WWU MÜNSTER

Measurement of Neutral Mesons and Direct Photons in pp Collisions with ALICE

Daniel Mühlheim, Dissertation 2018

wissen.leben

Experimentelle Physik

Measurement of Neutral Mesons and Direct Photons in pp Collisions with ALICE

Inaugural-Dissertation
zur Erlangung des Doktorgrades
der Naturwissenschaften im Fachbereich Physik
der Mathematisch-Naturwissenschaftlichen Fakultät
der Westfälischen Wilhelms-Universität Münster

vorgelegt von
Daniel Mühlheim
aus Gießen

– 2018 –

Dekan:	Prof. Dr. Michael Klasen
Erster Gutachter:	PD Dr. Christian Klein-Bösing
Zweite Gutachterin:	Prof. Dr. Anna Kulesza
Tag der mündlichen Prüfung:	____________________
Tag der Promotion:	____________________

Contents

Chapter 1

Introduction

The European Organization for Nuclear Research (CERN) is established as the largest particle physics laboratory in the world. It currently operates the Large Hadron Collider (LHC) which is the most powerful accelerator mankind has built so far, representing the latest centerpiece in the long history of particle and nuclear physics at CERN [1]. This work has been carried out within the ALICE collaboration which is the only experiment at the LHC dedicated to the study of the Quark-Gluon Plasma (QGP). The QGP is a state of matter consisting of free quarks and gluons that undergo strong interactions. It can be created in high energy collisions of heavy ions; a collision system which the LHC can provide up to a nominal center of mass energy of $\sqrt{s_{\mathrm{NN}}} = 5.5\,\mathrm{TeV}$ for Pb-Pb. In Chap. 2, the theoretical background related to the QGP and its underlying theory of strong interactions, Quantum Chromodynamics (QCD), is introduced and elaborated. The presence of the QGP, which is formed shortly after a heavy-ion collision took place, leads to many different signatures which can be measured by an experiment. The present experimental environment used for this purpose is introduced in Chap. 3, where, besides the accelerator chain around the LHC and the ALICE detector, the software framework is introduced. To explore the signatures of the QGP, hadronic collisions of different system sizes are studied involving pp, p-Pb and Pb-Pb collisions. Each system is unique and all of them are needed to develop a consistent picture and understand the respective measurements, which includes disentangling initial and final state effects in the nuclear modification of particle spectra. The presence of a QGP or simply the presence of cold matter, like a Pb-ion in case of the p-Pb system for example, may modify the particle yields as a function of p_{T} and rapidity.

In this thesis, neutral mesons, namely π^0 and η mesons, are studied in this context setting the focus on maximally improving the measurements in pp collisions so that a reliable reference for heavy-ion collisions can be established. Hence, the mesons' production cross sections are measured in pp collisions, which were recorded during LHC Run 1, involving four different center of mass energies: $\sqrt{s} = 0.9$, 2.76, 7 and 8 TeV. An overview of the analyzed data sets in this thesis is given in Chap. 4 that also introduces the corresponding Monte Carlo simulations used and further exemplifies the extensive studies on the quality assurance of simulations and data. The neutral mesons are reconstructed via their two-photon decay channels by means of invariant mass analysis, for which photons are reconstructed using two fundamentally different detection techniques: via the Photon Conversion Method (PCM) and using the Electromagnetic Calorimeter (EMCal) as described in Chap. 5. Furthermore, the chapter includes details about the applied photon selection criteria and the energy calibration of the EMCal. As already introduced, neutral mesons and photons are studied in this work, in particular the most abundant light neutral mesons π^0 and η. In Chap. 6, the techniques exploited to reconstruct neutral mesons are introduced and the determined production cross sections as well as particle ratios, integrated yields and mean transverse momenta are presented. Furthermore, the obtained results are compared with Monte Carlo event generators as well as recent NLO perturbative QCD (pQCD) calculations. The neutral meson measurements also involve the application of the so-called hybrid method PCM-EMCal which was established in ALICE in the context of this thesis. Hence, various meson reconstruction methods are exploited and their results are combined in order to minimize the uncertainties of the neutral meson spectra. Here, the goal is to provide high precision baselines for the corresponding measurements involving heavy ions. All the different approaches are also followed to apply them to heavy-ion analysis in the future. High precision measurements of neutral meson cross sections are also needed to obtain essential knowledge about decay photons which are a dominant background source for many measurements related to direct photons, dileptons and heavy-quark production. Moreover, π^0 and η mesons are of relevance and interest since no other ALICE measurement of identified particle spectra is possible for such wide p_{T} ranges from the order of a hundred MeV/c up to more than 100 GeV/c. The neutral meson spectra are also a relevant input and provide important constraints for Parton Distribution Functions (PDFs) and Fragmentation Functions (FFs) in the context of pQCD calculations. Here, the LHC energies enable to probe rather low values of $x \sim 0.001$ and $z \sim 0.1$. In this context, the π^0 is of interest because it is the lightest hadron being produced most abundantly, originating dominantly from gluon fragmentation. Only above 20 GeV/c, quark fragmentation also starts to play a role. On the other hand, the η is relevant because of its hidden strangeness component. Furthermore, the neutral meson measurements are carried out at different center of mass energies to study the evolution of spectra as a function of $\sqrt{s}$ and to study scaling laws with respect to relative particle yields like m_{T} scaling. Hence, precise measurements of identified hadron spectra over wide p_{T} ranges at different LHC energies are of particular importance for the quantitative description of particle production at the LHC.

Another focus of this thesis is the measurement of inclusive and direct photon spectra, where the latter term is defined by all photons not originating from particle decays. Usually, direct photons are further classified into prompt, fragmentation and thermal components. While the amount of prompt photons can be reliably calculated with pQCD, the contributions from fragmentation photons and thermal photons remain to be a key subject of recent studies. The results concerning inclusive and direct photon production are elaborated and summarized in Chap. 7, also being compared with recent theory predictions. Photons are of special interest since they can escape a strongly interacting medium like the QGP basically unaffected as their mean free path is much larger than the relevant length scales of the expanding fireball. Moreover, they are produced at all stages of hadronic collisions with negligible final-state interactions so that they are sensitive to the early stages of the system's evolution. Since a variety of QGP signatures are also present in high multiplicity p-Pb or pp collisions at the LHC [2], the search for a direct photon signal at low p_{T} in minimum bias pp collisions is of interest, i.a. predicted in Ref. [3] for $\sqrt{s} = 7$ TeV.

The reported measurements carried out for pp collisions at $\sqrt{s} = 8$ TeV are published by the ALICE collaboration, in particular the neutral meson results [4, 5] and the measurement of direct photons [6, 7] which also includes data recorded in pp at $\sqrt{s} = 2.76$ TeV. Furthermore, the neutral meson results for $\sqrt{s} = 2.76$ TeV are published by ALICE [8] as well, for which analysis contributions were provided in the context of this thesis. This also applies to the EMCal-related neutral meson measurements reported for p-Pb collisions at $\sqrt{s_{\mathrm{NN}}} = 5.02$ TeV [9]. The presented meson results for pp collisions at $\sqrt{s} = 0.9$ and 7 TeV are foreseen to enter an upcoming ALICE publication which is planned to update the current Ref. [10]. Back then, the EMCal-related measurements, reported in this thesis, were not available and only half of the recently available statistics was reconstructed.

Chapter 2

Theoretical Background

This chapter introduces the relevant theoretical background in the context of this thesis. After a short introduction of the Standard Model (SM) and the fundamental forces of nature, the focus is set on Quantum Chromodynamics (QCD) and its bound-states, so-called hadrons. Subsequently, the particle and photon production in hadronic collisions are elaborated and different hadronization models are introduced. Some important signatures of the Quark-Gluon Plasma (QGP) are furthermore summarized with regard to neutral meson and photon measurements and the importance of small systems is outlined in this context. The chapter is concluded by an introduction to the relevant Monte Carlo (MC) event generators for this thesis.

2.1 The Standard Model

In the late 1960s, Glashow [12], Salam [13] and Weinberg [14] conceived major parts of the Standard Model (SM) of particle physics, for which the Nobel Prize was consequentially awarded in 1979 [15]. The SM is a gauge Quantum Field Theory (QFT) combining the theories of strong and electroweak interactions, where the latter represents the unified description of electromagnetism and the weak interaction [16]. The fundamental building blocks of the SM are six quarks and six leptons which both are fermions carrying a spin of 1/2. The fermions are organized in three generations representing some kind of mass hierarchy. From the fit of the Z^0 boson resonance as shown in Ref. [17], the number of light neutrino species is confirmed to be three, which is in agreement with the three observed generations of fundamental fermions. Furthermore, the SM is composed of four gauge bosons, associated to the electroweak and strong interactions, and the Higgs boson that was recently discovered [18, 19]. The Higgs boson, which is the quantum excitation of the Higgs field, is the first elementary scalar particle to be discovered in nature. This field is pivotal in generating the masses of the fundamental building blocks of the SM that are shown in Fig. 2.1.1. In fact, the SM has proven to be a very successful model over the last decades. There is no persistent deviation from SM predictions which is observed so far [20].

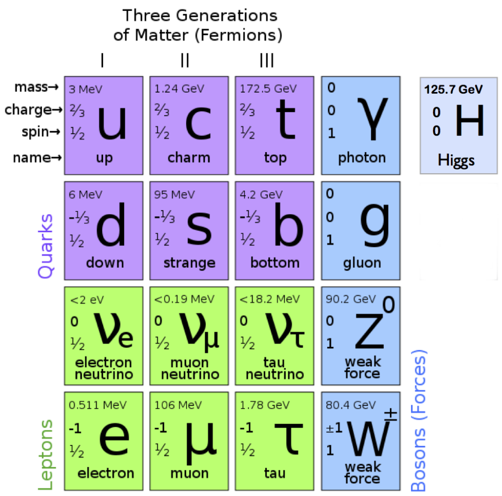

Figure 2.1.1: The SM of particle physics, adapted from Ref. [11].

The gauge bosons contained in the SM, see Fig. 2.1.1, mediate the fundamental forces of nature that are known as of today, which are introduced in the following with decreasing relative strength. The strong interaction is mediated by the gluon, representing the strongest of all forces, whereas the photon is the gauge boson of electromagnetism. Z^0 and $W^\pm$ are the gauge bosons of the weak interaction. The fourth fundamental force is gravity which is described by general relativity [21]. It is the weakest of all forces but the only relevant force in the universe on the scale of galaxies and beyond. General relativity has not only proven to work on large scales, but it was also able to predict the existence of gravitational waves; an astonishingly tiny signal which was recently discovered [22]. However, gravity is not contained in the SM at all and it remains to be resolved how to merge the two successful theories in the future. Since a unification could already be achieved for electromagnetism and the weak interaction, much effort is put into a Grand Unified Theory (GUT) which would be able to unify the electroweak and strong interactions [23]. Moreover, the ultimate goal of theoretical and experimental particle physics is to further incorporate gravity to obtain a theory of everything [24]. In this context, the existence of a graviton as the mediator of the gravitational interaction is speculated, however, without experimental evidence so far [25]. Another speculative field is the search for dark matter although there is compelling observational evidence for the existence of such matter [26]. As the nature of dark matter still remains to be a mystery, there are nevertheless extensive searches going on by various experiments exploiting colliders [27] as well as direct [28] and indirect [29] detection techniques. Taken together, there are four known fundamental forces in nature which are summarized in Tab. 2.1.1, ordered by their relative strength.

	fundamental forces			
	strong	electromagnetism	weak	gravity
relative strength	1	10^{-3}	10^{-8}	10^{-37}
boson	g	γ	Z^0, $W^\pm$	graviton?
spin	1	1	1	2
mass (GeV/c^2)	0	0	91.2, 80.4	0

Table 2.1.1: The basic properties of the four fundamental forces of nature, adapted from Ref. [30]. The relative strengths are approximate values for two fundamental particles at a distance of 1 fm which is roughly the radius of a proton [30].

2.2 Theory of Quarks & Gluons: Quantum Chromodynamics

The theory of strong interactions is QCD [31], which is a SU(3) non-abelian gauge field theory describing the interactions between quarks and gluons. The fundamental parameters of QCD are the strong coupling g_s, or $\alpha_\mathrm{S} = g_\mathrm{S}^2/4\pi$, and the quark masses m_q. In total, there are six different quark flavors, each of them existing as particle and antiparticle, and eight kinds of gluons. The quarks carry a spin of 1/2 while gluons are massless pointlike particles of spin 1. All strongly interacting particles carry color charge, degenerated in three different states $N_c = 3$. The Lagrangian of QCD [32] is given by:

$$\mathcal{L} = \sum_q \bar{\psi}_{q,a} \left(i\gamma^\mu \partial_\mu \delta_{ab} - g_\mathrm{S} \gamma^\mu t^C_{ab} \mathcal{A}^C_\mu - m_q \delta_{ab} \right) \psi_{q,b} - \frac{1}{4} F^A_{\mu\nu} F^{A\,\mu\nu}, \tag{2.2.1}$$

where γ^μ are the Dirac γ-matrices and repeated indices are summed over. The quark-field spinors are represented by $\psi_{q,a}$ for quarks of flavor q with a color index a running from $a = 1$ to $N_c = 3$. The $\mathcal{A}_\mu^C$ correspond to gluon fields with C running from 1 to $N_c^2 - 1 = 8$. The t_{ab}^C correspond to eight 3×3 matrices, the generators of the SU(3) group, encoding the fact that a gluon's interaction with a quark rotates the quark's color in SU(3) space. The variable g_S is the QCD coupling constant and the field tensor $F_{\mu\nu}^A$ is given by:

$$F_{\mu\nu}^A = \partial_\mu \mathcal{A}_\nu^A - \partial_\nu \mathcal{A}_\mu^A - g_s f_{ABC} \mathcal{A}_\mu^B \mathcal{A}_\nu^C \quad \text{with} \quad \left[t^A, t^B\right] = i f_{ABC} t^C, \tag{2.2.2}$$

where f_{ABC} are the structure constants of the SU(3) group. The Feynman rules of QCD, shown in Fig. 2.2.2a, involve a quark-antiquark-gluon vertex and a 3-gluon vertex proportional to g_s as well as a 4-gluon vertex that is proportional to g_S^2 [16].

The QCD lagrangian is invariant under the exchange of left- and right-handed components of the quark spinor which is called chiral symmetry. This symmetry is explicitly broken since quarks have masses. However, even for massless quarks the strong force would give rise to a so-called chiral condensate that is not invariant under exchange of left- and right-handed fermions. Thus, chiral symmetry of the QCD Lagrangian is spontaneously broken which generally leads to the existence of massless Goldstone bosons. For QCD, these bosons can be identified with the three pions, see also Sec. 2.2.2, which are observed to have masses of approximately 140 MeV/c^2 though. Therefore, these mesons are found to be Pseudo-Goldstone bosons as their masses are nonzero but significantly smaller than typical hadron masses [33].

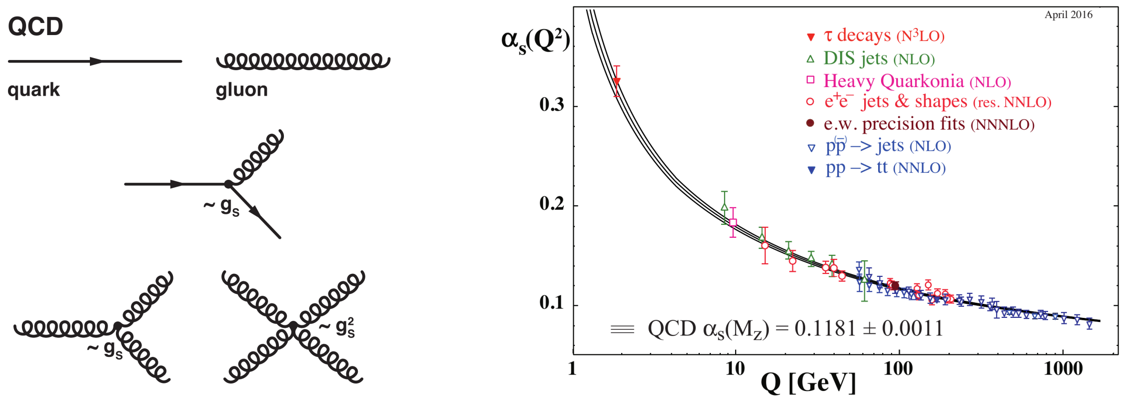

a) b)

Figure 2.2.2: a) QCD Feynman graphs showing free particles and the interaction vertices, adapted from Ref. [34]. b) Latest results on α_S from various experiments as contained in the latest PDG review [32]. There are also very recent measurements of α_S from the CMS collaboration which can be found in Refs. [35, 36].

The coupling strength $\alpha_\mathrm{S} = g_\mathrm{S}^2/4\pi$ is one of the fundamental input parameters of QCD. It cannot be predicted by theory but must be determined from experiments. It is often considered as the running coupling constant of QCD since it is found to vary as a function of momentum transfer Q^2. The dependence of α_S on Q^2 [37] is given at leading order by:

$$\alpha_\mathrm{S}(Q^2) = \frac{12\pi}{(33 - 2n_f) \ln\left(\frac{Q^2}{\Lambda^2}\right)}, \tag{2.2.3}$$

which only holds for $Q^2 \gg \Lambda^2$. Furthermore, n_f is the number of quark flavors and $\Lambda \sim 200\,\mathrm{MeV}$ is the QCD scaling parameter that specifies the energy scale at which the perturbative coupling would nominally become infinite, called Landau pole. The coupling α_S is often quoted at the Z^0 boson mass M_{Z^0}, for which the current world average is found to be $\alpha_\mathrm{S}(M_{Z^0}^2) = 0.1181 \pm 0.0011$, afflicted with an uncertainty of 0.9 % [32]. In Fig. 2.2.2b, the running coupling α_S is shown as a function of momentum transfer for various measurements. For small Q^2, the coupling α_S becomes large and quarks are bound to hadrons. This is a basic feature of QCD called confinement, which denotes the property that only color singlet particles can exist. Hence, no isolated colored charge can be observed. The effect of confinement can be described by a phenomenological potential between a quark q and an anti-quark $\bar{q}$. It has a coulomb part, which is dominant at short ranges, and a linearly rising term at long distances:

$$V_{q\bar{q}}(r) \approx \frac{4}{3}\frac{\alpha_\mathrm{S}}{r} + kr, \tag{2.2.4}$$

where r is the radial distance between the quarks and k is $0.85\,\mathrm{GeV\,fm^{-1}}$ [38]. The linearly rising term makes it energetically impossible to separate a $q\bar{q}$ pair. If both quarks are moving away from each other in their center of mass frame, e.g. after they were created in a collision of particles, it soon becomes energetically favorable to create new $q\bar{q}$ pairs to neutralize color charge, so that in the final state two distinct jets will be observed. Confinement further explains that nuclear forces have very short ranges because nucleons are color singlets. Hence, they cannot exchange gluons but only colorless states. The lightest color singlet hadronic particle is the pion so that the range of nuclear forces is fixed by the pion mass, $r \sim m_\pi^{-1} \approx 1\,\mathrm{fm}$. In the limit of high momentum transfers, the coupling strength α_S decreases so that particles behave as if they were free. This behavior is called asymptotic freedom since α_S vanishes asymptotically at large Q^2 [39].

Ab-initio predictive methods for QCD include Lattice QCD (LQCD) and perturbative QCD (pQCD). LQCD [40–42] is a way to probe non-perturbative aspects of QCD by reformulating the theory on a lattice of discrete space-time points. The lattice spacing a gives a minimum distance and, thus, also a maximum momentum scale that acts as a momentum cutoff for integrals. Therefore, terms stay finite, which otherwise would become infinite, so that the result depends on a in the end. To remove this dependence, repeated calculations with decreasing a need to be performed until the scaling regime is reached, where the lattice spacing can be related to a physical scale. An overview of recent results is given in Ref. [43]. On the other hand, pQCD [44] can be considered as the main tool for solving QCD at high energy scales $Q^2 \gg \Lambda^2$. In that region, α_S becomes small and allows perturbation theory techniques to be applied.

For high-energy scattering problems with hadrons in the final state, many processes at the LHC involve large Q^2 for which pQCD can be applied. Most processes in QCD cannot be calculated with pQCD methods, though, since neither free quarks nor free gluons can be observed due to color confinement. In particular, the structure of hadrons has a non-perturbative nature, for example, as they are composite with a time-dependent structure. Partons are within clouds of further partons, constantly being emitted and absorbed. However, as hadrons remain intact, fluctuations must involve momentum transfers Q^2 smaller than the confinement scale of Λ that gives an estimate for the timescale of most fluctuations of about $\sim 1/\Lambda$ [31]. A hard perturbative probe interacts over a much shorter timescale $1/Q \ll 1/\Lambda$ with the partons of the participating hadrons. Hence, partonic fluctutations appear to be basically frozen so that an instantaneous snapshot of the hadron structure is taken at a characteristic resolution given by $\sim 1/Q$. This is formalized in the QCD factorization theorem [45], separating the cross section into two parts to be able to obtain predictions from QCD. As QCD quanta are asymptotically free, pQCD is used to calculate the elementary short-range scattering processes involving large Q^2. The long-range universal properties of QCD are, on the other hand, constrained by global fits to experimental data [44]. These universal properties are modeled by Parton Distribution Functions (PDFs), describing the kinematic distributions of quarks and gluons within the hadrons in the collinear approximation [46]. Furthermore, the QCD matrix element [32] needs to be calculated and so-called parton-to-hadron Fragmentation Functions (FFs) provide the probability for a quark or gluon to fragment into hadrons of a certain type [47]. Then, the cross section to produce a certain hadron of type H can be written as the sum over parton types:

$$E\frac{\mathrm{d}^3\sigma^H}{\mathrm{d}p^3} = \sum_{a,b,c} f_a\left(x_1, Q^2\right) \otimes f_b\left(x_2, Q^2\right) \otimes D_c^H(z_c, Q^2) \otimes \mathrm{d}\hat{\sigma}_{ab\to cX}\left(x_1, x_2, Q^2\right), \tag{2.2.5}$$

where $f_i(x, Q^2)$ denotes the proton PDF of parton i carrying a fraction x of the proton's longitudinal momentum, $D_i^H(z_i, Q^2)$ the FF of parton i forming hadron H carrying a fraction z_i of the parton's momentum and $\mathrm{d}\hat{\sigma}_{ij\to kX}\left(x_1, x_2, Q^2\right)$ the parton-level cross section for the production of the final state k through the initial partons i and j.

2.2.1 The Quark-Gluon Plasma

A consequence of asymptotic freedom is that at very high energies or baryon densities hadronic matter dissolves into its constituents, passing a phase transition from the hadronic to a guark-gluon phase. This state of matter is called Quark-Gluon Plasma (QGP). The QGP was predicted shortly after the formulation of QCD [48, 49] and is believed to have existed shortly after the Big Bang. In this state of matter, quarks and gluons are quasi-free and can cover path lengths much larger than the scale of a proton. Hence, confinement is no longer given which is generally denoted deconfinement. This is an intrinsically non-perturbative feature of the QCD which occurs at the critical temperature T_c, at which normal matter transitions into a QGP. The system needs to consist of a large number of degrees of freedom and needs to be in local equilibrium so that quantities like pressure, temperature, energy and entropy density are well-defined. Therefore, the lifetime of the system has to be significantly larger than the inverse rate of interactions to allow enough interactions among particles to drive the system towards an equilibrium state [50]. In the late 1960s, Hagedorn already proposed a limiting temperature for hadronic systems of 140 MeV [51]. Recent lattice QCD calculations determined the critical temperature and extracted values of T_c in the range of $\sim 150-190$ MeV [52–54], depending on the number of quark flavors n_f and their masses m_q.

The phase diagram of QCD [55] is shown in Fig. 2.2.3a, showing the current knowledge as a function of temperature T and baryo-chemical potential μ_B. The theoretical knowledge about the phase diagram is mainly coming from LQCD which depicts the transition of confined to deconfined matter depending on the temperature and the baryo-chemical potential. Moreover, using the LQCD formalism it was found that the scaled energy density ϵ/T^4 steeply increases at T_c. This can be understood by rapidly rising number of degrees of freedom since deconfinement takes place. This is illustrated in Fig. 2.2.3b where the energy density can be seen for two and three degenerated quark flavors [56]. The LQCD calculations shown in this figure predict a value of $T_\mathrm{c} = 173 \pm 15$ MeV at a given energy density of $\epsilon \sim 0.7\,\mathrm{GeV/fm^3}$ for the phase transition.

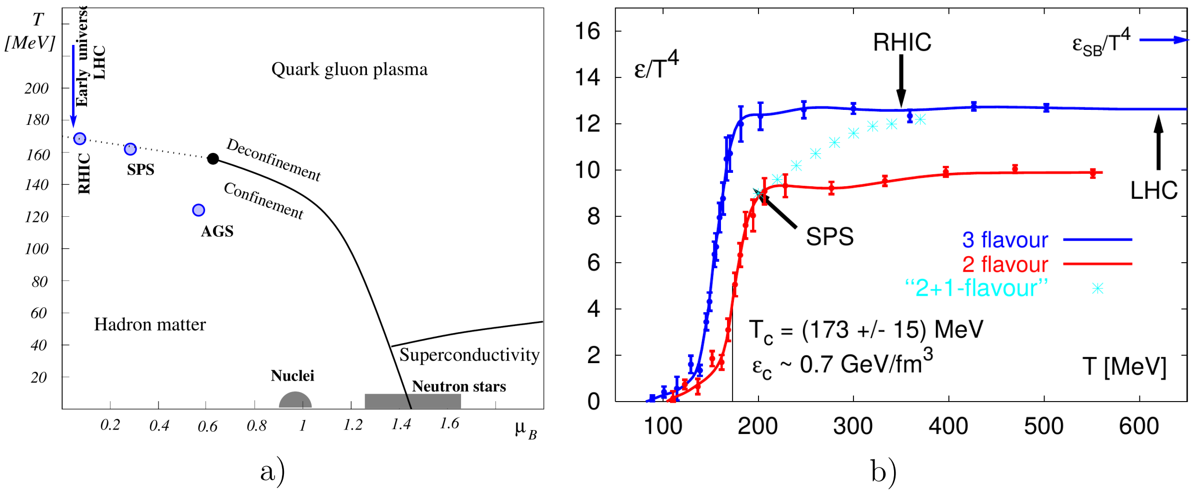

Figure 2.2.3: a) A schematic of the QCD phase diagram [57] as a function of T and μ_{B}. Ordinary nuclear matter is found for $\mu_{\mathrm{B}} \approx 1\,\mathrm{GeV}$ and small T, whereas for higher T a phase transition to the QGP takes place. A critical point is expected to be present as indicated in the plot. b) The scaled energy density in QCD [56] for two or three degenerated quark flavors as a function of T. The arrows denote energy densities that are reached in the initial stages of heavy-ion collisions at the different accelerators which were estimated by the Bjorken formula [58].

Experiments at the LHC can cover the region at low μ_{B} and high temperatures above T_{c} in heavy-ion collisions of Pb (Xe) nuclei which were delivered at center of mass energies of $\sqrt{s_{\mathrm{NN}}} =$ 2.76 and 5.02 TeV (Xe: 5.44 TeV) so far. Previously, high energy heavy-ion collisions were already provided at different laboratories. The Alternating Gradient Synchrotron (AGS) at BNL featured such collisions at $\sqrt{s_{\mathrm{NN}}} = 4.6\,\mathrm{GeV}$ already in 1986, whereas the SPS at CERN could provide collisions at $\sqrt{s_{\mathrm{NN}}} = 17.2\,\mathrm{GeV}$ per colliding nucleon pair reaching at least an intermediate state between the hadron gas and the QGP. The accelerator facilities at BNL were further upgraded so that the RHIC was constructed which went into operation in 2000. It was able to reach $\sqrt{s_{\mathrm{NN}}} = 200\,\mathrm{GeV}$ in Au-Au collisions for which clear evidence for the creation of a QGP could be provided.

2.2.2 Hadrons: Mesons, Baryons & Exotics

Due to confinement, neither quarks nor gluons can be observed as free particles. Instead, they form bound states denoted hadrons which must be colorless. In this context, the three color charges of QCD can be associated with the colors red, blue and green (r, b, g) in analogy to the primary colors of the chromatic circle. Hence, the superposition of colors must overlap to white to form hadrons which are color-singlet combinations of quarks, antiquarks and gluons. These quarks determine the quantum numbers of a hadron and are thus denoted valence quarks. In addition, there are constantly virtual $q\bar{q}$ pairs created and annihilated within a hadron, which are the so-called seaquarks [59]. In general, any number of valence quarks within a hadron is allowed by QCD as long as a color-singlet is formed. Therefore, hadrons are categorized into mesons, baryons and exotic hadrons. A meson is a combination of a quark-antiquark pair $q\bar{q}$, whereas baryons are composed of three quarks or antiquarks, which both form the ordinary visible matter. Bound-states involving explicit valence gluon content or systems composed of more than three quarks are considered exotic hadrons. Recently, hadrons composed of four and five quarks were discovered experimentally which are named tetraquarks [60] and pentaquarks [61]. Moreover, there are many candidates for hybrids which are composed of quarks and a gluonic component, but also for glueballs that solely consist of valence gluons. Some overviews of this field are given in recently published Refs. [62, 63]. In the following, only mesons and baryons will be further considered as they form ordinary matter and are of relevance for this thesis.

As shown in Fig. 2.1.1, the d, s and b quarks have an electric charge of -1/3, whereas u, c and t quarks have +2/3. Another quantum number related to quarks is the isospin I which is associated to both u and d quarks with a magnitude of $I = 1/2$, for which the z-component is found to be $I_z = +1/2$ and $I_z = -1/2$ respectively. The heavier quarks s, c, b and t posses strangeness $S = -1$, charm $C = +1$, bottomness $B = -1$ and topness $T = +1$, for which the sign is defined to be opposite for antiquarks. The quantum numbers can be related to the electrical charge Q through the generalized Gell-Mann-Nishijima formula [32] as follows:

$$Q = I_z + \frac{\mathcal{B} + S + C + B + T}{2}, \tag{2.2.6}$$

where Q is given in unites of elementary charge e and $\mathcal{B}$ is the baryon number which is +1/3 for quarks and -1/3 for antiquarks. In this context, the hypercharge Y is defined by:

$$Y = \mathcal{B} + S - \frac{C - B + T}{3}. \tag{2.2.7}$$

Although topness is considered in this theoretical formalism, the very short lifetime of t quarks makes it probable that bound-state hadrons containing t quarks do not exist.

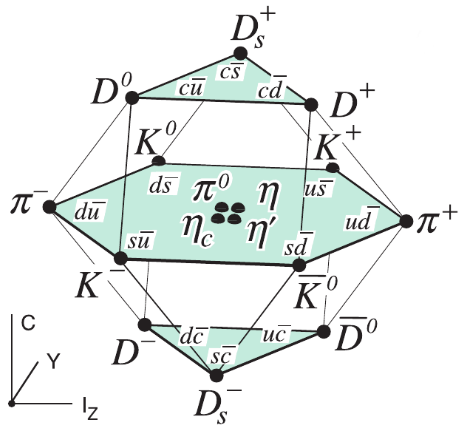

Figure 2.2.4: The 16-plet [32] of pseudoscalar mesons made of u, d, s and c quarks.

There are various quantum numbers that can be associated to hadrons. First of all, there is an intrinsic angular momentum that every quark in the system carries which is called spin. Depending on how the spins of the respective quarks of the hadron add up, the total spin S of the hadron is found. By adding up the contributions of all quarks, the total isospin I is found analogously. In addition, there may be an orbital angular momentum L by quarks and gluons. The total spin of the particle J is a combination of the spin S and orbital angular momentum L and given by $|L-S| \leq J \leq |L+S|$. Based on the introduced quantum numbers, the parity P is defined by $P = (-1)^{L+1}$. Furthermore, the charge conjugation, also called C-parity, is found to be $C = (-1)^{L+S}$. The C-parity is only defined if a particle is its own antiparticle. Hence, by replacing all valence quarks by the corresponding antiquarks results in the same quark content again, see also Tab. 2.2.2. This quantum number can be further generalized by the G-parity, $G = (-1)^{I+L+S}$, which is only defined for multiplets with average charge of zero for which $\bar{Q} = \bar{B} = \bar{Y} = 0$ is valid. Further radial radial excitations, characterized by N, are possible for hadrons. However, only ground-states with $N = 1$ are described in the following.

Mesons are $q\bar{q}$ bound-states which have $\mathcal{B} = 0$. They can be classified in J^{PC} multiplets. If a meson is not its own antiparticle, C-parity is not defined and the corresponding symbol needs to be omitted. The spins of the two quarks in the system can be antiparallel, hence $S = 0$, or can be found to be parallel yielding $S = 1$ for the meson. For $L = 0$, mesons are denoted pseudoscalar if $J^{PC} = 0^{-+}$ holds, whereas they are named vectors if 1^{--} is found. The orbital excitations possessing $L = 1$ are named scalars, characterized by 0^{++}, or axial vectors if the cases 1^{++} or 1^{+-} apply. Furthermore, mesons are denoted tensors if J^{PC} is found to be 2^{++}. The following Tab. 2.2.2 gives an overview of the mesons which are relevant for this thesis. Their rest masses and quarks contents are quoted in addition to their quantum numbers. Furthermore, the mean lifetimes of mesons are listed as well as their leading decay modes are given which are of importance for estimating the decay photon background in Chap. 7.

	meson	rest mass (MeV/c^2)	quark content	$I^G(J^{PC})$	mean lifetime (s)	leading decay modes [BR $\gtrsim 5\,\%$]
pseudoscalar	π^0	≈ 135	$\frac{1}{\sqrt{2}}(u\bar{u} - d\bar{d})$	$1^-(0^{-+})$	$8.5 \cdot 10^{-17}$	$\gamma\gamma$
	π^+	≈ 140	$u\bar{d}$	$1^-(0^-)$	$2.6 \cdot 10^{-8}$	$\mu^+\nu_\mu$
	K^+	≈ 494	$u\bar{s}$	$\frac{1}{2}(0^-)$	$1.2 \cdot 10^{-8}$	$\mu^+\nu_\mu$, $\pi^+\pi^0$, $\pi^+\pi^+\pi^-$
	K^0_S	≈ 498	$\frac{1}{\sqrt{2}}(d\bar{s} + s\bar{d})$	$\frac{1}{2}(0^-)$	$9.0 \cdot 10^{-11}$	$2\pi^0$, $\pi^+\pi^-$
	K^0_L	≈ 498	$\frac{1}{\sqrt{2}}(d\bar{s} - s\bar{d})$	$\frac{1}{2}(0^-)$	$5.1 \cdot 10^{-8}$	$\pi^\pm l^\mp \nu$, $3\pi^0$, $\pi^+\pi^-\pi^0$
	η	≈ 548	$\frac{1}{\sqrt{6}}(u\bar{u} + d\bar{d} - 2s\bar{s})$	$0^+(0^{-+})$	$5.0 \cdot 10^{-19}$	$\gamma\gamma$, $3\pi^0$, $\pi^+\pi^-\pi^0$
	η'	≈ 958	$\frac{1}{\sqrt{3}}(u\bar{u} + d\bar{d} + s\bar{s})$	$0^+(0^{-+})$	$3.3 \cdot 10^{-21}$	$\pi^+\pi^-\eta$, $\rho^0\gamma$, $\pi^0\pi^0\eta$
vector	ρ^+	≈ 775	$u\bar{d}$	$1^+(1^-)$	$4.4 \cdot 10^{-24}$	$\pi^+\pi^0$
	ρ^0	≈ 775	$\frac{1}{\sqrt{2}}(u\bar{u} - d\bar{d})$	$1^+(1^{--})$	$4.4 \cdot 10^{-24}$	$\pi^+\pi^-$
	ω	≈ 783	$\frac{1}{\sqrt{2}}(u\bar{u} + d\bar{d})$	$0^-(1^{--})$	$7.8 \cdot 10^{-23}$	$\pi^+\pi^-\pi^0$, $\pi^0\gamma$
	ϕ	≈ 1020	$s\bar{s}$	$0^-(1^{--})$	$1.5 \cdot 10^{-22}$	K^+K^-, $K^0_L K^0_S$

Table 2.2.2: The basic properties [32] of a selected sample of mesons which are relevant for the meson and photon measurements reported in this thesis. Each meson has a corresponding antiparticle for which quarks need to be replaced by their corresponding antiquarks and vice versa.

On the other hand, baryons have $\mathcal{B} = 1$ and J^P can be assigned to them. All established baryons are qqq configurations while antibaryons are represented by $\bar{q}\bar{q}\bar{q}$. If the total spin of all quarks couples to $S = 1/2$, the octet with $J^P = 1/2^+$ is found which contains protons and neutrons. For $S = 3/2$, a decuplet with the $\Delta(1232)$ makes up the ground states with $J^P = 3/2^+$. Further baryon resonances with angular momentum are possible which are being explored by various experiments [64]. In the following Tab. 2.2.3, all relevant baryons for this thesis are listed which, in particular, show π^0 mesons or photons in their decay modes.

Hadrons may decay via strong, electromagnetic or weak processes for which typical timescales of $t_{\text{strong}} \approx 10^{-23}\,$s, $t_{\text{em}} \approx 10^{-16}\,$s and $t_{\text{weak}} \gg 10^{-16}\,$s can be specified respectively. Besides the

J^P	baryon	rest mass (MeV/c^2)	quark content	mean lifetime (s)	leading decay modes [BR $\gtrsim$ 5 %]
$1/2^+$	p	≈ 938	uud	stable	N/A
	n	≈ 940	udd	$8.8 \cdot 10^{2}$	$\mathrm{p}e^-\bar{\nu}_e$
	Λ	≈ 1116	uds	$2.6 \cdot 10^{-10}$	$\mathrm{p}\pi^-$, $\mathrm{n}\pi^0$
	Σ^+	≈ 1190	uus	$8.0 \cdot 10^{-11}$	$\mathrm{p}\pi^0$, $\mathrm{n}\pi^+$
	Σ^0	≈ 1193	uds	$7.4 \cdot 10^{-20}$	$\Lambda\gamma$
	Σ^-	≈ 1197	dds	$1.5 \cdot 10^{-10}$	$\mathrm{n}\pi^-$
$3/2^+$	Δ^{++}	≈ 1232	uuu	$5.6 \cdot 10^{-24}$	$\mathrm{p}\pi^+$
	Δ^+	≈ 1232	uud	$5.6 \cdot 10^{-24}$	$\mathrm{n}\pi^+$, $\mathrm{p}\pi^0$
	Δ^0	≈ 1232	udd	$5.6 \cdot 10^{-24}$	$\mathrm{n}\pi^0$, $\mathrm{p}\pi^-$
	Δ^-	≈ 1232	ddd	$5.6 \cdot 10^{-24}$	$\mathrm{n}\pi^-$

Table 2.2.3: The basic properties [32] of a selected sample of baryons which are most relevant in the context of this thesis. The corresponding antiparticles can be constructed by exchanging quarks by respective antiquarks.

universal conservation of energy, the strong interaction preserves all quantum numbers introduced in this section: spin, electric charge, baryon number, lepton number, isospin, strangeness, charm, topness, bottomness, parity and the composite quantities CP and CPT. Electromagnetic processes, mediated by the photon having $J_\gamma^{PC} = 1^{--}$, preserve all these quantities as well but only the third component of the isospin. The weak interaction also agrees to the majority of this list but violates isospin, strangeness, charm, topness, bottomness, parity and CP.

As listed in Tab. 2.2.2, π^0 and η mesons may decay into $\gamma\gamma$ pairs via so-called triangle diagrams [65]. The η meson, which represents in fact a mixing of different eigenstates, shows a variety of decay modes which are reviewed in Ref. [66].

2.3 Particle Production in Hadronic Collisions

The LHC allows to study hadronic collisions of highly relativistic particles, commonly involving protons and/or Pb ions. In general, collisions of such particles can be divided into two categories:

i) elastic collisions with no further modification of the initial state particles except modifications of the particle's momentum vectors;

ii) inelastic collisions, in which hadrons are either excited or broken up so that new particles can be created.

The observed interaction rate (or collision rate, see also Eq. 4.2.4) can be computed from the luminosity $\mathcal{L}$, a quantity which is solely based on machine-dependent properties of the accelerator complex, and the cross section σ representing the processes of interest. Hence, the total cross section σ_{tot} for a hadronic collision of two hadrons is the sum of the elastic σ_{el} and inelastic σ_{inel} cross sections. In this thesis, the focus is set on proton-proton (pp) collisions for which only inelastic collisions are of interest as the production of photons and neutral mesons is studied. The situation before the collision is given by the two original particles, called initial state. The momentum vectors and energy of each particle is described using the general concept of four-vectors, $p = (E, \vec{p})$, and natural units. Squaring p leads to the identity $p^2 = E^2 - \vec{p}^2 = m^2$, where m is the rest mass of the given particle. For a collision of two particles, the Mandelstam variable $s = (p_1 + p_2)^2$ can be defined. This is a Lorentz-invariant quantity, where p_1 and p_2 denote the four-momenta of both incoming particles. In the center of mass frame at the LHC, where $\vec{p}_1 = -\vec{p}_2$ and $E_1 = E_2 \equiv E$ can be identified by the momenta and energies of the protons, the center of mass energy reads as follows: $\sqrt{s} = p_1 + p_2 = 2E$. All particles produced or remaining after the collision happened characterize the final state. The momentum vectors of these particles are usually split in longitudinal and transverse components with respect to the z-coordinate, representing the beam axis. As the transverse momenta p_T are found to be zero before the collision, the presence of $p_\mathrm{T} > 0$ can always be associated with interactions that occurred at the interaction point, also called collision vertex. The transverse momentum is defined by $p_\mathrm{T} = \vec{p} \cdot \sin(\theta)$, whereas the longitudinal momentum is found to be $p_\mathrm{L} = \vec{p} \cdot \cos(\theta)$. Furthermore, the transverse mass m_T can be defined which is invariant under Lorentz transformations in z-direction: $m_\mathrm{T}^2 = m^2 + p_\mathrm{T}^2 = E^2 - p_z^2$. The rapidity y as well as pseudorapidity η of a particle can be obtained by:

$$y = \frac{1}{2} \ln \left(\frac{E + p_\mathrm{L}}{E - p_\mathrm{L}} \right) \quad \text{and} \quad \eta = -\ln \left(\tan \left(\frac{\theta}{2} \right) \right) \quad \text{respectively,} \tag{2.3.8}$$

using E, p_L and θ which depicts the angle between the particle's momentum vector and the beam axis. These quantities are relevant in the context of hadronic collisions. Approximately the same particle flux is observed per unit interval of rapidity. The rapidity y is additive under Lorentz transformations so that Δy is found to be Lorentz invariant. However, y requires the knowledge of energy and momentum of a particle. Therefore, it must be identified. Hence, experiments often employ the pseudorapidity η, which only requires the measurement of the momentum vector, so that an analogon to y for unidentified particles is available. Both definitions become equivalent, $\eta \approx y$, in the limit of $m \ll p$.

The inelastic cross section for pp collisions is determined to be $\sigma_\mathrm{inel} \approx 30\,\mathrm{mb}$ for $\sqrt{s} = 10\,\mathrm{GeV}$ and changes only little with increasing center of mass energies [67]. It is found to be $\sigma_\mathrm{inel} \approx 70\,\mathrm{mb}$ for a typical LHC center of mass energy of $\sqrt{s} = 7\,\mathrm{TeV}$ for pp collisions. Furthermore, Ref. [67] also gives the parameterizations of these cross sections as a function of $\sqrt{s}$. Beyond total cross sections, the differential equivalents define σ as a function of a final-state variable. In the context of measuring particle production rates in hadronic collisions, the differential cross section is usually given with respect to the particle's momentum $\vec{p}$, hence $\mathrm{d}^3\sigma/\mathrm{d}p^3$. However, the phase space element $\mathrm{d}^3p = \mathrm{d}p_x\mathrm{d}p_y\mathrm{d}p_z = \mathrm{d}p_\mathrm{T}\mathrm{d}p_\mathrm{L}\mathrm{d}p_\varphi$, given in different coordinate systems, is not invariant under Lorentz transformations but d^3p/E is found to be invariant. Therefore, the invariant differential cross sections can be identified with $E\mathrm{d}^3\sigma/\mathrm{d}p^3$. By further substituting $\mathrm{d}p_L/\mathrm{d}y = E$ and applying φ-symmetry, the following relations are found:

$$E\frac{\mathrm{d}^3\sigma}{\mathrm{d}p^3} \overset{(i)}{=} \frac{1}{2\pi p_\mathrm{T}} \frac{\mathrm{d}^2\sigma}{\mathrm{d}p_\mathrm{T}\mathrm{d}y} \overset{(ii)}{=} \frac{1}{2\pi p_\mathrm{T}} \frac{\sigma_\mathrm{trigger}}{N_\mathrm{events}} \frac{\mathrm{d}^2N}{\mathrm{d}p_\mathrm{T}\mathrm{d}y}, \tag{2.3.9}$$

representing the production cross section of a particle with transverse momentum p_T for the given hadronic collision system (i). The right part of the equation beyond (ii) introduces the quantities which are determined by an experiment in order to measure the differential invariant cross section, for which N_{events} is the number of analyzed events, σ_{trigger} the fraction of the total cross section that the trigger condition of the experiment is able to sample and N is the number of reconstructed particles for each p_{T} bin defined for analysis. By integrating over p_{T}, the average multiplicity of particles per rapidity interval y is found, also denoted integrated yield $\mathrm{d}N/\mathrm{d}y$.

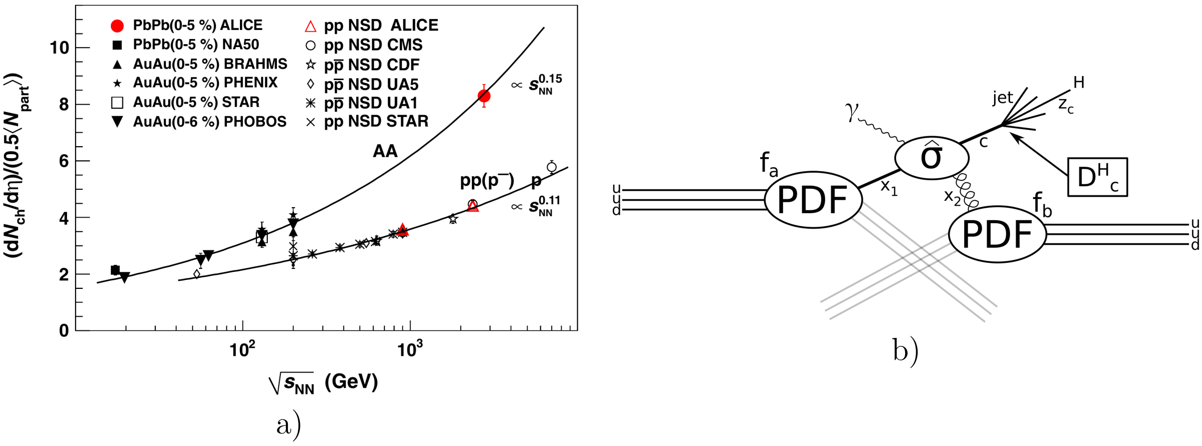

Figure 2.3.5: a) The charged-particle pseudorapidity density per participant pair of hadrons [68] measured by different experiments, which can be parameterized by the indicated curves. b) A schematic drawing visualizing the QCD factorization theorem as introduced in Eq. 2.2.5, given the example of a quark-gluon compton scattering with a photon and a jet in the final state.

In Fig. 2.3.5a, the charged-particle pseudorapidity density per participant pair of hadrons is shown for pp ($\mathrm{p\bar{p}}$) collisions and heavy-ion collisions, involving Pb-Pb and Au-Au, measured by different experiments as indicated in the legend. The densities are found to increase with $\sqrt{s}$, following a dependency of $s_{\mathrm{NN}}^{0.11}$ for pp ($\mathrm{p\bar{p}}$) and $s_{\mathrm{NN}}^{0.15}$ for heavy-ions which clearly indicate differences of particle production mechanisms in both systems. Furthermore, the average transverse momentum $\langle p_{\mathrm{T}}\rangle$ can be obtained by calculating the weighted arithmetic mean of Eq. 2.3.9.

The production of particles in inelastic hadronic collisions is generally divided into two basic categories:

i) low momentum transfer reactions, $Q^2 \lesssim \Lambda^2$, so-called soft processes;

ii) high momentum transfer reactions, $Q^2 \gg \Lambda^2$, so-called hard processes.

The majority of particles is produced with low p_{T} in soft processes involving small momentum transfers Q^2. On the other side, hard processes are mainly responsible for producing particles with momenta of several GeV/c or more. In addition to these processes, simultaneous parton interactions due to the rest of the proton's constituents may also occur. They are denoted underlying event which can be described by multiple parton interactions.

In the soft regime, pQCD calculations are not applicable to describe the particle production mechanisms. Hence, phenomenological models need to be employed which are based on previous measurements of particle production cross sections by other experiments at lower collision energies. Fig. 2.3.6 shows the invariant p_{T}-differential cross sections of neutral pion production in pp collisions at $\sqrt{s} = 62.4$, 200, 900 and 7000 GeV. At low p_{T}, the spectra can be universally described by an exponential:

$$E\frac{\mathrm{d}^3\sigma}{\mathrm{d}p^3} \propto e^{-\alpha p_{\mathrm{T}}}, \tag{2.3.10}$$

for which $\alpha \approx 6$ GeV/c yields a remarkably well agreement independent of $\sqrt{s}$.

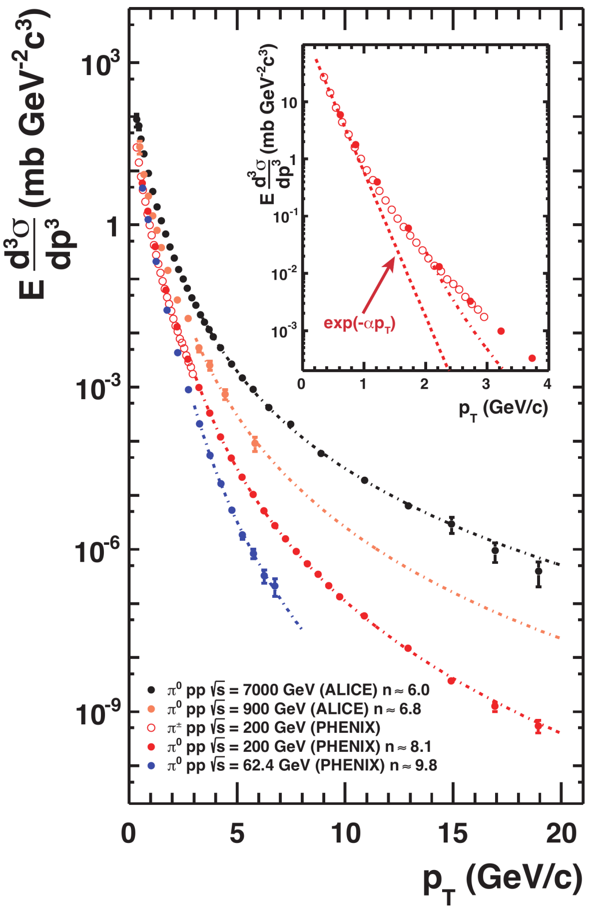

Figure 2.3.6: The p_{T}-differential cross sections of π^0 production in pp at $\sqrt{s} = 62.4$, 200, 900 and 7000 GeV [34], each fitted with an exponential for $p_{\mathrm{T}} < 1$ GeV/c and a power law for $p_{\mathrm{T}} > 2$ GeV/c.

For $p_{\mathrm{T}} \gtrsim 2$ GeV/c, clear differences between the collision energies can be stated. The power law exponents are observed to decrease from about $n \sim 10$ to $n \sim 6$ with increasing center of mass energies, indicating the hardening of the spectra since the relative contribution of particles originating from hard scatterings compared to the total multiplicity increases with $\sqrt{s}$. This regime dominated of hard processes can be parameterized by:

$$E\frac{\mathrm{d}^3\sigma}{\mathrm{d}p^3} \propto p_{\mathrm{T}}^{-n} \tag{2.3.11}$$

where n is found to evolve with $\sqrt{s}$. These processes can be described by means of pQCD and the factorization theorem as introduced in Sec. 2.2. The theorem is furthermore visualized in Fig. 2.3.5b by showing a schematic pp collision, where the different terms of the factorization theorem are drawn. The incoming two protons are illustrated by the constituent quarks, whereas the grey lines represent the outgoing remnants of the protons after the collision. The two PDFs f_a and f_b represent the initial state. The hard scattering of a quark and gluon, each carrying the respective momentum fraction of the proton x_i, is illustrated by the matrix element $\hat{\sigma}$. A quark-gluon compton scattering takes place producing a photon and a high energetic parton c which hadronizes into a collimated spray of particles, a so-called jet. The FF describes the non-perturbative production of hadron H which is one of the final state particles within the jet. It fragmented from the original parton c carrying a momentum fraction z_c.

For various purposes, the measured production cross sections need to be parameterized by closed-form expressions. The functional shapes are hereby motivated by the underlying physics processes, combining the characteristics of soft and hard interactions in order to arrive at fit functions being able to parameterize the particle spectra measured at LHC energies. A recent development in this context is the Two-Component Model (TCM), proposed in Ref. [69]. Its functional form is a combination of a Boltzmann component and a power law part. In general, they should be the dominant components at low and high p_{T} respectively. The fit function is able to reproduce measured spectra at LHC energies over the full p_{T} range and is defined as follows:

$$E\frac{\mathrm{d}^3\sigma}{\mathrm{d}p^3} = A_e\, e^{-E_{\mathrm{T,kin}}/T_e} + A\left(1+\frac{p_{\mathrm{T}}^2}{T^2 n}\right)^{-n}, \tag{2.3.12}$$

where $E_{\mathrm{T,kin}} = \sqrt{p_{\mathrm{T}}^2+m^2} - m$ is the transverse kinematic energy with the particle's rest mass m and A_e, A, T_e, T as well as n are free parameters. It is used as default in this thesis, see Chap. 6 and Chap. 7. Another common parameterization is the Tsallis function [70] which was used by default to describe the spectra reported by previous measurements of neutral meson production in pp collisions published by ALICE [10, 71]:

$$E\frac{\mathrm{d}^3\sigma}{\mathrm{d}p^3} = \frac{C}{2\pi}\,\frac{(n-1)(n-2)}{nT(nT+m(n-2))}\left(1+\frac{m_{\mathrm{T}}-m}{nT}\right)^{-n}, \tag{2.3.13}$$

where C, n and T are free parameters of the fit with m and m_{T} being the rest as well as the transverse mass of the particle. Furthermore, a modified Hagedorn [72] is used in this context:

$$E\frac{\mathrm{d}^3\sigma}{\mathrm{d}p^3} = A\left(e^{-\left(ap_{\mathrm{T}}+bp_{\mathrm{T}}^2\right)} + \frac{p_{\mathrm{T}}}{p_0}\right)^{-n}, \tag{2.3.14}$$

where A, a, b, p_0 and n are the free parameters. If the spectra should only be fitted for higher p_{T} above several GeV/c, a simple power law can also be used:

$$E\frac{\mathrm{d}^3\sigma}{\mathrm{d}p^3} = A\cdot p_{\mathrm{T}}^{-n}, \tag{2.3.15}$$

where A and n are the two free parameters.

2.3.1 Hadronization

Hadronization denotes the process which transforms a set of colored partons into a set of color-singlet hadrons for which confinement is preserved. It is a non-perturbative transition mapping partons onto on-shell primary hadronic states. These hadrons may decay further to produce secondary particles. However, this subsequent step is independent from the hadronization process itself. Nonetheless, hadronization leads to a fragmentation of initial partons into collimated sprays of particles. These particles contained in a tight cone are denoted jet. There are several jet finding algorithms [73] to cluster such adjacent particles in order to reconstruct energy and momentum of the initial parton, however, the definition of a jet is essentially ambiguous. Therefore, experiment and theory need to use the same definition to be able to compare their findings [73].

Fixed-order pQCD calculations exploiting the QCD factorization theorem, see Eq. 2.2.5, use parton-to-hadron FFs $D_i^H(z_i, Q^2)$ which provide the probability for a quark or gluon i to fragment into a certain type of hadron H carrying a fraction z_i of the parton's momentum. These FFs describe the non-perturbative processes of QCD of partons fragmenting into hadrons in one parton-to-hadron FF. Therefore, they need to be obtained from actual experimental data. Once the FFs are determined for a certain scale and if the factorization scale μ_f is large compared to Λ, the change of the FFs for different scales can be obtained from the DGLAP equations [74].

Comprehensive parameterizations of FFs are derived from global fits to experimental data from a large variety of processes at various collision energies, for which LHC data opens up new domains of x and z not accessible at lower energies. Examples for such FFs for neutral mesons are DSS07 [75] and AESSS [76] based on pre-LHC data. Deviations from these FFs were observed at LHC energies [75], leading to recent progress made by including first LHC data in these global fits, e.g. DSS14 [77]. However, for some neutral mesons like the η meson such updates are still pending.

On the other hand, MC event generators attempt to simulate the hadronization process on its own after the parton showering has terminated which is modeled independently. By construction, the hadronization scale is identical to the infrared cutoff of the parton shower [78]. Different QCD-inspired phenomenological models are used to describe the process of hadronization in this context. There are two main classes of models currently being used: the string and cluster fragmentation models. The generators PYTHIA [79–81] and PHOJET [82, 83] use string fragmentation models [84], whereas HERWIG [85] is an example using the cluster fragmentation model [86]. Another recent successful model is rope fragmentation [87, 88] which essentially is a generalization of the string model. In the following, these three different hadronization models are introduced and further elaborated.

String Model

Besides some early developments, the most sophisticated and well-known string model is the Lund string model [89, 90] which is widely used, i.a. in PYTHIA. The starting point of this model is the linear confinement of QCD at large distances; $V(r) \sim kr$ with an energy per unit length of $k \approx 0.85\,\mathrm{GeV/fm}$ [38], hence any Coulomb-related terms are neglected. If a pair of partons, e.g. $q\bar{q}$, moves apart, the color flux tube in between is being stretched. The potential energy stored in the string increases, until it can finally break at a vertex producing a new $q'\bar{q}'$ pair. Then, the system splits into two color-singlet systems which move apart further. In between both systems, a widening no-field region opens up as shown in Fig. 2.3.7a. In that figure quarks are assumed to be massless, hence moving with speed of light. The color-singlet systems may undergo further breaking processes, equivalent to creating additional vertices, if the invariant mass of the respective system is large enough. If masses are small, however, the quarks may turn around when the string is maximally extended to create a so-called ‘yo-yo’ movement pattern. Such color-singlet bound states of partons represent hadrons created in the fragmentation process which are required to be produced on mass shell having $E = k\Delta z$ and $p_z = k\Delta t$ with a transverse mass of $m_{\mathrm{T}}^2 = k^2((\Delta z)^2 - (\Delta t)^2)$ [78], where Δz and Δt denote the distances between the two vertices forming the hadron. The different breaks are spacelike separated, $(\Delta t)^2 - (\Delta z)^2 < 0$, hence they can be viewed to occur independently of each other. In that way, the system may fragment into n primary hadrons, where $n \in \mathbb{N}$.

In the Lund model, the string break processes are simulated by an iterative procedure. Since there is no natural order, the system exhibits a ‘left-right’ symmetry so that one is free to consider the breaks in any order. Reflecting this characteristic, the Lund symmetric fragmentation function $f(z)$ is defined, where z is the fraction of the remaining lightcone momentum $E \pm p_z$ (+ for q, - for $\bar{q}$) that the newly produced hadron takes:

$$f(z) \propto \frac{(1-z)^a}{z} \exp\left(-\frac{bm_{\mathrm{T}}^2}{z}\right), \tag{2.3.16}$$

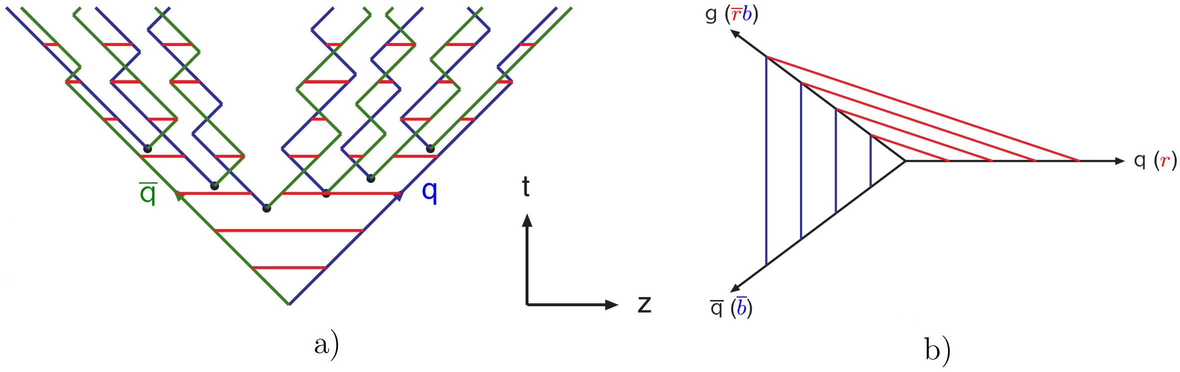

Figure 2.3.7: a) The breakup of an initial $q\bar{q}$ pair into several color-singlet 'yo-yo' states, representing produced hadrons, is shown in the picture of the Lund string model [78]. b) The schematic drawing visualizes how additional gluons, stretching the color string, are treated within the Lund string model [78].

where a and b are the free parameters of the model and m_{T} is the transverse mass. For a string break in the classical picture, the new $q\bar{q}$ pair can be created in one point and be pulled apart. However, the pair must be produced at a certain distance if quarks have mass or transverse momentum, so that the field energy between them can be transferred into m_{T}. Hence, considering quantum dynamics, the quarks are created in one point and have to tunnel out to the classically allowed region. This is represented by the exponential factor in Eq. 2.3.16, $f(z) \propto \exp\left(-\frac{bm_{\mathrm{T}}^2}{z}\right)$, which is found in analogy to similar QED processes. This formula also implies a suppression of heavy quark production, $u : d : s : c \approx 1 : 1 : 0.3 : 10^{-11}$. Moreover, the Lund string model does also include the production of baryons B. A simple scheme is the occasional production of antidiquark-diquark pairs. Furthermore, there is the so-called popcorn model, in which baryons appear from successive production of several $q\bar{q}$ pairs. Note that each of these schemes preserves baryon number conservation as in any case at least one $B\bar{B}$ pair is produced. If the system does not only consist of a $q\bar{q}$ pair but also contains additional gluons, e.g. a $gq\bar{q}$ system moving apart, the Lund string model does also provide a meaningful description. The gluon stretches the string as shown in Fig. 2.3.7b and can be viewed as an energy- and momentum-carrying kink on the string. One of the key predictions is that the qg and $\bar{q}g$ angular regions should receive enhanced particle production while the $q\bar{q}$ region should be depleted which was confirmed by Ref. [91]. In general, the string fragmentation approach is collinear and infrared safe [78]. One of the limitations of this model is, however, that it treats all string fragmentations independently as it was originally formulated for one isolated string.

Cluster Model

The cluster model [86] is based on the preconfinement property of parton showers. That means that at any evolution scale Q_0 the color structure of a parton shower is such that color-singlet combinations of neighboring partons can be formed, having asymptotically universal invariant mass distributions. In this context, universal denotes a dependence only on Q_0 and the QCD scale Λ but not on the nature of the hard process initiating the shower [78]. Hence, the mass distribution can be calculated perturbatively if $Q_0 \gg \Lambda$. In Fig. 2.3.8a, the color structure of a parton shower is shown, visualizing the splitting processes. In the shower, the gluons are represented by pairs of color-anticolor lines that are connected at vertices. Each color line at the low-scale end of the shower is connected to an anticolor partner line at the same scale. Hence, the color structure of a shower can be drawn on a plane so that color-anticolor partners are adjacent. Such adjacent partners may form color-singlets which are closer in phase space. After the perturbative phase, these color-singlet clusters subsequently decay into the observed hadrons. Hence, non-perturbative splittings of gluons into quark-antiquark pairs is enforced at the shower cutoff scale to form physical clusters with mesonic quantum numbers. The hadrons, emerging from the decay of each cluster, are spread over a limited region in phase space. This leads to a distribution of final-state hadrons closely connected to that of partons at the cutoff scale. The cluster decays can also produce heavy flavors as well as $B\bar{B}$ pairs. Baryons may also originate from gluon splittings into light diquark-antidiquark pairs. These transitions of clusters into observed hadrons is one of the key points of the cluster model. A simple model in this context is to randomly select from all allowed decay channels with probabilities according to phase space and, i.a. flavor and spin degeneracy. This naturally leads to limited transverse momenta and a suppression of heavy flavor, strangeness and baryon production. One of weaknesses of the cluster model is that it does not include any interaction between the clusters, a comparable limitation as in the case of the string model which treats all string fragmentations independently.

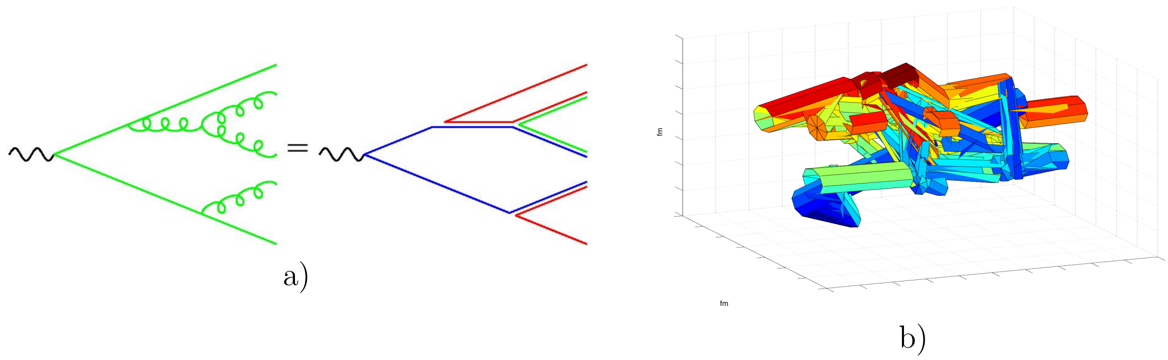

Figure 2.3.8: a) The color structure of a parton shower [78]. b) A schematic of a typical event in impact parameter space and rapidity is shown before hadronization [88] according to the rope model. The color strings are illustrated for a pp event at $\sqrt{s} = 7\,\text{TeV}$ from a MC simulation.

Rope Model

The rope model [87, 88] can be viewed as a natural extension of the successful Lund string model by incorporating interactions of overlapping strings in the formalism. When many strings are produced within a limited space, they are expected to overlap in space and time during the fragmentation process and hence interact, so that the independent fragmentation scheme does not hold anymore. In the dense environment of hadronic collisions, so-called color ropes are expected to be formed by coherent interactions of nearby strings, resulting in a stronger color field which leads to an enhancement strangeness and baryon production. At LHC energies, many overlapping strings are already expected in pp collisions and naturally for larger systems as well. Fig. 2.3.8b shows a schematic obtained from MC simulation for pp collisions $\sqrt{s} = 7\,\text{TeV}$, visualizing an event before hadronization. The transverse dimension of color flux tubes are of typical hadronic sizes, the confinement scale of roughly 1 fm, each with the standard value of the string tension, represented by k as already introduced [88]. A key point of the rope model is to increase the local string tension by estimating the transverse-space overlap by string pieces which may show up in parallel or antiparallel pieces. This is done with help of LQCD calculations [92]. Random color charges for the individual strings are assumed. Furthermore, it is also assumed that color ropes break by successive production of new $q\bar{q}$ pairs, leading to a reduction of the rope tension with each individual breakup. The model drastically improves the description of strange hadron generation as a function of event multiplicity in all systems from e^-e^+ to AA [92].

2.3.2 Photon Production & Interaction with Matter

Photons are produced during all stages of hadronic collisions with negligible final-state interactions, making them a very interesting probe to study the different stages of such collisions. They are of special interest in the context of studying the QGP as they are not influenced by the strong interaction and hadronization processes, thus having mean free paths much larger than the collision volume. A variety of production mechanisms are superimposed to yield the inclusive photon spectra which can be directly measured by experiments. In general, the inclusive set of photons can be categorized into two distinct classes:

i) decay photons, γ_{dec}, which originate from hadronic decays;

ii) direct photons, γ_{dir}, defined as all photons which do not originate from decays.

Usually, direct photons are further classified into prompt, fragmentation and thermal components. For high transverse momenta above several GeV/c, the dominant contribution of prompt photons is created by initial $2 \rightarrow 2$ hard scattering processes. The main components in this regime are the Leading Order (LO) processes quark-gluon Compton scattering, $qg \rightarrow q\gamma$, and quark-antiquark annihilation, $q\bar{q} \rightarrow g\gamma$, which are calculable in the framework of pQCD. The outgoing partons will hadronize and most likely form jets, being sensitive to the presence of a strongly interacting medium. On the other hand, the outgoing photons are able to escape such a medium basically unaffected. Hence, these γ-jet correlations are generally denoted as golden channel to study i.a. energy loss effects as the photon balances the original momentum of the opposing parton [93]. A further class is represented by fragmentation photons being directly produced by fragmenting partons. Additional photon production mechanisms are expected to contribute especially in heavy-ion collisions via jet-medium interactions and thermal emissions. In this context, jet-medium interactions summarize the production of photons in scatterings of hard partons with thermalized partons and in-medium photon bremsstrahlung emitted by quarks. On the other hand, thermal photons originate from thermal radiation of the QGP and, subsequently, the hot hadron gas. These contributions are expected to produce the dominant photon component at low p_{T} in heavy-ion collisions which is exponentially suppressed for increasing momenta though. It remains a big challenge to pin down the relative contributions of the different processes and to describe all the experimental findings concerning direct photons in theory which also includes the famous "photon puzzle", see Refs. [94–97] for further reference on this topic.

The direct photon component can be accessed by subtracting the decay photon background as follows:

$$\gamma_{\mathrm{dir}} = \gamma_{\mathrm{inc}} - \gamma_{\mathrm{dec}} = \left(1 - \frac{1}{R_\gamma}\right) \cdot \gamma_{\mathrm{inc}}, \tag{2.3.17}$$

where $R_\gamma \equiv \gamma_{\mathrm{inc}}/\gamma_{\mathrm{dec}}$ is introduced as the ratio of the amount of inclusive photons over the number of photons originating from particle decays. If $R_\gamma > 1$ is found, a direct photon signal can be deduced. Experimentally, R_γ can be accessed via the following relation:

$$R_\gamma = \frac{\left(\gamma_{\mathrm{inc}}/\pi^0\right)_{\mathrm{meas}}}{\left(\gamma_{\mathrm{dec}}/\pi^0_{\mathrm{param}}\right)_{\mathrm{sim}}}, \tag{2.3.18}$$

where the numerator can be directly extracted from data by measuring the inclusive photon production γ_{inc} and the π^0 spectrum. The denominator is obtained by a particle decay simulation which includes all relevant photon sources from hadron decays, for which the parametrizations of measured hadron spectra are used as input so that a realistic decay photon spectrum can be estimated for the given collision system.

Photons can be detected by exploiting their interactions with matter. In this context, the three main processes are the photoelectric effect, Compton scattering and pair production. The total cross section for a photon to interact with matter is given by the sum of the different contributions, $\sigma_{\mathrm{all}} = \sigma_{\mathrm{photo}} + \sigma_{\mathrm{compton}} + \sigma_{\mathrm{pair}}$, each depending on different powers of the proton number Z. Given high values of Z, the photoelectric effect is dominant at low photon energies of $E_\gamma \lesssim 0.1\,\mathrm{MeV}$, whereas Compton scattering is the leading process in the intermediate energy regime complemented by pair production as the dominant process at high photon energies of $E_\gamma \gtrsim 10\,\mathrm{MeV}$. The latter process describes the conversion of a photon into a e^-e^+ pair, $\gamma \to e^-e^+$ which is of main relevance for this thesis as it can be used to detect and reconstruct high energetic photons. For this purpose, the trajectories of both leptons can be experimentally determined by means of tracking detectors so that the converted photon can be reconstructed, see also Sec. 5.1. The part of the photon energy exceeding the rest masses of the created e^-e^+ pair is converted into its kinetic energy and some further part is transferred to an additional recoil particle which is necessary to fulfill energy and momentum conservation laws at all times. Such a conversion of a photon into a e^-e^+ pair usually occurs in the magnetic field of a nucleus which acts as recoiling particle, however, it is also possible in the field of an electron. Pair production may occur if the following condition is fulfilled which can be deduced from the energy and momentum conservation laws:

$$E_\gamma \geq 2m_e \left(1 + \frac{m_e}{m_{\mathrm{nucleus}}}\right), \tag{2.3.19}$$

where the masses of the electron and the nucleus enter. In good approximation $E_\gamma \geq 2m_e$ holds since $m_{\mathrm{nucleus}} \gg m_e$. The relation further simplifies to $E_\gamma \geq 4m_e$ if the process occurs in the field of an electron. The cross section for pair production at high photon energies of $E_\gamma \gg 137 m_e/Z^{1/3}$ is given by [98]:

$$\sigma_{\mathrm{pair}} = \frac{Z^2 r_0^2}{137}\left(\frac{28}{9}\ln\left(\frac{183}{Z^{1/3}} - \frac{2}{27}\right)\right) \overset{(i)}{\approx} \frac{7}{9} \cdot \frac{A}{N_A} \cdot \frac{1}{X_0} \propto Z^2, \tag{2.3.20}$$

where Z is the proton number of the nucleus and r_0 the classical electron radius. Introducing the radiation length X_0, the Avogadro constant N_A and the mass number A, the relation (i) is obtained which shows a proportionality of Z^2 of the pair production cross section. The parameter X_0 describes the length after which the energy E of an initial electron/positron with energy E_0 is reduced to E_0/e, where e is the Euler number:

$$-\frac{\mathrm{d}E}{\mathrm{d}x} = \frac{E}{X_0}, \quad \text{where} \quad X_0 = \frac{716,4 \cdot A}{Z(Z-1)\ln(287/\sqrt{Z})}. \tag{2.3.21}$$

The variable X_0 is a material constant, only depending on Z and A [99]. Hence, a proportionality of $X_0 \sim A/Z^2$ is found in good approximation. Separating the variables in Eq. 2.3.21 and solving for E finally leads to the following relation: $E(x) = E_0\, e^{-x/X_0}$.

On the other hand, if heavy charged particles are considered $m \gg m_e$, the energy loss per path length within matter is described by the Bethe-Bloch formula [100]. In analogy to the radiation length X_0 for the emission of bremsstrahlung, the mean free path of a photon Λ_γ is defined as the length after which the number of primary photons is reduced by the factor $1/e$:

$$\Lambda_\gamma = \frac{9}{7} X_0. \tag{2.3.22}$$

Besides exploiting the pair production to reconstruct photons, electromagnetic calorimeters are also used for this purpose as introduced in Sec. 5.2. If photons enter such a calorimeter, an electromagnetic shower is created. The development of such a shower is schematically drawn in Fig. 2.3.9. For $E_\gamma \gtrsim 10\,\mathrm{MeV}$, pair production is already the dominating interaction process of photons with matter, whereas for further increasing photon energies it is basically the only contributing process to the total cross section. If such a high energetic photon enters some material, it will travel one free path length Λ_γ on average before a pair production occurs as indicated in Fig. 2.3.9 at $n = 0$. A high energetic e^-e^+ pair is hence created which further crosses the material until losing energy by bremsstrahlung at $n = 1$, a process which scales with the radiation length X_0. Such bremsstrahlung photons can further create e^-e^+ pairs while the electrons and positrons may further radiate photons by bremsstrahlung, increasing the number of particles in each step. The cascade continues in this fashion until the energy of the bremsstrahlung photons is below the threshold level for pair production so that they are finally absorbed by an occurring photo effect while for the electrons and positrons the process continues until the critical energy E_c is reached. The critical energy E_c is defined by the energy at which $(dE/dx)_{\text{bremsstrahlung}} = (dE/dx)_{\text{ionization}}$ holds. Below E_c, the energy loss per path length by ionization is more probable than the energy loss by the emission of bremsstrahlung, defining the formal stopping point of the shower development. The critical energy can be estimated for solid and liquid materials by $E_c = 610\,\mathrm{MeV}/(Z + 1.24)$. The transverse dimension of an electromagnetic shower is described by the Molière radius [99]:

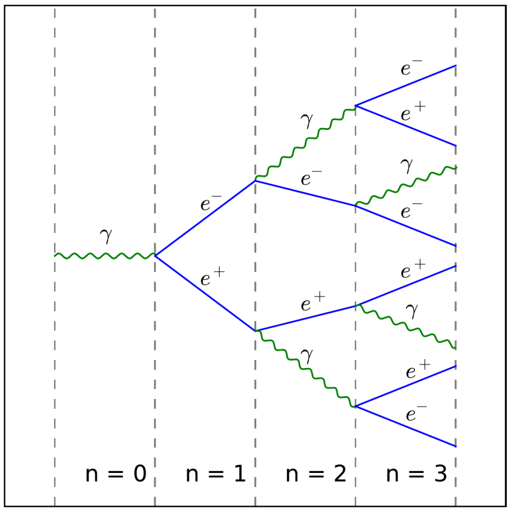

Figure 2.3.9: A schematic drawing visualizing the substructure of an electromagnetic shower, taken from Ref. [101].

$$R_M = \frac{21.2\,\mathrm{MeV}}{E_c} X_0 \approx \frac{7A}{Z\rho}, \tag{2.3.23}$$

where ρ is the density of the material. Within R_M about 90 % of the deposited energy is contained, whereas within $2 \cdot R_M$ in transverse direction about 95 % of the energy deposition takes place.

2.3.3 Selected Signatures of the Quark-Gluon Plasma

The hot and dense QGP phase can be probed in heavy-ion collisions, e.g. at the LHC typically Pb-Pb collisions are provided. However, such studies are difficult to interpret without any baseline. Therefore, measurements in so-called small systems are of high importance in this context to obtain a reference for the heavy-ion results. Small systems include for example pp but also p-Pb collisions for which the formation of a QGP fireball is commonly not expected. The QCD vacuum is probed with pp collisions, whereas in p-Pb the influence of cold nuclear matter can be investigated. Both systems complement Pb-Pb collisions, where the effects of the presence of the QGP can be studied. Hence, it is crucial to perform all measurements for pp, p-Pb and Pb-Pb collisions to develop a consistent picture. Each system is unique and can probe different environments, enabling the possibility to disentangle the various observations and to interpret the results. Furthermore, measurements at different center of mass energies are of importance to study the evolution of e.g. particle production spectra with energy and to test scaling laws.

In central heavy-ion collisions, the same initial interactions as for small systems take place, although many more binary nucleon-nucleon collisions occur in the reaction zone at the same time. Lots of energy is deposited in this reaction zone via soft processes so that after a certain thermalization time, given high enough temperatures, a QGP can be formed. The system subsequently expands into the QCD vacuum and cools down, undergoing a transition into a hadronic phase, in which the deconfined partons finally hadronize. They may undergo further interactions until the complete decoupling of hadrons is reached, the freeze-out. This medium evolution of existing QGP phase influences the experimental observables in various ways, leading to a variety of signatures for the presence of a QGP for which comprehensive overviews can be found in Refs. [50, 102]. In the following, only a selection of these signatures are elaborated which are closely related to neutral meson and photon measurements.

The modification of particle yields in heavy-ion collisions, AA, with respect to pp collisions can be studied using the R_{AA}. This observable corresponds to the ratio between the AA and the pp production cross sections, normalized to the number of nucleon-nucleon collisions:

$$R_{AA}(p_{\mathrm{T}}) = \frac{\mathrm{d}^2 N/\mathrm{d}p_{\mathrm{T}}\mathrm{d}y|_{\mathrm{AA}}}{\langle T_{AA}\rangle \cdot \mathrm{d}^2\sigma/\mathrm{d}p_{\mathrm{T}}\mathrm{d}y|_{\mathrm{pp}}}, \tag{2.3.24}$$

where $\langle T_{AA}\rangle$ is the average nuclear overlap function. It is related to the average number of inelastic nucleon-nucleon collisions $\langle N_{\mathrm{coll}}\rangle$ as follows: $\langle T_{AA}\rangle = \langle N_{\mathrm{coll}}\rangle/\sigma^{\mathrm{pp}}_{\mathrm{inel}}$, where $\sigma^{\mathrm{pp}}_{\mathrm{inel}}$ is the cross section for inelastic pp collisions. $\langle N_{\mathrm{coll}}\rangle$ depends on the impact parameter b between the two heavy nuclei. In this context, the Glauber model is used to determine $\langle N_{\mathrm{coll}}\rangle$ as a function of impact parameter between the two interpenetrating nuclei [103]. For this purpose, realistic initial distributions of nucleons inside the nucleus are utilized, assuming the nucleons follow straight trajectories. Directly related to the impact parameter, the concept of centrality can be introduced [103]. The centrality c is a measure of the percentage of the total nuclear interaction cross section. Head-on collisions of nuclei with $b \to 0$, hence $c \to 0\%$, are denoted central, whereas the opposite case is identified as peripheral collision for which $c \to 100\,\%$. Hard processes are expected to scale with $\langle N_{\mathrm{coll}} \rangle$. Hence, the R_{AA} is expected to be at unity in the absence of any nuclear effects. Therefore, a suppression, $R_{AA} < 1$, at larger momenta gives evidence for a medium modification of the measured particle spectra which is one of the key signatures of a QGP. The R_{AA} of neutral pions for Pb-Pb collisions at $\sqrt{s_{\mathrm{NN}}} = 2.76\,\mathrm{TeV}$ was measured by ALICE [71], for which an example is shown in Fig. 2.3.10a. It can be seen that the suppression increases with centrality from peripheral ($60-80\,\%$) to most central events ($0-5\,\%$). This can be interpreted by partons losing more and more energy since the reaction zone and hence the volume of the QGP fireball increases. The R_{AA} exhibits a maximum at around $1-2\,\mathrm{GeV}/c$, where soft processes are dominant which are affected by collective effects.

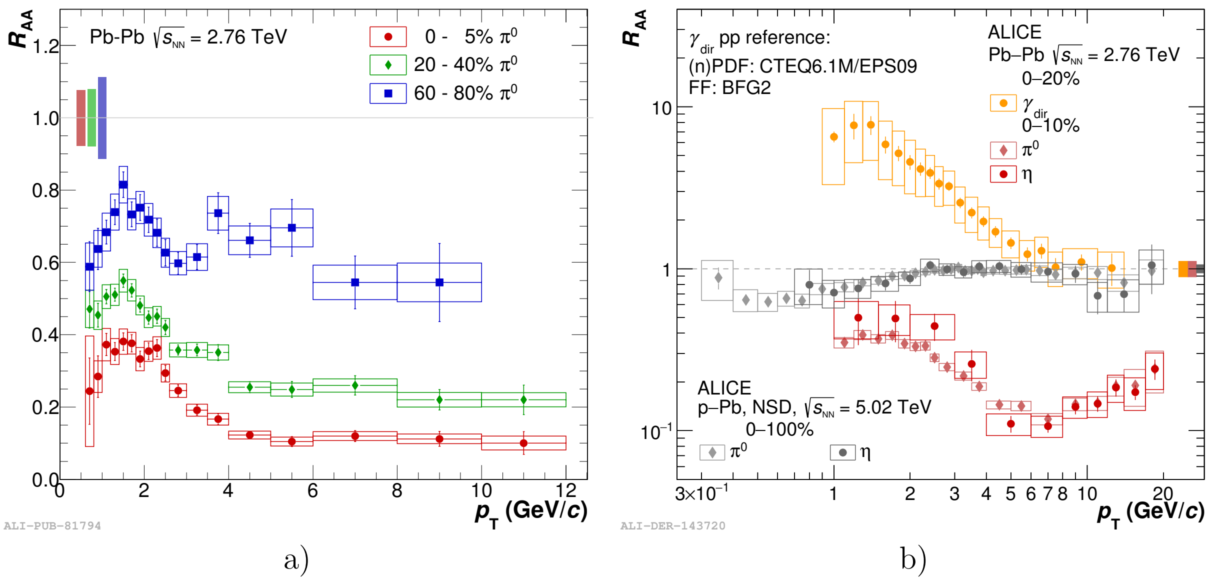

Figure 2.3.10: a) The nuclear modification factor R_{AA} for three different centralities measured in Pb-Pb collisions at $\sqrt{s_{\mathrm{NN}}} = 2.76\,\mathrm{TeV}$ [71]. b) The corresponding factors are shown for direct photons as well as neutral mesons for most central events, whereas the R_{pA} measured in p-Pb collisions at $\sqrt{s_{\mathrm{NN}}} = 5.02\,\mathrm{TeV}$ is shown in addition [104]. The colored vertical boxes around unity represent the uncertainty of $\langle T_{AA} \rangle$ and the normalization uncertainty of the reference pp spectra, added in quadrature.

In analogy to Eq. 2.3.24, the R_{pA} can be defined relating the invariant yields in pp collisions and p-Pb collisions. Fig. 2.3.10b shows a summary of the results on R_{AA} and R_{pA} on the modification of neutral meson and direct photon spectra [9, 105, 106]. The R_{AA} of the neutral mesons π^0 and η for $0-10\,\%$ centrality are shown for Pb-Pb collisions at $\sqrt{s_{\mathrm{NN}}} = 2.76\,\mathrm{TeV}$ which are found to be consistent within given uncertainties. The direct photon R_{AA} proofs the expectations to be consistent with unity for high p_{T} above $6\,\mathrm{GeV}/c$. This is the case since hard processes scale with $\langle N_{\mathrm{coll}} \rangle$ and photons do not interact strongly, enabling them to leave the medium basically unaffected. On the other hand, the R_{AA} is observed to be larger than unity for lower p_{T}. This observation is interpreted as the thermal photon signal of a hot QCD medium. Due to the absence of a QGP in pp collisions, the R_{AA} is hence found to be larger than unity. Moreover, the R_{pA} is found to be consistent with unity above several GeV$/c$, further strengthening the interpretation of the observed suppression in central Pb-Pb collisions which is facilitated by the presence of a QGP medium.

The following Fig. 2.3.11a shows the direct photon spectra for three different centrality classes measured by ALICE [105]. The spectra are obtained from inclusive photon measurements and R_γ, which is shown in Fig. 2.3.11b, by exhibiting the relation from Eq. 2.3.17. If the R_γ is not above unity within $1\,\sigma$ of statistical or systematic uncertainty, corresponding upper limits at 90 % C.L. are drawn. The reference is provided by N_{coll}-scaled NLO pQCD calculations. For high p_{T}, an agreement with theory calculations is given while for low p_{T} a direct photon excess can be deduced due to thermal photon radiation of the QGP. Such photons are expected to be produced with an exponentially falling spectrum $\propto \exp(-p_{\mathrm{T}}/T)$. Hence, the data for most central collisions is fitted using an exponential in the range of $0.9 < p_{\mathrm{T}} < 2.1\,\mathrm{GeV}/c$ to extract the inverse slope parameter, the effective temperature $T_{\mathrm{eff}} = 297 \pm 12_{\mathrm{(stat)}} \pm 41_{\mathrm{(sys)}}\,\mathrm{MeV}$. Furthermore, the measured direct photon excess via R_γ, shown in Fig. 2.3.11b, is found to be consistent with NLO pQCD predictions for $p_{\mathrm{T}} \geq 5\,\mathrm{GeV}/c$ for all centrality classes. For the momentum interval $0.9 < p_{\mathrm{T}} < 2.1\,\mathrm{GeV}/c$, however, a direct photon excess of $2.6\,\sigma$ is found for the most central class which is due to the presence of additional direct photons by thermal radiation. Hence, in this context actual measurements of direct photon spectra and R_γ in pp collisions are important to further settle the interpretations of heavy-ion results.

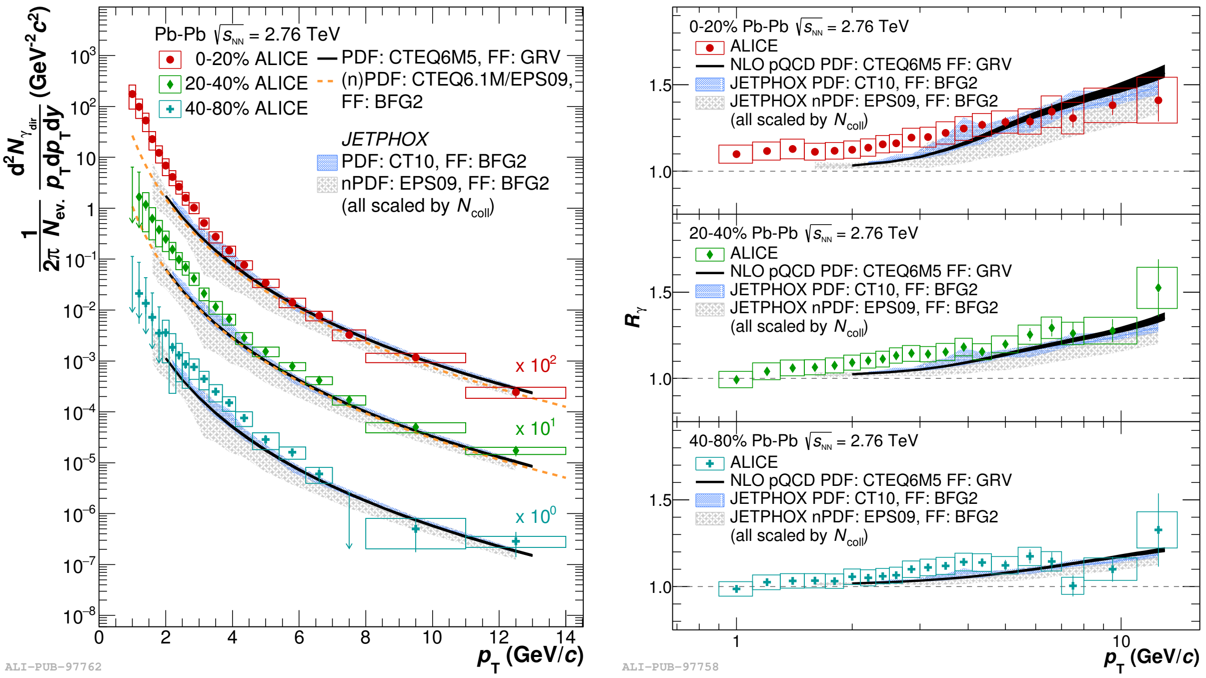

a) b)

Figure 2.3.11: The invariant yields of direct photon production, a), and the corresponding values of R_γ, b), measured for three different centrality classes of Pb-Pb collisions at $\sqrt{s_{\mathrm{NN}}} = 2.76\,\mathrm{TeV}$ which are compared to various theory predictions [105].

Furthermore, the direct photon flow was also measured by ALICE [107]. The flow of particles denotes their anisotropic momentum distribution caused by the initial state of the colliding heavy nuclei [108]. In general, their overlap region is found to be almond shaped for finite impact parameters, thus yielding different pressure gradients in space which modify the momentum distributions as a function of the particle's trajectory. For direct photons, no significant flow was expected, however, a high photon flow was measured [107] across all centrality classes which is comparable in its magnitude to the results for charged particles. This points to a late photon production since flow needs to time to develop [109]. On the other hand, the photon excess in heavy-ion collisions at low p_{T} is interpreted to be thermal radiation which in contrast points to an early production of photons where the hot QGP matter is still present and no hadrons are formed yet. This contradiction is the so-called photon puzzle, for which a selection of relevant references is given by Refs. [94–97]. For the ALICE measurement there only is a $1.4\,\sigma$ effect in the most central class [107] given the current experimental uncertainties, whereas the puzzle is present for the corresponding PHENIX measurement which finds a substantial v_2 of direct photons [110].

2.4 Monte Carlo Event Generators

General purpose Monte Carlo (MC) event generators [78] are software libraries which are used for various applications including the simulation of high-energetic hadronic collisions. Hence, they are used to randomly generate events as those produced in real collisions at collider experiments. In this thesis, there are essentially two different event generators used for analysis: PYTHIA and PHOJET which are two commonly used generators in high-energy physics. The event generators produce the outgoing particles in vacuum and no further interaction with detector material is considered at this stage. Both are introduced in the remaining part of this section.

PYTHIA

PYTHIA [79–81] is a general purpose MC event generator. In high-energy physics it is one of the standard event generators widely used. There are different versions of the program available: while PYTHIA 6 is written in Fortran 77, its successor PYTHIA 8, for example, stands for the first release completely written in C++ adding more features and fixing existing bugs. PYTHIA 8 can be linked with other program packages following the Les Houches Accord (LHA) and its associated Les Houches Event Files (LHEF) so that external matrix element calculations can be used for example. The implemented physics models in PYTHIA focus on high-energy particle collisions, defined as having center of mass energies of larger than 10 GeV. This limitation is given by approximations of a continuum of allowed final states for hadron-hadron cross section calculations for example [81]. Below the energy threshold of 10 GeV, the hadronic resonance region is entered where these implemented approximations break down [81] and where, at some point as well, perturbation theory is also not applicable anymore. Hence, the program can handle only hadronic collisions, whereas γp and $\gamma\gamma$ are not yet addressed in PYTHIA 8. The PYTHIA machinery features hard processes at LO level, mainly focusing on $2 \longrightarrow 1$ and $2 \longrightarrow 2$ processes but also some $2 \longrightarrow 3$ processes are available. Soft processes are also modeled in PYTHIA which is intended to describe all components of the total cross section in hadronic collisions. Therefore, total, elastic and inelastic cross sections are obtained from Regge [111] fits to data. The default cross section for pp collisions is described by the Donnachie-Landshoff parameterisation [112] with one Pomeron and one Reggeon term. Several sets of PDFs are available, e.g. CTEQ [113] and MSTW PDFs [114], whereas others can be used via LHA interface. The shower evolution is based on standard LO DGLAP splitting kernels [81]. The Initial State Radiation (ISR) and Final State Radiation (FSR) algorithms follow a p_{T}-ordered evolution and are based on these DGLAP splitting kernels which express the probability of emitting radiation when moving to lower values of the shower evolution variable. In hadronic collisions, Multiparton Interactions (MPIs) are a natural consequence of the composite structures of the colliding particles which are also modeled in PYTHIA spanning both soft and hard MPI processes with a variety of tuning parameters [81]. The hadronization of colored partons into final state hadrons is based on the LUND string model [115], introduced in detail in Sec. 2.3.1. These produced hadrons are not necessarily stable particles so that they are decayed subsequently. The according decay properties of the hadrons are stored in decay tables, as summarized in Ref. [32]. In summary, PYTHIA has many tunable parameters with significant influence on the generated distributions. Therefore, specific sets of predefined parameters are available. Such a set is called tune which is obtained from comparisons with data. A variety of tunes is available, for example one of the early tunes is 4C [116] that already includes early 7 TeV LHC data. A very recent tune is Monash 2013 [117], covering LEP, Tevatron and LHC data. It is used by default since PYTHIA 8.2. In the context of this thesis, a further relevant feature of PYTHIA is the possibility to run with cuts on the momentum of the initial parton from the hard scattering, so-called $p_{\mathrm{T,hard}}$ bins. This allows to generate samples with larger statistics for higher transverse momenta without the need to arbitrarily embed high momentum particles, see also Sec. 4.1.1.

PHOJET

PHOJET [82, 83, 118] is a Monte Carlo event generator written in FORTRAN which provides an alternative to PYTHIA. The generator uses an implementation of the two-component Dual Parton Model (DPM) [119], combining results from Regge theory, reggeon calculus [120] and AGK cutting rules [121] to describe soft processes. For the hard interaction processes, the framework of pQCD is used to derive predictions. In that way, PHOJET gives an almost complete picture of hadron-hadron, photon-hadron and photon-photon interactions at high energies [83, 122]. In the framework of DPM, the description of hadronic interactions involves the exchange of pomerons. The pomeron is a theoretical object which is a color neutral object providing an effective description of important degrees of freedom in Regge limit [118]. The exchange of such pomerons can be subdivided into soft processes and hard processes, enabling the predictive power of the QCD-improved parton model and PDFs [118]. These processes are distinguished by a transverse momentum cutoff of about $p_{\mathrm{T,\,cut\text{-}off}} \approx 3\,\mathrm{GeV}/c$. Within the two-component DPM, the connection of the soft and hard subprocesses is given by an unitarization scheme, chosen in a way that the sum of the hard and soft cross sections is nearly independent of the choice of $p_{\mathrm{T,\,cut\text{-}off}}$. Therefore, the tuning parameters are connected to each other unlike for PYTHIA. On the other hand, parton showers are initiated following the DGLAP evolution equations [123] similar to PYTHIA. The process of hadronization is based on the LUND string model, see also Sec. 2.3.1.

Chapter 3

Experimental Environment

This chapter gives an overview of the experimental environment which is based on the beam facilities and detectors being located at the European Organization for Nuclear Research (CERN). The ALICE detector is introduced with its sub-detector systems as well as its trigger system. Moreover, its Data Acquisition (DAQ) chain is described and the basic data reconstruction steps are explained. Furthermore, the analysis framework is described which is used for analysis.

3.1 The LHC @ CERN

CERN is a major research institution located in the border area of Switzerland and France in Geneva. Since it was founded back in 1953 by twelve European countries, it has grown to be one of the most important research institutions in the world in the field of nuclear and particle physics. During its long history, it has been running several groundbreaking accelerators like the Synchrocyclotron (SC) [124], the Proton Synchrotron (PS) [125], the Super Proton Synchrotron (SPS) [126] and the Large Electron Positron Collider (LEP) [127] for example. Some of these accelerators are still in use for the particle injection chain of the Large Hadron Collider (LHC) [128] which is the largest and most powerful particle accelerator that mankind has built up to now. In 1994, the LHC project was approved by the CERN council to succeed LEP and prolong its successful era. The LHC is located inside the old LEP tunnel which has a circumference of 26.7 km, about 45 to 170 m below ground level. The accelerator was designed to deliver particle collisions with unprecedented center of mass energies of $\sqrt{s} = 14\,\mathrm{TeV}$ for proton-proton (pp) collisions with a design luminosity of $\mathcal{L} = 10^{34}\,\mathrm{cm}^{-2}\,\mathrm{s}^{-1}$ and $\sqrt{s_{\mathrm{NN}}} = 5.5\,\mathrm{TeV}$ for heavy ions, e.g. Pb or Xe, at $\mathcal{L} = 10^{27}\,\mathrm{cm}^{-2}\,\mathrm{s}^{-1}$.

The LHC features four main experiments each located at a dedicated experimental cavern at different positions in the ring: ALICE [129], ATLAS [130], CMS [131] and LHCb [132]. Furthermore, three smaller experiments, LHCf [133], MoEDAL [134] and TOTEM [135], are collecting data and complete the set of running experiments at the LHC. The accelerator has been designed as a discovery machine, amongst others for the hunt for the Higgs-Boson which was finally discovered by ATLAS [18] and CMS [19] on July, 4th in 2012. Besides the quests to discover new particles or (yet) unknown signals mainly followed by these two collaborations, there is the LHCb experiment which mainly focuses on heavy flavor (beauty and charm), electroweak as well as QCD physics. The list of main experiments at the LHC is completed by ALICE, introduced with more detail in Sec. 3.2, which is the only dedicated experiment to study the QGP.

The LHC can be divided into eight main sectors, so-called Octants, which host the major components of the full accelerator complex. This substructure is illustrated using a schematic, see Fig. 3.1.1. The Octants feature the following components:

- the four beam Interaction Points (IPs), labeled by their corresponding Octant, hosting the four main experiments: IP1 → ATLAS, IP2 → ALICE, IP5 → CMS and IP8 → LHCb;
- beam pipes including dipole magnets to bend the beam and focusing structures (using quadrupole, sextupole, octupole and decapole magnets) to control the beam orbit [136];
- acceleration system using radiofrequency cavities [136] at Octant 4 to increase the beam energies;
- a cleaning system, located at Octants 3 and 7, which uses a various set of collimators to scatter and absorb particles with large momentum offsets or large betatron amplitudes;
- the beam dump [136] in Octant 6;
- and the two injection points within Octant 2 and Octant 8 to feed the preaccelerated beams from the SPS into the LHC.

The LHC has two separate beam pipes for the two counter-rotating beams which consist of eight straight sections and eight arcs, see also Fig. 3.1.1. These arcs are equipped with superconducting twin bore dipole magnets which consist of two sets of coils and beam channels within the same mechanical structure and cryostat. The dipole magnets are operated below a temperature of 2 K, yielding peak dipole fields of 8.33 T to be able to bend the particles trajectories at the nominal beam energies. A powerful ultra-high vacuum system is installed which reaches a quality of $\sim 10^{-13}$ atm for the total volume of 150 m^3 in order to minimize beam-gas interactions. The beam pipes with their vacuum structures and magnetic fields are separated throughout the ring and only share common parts around the IPs, where the main experiments are located and the two beams are brought to collision by means of focusing magnets. At these IPs, the beams hence cross the magnetic bores as indicated in Fig. 3.1.1.

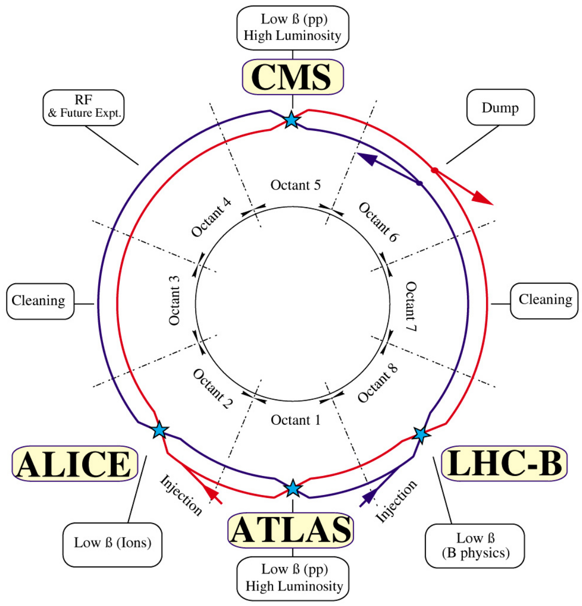

Figure 3.1.1: A schematic of the general layout [137] of the LHC, subdivided into two beam pipes and eight octants with four beam interaction points, indicated by blue stars.

The particles are filled in bunches into the accelerator which can host at nominal operation up to 2,808 proton bunches with a bunch spacing of 25 ns that translates to a distance of about 7.5 m. The maximum bunch intensity is restricted to about $1.15 \cdot 10^{11}$ protons, limited by the geometrical aperture of the LHC [128]. Approximately 362 MJ of energy is hence stored by the beams and about 600 MJ are stored in the magnetic system of the LHC, requiring an efficient beam loss system [138] in case of technical issues, if bunches leave their dedicated orbits, if a magnet quenches or in case of any other emergency. Running with heavy ions, the LHC has been able to operate up to 518 bunches per beam with about 10^8 lead ions per bunch, exceeding the design luminosity at IP1 by a factor of approximately four [139].

Several preacceleration steps are needed to exceed the minimum momentum, determined by the beam rigidity of the LHC, before the particle bunches may finally be injected into the LHC which is then capable of accelerating them up to the nominal energies. The following Fig. 3.1.2 shows the latest overview of the full accelerator complex at CERN which includes the full preaccelerator chain used to feed particle bunches into the LHC.

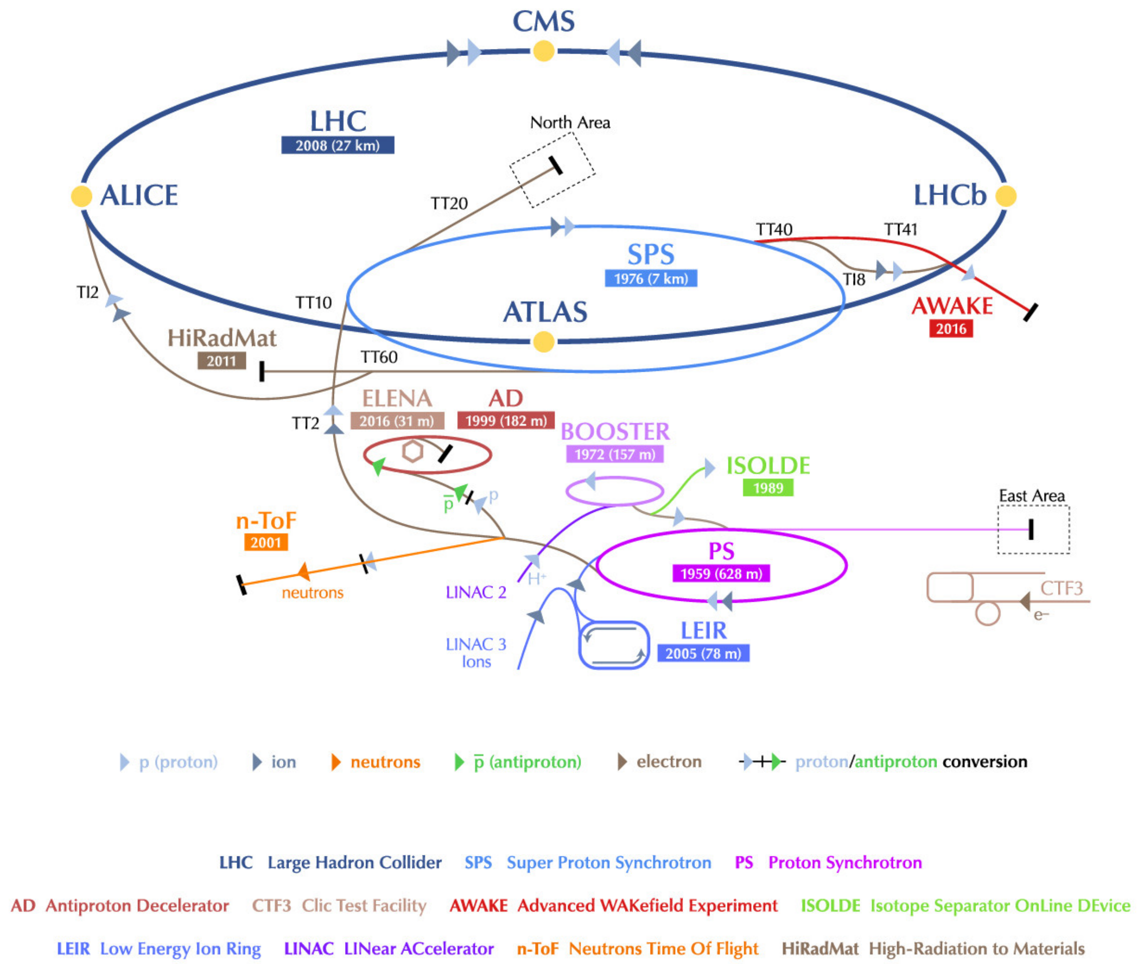

Figure 3.1.2: An overview [140] of the full accelerator complex at CERN including the LHC, hosting the four main experiments ALICE, ATLAS, CMS and LHCb.

There are different preacceleration chains employed to deliver beams of protons and heavy ions to the LHC. The protons are obtained from a bottle of hydrogen gas which is connected to a duoplasmatron proton source [141] that feeds LINAC 2. Further preacceleration steps are carried out with help of the BOOSTER, the PS and the SPS, as it can be followed with nominal endpoint energies quoted in brackets:

PROTONS ▷ LINAC 2 (50 MeV) → BOOSTER (1.4 GeV) → PS (26 GeV) → SPS (450 GeV)

Lead ions are extracted from a Electron Cylcotron Resonance Ion Source (ECRIS) [141] from isotopically pure solid lead which are fed into LINAC 3 that accelerates the particles up to 4.2 MeV per nucleon. The subsequent step involves the Low Energy Ion Ring (LEIR), after which the same accelerators are used as for the protons; the PS and the SPS:

HEAVY IONS $\triangleright$ LINAC 3 (4.2 MeV/u) $\rightarrow$ LEIR (72 MeV/u) $\rightarrow$ PS (5.9 GeV/u) $\rightarrow$ SPS (177 GeV/u)

The beam energies reached at the SPS are finally high enough to be able to feed the beams into the LHC which is then able to circulate them. The injection into the LHC is realized by the transfer lines Tl2 and Tl8, see Fig. 3.1.2, each of a length of approximately 2.5 km which are used to populate both beam pipes with bunches. As soon as the desired bunch scheme has been injected, it takes a minimum of 20 min to ramp up the beam energies to the nominal center of mass energies of 7 TeV for protons and 2.56 TeV/u for heavy ions.

3.2 The ALICE Experiment

ALICE (A Large Ion Collider experiment) [129] is the only major experiment at the LHC which is dedicated to the study of heavy-ion collisions. Its most challenging design goals were defined by the huge track densities of up to $\mathrm{d}N/\mathrm{d}y \approx 8,000$ particles at mid-rapidity which were predicted during its design phase [142] for central heavy-ion collisions at LHC energies. In addition, the experiment is able to perform full reconstructions of such events, still being able to reconstruct trajectories of charged particles down to lowest transverse momenta of $p_{\mathrm{T}} \approx 100\,\mathrm{MeV}/c$ up to $100\,\mathrm{GeV}/c$ while serving excellent Particle Identification (PID) capabilities with many different techniques up to $20\,\mathrm{GeV}/c$. Furthermore, the ALICE experiment features two different calorimeters to reconstruct neutral particles and enables the reconstruction of photon candidates via conversions within the detector material because of its excellent tracking capabilities. These requirements, together with the spatial restrictions of the old LEP magnet being reused for ALICE, led to a unique design of the detector highlighting the world's largest TPC to perform reliable tracking down to lowest momenta. The ALICE apparatus has dimensions of about $16 \times 16 \times 26\,\mathrm{m}^3$ with a total weight of about 10,000 t. A schematic of the complete apparatus is shown in Fig. 3.2.3. An extensive set of documentation concerning the sub-detector systems of ALICE with special focus on the excellent physics performance that has been achieved can be found in Refs. [143–145].

3.2.1 Detectors

Three major parts of ALICE can be identified which are used to categorize all sub-detector systems: the central barrel detectors, the forward detectors and the MUON spectrometer. The following Tab. 3.2.1 lists all detectors belonging to the central barrel, further quoting their nominal acceptances and radial positions. In addition, the material thickness of each detector is given in units of X/X_0 relative to the radiation length X_0 [32], since these values are of importance for the photon-related measurements reported in this thesis. Subsequently, the forward detectors and the MUON spectrometer are introduced in Tab. 3.2.2 which complete the list of sub-detectors of ALICE. The discussion of these parts is restricted to their essential elements as the central barrel plays the main role in the context of this thesis. Both Tab. 3.2.1 and Tab. 3.2.2 list the main purposes of each sub-detector system of ALICE and cite the respective Technical Design Reports (TDRs) where further details may be found about each system.

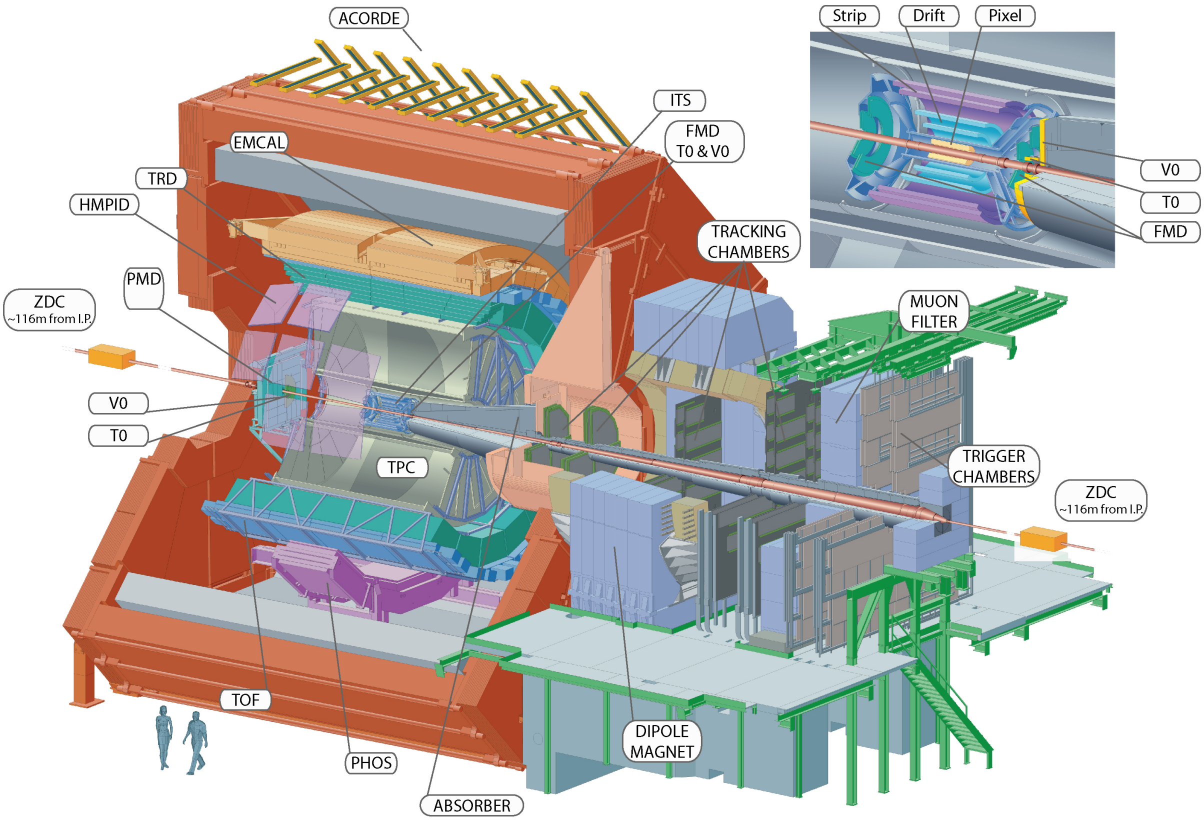

Figure 3.2.3: The ALICE experiment with its sub-detector systems [146] as installed in 2012. The central barrel detectors (ITS, TPC, TRD, TOF, EMCal (DCal), PHOS and HMPID) are located within the solenoid magnet while the forward detectors (V0, T0, PMD, FMD and ZDC) are also shown together with the MUON spectrometer which features a large dipole magnet. In addition, the cosmic ray trigger ACORDE is positioned on top of the solenoid magnet.

The Central Barrel

The central barrel detectors cover polar angles of 45° to 135° around the nominal center of ALICE defined at the IP2 [147]. They are mounted on the space frame [148] and are located within the huge solenoid magnet [149], shown in red color in Fig. 3.2.3. This magnet is often named "L3 magnet" since it had already been used for the L3 experiment [150] at LEP before. ALICE decided to reuse the solenoid which is the biggest normal conducting magnet in the world, having 150 MJ of magnetic energy stored at its design parameters with an operating current of 30 kA [129]. The solenoid coil is surrounded by an iron yoke, which can be seen in red color in Fig. 3.2.3, and is closed at its ends by two poles equipped with hinged doors. The magnet weighs about 7,800 t and generates a nominal magnetic field of $B = 0.5\,\mathrm{T}$. It is a central component of the tracking system as the B field causes the charged particle trajectories to bend by the Lorentz force, enabling measurements of their momenta by the central tracking detectors. The central barrel features further detector systems to provide PID and photon reconstruction on that basis. A complete list of central barrel detectors can be found in the following Tab. 3.2.1, after which detailed descriptions of the respective sub-detector systems follow.

	detector	acceptance polar	acceptance azimuthal	position r (cm)	X/X_0 $\sim$ (%)	main purpose
central barrel	ITS [151]					
	SPD	$\|\eta\| < 2.0$	full	3.9	1.14	tracking, vertex
		$\|\eta\| < 1.4$	full	7.6	1.66	tracking, vertex
	SDD	$\|\eta\| < 0.9$	full	15.0	1.38	tracking, PID
		$\|\eta\| < 0.9$	full	23.9	1.26	tracking, PID
	SSD	$\|\eta\| < 1.0$	full	38	1.36	tracking, PID
		$\|\eta\| < 1.0$	full	43	0.86	tracking, PID
	TPC [152]	$\|\eta\| < 0.9$	full	85 – 247	3.50	tracking, PID
	TRD [153]	$\|\eta\| < 0.8$	full	290 – 368	23.4	track., PID, trig.
	TOF [154, 155]	$\|\eta\| < 0.9$	full	370 – 399	29.5	PID
	EMCal [156]	$\|\eta\| < 0.7$	$80° < \varphi < 187°$	430 – 455	$2 \cdot 10^3$	photons, trigger
	DCal [157]	$0.22 < \|\eta\| < 0.7$ $\|\eta\| < 0.7$	$260° < \varphi < 320°$ $320° < \varphi < 327°$	430 – 455	$2 \cdot 10^3$	photons, trigger
	PHOS [158]	$\|\eta\| < 0.12$	$220° < \varphi < 320°$	460 – 478	$2 \cdot 10^3$	photons, trigger
	HMPID [159]	$\|\eta\| < 0.6$	$1.2° < \varphi < 58.8°$	490	18.0	PID

Table 3.2.1: The sub-detectors of ALICE located in the central barrel, all values are taken from the quoted TDRs for each detector and Ref. [129]. The geometrical acceptances of the detectors are given in addition to their radial positions with respect to the nominal center of ALICE which is specified in the definition of the ALICE coordinate system [147]. The main purposes of the detectors are listed as well as their material thicknesses measured in X_0 which are important in the context of photon measurements, see Chap. 5. The given values for the ITS include its thermal shielding and support structures.

Inner Tracking System (ITS):
The ITS [160] is one of the major tracking detectors of ALICE. It is composed of six cylindrical layers of silicon detectors using three different detector techniques, each installed at two neighboring layers as shown in Fig. 3.2.4a. The two innermost layers use silicon pixel technology. The Silicon Pixel Detector (SPD) closely surrounds the beam pipe, made out of a beryllium cylinder of 800 μm thickness, for which it provides mechanical support. The pixel design was chosen since it offers the highest granularity and good spatial resolution in z-direction which is of highest importance because of the vicinity to the interaction point where highest track densities of up to 50 tracks/cm^2 may be present. Furthermore, it is a fundamental element to localize the primary vertex as well as for the measurement of impact parameters of secondary tracks from weakly decaying particles [143]. The two intermediate layers are made of drift detectors which form the Silicon Drift Detector (SDD). The SDD features a very good multitrack capability with a very high spatial resolution in z-direction. Moreover, it provides two of the four dE/dx samples for the PID capability of the ITS. The two outermost layers of the ITS, as shown in Fig. 3.2.4a, compose the Silicon Strip Detector (SSD). It is crucial for the matching of tracks between ITS and TPC for which it was designed to provide optimal performance. Furthermore, the SSD is optimized for low mass in order to minimize X/X_0 to reduce multiple scatterings and it additionally provides two dE/dx samples for the PID. All radial positions as well as the acceptances of the different sub-detector systems of the ITS can be obtained from Tab. 3.2.1 which also lists the respective material thickness of each layer measured in X/X_0.

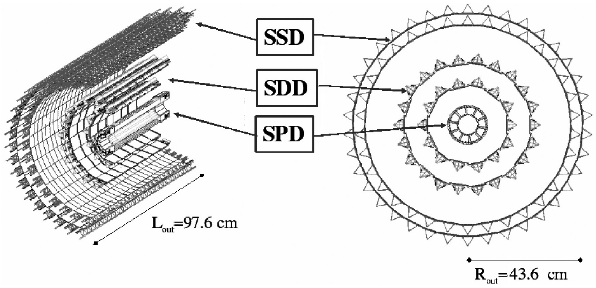

a)

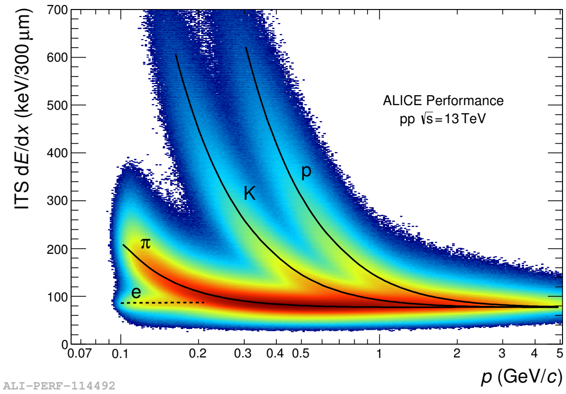

b)

Figure 3.2.4: a) A schematic [161] of the sub-structure of the ITS which is composed of SPD, SDD and SSD. b) A performance plot for pp collisions at $\sqrt{s} = 13\,\mathrm{TeV}$ [162] showing the PID capabilities of the ITS at lowest momenta, being able to separate electrons/positrons, charged pions, kaons and protons in that region.

Combining the information of the different sub-systems, the ITS is able to localize the primary vertex with a resolution of better than $100\,\mu$m and is able to reconstruct secondary vertices from weak decays from strange, charm and beauty particles, for which the impact parameters of the secondary tracks can be measured with a resolution of better than $60\,\mu$m in the $r\varphi$-plane for $p_{\mathrm{T}} > 1\,\mathrm{GeV}/c$ [129]. Furthermore, the ITS improves the momentum and angle resolution for particles reconstructed by the TPC as it participates in the global tracking in ALICE. Additionally, it provides the possibility for standalone tracking to cover dead regions of the TPC and to track and identify tracks with low momenta as it is shown in Fig. 3.2.4b. The PID capabilities of the ITS are based on its outer four layers which provide a measurement of the ionization energy loss of traversing particles, from which the $\mathrm{d}E/\mathrm{d}x$ values are determined, hence complementing the excellent tracking capabilities of the TPC.

Time Projection Chamber (TPC):
The TPC [163] is the main tracking detector of ALICE which is optimized to provide a good two-track separation, reliable PID capabilities and a solid vertex determination in environments of high track densities of more than 10,000 charged particles within acceptance at the same time. It covers a phase space of $|\eta| < 0.9$ in pseudo-rapidity for tracks with full radial track lengths from the ITS to the TRD with a full coverage of the azimuth, only short of the dead regions. A schematic drawing of the detector is shown in Fig. 3.2.5a. The TPC consists of the field cage and the readout chambers at its end plates, defining a gas volume of about $90\,\mathrm{m}^3$ which had been filled with Ne-CO_2-N_2 (85.7 % − 9.5 % − 4.8 %) during the first year of detector operation. In 2011, the nitrogen was removed after a year of data taking since it did not have the desired impact on the stable operation of the detector, leaving a gas mixture of Ne-CO_2 (90 % − 10 %) for the remainder of the first LHC run. For the second LHC run, the nitrogen was replaced by argon, which unfortunately led to strong space charge distortions [164] so that the well-proven gas mixture Ne-CO_2 has been restored in the end. The field cage has an inner radius of about 85 cm, determined by the maximum acceptable hit density, and an outer radius of about 247 cm which is required to achieve a $\mathrm{d}E/\mathrm{d}x$ resolution of better than 5 − 7 %. Its overall length along the beam direction is 500 cm, in which the cage is divided into two parts by the central HV

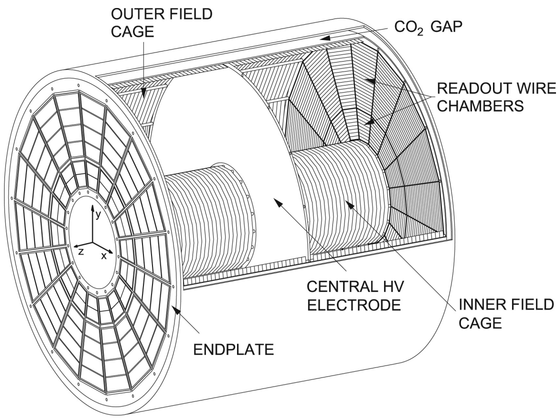

a)

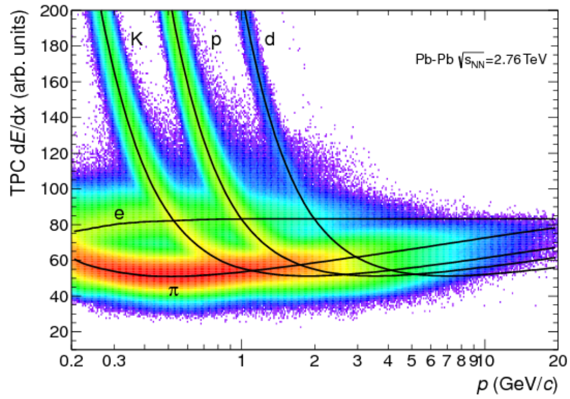

b)

Figure 3.2.5: a) A schematic drawing [163] of the TPC, giving insight into the drift volume which is limited by the inner/outer field cages as well as the readout chambers. b) An example plot from Pb-Pb collisions at $\sqrt{s_{\mathrm{NN}}} = 2.76\,\mathrm{TeV}$ [145] showing the performance of $\mathrm{d}E/\mathrm{d}x$ measurements of charged particles by the TPC.

electrode, an aluminized Mylar foil of $22\,\mu$m thickness. Between the electrode and the end plates of the TPC a voltage of 100 kV is applied which results in a drift field of 400 V/cm. Therefore, ionization electrons move towards the end plates with a drift velocity of $2.65\,\mathrm{cm}/\mu\mathrm{s}$, resulting in a maximum drift time of $94\,\mu$s [163]. The end plates are segmented in 18 sectors in φ with two readout chambers per sector. A pad readout of the chambers is realized using the Multi-Wire Proportional Chamber (MWPC) technique, yielding a total of 557,568 readout channels. Therefore, the spatial arrival points of the ions can be precisely measured, giving access to the projection of the particles trajectory in the $r\varphi$-plane. A maximum of 159 space points are theoretically reconstructable, depending on how many pads the particles trajectory traverses. In addition, an accurate measurement of the arrival times of ionization electrons is performed so that the full trajectory in 3D space can be determined. In the present case, the drifting ions are created by charged particles traversing the active volume of the TPC, ionizing the gas molecules inside the field cage via electromagnetic interactions. The particles energy loss can be described by the Bethe-Bloch formula [32] which is valid for heavy ($\mathrm{m} \gg \mathrm{m}_e$), charged particles which traverse matter. Using the representation proposed by the ALEPH collaboration [165], the energy loss per path length $\mathrm{d}E/\mathrm{d}x$ is hence parameterized by the following formula:

$$f(\beta\gamma) = \frac{A}{\beta^D}\left(B - \beta^D - \ln\left(C + \frac{1}{(\beta\gamma)^E}\right)\right), \tag{3.2.1}$$

where β is the particles velocity, γ its Lorentz factor and A to E are fit parameters. An example of a $\mathrm{d}E/\mathrm{d}x$ measurement in Pb-Pb collisions at $\sqrt{s} = 2.76\,\mathrm{TeV}$ is shown in Fig. 3.2.5b, where the black lines correspond to the parameterizations of the $\mathrm{d}E/\mathrm{d}x$ curves for different particle species using Eq. 3.2.1. The achieved resolution of the $\mathrm{d}E/\mathrm{d}x$ for isolated tracks is 5 %, whereas for the nominal design goal of $\mathrm{d}N/\mathrm{d}y \approx 8,000$ a resolution of 6.8 % can still be accomplished. Furthermore, reliable tracking can be performed down to $100\,\mathrm{MeV}/c$ for primary tracks and $50\,\mathrm{MeV}/c$ for secondary tracks, reaching position resolutions of 1100 to $800\,\mu$m in $r\varphi$ and 1250 to $1100\,\mu$m in z-direction for inner and outer radii respectively. To reduce multiple scattering, a low material budget of only $X/X_0 = 13\,\%$ up to the radial endpoint of TPC could be realized.

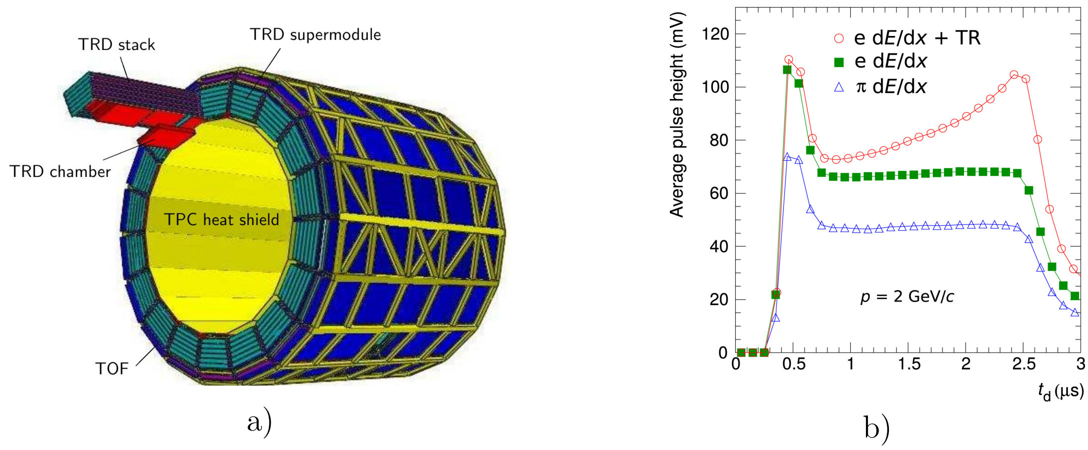

Figure 3.2.6: a) The schematic layout [129] of the TRD detector is shown for which one supermodule is displaced from its original position in the space frame to visualize its stacks and chambers. The outer side of the TRD is surrounded by the TOF detector which follows the same segmentation into 18 modules. b) The characteristic signals [166] generated by $e^{\pm}$ and $\pi^{\pm}$ which are used for PID purposes.

Transition Radiation Detector (TRD):
The TRD [166] provides electron identification in the central barrel for $p > 1\,\mathrm{GeV}/c$ and also makes a fast trigger for charged particles with high momenta available in order to enhance the number of recorded jets or high-p_{T} J/ψ, for example. It is located in the space frame, as shown in Fig. 3.2.6a, and segmented in φ into 18 so-called supermodules which are composed of 30 readout chambers arranged in five stacks along z and six layers in radius r. The readout chambers are subdivided into a radiator, a drift section and an amplification region. The signal is obtained by MWPC chambers with pad readout with an overall channel count of $1.18 \cdot 10^6$ of the full TRD detector. The chambers are filled with a gas mixture, Xe-C0_2 (85 % − 15 %), which traversing charged particles ionize. In addition, particles exceeding the threshold for TR production of about $\gamma \approx 1000$ will produce in average 1.45 X-ray photons in the energy range of 1 to 30 keV within the radiator which are converted with high efficiency by the high-Z counting gas Xenon. All electrons from regular ionization processes as well as the electrons from X-ray conversions will drift towards the amplification region where a gas amplification in the vicinity of the anode wires takes place which induces the signal on the readout pads. Fig. 3.2.6b shows the characteristic signals which electrons and pions generate. The discrimination of electrons can be achieved via their increased energy loss $\mathrm{d}E/\mathrm{d}x$ and the absorption of TR photons predominantly at the beginning of the drift section, hence causing the signal peak at larger drift times. The design goal for the pion rejection capability was in the order of a factor of 100 for momenta above $1\,\mathrm{GeV}/c$ but finally 410 could be achieved for p-Pb collisions [166]. Furthermore, the TRD takes part in the global track reconstruction of ALICE for which it provides input at large radial positions, thus improving the resolution for high track momenta by about 40 % [166].

Time-Of-Flight Detector (TOF):
The TOF detector enables PID for the intermediate momentum region to distinguish between pions, kaons and protons. In that region, a separation power better than $3\,\sigma$ for π/K and K/p is obtained. The detector is installed within the space frame and follows the TRD as the subsequent detector system in radial direction as indicated in Fig. 3.2.6a. It is segmented into

18 sectors in φ, so-called supermodules, each consisting of five modules in z-direction. Due to the large area of about $160\,\mathrm{m}^2$ which needs to be covered, a gaseous detector design was chosen. Every module consists of a group of Multi-gap Resistive Plate Chamber (MRPC) strips closed inside a box which defines and seales a gas volume, summing up to a total volume of $17.5\,\mathrm{m}^3$ for all modules being filled a with mixture of $C_2H_2F_4$-(i-C_4H_{10})-SF_6 (90 % – 5 % – 5 %). Any ionization of a traversing charged particle starts an avalanche process, driven by an applied high voltage (HV) of 13 kV, and generates a signal on the pick-up electrodes. In total, there are 157,248 readout channels available for the complete TOF detector. Since there is no drift time associated with the movement of electrons in an electric field, a time jitter is solely caused by fluctuations in the growth of the avalanche. With the given detector design, an intrinsic time resolution of better than 40 ps is accomplished with an efficiency close to 100 %.

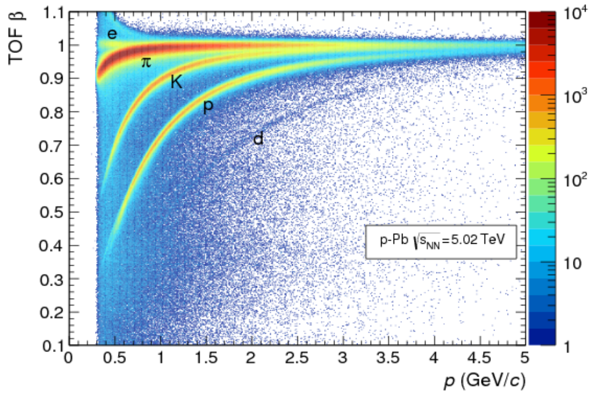

Figure 3.2.7: A performance plot [145] showing an example of the PID capabilities of the TOF detector for p-Pb collisions at $\sqrt{s_{\mathrm{NN}}} = 5.02\,\mathrm{TeV}$, being able to separate π, K and p.

Electromagnetic Calorimeter (EMCal) / Di-jet Calorimeter (DCal):
The EMCal [167] detector allows the measurement of high momentum photons and electrons, thus enabling the reconstruction of particles decaying via electromagnetic processes like neutral, light mesons for example. Furthermore, it provides access to the neutral energy component of jets, making their full reconstruction possible. In addition, it offers a fast and efficient trigger for jets as well as for photons and electrons. The EMCal is a sampling electromagnetic calorimeter, constructed in a so-called shashlyk [168] design. Its active elements, also referred to as cells, are composed of 77 alternating layers of lead and plastic scintillator [169]. The material thickness per layer is 1.44 mm for the lead absorber and 1.76 mm for the active scintillating part, resulting in an average density of $5.68\,\mathrm{g/cm}^3$ of the complete detector material. Adding up all layers, the total length of a cell is found to be 24.6 cm which can also be measured in radiation length X_0 [32], where $20.1\,X_0$ is found. Such a high value is required to contain the full electromagnetic shower within the active detector material. High energetic photons and electrons/positrons entering the detector create such a shower which usually spreads over multiple adjacent cells which can be grouped into so-called clusters to reconstruct the particle's energy. Heavier particles, on the other hand, do not create showers and, hence, loose their energy only partly as they are either minimum ionizing (Minimum Ionizing Particles (MIPs)) or they only exhibit hadronic interactions in case they are neutral. The deposited energy into the active elements of the calorimeter is converted into scintillation light by fluorescence processes involving benzene ring molecules, an organic scintillator [170]. Each cell of the EMCal has a size of $\Delta\eta \times \Delta\varphi = 0.0143 \times 0.0143$ which translates to a sensitive surface of about $\sim 6.0 \times 6.0\,\mathrm{cm}^2$, corresponding to approximately twice the Molière radius of R_M=3.2 cm. This radius is a measure of the transverse dimension of the electromagnetic shower, defined as the radius of a cylinder containing on average 90 % of the shower's energy deposition. The scintillation light in each layer is collected by wavelength shifting fibers perpendicular to the face of each cell that cross all active layers. A $5 \times 5\,\mathrm{mm}^2$ active area Avalanche Photodiode (APD) is used for every cell

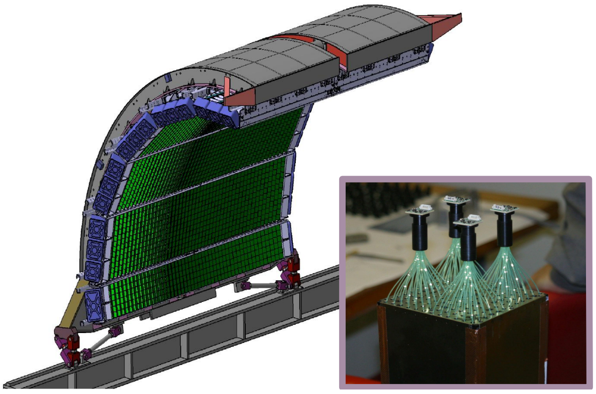

a)

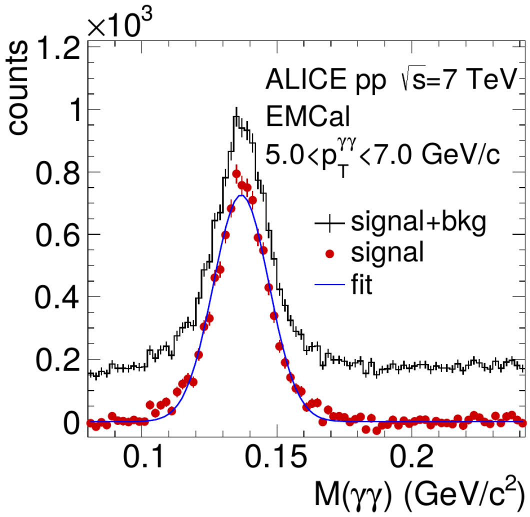

b)

Figure 3.2.8: a) A schematic drawing of the EMCal detector [167] as it is installed in ALICE. The single modules are visible which compose the supermodules. Within the box, one example module [156] is shown for which the enclosing structure was removed. The wavelength shifting fibres from the four different cells can be seen which compose one module. b) The performance of the EMCal [145] is demonstrated for pp collisions at $\sqrt{s} = 7\,\text{TeV}$. A clear π^0 peak can be seen for the given p_T interval.

to detect the generated scintillation light which is guided by the fibres towards the APDs. The EMCal is structured into modules which consist of groups of 2×2 cells. The modules are further combined into arrays of 12×24 modules called supermodules. In total, there are ten full and two one-third-sized EMCal supermodules installed, covering $\Delta\varphi = 107°$ in azimuth and $|\eta| < 0.7$ in pseudorapidity with a total number of 12,288 cells [167]. A schematic drawing of the EMCal is shown in Fig. 3.2.8a, where the full EMCal is shown with its mechanical support structures. The single modules can be identified which are drawn in green color. Furthermore, an example of a module is shown which is the smallest building block of the EMCal, for which the separation into the four cells is clearly visible by following the wavelength shifting fibres. The EMCal detector is located at a radial distance of 4.28 m at the closest point from the nominal collision vertex. Its intrinsic energy resolution is parametrized as follows:

$$\frac{\sigma_E}{E} = \frac{4.8\%}{E} \oplus \frac{11.3\%}{\sqrt{E}} \oplus 1.7\%, \tag{3.2.2}$$

with E in units of GeV [167]. The performance of the EMCal is exemplified by the invariant mass distribution of π^0 meson candidates shown in Fig. 3.2.8b, whose width relates to the energy resolution quoted in Eq. 3.2.2 that is expectedly larger than the width observed for the high-resolution PHOS, see Eq. 3.2.3 and Fig. 3.2.9b. The EMCal is complemented by the DCal [157] which is installed across the space frame, 180° in azimuth away from the EMCal, surrounding the PHOS modules as shown in Fig. 3.2.9a. The DCal enables the possibility to fully reconstruct jets which are emitted back-to-back with $\Delta\varphi = 180°$. It follows the same specifications as the EMCal with the difference that only 12×16 modules compose a supermodule. The detector covers $\Delta\varphi = 60°$ with $\pm 0.22 < \eta < \pm 0.7$, at the same time the maximum back-to-back coverage available. In addition, there are two more modules installed covering $\Delta\varphi = 7°$ with $|\eta| < 0.7$.

Photon Spectrometer (PHOS):
The PHOS [129] spectrometer is an electromagnetic calorimeter enabling the measurement of high momentum photons and electrons independent from the EMCal. In principle, the same measurements can be carried out as with the EMCal, although much better position and energy resolutions are reached given the downside of a very limited acceptance in comparison. However, the excellent energy resolution allows to strengthen the focus on the low p_{T} region which is of particular interest for the measurement of thermal photons radiated by a QGP, for example, but also to push neutral meson spectra measurements to lower p_{T}. In addition, the PHOS also provides triggering capabilities to enhance the collected statistics at high p_{T}.

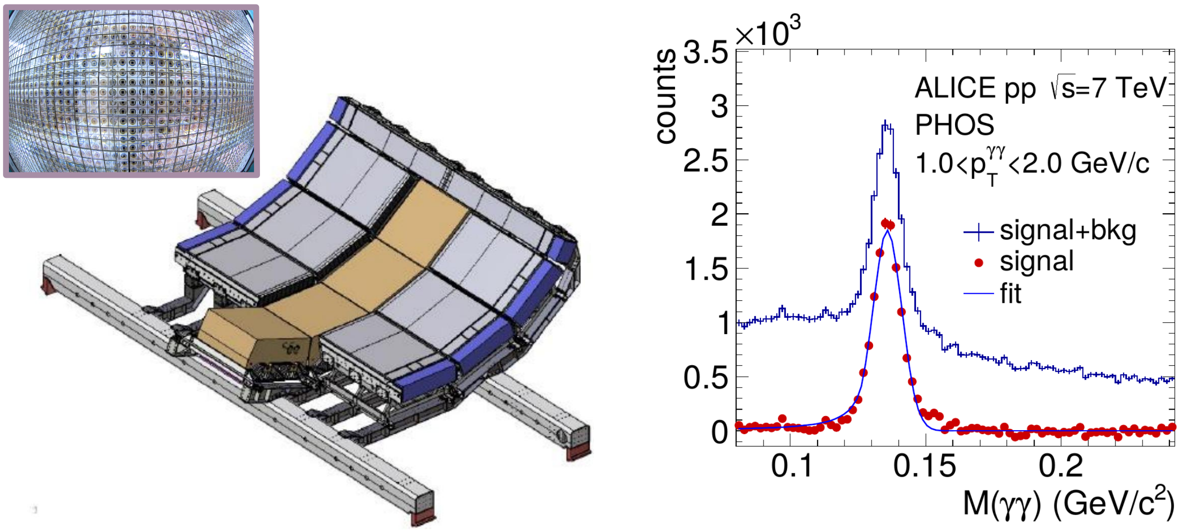

a) b)

Figure 3.2.9: a) A schematic drawing of the PHOS detector [171], shown in brown color, as it is currently installed in ALICE with 3½ active modules, see Tab. 3.2.4. The DCal is displayed in light blue color, surrounding the PHOS modules. Within the box, a photograph of one full PHOS module [172] is shown, where the single crystals as well as the readout APDs can be clearly identified. b) An illustration of the performance of the PHOS [145]. A narrow π^0 peak is observed for the given low p_{T} interval due to the excellent energy resolution of the PHOS.

The PHOS detector is a homogeneous electromagnetic calorimeter composed of lead tungstate, $PbWO_4$, crystals. These crystals are the active elementary units which are also called cells. They have dimensions of $\Delta\eta \times \Delta\varphi = 0.004 \times 0.004$ translating to $\approx 2.2 \times 2.2\,\mathrm{cm}^2$. Thus, the lateral dimension of the cells is slightly larger than the $PbWO_4$ Molière radius of $\mathrm{R}_M = 2\,\mathrm{cm}$. The crystals have a length of 18 cm which is $20\,X_0$ expressed in radiation lengths. The detector is structured into modules consisting of an array of 56×64 cells that add up to 3,584 crystals in total for one module. In nominal configuration, there are five modules installed yielding a total number of 17,920 crystals being operated. Therefore, the spectrometer covers $\Delta\varphi = 100°$ in azimuth and $|\eta| < 0.12$ in pseudorapidity and is located at a distance of 4.6 m from the IP. In contrast to the EMCal, the PHOS uses anorganic scintillator [170] material, in which the scintillation process is due to the electronic band structure found in crystals. The $PbWO_4$ acts as an absorber as well as active material at the same time. The scintillation light generated within the crystals is detected using APDs with an active area of $5 \times 5\,\mathrm{mm}^2$. The crystals are operated at a temperature of $-25°C$, at which the light yield of $PbWO_4$ increases by about a factor of three compared to room temperature. The energy resolution of the PHOS is parameterized by the following formula:

$$\frac{\sigma_E}{E} = \frac{1.8\%}{E} \oplus \frac{3.3\%}{\sqrt{E}} \oplus 1.1\%, \tag{3.2.3}$$

where E is given in units of GeV. The TRD and TOF detectors are partly not installed in front of PHOS in order to minimize the material budget for the high resolution calorimeter. Additionally, a Charged Particle Veto (CPV) [173] is foreseen for all PHOS modules which was installed during LS1 in front of only one module for testing purposes. A CPV adds 5 % of X/X_0 and uses MWPCs filled with a gas mixture of Ar-CO_2 (80 %−20 %). It reaches a charged particle detection efficiency of better than 99 %. Thus, it is possible to efficiently distinguish between charged and neutral particles hitting the calorimeter, further being able to increase the signal to background ratio.

High Momentum Particle Identification Detector (HMPID):
The HMPID is dedicated to inclusive measurements of identified hadrons for $p_T > 1\,\mathrm{GeV}/c$. It enhances the PID capabilities of ALICE beyond the momentum interval accessible through energy-loss measurements by the ITS and the TPC and time-of-flight measurements by the TOF, extending the π/K and K/p discrimination up to higher p_T.

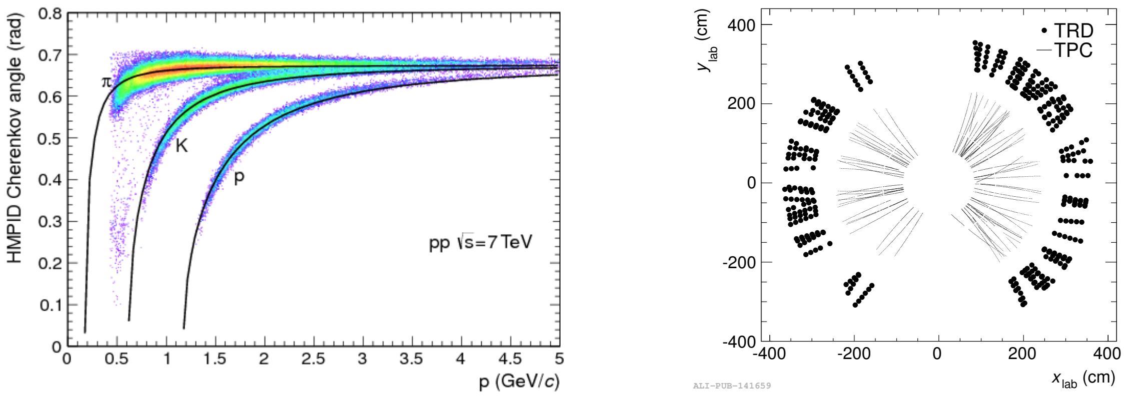

a) b)

Figure 3.2.10: a) The PID performance [145] of the HMPID is indicated in this figure for pp collisions at $\sqrt{s} = 7\,\mathrm{TeV}$. The particle species π, K and p can be clearly separated up to momenta of several GeV/c. b) The track matching performance [166] of TPC to TRD is visualized by the reconstructed tracklets of each detector system. The lines represent cosmic muons traversing the central barrel of ALICE, which were recorded with help of the muon trigger provided by ACORDE.

The HMPID is based on proximity-focusing Ring Imaging Cherenkov (RICH) counters and consists of seven modules of about $1.5 \times 1.5\,\mathrm{m}^2$ each which are fixed to the space frame. The modules contain radiators with a 15 mm thick layer of low chromaticity C_6F_{14} liquid with an index of refraction of $n = 1.2989$ at $\lambda = 175\,\mathrm{nm}$. Particles that travel faster than the speed of light in the radiator hence emit Cherenkov photons which are detected by a photon counter. For this purpose, a thin layer of CsI, acting as photon converter, is deposited onto the pad cathode of a MWPC. The full detector has an acceptance of 5 % of central barrel phase space, covering

$\Delta\varphi = 57.6°$ in azimuth and $|\eta| < 0.6$ in pseudorapidity. The PID performance of the HMPID concerning separation of π, K and p is shown in Fig. 3.2.10a.

The Forward Detectors, the MUON spectrometer and ACORDE

The forward detectors, composed of five independent systems, are used for triggering purposes, event characterization and calibration. Moreover, a MUON spectrometer is available in ALICE, offering acceptance in the forward rapidity region which is able to detect and reconstruct muons. Part of this spectrometer is a large dipole magnet [129], placed 7 m away from the IP, which is in fact the largest warm dipole magnet in the world. It has a weight of about 835 t and a 6 kA operating current is needed to provide a magnetic field of $B = 0.67\,\mathrm{T}$ at the center of its coils [174]. This magnetic field is of crucial importance for the MUON spectrometer since it enables the determination of muon momenta. In addition, the cosmic ray trigger ACORDE complements the detector sub-systems of ALICE, enabling the measurement of cosmic muons with the central barrel detectors in order to carry out alignment and calibration processes. The following Tab. 3.2.2 summarizes all ALICE sub-detectors introduced in this paragraph, after which short descriptions of the respective detectors follow.

	detector	acceptance polar	acceptance azimuthal	main purpose
forward	V0 [175]			
	V0A	$2.8 < \eta < 5.1$	full	charged particles, trigger
	V0C	$-3.7 < \eta < -1.7$	full	charged particles, trigger
	T0 [175]			
	T0A	$4.6 < \eta < 4.9$	full	time, trigger
	T0C	$-3.3 < \eta < -3.0$	full	time, trigger
	PMD [176, 177]	$2.3 < \eta < 3.9$	full	photons
	FMD [175]			
	FMD1	$3.6 < \eta < 5.0$	full	charged particles
	FMD2	$1.7 < \eta < 3.7$	full	charged particles
	FMD3	$-3.4 < \eta < -1.7$	full	charged particles
	ZDC [178]			
	ZN	$\|\eta\| > 8.8$	full	forward neutrons
	ZP	$6.5 < \eta < 7.5$	$\|\varphi\| < 10°$	forward protons
	ZEM	$4.8 < \eta < 5.7$	$\|2\varphi\| < 32°$	photons
muon	MCH [179, 180]	$-4 < \eta < -2.5$	full	muon tracking
	MTR [179, 180]	$-4 < \eta < -2.5$	full	muon trigger
	ACORDE [181]	$\|\eta\| < 1.3$	$30° < \varphi < 150°$	cosmics

Table 3.2.2: The five independent forward detectors and the two muon-related detectors of ALICE: the MUON spectrometer and ACORDE. The geometrical acceptances of the detector systems are given in addition to naming their main purposes. Furthermore, the TDRs for the different detectors are cited.

Forward Detectors:
The V0 detector is a small angle detector composed of two arrays of scintillator counters, called

V0A and V0C, installed on either side of the ALICE IP. In this context, C-side which stands for clockwise with respect to the LHC ring, where the MUON spectrometer of ALICE is located, seen in right part of Fig. 3.2.3. Hence, A-side refers to counter-clockwise direction from the IP and the left side of ALICE in Fig. 3.2.3. The V0 provides Minimum Bias (MB) triggers for the central barrel detectors and also serves as an indicator of centrality of heavy-ion collisions via the multiplicity recorded in the event. Furthermore, it is used to trigger on centrality by cutting on the number of fired counters and the total charge seen by the detector. Moreover, it participates in luminosity measurements. The V0A is located 340 cm from the IP and the V0C is fixed to the front face of the MUON absorber, therefore being installed at a distance of 90 cm from the IP. The peusdorapidity ranges covered of both detectors are given in Tab. 3.2.2 which are segmented into 32 individual counters each, distributed in four rings and eight sectors. The detector material consists of BC-404 [175] plastic scintillator based on polyvinytoluene. Charged particles arising from initial collisions but also from various background sources will cross the detector material and generate scintillation light which is guided by wavelength shifting fibres with 1 mm in diameter to Photomultiplier Tubes (PMTs) reading out the signal.

The T0 detector determines the real time of the collision to provide the start time for the TOF detector and a wake-up signal for the TRD detector. In addition, it measures the primary vertex position for each interaction and provides a fast trigger signal if the position is within preset values in order to discriminate background in form of beam-gas interactions. Moreover, it offers redundancy for the V0 detector as it may also provide a MB trigger signal as well as multiplicity triggers. The T0 detector consists of two arrays of Cherenkov counters with 12 counters per array. The signal is read out by PMTs which are coupled to quartz radiators of each 20 mm in diameter and thickness. The T0C is placed 72.7 cm away from the IP, whereas the T0A is located at a distance of about 375 cm. Both detectors are mounted as close as possible to the beam pipe to maximize efficiency.

The Photon Multiplicity Detector (PMD) is able to measure the multiplicity and spatial distribution of photons in the forward pseudorapidity region of $2.3 < \eta < 3.7$. It can provide estimates of the transverse electromagnetic energy and the reaction plane. Fur this purpose, the detector exhibits a preshower method involving a converter of $3\,X_0$ thickness which is placed in between two detector planes of high granularity gas proportional counters, for which a mixture of Ar-CO_2 (70 % – 30 %) is used. The first plane is used as CPV and the second for photon PID, reaching a nominal photon purity of 65 %. The proportional counters are operated at a HV of 1,400 V, yielding an efficiency of about 96 % for charged pions at the operating conditions. Both detector planes consist of 24 modules, each containing 4,608 cells, to cover an active area of about $2.59\,\mathrm{m}^2$.

The Forward Multiplicity Detector (FMD) provides charged particle multiplicity measurements in the forward pseudorapidity regions quoted in Tab. 3.2.2. It enables to study multiplicity fluctuations event-by-event, the determination of reaction plane and to perform particle flow analysis. It is separated into FMD1, FMD2 and FMD3, consisting of one, two and two detector rings respectively. Such a detector ring is composed of silicon sensors, segmented into different number of strips depending on the ring location [175] with radii of 4.2 cm up to 28.4 cm. Their inner and outer radii are constrained by the beam pipe and the inner radius of the TPC, compromising a total number of channels of 51,200.

The Zero Degree Calorimeter (ZDC) measures the energy carried in forward direction by spectator nucleons that do not take part in the actual collision in order to estimate the number of participant nucleons which is directly related to the geometry of a AA collision. This centrality information is also used for triggering purposes and the ZDC is also able to give an estimate of the reaction plane in nuclear collisions. Two sets of hadronic ZDCs are located at 116 m on either side of the IP and two small electromagnetic calorimeters, Zero Degree Electromagnetic Calorimeter (ZEM), are placed at about 7 m from the IP. The ZDC consists of two distinct detectors: the Zero Degree Neutron Calorimeter (ZN) for spectator neutrons, placed at $0°$, and the Zero Degree Proton Calorimeter (ZP) for spectator protons, being displaced to match the deflection of charged particles by the magnetic elements of the LHC beam line. The ZN, the ZP and the ZEM are sampling calorimeters with a dense absorber and active elements, having quartz fibres interspersed in the absorber. These fibres collect the Cherenkov radiation produced by incident particles within the absorber material which is then detected by PMTs.

Muon Spectrometer (MUON):
The MUON spectrometer [182], shown in right part of Fig. 3.2.3, is able to detect and reconstruct muons in the pseudorapidity region $-4 < \eta < -2.5$, enabling the measurement of the complete spectrum of heavy-quark vector-mesons resonances (J/ψ, ψ', Υ, etc.) that decay into muon pairs, $\mu^+\mu^-$. As all the resonances can be measured with the same device, their production rates can be efficiently compared as systematic uncertainties related to the detectors can be partly canceled out for the ratios. Furthermore, the device opens up studies of the production of open heavy flavors. The system can handle high luminosities so that stand-alone data taking is performed together with ZDC, SPD, PMD, T0, V0 and FMD which all can take high rates. In principle, the spectrometer consists of a passive absorber, a tracking system (MCH), the large dipole magnet and the muon trigger chambers (MTR). The absorber is made out of carbon and concrete to limit small-angle scattering, having a length of $60\,X_0$ to efficiently absorb hadrons and photons. Therefore, only muons with a minimum p_T of $4\,\mathrm{GeV}/c$ are able to traverse the full system. Their tracking is performed by the Muon Chambers (MCH) which are composed of five different stations with two planes per station. Each plane consists of a 5 mm gas gap drift MWPC with segmented cathode planes, using a gas mixture of Ar-CO_2 ($80\,\%-20\,\%$), yielding a spatial resolution of $70\,\mu$m in the bending plane. The triggering detector is the Muon Trigger (MTR) which is composed of four Resistive Plate Chamber (RPC) planes arranged in two stations with two planes per station. Each plane consists of 18 RPC modules using a gas mixture of Ar-$C_2H_2F_4$-(i-butane)-SF_6 ($50.5\,\%-41.3\,\%-7.2\,\%-1\,\%$). The system is able to trigger on muons for which the threshold can be varied from $\sim 0.5-2\,\mathrm{GeV}/c$.

ALICE Cosmic Ray Detector (ACORDE):
The ACORDE [183] detector consists of an array of plastic scintillator counters placed on top of the L3 magnet as it can be seen in Fig. 3.2.3. The cosmic ray detector provides a fast trigger signal for commissioning, calibration and alignment procedures for the ALICE detectors. For this purpose, a single atmospheric muon rate of about $4.5\,\mathrm{Hz/m^2}$ is available at the underground level of the ALICE detector. An example of a calibration procedure for TPC and TRD is shown in Fig. 3.2.10b, recorded with help of the ACORDE cosmics trigger, where the trajectories of muons can be followed that traverse the central barrel in order to perform alignment studies and to investigate the track matching performance between the two detector systems. ACORDE is also used to study high-energy cosmic rays for which it is operated in parallel to the data taking of ALICE. The detector consists of 60 modules covering $\Delta\varphi = 120°$ in azimuth and $|\eta| < 1.3$ in pseudorapidity. Each module is composed of two plastic scintillator counters placed on top of each other which are operated in coincidence.

3.2.2 Data Taking Periods by ALICE

The data taking periods performed by ALICE are labeled according to the operation scheme of the LHC which is generally structured in running and shutdown periods. After a long preparation time, LHC Run 1 was carried out from 2009 to 2013 featuring a variety of collision systems as listed in Tab. 3.2.3. This table also lists the current progress regarding LHC Run 2 as well as the planned data taking campaigns by ALICE. Such a campaign may consist of several periods which are represented by the prefix 'LHC', the last two digits of the given year and a single letter that stands for approximately one month of data taking.

LHC	year	system	$\sqrt{s_{(\mathrm{NN})}}$ (TeV)	data taking periods	specialty & running mode
Run 1	2009	pp	0.9/2.36	LHC09a-d	cosmics & commissioning
	2010	pp	0.9	LHC10c	MB
			7	LHC10b-f	
		Pb-Pb	2.76	LHC10h	first Pb-Pb run, MB
	2011	pp	2.76	LHC11a	MB
			7	LHC11c,d	rare triggers
		Pb-Pb	2.76	LHC11h	MB & rare triggers
	2012	pp	8	LHC12a-i	
	2013	p-Pb	5.02	LHC13b-f	first p-Pb run, MB & rare
		pp	2.76	LHC13g	rare triggers
LS1				mid-2013 & 2014	
Run 2	2015	pp	13	LHC15f-k	MB & rare
			5.02	LHC15n	
		Pb-Pb	5.02	LHC15o	record $\sqrt{s_{\mathrm{NN}}}$, MB & rare
	2016	pp	13	LHC16d-e	MB & rare triggers
		p-Pb	5.02	LHC16q,t	
			8	LHC16r,s	record $\sqrt{s_{\mathrm{NN}}}$, MB & rare
	2017	pp	13	LHC17c-m,o,r	MB & rare triggers
			5.02	LHC17p,q	
		Xe-Xe	5.44	LHC17n	first Xe run, MB
	2018	pp	13	- planned / to be recorded -	
		Pb-Pb	5.02		
LS2				2019 & 2020	
Run 3	2021	pp	14	- planned / to be recorded -	
		Pb-Pb	5.02		
	2022	pp	14		
			5.02		
	2023	pp	14		
		Pb-Pb	5.02		
LS3				2024 & 2025	
HL-LHC [184] with Runs 4, 5 and 6 until 2037					

Table 3.2.3: An overview of the recent and upcoming, planned data taking periods of ALICE, listing the collision systems recorded at the given energies provided by the LHC. Their special features are given in addition to the naming scheme of each period.

During 2013, the first Long Shutdown (LS), LS1, campaign followed which was crucially needed to perform maintenance work on the system and to install machine and detector upgrades, see also Tab. 3.2.4 for the upgrades of ALICE during that time. LHC Run 2 succeeded, currently still ongoing, which will conclude with the fourth Pb-Pb data taking period in the end of 2018. The LS2 will include significant upgrades of ALICE featuring major detector and readout upgrades [185], introducing as well a new Online and Offline Computing System (O^2) [186] as the delivered luminosities of the LHC will significantly increase and Pb-Pb interaction rates of 50 kHz will be provided. A new readout scheme for the TPC is needed for this purpose which will be changed from gating grid operation using MWPC technique to a continuously operating Gas Electron Multiplier (GEM) based readout system [187]. Moreover, the ITS will be completely replaced by a new high resolution, low-material ITS [188] and also the MUON system will face improvements [189]. In 2021, data taking will then restart again which will be LHC Run 3. After LS3, the era of High Luminosity (HL)-LHC will follow with Run 4, Run 5 and Run 6 currently being planned until 2037 [184].

When data taking started in 2009, some ALICE sub-detector systems, due to various reasons, were not fully installed and/or not fully operational according to their nominal configurations which are described in Sec. 3.2.1. The following Tab. 3.2.4 gives an overview of the affected detector systems, all located at the central barrel, and their limitations concerning acceptance. The TRD had seven of its 18 supermodules installed in the beginning which could be improved with further supermodules being completed and installed during longer technical stops of the LHC to achieve its completion during LS1 with full coverage in φ. The EMCal had four supermodules installed, covering $\Delta\varphi = 40°$, until the end of 2010 and was basically operated with nominal acceptance of ten (+ two one-third-sized) active modules since then. The DCal was an addendum to the calorimeter system being installed during LS1. Finally, the PHOS was operated with three installed modules for the whole period of LHC Run 1, having half a module added to the acceptance in LS1 which, however, had special focus on improving the percentage of dead areas of the existing modules.

LHC	year	TRD	TOF	EMCal	DCal	PHOS
		sectors installed, each $\Delta\varphi = 20°$				
Run 1	2009	7	18	2	-	3
	2010	7	18	2	-	3
	2011	10	18	5	-	3
	2012	13	18	5⅓	-	3
	2013	13	18	5⅓	-	3
LS1						
Run 2	2015	18	18	5⅓	3⅓	3½
	2016	18	18	5⅓	3⅓	3½
	2017	18	18	5⅓	3⅓	3½
	2018	18	18	5⅓	3⅓	3½
nominal:		18	18	5⅓	3⅓	5

Table 3.2.4: The number of installed sectors, each $\Delta\varphi = 20°$, of the listed central barrel detectors of ALICE with respect to the nominal acceptances. The TRD, EMCal and DCal were completed until the end of LS1 while the TOF was fully installed throughout. For the PHOS, 1½ modules are still to be installed [158].

3.2.3 Trigger System & DAQ

The ALICE Trigger System (TRG) [190, 191] is designed to combine and synchronize information from all triggering detectors of ALICE and to send out the correct sequences of trigger signals to start their readouts. Driven by the design requirements of ALICE, see Sec. 3.2, many gaseous detector layouts were chosen that limit the maximum inspection rate. The TRG is required to operate in varying running modes with significantly different characteristics to comply with the physics goals of the collaboration, from pp collisions with rather low multiplicities up to central Pb-Pb interactions with especially high multiplicities varying in their collision rates by about two orders of magnitude. Although it is not possible to connect all trigger signals from different detectors due to the short timescale allowed for the trigger decision, it is sufficient to trigger on the level of centrality or the existence of high-p_{T} hadrons, leptons or photons. Furthermore, the TRG enables the possibility of dynamic partitioning to only send trigger signals to specific detectors chosen to be combined in a detector cluster, for example, to independently operate the MUON system and central barrel detectors in different partitions at the same time. Tab. 3.2.5 shows a selection of triggers which are especially important in the context of this thesis as they were used for analysis, see Chap. 4. A much more complete list of major triggers running in ALICE can be found in Ref. [145].

trigger	description	acronym	condition
minimum bias (MB)	V0OR	INT1	signal in V0A $\vee$ V0C $\vee$ SPD
	V0AND	INT7	signals in V0A $\wedge$ V0C
rare	EMCal-L0	EMC7	specific energy deposit in EMCal $\wedge$ MB
	EMCal-L1	EGA	EMCal photon algorithm $\wedge$ EMC7
	PHOS-L0	PH	specific energy deposit in PHOS $\wedge$ MB

Table 3.2.5: A small subset of ALICE triggers, relevant for this thesis, which are involved in the data analysis presented in Chap. 4. There are many more triggers being recorded by ALICE [145, 191]: e.g. additional MB triggers issued by the T0 and rare triggers by the TRD, the MUON system, ACORDE etc.

The core of the TRG is the Central Trigger Processor (CTP) [191]. It needs to make optimum use of the available detectors which are being busy for very different time windows following a valid trigger signal. Moreover, the restrictions imposed by the available bandwidth of the DAQ system and the High-Level Trigger (HLT) need to be respected. The CTP basically consists of a Field Programmable Gate Array (FPGA) containing the trigger logic needed to perform the trigger decision which is then propagated to the Local Trigger Unit (LTU) of each detector, subsequently being forwarded to the Front End Electronics (FEE) of the detectors. It evaluates the trigger inputs from the various detectors on every machine clock cycle which is $\sim 25\,$ns. The ALICE trigger system consists of three trigger levels:

- Level-0 (L0) after $1.2\,\mu$s;
- Level-1 (L1) after $6.5\,\mu$s;
- Level-2 (L2) after $88\,\mu$s,

where the quoted periods represent the available time to deliver a trigger decision to the detectors. A first response of the TRG needs to be fast as the FEE of some detectors needs a strobe rather early within 1.2 μs, e.g. the TRD. Therefore, the fast logic is split into two stages: everything that can be achieved within 1.2 μs is used for the L0 decision and those detectors that require longer contribute to the L1 decision. An important part of the TRG is the 'past-future protection', for which the forward detectors are monitoring the interactions to prevent multiple collisions occurring at the same readout interval since overlapping central Pb-Pb collisions would not be reconstructable at all. The final L2 decision is waiting 88 μs, determined by the drift time of the TPC, to record the event. In case of a positive L2 trigger decision, the collected data is streamed to the DAQ. Consecutively, the DAQ sends a copy of the raw data to the HLT which is able to further reduce the data volume by applying other trigger conditions or by compressing the data. For this purpose, a farm of up to 1,000 multiprocessor computing systems is available which perform an online analysis of the collected data. If the HLT is operated in analysis mode, further information may be added to the data which is then stored to tape by the DAQ. If the HLT is fully enabled, it can sent a trigger decision back to the DAQ via the DAQ-HLT interface or its output can even replace information that was streamed in parallel to the DAQ. This functionality is needed for data compression which is especially important for the TPC due to its enormous event sizes of up to 70 MB per central Pb-Pb collision, yielding a total bandwidth of up to 35 GByte/s [163]. The readout electronics of the detectors is interfaced using the ALICE-standard Detector Data Links (DDLs) which is a major architectural feature of the ALICE DAQ, enabling a data transmission rate of 200 MB/s in both directions. Using this interface, the recorded data is transferred to Local Data Concentrators (LDCs) preparing sub-events which are furthermore shipped to Global Data Collectors (GDCs), where the full event is assembled. This event building is managed by the Event Building and Distribution System (EBDS) using the standard TCP/IP as transport mechanism which thereafter stores the data on disk at the experimental pit on a so-called Transient Data Storage (TDS). Finally, the data is transferred to a Permanent Data Storage (PDS) managed by the CERN Advanced Storage Manager (CASTOR).

While ATLAS and CMS may take up to 40 MHz collision rates, ALICE should initially handle up to 200 kHz [190]. The running experience showed that ALICE can be run safely at 700 kHz pp collisions with all detectors including contributions from beam-beam and beam-gas interactions [145], corresponding to $\mathcal{L} = 10^{29}\,\mathrm{cm}^{-2}\,\mathrm{s}^{-1}$ during MB data taking and $\mathcal{L} = 10^{31}\,\mathrm{cm}^{-2}\,\mathrm{s}^{-1}$ for rare triggers. For p-Pb, about 200 kHz were reached, roughly corresponding to $\mathcal{L} = 10^{29}\,\mathrm{cm}^{-2}\,\mathrm{s}^{-1}$ [145] and for Pb-Pb about 2 kHz could be realized, for central collisions up to 200 Hz due to the limitations of the TPC, corresponding to $\mathcal{L} = 10^{27}\,\mathrm{cm}^{-2}\,\mathrm{s}^{-1}$ [145]. Due to the limitations of the readout speed of many ALICE detectors, i.a. the TPC, the luminosity was leveled for ALICE using a transverse beam offset and was kept constant at the predefined value which the detector can handle [192]. During operation of ALICE, the full detector system is monitored and controlled using the Detector Control System (DCS) to ensure a safe and correct operation. All the different systems described in this section, DCS, TRG, DAQ and HLT, are part of the Experiment Control System (ECS) [191].

3.3 Analysis Framework

The analysis framework includes the full software chain which is needed to reconstruct and analyze the raw data which has been recorded using the ALICE DAQ, see Sec. 3.2.3. A general description of the basic parameters and raw data structure of ALICE as well as its computing and reconstruction/simulation framework can be found in Ref. [193]. The full software framework of ALICE is based on C++ [194, 195], an object oriented programming language suiting the needs of a complicated large scale experiment since it provides high performance, efficient memory usage and flexibility. For all software described in this chapter, the version control system Git [196] is used to track the evolution of the code and to be able to restore previous versions which is widely accepted as the standard tool for such a task. All software is based on ROOT [197], an object-oriented program and library which is being developed by CERN. It offers integrated I/O, efficient hierarchical object storage and a C++ interpreter. Moreover, it provides tools for efficient data storage and analysis as well as visualization and has evolved over the last two decades to be the standard package in High Energy Physics (HEP) software. More information, manuals and downloads can be found in Ref. [198]. In the following, the analysis framework will be introduced from the reconstruction of raw data, the preparation of simulations up to the higher level offline analysis which is performed in two distinct steps described in Sec. 3.3.2.

3.3.1 Data Reconstruction & Simulations

The ALICE computing framework needs to fulfill diverse objectives: the reconstruction and analysis of recorded data including alignment and calibration procedures need to be performed as well as simulations from pp to heavy-ion collisions need to be generated including a proper detector response. All these tasks are realized by AliROOT [199], being continuously developed since 1998, which is an object oriented framework based on ROOT adding extensions especially implemented for ALICE. AliROOT also contains the complete detector geometries which are modeled with great detail including support structures, detector services, beam pipe, flanges and pumps. Moreover, the magnetic field distributions of the solenoid and the dipole are described in detail.

Different MC event generators are implemented in AliROOT which can be used to simulate full events or single particles, e.g. PYTHIA [79, 80], PHOJET [82], DPMJET [200], HIJING [201] or AMPT [202], see also Sec. 2.4. All particles from the event generator are subsequently propagated through the detector material of ALICE by means of a detector response simulation, where different programs can be used. In this context, GEANT3 [203], GEANT4 [204] and FLUKA [205] are available. All of these are able to generate a detailed energy deposition in the detector, composed of so-called hits. Following the terminology from GEANT, such a hit is defined as the energy deposition at a given point and time. They are then transformed to ideal detector responses taking into account their characteristics and the electronic manipulation of signals including digitization steps, leading to so-called digits. Afterwards, these are further transformed to the specific output format of the respective detector electronics called raw format. From this point on, the processing of MC events and real data is identical.

The simulations produced by the MC event generators contain the complete true information about the generated particles, e.g. PID, momentum and energy. Within the simulation chain, this true information is disintegrated and finally disregarded as only the particle's interactions with the detector material is used by the reconstruction algorithms to reconstruct the particle's momenta and energies in order to develop a PID hypothesis. Hence, this provides a powerful tool to evaluate the detector performance since the true information about the particles stays always accessible in a separate storage location. Therefore, the fully reconstructed particles in MC simulations, only based on the hits in the detector, can be compared to the true MC information to obtain purity estimates and reconstruction efficiencies.

The underlying raw data format of the detectors is described in Ref. [193] which is the direct output of real data taking. Within the AliROOT framework, the calibration and alignment information is saved in addition to relevant data from the ECS which is needed for the proper reconstruction of raw data, e.g. gas pressure or temperatures. The data reconstruction uses the digits, e.g. ADC or TDC counts, together with further information like module number, readout channel or similar as input. For the reconstruction of both data and simulations, neighboring digits are combined to so-called clusters assuming they originate from the same particle which is followed by the full event reconstruction described later in this section. The output of this step is stored in the Event Summary Data (ESD) format for real data and MC which is about one order of magnitude smaller in size compared to raw data. It contains the reconstructed particle trajectories, called tracks, together with a PID hypothesis associated to each particle candidate. The output also contains reconstructed secondary vertices including kink or cascade topologies. Secondary Vertex (V^0) candidates represent the decays of a neutral mother into two charged daughter particles, e.g. $\gamma \rightarrow e^+e^-$ or $\Lambda^0 \rightarrow p\pi^-$. On the other hand, kinks denote particle decays for which one daughter is invisible for the detector, e.g. $K^- \rightarrow \mu^-\overline{\nu}_\mu$. Finally, cascade topologies are included, e.g. $\Xi^- \rightarrow \Lambda^0\pi^- \rightarrow p\pi^-\pi^-$. In addition, neutral particles are reconstructed in the electromagnetic calorimeters, represented by clusters. All these event characteristics are also saved in another data format called Analysis Object Data (AOD) which is being produced during reconstruction as well. These AODs contain a compressed version and, in principle, a minimum set of information for all the relevant data needed for analysis, further reducing the computing needs for running an analysis.

After the reconstruction steps performed independently for each detector, e.g. cluster finding, the following sequence is obeyed for full event reconstruction:

1. the primary vertex reconstruction;
2. the track reconstruction with subsequent PID;
3. the secondary vertex reconstruction.

1. Primary Vertex Reconstruction

The reconstruction of the primary vertex [129] is based on the information provided by the SPD, the two innermost layers of the ITS. For this purpose, pairs of reconstructed points in the two layers are selected which are close in azimuth in the transverse plane to obtain so-called SPD tracklets. The z-position of the vertex is estimated by linear extrapolation using their z-coordinates. Subsequently, the same procedure is performed in the transverse plane although trajectories of charged particles are bend due to the present magnetic field. However, due to the short distances this approximation is sufficient enough to be used for the first tracking pass. The transverse position of the interaction point can also be determined by averaging over many events, provided the beams are well focused and their position is sufficiently stable in time. As shown in Fig. 3.3.11a, the efficiency of vertex reconstruction rises with charged particle density $\mathrm{d}N_{\mathrm{ch}}/\mathrm{d}\eta$ since more and more information or rather constraints are available. For $\mathrm{d}N_{\mathrm{ch}}/\mathrm{d}\eta > 10$, the vertex is basically reconstructed for any event. On the other side, the resolution of the primary vertex determination is also a function of track multiplicity and, hence,

$dN_{ch}/d\eta$. The dependence on charged particle density for the obtained resolutions $\sigma_{x,y}$ and σ_z in pp collisions are shown in Fig. 3.3.11b which can be fitted by the expression:

$$\sigma_z = \frac{A}{\sqrt{dN_{ch}/d\eta}} + B, \tag{3.3.4}$$

where A and B are the fitting constants, found to be $A = 208 \pm 13\,\mu$m and $B = -6 \pm 4\,\mu$m for $\sigma_{x,y}$ and $A = 272 \pm 13\,\mu$m and $B = -3 \pm 4\,\mu$m for σ_z. For an average track density in pp collisions, $dN_{ch}/d\eta \approx 8$, primary vertex resolutions of $110\,\mu$m for the z-coordinate and $70\,\mu$m for the transverse direction can finally be achieved as shown in Fig. 3.3.11b. On the other hand, a resolution of around $\sigma_z \sim 10\,\mu$m can be obtained for high particle densities corresponding to heavy-ion collisions. The predetermined primary vertex position is used for the full track reconstruction, after which the position of the primary vertex is recalculated including all measured tracks.

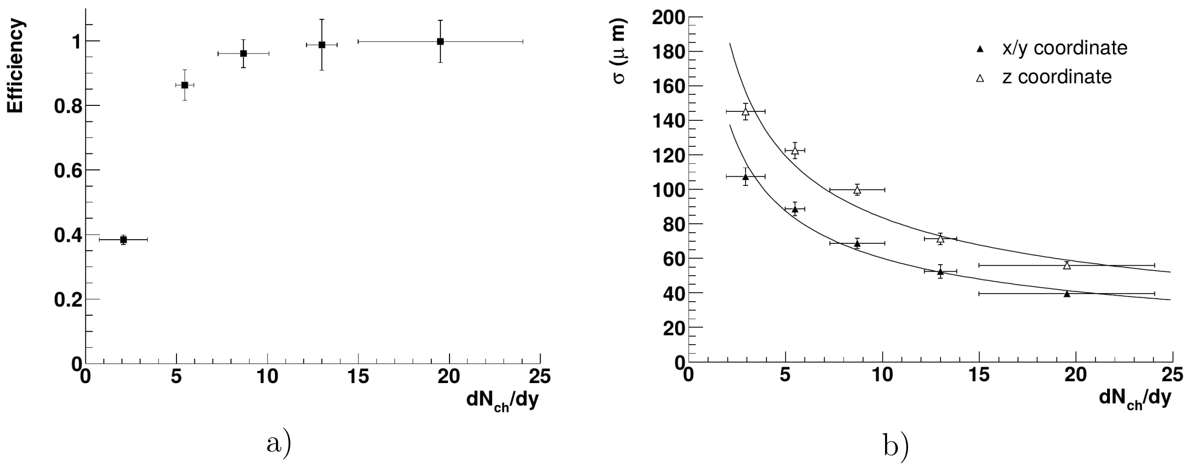

Figure 3.3.11: The efficiency [129], a), and resolution [129], b), of primary vertex reconstruction in pp collisions as a function of charged particle density.

2. Track Reconstruction

The track reconstruction begins with the TPC on its own for which, in the first step, space points are reconstructed by calculating the center of gravity of the 2D clusters in pad row and time direction. For higher particle densities, a cluster unfolding procedure is applied which takes into account the cluster structure [129]. These space points are used to obtain seeds for the track reconstruction which is based on a Kalman filter approach [206, 207], originally introduced in Ref. [208]. This approach critically depends on the determination of a proper set of initial seed values for the track parameters and their covariance matrix. Therefore, the seeding is a very important part of the reconstruction chain which is performed twice: (i) by assuming the track originated from the primary vertex; (ii) by assuming it originated from elsewhere, e.g. a secondary interaction or particle decay. Using the primary vertex as a constraint which is independently determined by the ITS, pairs of space points in the TPC are combined which can project to the primary vertex. Some geometrical and momentum restrictions are applied in this step to reduce the number of possible combinations [144]. If an additional cluster is found in between the two space points, the track parameters and covariance matrix are calculated for the respective helix connecting all points. This procedure is repeated several times, choosing a set of pad rows closer and closer to the center of the TPC to obtain all track seeds. Their track parameters and covariance matrices are then fed into the Kalman filter which essentially consists of the following steps: (i) the state vector of the track parameters and covariance matrix is propagated to the next pad row; (ii) a noise termin, representing the information loss due to stochastic processes like multiple scattering and energy-loss fluctuations, is added to the inverted covariance matrix that describes the current knowledge of the track parameters; (iii) if the filter finds a space point compatible with the track prolongation in the new pad row, this new measurement is added and the track is updated with the increased information level. After completing these steps, the full procedure is repeated using seeds that were obtained without primary vertex constraint. As a result, the track finding efficiency is found to be nearly 100 %, normalized to the number of tracks theoretically reconstructable in the TPC.

After the successful reconstruction of TPC tracks, they are matched to the ITS. This is realized by propagating them to the outer layers of the ITS, starting from highest momentum tracks and continuing with lower momenta in order to make the most precise assignments first. The primary track candidates found in the TPC are then followed by the Kalman filter processing the tracking information of the ITS. Again, this is done in two independent passes; with and without primary vertex constraint for which both sets of parameters are stored for subsequent analysis of short-lived particle decays, such as charm and beauty decays. The tracks found during the TPC pass without vertex constraint are followed in the ITS, if applicable. Each reconstructed TPC track can have several candidate paths through the ITS as all possible assignments in the search window around the prolongation of the TPC track are used as different hypotheses, being followed independently. A decision is made in the end based on the sum of χ^2 along the track candidate's path.

When this ITS tracking step is completed, the Kalman filter is reversed and the track is propagated from the inner ITS layer outwards. As much more precise track parameters are available now, the focus is set to eliminate improperly assigned space points. The tracks are continued beyond the TPC and space points are assigned from the TRD. Tracks are furthermore matched with hits in the TOF, cluster in the HMPID or space points in the CPV in front of PHOS. Then, the tracks are propagated inwards again by reversing the Kalman filter to refit all tracks to obtain their final set of parameters at or nearby the primary vertex. After having removed all the ITS space points already assigned to other tracks, there may be an optional track finding step with the ITS only which is useful for tracks that do not have seeds in the TPC since they cross dead areas.

After applying the full procedure on track finding, the track reconstruction efficiencies as shown in Fig. 3.3.12a are obtained for pp collisions which are normalized to the total number of primary charged tracks in the acceptance. The efficiency is at around 90 % for high momenta, essentially reflecting the dead areas of the TPC which cover $\sim 10\%$ of the azimuthal angle. The large drop of efficiency including the TRD is due to interactions with the material, decays and additional dead zones so that the TRD is only used if it improves the precision. The momentum resolution for tracks in pp collisions is shown in Fig. 3.3.12b for different detector combinations as well, where the TPC standalone efficiency requires no primary vertex constraint. A significant improvement can be observed when combining ITS and TPC due to an increased track length and the addition of further high resolution space points of the ITS. Finally, the primary vertex is recalculated taking into account the full reconstructed tracking information, as already described in the

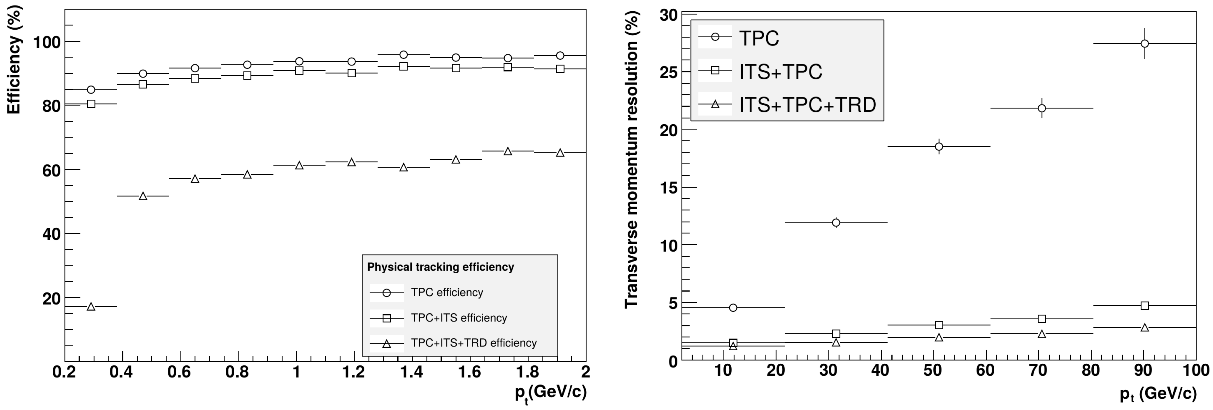

a) b)

Figure 3.3.12: a) The tracking efficiencies [129] for pp collisions when requiring different sets of participating detectors. Deviations from one are mainly due to dead areas in the acceptance. b) The achieved transverse momentum resolutions [129] for different sets of detectors involved in the reconstruction. The TRD especially helps for high momentum tracks, improving the resolution by up to 40 %.

previous section about primary vertex reconstruction, so that resolutions $\sigma_{x,y}$ and σ_z as shown in Fig. 3.3.11b can be obtained.

3. Secondary Vertex Finding

Particles originating from the primary collision may decay after a certain distance or interact with the detector material, creating so-called secondary vertices which are distinguishable from the primary vertex. Neutral particles decaying in secondary vertices are referred to as V^0 candidates, where the 'V' reflects the decay topology of a neutral invisible particle decaying into two charged daughter particles. The vertex itself can be identified with the tip of the two lines connected in the middle. Typical candidates with suitable lifetimes are strange particle decays of, for example $K_S^0 \to \pi^+\pi^-$ or $\lambda^0 \to p\pi^-$, but also photons may interact with the detector material and convert within the magnetic field of a nucleus or an electron into an electron-positron pair, $\gamma \to e^+e^-$, offering a powerful method for photon detection, see Sec. 5.1.

The secondary vertex finding is illustrated in Fig. 3.3.13 giving two examples of K_S^0 and λ^0 decays, where the latter is part of a cascade decay of a Ξ^-. The trajectories of the secondary tracks are shown together with their generated hits in the different layers of the ITS. A secondary track is defined by the requirement to have a Distance of Closest Approach (DCA) to the primary vertex of at least 0.5 mm for pp and 1 mm for Pb-Pb collisions. Only such tracks are used for the reconstruction of secondary vertices for which tracks with opposite signs are paired. Subsequently, their Point of Closest Approach (PCA) is calculated and a first V^0 sample is retrieved. The following cuts are then applied to the sample: (i) the PCA is requested to be below 1.5 cm; (ii) this point needs to be closer to the primary vertex than the first hit of both secondary tracks; (iii) the cosine of the so-called pointing angle θ between the total momentum vector of the pair $\vec{p}_{\text{pair}}$ and the straight line connecting the primary and secondary vertex candidate must exceed 0.9 which is relaxed for V^0 candidates with momenta below 1.5 GeV/c. If these conditions are fulfilled, a secondary vertex candidate is found during reconstruction. Additional cuts can then be imposed on analysis level.

In general, two different sets of V^0 candidates are available which are determined by an 'on-the-fly V^0-finder' and on the other side by an 'offline V^0-finder'. The first one is running during reconstruction, as its name indicates, allowing the tracks to be refitted by the Kalman filter using the secondary vertex to seed the daughter tracks. During this procedure, the full tracking information is reevaluated and an updated covariance matrix as well as tracking parameters can be stored. This improves the position and momentum resolution compared to the offline version which needs to perform the finding procedure after the full tracking chain has already been processed. The offline V^0-finder, however, can deal with adjusted selection parameters without the need of a full reconstruction pass.

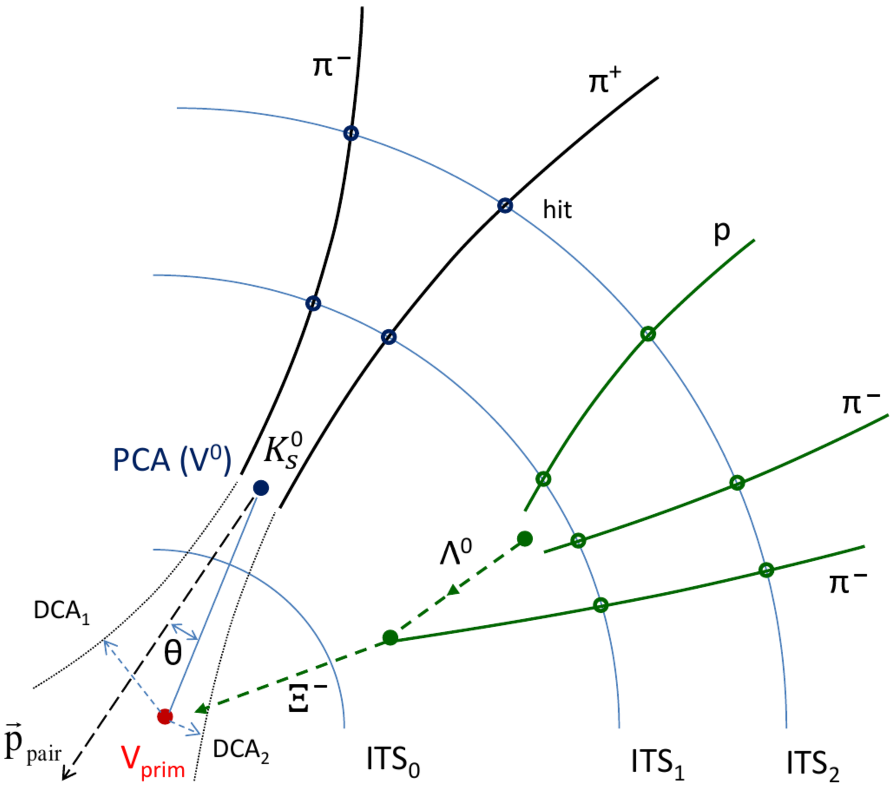

Figure 3.3.13: The principle of secondary vertex reconstruction [145] showing decays of K_S^0 and Ξ^-. The different layers of the ITS are sketched including the hits generated by the decay daughters. Solid lines represent the reconstructed secondary tracks of the charged particles which are extrapolated to obtain the secondary vertex candidates indicated by full dots. The dashed lines represent extrapolations to the primary vertex as well as auxiliary vectors.

The pointing angle cut is relaxed for the cascade reconstruction which are reconstructed by means of invariant mass techniques. During reconstruction, special attention is also devoted to find kink topologies, where a particle decays in flight within the fiducial volume of the TPC. This is done by combining primary tracks which disappear before the end of the TPC with secondary tracks of the same sign which are matched closely in space.

Full event reconstruction

Two so-called event displays are shown in Fig. 3.3.14, exemplifying the result of the event reconstruction as described in this chapter. In general, several reconstruction passes may be available for the same dataset if the PID could be improved afterwards, for example, or if part of the collected statistics could be recovered by resolving issues concerning reconstruction, alignment or basic detector calibration. In Fig. 3.3.14, primary tracks are visualized by continuous gray lines, secondary tracks by dotted gray lines. Electron candidates are highlighted in blue, positron candidates in red and the amount of energy deposited into the EMCal is represented by the length of the red boxes. The upper event display represents a usual MB triggered pp collision with average multiplicity and one conversion photon candidate, whereas the lower display was recorded by an EMCal-L1 trigger. Clearly, there is much more activity in the latter event and multiple conversion photon candidates can be constructed in addition to the EMCal photon candidates.

3.3.2 Data Analysis - the LCG & the PCM Framework

The central data analysis framework used in ALICE is called AliPhysics [209]. There are different Physics Working Groups (PWGs) of the ALICE experiment that contribute to this framework which is based on the previously described AliROOT package. This thesis was carried out within the subgroup which is related to Gammas and Neutral Mesons (GA), in short PWG-GA. Each PWG has its own dedicated code committed to AliPhysics which is able to perform the respective analysis of specific interest. Daily tags are deployed containing the latest snapshot of the software framework which can be used for analysis. For this purpose but also for data reconstruction and simulation, a large amount of computing resources needs to be operated for such an experiment like ALICE. Therefore, the available computing resources and data storages are spread all over the world in many major computing centres which are linked and accessible via the LHC Computing Grid (LCG) [210, 211], for which ROOT is a major foundation of the framework. In fact, the LCG provides the computing infrastructure for the entire high-energy physics community at the LHC. ALICE has developed a special interface to access these resources, called ALICE Environment (AliEn) [212].

As already stated, this thesis was carried out in the context of the PWG-GA, in particular within its subgroup dedicated to the reconstruction of photon conversions: the Photon Conversion Group (PCG) [213]. All the software of the PCG can be found in the AliPhysics repository, see Ref. [209], within the folder ‘PWGGA/GammaConv’. Since there are huge amounts of computing resources needed for the processing of the datasets and simulations, a centralized analysis framework has been developed to efficiently manage the available resources; the Lightweight Environment for Grid Operations (LEGO) train system [214]. Using such LEGO trains, the datasets and simulations can be processed on the LCG using the latest tags of software deployed from the AliPhysics repository [209]. All the relevant information from this analysis step for the full dataset and/or simulation is saved to ROOT files, containing various histograms for all observables of interest which can be further used for offline analysis. This offline part of data analysis is performed by means of the so-called PCM framework, also named afterburner software [215] in common speech. It contains the required code to extract the quantities of interest and to obtain efficiencies and corrections from MC to be applied to real data. Moreover, it includes the possibility to combine multiple measurements and to evaluate systematic variations as well as to properly reflect the correlations of uncertainties for the combination steps. The full Quality Assurance (QA) framework is also contained in this package, see Sec. 4.3, as well as many more applications which may all be found in the repository following Ref. [213]. A detailed documentation is available in this context which can be found in Ref. [216], explaining with great detail the features of the framework and also giving some further examples. The related Git repository of the GitBook is found in Ref. [217].

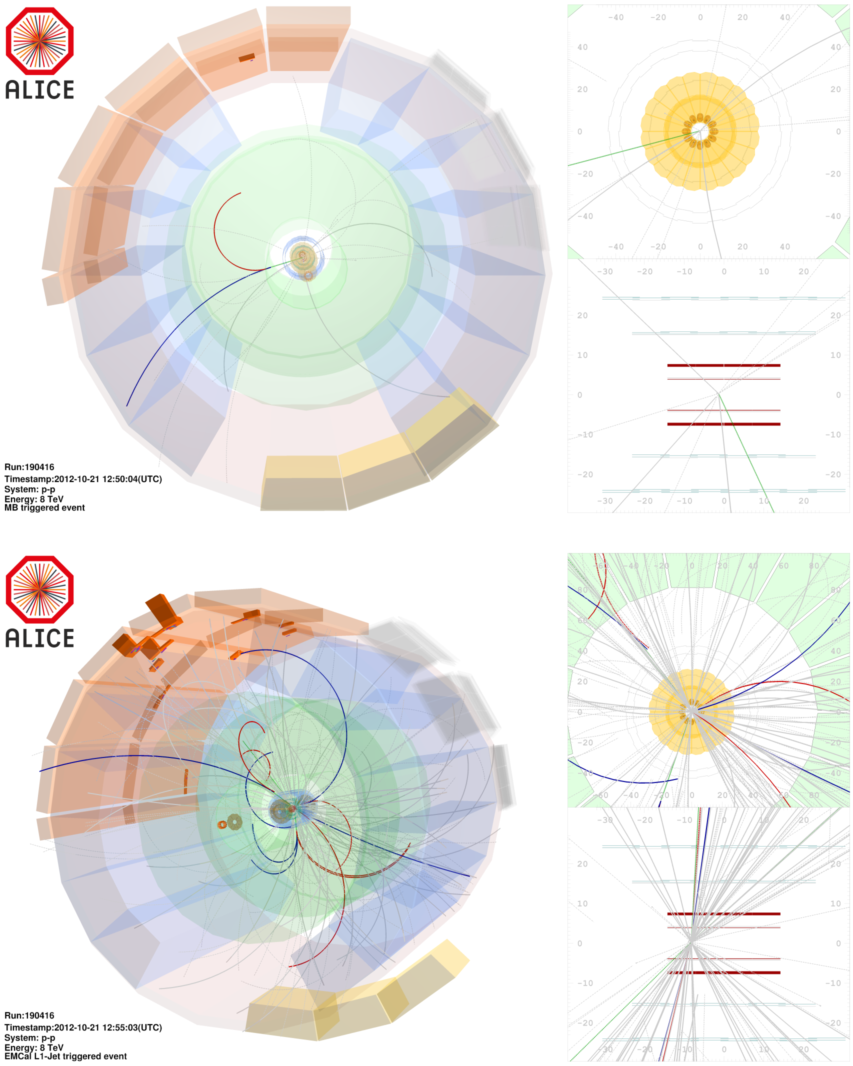

Figure 3.3.14: Two ALICE event displays [218] showing recorded MB (top) and EMCal-L1 triggered (bottom) pp collisions at $\sqrt{s} = 8\,\text{TeV}$. All reconstructed tracks are clearly visible as well as the energy deposition into the EMCal. Different views of the same collision are presented in each event display: (i) a 3D view of the full central barrel including ITS, TPC, EMCal and PHOS, (ii) a projection onto the r-φ plane in the top right detail, highlighting the ITS and (iii) a projection onto the r-z plane where the location of the reconstructed primary vertex can be seen.

Chapter 4

Datasets & Quality Assurance

This chapter introduces the datasets and MC productions used for photon and neutral meson analysis, see Chaps. 6 and 7, which were carried out in the context of this thesis for pp collisions at $\sqrt{s}$ = 0.9, 7 and 8 TeV [4–6]. For the latter system at $\sqrt{s}$ = 8 TeV, a large sample of rare calorimeter triggers was recorded which are introduced in detail in combination with the corresponding MC simulations needed for analysis. Furthermore, the event selection and pileup removal procedures are elaborated and the integrated luminosities being recorded for the different datasets are quoted. Finally, the Quality Assurance (QA) framework is described with focus on the most important observables to examine in order to decide if the recorded data is of good quality and, therefore, may be used for analysis.

4.1 Datasets & Monte Carlo Simulations for pp, $\sqrt{s}$ = 0.9, 7 & 8 TeV

During LHC Run 1, ALICE was recording data for pp collisions at $\sqrt{s}$ = 0.9, 2.76, 7 and 8 TeV. An overview of these data taking periods can be found in Tab. 3.2.3 which is part of the dedicated Sec. 3.2.2. Since part of the detector systems of ALICE were not fully installed with nominal acceptances from the beginning of data taking in 2009, it is particularly important in the context of this section to recall the actual detector configurations of ALICE as datasets from 2010 and 2012 will be introduced in this section. The respective configurations are summarized in Tab. 3.2.4 for the different years of the experimental program. Whereas the measurements at $\sqrt{s}$ = 2.76 TeV were carried out and published in Refs. [8, 219], the analysis of the remaining three collision systems is subject of this thesis.

The data samples analyzed in this thesis are summarized in Tab. 4.1.1, covering pp collisions at $\sqrt{s}$ = 0.9, 7 and 8 TeV. In 2010, pp collisions at $\sqrt{s}$ = 0.9 and 7 TeV were provided by the LHC. The corresponding data taking periods of ALICE are identified by a single period 'LHC10c' for $\sqrt{s}$ = 0.9 TeV and accordingly 'LHC10b-f' for 7 TeV which is an abbreviation for a total of five periods: 'LHC10b,c,d,e,f'. In 2012, ALICE recorded pp collisions at $\sqrt{s}$ = 8 TeV which are labeled with 'LHC12a-i', an acronym for altogether seven different periods: 'LHC12a,b,c,d,f,h,i'. In general, each data taking period corresponds to approximately one month of data taking which is furthermore split into a subset of runs. Ideally, each run corresponds to one physics devoted fill of the LHC which can typically provide collisions for many hours. Depending on the running conditions, this time span may also be shortened to the order of a single hour or even below. All runs used for data analysis can be found in the appendix in Tab. B.1.1 for $\sqrt{s}$ = 0.9 TeV, in Tab. B.1.2 for 7 TeV and in Tabs. B.1.3, B.1.4 and B.1.5 for 8 TeV.

The reconstruction passes used for analysis are also given in Tab. 4.1.1. For all datasets, the table also lists the number of events used for normalization $N_{\text{norm, evt}}$ and the total number of recorded minimum bias events N_{MB}. Furthermore, the integrated fraction of events with a reconstructed z-vertex within $|z_{vtx}| < 10\,\text{cm}$ is given in addition to the fraction of events with a primary vertex outside the given interval $|z_{vtx}| > 10\,\text{cm}$. The fraction for events without any vertex reconstructed is also listed and the respective fraction of pileup events is calculated, see Sec. 4.2 for further details.

pp, $\sqrt{s}$ (TeV)	data, MB trig. / MC, event gen.	pass	periods	$N_{\text{norm, evt}}$	N_{MB}	A (%)	B (%)	C (%)	D (%)
0.9	V0OR (INT1)	4	LHC10c	$5.81 \cdot 10^6$	$6.64 \cdot 10^6$	80.6	11.2	7.9	0.3
	MC, PYTHIA 6		LHC14j4c	$5.81 \cdot 10^6$	$6.63 \cdot 10^6$	80.0	11.1	8.9	0
7	V0OR (INT1)	4	LHC10b-f	$3.14 \cdot 10^8$	$3.56 \cdot 10^8$	80.5	9.8	8.6	1.1
	MC, PYTHIA 6		LHC14j4b-f	$3.78 \cdot 10^8$	$4.18 \cdot 10^8$	82.0	8.5	9.5	0
8	V0AND (INT7)	2	LHC12a-i	$1.08 \cdot 10^8$	$1.18 \cdot 10^8$	90.7	1.3	6.8	1.1
	MC, PYTHIA 8		LHC15h1a-i	$2.38 \cdot 10^8$	$2.58 \cdot 10^8$	79.5	13.9	6.5	0
	MC, PHOJET		LHC15h2a-i	$2.37 \cdot 10^8$	$2.56 \cdot 10^8$	84.4	8.7	6.8	0

Table 4.1.1: An overview of all pp datasets used for analysis. The reconstruction pass of each dataset is listed as well as the corresponding MB trigger. Furthermore, the number of events used for normalization is quoted as well as the number of recorded MB triggers. In addition, the following fractions are given: (A) $\frac{\text{MB,vtx,}|z_{vtx}|<10\text{ cm}}{\text{MB}}$, (B) $\frac{\text{MB,vtx,}|z_{vtx}|>10\text{ cm}}{\text{MB}}$, (C) $\frac{\text{MB,no vtx}}{\text{MB}}$ and (D) $\frac{\text{MB,pileup}}{\text{MB}}$.

Different MC event generators are available as input for the full detector simulations which are needed to obtain the reconstruction efficiencies and geometrical acceptance corrections which are then applied to the measured raw spectra in data. The general purpose event generators used in this context for the collisions systems quoted in Tab. 4.1.1 are PYTHIA 6 [79], PYTHIA 8 [80, 81] and PHOJET [82, 83] which were tuned on results of previous lower energy experiments and, in addition, on early LHC data in the case of PYTHIA 8. All generators are able to describe the spectral shape of particle production with limited but decent accuracy which is sufficient to extract realistic acceptances and reconstruction efficiencies. As they are based on different models, see Sec. 2.4, each event generator has a different momentum interval where it is able to reproduce the neutral meson and photon spectra better than other generators. The impact of such discrepancies on the final results will be reflected for the systematic uncertainties of the measurements, see Sec. 6.2.4 and Sec. 6.3.2.

All MC simulations used for analysis can be found in Tab. 4.1.1 where the same properties are quoted as for data. The simulations follow a similar naming scheme as data which involves the year of production followed by a letter and a number, representing the ALICE internal MC name cycle, and finally being concluded by the label of the respective data taking period to which the simulation was anchored to. This means that the simulation properly reflects the statistics of each run recorded in data which is of importance as the set of active detectors may vary from run to run. By anchoring the MC simulations, the event characteristics of real data, e.g. z-vertex distributions and environmental conditions such as gas pressures and temperatures, are also reflected aiming to reproduce the actual running conditions as well as possible. All the simulations listed in Tab. 4.1.1 use GEANT3 [203] to realistically reproduce the interactions between the generated particles and the detector material. As introduced in Sec. 3.3.1, the simulations are treated as data but the information on true MC level can always be recovered on request.

Tab. 4.1.1 also lists the minimum bias triggers that were active for the respective datasets which are generally introduced in Tab. 3.2.5. These triggers are issued on L0, therefore being generated $1.2\,\mu$s after the interaction [175], see also Sec. 3.2.3. The V0AND (also known as INT7) requires at least one hit in each V0A and V0C, whereas the V0OR (INT1) requires a hit either in the V0A, the V0C or the SPD [220]. For pp collisions at $\sqrt{s} = 8$ TeV, large amounts of calorimeter triggers provided by the EMCal [221] and the PHOS [222] were recorded in addition to the MB running. They are introduced in detail in the following Sec. 4.1.1.

4.1.1 Rare Calorimeter Triggers & Jet-Jet MC Simulations for pp, $\sqrt{s} = 8$ TeV

The EMCal and the PHOS provide rare triggers, see Sec. 3.2.3, to enhance statistics at high p_{T} by selectively recording events with high energy deposits in the calorimeters. For the data taking campaign at $\sqrt{s} = 8$ TeV, both calorimeters were issuing L0 triggers and the EMCal was recording L1 photon triggers in addition.

The L0 triggers provided by the calorimeters are the EMCal-L0 [167] and the PHOS-L0 [222]. They are of the same latency as the V0AND, which was the active minimum bias trigger for pp collisions at $\sqrt{s} = 8$ TeV in 2012, and are required to be in coincidence with this MB trigger. The EMCal-L0 trigger, named EMC7, inspects the energy sum over sliding windows of 4×4 cells which are limited to be located at one Trigger Region Unit (TRU). Such a TRU corresponds to 8×48 cells and, in general, three TRU compose one EMCal supermodule. The EMC7 trigger is hence issued if the detected energy sum in one TRU exceeds a certain threshold above the background noise and if a MB trigger was detected in addition. The L0 trigger of the PHOS is realized analogously but in this case 16×14 cells compose one TRU. For the given dataset at $\sqrt{s} = 8$ TeV, the thresholds for the EMCal- and PHOS-L0 triggers were set to $\overline{E}_{\mathrm{EMC7}} \approx 2$ GeV and $\overline{E}_{\mathrm{PHOS\text{-}L0}} \approx 4$ GeV respectively.

A L1 photon trigger, named EGA, is also deployed for the EMCal which inspects events preselected by the EMCal-L0 trigger [223, 224]. The trigger algorithm of the EGA is similar to the EMCal-L0 but combines information from the different TRUs to enhance the trigger efficiency and overcome hardware boundary effects, thus increasing the effective area by about one third. Compared to the L0 trigger, a larger threshold of $\overline{E}_{\mathrm{EGA}} \approx 10$ GeV is set to further improve the p_{T} reach of the EMCal related measurements. For the PHOS, a L1 trigger is under consideration [225] which was not exploited in 2012, however. The respective statistics collected for each of the EMCal triggers at L0 and L1 can be found in Tab. 4.1.2 together with the related quantities needed for normalization analog to Tab. 4.1.1. The EMC7 was active for the periods 'LHC12b-i', whereas the EGA was running during data taking period 'LHC12c' for the first time.

By using the rare triggers provided by the EMCal, as already stated, the obtained statistics for photons at higher momenta can be significantly increased. For the reconstruction of neutral mesons, two photons are combined and the invariant mass is calculated for the pair, see Sec. 6.1. As the reconstruction efficiencies depend on the energy sharing between the two photons denoted with α which follows a rather broad distribution, the trigger turn-on will be fairly washed out on the meson level compared to the single photon level. Therefore, it is crucial that the trigger is sufficiently simulated on MC level to properly describe these distributions. Since a full simulation

pp, $\sqrt{s}$ (TeV)		periods	EMCal rare trigger	$N_{\text{norm, evt}}$	N_{Y}	A (%)	B (%)	D (%)
8	data	LHC12b-i	L0 (EMC7)	$3.58 \cdot 10^7$	$3.93 \cdot 10^7$	91.1	6.6	2.3
		LHC12c-i	L1 (EGA)	$2.12 \cdot 10^6$	$2.35 \cdot 10^6$	90.3	6.0	3.7
	PYTHIA 8, Jet-Jet	LHC16c2	mimic EMC7	$5.98 \cdot 10^7$	$7.85 \cdot 10^7$	76.5	23.4	0
			mimic EGA	$1.87 \cdot 10^7$	$3.71 \cdot 10^7$	50.6	49.3	0

Table 4.1.2: The statistics collected for the different EMCal triggers. Moreover, the following integrated fractions are given: (A) $\frac{\text{Y,vtx,}|z_{vtx}|<10\text{ cm}}{\text{Y}}$, (B) $\frac{\text{Y,vtx,}|z_{vtx}|>10\text{ cm}}{\text{Y}}$ and (D) $\frac{\text{Y,pileup}}{\text{Y}}$, where Y stands for the respective trigger class. The fraction of events without vertex, introduced with (C) in Tab. 4.1.1, is practically zero for all cases and is therefore omitted.

of the EMCal triggers in the ALICE simulations is still missing, a simple algorithm to mimic the trigger was implemented on the analysis level. The trigger algorithms are mimicked by tagging events with at least one cluster of adjacent cells exceeding a predefined energy threshold. For each event, this energy threshold is sampled from a Gaussian distribution around its mean μ_{Trigger} with a standard deviation of σ_{Trigger} to simulate the observed non-uniformity of the trigger thresholds for the different TRUs. These two parameters are adjusted according to the actual threshold of the respective EMCal trigger which is analyzed, summarized in Tab. 4.1.3. Given the simplicity of this procedure compared to a detailed simulation of calorimeter triggers, the trigger mimicking has proven to be a fast and reliable method to reproduce the trigger turn-on curves at the analysis level which has been cross-checked in detail, see Sec. 4.2 and Sec. 4.3.

pp, $\sqrt{s}$ (TeV)	rare trigger	approx. threshold	sim. threshold μ_{Trigger}	σ_{Trigger}	RF
8	EMCal-L0 (EMC7)	$\sim 2\,\text{GeV}$	$1.85\,\text{GeV}/c$	$0.2\,\text{GeV}/c$	67.0 ± 1.1
	EMCal-L1 (EGA)	$\sim 10\,\text{GeV}$	$9.50\,\text{GeV}/c$	$1.0\,\text{GeV}/c$	$(14.9 \pm 0.3) \cdot 10^3$

Table 4.1.3: The approximate trigger thresholds for the EMCal-L0 and L1 triggers that were active for the data recording for pp, $\sqrt{s} = 8\,\text{TeV}$. The trigger mimicking settings are quoted in addition to the Trigger Rejection Factor (RF) defined in Sec. 4.2.

As the calorimeter triggers enhance the statistics at higher p_{T}, adequate MC simulations are needed which are able to provide the geometrical acceptances and reconstruction efficiencies with sufficient precision in this high-p_{T} region. However, minimum bias MC simulations are an inadequate choice for this purpose in particular with respect to large computing resources and enormous disk space needed to process and store huge amounts of generated events. A better choice is to exploit the possibility of PYTHIA to generate events which are enriched by jets, generated in bins of hard scatterings $p_{\text{T,hard}}$. Such productions are called Jet-Jet MC productions and are a very useful instrument to obtain sufficient MC statistics at higher p_{T} requiring rather limited computing resources compared to pure MB MC simulations. The produced Jet-Jet MC production for $\sqrt{s} = 8\,\text{TeV}$ is listed in Tab. 4.1.2 which further quotes the available statistics for both mimicked triggers. It has been carefully studied that the obtained corrections from this Jet-Jet MC are fully compatible with those extracted from the standard minimum bias MC simulations. The selected $p_{\text{T,hard}}$ bins for the Jet-Jet production ‘LHC16c2’ can be obtained from Fig. 4.1.1a which shows the unweighted raw p_{T} spectra of neutral pions from that production.

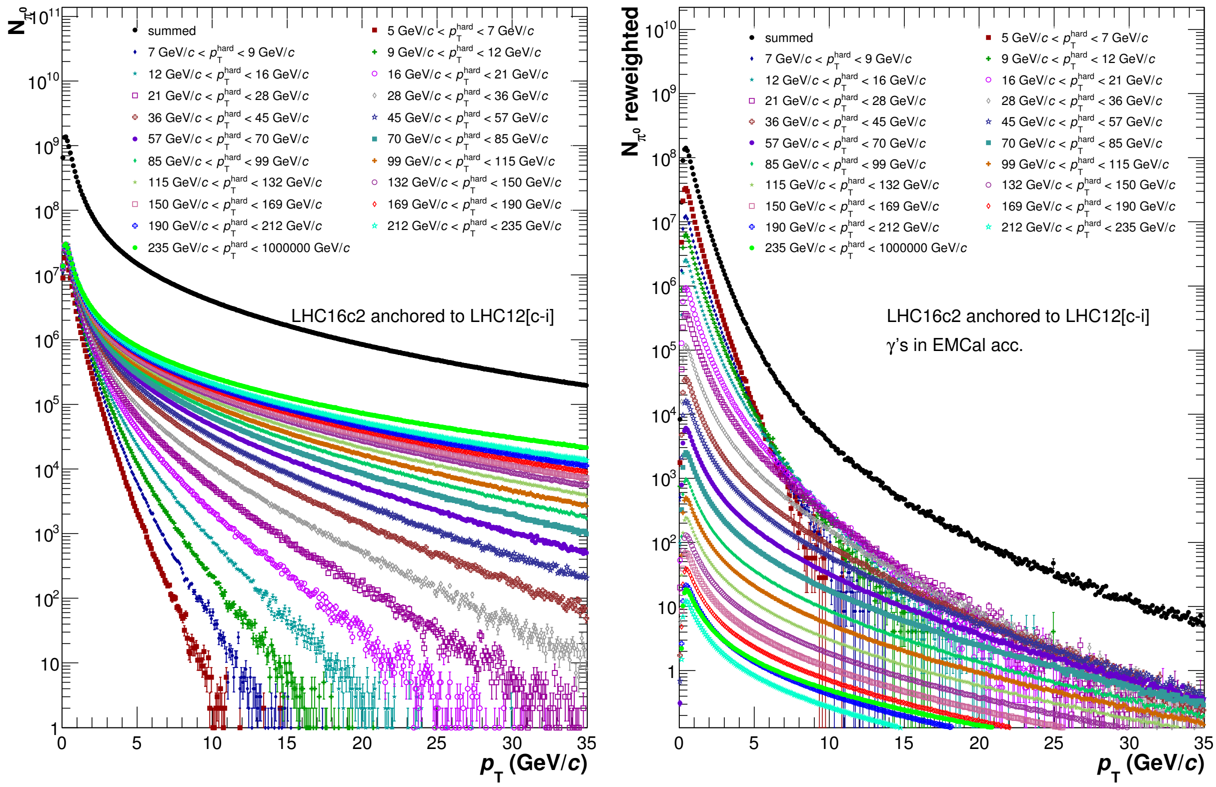

a) b)

Figure 4.1.1: a) The unweighted raw p_T distributions of neutral pions are shown for the respective $p_{T,hard}$ bins of the Jet-Jet MC production. The black points represent the sum of all 20 $p_{T,hard}$ bins. b) After applying the weights calculated with Eq. 4.1.1, also listed in Tab. B.1.7, the weighted p_T spectra are shown for the π^0.

Several trials N_{trials} are necessary to generate the requested number of events for each $p_{T,hard}$ bin. This is due to the requirement that a jet needs to be found with a transverse energy of $E_T \geq 5\,$GeV in order to accept the generated event. Furthermore, PYTHIA provides the respective cross section of each hard scattering process which is simulated. It is denoted σ_{event} in this context, which corresponds to the average cross section of the complete sample of events generated for a $p_{T,hard}$ bin. To build up the full spectrum, a certain weight ω_{JJ} needs to be applied for every $p_{T,hard}$ as only a small part of the full space is sampled by each of them. These weights are calculated as follows:

$$\omega_{JJ} = \frac{\sigma_{event}}{N_{trials}/N_{generated\ events}}, \tag{4.1.1}$$

which need to be applied on an event by event basis for each particle as it is demonstrated in Fig. 4.1.1b for the π^0 meson. The figure indicates that fluctuations, which occur in an individual $p_{T,hard}$ bin, can have a fairly large impact after the weighting procedure which is especially the case for more rare particles than the π^0. Therefore, all events which contain a single particle with a momentum of $p_{T,\ part} > 1.5 \cdot p_{T,hard}$ or a jet with $p_{T,\ jet} > 2 \cdot p_{T,hard}$ are rejected which anyways happens rarely. More information about the respective $p_{T,hard}$ bins and the obtained weights can be found in the appendix B in Tab. B.1.7.

4.2 Event & Trigger Selection for pp, $\sqrt{s}$ = 0.9, 7 & 8 TeV

The event and trigger selection is applied during offline analysis on the LCG, see Sec. 3.3.2. Depending on the respective dataset to be analyzed, only events with the proper trigger decision are taken into account. For $\sqrt{s} = 0.9$ and 7 TeV, only events flagged with the MB trigger V0OR (INT1) are selected, whereas the V0AND (INT7) as well as the two rare EMCal triggers, EMC7 and EGA, are analyzed for the pp dataset at 8 TeV. A so-called Physics Selection (PSEL) is further applied which rejects events which are not of physics type, e.g. calibration events. Moreover, it discards events assigned to noise or contamination from Machine-Induced Background (MIB) [145], for example by inelastic beam-gas interactions. In addition to these criteria, an event has to have a primary vertex reconstructed that obeys the condition $|z_{vtx}| < 10\,\mathrm{cm}$ with respect to the center of ALICE to be considered for further analysis. In this regard, the primary vertex may be reconstructed either with global or simply SPD-only tracks, see Sec. 3.3.1. Hence, the number of events used for the normalization of spectra is obtained by:

$$N_{\mathrm{norm,\ evt}} = N_{\mathrm{Y,vtx,}|z_{vtx}|<10\mathrm{cm}} + \frac{N_{\mathrm{Y,vtx,}|z_{vtx}|<10\mathrm{cm}}}{N_{\mathrm{Y,vtx,}|z_{vtx}|<10\mathrm{cm}} + N_{\mathrm{Y,\ vtx,}|z_{vtx}|>10\mathrm{cm}}} \cdot N_{\mathrm{Y,no\ vtx}}, \tag{4.2.2}$$

where Y is corresponds to the respective trigger class analyzed. The other quantities contained in this formula are quoted in Tabs. 4.1.1 and 4.1.2 for the respective datasets and trigger classes.

Since the beginning of operation in 2009, the LHC has been able to constantly increase the delivered instantaneous luminosity for all experiments. However, ALICE can only take data at a limited rate due to its variety of gaseous detectors, mainly restricted by the TPC due to the long ion drift times of up to 94 μs, see Sec. 3.2.1. Thus, both beams at the ALICE IP are usually displaced to limit the interaction rate to the maximum possible value as introduced in Sec. 3.2.3. However, this procedure is not enough to guarantee that there is not more than one interaction occurring in a small time frame. If such a situation occurs, though, the different interactions cannot be resolved any more by the sub-detector systems of ALICE, which is generally denoted pileup. Hence, an effective rejection of pileup is needed to identify and discriminate such events. As such, two different subclasses of pileup are differentiated: in-bunch and out-of-bunch pileup. The first case, in-bunch pileup, is defined by the reconstruction of multiple primary vertices for the same event. Therefore, several interactions occurring during the same bunch crossing cause more than one primary vertex to be reconstructed for the respective event. On the other hand, there may also occur out-of-bunch pileup. Since multiple events will generally overlap in the TPC drift region depending on the bunch spacing of the LHC, this term describes the case of too many overlaps too close in time which cannot be distinguished anymore.

To reject the in-bunch part, a pileup rejection based on the number of reconstructed vertices using the SPD is applied. This rejection method removes events from analysis which have more than one primary vertex reconstructed based on the SPD tracking information. In combination with the SPD background cut which is described later in this section, in-bunch pileup is removed with an efficiency of 92 %, as shown in Fig. B.0.1a for pp at $\sqrt{s} = 8$ TeV. By implication, the finite efficiency of this procedure is reflected in the systematic uncertainties, see Secs. 6.2.4, 6.3.2 and 7.2.2. In general, the fraction of rejected events by the SPD pileup rejection highly depends on the actual beam conditions. The higher the luminosity or the smaller the beam diamond is, the larger becomes the fraction of rejected events due to this constraint. Whereas the fraction of events without vertex in data only depends on the collision energy, the z-vertex position, on the other hand, highly depends on the luminosity and the resolution of the involved detectors and much less on the collision energy itself. Both quantities are exemplary shown in Fig. 4.2.2 for the different runs recorded for pp collisions at $\sqrt{s} = 8$ TeV which are listed in Tab. B.1.3.

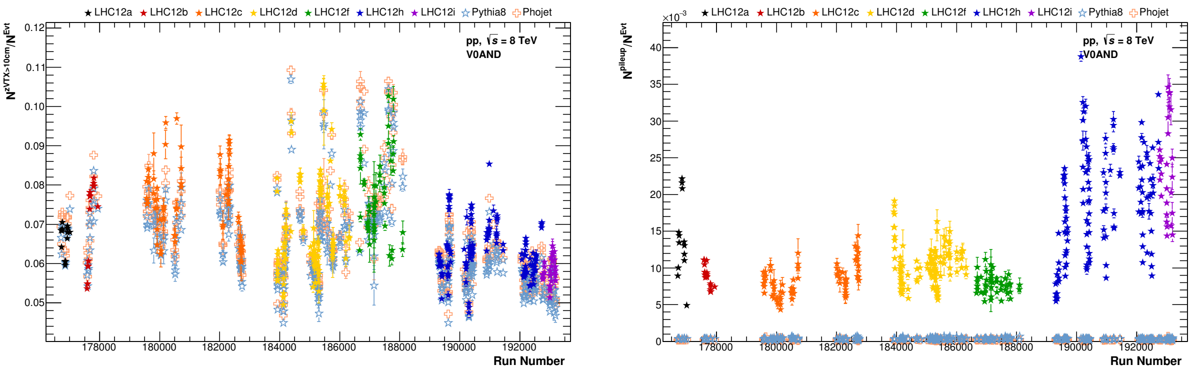

a) b)

Figure 4.2.2: a) The fraction of events fulfilling $|z_{vtx}|$ >10 cm as a function of run number for $\sqrt{s} = 8$ TeV, see Tab. B.1.3. The anchored MC simulations, see Tab. 4.1.1, are able to reproduce the run dependence seen in data. b) The fraction of rejected events due to the SPD pileup removal per run are shown. The observed pattern corresponds to the delivered luminosities by the LHC which are shown in Fig. B.0.1b.

A comparison with simulations shows that the run dependence is properly taking into account by the MC productions, although they slightly miss the absolute fractions in Fig. 4.2.2a. Since only single collisions were simulated for MC productions, the fraction in Fig. 4.2.2b is found to be always zero for these cases.

On the other hand, the contribution from out-of-bunch pileup has to be treated on analysis level. Due to the fact that the EMCal has a fairly fast readout and given that the LHC bunch spacing was never below the value of 50 ns for the analyzed datasets, the constraint on the triggering collision is therefore given when including an EMCal photon candidate in the analysis for which a timing cut on the cell readout time is used as introduced in Sec. 5.2. In contrast, the contribution from out-of-bunch pileup can only be estimated during analysis using a statistical subtraction method for the reconstruction of photons based on secondary vertices V^0, see Sec. 5.1. Since multiple events are basically always present in the TPC drift region, it may happen that secondary vertices are erroneously associated to the wrong event as it is only possible to distinguish between events with limited efficiency given the operating conditions of the detector. The correction is carried out by using the DCA_z information of the momentum vector of the V^0 candidates with respect to the reconstructed primary vertex, where z represents the beam direction. V^0 candidates from different events generate a broad underlying Gaussian-like DCA distribution which is approximated to estimate the contribution of out-of-bunch pileup.

To further reject background events, a cut on the correlation of SPD tracklets and SPD clusters is applied which is shown in Fig. 4.2.3 for data and MC. If there are way more SPD clusters are found compared to the number of SPD tracklets in an event, a so-called background event is found being discarded from analysis. In detail, the applied cut condition reads as follows:

$$N_{\text{Clusters}} > 4 \cdot N_{\text{Tracklets}} + 65, \tag{4.2.3}$$

where the number of SPD clusters and tracklets enter, N_{Clusters} and $N_{\text{Tracklets}}$ respectively.

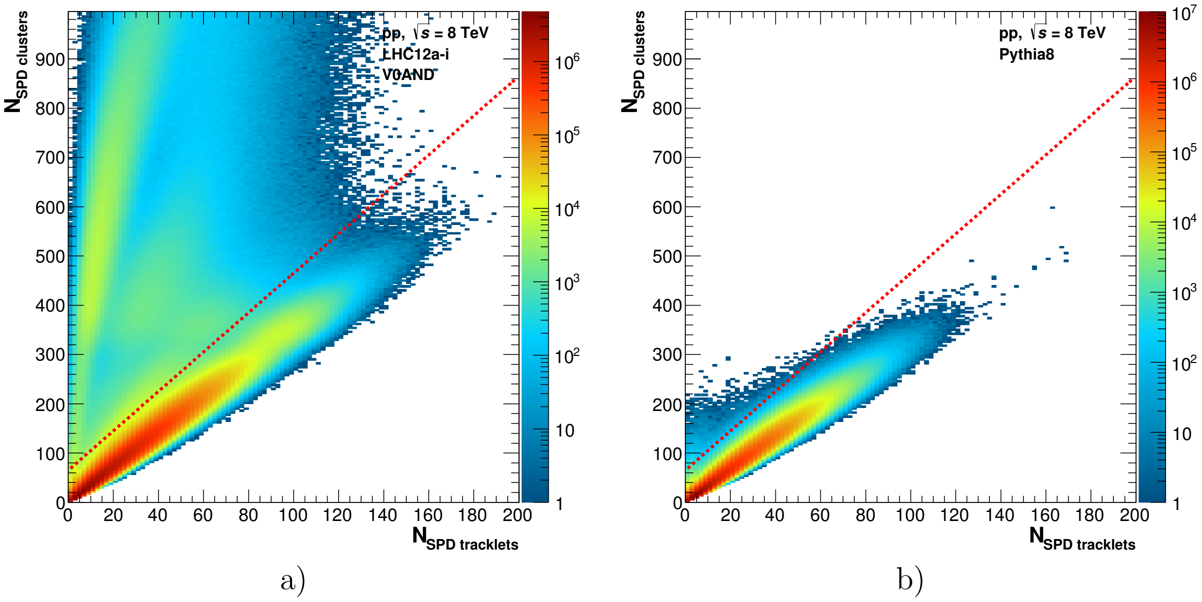

Figure 4.2.3: The number of SPD clusters plotted vs. the number of SPD tracklets for data, a), recorded in pp, $\sqrt{s} = 8\,\mathrm{TeV}$ and for the anchored PYTHIA 8 MC simulation, b). The dotted red lines display the cut condition introduced in Eq. 4.2.3 which is applied for both cases.

In the following Fig. 4.2.4a, the number of reconstructed tracks per event is shown for MB triggered data at $\sqrt{s} = 8\,\mathrm{TeV}$ and the corresponding MC simulations, where each distribution is normalized to an integral of one. One can clearly see differences for the charged track multiplicities between data and MC, in particular for the Jet-Jet MC production. In general, PYTHIA 8 provides a better description of the measured charged particle multiplicity compared to PHOJET, although both are able to provide a reasonable description for lower multiplicities. This is an important requirement as, in general, the reconstruction efficiencies of photons depend on the charged particle density $\mathrm{d}N_{\mathrm{ch}}/\mathrm{d}\eta$ especially for low numbers of charged tracks. This is the case since the efficiencies are coupled to the primary vertex resolution which intrinsically depends on $\mathrm{d}N_{\mathrm{ch}}/\mathrm{d}\eta$. Whereas the effect is considerable for the reconstruction of photons via secondary vertices V^0, it is somewhat smaller for EMCal photons. Therefore, the events are weighted in order to adapt the multiplicity distributions from MC to data. This weighting procedure yields corrections of the order of $1-2\,\%$ for MB triggered events when including V^0 photon candidates. If only EMCal photons are considered, the correction is rather small throughout and well below $1\,\%$. As for Jet-Jet MC productions, also shown in Fig. 4.2.4a, the charged track multiplicities are found to be heavily depleted for lower values, so that such productions should not be used to correct MB triggered data.

Above ~ 7 tracks per event the reconstruction efficiencies for photons are found to be rather stable. The following Fig. 4.2.4b compares the measured charged particle multiplicities from data with the corresponding Jet-Jet MC for which trigger mimicking is applied as introduced in Sec. 4.1.1. The shapes of the distributions are much more alike compared to the previous MB case. Thus, for events recorded with rare EMCal triggers the weighting plays a much smaller role with an effect of $< 0.1\,\%$. Consequently, no weighting is used for the Jet-Jet MC simulations.

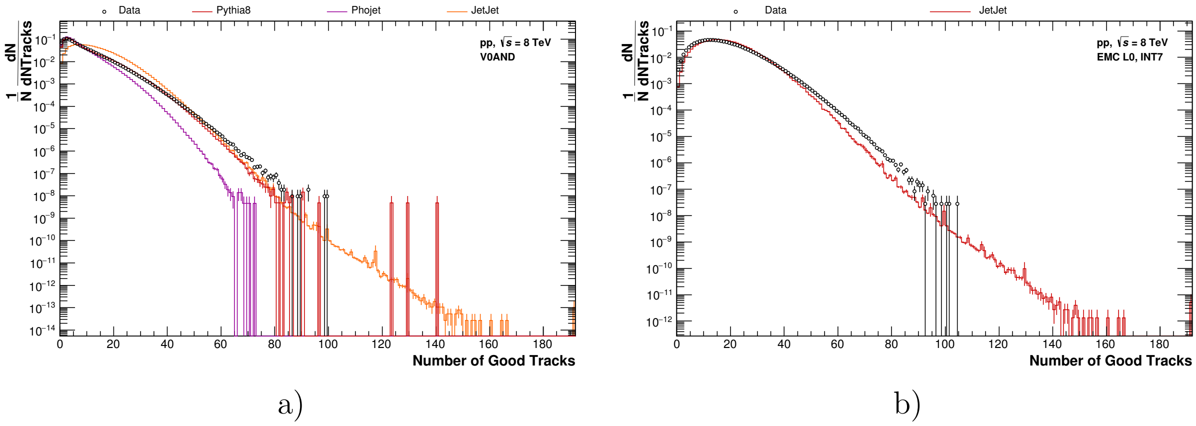

Figure 4.2.4: The number of reconstructed tracks per event before the multiplicity weighting procedure for MB triggered data and its anchored MC productions, a), and for the EMCal-L0 EMC7 trigger, b), which is plotted with the distribution obtained from the corresponding Jet-Jet MC simulation.

As introduced in Sec. 4.1.1, a large sample of rare EMCal triggers, EMC7 and EGA, was recorded during pp data taking at $\sqrt{s}$ = 8 TeV in 2012. These triggers require a proper normalization in order to correctly consider them for analysis. For this purpose, the Trigger Rejection Factors (RFs) are determined which quantify the rejection power of the given trigger condition with respect to the MB trigger. The RFs are calculated on the level of reconstructed EMCal clusters which are defined by an accumulation of adjacent cells exhibiting an energy deposition in an event. Such a cluster represents the complete energy deposition of a particle entering the EMCal. More information in this regard is given in the dedicated Sec. 5.2, where the reconstruction of clusters and the subsequent selection criteria are described. The cluster energy spectra for the different triggers available for $\sqrt{s}$ = 8 TeV are shown in Fig. 4.2.5, in which the enhancement of statistics at higher energies by using EMCal triggers becomes evident. Basic photon identification cuts are applied to the clusters as introduced in Sec. 5.2 so that distributions are labeled as raw photon candidate spectra.

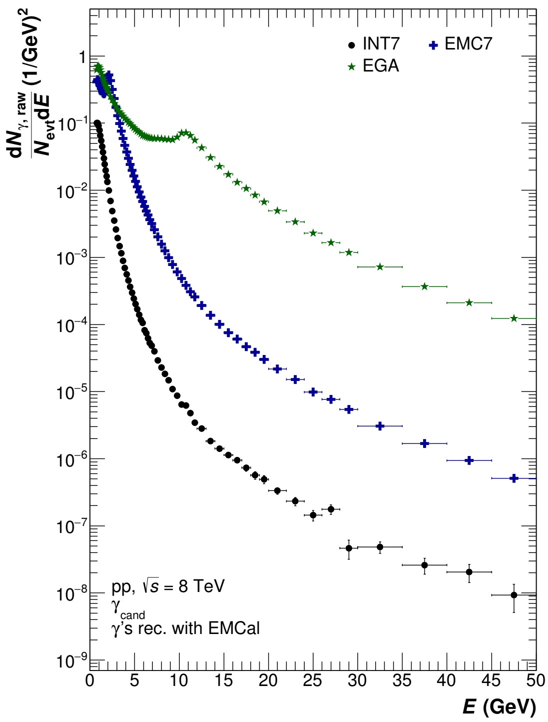

Figure 4.2.5: The raw cluster energy distributions for the EMCal, normalized to $N_{\text{norm, evt}}$.

Using the cluster energy spectra from MB and EMCal triggered events, shown in Fig. 4.2.5 as a function of cluster energy E, the RFs are determined by constructing the ratios of both distributions which are presented in Fig. 4.2.6a for data. These ratios are expected to follow a constant for high cluster energies, the so-called plateau region, assuming the triggers only enhance the rate of clusters but do not affect their reconstruction efficiency. In fact, Fig. 4.2.6a demonstrates that this assumption is valid. Moreover, the cluster energy ratios have a steep turn-on near the respective trigger threshold energies before the plateau regions are reached. By fitting the constructed ratios in the plateau regions with a constant, the trigger rejection factors are obtained that are mainly relevant for analysis. The RFs are always determined with respect to the next lower threshold trigger to reduce statistical uncertainties which is achieved because larger p_{T} ranges can be used for the fitting step. Tab. 4.1.3 summarizes the obtained RFs for the different EMCal triggers which are also contained in Fig. 4.2.6a. To obtain the RF for the EGA which is quoted in Tab. 4.1.3, the two given rejection factors from MB to EMC7 and EMC7 to EGA need to be multiplied as the RF with respect to the MB trigger is only of relevance. Since the EMC7 becomes fully efficient only above its triggering threshold of $\overline{E}_{\mathrm{EMC7}} \approx 2\,\mathrm{GeV}$, there is a change of slope visible in the turn-on region of the EGA. The determination of the quoted systematic uncertainties of the RFs are introduced later in the corresponding Sec. 6.2.4.

In Fig. 4.2.6b, a comparison of the cluster energy ratios obtained from data and MC simulation is shown for the EGA. The simple trigger mimicking algorithm was used, introduced in Sec. 4.1.1 using the parameters quoted in Tab. 4.1.3, which fulfills the requirement to reasonably reproduce the cluster energy ratios in MC simulations. Since the actual shape of the cluster energy spectra may be different between data and MC, the latter is properly normalized to match the absolute amount of the RF. It is more important that the characteristics of the distributions, the turn-on region and, most importantly, the plateau region are well reproduced which is demonstrated in Fig. 4.2.6b.

In the end, the measured invariant yields of photons and neutral mesons with the different MB and rare trigger conditions of ALICE need to be transformed into invariant cross sections in order to obtain universal results which may be compared to the findings of other experiments. In general, every trigger condition Y used in an experiment only samples part of the full inelastic cross section σ_{inel}, which is described by the visible cross section $\sigma_{\mathrm{Y}}^{\mathrm{VIS}}$ that is identified by σ_{Y} in the following. As a result, σ_{Y} is specified as the cross section seen by a given trigger condition with respect to σ_{inel}, defined as follows: $\sigma_{\mathrm{inel}}/\sigma_{\mathrm{Y}} = \epsilon{\cdot}\sigma_{\mathrm{inel}}$, where ϵ is the fraction of inelastic events satisfying the trigger condition Y. The observed reaction rate $\mathrm{d}N/\mathrm{d}t$ can then be determined as follows:

$$\frac{dN}{dt} = \sigma_{\mathrm{Y}} \cdot \mathcal{L}, \tag{4.2.4}$$

where σ_{Y} is defined as above and $\mathcal{L}$ is the provided instantaneous luminosity of the LHC.

To determine σ_{Y} for a given trigger, van der Meer (vdM) scans [226, 227] are performed in order to study the geometry of the beam interaction region in ALICE. For this purpose, both beams are separately moved across each other in the two transverse directions x and y which denote the horizontal and vertical direction respectively. By measuring the rate R of a reference process as a function of the beam separation Δx and Δy, the instantaneous luminosity $\mathcal{L}$ for head-on collisions of a pair of bunches is given by:

$$\mathcal{L} = \frac{f_{\mathrm{rev}} N_1 N_2}{h_x h_y}, \tag{4.2.5}$$

where $f = 11245.5\,\mathrm{Hz}$ is the revolution frequency of the LHC, N_1, N_2 the number of protons in each bunch and h_x, h_y the effective convolved beam widths in the two transverse directions [228]. The cross section σ_{Y} for the chosen reference process can then be determined by $\sigma_{\mathrm{Y}} = R/\mathcal{L}$.

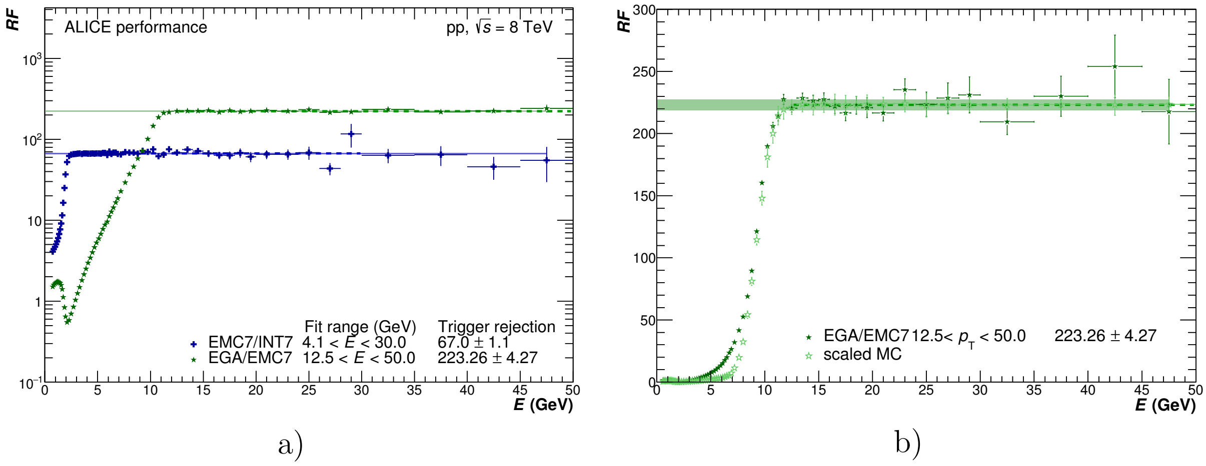

Figure 4.2.6: a) The determination of trigger rejection factors (RFs) is shown. The fitting ranges are indicated by dotted lines, whereas the colored bands around the RFs indicate their systematic uncertainties. b) A comparison of the cluster energy ratios for the EGA for data, dark green, and the Jet-Jet MC simulation using trigger mimicking in light green.

Ideally, a perfect MB trigger samples the minimal fraction of σ_{inel}, at which all physics observables of interest are not influenced and still remain unaffected. In reality, experiments follow a variety of physics observables but also have to deal with different background sources. Therefore, large parts of σ_{inel} are typically visible for MB triggers reaching values of $\epsilon \sim 0.7-0.9$. For the different collision systems analyzed in this thesis, the respective cross sections are listed in Tab. 4.2.4.

The visible cross sections σ_{Y} of the different MB triggers were determined by vdM scans for $\sqrt{s} = 7$ TeV [220] and 8 TeV [228]. However, no vdM scan was carried out for $\sqrt{s} = 0.9$ TeV but σ_{inel} is provided by previous measurements at the SPS [229]. To derive the visible cross sections also in this case, MC simulations were performed to obtain the trigger efficiencies [220] which are represented by ϵ. The respective values for σ_{V0AND} and σ_{V0OR} for $\sqrt{s} = 0.9$ TeV, which were obtained by this procedure, are also quoted in Tab. 4.2.4. The simulations are cross-checked by a comparison with the measured ratios of the different MB event rates which are also given in Tab. 4.2.4. Within the given uncertainties, they are found to be in good agreement with the predictions from the simulations.

Taken together, the integrated luminosities $\mathscr{L}_{\text{int}}$ can be calculated which quantify the collected statistics for the different MB and rare EMCal triggers that were recorded for pp collisions at $\sqrt{s} = 0.9$, 7 and 8 TeV. By separation of variables in Eq. 4.2.4 and integrating over time, they can be obtained by:

$$\mathscr{L}_{\text{int}} = \frac{N_{\text{events}}}{\sigma_{\text{Y}}} \cdot \text{RF}, \tag{4.2.6}$$

where N_{events} is the number of analyzed events, σ_{Y} is the visible cross section of the given MB trigger and RF is the respective trigger rejection factor. For the case of rare EMCal triggers at 8 TeV, σ_{Y} represents the underlying MB trigger condition σ_{V0AND} which is input for the trigger algorithm of the calorimeter. For the MB triggered datasets, the RF is defined to be unity. All obtained values are summarized in Tab. 4.2.5 for the different datasets, where the uncertainties of

pp, $\sqrt{s}$ (TeV)	σ_{V0AND} (mb)	$\sigma_{\mathrm{V0AND}}/\sigma_{\mathrm{V0OR}}$ measured	$\sigma_{\mathrm{V0AND}}/\sigma_{\mathrm{V0OR}}$ simulated	σ_{V0OR} (mb)	σ_{inel} (mb)
0.9	$40.1^{+2.0}_{-1.6}$	0.8401 ± 0.0004	$0.839^{+0.006}_{-0.008}$	$47.8^{+2.4}_{-1.9}$	$52.5 \pm 2.0_{\mathrm{(sys)}}$
7	54.3 ± 1.9	0.8727 ± 0.0001	0.871 ± 0.007	62.4 ± 2.2	$73.2^{+2.0}_{-4.6}{}_{\mathrm{(model)}} \pm 2.6_{\mathrm{(lumi)}}$
	σ_{V0AND} (mb)		$\sigma_{\mathrm{T0AND}}/\sigma_{\mathrm{V0AND}}$ measured	σ_{T0AND} (mb)	
8	55.8 ± 1.5		0.457 ± 0.015	25.5 ± 0.5	$74.7 \pm 1.7_{\mathrm{(sys)}}$

Table 4.2.4: The visible cross sections σ_{Y} for the different MB triggers used for analysis, σ_{V0AND} and σ_{V0OR}, for pp collisions at $\sqrt{s} = 0.9$, 7 and 8 TeV. The value for σ_{T0AND} at 8 TeV is given for further reference. The measured and simulated ratios of the MB trigger rates are furthermore quoted, showing good agreement within uncertainties. The given values for 0.9 and 7 TeV are obtained from Refs. [220, 229] which are also summarized in Ref. [10]. For 8 TeV, the visible cross sections are provided by Ref. [228] and the total cross section is given by Ref. [230]. Unless labeled differently, the uncertainties always reflect a combination of both statistical and systematic contributions.

the visible cross sections, which are quoted in Tab. 4.2.4, are indicated by the term “norm”. The systematic uncertainties entering from the determination of the RFs are labeled with “sys”.

	$\mathscr{L}_{\mathrm{int}}$ (nb^{-1})		
pp, $\sqrt{s}$ (TeV)	MB (INT1, INT7)	EMCal-L0 (EMC7)	EMCal-L1 (EGA)
0.9	$0.12 \pm 0.01_{\mathrm{(norm)}}$	-	-
7	$5.03 \pm 0.18_{\mathrm{(norm)}}$	-	-
8	$1.94 \pm 0.05_{\mathrm{(norm)}}$	$40.9 \pm 0.7_{\mathrm{(sys)}} \pm 1.1_{\mathrm{(norm)}}$	$615.0 \pm 15.0_{\mathrm{(sys)}} \pm 16.0_{\mathrm{(norm)}}$

Table 4.2.5: The integrated luminosities for the different pp datasets recorded at $\sqrt{s} = 0.9$, 7 and 8 TeV, calculated according to Eq. 4.2.6 which are available for analysis.

4.3 Quality Assurance

All the datasets and corresponding MC simulations analyzed in this thesis, which are quoted in Tabs. 4.1.1 and 4.1.2, were subject to a detailed Quality Assurance (QA) procedure. The aim of this procedure is to ensure that the detectors were operated under stable conditions for each recorded run and showed no malfunction during data taking. Furthermore, the anchored MC simulations are cross-checked with data to make sure that varying detector conditions, e.g. changing acceptances, are properly reflected by the simulations. Such varying detector conditions are frequently occurring between subsequent runs during data taking due to specific detector related reasons. In this case, it is highly important that the simulations are able to describe these varying conditions and follow the trends seen in data. For this purpose, a powerful framework has been developed in the context of this thesis [215] which is able to address all the needs for a reliable QA, for which further documentation can be found in Ref. [217].

In general, the QA has been carried out on two levels: (i) run-by-run; (ii) each period and the whole dataset. All observables and derived quantities relevant for the measurements were cross-checked in detail on both levels. As different event generators are used for the simulations which are based on different models, being constantly developed further, so that not all aspects of real data can be described entirely. In this context, it is more important that the MC simulations do not miss the total number of particles, for example, by an order of magnitude and are able to reproduce the detector response correctly which may vary from run to run, as already explained, so that they can be used for the extraction of reconstruction efficiencies. The framework is generally split into an event-related part which monitors basic event properties and global observables and the QA on photon reconstruction which is furthermore subdivided the V^0-related and calorimeter-related branches.

The run-by-run level QA yields a set of good runs for each data taking period to be used for analysis. These lists can be found in Tabs. B.1.1, B.1.2, B.1.3, B.1.4, B.1.5 and B.1.6 for the analyzed datasets in this thesis. The selection is based on the central information summarized in the Run Condition Table (RCT) of ALICE which gives insight about the quality of the recorded runs since it collects known issues which occurred during data taking. All runs have to be declared as good runs in the RCT, in which the tracking detectors, most importantly ITS and TPC, as well as the EMCal are required to be labeled as properly running under stable conditions during data taking. All relevant observables were investigated but the most important ones to distinguish between good runs to be accepted for analysis and bad runs to be discarded are the following:

- number of π^0 candidates per event as well as reconstructed π^0 (η) mass and width on run-by-run level;
- number of photon conversion candidates obtained from the V^0 sample and number of EMCal photon candidates per event;
- energy and momentum distributions of photon candidates;
- η/φ-distributions of selected photon candidates;
- general event properties, e.g. number of charged tracks per event, z-vertex distributions as well as fraction of events discarded due to pileup or missing primary vertices.

If a run significantly deviates from the global mean value of a respective observable, it is discarded for further analysis. This condition is enforced unless there is no clear explanation for the varying behavior of the observable which the anchored MC simulation can reproduce. The following Figs. 4.3.7a and 4.3.7b summarize the good runs accepted for analysis for $\sqrt{s} = 7$ and $8\,\mathrm{TeV}$ and show the recorded as well as simulated number of events for each run. The anchoring of the MC simulations can be followed from the plots.

In Fig. 4.3.8a, the average number of reconstructed primary tracks per event is shown for data and MC simulations at $\sqrt{s} = 8\,\mathrm{TeV}$. In principle, the event generators are able to describe the observed multiplicities and, most importantly, the run dependence is obeyed by simulations. Alongside, Fig. 4.3.8b shows the mean z position of the reconstructed primary vertex for pp, $\sqrt{s} = 7\,\mathrm{TeV}$. Also in this case, the anchored simulation properly reflects the running conditions.

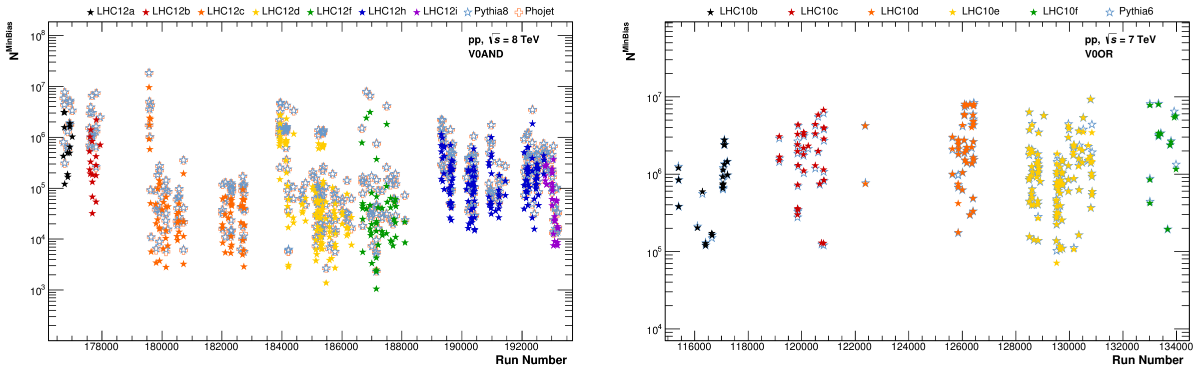

a) b)

Figure 4.3.7: The available runs which are used for analysis for the respective MB triggers recorded at $\sqrt{s} = 8\,\mathrm{TeV}$, a), and $7\,\mathrm{TeV}$, b). The datasets are introduced in Tab. 4.1.1 with the corresponding statistics recorded, which is broken down into the available statistic per run in a) and b).

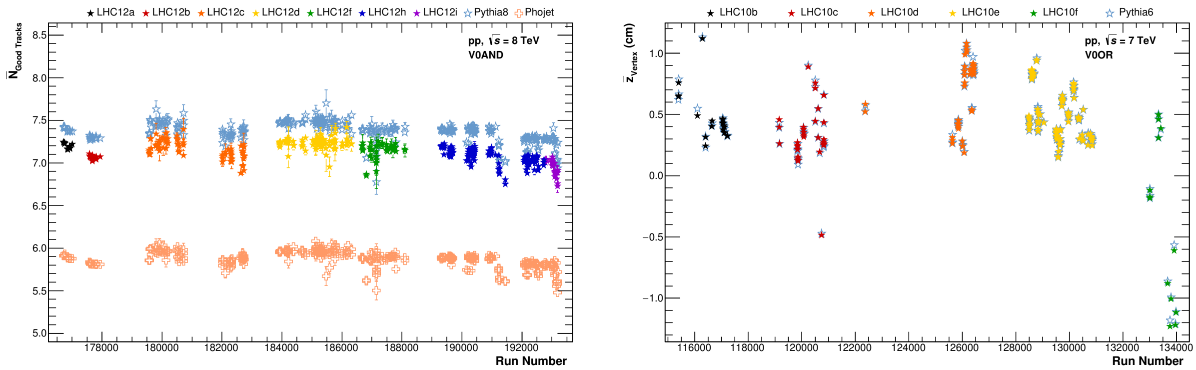

a) b)

Figure 4.3.8: The average number of reconstructed primary tracks per event, a), and the mean z-vertex position, b), for pp collisions at $\sqrt{s} = 7$ and $8\,\mathrm{TeV}$.

The following Fig. 4.3.9a shows the average number of V^0 photon candidates per event. The data points follow the trend seen in Fig. B.0.1b since no out-of-bunch pileup has been removed yet, which is generally not present in simulations. The average number of EMCal clusters per event is shown in Fig. 4.3.9b. The response of each of the total of 12,288 cells of the EMCal was studied and compared to MC simulations in each run. These studies were carried out to ensure that varying acceptances of the detector are correctly mapped to MC, which can be followed in Fig. 4.3.9b, and that the response of each cell is properly reflected in MC, i.a. excluding so-called “hot” and “cold” cells which fire more often and less, respectively, in real data than in simulations.

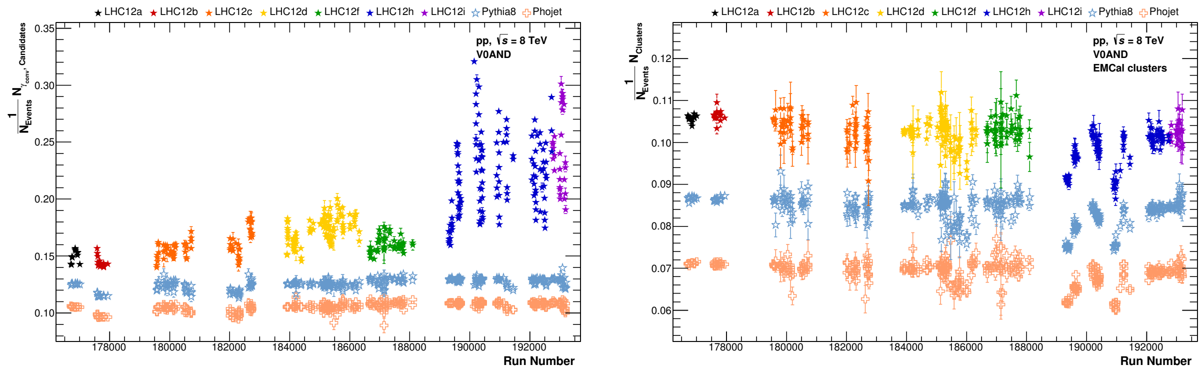

a) b)

Figure 4.3.9: The average number of V^0 photon candidates, a), and EMCal cluster candidates, b), for pp collisions at $\sqrt{s} = 8\,\mathrm{TeV}$, obtained after applying all cuts described in Chap. 5.

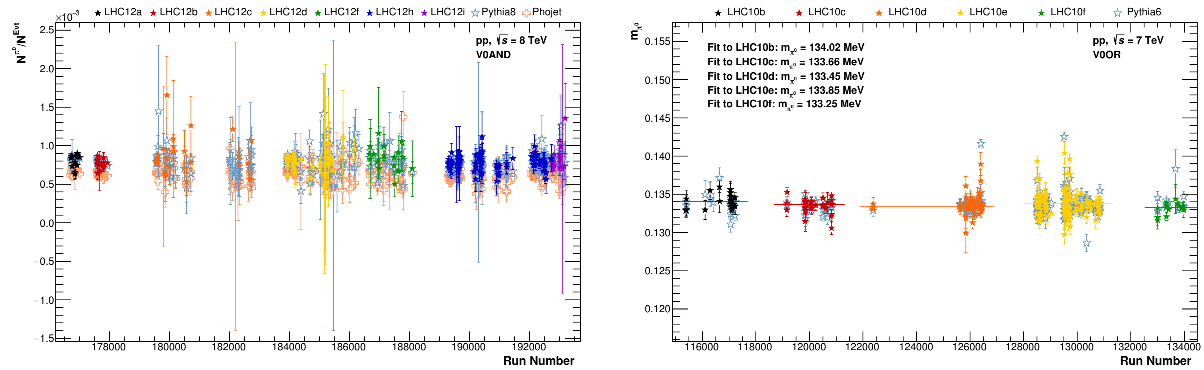

a) b)

Figure 4.3.10: The average number of π^0 candidates per event, a), for $\sqrt{s} = 8\,\mathrm{TeV}$ and the reconstructed π^0 mass, b), in units of GeV/c^2 for each run which was recorded for $\sqrt{s} = 7\,\mathrm{TeV}$.

Chapter 5

Photon Reconstruction

In ALICE, photons are measured via two fundamentally different detection methods: exploiting the Photon Conversion Method (PCM) and employing the installed electromagnetic calorimeters, namely the EMCal and the PHOS. Both methods are introduced in this chapter and their basic reconstruction principles are elaborated. Concerning the electromagnetic calorimeters, the focus is set on the EMCal as it is exclusively used for the reported analysis in this thesis. The photon reconstruction using the PHOS is not explicitly described, however, the concept is identical compared to the EMCal. Furthermore, the photon selection criteria are established which are used to perform reliable photon reconstruction with high purity for each of the two methods. Finally, some more detail is given about the refined energy calibration scheme for the EMCal which is used to precisely tune the MC simulations to measured data.

5.1 Photon Conversion Method

Photons may convert into electron-positron pairs e^-e^+ within the detector material of ALICE. Thus, secondary vertices V^0s are generated from which two secondary particles originate. Such photon conversions can be reconstructed by means of the tracking system of ALICE. This procedure is named Photon Conversion Method (PCM). In this context, the secondary tracks represent electron and positron candidates, generally denoted daughters of the V^0, which itself represents the so-called mother particle. Furthermore, V^0 is also identified as conversion photon candidate in the context of the PCM and the actual location of the V^0 in detector space is also referred to as conversion point. The reconstruction of PCM photons may be divided into three major steps:

(i) tracking and V^0 finding;

(ii) track selection, PID;

(iii) photon candidate reconstruction and subsequent selection.

Every step is further elaborated in the following, for which all applied photon selection criteria are summarized in the following Tab. 5.1.1. The PCM uses the main tracking systems of ALICE which consist of the ITS and the TPC. With this method, it is feasible to reconstruct photon conversion candidates between the IP and a radius which approximately corresponds to the midpoint of the TPC in radial direction. In the given region, photons convert with a probability of about 9 % in ALICE, see also Fig. 7.2.8a in Sec. 7.2, enabling a direct measurement of the integrated radiation length of the complete ALICE detector up to this radius.

The secondary vertices are determined using the on-the-fly V^0-finder. It provides better efficiencies in particular for low momenta and an improved conversion point resolution with regard to the offline V^0-finder, see also Sec. 3.3.1. No assumption on the mass of the two daughter particles is applied during this procedure. However, the standard hypothesis used for the V^0 reconstruction is the decay of a K^0_S. Therefore, the precision of the reconstructed conversion points is improved by recalculating the position of the V^0 under the assumption that the momenta of its daughter particles are parallel at the point of their creation. This is a truly valid assumption for real photons since they have no mass. The recalculation is described in detail in Refs. [231, 232] and accordingly Ref. [233], where also more information about the achieved spatial resolutions of the photons can be found.

	pp, $\sqrt{s} = 0.9$, 7 and 8 TeV
track selection criteria	
general	$p_{\mathrm{T,track}} > 0.05\,\mathrm{GeV}/c$
	$N_{\text{cluster TPC}}/N_{\text{reconstructable clusters}} > 60\,\%$
	$\lvert\eta_{\mathrm{track}}\rvert < 0.9$
electron PID	$-4 < n\sigma_e < 5$
	$n\sigma_\pi > 1$ for $p > 0.4\,\mathrm{GeV}/c$
photon (V^0) selection criteria	
general	on-the-fly V^0-finder
	$5\ \mathrm{cm} < R_{\mathrm{conv}} < 180\,\mathrm{cm}$
	$\lvert Z_{\mathrm{conv}}\rvert < 240\,\mathrm{cm}$
	$0 \leq \lvert\varphi_{\mathrm{conv}}\rvert \leq 2\pi$
	$\lvert\eta_{\mathrm{V}^0}\rvert < 0.9$
	$\cos(\theta_{\mathrm{PA}}) > 0.85$
photon quality	$\lvert\psi_{\mathrm{pair}}\rvert < \psi_{\text{pair, max}}(1 - \chi^2_{\mathrm{red}}/\chi^2_{\text{red, max}})$
	with $\psi_{\text{pair, max}} = 0.1$ and $\chi^2_{\text{red, max}} = 30$
Armenteros-Podolanski	$q_{\mathrm{T}} < q_{\text{T, max}}\sqrt{1 - \alpha^2/\alpha^2_{\max}}$
	with $q_{\text{T, max}} = 0.05\,\mathrm{GeV}/c$ and $\alpha_{\max} = 0.95$

Table 5.1.1: The track and photon selection criteria, also denoted cuts, which are applied for the reconstruction of photons using the PCM. All listed criteria are likewise applied for $\sqrt{s} = 0.9$, 7 and 8 TeV.

The daughter tracks of the V^0s are required to have opposite charges and not to exhibit any kink topology. Furthermore, each track associated with a secondary vertex has to have a minimum transverse momentum of $p_{\mathrm{T,track}} > 0.05\,\mathrm{GeV}/c$. In addition, at least 60 % of TPC clusters from the maximum possible number of clusters, which a daughter track can create in the TPC along its path, need to be found. The daughter tracks also have to pass the condition $\lvert\eta_{\mathrm{track}}\rvert < 0.9$, where η is determined based on the angle between the beam axis and the orientation of the momentum vector of the daughter particle in the ZR-plane.

In order to primarily select the photons among the remaining set of V^0s and, at the same time, to reject contributions from K^0_S, Λ and $\bar{\Lambda}$ which partially have charged pions in their decay channels, electron/positron PID criteria and additional charged pion rejection cuts are applied as listed in Tab. 5.1.1. For this purpose, the PID information of the TPC is mainly used to identify electrons and positrons. All cuts are applied independent of the actual charge

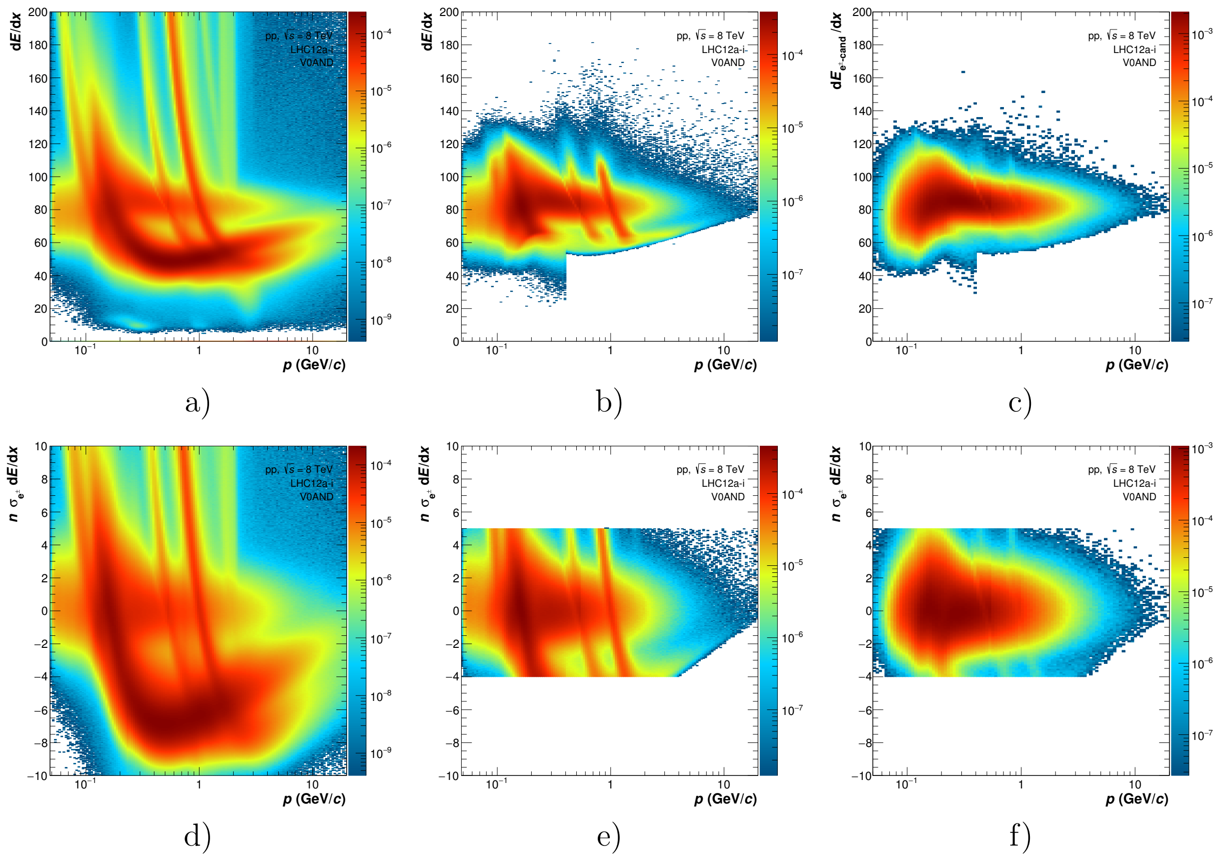

Figure 5.1.1: The measured raw TPC $\mathrm{d}E/\mathrm{d}x$ distribution, a), and the corresponding quantity $n\sigma_e$, d), defined in Eq. 5.1.1, for the full sample of positively and negatively charged V^0 daughter tracks after solely enforcing the general selection criteria from Tab. 5.1.1. By further applying the electron PID cuts, the respective plots shown in b) and e) are obtained. After applying the full set of selection criteria given in Tab. 5.1.1, the distributions shown in c) and f) are obtained which correspond to rather clean electron samples with high purity. All 2D-histograms shown from a) to f) are normalized to an integral of one.

of the track so that the term 'electrons' always denotes the combined sample of e^- and e^+ in the following, unless specified differently. Other techniques, e.g. using the provided PID information from the ITS, TOF and TRD detectors, are not considered in this context since each of these are only applicable to a small fraction of secondary tracks. Therefore, the available statistics would be significantly reduced and new sources of systematic uncertainties would be introduced in addition so that no major improvement would be possible.

Hence, electrons from photon conversions are identified by means of the TPC via their measured energy deposit per path length $\mathrm{d}E/\mathrm{d}x$. This quantity is plotted in Fig. 5.1.1a for all V^0 daughter tracks after only applying the general selection criteria for tracks and V^0s from Tab. 5.1.1. The different bands, which are observed, can be related to different particle species as already introduced in Fig. 3.2.5b. The electron band is located around a $\mathrm{d}E/\mathrm{d}x$ value of 80 while the most abundant particle is the charged pion which is represented by the broad distribution around $\mathrm{d}E/\mathrm{d}x \approx 50$ at $p = 1\,\mathrm{GeV}/c$, followed by protons and kaons. The difference of the measured $\mathrm{d}E/\mathrm{d}x$ value from the hypothesis of the electron energy loss is used for PID, which is shown in Fig. 5.1.1d for the corresponding case. The measured TPC $\mathrm{d}E/\mathrm{d}x$ of the daughter tracks is required to be within $-4 < n\sigma_e < 5$ of the expected electron energy loss which is a momentum-dependent observable defined by:

$$n\sigma_e = \frac{\mathrm{d}E/\mathrm{d}x - \langle \mathrm{d}E/\mathrm{d}x \rangle_e}{\sigma_e}, \tag{5.1.1}$$

with the average energy loss of the electron $\langle \mathrm{d}E/\mathrm{d}x \rangle_e$ and the Gaussian width σ_e of the fit to the measured $\mathrm{d}E/\mathrm{d}x$ distribution. To further reduce charged pion contamination as the pion $\mathrm{d}E/\mathrm{d}x$ band begins to merge with the electron $\mathrm{d}E/\mathrm{d}x$ band above $p \gtrsim 4\,\mathrm{GeV}/c$, a cut based on the separation from the hypothesis of charged pion energy loss is applied in $n\sigma_\pi$, analog to the previous definition in Eq. 5.1.1. Tracks with energy losses closer to the pion line than $|n\sigma_\pi| < 1$ are removed. Taken together, both PID cuts remove about 97 % of the full sample of secondary tracks for pp collisions and clearly enhance the fraction of electron candidates as demonstrated in Fig. 5.1.1b and, accordingly, Fig. 5.1.1e. After applying all remaining cuts from Tab. 5.1.1, which will be described in the upcoming part of this section, Fig. 5.1.1c and Fig. 5.1.1f are finally obtained, indicating electron candidates with high purity.

Conversion photon candidates are only considered if they are reconstructed at a radial distance of at least $R > 5\,\mathrm{cm}$ in order to reduce the contamination from Dalitz decays, $\pi^0 \rightarrow \gamma e^- e^+$. Additional constraints are imposed on $R_\mathrm{conv} < 180\,\mathrm{cm}$ and $|Z_\mathrm{conv}| < 240\,\mathrm{cm}$ to ensure that the reconstruction of secondary tracks is performed inside the TPC. A so-called line-cut is further applied to restrict the geometrical η distribution of the V^0s in order to remove photon candidates that would otherwise appear outside the angular dimensions of the detector. Therefore, the following constraint is enforced for the V^0s:

$$R_\mathrm{conv} > |Z_\mathrm{conv}| \cdot S_\mathrm{ZR} - Z_0, \tag{5.1.2}$$

where $S_\mathrm{ZR} = \tan\left(2 \cdot \arctan(\exp(-\eta_\mathrm{cut}))\right)$, $Z_0 = 7\,\mathrm{cm}$ and $\eta_\mathrm{cut} = 0.9$. The coordinates R_conv and Z_conv are determined with respect to the nominal center of the detector, $(X, Y, Z) = (0, 0, 0)$, and thus do not depend on the primary vertex position.

Furthermore, a cut on the cosine of the pointing angle of $\cos(\theta_\mathrm{PA}) > 0.85$ is performed to remove fake photon candidates. Here, the pointing angle θ_PA is the angle between the reconstructed photon momentum vector and the vector joining the collision vertex and the conversion point. The cut is already applied on reconstruction level but is repeatedly applied after recalculating the conversion point to remove the candidates which do not fulfill the condition anymore.

The non-photon contamination of V^0 candidates is further suppressed by a triangular two-dimensional cut:

$$|\psi_\mathrm{pair}| < \psi_\mathrm{pair,\,max}(1 - \chi^2_\mathrm{red}/\chi^2_\mathrm{red,\,max}), \tag{5.1.3}$$

with $\psi_\mathrm{pair,\,max} = 0.1$ and $\chi^2_\mathrm{red,\,max} = 30$. The cut is based on the reduced χ^2_red $\left(\equiv \chi^2_\gamma/\mathrm{ndf}\right)$ of the Kalman-Filter [206, 207] hypothesis for the $e^- e^+$ pair, thus selecting the reconstructed photon candidates by their quality. In this context, Fig. 5.1.2a compares the χ^2_red distributions for data and MC, further breaking down the different contributions observed in simulations. Moreover, the angle ψ_pair denotes the angle between the plane perpendicular to the magnetic field of the ALICE solenoid magnet and the $e^- e^+$ pair plane. The first plane can be identified with the xy-plane and within the second, the opening angle of the $e^- e^+$ pair is defined by: $\xi_\mathrm{pair} = \arccos\left(\vec{p_{e^-}} \cdot \vec{p_{e^+}} / |\vec{p_{e^-}}| \cdot |\vec{p_{e^+}}|\right)$ [234]. By using the difference of the polar angle for that pair in addition, $\Delta\theta_{e^-e^+} = \theta_{e^-} - \theta_{e^+}$, the following definition follows: $\psi_{\text{pair}} = \arcsin\left(\Delta\theta_{e^-e^+}/\xi_{\text{pair}}\right)$. The ψ_{pair} angle, being evaluated after a propagation of both daughter tracks for 50 cm in outside radial distance, is able to distinguish between real signal and random combinations since it is a measure of the contribution of the azimuth component to the total opening angle of the e^-e^+ candidate pair. For real photon conversions, ψ_{pair} is peaked at zero radiant as it can be followed from Fig. 5.1.2b, where a comparison between data and simulation for the accepted photon candidates is shown. On the other hand, decays of particles with rest mass or arbitrary combinations basically yield random values of ψ_{pair}. Both quantities, χ^2_{red} and ψ_{pair}, are used in conjunction as they span a plane in which signal and background can be well distinguished. While the combinatorial background is distributed flat in the whole plane, the signal is concentrated close to zero for both quantities.

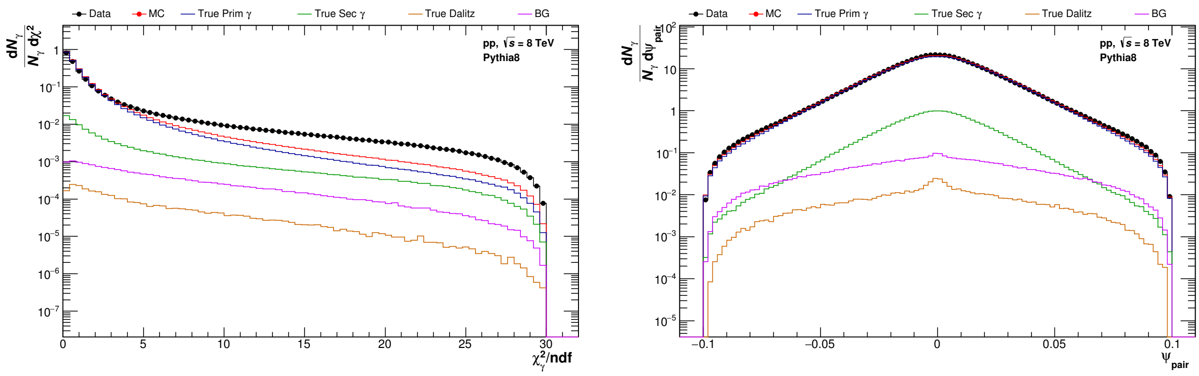

Figure 5.1.2: Comparisons of the χ^2_{red}, a), and ψ_{pair}, b), distributions for data and MC simulations. For the latter case, the different categories are plotted separately which are based on the MC true information: true primary and true secondary photons, true Dalitz decays and contributions from background, e.g. random combinations or falsely identified particles. The distributions are not fully matched between data and MC in the tails which could stem from the underestimation of secondaries in PYTHIA 8 compared to data while noting the logarithmic y-axis. Both plots show distributions which are normalized by the total number of photon candidates passing all selection criteria.

The remaining contamination from K^0_S, Λ and $\overline{\Lambda}$ can be further reduced by means of the Armenteros-Podolanski [235] plot which is shown in Fig. 5.1.3a for the V^0 sample, obtained after applying the general selection criteria from Tab. 5.1.1. The plot shows the projection of the momentum of the daughter particle with respect to the V^0 in the transverse direction, $q_{\text{T}} = p \times \sin\theta_{\text{mother-daughter}}$, plotted versus the longitudinal momentum asymmetry $\alpha = (p^+_L - p^-_L)/(p^+_L + p^-_L)$ of both daughters. In the laboratory frame, the opening angle between both daughter particles of the conversion photon candidate are very small due to the vanishing rest mass of the photon. Hence, q_{T} is close to zero for real photon conversions but yields larger values if the mother particle has a non-vanishing rest mass. Moreover, the distribution is symmetric around $\alpha = 0$ if the daughters have the same mass. In Fig. 5.1.3a, four different structures are distinguishable which are marked in the plot: the symmetric distributions of real photons with q_{T} close to $0\,\text{GeV}/c$ as well as K^0_S where the same quantity ranges from 0.05 to approximately $0.20\,\text{GeV}/c$ plus the Λ and $\overline{\Lambda}$ represented by the asymmetric distributions around $\alpha = \pm 0.7$, which are caused by the mass difference of the decay products. Therefore, the Armenteros-Podolanski is used to further reject non-photon contribution concerning the remaining sample of V^{0}s by applying the following criterion for q_T which depends on α:

$$q_\mathrm{T} < q_{\mathrm{T,\,max}}\sqrt{1-\alpha^2/\alpha^2_\mathrm{max}}, \tag{5.1.4}$$

with $q_{\mathrm{T,\,max}} = 0.05\,\mathrm{GeV}/c$ and $\alpha_\mathrm{max} = 0.95$. The resulting distribution is shown in Fig. 5.1.3b after all cuts from Tab. 5.1.1 are applied. For further illustration, the different structures from Fig. 5.1.3a are visualized as well.

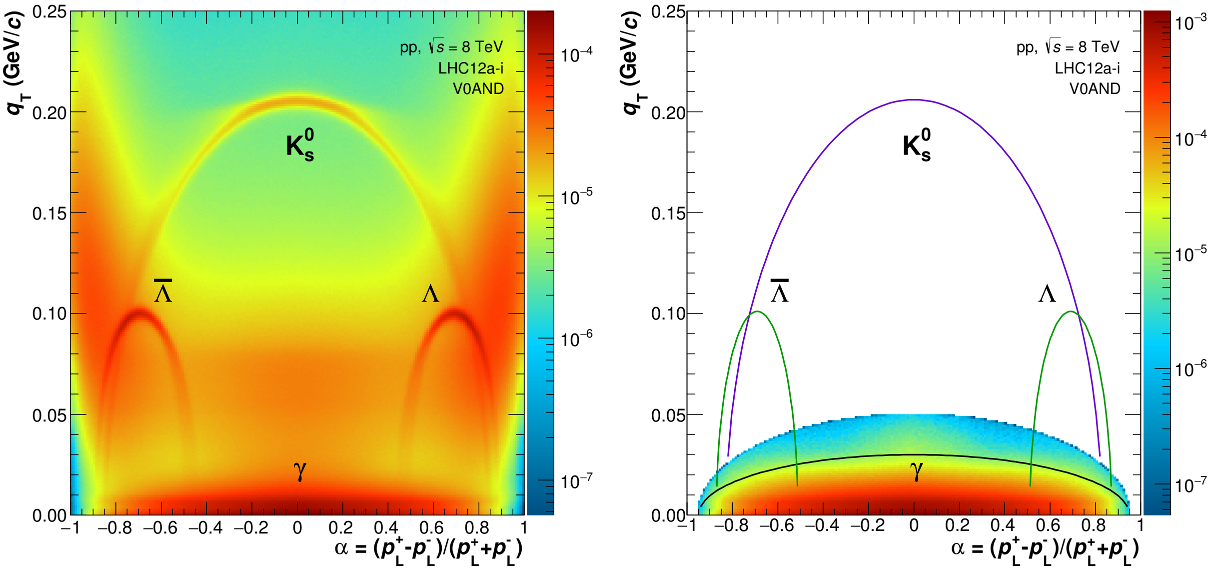

a) b)

Figure 5.1.3: Displays of Armenteros-Podolanski plots after only applying the general selection criteria, a), and after applying all criteria, b), which are listed in Tab. 5.1.1. Both plots are normalized by the total number of photon candidates passing the respective selection criteria.

After applying all selection criteria given in Tab. 5.1.1, high photon purities of more than 98% are reached up to momenta of $p_\mathrm{T} \approx 10\,\mathrm{GeV}/c$ for pp collisions. The following Fig. 5.1.4a and Fig. 5.1.4b show the conversion points of all these accepted photon candidates in the XY- and ZR-plane of ALICE. The more material is present, the more conversions can be observed. Some important structures visible in the plots are exemplary listed in the following:

- $R \lesssim 10$ cm: all structures from the beam pipe up to both layers of the SPD;
- $R \approx 15$; 25 cm: both layers of the SDD;
- $R \approx 40$ cm: both layers of the SSD;
- $R \approx 60$; 80 cm: the TPC inner containment vessel and the TPC inner field cage, followed by the TPC gas for $R \gtrsim 85$ cm.

Thus, the PCM is also a powerful tool to perform a detector tomography of ALICE [232] as the method is very sensitive on the amount of material which is actually present.

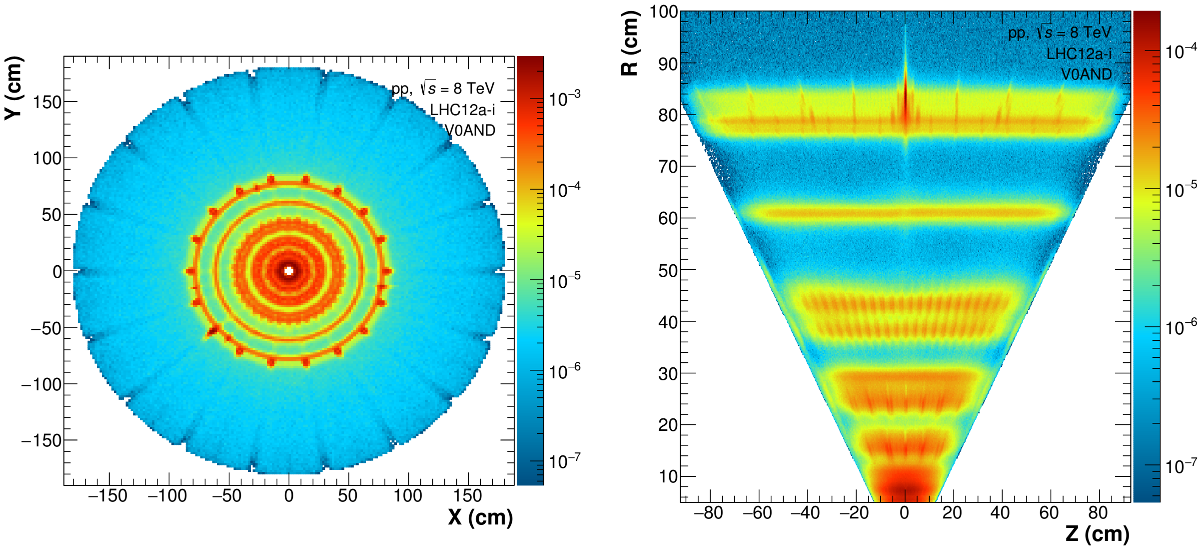

a) b)

Figure 5.1.4: The conversion points of photon candidates passing all selection criteria which are plotted for the XY- and ZR-plane in a) and b) respectively. The number of reconstructed photon candidates in each bin of the 2D histograms visualize the amount of present detector material of ALICE, which is quantified in Tab. 3.2.1.

On analysis level, an out-of-bunch pileup correction is furthermore required if the PCM is used standalone which estimates the contamination of photon candidates from multiple events overlapping in the TPC, introduced in Sec. 4.2 and further elaborated in Sec. 7.2.

5.2 Electromagnetic Calorimeter

When photons, but also electrons and positrons, enter an electromagnetic calorimeter like the EMCal, they generate electromagnetic showers and deposit their energy in this way. By design, these showers usually cover multiple adjacent cells of the calorimeter for the energy range of interest. Hence, the full response of the EMCal to an impinging particle is obtained by grouping such sets of adjacent cells into so-called clusters which represent the complete deposited energy of a given particle. Since the rest mass of photons is zero, which is in good approximation also true for electrons in the GeV range, the full four-momentum vector can be reconstructed by computing the center of gravity of the cluster and assuming that the particle originated from the primary vertex. Therefore, the EMCal can be used to measure photons so that in this context a cluster is referred to as EMCal photon candidate. However, any particle generally deposits at least some energy when entering a calorimeter so that also contributions from hadrons and heavier leptons need to be suppressed. Charged particles, such as electrons and positrons, can be rejected from the photon candidate sample by a track-to-cluster matching procedure. To reject MIPs, which deposit $E \lesssim 300\,\mathrm{MeV}$, low-energy hadrons and detector noise, specific energy thresholds are applied for each cell and cluster. In addition, further selection criteria are applied to primarily select photon clusters which are summarized in Tab. 5.2.2.

	pp, $\sqrt{s} = 0.9$, 7 and 8 TeV	
cluster reconstruction		
clusterizer	V2	
	$\lvert t_{\text{cell}}\rvert < 500\,\text{ns}$	
	$E_{\text{seed}} = 500\,\text{MeV}$	
	$E_{\text{min}} = 100\,\text{MeV}$	
energy correction	CCRF	
cluster selection criteria		
general criteria	$\lvert\eta_{\text{cluster}}\rvert < 0.67$	
	$1.40\,\text{rad} < \varphi_{\text{cluster}} < 3.15\,\text{rad}$	
	$E_{\text{cluster}} > 0.7\,\text{GeV}$	
	$N_{\text{cells}} \geq 2$	
cluster time	-30 ns $< t_{\text{cluster}} <$ 35 ns	-130 ns $< t_{\text{cluster}} <$ 130 ns
	for $\sqrt{s} = 8$ TeV	for $\sqrt{s} = 0.9$ and 7 TeV
cluster shape		
PCM-EMCal	$0.1 \leq \sigma^2_{\text{long}} \leq 0.5$	
EMCal	$0.1 \leq \sigma^2_{\text{long}} \leq 0.7$	
EMCal γ_{dir}	$0.1 < \sigma^2_{\text{long}} < 0.32 + 0.0072 \cdot E^2_{\text{cluster}}/\text{GeV}^2$ for $E_{\text{cluster}} \leq 5$ GeV	
	$0.1 < \sigma^2_{\text{long}} < 0.5$ for $E_{\text{cluster}} > 5$ GeV	
track matching	$\lvert\Delta\eta\rvert < 0.010 + \left(\frac{p_{\text{T}}}{\text{GeV}/c} + 4.07\right)^{-2.5}$	
	$\lvert\Delta\varphi\rvert < 0.015 + \left(\frac{p_{\text{T}}}{\text{GeV}/c} + 3.65\right)^{-2}$	

Table 5.2.2: The parameters used to reconstruct EMCal clusters and subsequently select photon candidates. All listed criteria are likewise applied for $\sqrt{s} = 0.9$, 7 and 8 TeV, unless otherwise specified as for the cluster timing or for the shape parameter which somewhat varies for different reconstruction methods.

The FEE of the EMCal detector is only able to register ADC counts for each cell, obtained from the amount of scintillation light hitting the APD. Hence, a translation function is needed to convert ADC counts to a calibrated energy information. Since the gain of the different APDs may vary, a response to a given signal would be different for each of them. Therefore, a pre-calibration is performed by using MIPs from cosmics [156]. The high voltages applied to each APDs are tuned so that ideally all cells give the same response for the MIPs. Residual differences are corrected for on software level by additional coefficients which are obtained from physics data. For this purpose, the MIP peak from high statistics data is also used to adjust the gain factors for each cell. Moreover, the relative energy calibration of the detector is performed by measuring, in each cell, the reconstructed π^0 mass in the invariant mass distribution of photon pairs built with one photon in the given cell. In addition, identified electrons are further used to verify the energy scale of the EMCal by comparing their reconstructed energies to their momenta determined by the tracking system [167]. The achieved relative calibration level is estimated to be 3% and adds up quadratically to the constant term of the energy resolution [4]. On analysis level, an additional energy correction is applied to MC simulations which improves the MC description of measured data in the relevant p_{T} range used for analysis by exploiting the high resolution of PCM photons. The procedure is introduced and further elaborated in Sec. 5.2.1.

Due to different cable lengths, for example, a time calibration is also performed for each cell [236]. The calibration is of high importance for the analysis since the time of a cluster is inherited from the highest energetic cell of the cluster. Since the bunch spacing within the LHC can be as low as 25 ns, a proper timing information is required to be able to assign the clusters to the correct bunch crossing, hence event, since the readout window of the EMCal spans about 1 μs. There is no proper timing simulation of the EMCal available for MC, however, no pileup is present at all by definition. Consequently, no timing cuts are applied in this case.

The EMCal is able to reconstruct photons by combining adjacent cells with deposited energies into clusters which is realized by a clusterization algorithm. Although many different algorithms are possible in theory, there are two dominantly used clusterizer versions in ALICE which have proven to be reliable and robust, the so-called V1 and V2. The latter one is used per default, whereas the V1 serves as cross-check in this thesis. In Fig. 5.2.5, the outcome of applying the V2 clusterizer algorithm can be followed which is described in the following:

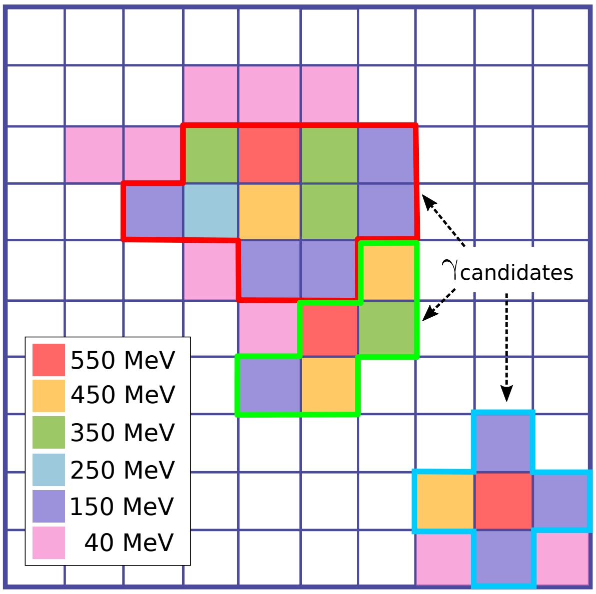

Figure 5.2.5: A schematic [237] of the working principle of the V2 clusterizer, reconstructing three different photon candidates in the example.

At first, the V2 algorithm looks for the cell that recorded the highest energy in the event, exceeding the seed energy threshold E_{seed}. After the identification of such a seed cell, adjacent cells with recorded energies above a minimum energy E_{min} are added to the cluster. The algorithm adds cells to the cluster as long as their recorded energy is smaller than the previous cell's energy. However, the V2 does not aggregate the respective cell if it recorded a higher energy than the previous one. The clusterization process continues in the same way with the remaining cells until all of them, which detect a signal above the required energy thresholds, are grouped into clusters. Cluster energies are then calculated by $E = \sum_i^{N_{\text{cells}}} e_i$, where e_i stands for the energy recorded by the indicated cell. The values of E_{seed} and E_{min} depend on the energy resolution and the noise level of the FEE. For the EMCal, they are set to $E_{\text{seed}} = 500\,\text{MeV}$ and $E_{\text{min}} = 100\,\text{MeV}$ to reject MIPs and suppress detector noise. The only difference of the V1 clusterizer compared to the V2 is that the V1 does not enforce the condition that an adjacent cell needs to have less energy than the current one, so that neighboring clusters do merge much faster into single clusters compared to the V2. In both cases, no cuts on potential time differences between cells in a cluster are applied as the cell's timing information is only reliable above E_{seed}.

After the cluster finding step is performed, some general selection criteria are applied to the clusters. Trivially, they are required to fulfill $|\eta_{\text{cluster}}| < 0.67$ and $1.40\,\text{rad} < \varphi_{\text{cluster}} < 3.15\,\text{rad}$ to be located on the EMCal surface. Furthermore, clusters need to be composed of at least two cells $N_{\text{cells}} \geq 2$ and need to have an energy of $E_{\text{cluster}} > 0.7\,\text{GeV}$. Moreover, a cut on the cluster timing is performed in order to only select clusters that belong to the given event. Due to the fact that EMCal has a fairly fast readout, the constraint to the triggering collision is therefore given for a photon candidate if a timing cut on the cluster level is used. The actual cut to be applied depends on the present bunch spacing in the LHC which may vary from fill to fill. For pp data recorded at $\sqrt{s} = 8\,\text{TeV}$, the bunch spacing was throughout 50 ns so that a cut of -30 ns $< t_{\text{cluster}} <$ 35 ns was used. For $\sqrt{s} = 0.9$ and 7 TeV, much larger spacings were present so that the condition could be loosened to -130 ns $< t_{\text{cluster}} <$ 130 ns.

The shape of clusters, characterized by the common shower shape parameter σ^2_{long} on the EMCal surface, can be used for PID purposes [8, 238]. The parameter represents the long axis of the shower surface ellipse and is defined as follows:

$$\sigma^2_{\text{long}} = 0.5 \left(\sigma_{\varphi\varphi} + \sigma_{\eta\eta} + \sqrt{(\sigma_{\varphi\varphi} - \sigma_{\eta\eta})^2 + 4\sigma^2_{\eta\varphi}} \right), \tag{5.2.5}$$

where $\sigma_{\varphi\varphi}$, $\sigma_{\eta\eta}$ and $\sigma_{\eta\varphi}$ are coefficients weighted by the cell energy:

$$\sigma_{\alpha\beta} = \sum_i \frac{w_i \alpha_i \beta_i}{w_{\text{tot}}} - \sum_i \frac{w_i \alpha_i}{w_{\text{tot}}} \sum_i \frac{w_i \beta_i}{w_{\text{tot}}}, \tag{5.2.6}$$

where the relations $w_{\text{tot}} = \sum_i w_i$ and $w_i = \max\left(0, 4.5 + \log\left(E_i/E_{\text{cluster}}\right)\right)$ [239] apply. The shower shape of pure photons tends to be circular as they enter the EMCal basically perpendicular, unaffected from magnetic fields. Hence, most photons will be reconstructed with a shower shape of $\sigma^2_{\text{long}} \approx 0.25$. Charged particles are, however, bend by the magnetic field generated by the solenoid magnet of ALICE so that they preferably generate elongated clusters in contrast. Although electrons cause a response very similar to photons, late photon conversions within the detector material of the TRD and TOF may generate elongated clusters as well. Therefore, requiring the condition $\sigma^2_{\text{long}} \leq 0.7$ sufficiently rejects contamination from these sources when reconstructing neutral mesons with two EMCal photons. If using only one EMCal photon, this condition is tightened to $\sigma^2_{\text{long}} \leq 0.5$. Since there is no further constraint by invariant mass technique for the direct photon analysis with EMCal, the cut is even more tightened for lower energies to an energy-dependent condition of $\sigma^2_{\text{long}} < 0.32 + 0.0072 \cdot E^2_{\text{cluster}}/\text{GeV}^2$ for $E_{\text{cluster}} \leq 5\,\text{GeV}$. The lower value of $\sigma^2_{\text{long}} \geq 0.1$ is chosen to reject clusters generated by nuclear interactions, in particular from neutrons hitting the APDs of cells. Such cases create abnormal clusters for which the signal is localized within one very high energetic cell. Even if there is some minor cross-talk between cells, any noise or neighboring energy depositions present, a cluster may be reconstructed.

As it is mentioned in Tab. 5.2.2, a track-to-cluster matching procedure is performed during analysis to reject clusters which can be associated to a charged particle. For this purpose, the reconstructed particle trajectories are used as a starting point and are consecutively propagated to the radius of the EMCal surface, if possible. The particle's energy loss is taken into account so that the propagation may fail if the particle has not enough momentum to reach the radial position of the EMCal or if the particles simply misses its surface. If the propagation is successful, the distance between the track and the cluster's center of gravity is calculated in the η-φ plane. The respective residuals are labeled with $\Delta\eta$ and $\Delta\varphi$ accordingly which are plotted in Fig. 5.2.6a for $\sqrt{s} = 8\,\text{TeV}$ without further distinguishing the particle's charge. Besides random associations represented by the blue background, the actual matches at $\Delta\eta = 0$ and $\Delta\varphi = 0$ can be clearly distinguished from that background. If the residuals fulfill the p_{T}-dependent conditions $|\Delta\eta| < 0.01 + \left(\frac{p_{\text{T}}}{\text{GeV}/c} + 4.07\right)^{-2.5}$ and $|\Delta\varphi| < 0.015 + \left(\frac{p_{\text{T}}}{\text{GeV}/c} + 3.65\right)^{-2}$, the matching was successful and the cluster is discarded. Hereby, true MC information was used to determine these matching conditions.

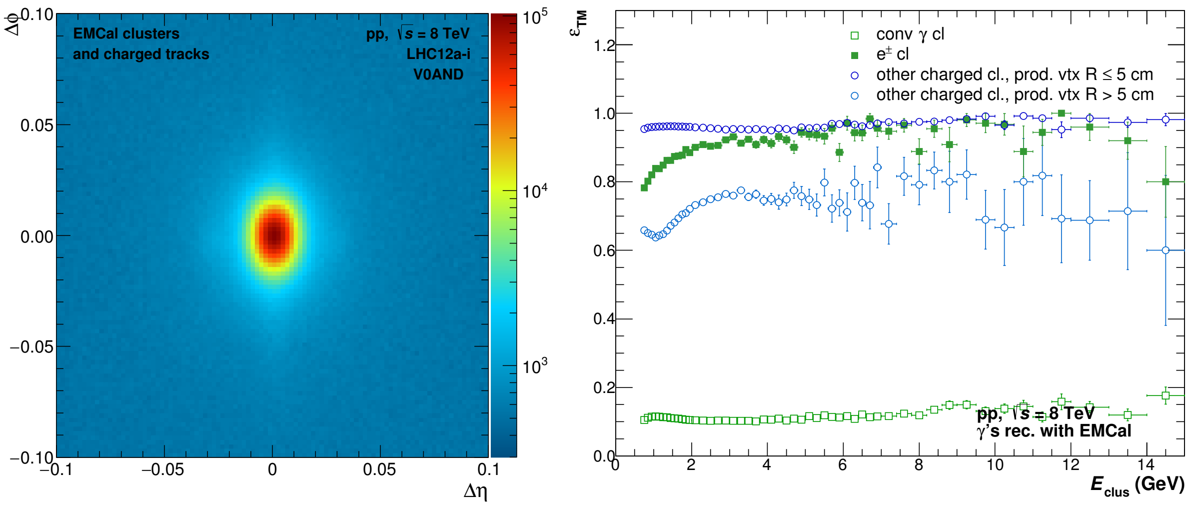

a) b)

Figure 5.2.6: a) The track-to-cluster matching residuals $\Delta\eta$ and $\Delta\varphi$ for data at $\sqrt{s} = 8\,\text{TeV}$. The successful matches are located in the vicinity of $(\Delta\eta/\Delta\varphi) = (0/0)$, whereas the residuals of random combinations are equally distributed in the background. b) The track matching efficiencies obtained from MB MC simulations for primary and secondary tracks as well as electrons are shown. The efficiencies were also verified for the Jet-Jet MC production which show continuous trends of all efficiencies as seen in this figure. Hence, a stable and efficient track matching up to $100\,\text{GeV}/c$ is ensured.

The track-to-cluster matching efficiencies are shown in Fig. 5.2.6b for the EMCal for different categories obtained from a MB MC simulation at $\sqrt{s} = 8\,\text{TeV}$, demonstrating the performance and validity of the matching procedure. For $p_{\text{T}} > 2\,\text{GeV}/c$, efficiencies are well above 95 % for primary electrons and other charged particles with production radii of $R \leq 5\,\text{cm}$. Secondary charged particles with production radii above $R > 5\,\text{cm}$ are still matched with rather high efficiencies. On the other hand, photon conversions occurring within the detector material directly in front of the EMCal, where no tracking detectors are present anymore, cannot be tracked and matched which explains the rather small efficiencies shown in open green squares.

The following Figs. 5.2.7a and 5.2.7b show the η-φ distributions of EMCal clusters which passed all selection criteria from Tab. 5.2.2. During pp data taking at $\sqrt{s} = 8\,\text{TeV}$ in 2012, the EMCal was only partially obscured by the TRD as only 13 out of 18 TRD sectors were installed at that time, see also Tab. 3.2.4. For the four EMCal supermodules located at $\varphi_{\text{cluster}} < 2.1$, there were no TRD modules present. On the other hand, the remaining supermodules at $\varphi_{\text{cluster}} > 2.1$ had the additional detector material of the TRD in front, causing a decrease of the reconstruction efficiency of low momentum photons in particular. This is due to the fact that photons also convert in the outer detector material, which is present, so that the conversion daughters may not be reconstructed anymore. Furthermore, the photon reconstruction efficiencies are observed to increase with larger values of $|\eta|$, also reproduced by the simulations, which also coincides with the η dependence of the photon conversion reconstruction efficiencies. All further features of the distribution seen in data are reproduced by MC simulations as well, which was ensured in great detail during the QA procedure described in Sec. 4.3.

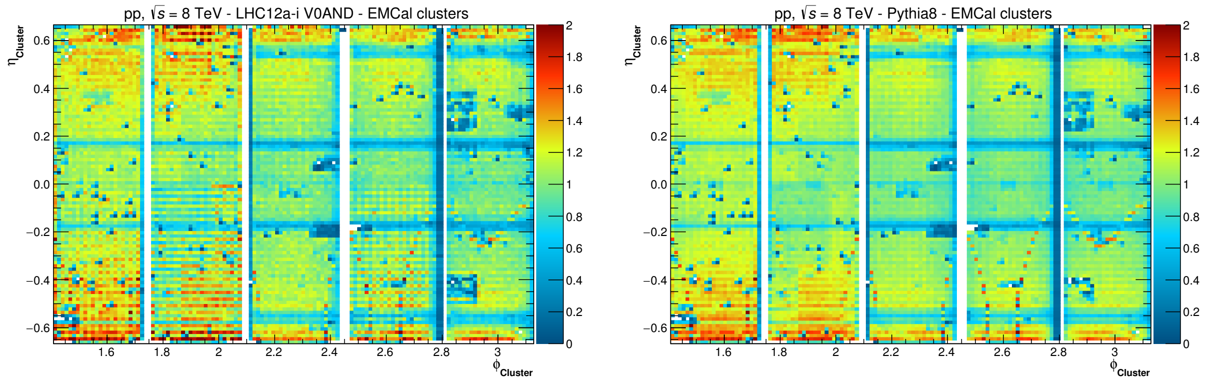

a) b)

Figure 5.2.7: The η-φ distributions of EMCal clusters for data, a), and the anchored PYTHIA 8 simulation, b). The histograms are normalized by the respective number of recorded events as well as the global average of cluster density per cell.

5.2.1 EMCal Cluster Energy Calibration

The existing relative energy as well as time calibrations for the EMCal, as described in Sec. 5.2, are applied for analysis, yielding an agreement within a few percent of the EMCal energy scale between data and MC simulations. These residual differences are important to correct for since a mass position difference of one percent may generate a bias in the final result of approximately n percent, assuming a power law behavior of the spectrum of $(1/p_{\mathrm{T}})^n$ with the power n. Instead of using an energy calibration scheme based on testbeam data to correct for the residual differences, from which at the same time a classical non-linearity correction is deduced [240], a new calibration method was developed in the context of this thesis which makes use of the good momentum resolution of the PCM photons. The philosophy is to take the measured data as is and to calibrate the EMCal cluster energies E_{cluster} in MC to data by exploiting the reconstructed mass position of the π^0 and η mesons. For this purpose, the neutral mesons are reconstructed via their two-photon decay channels, utilizing the invariant mass technique, see also Sec. 6.1 for further details:

$$M_{\gamma_1\gamma_2} = \sqrt{2E_{\gamma_1}E_{\gamma_2}\,(1-\cos\theta_{\gamma_1\gamma_2})}, \tag{5.2.7}$$

where E_{γ_1} and E_{γ_2} are the energies of the two photons and θ is the angle between the three-momentum vectors of both photons. By reconstructing the mesons using the so-called hybrid method which combines PCM with EMCal photons, the energy of the daughter particle reconstructed with the PCM is well known so that a direct access to the difference of the cluster energy scales in data and MC is given by evaluating the mesons' masses as a function of EMCal cluster energy. Hence, the central advantage of this method is the good energy resolution of the PCM photon which is reconstructed by means of the tracking detectors of ALICE, improving the precision of the energy calibration of the EMCal. Moreover, this improved correction scheme is able to correct for remaining geometrical misalignments of the EMCal between data and MC simulations as it is impossible to distinguish between the energy calibration and an alignment correction of the detector. Furthermore, it has the advantage of considering the latest version of the EMCal detector setup as the testbeam was not performed with identical readout and running conditions as compared to the present conditions during actual data taking. Therefore, the residual mismatch between the peak positions in data and MC simulations could be minimized compared to the testbeam calibration [240], leading to a reduction of the associated systematic uncertainty assigned to the energy scale. Taken together, the new calibration scheme provides the overall energy scale calibration and implicitly incorporates non-linearity effects as well. The following Fig. 5.2.8 shows the reconstructed mass positions of π^0 and η mesons plotted for data and MC simulations after applying all calibrations described in Sec. 5.2, but before applying any further calibration which will be introduced in this section.

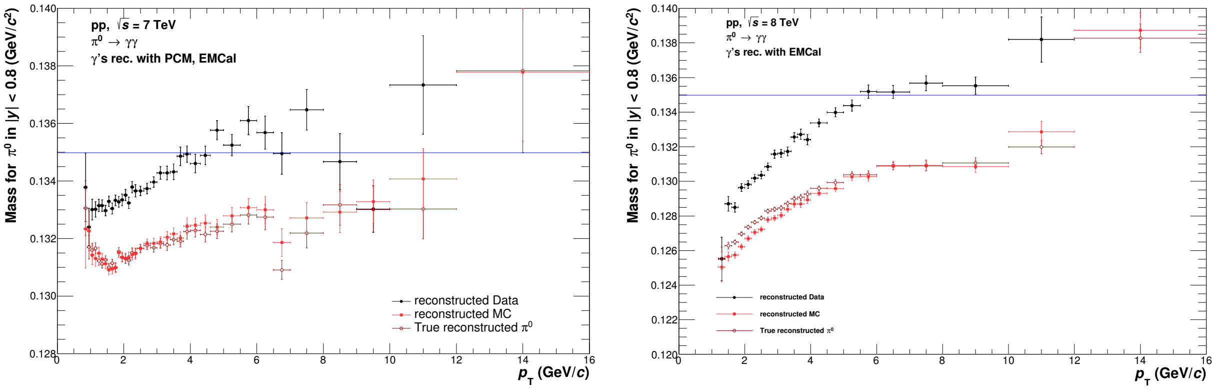

a) b)

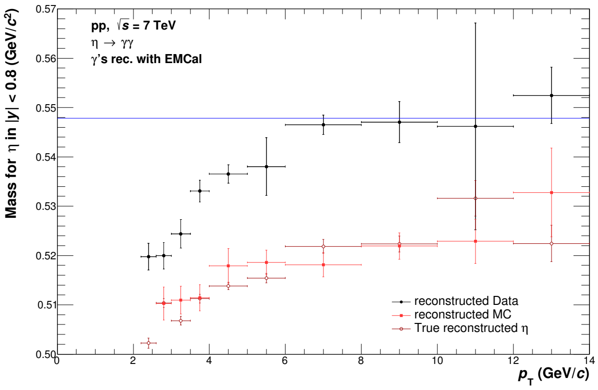

c)

Figure 5.2.8: Examples of the reconstructed π^0 and η mass positions for data, MC simulations and true MC plotted as a function of meson p_{T} for the hybrid method PCM-EMCal, a), and EMCal standalone, b) and c), for pp collision at $\sqrt{s} = 7$ and 8 TeV. The invariant mass peaks of the neutral mesons are fitted using a Gaussian convoluted with an exponential to obtain the mass positions, see Sec. 6.1 for further details.

The π^0 and η mass positions are plotted in Fig. 5.2.8 for the different p_{T} bins used for analysis which are obtained from data, MC simulations and true MC information. It can be followed that the mass positions agree within a few percent which is the starting point for the energy calibration scheme described in this section that has the purpose to correct for these residual differences.

In the following, the energy calibration scheme based on the PCM-EMCal method is introduced and further elaborated which is used as standard for analysis. Moreover, an alternative scheme based on pure EMCal information by selecting symmetric π^0 decays is also described which is used for estimation of systematic uncertainties. The general strategy of both calibration procedures is the following: (i) fitting of π^0 invariant mass peaks peaks for the different p_{T} bins to extract the mass positions; (ii) obtain ratios of mass peak positions in data and MC simulations; (iii) parametrize the ratios to obtain a calibration function which, then, is used to correct the EMCal cluster energies in the simulations to match the peak positions with data.

Energy Calibration using PCM-EMCal

Using the hybrid method PCM-EMCal, neutral mesons are reconstructed by combining PCM and EMCal photon candidates. The invariant masses of the meson candidates are computed according to Eq. 5.2.7 which are then plotted as a function of EMCal cluster energy. The combinatorial background is estimated by event mixing technique, as described in Sec. 6.1, and subtracted from the invariant mass distributions. The distributions are then fitted using a Gaussian convoluted with an exponential to obtain the mass positions which is performed independently for data and MC simulations. The obtained mass positions are exemplary shown in Fig. 5.2.9a for data and MC simulations for pp, $\sqrt{s} = 8\,\text{TeV}$. To improve the precision and high-p_{T} reach, the available rare calorimeter triggers are considered as well. Subsequently, the mass position ratios for each p_{T} bin from data and simulation are computed which are shown in Fig. 5.2.9b. This ratio is fitted with the following empirical parameterization:

$$f(E_{\text{Cluster}}) = p_0 + \exp\left(p_1 + p_2 \cdot E_{\text{Cluster}}\right), \tag{5.2.8}$$

where p_0, p_1 and p_2 are free parameters and E_{Cluster} represents the EMCal cluster energy. The function from Eq. 5.2.8 is then applied to the reconstructed cluster energies in MC simulations in order to perform the calibration. Since the correction is based on conversion and calorimeters photons, it is referred to as Conv-Calo Ratio Fit (CCRF) in the following.

Alternatively, as shown in Fig. 5.2.9a the mass positions in data and simulations can be fitted individually using the following function:

$$M(E_{\text{Cluster}}) = p_0 + p_1 \cdot E_{\text{Cluster}}^{p_2}, \tag{5.2.9}$$

where p_0, p_1 and p_2 are free parameters and E_{Cluster} represents the EMCal cluster energy again. The parameterizations of the masses for both data and MC simulations can then be divided by each other according to:

$$f(E_{\text{Cluster}}) = \frac{M_{Data}\left(E_{\text{Cluster}}\right)}{M_{MC}\left(E_{\text{Cluster}}\right)} + C = \frac{p_0 + p_1 \cdot E_{\text{Cluster}}^{p_2}}{p_3 + p_4 \cdot E_{\text{Cluster}}^{p_5}} + p_6, \tag{5.2.10}$$

where the free parameters can be identified as in Eq. 5.2.9 and p_6 is an additional degree of freedom to correct potential offsets due to fitting biases. This calibration procedure using Eq. 5.2.10 is called Conv-Calo Mass Fit (CCMF). This method has the advantage to be able to reduce statistical fluctuations if only low statistics is available for a given dataset. As this does not apply for all datasets analyzed in this thesis, this method will primarily serve as a cross-check and for systematic uncertainty estimation.

Energy Calibration using EMCal

Neutral mesons are reconstructed by computing the invariant mass of two EMCal clusters. To be able to carry out an energy calibration of the EMCal in this case, only such neutral meson candidates are selected that are reconstructed with two photons having approximately the same energy in the lab frame. For this purpose, the absolute value of the energy asymmetry $\widetilde{\alpha}_{\gamma\gamma}$ is defined as:

$$\widetilde{\alpha}_{\gamma_1\gamma_2} = \frac{|E_{\gamma_1} - E_{\gamma_2}|}{E_{\gamma_1} + E_{\gamma_2}}, \tag{5.2.11}$$

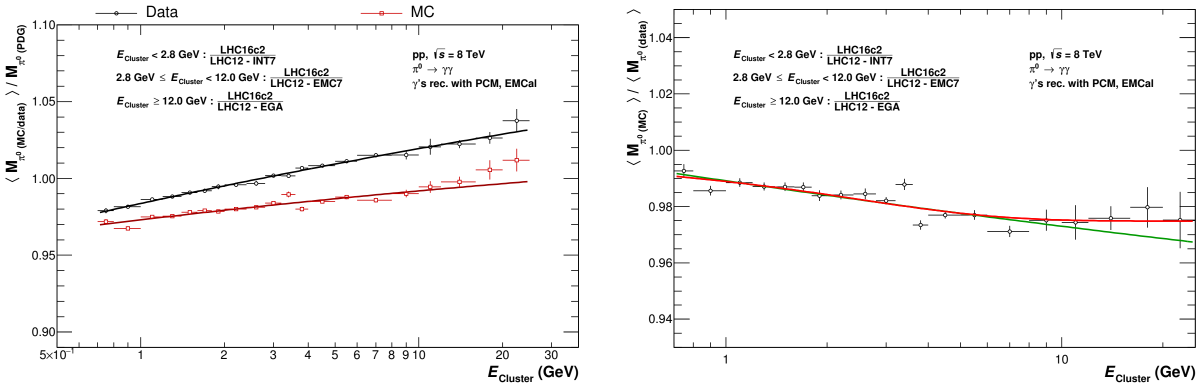

a) b)

Figure 5.2.9: In a), the obtained mass positions for data (black) and MC simulation (red) are shown for pp, $\sqrt{s} = 8\,\text{TeV}$, normalized to the PDG mass of the π^0 [32]. The lines with corresponding color represent the fits by Eq. 5.2.9. The mass position ratios from data and MC are shown in b), where the red line displays the outcome of the CCRF correction for which Eq. 5.2.8 is fitted to the data points. The green line indicates the CCMF calibration from Eq. 5.2.10 used to estimate systematic effects. As indicated in the legend, all available EMCal triggers are used to achieve the best possible precision.

where E_{γ_1} and E_{γ_2} are the energies of the two photon candidates represented by EMCal clusters. Here, the absolute value is applied because the energy asymmetry distribution of two clusters is found to be symmetric around zero. By enforcing a strict cut of $\widetilde{\alpha}_{\gamma\gamma} < 0.1$, the condition $E_{\gamma_1} \approx E_{\gamma_2} \equiv E_{\text{cluster}}$ holds and the invariant mass, see Eq. 5.2.7, can be employed to obtain the following relation:

$$M(E_{\text{Cluster}}) = \sqrt{2E^2_{\text{cluster}}\left(1 - \cos\theta_{\gamma_1\gamma_2}\right)} \propto E_{\text{cluster}}. \tag{5.2.12}$$

Furthermore, the condition $p_{\text{T}}^{\pi^0} \approx E^{\pi^0} \approx 2E_\gamma$ holds so that the invariant masses of neutral meson candidates can be sliced in cluster energy. All remaining steps are equivalent to the CCRF and CCMF calibration schemes so that in the end the two analogue energy calibrations Calo Ratio Fit (CRF) and Calo Mass Fit (CMF) are obtained. They serve as cross-checks and further input for the systematic uncertainty estimation.

Both introduced calibration procedures based on PCM-EMCal and EMCal were performed for the different MC simulations anchored to the datasets analyzed, see Tabs. 4.1.1 and 4.1.2, as they depend on the spectral shape of the input meson spectra which may vary between different generators in general. The resulting calibration factors, also denoted correction factors that need to be applied to the MC cluster energies, are summarized for the different MC simulations available for pp, $\sqrt{s} = 8\,\text{TeV}$ in Fig. 5.2.10a for CCRF and CRF and accordingly in Fig. 5.2.10b for CCMF and CMF. Moreover, the correction factor for the calibration based on EMCal testbeam data is also shown which clearly shows differences especially for lower energies. The parameters found for the standard calibration CCRF are also summarized in Tab. B.1.8.

As already pointed out, the CCRF calibration scheme is used by default throughout this thesis. It offers a much better precision as it is based on one PCM photon candidate. Furthermore, it can sample a much wider p_{T} range as only one EMCal cluster is needed for the calibration as

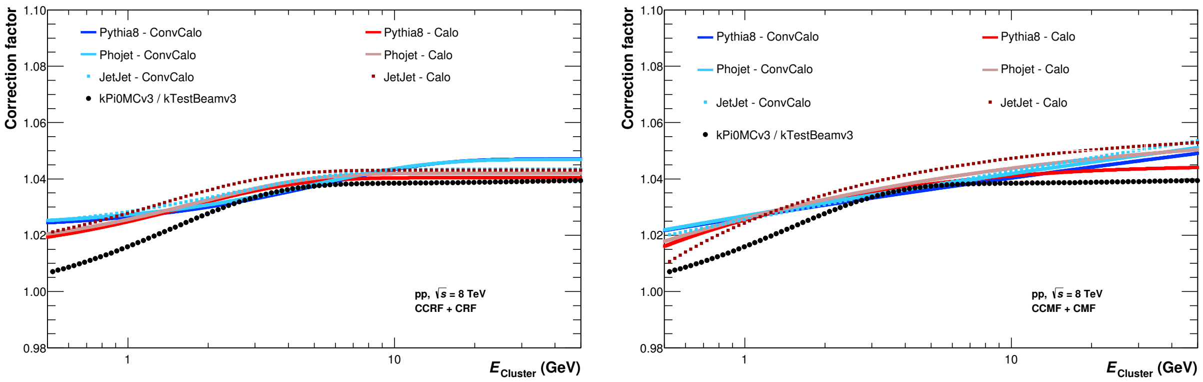

Figure 5.2.10: The correction factors, to be directly multiplied to the obtained EMCal cluster energies in MC simulations, are shown for the CCRF and CRF in a) and for the CCMF and CMF in b) for all simulations available for pp, $\sqrt{s} = 8\,\text{TeV}$.

compared to the requirement of having two symmetric clusters for the CRF. In addition, the latter method suffers more from cluster merging effects at higher p_{T}. In this region, clusters are getting even closer on the EMCal surface as the opening angle of the photon pair decreases due to the Lorentz boost. At some point, the clusterization algorithm cannot separate both photons any longer, thus reconstructing a single cluster. Given these limitations of the CRF, however, all presented schemes in Fig. 5.2.10a are able to provide reasonable calibrations although the CCRF minimizes the level of disagreement of mass positions in data and MC simulations, whereas all other calibrations are used to estimate the associated systematic uncertainty. In Fig. 5.2.10b, the corresponding calibrations for CCMF and CMF are shown which have a similar shape for lower energies. However, the plateau region for higher energies which is seen in Fig. 5.2.10a cannot be reproduced so that these calibrations need to be handled with special care. This is due to the choice of the parameterization of the mass positions and the arising fitting bias for higher energies which can be followed in Fig. 5.2.9a and Fig. 5.2.9b. Though, the parameterizations can be used for systematic uncertainty estimations as they provide a decent calibration in the relevant energy region for this thesis.

Examples for the final mass positions that are obtained in data and MC simulations using the CCRF calibration are shown in Fig. 5.2.11a, whereas their corresponding ratios can be found in Fig. 5.2.11b. Compared to the initial situation shown in Fig. 5.2.8, the ratios now agree with unity within their uncertainties. As the calibration was performed based on the π^0 alone, the η meson serves as a reliable cross-check of the validity of the procedure for which a reasonable agreement can also be stated given the uncertainties. Hence, the same calibration, CCRF in this example, is found to be consistently working for the EMCal and PCM-EMCal methods for the π^0 as well as η meson reconstruction, demonstrating a reliable and stable procedure. This is further illustrated in Fig. 5.2.12 for rare EMCal triggers in addition for which the procedures work as well. The ratios in Fig. 5.2.12 are fitted with constants, obtaining residual offsets for pp collisions at $\sqrt{s} = 8\,\text{TeV}$ of $0.005{\pm}0.043\,\%$ and $0.14{\pm}0.13\,\%$ for π^0 and η mesons for the EMCal analysis, whereas $0.002{\pm}0.042\,\%$ and accordingly $0.02{\pm}0.14\,\%$ are obtained for PCM-EMCal. For $\sqrt{s} = 7\,\text{TeV}$, the corresponding values are found to be $-0.045{\pm}0.045\,\%$ and $0.057{\pm}0.219\,\%$ for EMCal and $0.113{\pm}0.043\,\%$ as well as $-0.44{\pm}0.22\,\%$ for PCM-EMCal.

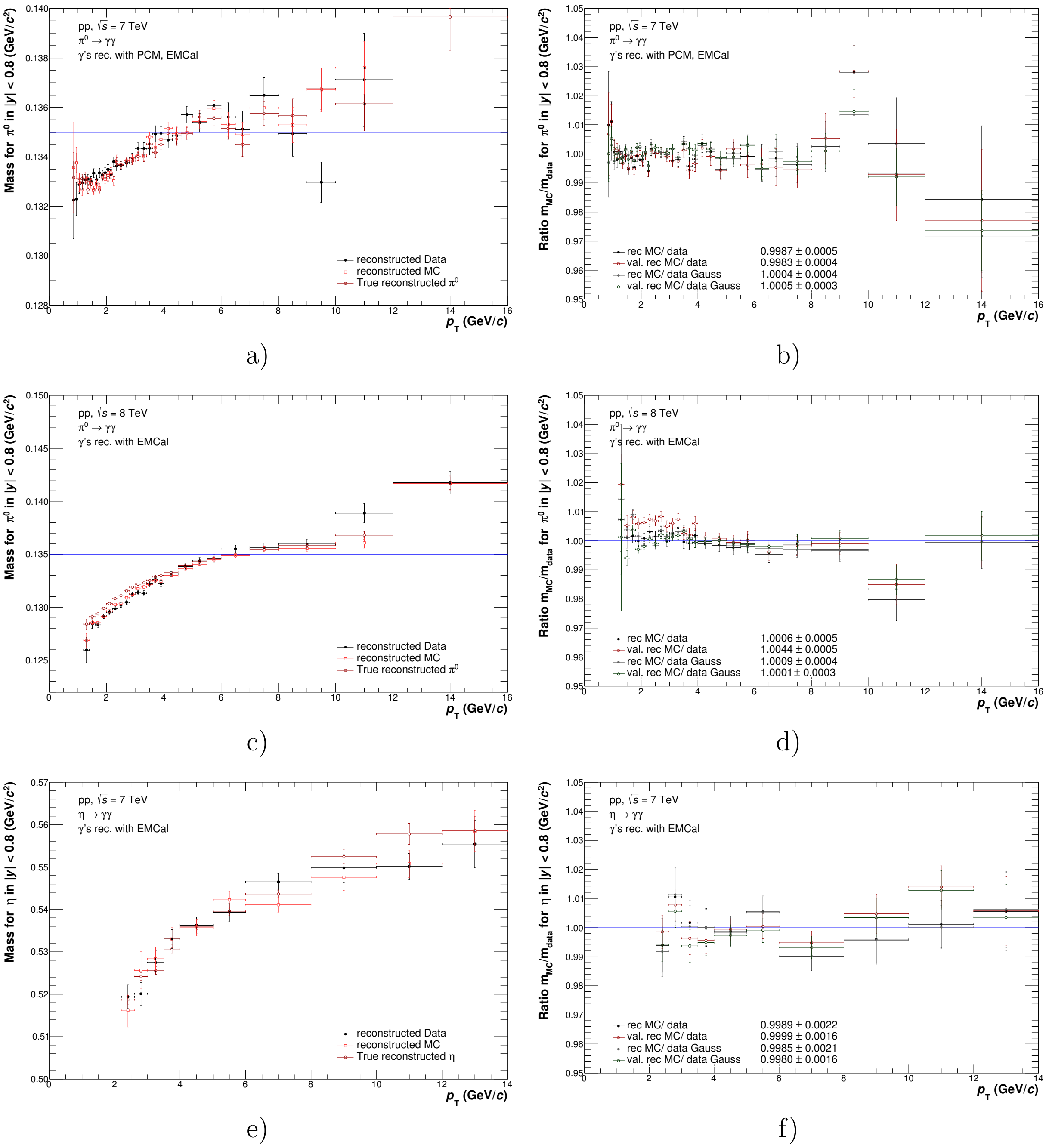

Figure 5.2.11: The reconstructed π^0 and η mass positions for data, MC simulations and true MC information in a), c) and e), for which the invariant mass peaks were fitted using an Gaussian convoluted with an exponential. In b), d) and f), the corresponding mass positions ratios are shown which are fitted with constants. In addition, the meson peak fitting was performed with Gaussian fits only for which the ratios are also given in the legend.

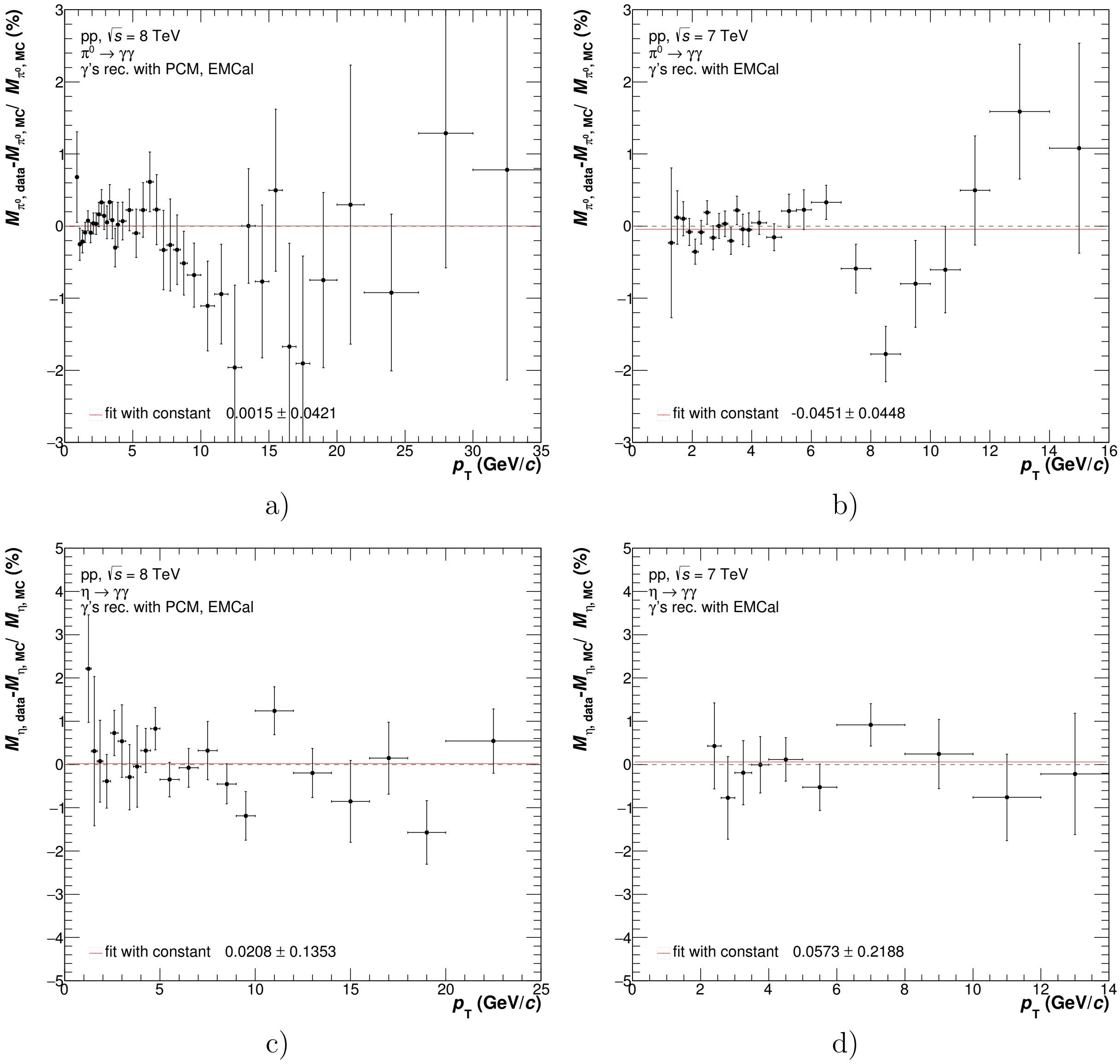

Figure 5.2.12: The mass position differences for π^0 and η mesons relative to the reconstructed mass position in MC simulations. The plots show the mass ratios for the combined measurements that are performed with each method, involving the respective MB triggers as well as rare EMCal triggers if available. The plots indicate a valid energy calibration for the EMCal also for triggered data in a) and c). The ratios are fitted by constants, drawn in red color which reflect the residual offsets from unity. If such deviations are still present, they will be reflected in the estimation of systematic uncertainties which can be found in Secs. 6.2.4, 6.3.2 and 7.2.2.

Chapter 6

Neutral Meson Measurements

This chapter presents measurements of neutral meson production in pp collisions which were carried out in the context of this thesis for $\sqrt{s} = 0.9$, 7 and 8 TeV using the ALICE detector. Neutral mesons, π^0 and η, are reconstructed via their two-photon decay channels by means of the general concept of invariant mass analysis which is introduced in the first section. Photons are measured by detecting conversions in the detector material of ALICE, see Sec. 5.1, and using electromagnetic calorimeters, see Sec. 5.2. Subsequently, the so-called hybrid method PCM-EMCal is established which combines two photons from the respective methods. The presented neutral meson measurements in pp collisions at $\sqrt{s} = 8$ TeV utilizing the reconstruction methods PCM-EMCal and EMCal are published by ALICE in Ref. [4] for which additional figures can be found in Ref. [5]. ALICE did already publish a paper on neutral meson production at $\sqrt{s} = 0.9$ and 7 TeV [8], however, no EMCal-related measurements were available back then. Therefore, in this thesis the first measurements of neutral mesons are reported using the EMCal and PCM-EMCal methods which are foreseen to enter an upcoming ALICE publication that will update the measurements published in the previous paper of ALICE. The measurement of neutral mesons in pp collisions at $\sqrt{s} = 2.76$ TeV was lead by F. Bock [219] and was also published by ALICE [8], for which also analysis contributions were provided in the context of this thesis. Finally, this chapter concludes with a comparison of the neutral meson measurements of ALICE at all available LHC Run 1 center of mass energies: $\sqrt{s} = 0.9$, 2.76, 7 and 8 TeV.

6.1 Reconstruction of Neutral Mesons via Invariant Mass Analysis

Neutral mesons which decay into two photons, γ_1 and γ_2, can be reconstructed by means of the invariant mass $M_{\gamma\gamma}$ of the photon pair. In this thesis, π^0 and η mesons which both undergo two-photon decays are considered using this general concept of invariant mass analysis. The photon candidates used for this purpose are reconstructed and selected according to Sec. 5.1 from the V^0 sample and from the EMCal cluster sample according to Sec. 5.2. From these sets of candidates, the four-vectors of two photons with energies E_{γ_1} and E_{γ_2} can be added and their invariant mass can be calculated as follows:

$$M_{\gamma_1\gamma_2} = \sqrt{2E_{\gamma_1}E_{\gamma_2}\left(1 - \cos\theta_{\gamma_1\gamma_2}\right)}, \tag{6.1.1}$$

where $\theta_{\gamma_1\gamma_2}$ is the opening angle between the photons in the laboratory frame. Hence, the resulting four-vector of the photon pair represents their mother particle candidate having an invariant mass of $M_{\gamma\gamma}$. The π^0 and η meson candidates are obtained by statistical analysis from an excess yield, visible at their reconstructed invariant masses on top of a combinatorial background. The latest PDG world averages for the nominal mass values of both mesons are given by $\pi^0 = 134.9766 \pm 0.0006$ MeV$/c^2$ and $\eta = 547.862 \pm 0.017\,\mathrm{MeV}/c^2$ [32]. In the analysis, the invariant masses $M_{\gamma\gamma}$ are obtained and filled into 2D-histograms versus the p_{T} of the mother particle. Fig. 6.1.1 shows examples of the two-photon invariant mass distributions in the vicinity of the nominal rest masses of the π^0 and η meson respectively.

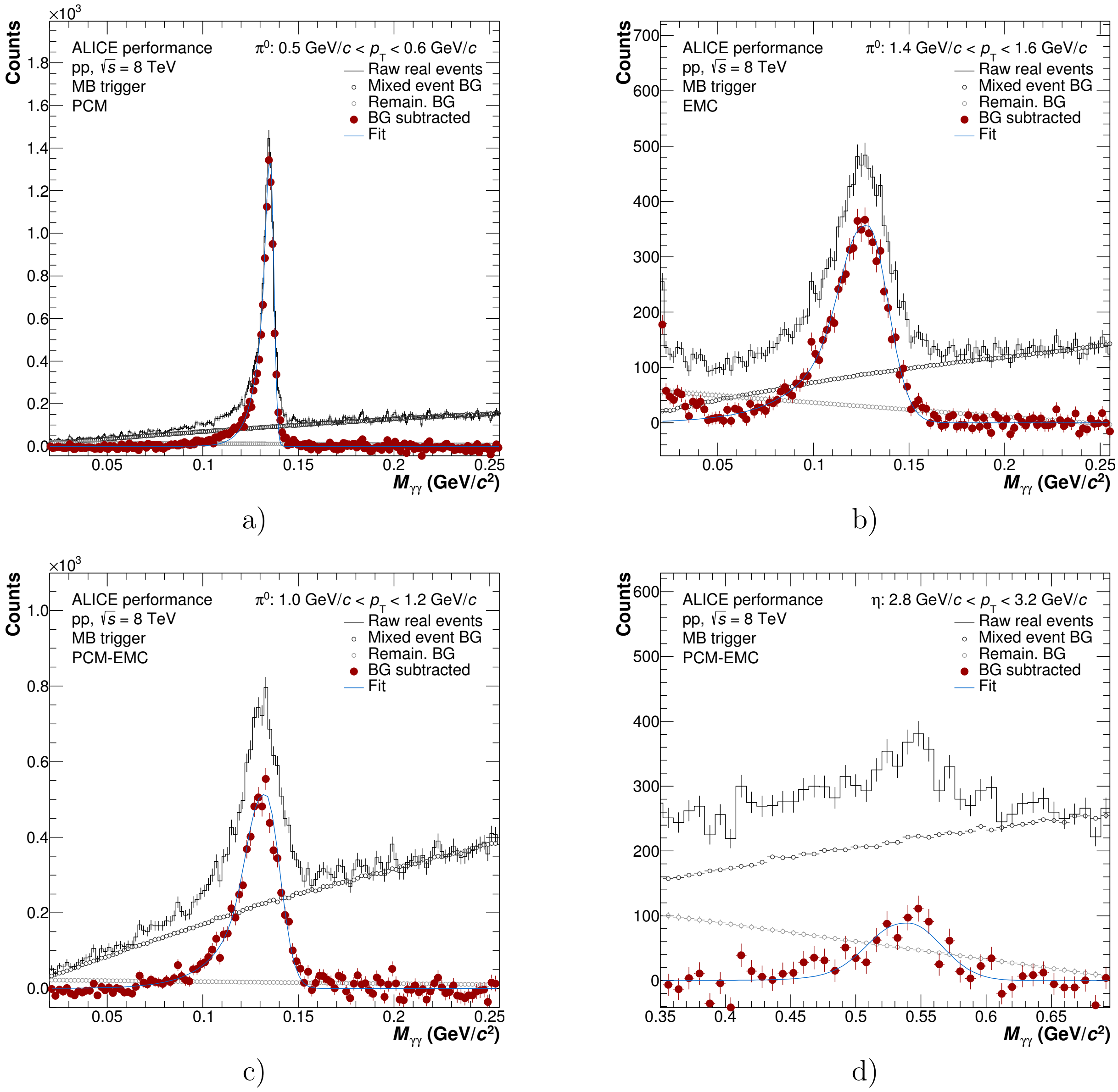

Figure 6.1.1: Example invariant mass distributions for the reconstruction methods PCM, a), and EMCal, b), as well as the hybrid method PCM-EMCal, c), for the π^0 for pp collisions at $\sqrt{s} = 8\,\mathrm{TeV}$. In addition, an example is given for the η meson in d).

In Fig. 6.1.1, the black histograms show the raw distributions of invariant masses from same-event combinations of photons obtained for the V0AND (INT7) MB trigger in pp collisions at $\sqrt{s} = 8\,\mathrm{TeV}$. These raw distributions include combinatorial background, BG, which enters via combinations of two uncorrelated photons. This means that both photons do not stem from the same particle leading to a more or less random $M_{\gamma\gamma}$ according to the phase space cuts on acceptance and momentum. The distributions are further composed of the neutral meson signal from photon candidate pairs that originate from the same mother particle. The background components are shown using gray data points, split into mixed-event and remaining background components. These components are subtracted from the raw signal in order to obtain the red data points representing the signal distributions. Clear peaks around the nominal mass positions of the π^0 and η mesons are visible. They are used to extract the mesons' raw yields in each p_{T} bin. The blue curves represent the fits to the signal according to Eq. 6.1.3.

Moreover, Fig. 6.1.1 shows invariant mass distributions obtained with different meson reconstruction methods. Two PCM photons can be combined as shown in Fig. 6.1.1a which is called PCM method. On the other hand, the invariant mass of two EMCal photons can be calculated,as seen in Fig. 6.1.1b which is named EMCal (in short EMC) method for neutral meson reconstruction. Furthermore, it is possible to use one photon of each reconstruction method, the so-called hybrid method PCM-EMCal (also PCM-EMC), exemplary shown in Fig. 6.1.1c and Fig. 6.1.1d for π^0 and η mesons. Although the p_{T} bins are not identical, a clear ordering of peak widths σ can be deduced from Fig. 6.1.1: $\sigma_{\mathrm{PCM}} < \sigma_{\mathrm{PCM\text{-}EMCal}} < \sigma_{\mathrm{EMCal}}$. This is a result of the resolution of the respective reconstruction methods: PCM is based on tracking yielding the best resolution, while the energy resolution of the EMCal is improving with increasing p_{T} but gets worse for decreasing p_{T}, see also Eq. 3.2.2 for the energy resolution of the EMCal. The hybrid method is observed to lie in between which is a natural consequence since it is a combination of both methods.

The invariant mass distributions shown in Fig. 6.1.1 are obtained with the meson cut selection given in Tab. 6.1.1. All listed cuts are applied to all constructed photons pairs independent from same and mixed-event combinations as well as signal or combinatorics which cannot be separated at this stage.

	pp, $\sqrt{s} = 0.9$, 7 and 8 TeV
meson selection criteria	
rapidity	$\lvert y\rvert < 0.8$
energy asymmetry	$-1.0 \leq \alpha_{\gamma\gamma} \leq 1.0$
opening angle	
PCM-EMCal	$\theta > 5\,\mathrm{mrad}$
EMCal	$\theta > 17\,\mathrm{mrad}$, no common edge of energy leading cells of both clusters

Table 6.1.1: The selection criteria applied to the reconstructed neutral meson sample in pp collisions at $\sqrt{s} = 0.9$, 7 and 8 TeV.

As only decays of neutral mesons into two photons are considered, a cut on $R_{\mathrm{conv}} > 5\,\mathrm{cm}$ is applied for PCM photons. Such a minimum radial distance of the conversion point from the center of the ALICE detector is applied for PCM photons in order to suppress the contribution from Dalitz decays, $\pi^0 \rightarrow \gamma e^- e^+$, which otherwise cannot be distinguished from real two-photon decays if at least one PCM photon is involved. As listed in Tab. 6.1.1, photon pairs are restricted to a rapidity of $\lvert y\rvert < 0.8$ for all methods. This condition is enforced due to the limited acceptance of the detectors located at the central barrel of ALICE, which covers $\lvert\eta\rvert < 0.9$, and to avoid edge effects. The energy asymmetry $\alpha_{\gamma\gamma}$ of a photon pair is defined as follows:

$$\alpha_{\gamma_1\gamma_2} = \frac{E_{\gamma_1} - E_{\gamma_2}}{E_{\gamma_1} + E_{\gamma_2}}, \tag{6.1.2}$$

where E_{γ_1} and E_{γ_2} represent the energies of both photons. In general, $\alpha_{\gamma_1\gamma_2}$ is not necessarily symmetric around zero which, in fact, depends on the reconstruction method. Hence, no cut on $\alpha_{\gamma\gamma}$ is performed indeed. However, the meson's reconstruction efficiency depends not only on p_{T} but also on this quantity $\alpha_{\gamma\gamma}$. This is the case in particular for the triggered data sets, see Sec. 4.1.1. Therefore, it is ensured and verified in the QA, see Sec. 4.3, that trigger mimicking is able to reproduce the features of the trigger reasonably well and notably provides reasonable efficiencies with a valid description of the $\alpha_{\gamma\gamma}$ distributions in data and MC simulation. As this is the case, the triggered data can even be used in p_{T} regions where the trigger is not fully efficient with decent systematic uncertainties. Furthermore, an opening angle cut of $\theta > 17\,\mathrm{mrad}$ for the angle between the momentum vectors of the two paired photon candidates is applied for the EMCal measurement. This condition is crucial for a proper mixed-event background description since two clusters from different events might be separated by an arbitrarily small distance in the event mixing step. If both clusters would be from the same-event, such configurations would overlap partially or even merge into single clusters which is closely connected to the working principle of the clusterizer that is used, see Sec. 5.2. The clusterizer is explicitly considered in event mixing by not allowing the cells with largest deposited energies of respective clusters to be direct neighbors on the EMCal surface so that a valid mixed-event background description can be achieved. For the hybrid PCM-EMCal method, an opening angle cut of $\theta > 5\,\mathrm{mrad}$ is applied between the momentum vectors of the pair of PCM and EMCal photon candidate to prevent double counting of the PCM photons.

The uncorrelated combinatorial background in Fig. 6.1.1 is indicated by black dots, being estimated by using an event mixing technique. Such an event mixing method destroys the correlations of the photon pairs by combining photons from different events, yielding the denoted mixed-event background. However, the shape of this combinatorial background depends on the photon multiplicity in the event, the primary vertex position in z and the transverse momentum of the particles. Instead of using the number of photons as a reference for multiplicity in the event, the number of primary particles is also found to be a valid approach to categorize the events. Hence, different event pools, binned by photon candidate multiplicity, z-vertex position and p_{T} as summarized in Tab. 6.1.2, are used to ensure a mixing of similar events only.

For both EMCal and PCM-EMCal methods, the EMCal photons are filled into a background pool related to multiplicity. To be able to reconstruct a neutral meson in an event, different number of EMCal photon candidates need to be found, two for EMCal or one for the hybrid method respectively, which is reflected in the difference of photon multiplicity listed in Tab. 6.1.2. The limits are defined in this table such that the statistics is equally shared among all bins in the best possible way. The mixing is performed only among photons which belong to the same bin in multiplicity and z-vertex position. For this purpose, the photons are stored in FIFO buffers which hold a maximum of 80 photons per bin to be mixed with all photons from the current event in the respective pool. Subsequently, the photons from the current event are added to the respective pool. In contrast to same-event combinations, the mixed-event background is hence obtained with up to 80 different events in order to minimize its statistical uncertainties. Therefore, the mixed-event background needs to be scaled to match the integral of the raw signal in the vicinity of the right side of the neutral meson peak, just outside the peak integration interval, after which it is subtracted from the raw distribution.

	pp, $\sqrt{s} = 0.9$, 7 and 8 TeV		
bin	photon multiplicity PCM-EMCal (EMCal)	charged particle multiplicity $N_{\text{primary tracks}}$	z-vertex coordinate (cm)
1	1 (2)	0 – 8	-50.00 – -3.38
2	2 (3)	9 – 16	-3.38 – -1.61
3	3 (4)	17 – 27	-1.61 – -0.23
4	≥4 (≥5)	27 – 200	-0.23 – 1.07
5	–	–	1.07 – 2.45
6	–	–	2.45 – 4.25
7	–	–	4.25 – 50.00

Table 6.1.2: The definition of event mixing classes. The three different classes photon multiplicity, charged particle multiplicity and z-vertex coordinate, can be used to categorize the events to provide a mixing of similar events. The photon multiplicity bin is filled with EMCal photons for both reconstruction methods EMCal and PCM-EMCal.

Once the background-subtracted invariant mass distributions are obtained which are exemplary shown in Fig. 6.1.1 visualized by red dots, the signal is fitted to determine the mass peak position and width of the π^0 and η meson distributions for every p_{T} bin. These fits are visualized by blue curves in Fig. 6.1.1 for which a function composed of a Gaussian modified by an exponential tail at the low mass side [241, 242] is used:

$$y = A \cdot \left(G\left(M_{\gamma\gamma}\right) + \exp\left(\frac{M_{\gamma\gamma} - M_{\pi^0(\eta)}}{\lambda}\right) \left(1 - G(M_{\gamma\gamma})\right) \theta(M_{\gamma\gamma} - M_{\pi^0(\eta)}) \right) + B + C \cdot M_{\gamma\gamma},$$

$$\text{with } G\left(M_{\gamma\gamma}\right) = \exp\left(-0.5 \left(\frac{M_{\gamma\gamma} - M_{\pi^0(\eta)}}{\sigma_{M_{\pi^0(\eta)}}} \right)^2 \right), \quad (6.1.3)$$

where the Gaussian G is defined by the width $\sigma_{M_{\pi^0(\eta)}}$, the amplitude A and the mean position $M_{\pi^0(\eta)}$ which is identified with the reconstructed mass position of the corresponding meson. The parameter λ represents the inverse slope of the exponential function. Above $M_{\pi^0(\eta)}$ the contribution of the exponential function is switched off by the Heaviside step function $\theta(M_{\gamma\gamma} - M_{\pi^0(\eta)})$. Furthermore, B and C are the free parameters of the linear component which is used to reflect the residual correlated background components remaining after the subtraction of the mixed-event background. This additional first order polynomial component is deduced from MC simulations and, hence, considered during the fitting process. In Fig. 6.1.1, this component is shown using open gray dots which is subtracted from the raw distributions in addition to the mixed-event background to obtain the background-subtracted invariant mass distributions represented by the red dots in Fig. 6.1.1. The low mass tail, represented by the parameter λ, accounts for late conversions of one or both photons for the EMCal-related methods. For the hybrid PCM-EMCal method it simultaneously accounts for energy loss effects due to bremsstrahlung in addition which is radiated by one of the leptons constituting the PCM photon candidate. This is demonstrated in Fig. 6.1.2 where validated invariant mass distributions for π^0 and η mesons are shown that are obtained from true MC information. Both photons are ensured to originate from the same mother particle which is validated to be a π^0 or η meson. The neutral meson peaks are decomposed according to the origin of the EMCal clusters to disentangle the composition of the exponential tails.

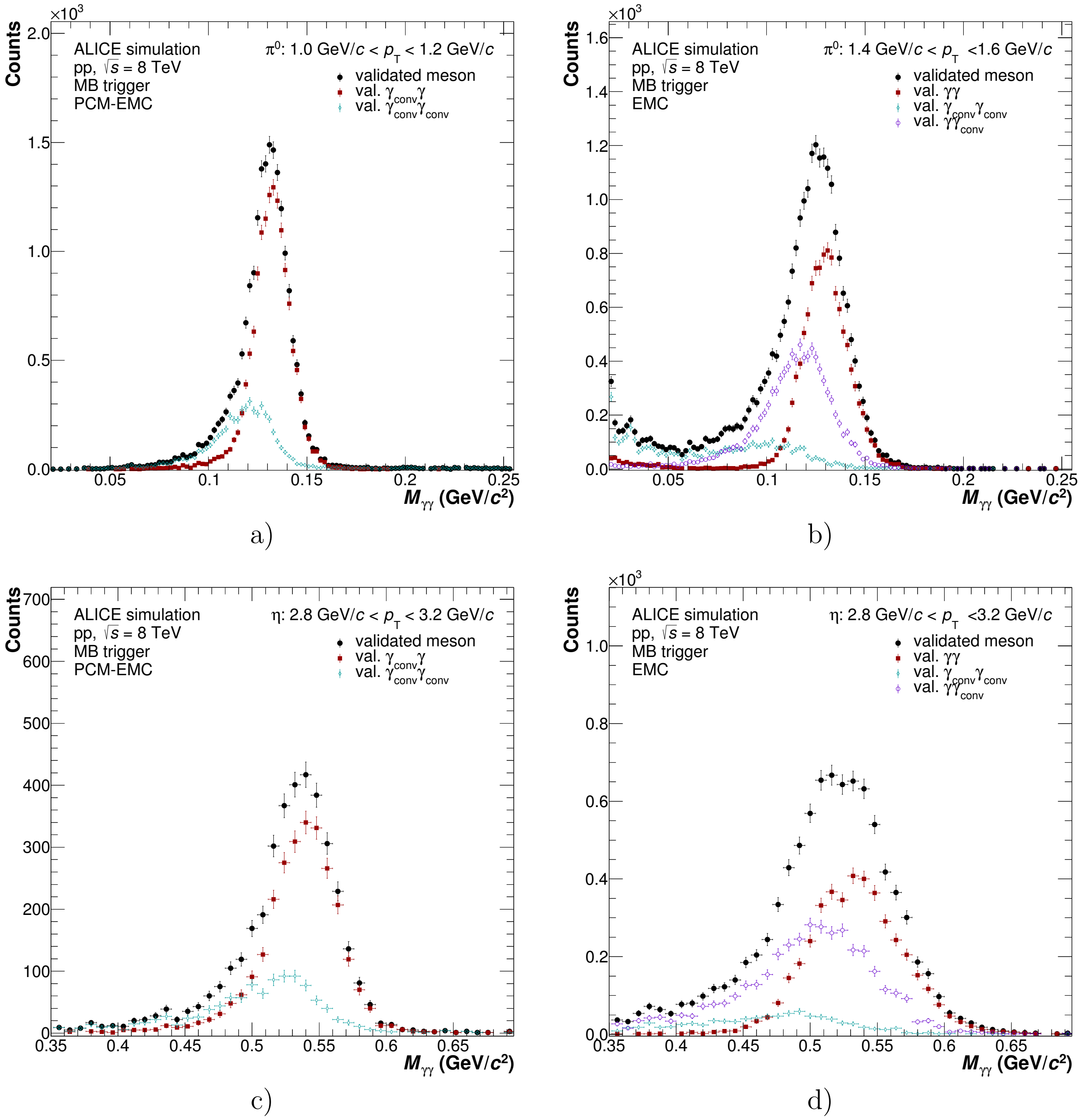

Figure 6.1.2: Example invariant mass distributions $M_{\gamma\gamma}$ of reconstructed validated photon pairs obtained from MC simulation for the PCM-EMCal, a) and c), as well as the EMCal, b) and d), reconstruction methods for V0AND (INT7) MB triggered pp collisions at $\sqrt{s} = 8$ TeV. The inclusive distributions of validated mesons are drawn in black, decomposed into the different groups as indicated in the respective legends.

The distributions, visualized by red dots in Fig. 6.1.2a and Fig. 6.1.2c, show the mesons' invariant mass distributions for a validated photon conversion combined with a true EMCal photon. Asymmetric peaks with clear tails at the low mass edges can be observed which is caused by energy loss of the conversion daughters due to bremsstrahlung. Because of the presence of material beyond the outer radius of the TPC, late photon conversions within this detector material may happen that cannot be tracked. If a photon converts in front of the EMCal, the cluster does not contain the full information about the original photon concerning energy and momentum in general. Requiring the occurrence of such late conversions with help of true MC, EMCal clusters may be selected with a leading contribution from an e^+ or e^- which is represented by cyan distributions in Fig. 6.1.2a and Fig. 6.1.2c. As the e^-e^+ pair is deflected from the original direction of the photon, a worse resolution as well as reduced average mass position for both mesons is observed. This effect increases for the EMCal method for which both photons may undergo a late conversion in the detector material of ALICE as shown in Fig. 6.1.2b and Fig. 6.1.2d. The violet points show the distributions in case one photon exhibited a late conversion, whereas the case of both photons converting lately is visualized by cyan distributions. Hence, the large tails at low invariant masses originate from mesons where both or one cluster have an electron as energy leading contribution and therefore the original photons converted lately within the detector material. As seen in Fig. 6.1.2b for two late conversions, the loss of information about the original photons can be significant as the distribution extends to lowest masses where most entries are observed. However, the mass shift is too small to be able to separate the different contributions for the various methods so that they superimpose to form the observed exponential tail at lower invariant masses for the EMCal method, whereas for the PCM-EMCal method the effect of bremsstrahlung also superimposes. This leads to the conclusion that the description of the material budget beyond the TPC agrees reasonably well within a few percent between real data and MC simulations since otherwise the peak shapes would differ significantly which is not observed though.

The fractions of late conversions in front of the EMCal can be obtained from true MC information and is shown in Fig. 6.1.3 for the two reconstruction methods PCM-EMCal and EMCal.

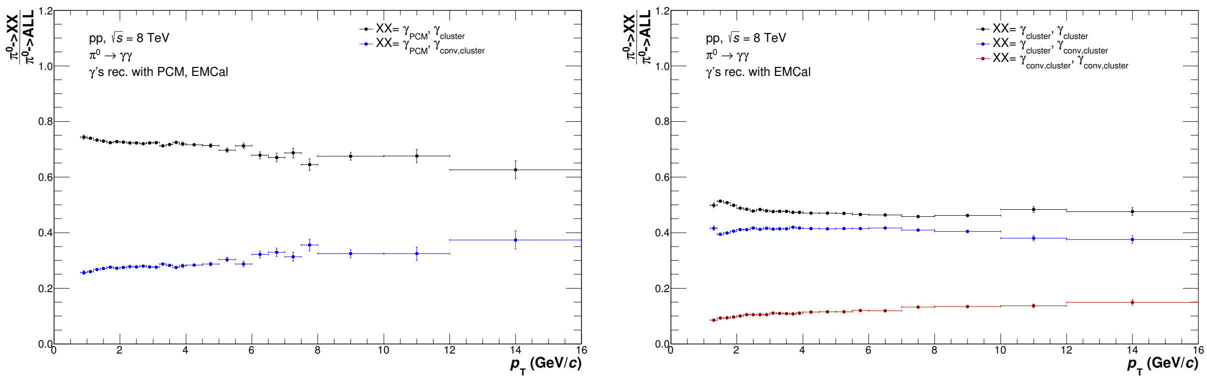

a) b)

Figure 6.1.3: The fractions of yield from the different contributions as introduced in Fig. 6.1.2 as a function of p_{T} of the validated meson.

The fractions in both plots partly show a small dependence on p_{T} caused by the track to EMCal cluster matching cut and can almost be considered independent in Fig. 6.1.2b. The fraction of late conversions for PCM-EMCal is about 30 %, whereas for EMCal in about 50 % of all cases at least one of the two photons converted lately.

In order to measure the differential production cross sections $\mathrm{d}^3\sigma/\mathrm{d}p^3$ of neutral mesons in pp collisions, $pp \to \pi^0(\eta) + X$, the recorded data as well as MC simulations need to be consulted.

For each p_T bin, the mesons' raw yields in data are extracted and corrected for detector acceptance and reconstruction efficiency using MC simulations. For this purpose, the raw yields of neutral mesons are extracted by integrating the background-subtracted invariant mass distributions for which examples are shown in Fig. 6.1.1. The integration windows are defined by the reconstructed mass position and width obtained by the respective fits, see Eq. 6.1.3, of the signal distribution for each p_T bin and cover at least three standard deviations on both sides. Then, the invariant differential cross sections of π^0 and η production for the given collision system, $E\mathrm{d}^3\sigma^{pp\to\pi^0(\eta)+X}/\mathrm{d}p^3$ in units of $(\mathrm{pb}\cdot c^3)/\mathrm{GeV}^2$, can be obtained following Eq. 2.3.9:

$$E\frac{\mathrm{d}^3\sigma^{pp\to\pi^0(\eta)+X}}{\mathrm{d}p^3} = \frac{1}{2\pi p_\mathrm{T}}\frac{\sigma_\mathrm{trigger}}{N_\mathrm{events}}\frac{\mathrm{d}^2N}{\mathrm{d}p_\mathrm{T}\mathrm{d}y} = \frac{1}{2\pi p_\mathrm{T}}\frac{1}{\mathscr{L}_\mathrm{int}}\frac{1}{A\cdot\varepsilon_\mathrm{rec}}\frac{1}{Br_{\pi^0(\eta)\to\gamma\gamma}}\frac{N^{\pi^0(\eta)}-N^{\pi^0}_\mathrm{sec}}{\Delta y\Delta p_\mathrm{T}}, \quad (6.1.4)$$

where, besides the factor $(2\pi p_\mathrm{T})^{-1}$, the respective experimental quantities are the following:

- $\mathscr{L}_\mathrm{int}$ is the integrated luminosity, see Tab. 4.2.5, for the given method and experimental trigger condition, see Chap. 4;
- $A\cdot\varepsilon_\mathrm{rec}$ is the product of the geometrical acceptance and reconstruction efficiency, in short also referred to as ϵ;
- $Br_{\pi^0(\eta)\to\gamma\gamma}$ is the Branching Ratio (BR) for the respective two-gamma decay channel which is found to be 98.823±0.034 % for the π^0 and 39.41±0.20 % for the η meson [32];
- $N^{\pi^0(\eta)}$ is the number of reconstructed π^0 (η) mesons for a given bin width in rapidity and transverse momentum, $\Delta y\Delta p_\mathrm{T}$;
- $N^{\pi^0}_\mathrm{sec}$ applies only for the π^0 analysis and represents the number of estimated secondary π^0 mesons from weak decays of K^0_S, K^0_L, Λ and material interactions,

which are further elaborated in Sec. 6.2 and Sec. 6.3.

6.1.1 The Hybrid Method PCM-EMCal

The hybrid PCM-EMCal method, introduced in the previous section in Fig. 6.1.1, combines photons reconstructed by the PCM and the EMCal. It provides an additional method to measure neutral mesons. Therefore, it contributes to reduce the size of statistical and systematic uncertainties for the neutral meson measurements as much as possible. As the two different methods PCM and EMCal are combined, the systematic uncertainties of the hybrid method are naturally correlated with the uncertainties from the respective methods. Possible statistical correlations between the methods, for instance due to the conversions at small distances relative to the beam axis, are negligible due to the small conversion probability and the small likelihood of reconstructing the respective electron in the EMCal leading to a meson candidate which finally ends up in the respective integration window. Furthermore, the hybrid method benefits from the high momentum resolution of the PCM on one side but also from the high reconstruction efficiency and, crucially, the triggering capabilities of the EMCal. Therefore, an extended p_T coverage is achieved compared to the standalone EMCal measurement as there is no limitation due to cluster merging effects, discussed later in Sec. 6.2.3. For the PCM-EMCal method, no out-of-bunch pileup needs to be taken into account because of the timing constraint of the EMCal as, in contrast, it is the case for a PCM standalone measurement, see Sec. 7.2.

When combining PCM and EMCal photon candidates in order to reconstruct neutral mesons, some special care needs to be taken with regard to the selection of EMCal clusters. The daughter particles of photon conversion candidates may also generate EMCal clusters. This situation is schematically drawn in Fig. 6.1.4a which displays the ALICE detector. In addition, a particle decaying into two photons, $\gamma_{\mathrm{CALO},1}$ and γ_{CONV}, is sketched. The latter photon converts and a daughter particle subsequently hits the EMCal, yielding $\gamma_{\mathrm{CALO},2}$.

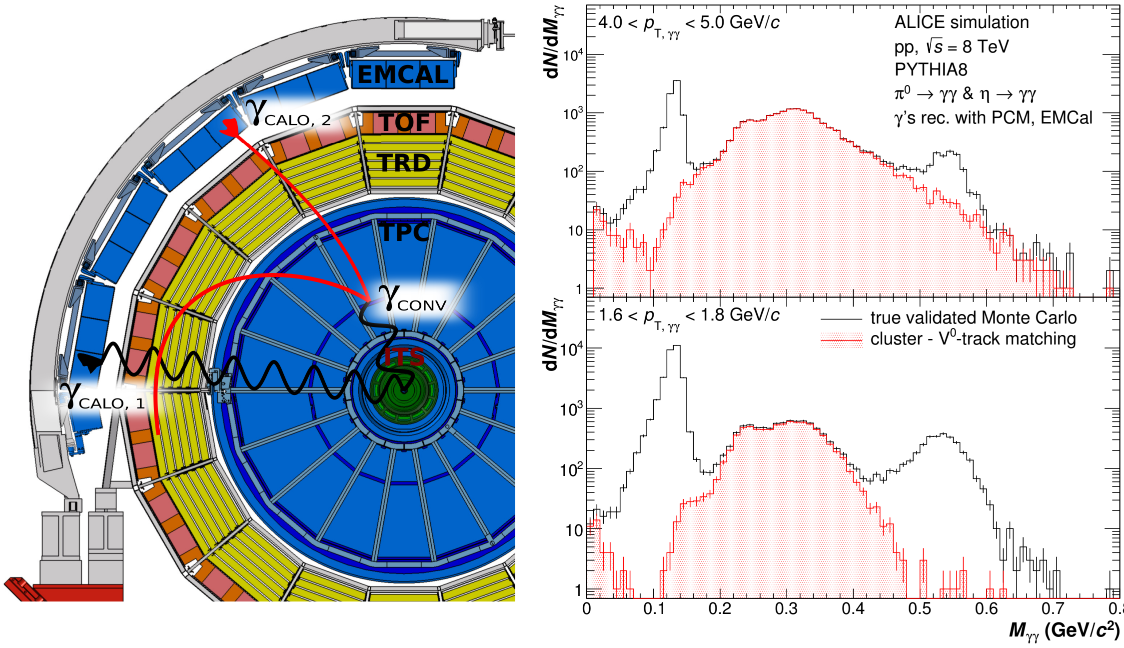

a) b)

Figure 6.1.4: a) A schematic cross section of the ALICE detector, adapted from Ref. [243], with different photon candidates drawn in addition. b) Invariant mass distributions of validated π^0 and η mesons from true MC for different p_{T} ranges of $1.6 < p_{\mathrm{T}} < 1.8\,\mathrm{GeV}/c$ and $4.0 < p_{\mathrm{T}} < 5.0\,\mathrm{GeV}/c$ for the hybrid method PCM-EMCal. The black histograms represent invariant masses of true meson candidates. In contrast, the red distributions indicate a double counting of the PCM photon if one of the legs of the V^0 itself generates the EMCal photon candidate. Such pairings are removed by matching the tracks of the conversion daughters to the EMCal clusters.

When reconstructing mesons using the hybrid methods, the photon combinations can be categorized into three general classes according to Fig. 6.1.4a:

(i) true signal – $\gamma_{\mathrm{CONV}} + \gamma_{\mathrm{CALO},1}$;

(ii) double counting of the PCM photon – $\gamma_{\mathrm{CONV}} + \gamma_{\mathrm{CALO},2}$;

(iii) background – all remaining combinations of all reconstructed photons in the event.

While case (i) yields the desired signal and (iii) gives combinatorial background, case (ii) leads to an autocorrelation which is visualized in Fig. 6.1.4b for two different p_{T} bins by the red histograms. The black distributions represent invariant masses of true meson candidates if the mother particle of the EMCal cluster is identical to the mother of the PCM photon which is validated to be a π^0 or η meson. As it can be seen, combinations of type (ii) generate a rather broad contribution between the invariant masses of the light neutral mesons π^0 and η which can be removed by propagating the V^0's daughter particle trajectories towards the EMCal surface and applying a matching condition with respect to the reconstructed clusters. This procedure is already performed implicitly by track matching procedure applied to EMCal clusters, see Sec. 5.2. From Fig. 6.1.4b it becomes evident that this matching procedure gains importance for higher p_{T} so that it is a essential analysis step for the hybrid method. Because of the importance of this procedure, MC simulations are used to evaluate its performance which is illustrated in Fig. 6.1.5 for true, a), π^0 and, b), true η candidates using the PYTHIA 8 MC simulation of pp collisions at $\sqrt{s} = 8\,\mathrm{TeV}$ for example.

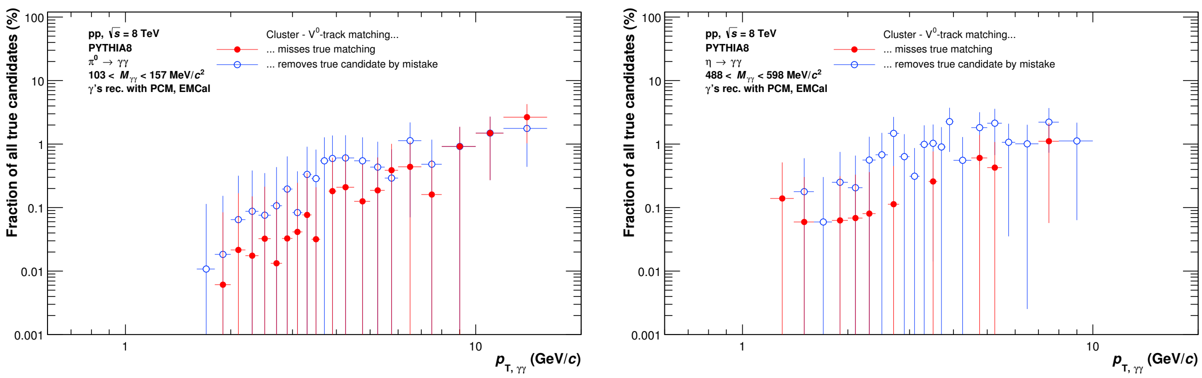

a) b)

Figure 6.1.5: The matching performance is demonstrated for true π^0, a), and true η, b), mesons for the given invariant mass regions. Red markers indicate true matches that were missed by the track matching procedure, whereas blue markers represent true meson candidates that were removed by mistake. If no data point is shown for a p_{T} bin, the respective fractions are vanishing.

At low p_{T} it rarely happens that a true matching of V^0-track and EMCal cluster is missed, indicated by red markers, as well as that a true meson candidate is removed by mistake, visualized by blue open markers. Both values are observed to slightly increase with p_{T}. This can be explained by the decreasing opening angle of the two photons due to the Lorentz boost of the mother particle so that the matching requirement is more likely to be fulfilled, EMCal clusters may simply merge and the conversion daughters e^-e^+ inherit more energy from the photon so that energy loss effects like bremsstrahlung occur more frequently. An integrated matching efficiency of approximately 99.1 % is found for the given example in Fig. 6.1.5, whereas nearly 0.6 % are missed and about 0.3 % are removed by mistake. Hence, Fig. 6.1.4b and Fig. 6.1.5 indicate that the procedure performs reasonably well to be used for meson reconstruction.

By combining PCM and EMCal photon candidates to reconstruct neutral mesons, a rather strict geometrical selection of PCM photon candidates is applied. The candidates pointing towards the EMCal surface, see Sec. 3.2.1, are predominantly selected. This is connected to the opening angles of the two photons originating from the meson decays. The angle depends on the Lorentz boost of the meson and its rest mass so that the effect is stronger for the π^0 than for the η meson. During the QA stage, see Sec. 4.3, it was ensured that there is no bias present due to this selection and that the MC simulations are able to properly describe this constraint.

6.2 Measurement of Neutral Mesons in pp Collisions at $\sqrt{s} = 8\,\mathrm{TeV}$

The results presented in this thesis concerning neutral meson production in pp collisions at $\sqrt{s} = 8\,\mathrm{TeV}$ are published by ALICE [4]. Additional figures can be found in Ref. [5]. An overview of the different meson reconstruction methods used in that publication is given in Tab. 6.2.3. The p_{T} reach of each method depends on the respective statistics available and, hence, in particular on the applicable set of triggers. Furthermore, the respective references are given and the covered p_{T} intervals of the full combination of all individual methods is listed.

reconstruction method	available p_{T} reach (GeV/c) π^0	η	η/π^0	reference
PCM	0.3 – 12.0	0.5 – 7.0	0.5 – 7.0	MSc thesis by N. Schmidt [244]
EMCal	1.2 – 20.0	2.0 – 35.0	2.0 – 20.0	this thesis
PCM-EMCal	0.8 – 35.0	1.2 – 25.0	1.2 – 25.0	this thesis
PHOS	1.0 – 35.0	N/A	N/A	PhD thesis by S. Yano [245]
combination	0.3 – 35.0	0.5 – 35.0	0.5 – 25.0	published by ALICE [4]

Table 6.2.3: A summary of the different reconstruction methods available measuring the neutral meson production in pp collisions at $\sqrt{s} = 8\,\mathrm{TeV}$. The PCM measurement is purely based on MB triggers and is provided by Nicolas Schmidt [244], whereas the PHOS reference is supplied by Satoshi Yano [245] including MB and PHOS-L0 triggers. The reconstruction of η mesons is not accessible by PHOS due to the limited detector acceptance for this dataset and the wider opening angle of the decay photons compared to the π^0.

The p_{T} ranges as introduced in Tab. 6.2.3 are split into p_{T} bins in which the respective analysis was carried out. The subdivision of bins can be deduced from the figures shown in the remaining part of this chapter or Sec. B.2.1. For the η/π^0 measurement, the π^0 signal is extracted using the same bin widths as defined for the η meson. The choice of bin widths reflects the available statistics of neutral meson candidates for each reconstruction method as a function of p_{T}. Moreover, the choice follows the goal to combine as many independent measurements as possible in each p_{T} bin which can only be done if the different methods share the same binning in their p_{T} overlap regions. All different analysis performed with each reconstruction method were carried out independently. The respective results are then combined as described in Sec. 6.2.5.

6.2.1 Signal Extraction

The measurement of neutral mesons in pp collisions at $\sqrt{s} = 8\,\mathrm{TeV}$ for both EMCal and PCM-EMCal methods involves the analysis of MB, EMCal-L0 and EMCal-L1 triggered events. The signal extraction for each trigger and reconstruction method is performed independently. Hence, the cross sections are obtained individually for each trigger according to Eq. 6.1.4 which are then combined as elaborated in Sec. 6.2.2. Example bins are shown in Fig. 6.2.6 for the EMCal-L0 (EMC7) and EMCal-L1 (EGA) triggers for both reconstruction methods. Clear π^0 and η meson peaks are visible on top of combinatorial background. Similar plots are already shown in the previous Sec. 6.1 in Fig. 6.1.1 for the MB trigger which can be used to look up the according definitions and explanations that also apply here.

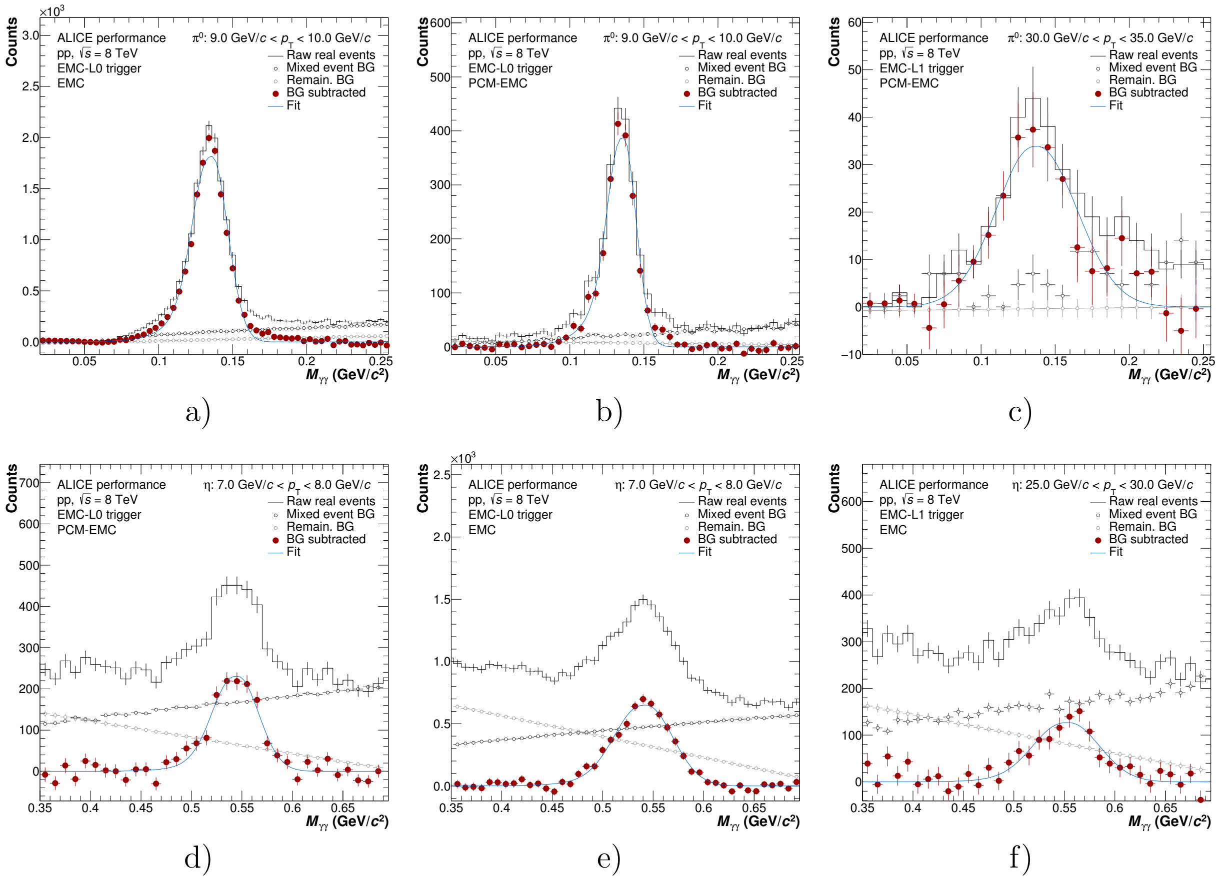

Figure 6.2.6: Example invariant mass distributions for the reconstruction methods PCM-EMCal and EMCal involving EMCal triggered events in pp collisions at $\sqrt{s} = 8\,\mathrm{TeV}$ showing π^0, a)−c), and η meson candidates, d)−f).

An overview of the complete signal extraction for all p_T bins for all three triggers used for the analysis is given in Sec. B.2.1 for both EMCal and PCM-EMCal methods. Compared to the MB trigger, the usage of EMCal triggers enables a higher momentum reach as such events are predominantly selected which include high energy deposits into the calorimeter. Thus, the probability to reconstruct mesons with high p_T is increased. However, the low p_T region is very difficult to access due to the present trigger biases so that it is better to use MB triggers for this regime. Fig. 6.2.6a, Fig. 6.2.6b, Fig. 6.2.6d and Fig. 6.2.6e show π^0 and η meson peaks for intermediate momenta of about $7-10\,\mathrm{GeV}/c$ for the EMCal and PCM-EMCal methods indicating a high significance of the signals. Much more statistics is available in the same p_T region compared to MB triggered invariant mass distributions. Fig. 6.2.6c and Fig. 6.2.6f show the highest p_T bin used for the analysis for the π^0, $30 < p_\mathrm{T} < 35\,\mathrm{GeV}/c$, and the second highest for the η meson, $25 < p_\mathrm{T} < 30\,\mathrm{GeV}/c$, which are only accessible using the EMCal triggers. A comparable p_T reach would be possible in theory by using MB triggers but enormous amounts of MB data would be needed so that an economic use of experimental resources always suggests a mixture of MB and calorimeter triggers to be recorded for an experiment like ALICE.

As introduced in Sec. 6.1, the mixed-event background needs to be scaled in order to subtract the uncorrelated background from the same-event distributions. The normalization ranges used for that purpose are given in Tab. 6.2.4 which are used for all invariant mass bins used in analysis. Hence, they apply to Fig. 6.1.1 and Fig. 6.2.6 as well.

reconstruction method	trigger	pp, $\sqrt{s} = 8\,\text{TeV}$ normalization range $[M_{\gamma\gamma}^{\text{low}}, M_{\gamma\gamma}^{\text{high}}]$ (GeV/c^2) π^0	η
EMCal	INT7	[0.19, 0.30]	[0.67, 0.80]
EMCal	EMC7	[0.25, 0.30]	[0.67, 0.80]
EMCal	EGA	[0.26, 0.30]	[0.67, 0.80]
PCM-EMCal	*all*	[0.19, 0.30]	[0.65, 0.75]

Table 6.2.4: The normalization ranges for the reconstruction methods PCM-EMCal and EMCal for the π^0 and η meson analysis.

Both same-event and mixed-event $M_{\gamma\gamma}$ distributions are integrated in the given ranges. The respective integrals are then divided by each other to obtain the scale factors for the mixed-event backgrounds. It is important that the normalization region is outside the actual peak region. However, it must be in close proximity to the peak to ensure a valid background description so that a proper amount of background is subtracted. It is verified that the signal extraction is stable and working correctly using true MC information, from which the linear shape of the remaining correlated background is also deduced. The values concerning the normalization range for the EMCal reconstruction method are bigger for the EMC7 and EGA triggers due to cluster merging effects leading to a shift of the mass position to higher values, see also Fig. 6.2.13.

The following Fig. 6.2.7 shows the extracted mass peak position M_{π^0} and width σ_{π^0} as a function of reconstructed p_{T} for both EMCal and PCM-EMCal reconstruction methods. The respective

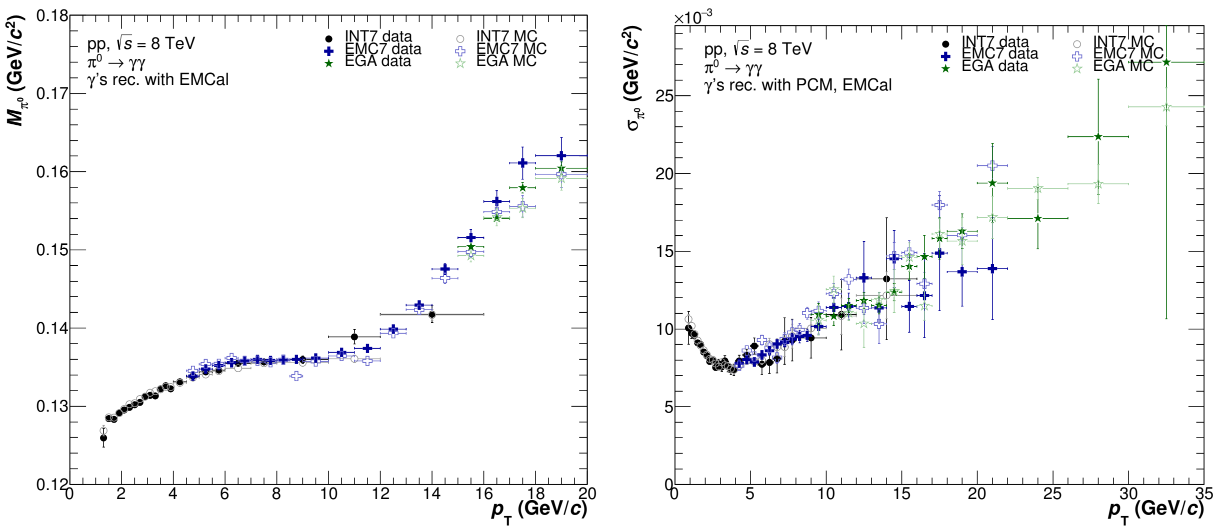

a) b)

Figure 6.2.7: The extracted mass positions M_{π^0} and peak widths $\sigma_{M_{\pi^0}}$ by fitting Eq. 6.1.3 to the background-subtracted signal, drawn as a function of p_{T} for real data and MC simulations for the three available triggers. The remaining distributions, M_{π^0} for PCM-EMCal and σ_{π^0} for EMCal, can be found in Fig. B.2.8.

values are obtained from fits of Eq. 6.1.3 to the background-subtracted signal distributions. Fig. 6.2.8 shows the equivalent for the signal extraction of the η meson. In both figures, the fit results for all three available triggers are superimposed which follow the same trends within the present uncertainties, thus confirming a proper detector response in MC simulations. Moreover, the triggers' overlap regions in p_{T} can be deduced from the plots.

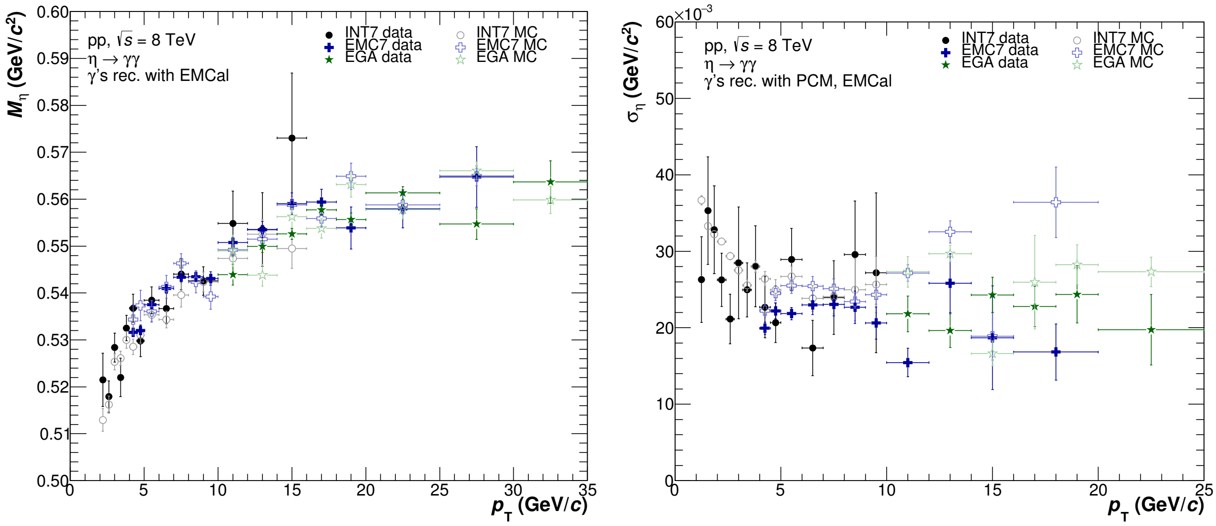

a) b)

Figure 6.2.8: The extracted mass positions M_η and peak widths σ_{M_η} by fitting Eq. 6.1.3 to the background-subtracted signal, drawn as a function of p_{T} for real data and MC simulations for the three available triggers. The remaining distributions, M_η for PCM-EMCal and σ_η for EMCal, can be found in Fig. B.2.8.

The integration ranges used to determine the mesons' raw yields are listed in Tab. 6.2.5 for the different reconstruction methods. For both neutral mesons they are chosen to cover at least $[-3\,\sigma, +3\,\sigma]$ around the reconstructed mass positions M_{π^0} and M_η, where σ is the standard deviation of the Gaussian part of the fit function.

		pp, $\sqrt{s} = 8\,\mathrm{TeV}$	
reconstruction method	trigger	integration range $[M_{\gamma\gamma}^{\mathrm{low}}, M_{\gamma\gamma}^{\mathrm{high}}]$ (GeV/c^2) π^0	η
EMCal	INT7	$[M_{\pi^0}$ - 0.050, M_{π^0} + 0.040$]$	$[M_\eta$ - 0.080, M_η + 0.080$]$
PCM-EMCal	INT7	$[M_{\pi^0}$ - 0.032, M_{π^0} + 0.022$]$	$[M_\eta$ - 0.060, M_η + 0.055$]$
EMCal	EMC7	$[M_{\pi^0}$ - 0.050, M_{π^0} + 0.060$]$	$[M_\eta$ - 0.064, M_η + 0.064$]$
PCM-EMCal	EMC7	$[M_{\pi^0}$ - 0.036, M_{π^0} + 0.025$]$	$[M_\eta$ - 0.072, M_η + 0.066$]$
EMCal	EGA	$[M_{\pi^0}$ - 0.060, M_{π^0} + 0.080$]$	$[M_\eta$ - 0.064, M_η + 0.064$]$
PCM-EMCal	EGA	$[M_{\pi^0}$ - 0.042, M_{π^0} + 0.029$]$	$[M_\eta$ - 0.072, M_η + 0.066$]$

Table 6.2.5: The integration ranges used to obtain the raw yields of π^0 and η mesons for the reconstruction methods PCM-EMCal and EMCal for the INT7, EMC7 and EGA triggers in pp collisions at $\sqrt{s} = 8\,\mathrm{TeV}$. The quoted values apply to all p_{T} bins used in the analysis.

The determination of the raw yields $N^{\pi^0(\eta)}$ for each p_T bin is performed by bin counting the background-subtracted signal in the given integration ranges. The results are shown in Fig. 6.2.9 for π^0 and Fig. 6.2.10 for η mesons. All distributions are normalized to the number of events recorded for each trigger. A clear ordering of the raw yields over a couple of magnitudes can be observed since the trigger rejection factors RF are yet to be considered. Since the Jet-Jet MC simulation used for the triggered datasets is only reliable above a meson momentum of $p_\mathrm{T} \approx 4\,\mathrm{GeV}/c$ due to the applied conditions during event generation in PYTHIA, e.g. a minimum transverse energy of 5 GeV, the EMCal-L0 trigger is basically operating at 100 % trigger efficiency since its threshold is at about 2 GeV. The EMCal-L1 trigger was running at a higher threshold of about 10 GeV so that the trigger turn-on region is indicated by the dips at around $10\,\mathrm{GeV}/c$ of the green distributions. In order to obtain a single result for each reconstruction method, the measurements of the same quantities provided by the three triggers are combined for each method according to Sec. 6.2.2.

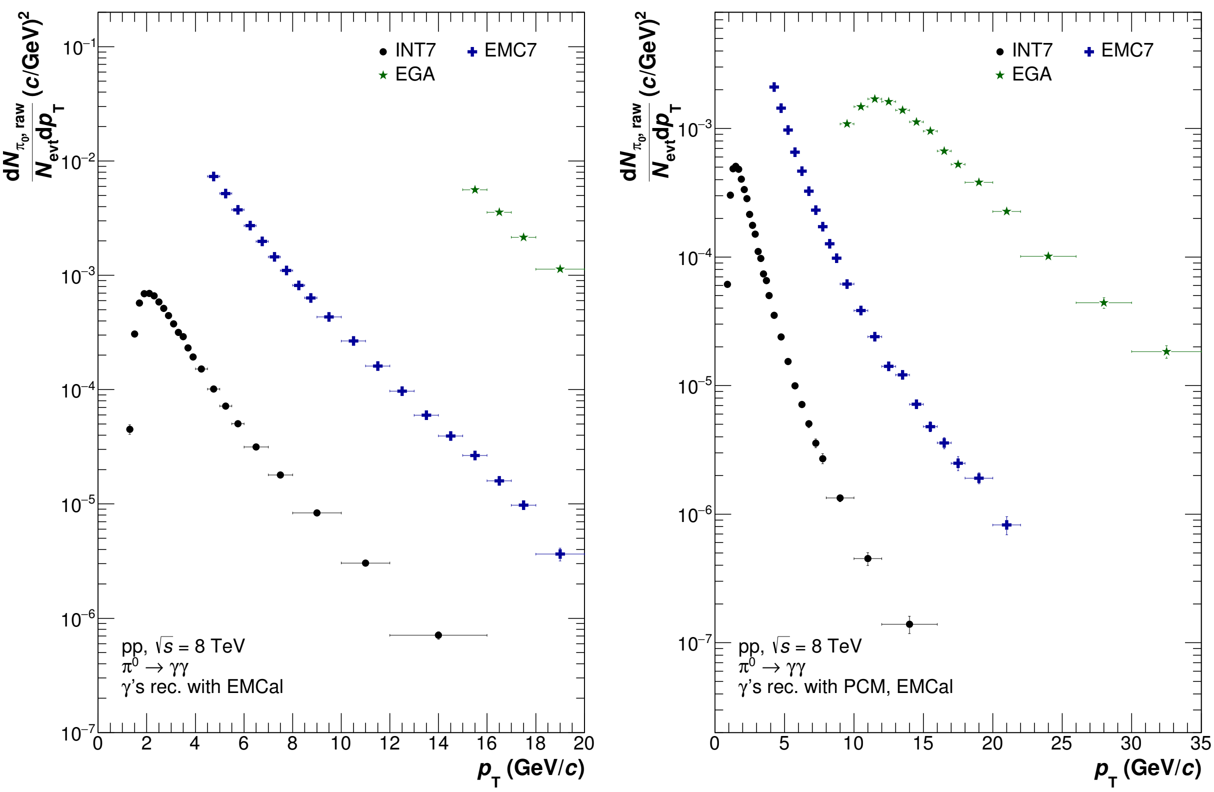

a) b)

Figure 6.2.9: The raw yields for π^0 mesons are shown as a function of p_T for the reconstruction methods EMCal and PCM-EMCal for the MB (INT7), EMCal-L0 (EMC7) and EMCal-L0 (EGA) triggers recorded at pp collisions at $\sqrt{s} = 8\,\mathrm{TeV}$. The distributions are normalized to the number of collected events in each trigger class. The enhancement of the triggered raw spectra due to the RFs is clearly visible.

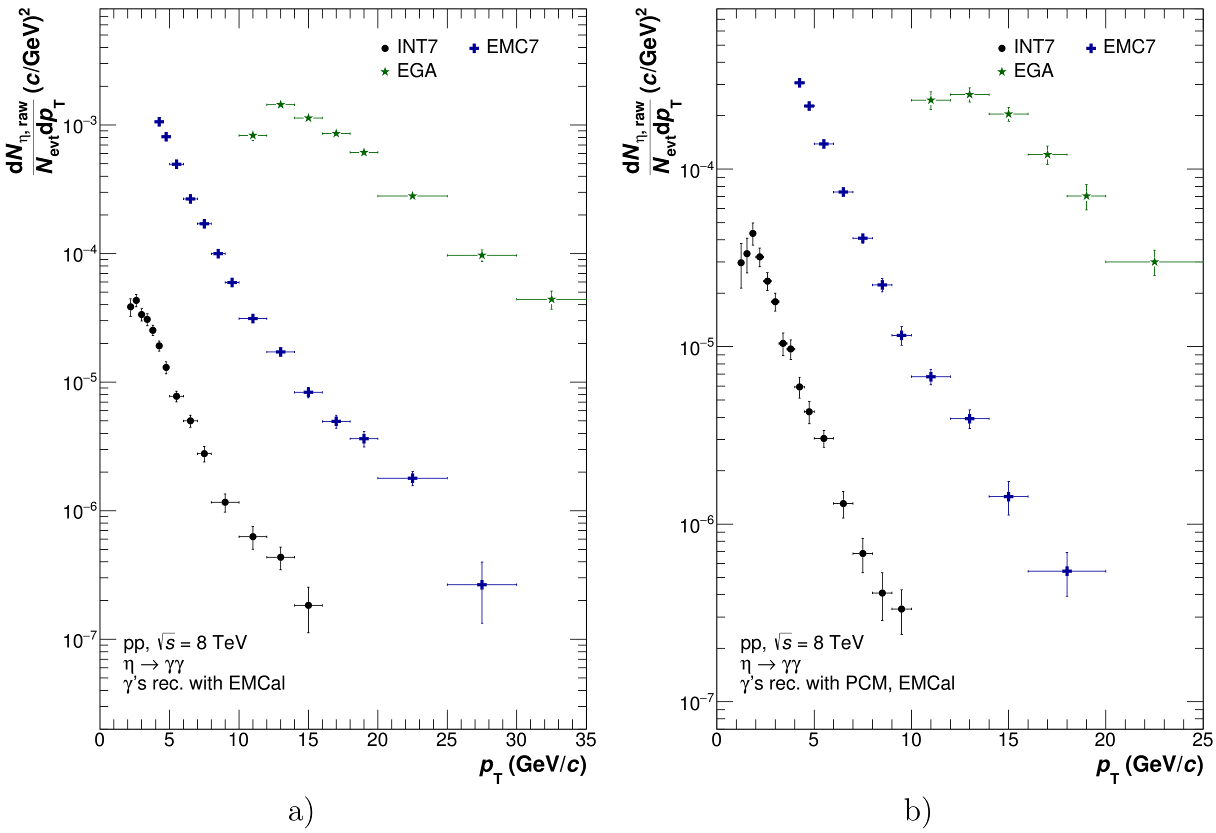

Figure 6.2.10: The raw yields for η mesons are shown as a function of p_{T} for the reconstruction methods EMCal and PCM-EMCal for the MB (INT7), EMCal-L0 (EMC7) and EMCal-L0 (EGA) triggers recorded at pp collisions at $\sqrt{s} = 8\,\mathrm{TeV}$. The distributions are normalized to the number of collected events in each trigger class. The enhancement of the triggered raw spectra due to the RFs is clearly visible.

6.2.2 Combination of Triggered Datasets

For both reconstruction methods EMCal and hybrid PCM-EMCal, neutral meson measurements are available for three different triggers; INT7, EMC7 and EGA, each covering certain p_{T} ranges of the same quantities as shown in the previous Sec. 6.2.1. The different measurements obtained with these triggers are combined in order to provide one result for each reconstruction method with improved uncertainties. This can be achieved since the combination profits from the partial overlap of different triggers in p_{T} and their varying performance: the INT7 triggered results dominate at low p_{T}, whereas the EMC7 provides the most precise measurement at intermediate and the EGA for highest p_{T}. Hence, the combination includes the strengths of each trigger and in the overlap regions the different measurements are combined according to the precision of each measurement which is reflected by the weights associated to each trigger as a function of p_{T}. These p_{T}-dependent weights are calculated according to the Best Linear Unbiased Estimate (BLUE) method [246–250] which is used to perform the combination. For each p_{T} bin, it reflects the respective statistical and systematic uncertainties obtained for each measurement as well as correlations of these uncertainties among the triggers.

The measurements provided by each trigger have specific statistical and systematic uncertainties, which may be completely correlated between the respective triggers in general. In this analysis, the statistical uncertainties are ensured to be fully uncorrelated since different triggers use non-overlapping data samples. However, only a few of systematic uncertainties are found to be uncorrelated, such as the uncertainty associated with the signal extraction and partly efficiency as well as uncertainties related to the even triggers, for which further details are summarized in Sec. 6.2.4. Hence, the systematic uncertainties are found to be largely correlated among the different triggers. The degree of correlation is represented by associated coefficients which are determined as a function of p_{T}. For the set of INT7, EMC7 and EGA triggers, the full correlation matrix contains nine elements:

$$\mathcal{C}(p_{\mathrm{T}}) = \begin{pmatrix} 1 & \mathrm{c\_EMC7\_INT7}(p_{\mathrm{T}}) & \mathrm{c\_EGA\_INT7}(p_{\mathrm{T}}) \\ \mathrm{c\_INT7\_EMC7}(p_{\mathrm{T}}) & 1 & \mathrm{c\_EGA\_EMC7}(p_{\mathrm{T}}) \\ \mathrm{c\_INT7\_EGA}(p_{\mathrm{T}}) & \mathrm{c\_EMC7\_EGA}(p_{\mathrm{T}}) & 1 \end{pmatrix}, \tag{6.2.5}$$

where $c\_i\_j(p_{\mathrm{T}})$ denote the p_{T}-dependent correlation coefficients of trigger i with respect to j. These coefficients, also identified by $\mathcal{C}_{ij}(p_{\mathrm{T}})$, are calculated according to Eq. 6.2.6:

$$\mathcal{C}_{ij}(p_{\mathrm{T}}) = \frac{\rho_{ij} S_i(p_{\mathrm{T}}) \rho_{ji} S_j(p_{\mathrm{T}})}{T_i(p_{\mathrm{T}}) T_j(p_{\mathrm{T}})}, \tag{6.2.6}$$

where $T_i(p_{\mathrm{T}})$ represents the total uncertainty of the respective measurement by trigger i which is obtained from the quadratic sum of the statistical $D_i(p_{\mathrm{T}})$ and systematic uncertainty $S_i(p_{\mathrm{T}})$. The formula already includes the assumption that the statistical uncertainties are completely uncorrelated. Hence, only the correlation factors ρ_{ij} need to be determined which represent the fraction of the correlated systematic uncertainty of a trigger i with respect to the trigger j as a function of p_{T}:

$$\rho_{ij}(p_{\mathrm{T}}) = \frac{\sqrt{S_i^2(p_{\mathrm{T}}) - U_{ij}^2(p_{\mathrm{T}})}}{S_i(p_{\mathrm{T}})}, \tag{6.2.7}$$

where U_{ij} is the uncorrelated systematic uncertainty of i with respect to j. It becomes clear that in general $\rho_{ij} \neq \rho_{ji}$ holds and that evaluating Eq. 6.2.6 and Eq. 6.2.7 yields unity for the diagonal elements in Eq. 6.2.5. By careful evaluation of the systematics of the respective measurements, the main uncertainty sources found to be partly uncorrelated among the different triggers are signal extraction, trigger normalization and efficiency uncertainties. Further details on the different sources may be obtained from Sec. 6.2.4. The following Fig. 6.2.11 shows the $\rho_{ij}(p_{\mathrm{T}})$ for π^0 mesons which are determined for all possible trigger combinations as a function of p_{T} for EMCal and PCM-EMCal. The remaining plots for the η and η/π^0 can be found in Fig. B.2.9 and Fig. B.2.10. Markers are only shown if two triggers have at least one overlapping p_{T} bin. The correlation coefficient are generally found to be above 0.8 for PCM-EMCal and above 0.7 for EMCal, indicating a high degree of correlations of systematic uncertainties showing a small dependency on p_{T} though.

With the knowledge of the correlation factors $\rho_{ij}(p_{\mathrm{T}})$, the combination of n different measurements provided by the triggers can be performed based on the BLUE method [246–250]:

$$\langle Q(p_{\mathrm{T}}) \rangle = \boldsymbol{\omega}^T(p_{\mathrm{T}}) \mathbf{Q}(p_{\mathrm{T}}) \tag{6.2.8}$$

$$= \sum_{a=1}^{n} \omega_a(p_{\mathrm{T}}) Q_a(p_{\mathrm{T}}), \tag{6.2.9}$$

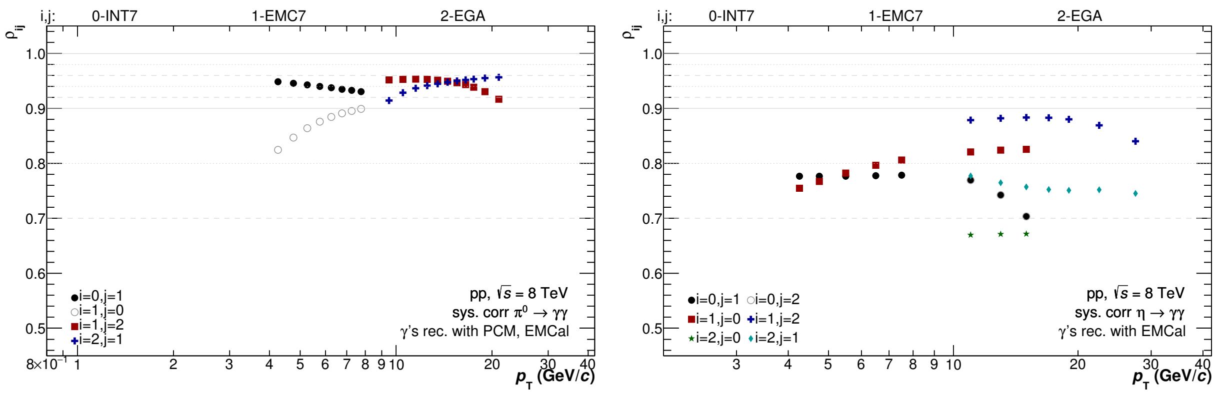

a) b)

Figure 6.2.11: The p_{T}-dependent correlation factors $\rho_{ij}(p_{\mathrm{T}})$ visualizing the fraction of correlated systematic uncertainty of trigger i with respect to trigger j. The factors are shown for the example of the π^0 for PCM-EMCal, a), and the η for EMCal, b). The remaining plots for the π^0, η and η/π^0 can be found in Fig. B.2.9 and Fig. B.2.10.

where $Q_a(p_{\mathrm{T}})$ with $0 < a < n$ represents the individual measurement a and where $\omega_a(p_{\mathrm{T}})$ is the respective weight applied to measurement a. The Q_a are summarized by the vector $\mathbf{Q}$, whereas the respective weights are represented by $\boldsymbol{\omega}$. According to the BLUE method, they are calculated in the following way:

$$\boldsymbol{\omega}(p_{\mathrm{T}}) = \mathcal{C}^{-1}\mathbf{U}/(\mathbf{U}^T\mathcal{C}^{-1}\mathbf{U}), \tag{6.2.10}$$

with the vector $\mathbf{U}$, whose components are all unity, and the inverse of the correlation matrix as defined in Eq. 6.2.5. This equation can be solved for ω_a as follows:

$$\omega_a(p_{\mathrm{T}}) = \frac{\sum_{b=1}^{n} \mathcal{H}_{ab}}{\sum_{a,b=1}^{n} \mathcal{H}_{ab}}, \tag{6.2.11}$$

where the definition $\mathcal{H} \equiv \mathcal{C}^{-1}$ with its elements $\mathcal{H}_{ab}$ applies.

The obtained weights $\omega_a(p_{\mathrm{T}})$ for the different triggers INT7, EMC7 and EGA are shown in Fig. 6.2.12 for the π^0 reconstructed with PCM-EMCal and, accordingly, the η meson using EMCal. The remaining plots showing the weights for all other cases can be found in Fig. B.2.11 and Fig. B.2.12. Markers are only shown in the plots if a trigger contributes to the combination in the given p_{T} bin.

The determined $\omega_a(p_{\mathrm{T}})$ enable not only the combination of the production cross section but also other related quantities are combined by applying these weights. Fig. 6.2.13 shows the reconstructed mass peak positions and extracted peak widths of π^0 and η mesons for the EMCal and PCM-EMCal measurements, having combined the peak positions and widths previously shown in Fig. 6.2.7 and Fig. 6.2.8 according to the obtained weights from Fig. 6.2.12. Furthermore, the same quantities obtained with the PCM method and the PHOS, see Tab. 6.2.3, are shown in the following Fig. 6.2.13. A comparison of the reconstructed mass peak positions and extracted peak widths from data and MC simulations, visualized by full and open markers respectively, confirms a proper detector response in the simulation for all reconstruction methods. The peak width ordering, $\sigma_{\mathrm{PCM}} < \sigma_{\mathrm{PHOS}} < \sigma_{\mathrm{PCM\text{-}EMCal}} < \sigma_{\mathrm{EMCal}}$ which is shortly discussed already in Sec. 6.1,

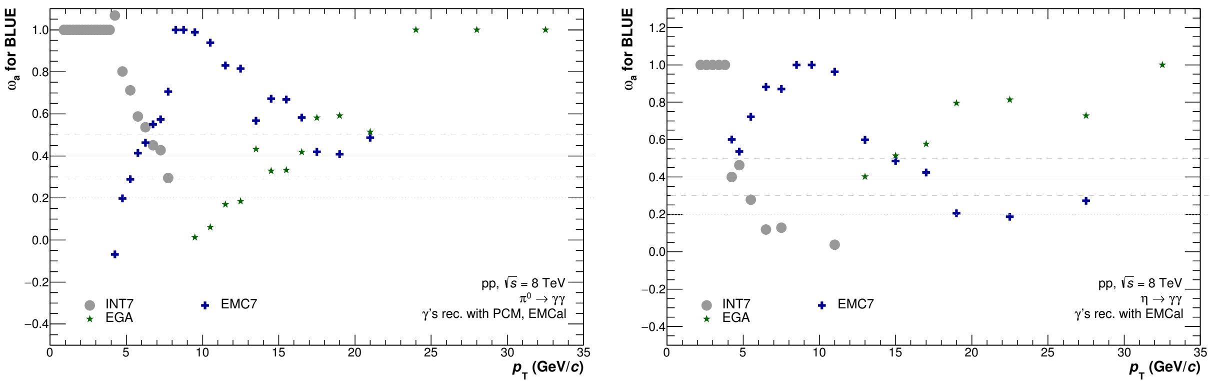

a) b)

Figure 6.2.12: The obtained weights $\omega_a(p_T)$ using the BLUE method for the combination of π^0 measurements using PCM-EMCal, a), and for the η using EMCal, b). The remaining plots showing the weights for all other cases can be found in Fig. B.2.11 and Fig. B.2.12.

can be observed as a function of p_T. It is a direct consequence of the respective energy and momentum resolutions of the different photon reconstruction techniques. Moreover, the mass positions using PCM and PHOS are found to be close to the nominal PDG masses which are indicated by the horizontal gray lines. The mass position for the EMCal method varies as a function of p_T since the MC cluster energies are calibrated to data as introduced in Sec. 5.2.1.

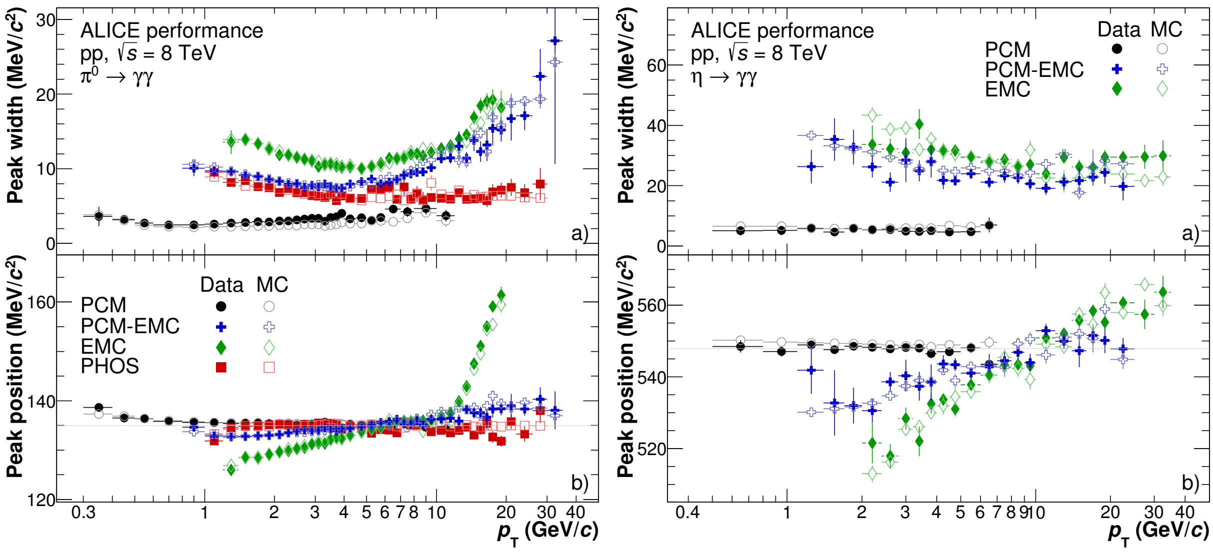

a) b)

Figure 6.2.13: The reconstructed peak widths and peak positions for π^0, a), and η, b), mesons for all reconstruction methods used in the analysis. The data points represent the merged result of all available triggers for each method according to the obtained weights shown in Fig. 6.2.12. Full markers indicate results from data, whereas open markers represent the obtained values from MC simulations.

If not otherwise specified, the plots shown in the upcoming sections always represent the combination of all triggers for a reconstruction method according to the weights introduced in this section.

6.2.3 MC Corrections of Raw Spectra

According to Eq. 6.1.4 in Sec. 6.1, the obtained raw spectra from Sec. 6.2.1 need to be corrected for secondary π^0 mesons from weak decays and material interactions $N^{\pi^0}_{\mathrm{sec}}$ in order to obtain the neutral meson production cross section $E\mathrm{d}^3\sigma^{pp\to\pi^0(\eta)+X}/\mathrm{d}p^3$ of interest. Furthermore, the geometrical acceptance A and reconstruction efficiency $\varepsilon_{\mathrm{rec}}$ need to be evaluated using MC simulations for that purpose. These two corrections are summarized by the correction factor ε, defined as the product of both quantities $\varepsilon \equiv A \cdot \varepsilon_{\mathrm{rec}}$.

As only primary mesons produced in pp collisions $pp \to \pi^0(\eta) + X$ are of interest, contributions of secondary π^0 mesons need to be removed. A secondary π^0 meson is defined to originate from weak decays or hadronic interactions with the detector material, thus being created at secondary vertices distinct from the initial collision point represented by the reconstructed primary vertex. Therefore, contributions from secondary π^0 are estimated and removed from the measurements. The occurrence of secondary η mesons can be neglected, hence the correction is only applied for the neutral pion. Weak decays of K^0_S represent the main source of secondaries but also decays of K^0_L and Λ into neutral pions contribute. However, π^0 mesons originating from K^0_L and Λ decays are suppressed at high p_{T} because of the particles' decay lengths and kinematics respectively. The decay properties of K^0_S, K^0_L and Λ are summarized in the following Tab. 6.2.6.

particle	decay channel	branching ratio	decay length ($c\tau$)
K^0_S	$\pi^0\pi^0$	30.69±0.05 %	2.6844 cm
K^0_L	$\pi^0\pi^0\pi^0$	19.52±0.12 %	15.34 m
	$\pi^+\pi^-\pi^0$	12.54±0.05 %	
Λ	$\mathrm{n}\pi^0$	35.8±0.5 %	7.89 cm

Table 6.2.6: The weakly decaying particles of relevance that yield secondary π^0 mesons to be corrected for in the analysis. The given values are taken from Ref. [32], further information can also be found in Tab. 2.2.2 and Tab. 2.2.3.

The production cross sections of the three main particles relevant for the secondary correction due to weak decays, K^0_S, K^0_L and Λ, are not well enough described by MC event generators for this analysis. Furthermore, they haven't been measured yet in pp collisions at $\sqrt{s} = 8\,\mathrm{TeV}$. However, the particle spectra were already published by ALICE for different $\sqrt{s}$ energies [251–253]. This data is used to obtain the particle spectra at $\sqrt{s} = 8\,\mathrm{TeV}$ by means of extrapolation. For that purpose, a power law for each p_{T} bin as function of $\sqrt{s}$ is assumed to estimate the yield at 8 TeV, see Sec. 7.1 for more details. In this context, the average of the charged kaon spectra serves as a meaningful proxy for both K^0_S and K^0_L, for which an agreement at the level of 1 % is found above 2 GeV/c. Hence, the charged kaon measurement is used as the default input for the production cross sections of the K^0_S and K^0_L due to its smaller uncertainties and larger p_{T} coverage. All obtained spectra for K^0_S, K^0_L and Λ are parametrized and extrapolated using Tsallis fits beyond the limited p_{T} range covered by measurements.

These parameterizations of spectra are used as weights in a PYTHIA 6.4 generator level simulation, where the respective particle decays are simulated taking into account the full decay kinematics. Using this procedure, the invariant yields of secondary π^0 mesons from weak decays of K^0_S, K^0_L and Λ are obtained. In order to obtain the raw spectra of secondary π^0 to perform the correction as indicated in Eq. 6.1.4, the acceptance and reconstruction efficiencies for secondary neutral pions are calculated using the full ALICE GEANT3 MC simulations. The comparison of the obtained secondary acceptances and efficiencies for the different sources is shown in Fig. 6.2.14 for EMCal and PCM-EMCal.

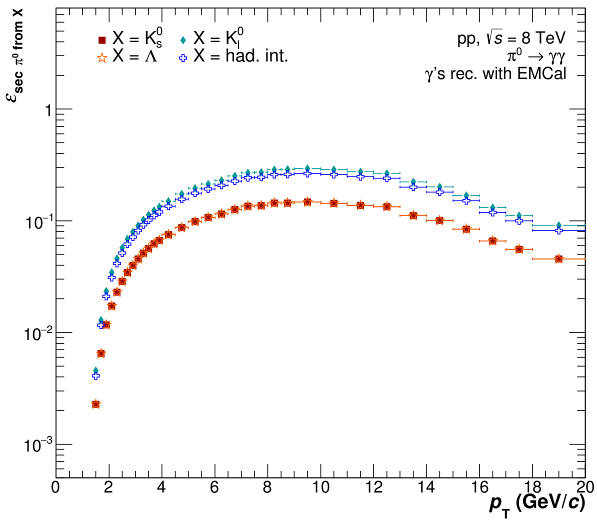

a)

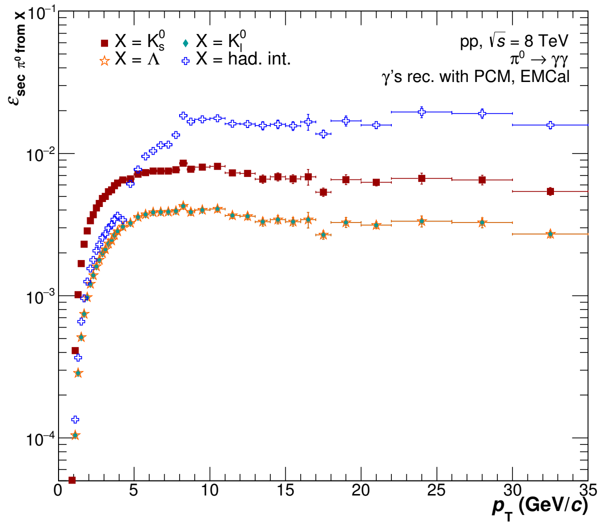

b)

Figure 6.2.14: Reconstruction efficiencies for secondary π^0 mesons for the different sources for EMCal, a), and PCM-EMCal, b), as a function of meson p_{T}.

In some cases, large fluctuations are seen in particular for K^0_L and Λ efficiencies due to limited statistics in the MC simulations. Hence, the ratio to the primary pion efficiency is computed for these cases and fitted with a constant which is used to scale the primary efficiency.

The obtained acceptances and reconstruction efficiencies for secondary π^0 mesons are multiplied with the respective invariant yields from the generator level MC simulation to arrive at the secondary π^0 raw yields from the different particles. The π^0 raw yield from interactions with the detector material is purely obtained from the full MC simulation using the true level of information which is the only viable approach. All the estimated secondary π^0 raw yields are then subtracted from the reconstructed number of π^0 mesons as indicated in Eq. 6.1.4. The effective secondary π^0 corrections are summarized in Fig. 6.2.15 for the reconstruction methods PCM, EMCal and PCM-EMCal. The corrections are of the order of $1-3\,\%$ for K^0_S, $<0.5\,\%$ for K^0_L, $\lesssim 0.02\,\%$ for Λ and $0.1-2\,\%$ for π^0 mesons from material interactions, varying within the given values for the different reconstruction methods.

After the contribution of secondary neutral pions is removed, the corrections for geometrical acceptance and reconstruction efficiencies need to be applied which are evaluated using the MC simulations introduced in Chap. 4. The correction factors ε for both PYTHIA and PHOJET MC productions are found to be consistent and, hence, are combined. To correct the raw yields obtained with triggered data, a PYTHIA 8 simulation is used enriched with jets, generated in

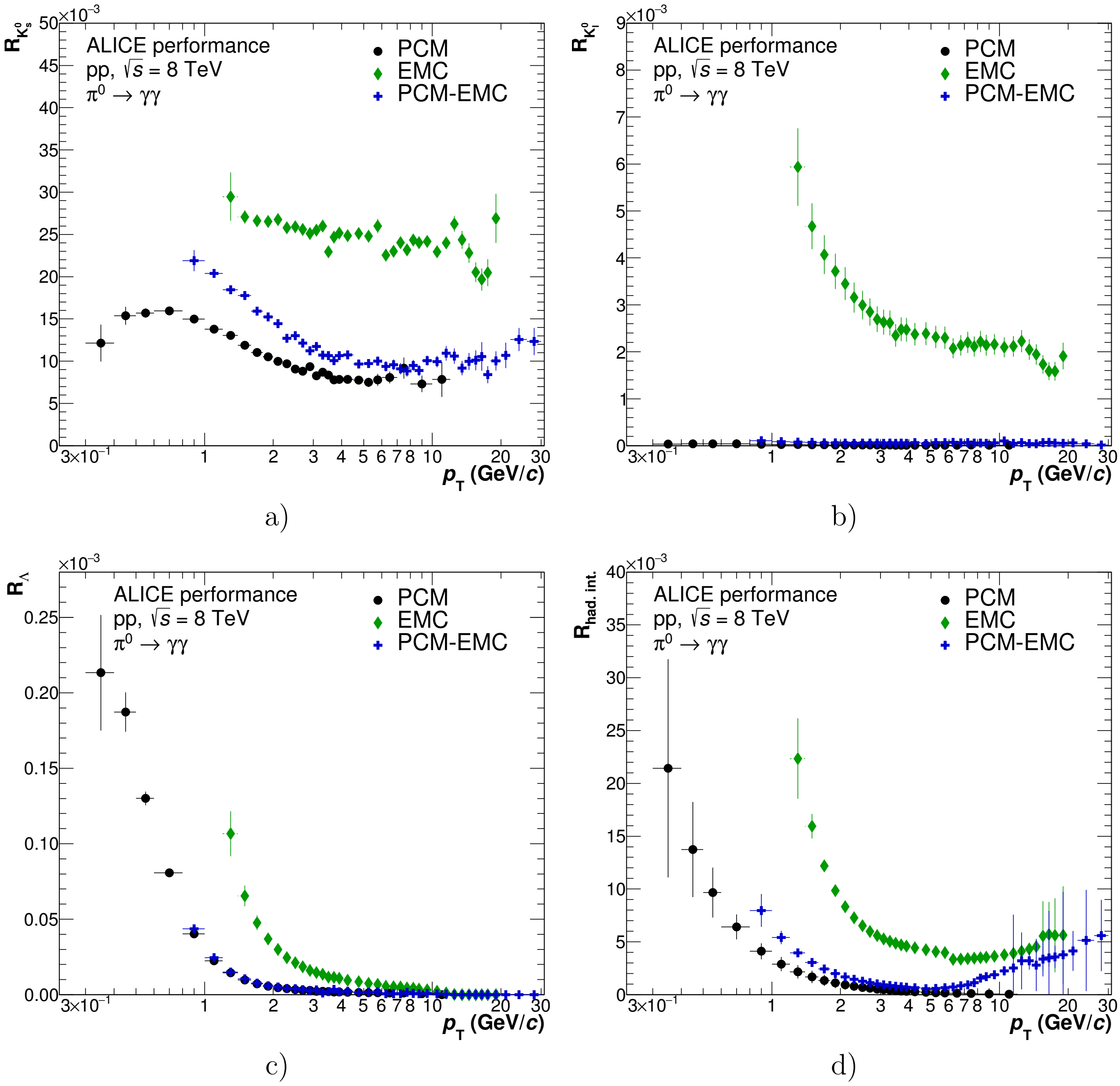

Figure 6.2.15: Effective corrections concerning secondary π^0 mesons originating from K^0_S, K^0_L and Λ decays as well as hadronic interactions with the detector material of ALICE, from a) to d), summarized for the methods PCM, PCM-EMCal and EMCal. The fractions of secondary π^0 mesons from the different sources are plotted as a function of p_{T}.

bins of hard scatterings $p_{\mathrm{T,\,hard}}$, see Sec. 4.1.1. For the simulations, the same reconstruction algorithms and analysis cuts are applied as for real data. The geometrical acceptance A_{meson} is defined as the ratio of the number of π^0 (η) mesons within $|y| < 0.8$, whose daughter particles are within the fiducial acceptance, and all π^0 (η) mesons generated in the same rapidity window:

$$A_{\mathrm{meson}}(p_{\mathrm{T}}) = \frac{N_{\mathrm{meson},\,|y|<0.8}(p_{\mathrm{T}}) \text{ with } \gamma_1, \gamma_2 \in \mathcal{A}}{N_{\mathrm{meson},\,|y|<0.8}(p_{\mathrm{T}})}, \tag{6.2.12}$$

where, depending on the reconstruction method, γ_1 and γ_2 represent PCM (γ_{conv}) and/or EMCal (γ_{calo}) photon candidates. The variable $\mathcal{A}$ stands for the respective detector acceptance, in which both photons have to be emitted. For the two different methods of photon detection $\mathcal{A}$ is defined as follows:

- $\mathcal{A}_{\text{PCM}}$: $\gamma_{\text{conv}} \in (\eta_{\text{conv}}, \varphi_{\text{conv}}) = (-0.90 < \eta < 0.90,\ 0 \leq \varphi < 2\pi)$;
- $\mathcal{A}_{\text{EMCal}}$: $\gamma_{\text{calo}} \in (\eta_{\text{calo}}, \varphi_{\text{calo}}) = (-0.67 < \eta < 0.67,\ 1.40\,\text{rad} < \varphi < 3.15\,\text{rad})$.

On the other hand, the reconstruction efficiency $\varepsilon_{\text{reco, meson}}$ is obtained via:

$$\varepsilon_{\text{reco, meson}}(p_{\text{T}}) = \frac{N_{\text{meson, reconstructed}}(p_{\text{T}})}{N_{\text{meson, }|y|<0.8}(p_{\text{T}}) \text{ with } \gamma_1, \gamma_2 \in \mathcal{A}}. \tag{6.2.13}$$

By performing the analysis on MC simulations which are treated like real data, the quantity $N_{\text{meson, reconstructed}}(p_{\text{T}})$ is determined by extracting the number of reconstructed mesons as a function of p_{T}. It is cross-checked with the so-called validated true efficiency which is based on true MC information by verifying that the photon candidates originate from the same mother particle, a π^0 or η meson. The obtained acceptances and reconstruction efficiencies are shown in Fig. 6.2.16 for π^0 and η mesons for both EMCal and PCM-EMCal methods.

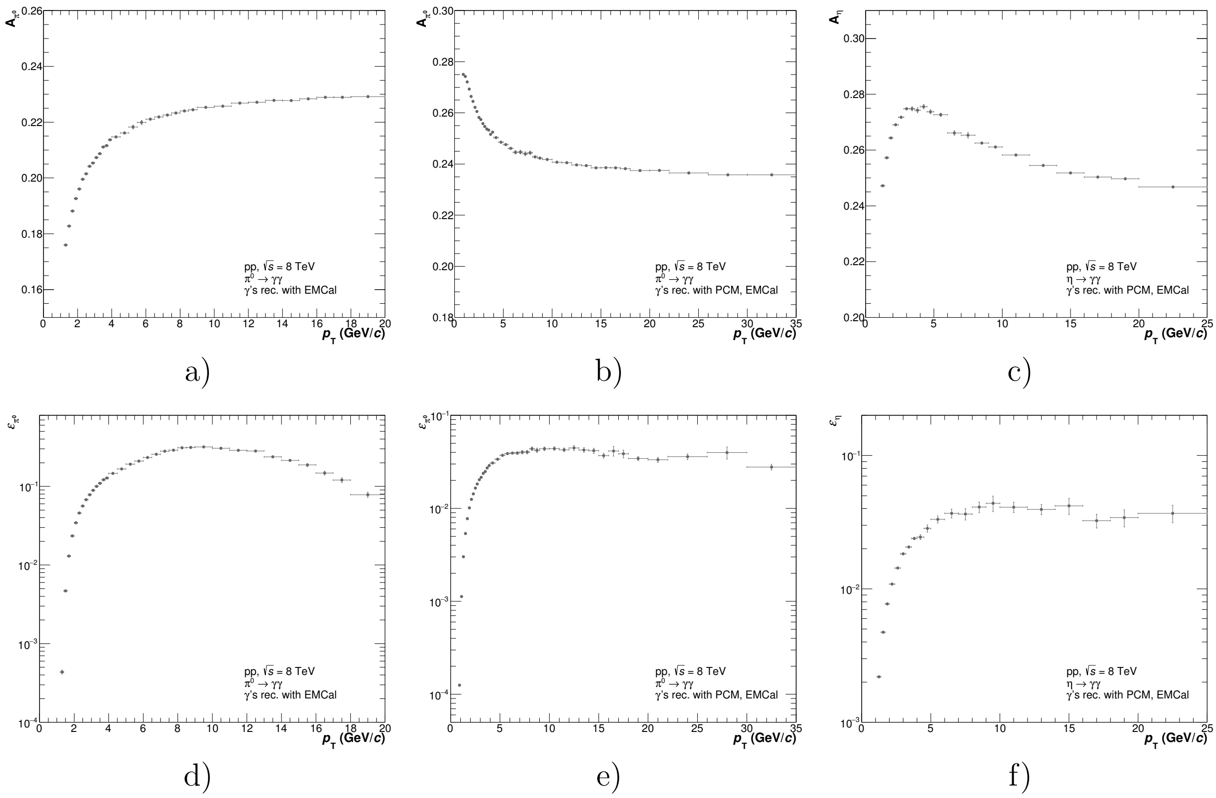

Figure 6.2.16: The geometrical acceptances A_{meson} for π^0 mesons are shown for EMCal, a), and PCM-EMCal, b), as a function of meson p_{T}. The acceptance for η mesons, c), is also presented for the latter method. Below, the corresponding reconstruction efficiencies $\epsilon_{\text{reco, meson}}$ are shown, again plotted versus meson p_{T}.

The corresponding plots for the η using EMCal are not shown in Fig. 6.2.16, however, they closely follow the shapes of the acceptance and efficiency plots for the π^0 with the exception that the decrease of efficiency beginning at around $p_{\mathrm{T}} \approx 10\,\mathrm{GeV}/c$ is not observed though. The normalized correction factors ε are shown in Fig. 6.2.17 for each reconstruction method used for the analysis of pp data at $\sqrt{s} = 8\,\mathrm{TeV}$. They contain the specific detector acceptances as well as reconstruction efficiencies.

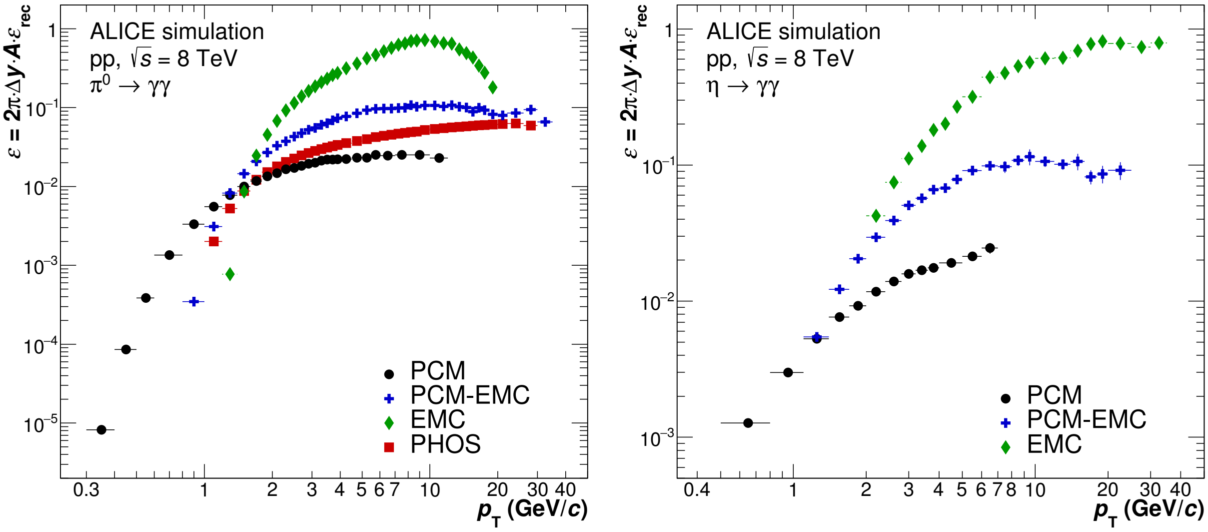

a) b)

Figure 6.2.17: The normalized correction factors ε for each reconstruction method for π^0, a), and η mesons, b), plotted as a function of p_{T}. The factors contain the detector acceptances and the respective reconstruction efficiencies, where acceptances are further normalized by the rapidity windows accessible with each method Δy and full azimuth coverage of 2π in order to enable a direct comparison between the different methods.

In Fig. 6.2.16, the acceptances are shown for EMCal and PCM-EMCal measurements in a), b) and c) as a function of meson p_{T}. The shape of the acceptance curve for the EMCal rises with increasing p_{T} due to the decreasing opening angle of the photon pair because of the Lorentz boost. Therefore, the likelihood that both photons of the mother particle are emitted into the geometrical acceptance of the EMCal detector increases with p_{T} and, hence, with the Lorentz boost. The same applies for the η meson which is not shown here but exhibits a similar shape as for the π^0. For the PCM-EMCal method, one photon needs to convert within the inner detector material of ALICE, whereas the other photon has to point towards the EMCal surface. Optimum values of the acceptance for both mesons are present which are represented by the peaks at around $1\,\mathrm{GeV}/c$ for the π^0 and approximately $4\,\mathrm{GeV}/c$ for the η. The acceptance decreases for lower p_{T} and for higher p_{T} as well. This is due to the requirement of a photon conversion to occur. At low p_{T}, the opening angles of the mesons are large and less energy is available for both daughter particles. Hence, the opening angles of the e^-e^+ pairs from the photon conversion are also large, leading to a reduced number of candidates within the detector acceptance. At high p_{T}, the opening angles of the mesons are small and, therefore, both photons essentially have to be in the geometrical acceptance of the EMCal as well. In between, an optimum is reached where the photons converting in the detector material of ALICE have enough energy to be within the TPC acceptance $|\eta| < 0.9$ for secondary track reconstruction while the calorimeter photon is pointing towards the EMCal surface. At high p_{T}, the acceptance asymptotically converges towards the same value as for the EMCal method. This is due to the fact that the acceptance for high momenta is basically given by the dimension of the EMCal detector, $|\eta| < 0.67$ and $\Delta\varphi = 100°$, yielding a coverage of approximately 23.3 % for $p_{\mathrm{T}} \to \infty$.

Furthermore, Fig. 6.2.16 shows the respective reconstruction efficiencies in d), e) and f). The shape of the reconstruction efficiency as a function of p_{T} for PCM-EMCal depends on the shape of the photon conversion probability which drops significantly with decreasing p_{T} while it is constant above several p_{T}. Hence, the meson reconstruction efficiencies rise until they reach plateaus above $p_{\mathrm{T}} \approx 6\,\mathrm{GeV}/c$. This hybrid method does not suffer from cluster merging as much as the EMCal method and the track matching procedure merely causes a slight decrease of the efficiency for higher p_{T}. For the EMCal, the shape of the reconstruction efficiency is a result of the minimum energy requirement for clusters of 700 MeV. Additionally, some of the photons convert in the detector material in front of the EMCal which might be lost, reducing the efficiency for low momenta even further. Moreover, the reconstruction efficiency for the π^0 is observed to decrease for $p_{\mathrm{T}} \gtrsim 10\,\mathrm{GeV}/c$ for the EMCal method which is also shown in Fig. 6.2.17, where the combination of acceptance and reconstruction efficiencies is drawn. The decrease is due to the effect of cluster merging which occurs due to the finite segmentation of the EMCal. Because of the Lorentz boost the opening angles of π^0 mesons become too small to resolve adjacent clusters with the given cell dimensions. The dominant symmetric decays are first to merge so that the asymmetric decay contributions become more relevant at higher momenta. Above a certain limiting momentum, it is no longer possible to separate the two decay photons of the π^0. Thus, merged clusters are created that significantly reduce the reconstruction efficiency for the EMCal as seen in Fig. 6.2.17. Therefore, the natural upper limit for the π^0 reconstruction with the EMCal is of the order of $p_{\mathrm{T}}^{\pi^0} \approx 20\,\mathrm{GeV}/c$. In contrast, the hybrid PCM-EMCal approach enables the possibility to overcome the limitations of the finite cell segmentation. Hence, it is possible to reconstruct π^0 mesons up to $p_{\mathrm{T}} \approx 35\,\mathrm{GeV}/c$ using the hybrid method. On the other hand, such cluster merging effects are negligible for the reported p_{T} range in case of PHOS because of its higher granularity compared to the EMCal. The merging effects are negligible for all methods for the η meson since the opening angles of the photon pairs are much larger compared to the π^0 in the given p_{T} interval.

The EMCal trigger efficiencies of EMC7 at L0 and EGA at L1, see Sec. 4.1.1, are implicitly reflected by the reconstruction efficiencies. However, the performance of these triggers can also be described by the efficiency biases κ_{trigg} which are shown in Fig. 6.2.18 for π^0, a), and η, b), mesons as a function of meson p_{T}. The κ_{trigg} are determined by comparing the MB efficiencies with those obtained from the trigger mimicking procedure. Fig. 6.2.18 demonstrates that for all p_{T} bins used in analysis the EMC7 trigger operates fully efficient. The corresponding Jet-Jet MC simulations limit the low p_{T} reach, see Sec. 4.1.1, which is well above the trigger threshold of approximately 2 GeV. On the other hand, the EGA trigger is rather efficient where it is used for the π^0. Cluster merging effects complicate the situation, however, in addition to the high energy threshold of the EGA of about 10 GeV leading to the limited number of p_{T} bins available. For the η meson, on the other side, triggered p_{T} bins can be used for the analysis which are well within the trigger turn-on region. This is possible because of the trigger mimicking for which adequate systematic uncertainties are associated in this region which reflect the level of description of the trigger turn-on in MC simulations.

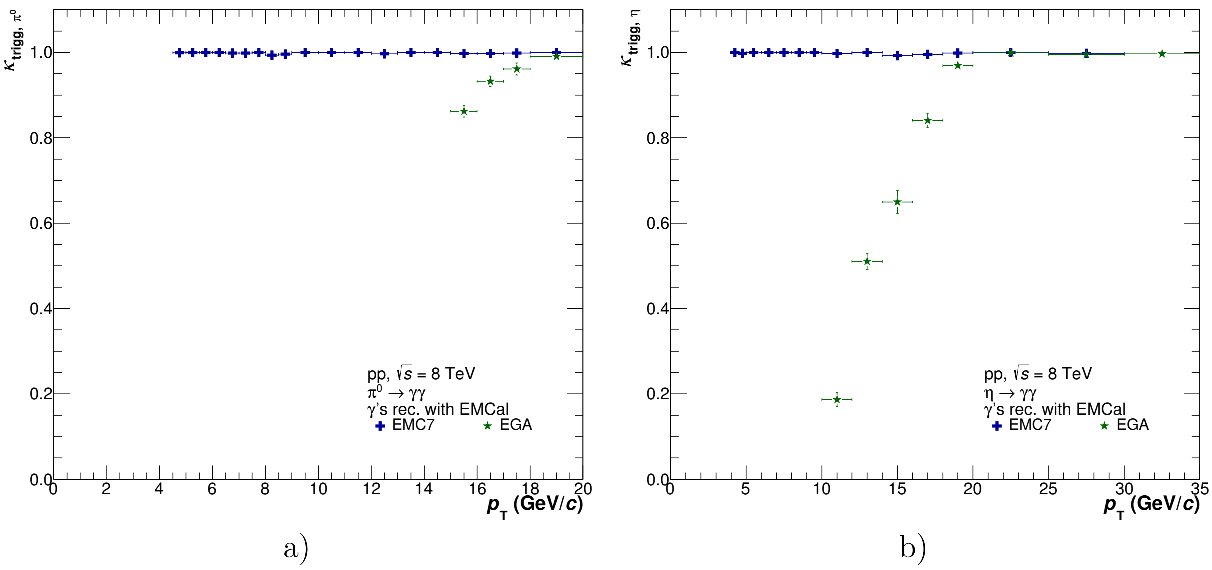

Figure 6.2.18: Efficiency biases κ_{trigg} for π^0, a), and η, b), mesons as a function of p_{T}, obtained for the two EMCal-related triggers EMC7 and EGA applying the trigger mimicking procedure to the Jet-Jet MC simulation, see Sec. 4.1.1.

6.2.4 Systematic Uncertainties

Statistical uncertainties are the result of stochastic fluctuations due to a finite set of observations which quantify how far a repeated measurement, using the same sample size and the same apparatus, would differ from the obtained result at most. In contrast, systematic uncertainties arise from the nature of the measurement apparatus itself but also from assumptions made during the analysis or from the specific choice of using a certain model. Hence, they play an important role in the context of evaluating measurements and assessing their significance as systematic uncertainties often dominate the total uncertainties. Therefore, they must be carefully evaluated so that the major part of an analysis deals with investigating and characterizing systematic effects. Different sources of such effects are identified for the described measurements using the reconstruction methods EMCal and PCM-EMCal which are summarized in Tab. 6.2.9, Tab. 6.2.10 and Tab. 6.2.11 for the neutral mesons π^0 and η as well as their ratio η/π^0. For each three different p_{T} bins, the uncertainties are given in percent and refer to relative systematic uncertainties of the measured values, illustrating the relative strengths of the reconstruction methods. Concerning the η/π^0 measurement, the π^0 signal is extracted using the same bin widths as defined for the η meson, for which the p_{T} bin widths are defined to be wider compared to the π^0 measurement, enabling a further possibility to separate statistical fluctuations from the actual systematic effects in particular for cut variations removing significant amounts of statistics.

The identification and estimation of systematic uncertainties follows Barlow's criteria [254]. By careful considerations and variations of the analysis cuts, the different sources of systematic uncertainty were found which are reported in the following. The systematic effects are estimated by varying different aspects of the analysis, for example by processing the analysis with modified event, photon and meson selection criteria, so-called cuts, as introduced in Chap. 4, Chap. 5

and Chap. 6. These variations are chosen such that either the underlying Gaussian distribution is sampled or that the maximum deviations can be accessed. Only one selection criterion is varied at the same time and the differences in the fully corrected spectra are calculated bin by bin as a function of p_{T}. In this way, the presence and magnitude of systematic effects is estimated. However, special care needs to be taken to disentangle statistical and systematic effects. Therefore, it is ensured that the selection criteria do not remove substantial amounts of statistics compared to the standard cut. The systematic uncertainties are determined from the set of cut variations and the present deviations in each p_{T} bin. Statistical effects can still play a role and cause non-physical fluctuations so that the systematic uncertainties are subsequently smoothed by reflecting the average of neighboring p_{T} bins. In order to estimate the systematic effects with best knowledge, each source of systematic uncertainty is considered in the global picture by incorporating all available information. This includes the different meson measurements as well as reconstruction methods and event triggers in order to profit from the improved statistics at higher p_{T} delivered by the triggered datasets and the insight how the systematic effects act on the different methods. For example, the same cut variations are performed for the hybrid method PCM-EMCal as for the standalone methods. Given the fact that only one photon candidate of each system is used in the hybrid approach, most systematic uncertainties are found to be of different size or behavior which is further elaborated in the following.

The different systematic uncertainty sources are summarized into eleven categories in the following. A detailed overview of the p_{T}-dependent systematic uncertainties decomposed into the different sources can be found in Fig. B.2.13. All these individual uncertainties from the different sources are summed quadratically for each p_{T} bin. The systematic uncertainty of the η/π^0 ratio is independently determined in addition to the uncertainties of the respective mesons π^0 and η. As indicated in Tab. 6.2.11, many uncertainties cancel in this case such as the material-related systematics. Furthermore, all uncertainties given in the following represent a $1\,\sigma$ level of deviation. They are visualized at the end of this section in Fig. 6.2.19 as a function of p_{T} for the different reconstruction methods for π^0, η and η/π^0 measurements, for which example bins are also quoted in Tab. 6.2.9, Tab. 6.2.10 and Tab. 6.2.11 as already introduced.

Signal Extraction

The signal extraction uncertainty is estimated by means of various modifications applied to the signal extraction procedure which is described in Sec. 6.2.1. The normalization range of the mixed-event background is changed as documented in Tab. 6.2.7 so that the normalization takes place on the left side of the meson peaks instead of the standard range on the right side.

		pp, $\sqrt{s} = 8$ TeV	
reconstruction method	trigger	left side normalization range $[M_{\gamma\gamma}^{\mathrm{low}}, M_{\gamma\gamma}^{\mathrm{high}}]$ (GeV/c^2) π^0	η
EMCal	*all*	[0.05, 0.08]	[0.34, 0.44]
PCM-EMCal	*all*	[0.03, 0.05]	[0.35, 0.46]

Table 6.2.7: The left side normalization ranges used for systematic uncertainty determination for the reconstruction methods PCM-EMCal and EMCal for the π^0 and η meson analysis. The standard ranges used for the analysis are listed in Tab. 6.2.4.

			pp, $\sqrt{s} = 8\,\mathrm{TeV}$	
	reconstruction method	trigger	integration range $[M_{\gamma\gamma}^{\mathrm{low}}, M_{\gamma\gamma}^{\mathrm{high}}]$ (GeV/c^2) π^0	η
narrow	EMCal	INT7	$[M_{\pi^0}$ - 0.030, M_{π^0} + 0.024]	$[M_\eta$ - 0.060, M_η + 0.060]
	PCM-EMCal		$[M_{\pi^0}$ - 0.016, M_{π^0} + 0.016]	$[M_\eta$ - 0.040, M_η + 0.045]
	EMCal	EMC7	$[M_{\pi^0}$ - 0.030, M_{π^0} + 0.036]	$[M_\eta$ - 0.048, M_η + 0.048]
	PCM-EMCal		$[M_{\pi^0}$ - 0.018, M_{π^0} + 0.018]	$[M_\eta$ - 0.048, M_η + 0.054]
	EMCal	EGA	$[M_{\pi^0}$ - 0.048, M_{π^0} + 0.064]	$[M_\eta$ - 0.048, M_η + 0.048]
	PCM-EMCal		$[M_{\pi^0}$ - 0.023, M_{π^0} + 0.023]	$[M_\eta$ - 0.048, M_η + 0.054]
wide	EMCal	INT7	$[M_{\pi^0}$ - 0.070, M_{π^0} + 0.056]	$[M_\eta$ - 0.100, M_η + 0.100]
	PCM-EMCal		$[M_{\pi^0}$ - 0.048, M_{π^0} + 0.028]	$[M_\eta$ - 0.080, M_η + 0.065]
	EMCal	EMC7	$[M_{\pi^0}$ - 0.070, M_{π^0} + 0.084]	$[M_\eta$ - 0.080, M_η + 0.080]
	PCM-EMCal		$[M_{\pi^0}$ - 0.053, M_{π^0} + 0.031]	$[M_\eta$ - 0.096, M_η + 0.078]
	EMCal	EGA	$[M_{\pi^0}$ - 0.072, M_{π^0} + 0.096]	$[M_\eta$ - 0.080, M_η + 0.080]
	PCM-EMCal		$[M_{\pi^0}$ - 0.062, M_{π^0} + 0.036]	$[M_\eta$ - 0.096, M_η + 0.078]

Table 6.2.8: The integration ranges used for systematic uncertainty estimation for π^0 and η mesons for the reconstruction methods PCM-EMCal and EMCal. The standard ranges used for the analysis are listed in Tab. 6.2.5.

Furthermore, the integration windows to obtain the raw yields are varied as summarized in Tab. 6.2.8. The ranges are modified to be narrower and wider than the standard ranges, which are given in Tab. 6.2.5. Moreover, higher order polynomials are used to describe the remaining correlated background after mixed-event subtraction and their influence on the signal extraction is studied compared to the standard choice of a linear background. The use of other functions to fit the signal is also considered in this context. For the EMCal, variations of the minimum opening angle cut enter as well down to 16 mrad and up to 18 mrad as well as applying the standard 17 mrad without the one cell distance cut, see Tab. 6.1.1. For the PCM-EMCal, cuts on the energy asymmetry α are performed. Furthermore, the signal extraction contains the uncertainty from the correction for secondary π^0 mesons which is estimated with help of the decay photon simulation, described in Sec. 7.1, and its uncertainties, see Sec. 7.2.2. The secondary correction uncertainty also enters the η/π^0 ratio with same size but obviously it is not applicable to the η meson. For the η/π^0 ratio, the signal extraction uncertainties of both π^0 and η mesons enter independently, representing the dominant contribution to the systematics for most p_T bins in that case.

Inner Material

This category denotes the systematic uncertainty arising from the limited knowledge about the present inner detector material of ALICE which is defined to include all material up to the midpoint of the TPC in radial direction. Any mismatch of the digital implementation of the existing ALICE detector leads to a discrepancy of the material budget between data and MC simulations which particularly is of importance for the PCM photon reconstruction as the photon conversion efficiency depends on the amount of the inner detector material, represented by the radiation length X_0. Therefore, this uncertainty also affects the R-distribution of photon conversion candidates which is a direct measure of the distribution of present detector material.

π^0 measurement	$1.4 - 1.6\,\mathrm{GeV}/c$		$5.0 - 5.5\,\mathrm{GeV}/c$		$15.0 - 16.0\,\mathrm{GeV}/c$	
category	PCM-EMCal	EMCal	PCM-EMCal	EMCal	PCM-EMCal	EMCal
signal extraction	1.9	2.3	2.4	1.5	3.3	4.6
inner material	4.5	–	4.5	–	4.5	–
outer material	2.1	4.2	2.1	4.2	2.1	4.2
PCM track reconstruction	0.5	–	0.9	–	2.1	–
PCM electron PID	0.6	–	1.3	–	3.1	–
PCM photon PID	0.5	–	1.1	–	3.5	–
cluster description	2.5	4.4	2.5	3.7	4.3	4.0
cluster energy calibration	1.8	2.5	1.9	1.8	2.8	2.0
track-to-cluster matching	0.2	3.1	0.5	2.0	3.3	3.7
efficiency	2.0	2.5	2.8	2.7	2.7	3.7
trigger normalization & pileup	0.1	0.1	0.7	0.3	2.3	2.4
total systematic uncertainty	6.5	8.0	7.3	6.9	10.6	9.6
statistical uncertainty	1.5	3.4	3.3	2.2	7.9	4.4

Table 6.2.9: Summary of the relative systematic uncertainties, which are given in percent, of the measurement of π^0 mesons for selected p_{T} bins for the reconstruction methods PCM-EMCal and EMCal in pp, $\sqrt{s} = 8$ TeV. The statistical uncertainties are given in addition to the total systematic uncertainties for each bin. The uncertainty from σ_{V0AND} determination of 2.6 %, see Ref. [228], is independent from the reported measurements and is separately indicated in the following plots in Sec. 6.2.6.

The systematic uncertainty is estimated to be 4.5 % per PCM photon for which further details can be found in Refs. [10, 232]. Furthermore, its estimation also involves the study on the difference between the two V^0 finding algorithms. For the η/π^0 measurement, this uncertainty cancels out completely.

Outer Material

The systematic uncertainty related to the outer material is only relevant for the EMCal photon reconstruction. The outer material includes all detector components from the radial center of the TPC up to the EMCal which amounts to approximately six times more material than the inner detector material, measured in X_0. In contrast to the inner material uncertainty for the PCM method, the influence of a mismatch of the material budget on the reconstruction of EMCal clusters is of completely opposite nature. For the PCM, any mismatch in the material causes a difference in the production rate, whereas the photon absorption rate as well as the production of secondary neutral pions is modified for the EMCal. In most cases, the photon simply converts within the outer detector material, of which at least one daughter electron may still be reconstructed in the EMCal. Hence, the neutral pion may still be reconstructed with a large probability but with a worse resolution, which is discussed in Fig. 6.1.2 as well. For these cases, the probability increases with increasing conversion radius. The majority of detector material is located within 1.5 m in front of the EMCal, namely the TPC outer wall, the TRD and the TOF including the respective support structures. Therefore, the assigned outer material uncertainty represents the mismatch between MC simulation and data which is estimated by comparing the results of the meson spectra using only EMCal supermodules with and without the TRD in front. This is possible since the data taking in 2012 occurred with the EMCal only partially obscured by the TRD. The uncertainty is estimated to be 3 % for the EMCal method and 1.5 % for the PCM-EMCal. As the TRD represents about half of the outer material budget and since TRD and TOF have similar material budgets, the same uncertainty is assigned to the TOF as well which already covered the full polar angle in 2012 so that a similar assessment as for the TRD is not feasible. It is added quadratically to the uncertainty from the TRD material budget so that values of 4.2 % for EMCal and 2.1 % for PCM-EMCal are found. The uncertainty does not apply for the η/π^0 ratio as it completely cancels out in this case.

PCM Track Reconstruction

This category summarizes the systematic uncertainties related to the secondary track finding used for PCM. It is estimated by varying the relevant selection criteria given in Tab. 5.1.1; the number of TPC clusters over all reconstructable clusters is varied down to 0.35, the minimum p_{T} cut up to 0.1 GeV/c and a various restrictions of the acceptance concerning φ_{conv} are applied. These uncertainties depend on the precision of the relative alignment of detectors and the track matching efficiency between TPC and TRD in different sectors in of the TPC in φ so that they may vary among different data taking periods or triggers used. For the PCM-EMCal method, such conversion photon candidates are mainly sampled which are reconstructed in front of the EMCal. The uncertainty is estimated to be of the order of 2 – 3 % for the different cases, being relevant for π^0, η and η/π^0 measurements.

PCM Electron PID

The systematic uncertainties related to the electron identification for the PCM method are summarized in this category which include the related cut variations from Tab. 5.1.1. In detail, this refers to the TPC dE/dx cuts on $n\sigma_e$ for electron identification and $n\sigma_\pi$ for charged pion suppression. Each cut is varied, so that the selection is tightened and loosened for which the respective results are compared. The corresponding uncertainty is found to be small at about 1 %, at low p_{T} with increasing magnitude for higher p_{T}, where the separation between electrons and pions becomes more and more difficult since both dE/dx bands are getting closer to each other, see Fig. 3.2.5b. It also applies for the η meson as well as for the η/π^0 ratio.

PCM Photon PID

This category summarizes the systematic uncertainties related to the selection of PCM photon candidates. It is obtained by varying the applied selection criteria to the 2D Armenteros-Podolanski plot; $q_{\mathrm{T,\,max}}$ down to 0.3 GeV/c and up to 0.7 GeV/c as well as variations of the ellipsoidal shape towards a quadratic cut as shown in Fig. 5.1.3b. Furthermore, the 2D photon quality selection criteria are varied which include the $\chi^2_{\mathrm{red,\,max}}$ down to 20 and the $\psi_{\mathrm{pair,\,max}}$ down to 0.05 and up to 0.2. The respective standard values are summarized in Tab. 5.1.1 which have the purpose to remove remaining contamination and random e^-e^+ combinations. The uncertainty is found to be approximately as large as the electron PID uncertainty with identical

η measurement	$2.0 - 2.4\,\mathrm{GeV}/c$		$5.0 - 6.0\,\mathrm{GeV}/c$		$18.0 - 20.0\,\mathrm{GeV}/c$	
category	PCM-EMCal	EMCal	PCM-EMCal	EMCal	PCM-EMCal	EMCal
signal extraction	9.0	9.3	7.2	6.0	10.6	8.1
inner material	4.5	–	4.5	–	4.5	–
outer material	2.1	4.2	2.1	4.2	2.1	4.2
PCM track reconstruction	1.8	–	2.4	–	3.3	–
PCM electron PID	1.8	–	2.9	–	6.5	–
PCM photon PID	2.9	–	3.0	–	7.9	–
cluster description	3.1	4.6	4.0	4.9	6.0	4.9
cluster energy calibration	3.2	3.5	3.9	3.4	4.5	3.5
track-to-cluster matching	1.5	4.0	1.7	3.2	4.2	3.3
efficiency	5.0	4.3	9.7	5.5	10.0	6.3
trigger normalization & pileup	0.1	0.1	1.4	1.5	3.0	2.8
total systematic uncertainty	13.0	13.1	15.2	11.5	20.9	13.3
statistical uncertainty	12.1	16.8	6.8	5.4	21.3	8.2

Table 6.2.10: Summary of the relative systematic uncertainties, which are given in percent, of the measurement of η mesons for selected p_{T} bins for the reconstruction methods PCM-EMCal and EMCal in pp, $\sqrt{s} = 8\,\mathrm{TeV}$. The statistical uncertainties are given in addition to the total systematic uncertainties for each bin, see also the explanations in caption of Tab. 6.2.9.

p_{T} dependence since the contamination increases with increasing p_{T}. For the η/π^0 ratio, it is one of the dominant uncertainties as only a small fraction of uncertainties cancel due to the different decay kinematics of the two mesons.

Cluster Description

The cluster description uncertainty quantifies the mismatch in the description of the clusterization process between data and MC simulations for the EMCal, giving rise to modified reconstruction efficiencies. The relevant selection criteria can be found in Tab. 5.2.2 which are listed in the following: The minimum energy cut on EMCal cluster level is varied down to 600 MeV and up to 900 MeV. Furthermore, the cluster shape cut is varied up to releasing the upper limit completely. The number of cells contained in the reconstructed cluster is varied down to one and up to three. Moreover, the cut on the cluster time is tightened and loosened and the results using the respective variations are compared. The energy thresholds E_{seed} and E_{min}, applied for the clusterization process, are varied between $400-600\,\mathrm{MeV}$ and $75-150\,\mathrm{MeV}$. Moreover, the time selection criterion on cell level $|t_{\mathrm{cell}}|$ is also varied down to $\pm 100\,\mathrm{ns}$. The effect of requiring certain minimum distances to bad channels of the EMCal was studied as well but no systematic effect could be deduced. All the different uncertainties from the various sources introduced in this paragraph are quadratically combined so that the values quoted in Tab. 6.2.9, Tab. 6.2.10 and Tab. 6.2.11 are obtained. The uncertainty applies for π^0, η and η/π^0 measurements and ranges between approximately 2 % up to 9 % for the example bins shown in the mentioned tables.

Cluster Energy Calibration

This category summarizes the uncertainty due to the finite accuracy of the EMCal cluster energy calibration. It is estimated by the remaining difference between data and MC simulations after the calibration procedure is performed which is described in Sec. 5.2.1. The difference is determined in percent and then multiplied by six, reflecting the power law behavior of the neutral meson spectra of approximately p_{T}^{-6}. In addition, the different calibration schemes, as introduced in Sec. 5.2.1, are used for the analysis and the respective results are compared. The uncertainty on the cluster energy calibration is of the order of a couple of percent and rises for decreasing p_{T} below momenta of approximately $2\,\mathrm{GeV}/c$. For the η meson (η/π^0) measurement, the uncertainties are found to be about 1.5 (2) times larger than for the π^0 meson.

Track-to-Cluster Matching

The uncertainty caused by imperfections of the track-to-cluster matching procedure when comparing data and MC simulations is reflected in this category. It is assessed by varying the three parameters of the track matching residuals $|\Delta\eta|$ and $|\Delta\varphi|$, which are listed in Tab. 5.2.2, and comparing the results. In this context, the matching conditions are modified to range from a tight selection, only removing centrally matched clusters, to rather loose conditions allowing a distance of a couple of cells depending on η and φ. The uncertainty applies for both the EMCal and PCM-EMCal method with different magnitude. For higher p_{T}, the track densities rise as the environment of the clusters is more and more populated by tracks belonging to jets, leading to increased uncertainties. The uncertainty applies for the π^0 and η measurements and only cancels partially for the η/π^0 ratio.

Efficiency

The systematic uncertainty denoted efficiency is estimated using different MC generators to vary the input spectra used for the determination of reconstruction efficiency. Moreover, the determined reconstruction efficiencies are compared with the obtained validated efficiencies using true MC information. Any mismatch between these efficiencies is also reflected in this category. For the analysis using EMCal triggers, the efficiency category further contains the uncertainty of the description of the actual trigger turn-on from real data by the trigger mimicking procedure in MC simulations as well as the modeling of the efficiency bias as introduced in Fig. 6.2.18. The respective sources of systematics are estimated by comparing the turn-on curves in data and MC simulations and assessing the performance and reliability of the trigger mimicking procedure describing the trigger biases. The uncertainties are present for π^0 and η mesons, respectively, and are being quadratically combined for the η/π^0 measurement for which trigger-related uncertainties largely cancel.

Trigger Normalization & Pileup

The uncertainty arising from the trigger normalization is estimated by varying the p_{T} ranges of the fits of the plateau regions, see Fig. 4.2.6a, for the determination of the trigger rejection factors (RFs). For this purpose, the starting points of the fits are varied by going three bins lower

η/π^0 measurement	$2.0 - 2.4\,\mathrm{GeV}/c$		$5.0 - 6.0\,\mathrm{GeV}/c$		$18.0 - 20.0\,\mathrm{GeV}/c$	
category	PCM-EMCal	EMCal	PCM-EMCal	EMCal	PCM-EMCal	EMCal
signal extraction	9.0	9.3	7.5	6.6	11.2	12.8
PCM track reconstruction	1.9	–	2.4	–	3.8	–
PCM electron PID	1.9	–	3.5	–	7.4	–
PCM photon PID	3.2	–	3.6	–	9.0	–
cluster description	3.5	4.9	4.1	5.1	8.9	5.5
cluster energy calibration	3.4	4.2	4.6	4.2	5.5	4.5
track-to-cluster matching	1.5	3.9	1.8	3.2	6.1	3.3
efficiency	5.4	4.5	9.8	5.8	10.5	7.5
total systematic uncertainty	12.4	12.8	15.0	11.6	23.1	16.8
statistical uncertainty	12.2	5.4	7.4	2.7	23.3	19.0

Table 6.2.11: Summary of the relative systematic uncertainties, which are given in percent, of the measurement of the η/π^0 ratio for selected p_T bins for the reconstruction methods PCM-EMCal and EMCal in pp, $\sqrt{s} = 8$ TeV. The statistical uncertainties are given in addition to the total systematic uncertainties for each bin, see also the explanations given in the caption of Tab. 6.2.9.

and six bins higher in p_T. The ten values obtained for the RF are then averaged reflecting the respective fit uncertainties. The largest uncertainty is then deduced from the biggest difference of the central value to the lowest and highest RF in accordance with the determined values. As the RF are always determined with respect to the next lower threshold trigger, the systematic uncertainty for the higher level threshold triggers are obtained by quadratically combining the respective uncertainties for the individual steps. Additionally, the RFs are independently determined for each EMCal supermodule and compared to each other. All factors are found to be consistent and in agreement within statistical uncertainties. Furthermore, the uncertainty of the pileup removal enters in this category. It relates to the systematic uncertainty due to the pileup rejection cuts by the SPD which have a finite efficiency to remove pileup events. It is estimated based on the knowledge of the inefficiency, see Fig. B.0.1a, running the analysis with/without any SPD cuts and comparing the obtained results.

The following Fig. 6.2.19 summarizes the statistical and systematic uncertainties for the different reconstruction methods contained in Tab. 6.2.3 for the π^0, η and η/π^0 measurements in pp collisions at $\sqrt{s} = 8$ TeV. The figures visualize the relative uncertainties in percent as a function of meson p_T. The observed steps of the statistical uncertainties illustrate changes in the bin widths. Furthermore, the strengths of each method can be read off at which p_T intervals the respective method provides the most accurate measurement of the corresponding quantities.

6.2.5 Combination of Individual Measurements

The individual measurements of π^0 and η meson production cross sections at mid-rapidity as well as the corresponding η/π^0 ratio in pp collisions at $\sqrt{s} = 8$ TeV are shown in Fig. 6.2.20 for which the available reconstruction methods, as introduced in Tab. 6.2.3, are used as input. The

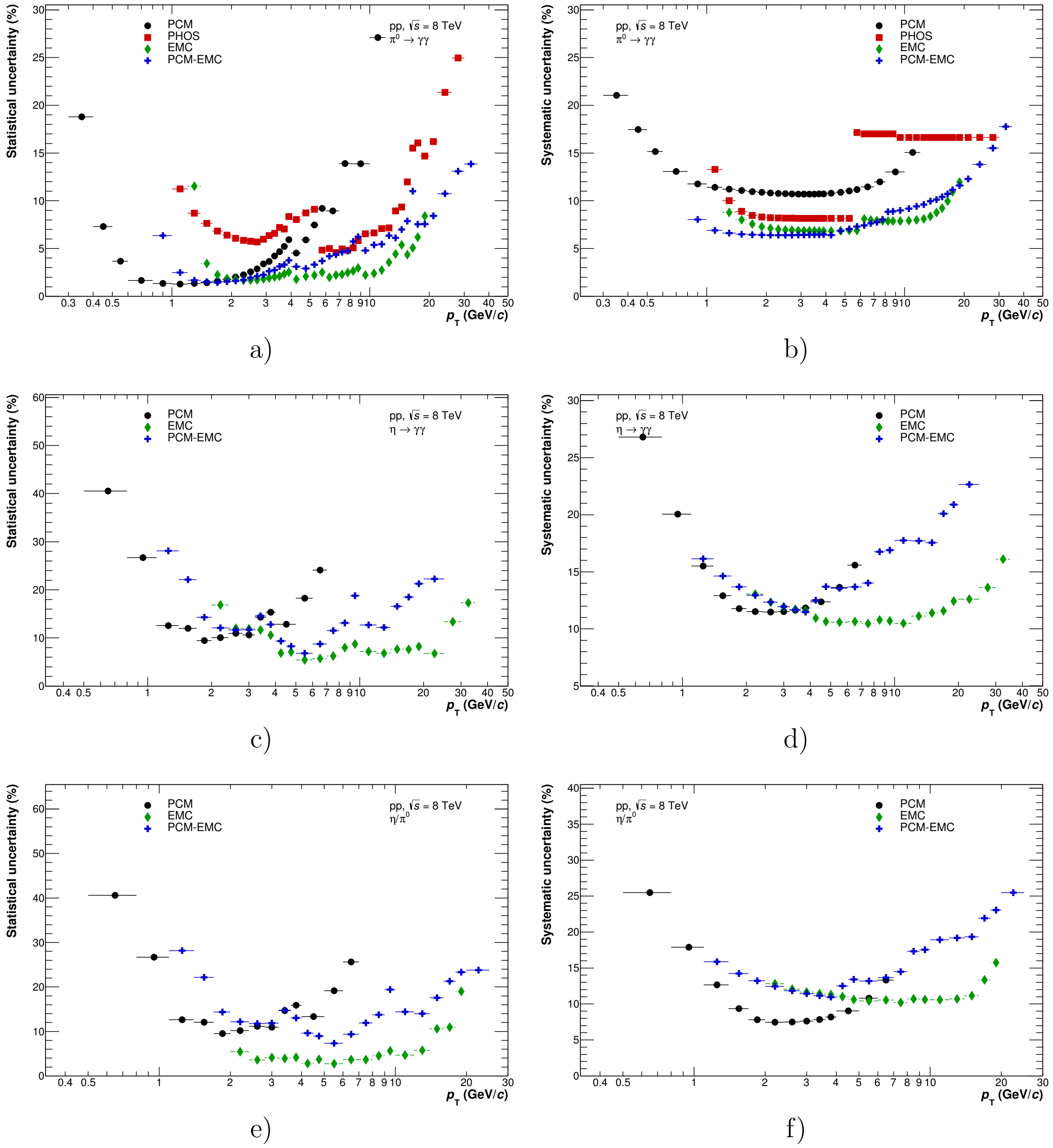

Figure 6.2.19: Relative statistical (left) and systematic (right) uncertainties in percent for all available reconstruction methods for π^0, η and η/π^0 measurements in pp collisions at $\sqrt{s} = 8\,\mathrm{TeV}$.

plots indicate a good agreement of all available measurements within their associated statistical and systematic uncertainties. All the respective results provided by the different reconstruction methods are independently obtained from each other. Moreover, Fig. 6.2.20 also visualizes the p_T ranges for which the respective measurements are available, representing the input for the combination procedure described in this section.

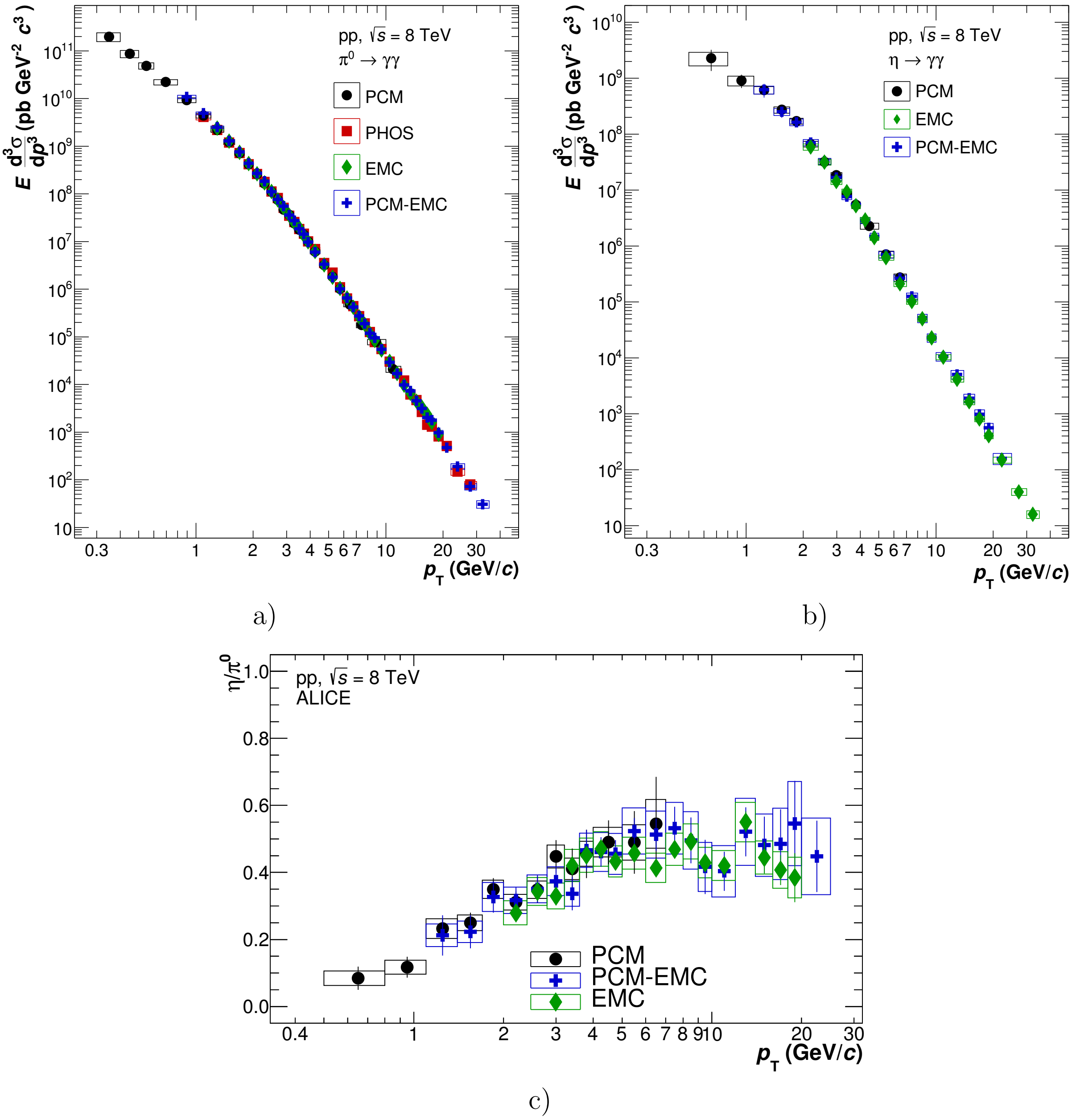

Figure 6.2.20: The neutral meson production cross sections for π^0, a), and η, b), mesons measured with the respective reconstruction methods which are input for the combination procedure. Furthermore, the η/π^0 ratio, c), is measured using the methods PCM, PCM-EMCal and EMCal. The vertical error bars represent statistical uncertainties, whereas the boxes quantify the p_{T} bin widths in horizontal direction as well as the systematic uncertainties in vertical direction.

In analogy to Sec. 6.2.2, the final results for the different measurements are obtained by combining the individual results provided by the different reconstruction methods by exploiting the BLUE method [246–250]. The correlations of the systematic uncertainties of the different methods have to be taken into account for this purpose. Possible statistical correlations between the available measurements, for instance due to photon conversions at small distances relative to the beam axis, are negligible due to the small conversion probability and the small likelihood of reconstructing the respective conversion daughters in the calorimeters leading to a meson candidate which finally ends up in the respective integration window. Concerning systematics, there are no common uncertainties present among PCM, EMCal and PHOS. Therefore, all systematic uncertainties are assumed to be completely uncorrelated for these cases. On the other hand, the correlations introduced by including the hybrid PCM-EMCal method have to be taken into account, for which a different number of photon candidates enters by construction when comparing with the respective standalone methods. Thus, all systematic uncertainties relevant for the PCM method are found to be partially correlated with their counterpart from the PCM-EMCal method. Half of the size of the material budget uncertainty, for example, is assumed to be uncorrelated since only one PCM photon enters for the hybrid method. Furthermore, the uncorrelated systematic uncertainties from PCM-EMCal with respect to PCM are, with full size, all the calorimeter-related uncertainties as well as trigger and efficiency uncertainties. Hence, the following correlation factors ρ_{ij} are found for the different cases which are shown in Fig. 6.2.21.

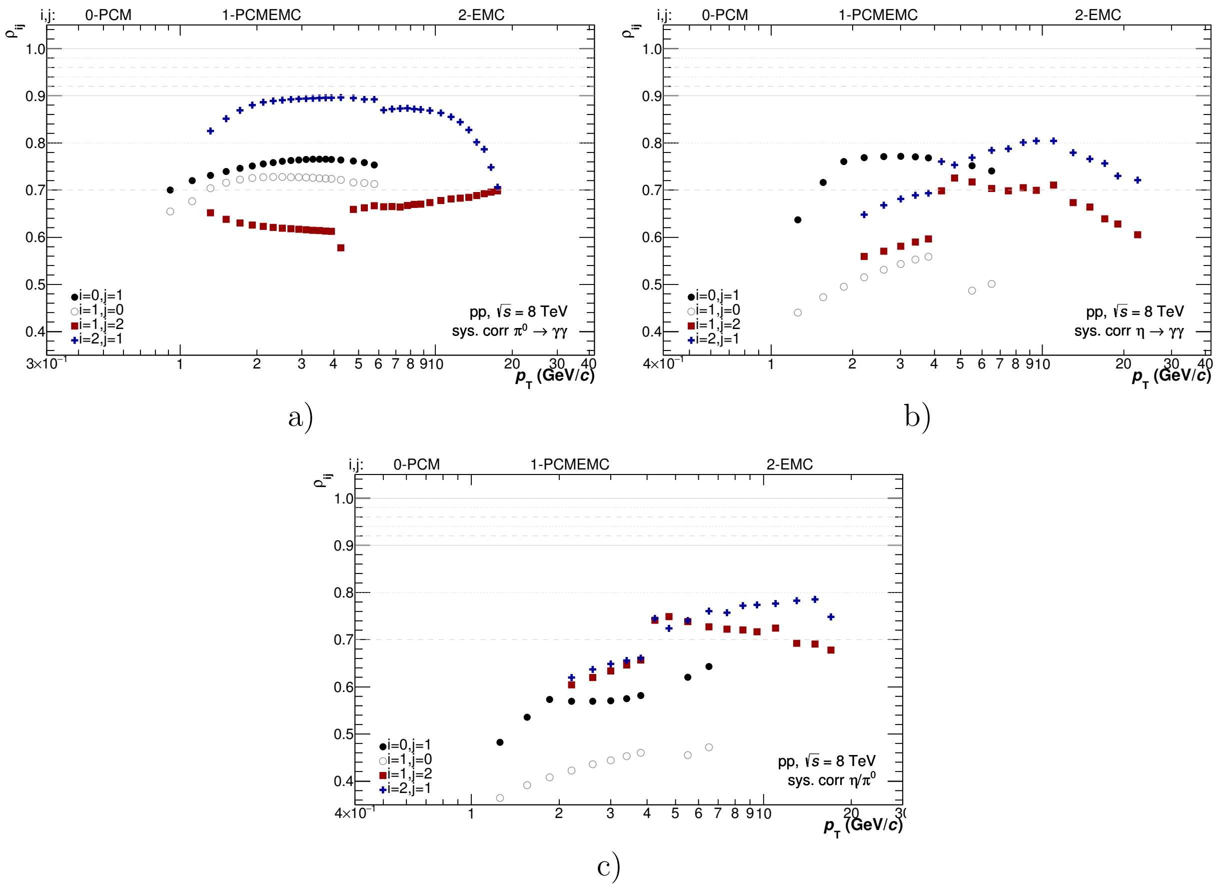

Figure 6.2.21: The p_{T}-dependent correlation factors $\rho_{ij}(p_{\mathrm{T}})$ visualizing the fraction of correlated systematic uncertainty of reconstruction method i with respect to method j. The factors are shown for the π^0 and the η, in a) and b), and the η/π^0 ratio, c), for different combinations of the methods PCM (0), PCM-EMCal (1) and EMCal (2), for which correlations of systematic uncertainties are present.

In Fig. 6.2.21, the horizontal gray lines provide orientation for the p_T dependence of the factors which is found to be rather small. The combinations, which are not contained in the legend, do not exhibit any correlations in between so that the factors are found to be zero. Therefore, the corresponding factors are not visualized.

After determining the correlation of the systematic uncertainties, the combination of the individual measurements is performed following the BLUE method [246–250] as introduced in Sec. 6.2.2. The obtained weights ω_a for the individual measurements provided by the different reconstruction methods are shown in Fig. 6.2.22.

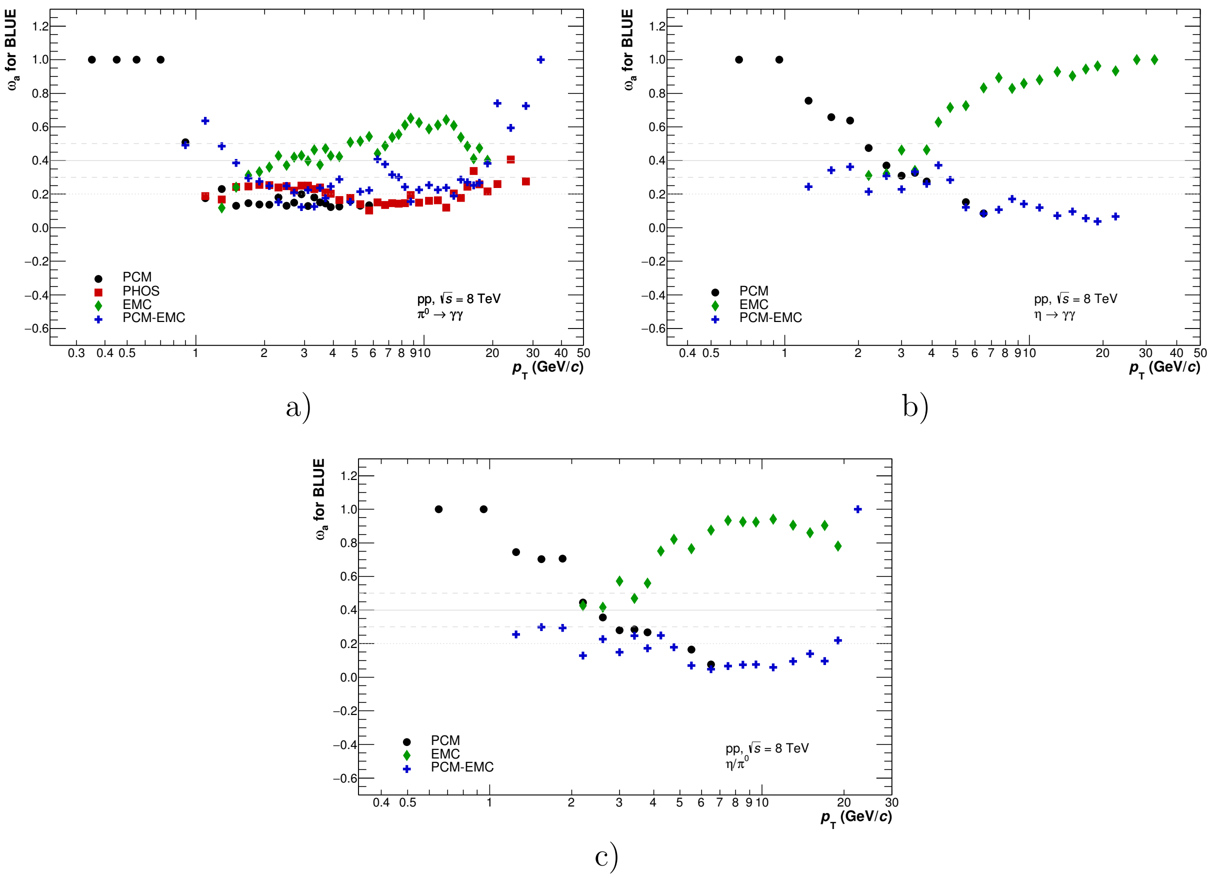

Figure 6.2.22: The obtained weights $\omega_a(p_\text{T})$ using the BLUE method for the combination of π^0, η and η/π^0 measurements using all inputs summarized in Tab. 6.2.3 for pp collisions at $\sqrt{s} = 8\,\text{TeV}$.

The figure further indicates the relevant p_T ranges for which the respective measurements provided by each individual method are considered for the final result. All reconstruction methods enter the final results with considerable weights. As a result, the combined uncertainties are found to be reduced by profiting from the pool of (partly) independent measurements. However, the EMCal measurements clearly dominate at high p_T, whereas the PCM method provides the most accurate measurements for low p_T.

The relative total, statistical and systematic uncertainties obtained after performing the combination of all individual measurements are shown in Fig. 6.2.23. The uncertainties are given in percent. For the majority of p_{T} bins, the systematic uncertainties are dominating, whereas for the lowest and highest p_{T} bins the statistical uncertainties are taking over.

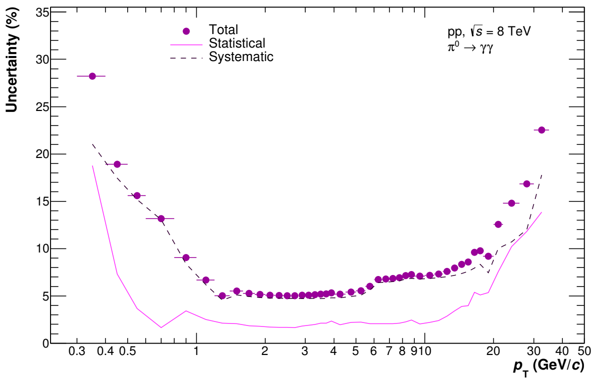

a)

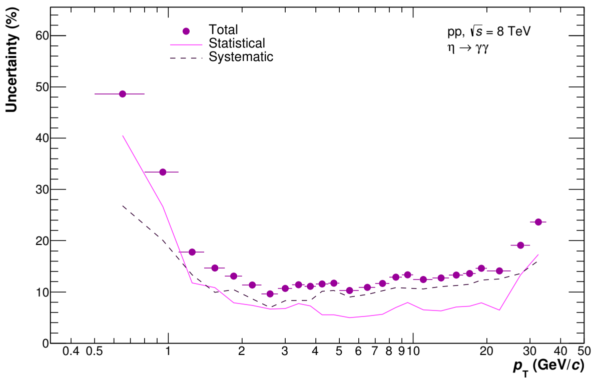

b)

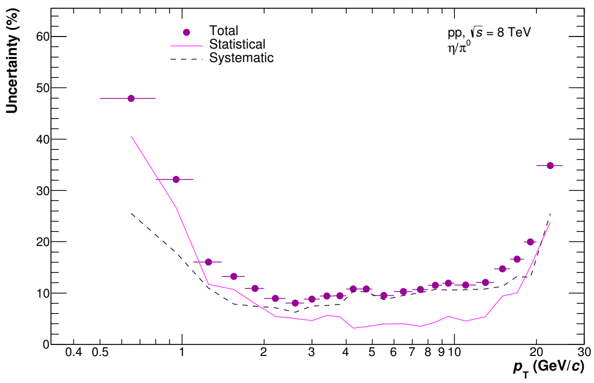

c)

Figure 6.2.23: Relative total, statistical and systematic uncertainties for the π^0, η and η/π^0 measurements in pp collisions at $\sqrt{s} = 8\,\mathrm{TeV}$ as a function of p_{T}. The plots visualize the final uncertainties obtained from the combination of all available measurements provided by the respective reconstruction methods.

Correction for Finite Bin Width

The measured production cross sections of π^0 and η mesons as well as the measurement of the η/π^0 ratio are performed for finite p_{T} bin widths which vary as a function of p_{T}. However, the underlying spectra are considerably changing within a given p_{T} bin, e.g. they are steeply falling for increasing p_{T}. Thus, the cross section or ratio determined for a p_{T} bin does not represent the value measured at the center of a p_{T} bin. Hence, a correction needs to be applied due to the finite p_{T} bin widths of the respective measurements [255] for which two different approaches are available. The data points can either be shifted horizontally in p_{T}, such that the modified p_{T} values truly represent the corresponding value measured in the given p_{T} bin. On the other hand, the data points can be shifted vertically so that they represent the correct measurement for the center of the respective p_{T} bin. Both approaches depend on the same underlying model assumptions. The neutral meson spectra are shifted by means of the assumption of a Tsallis [70] fit function, see Eq. 2.3.13, as an approximation of the respective underlying spectrum. The bin width correction is determined based on the combined neutral meson spectra and then applied to the individual spectra for the different methods. In the following Sec. 6.2.6 and Sec. 6.4, the described bin width correction is already applied for all shown results.

For the neutral meson spectra, the bin shift correction is performed along the horizontal axis by correcting the respective p_{T} values. Fig. 6.2.24 shows the bin width corrections for the final combined π^0 and η meson measurements. Throughout the p_{T} region covered, the bin width corrections are of the order of 1 % and below.

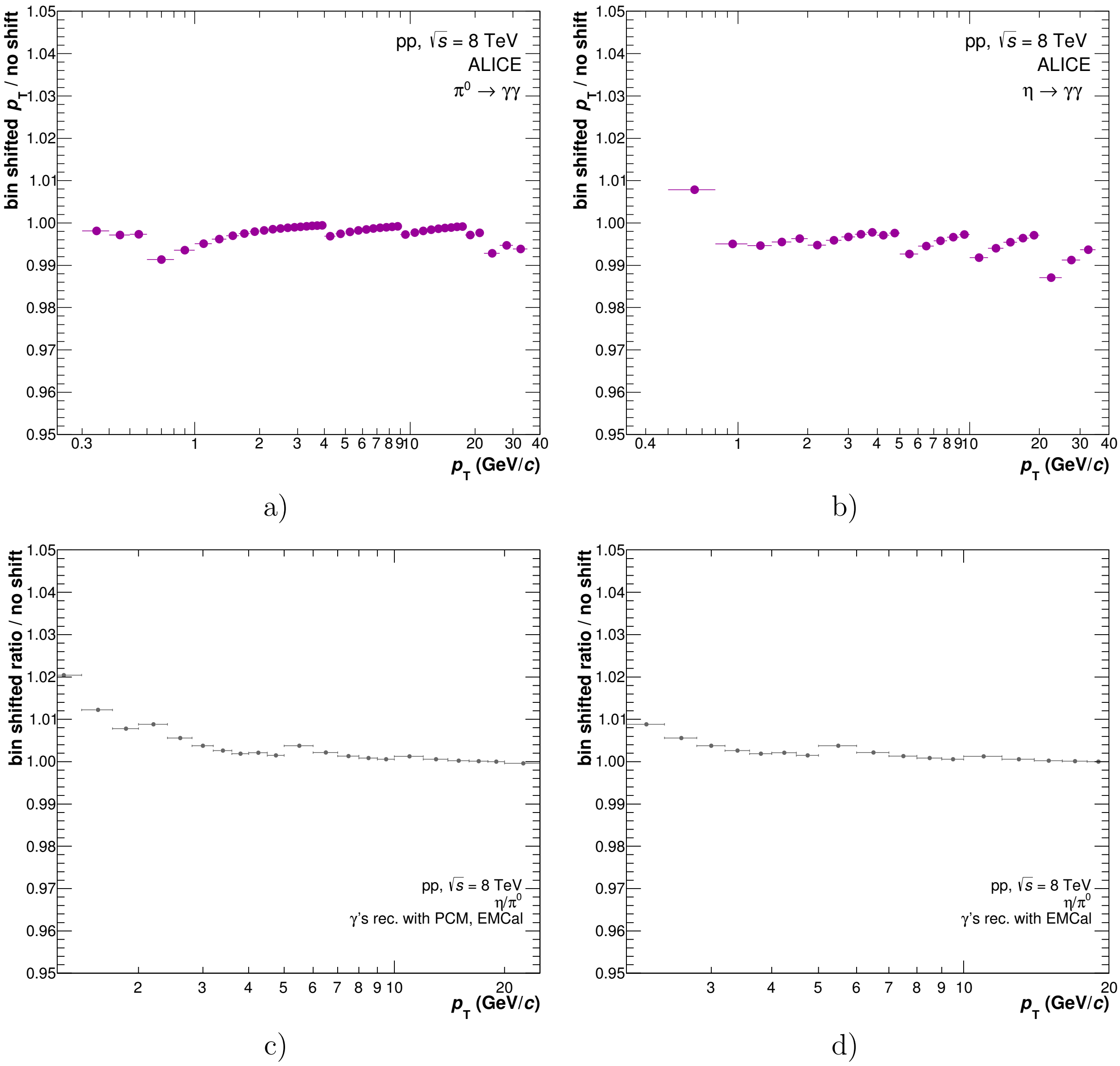

Figure 6.2.24: The size of the bin width corrections for the combined π^0, a), and η, b), meson spectra are shown. Furthermore, the obtained bin width corrections for the η/π^0 are shown for the PCM-EMCal and EMCal method in c) and d). For the η/π^0 case, the bin width corrections are applied for each individual input measurement, which is subsequently followed by the combination of the respective η/π^0 ratios.

For the calculation of η/π^0 ratio, in contrast, a bin shift correction along the vertical direction is applied as otherwise the ratio could not be computed and the different measurements could not be combined. This approach is chosen due to the fact that the π^0 and η meson spectra exhibit different shapes especially for low p_T. Fig. 6.2.24c and Fig. 6.2.24d visualize the bin width corrections for the final combined η/π^0 ratios for EMCal as well as PCM-EMCal method. The corrections are of the order of 1 % for most of the p_T region covered but go up to about 2 % for low p_T for the latter case. They become significant for even smaller p_T and rise up to 8 % for lowest p_T bin supplied by PCM for the η/π^0 measurement.

6.2.6 Results

The invariant differential cross sections of inclusive π^0 and η meson production at mid-rapidity cover transverse momentum ranges of $0.3 < p_\mathrm{T} < 35.0\,\mathrm{GeV}/c$ and $0.5 < p_\mathrm{T} < 35.0\,\mathrm{GeV}/c$. Both measurements are shown in Fig. 6.2.25 together with various theory predictions.

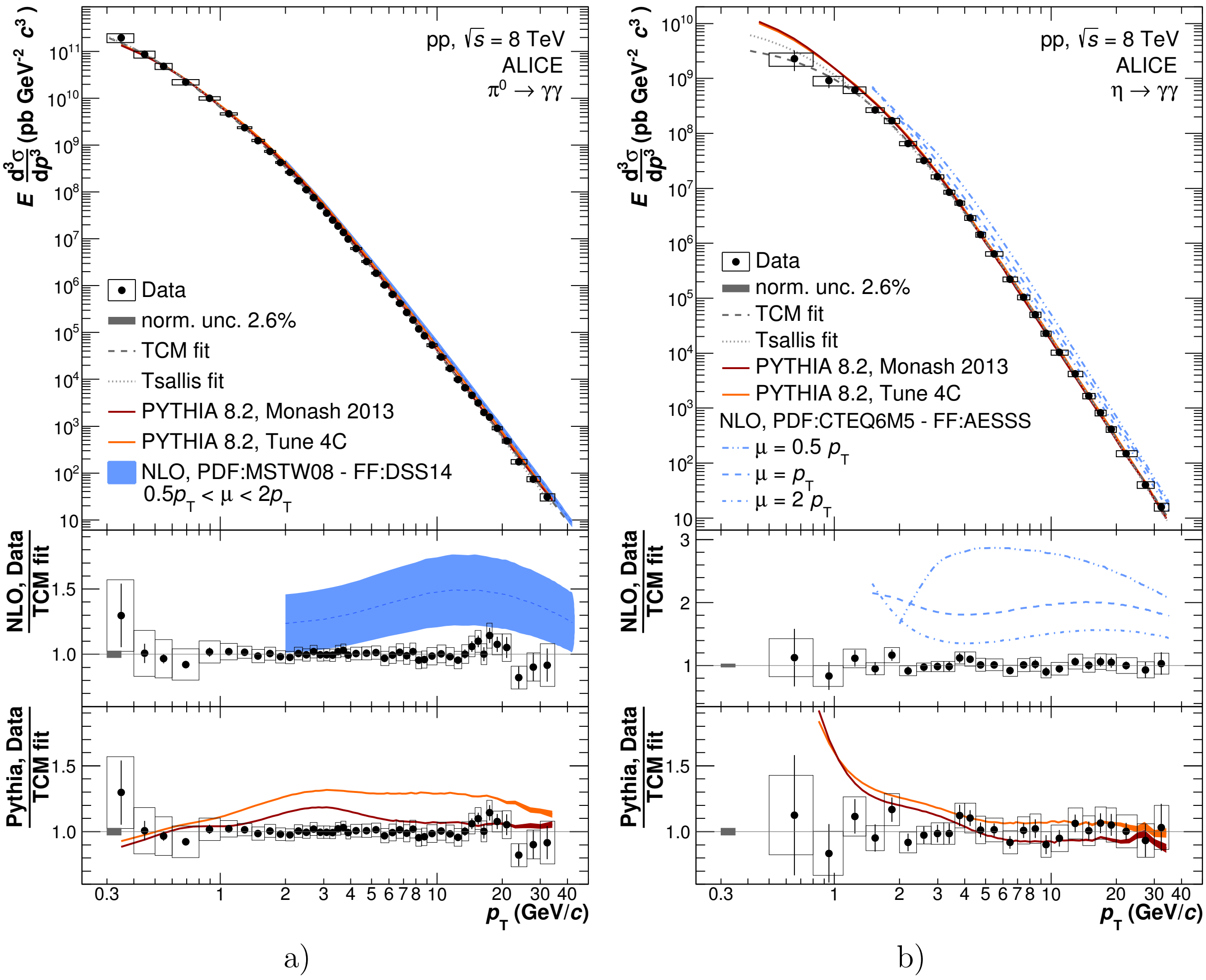

Figure 6.2.25: Combined invariant cross sections for neutral meson production in pp collisions at $\sqrt{s} = 8\,\mathrm{TeV}$ compared to PYTHIA 8.210 as well as NLO pQCD predictions using PDFs MSTW08 (CTEQ6M5) with FFs DSS14 (AESSS) for the π^0 (η).

The combined cross sections, shown in Fig. 6.2.25, are the result of the combination procedure described in Sec. 6.2.5. The total uncertainties of the measurements, calculated by quadratically adding the combined statistical and systematic uncertainties, are of the order of 5 % for the π^0 and 10 % for the η meson for most of the p_{T} bins covered as shown in Fig. 6.2.23. They increase for low and high momenta due to statistical limitations as well as systematic effects. Both combined neutral meson spectra are by default fitted with a TCM [69] fit function, see Eq. 2.3.12 in Sec. 2.3, using the total uncertainties for each p_{T} bin.

To compare the different reconstruction methods which entered the combination procedure described in Sec. 6.2.5, the ratios of spectra measured by each reconstruction method to the TCM fit of the combined spectrum are shown in Fig. 6.2.26. The vertical error bars represent the statistical uncertainties, whereas the boxes quantify the bin widths in horizontal direction and the systematic uncertainties in vertical direction. All measurements agree within uncertainties over the full p_{T} range.

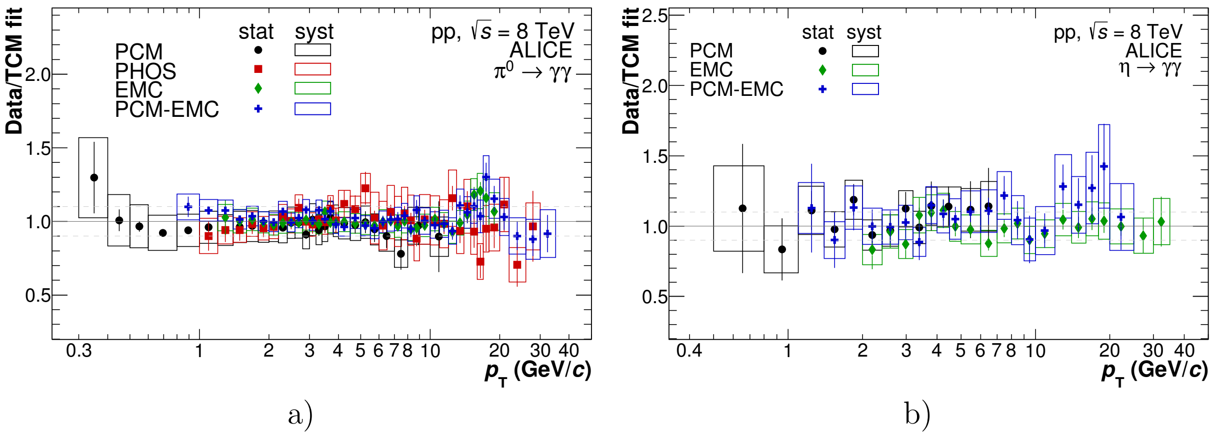

Figure 6.2.26: Ratios of the measured π^0, a), and η, b), spectra from each reconstruction method to the TCM fit of the combined spectrum.

Furthermore, they are also fitted with a Tsallis function [70], see Eq. 2.3.13 in Sec. 2.3, which was used as default in previous measurements of π^0 and η meson production in pp collisions reported by ALICE [10, 71]. The extracted fit parameters are summarized in Sec. 6.4 and can be found in Tab. 6.4.18 and Tab. 6.4.19. In this context, the TCM is chosen as default since it better describes the spectra at low and high p_{T} than the Tsallis counterpart, which is demonstrated in Fig. 6.2.27 for the π^0 and η respectively. This figure also includes a comparison with a modified Hagedorn fit, see Eq. 2.3.14, and a pure power law, see Eq. 2.3.15. All fit functions provide a reasonable description of the spectra which for the power law is a valid statement only beyond 4 GeV/c as expected.

The invariant differential cross sections of neutral meson production at mid-rapidity are compared in Fig. 6.2.25 with NLO pQCD calculations [76, 77] using the PDF MSTW08 [114] together with the FF DSS14 [77] for the π^0 and CTEQ6M5 [256] with AESSS [76] for the η meson respectively. The same factorization scale value, μ with $0.5p_{\mathrm{T}} < \mu < 2p_{\mathrm{T}}$, is chosen for the factorization, renormalization and fragmentation scales used in the NLO pQCD calculations for which the largest uncertainty is represented by the choice of μ. Furthermore, PYTHIA 8.210 calculations are superimposed for which two different tunes are available. In the bottom part of Fig. 6.2.25, the ratios of data and NLO pQCD predictions to the TCM fits of the neutral mesons

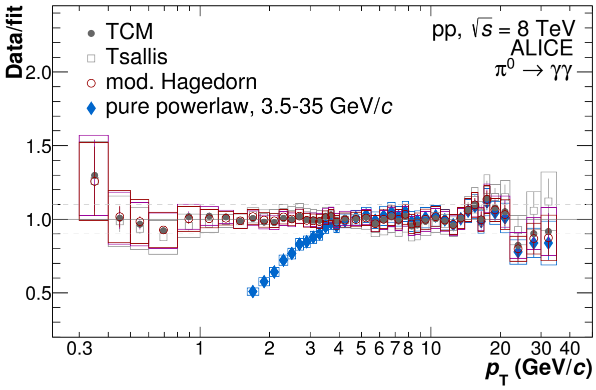

a)

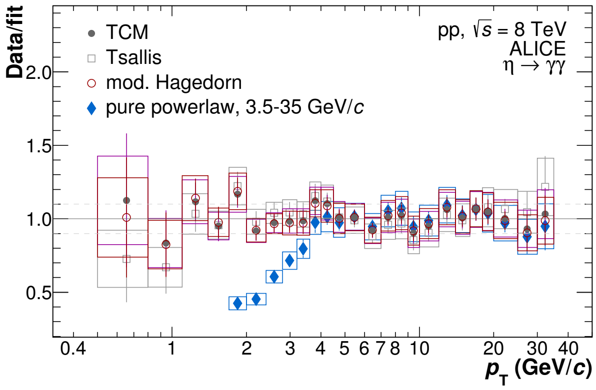

b)

Figure 6.2.27: Ratios of the combined results, shown in Fig. 6.2.25, to TCM, Tsallis, modified Hagedorn and power law fits of the same results obtained for the π^0 and η meson in a) and b).

are shown. For all μ values, the pQCD calculations overestimate the measured data for both π^0 and η mesons. For the π^0, the calculations are above data by $20-50\,\%$ depending on p_{T} for $\mu = p_{\mathrm{T}}$ although the same combination of NLO PDF, pQCD and FF describes the RHIC data at $\sqrt{s} = 510$ GeV rather well [257]. For $\sqrt{s} = 2.76$ TeV, the same pQCD prediction overshoots ALICE data by about 30 % at moderate p_{T} while agreeing at higher p_{T} [8]. For DSS14, the FF uncertainties could be considerably reduced by including the first ALICE publication on π^0 production in pp collisions at $\sqrt{s} = 7$ TeV [10]. In contrast, the FF used for the η meson, AESSS, only includes pre-LHC data so that the larger discrepancy of the pQCD prediction can be explained. Including the precise new data for η meson production measured at $\sqrt{s} = 2.76$ [8], 7 [10] and 8 TeV [4] will also help to considerably reduce the NLO pQCD uncertainty bands in that case.

Furthermore, the neutral meson measurements are compared to PYTHIA 8.210 [81] references as shown in Fig. 6.2.25. Two different tunes of the MC event generator are available in this context: the tune 4C [116] and the Monash 2013 tune [117]. In order to ensure a valid comparison of the PYTHIA tunes with the measurement, π^0 from decays of long-living strange particles, e.g. K^0_S, Λ, Σ and Ξ, are excluded. The tune 4C is about 30 % above the π^0 measurement for $p_{\mathrm{T}} > 1.5\,\mathrm{GeV}/c$. In contrast, the Monash 2013 tune reproduces the π^0 spectrum within 10 % for almost the complete p_{T} range. However, both tunes are not able to describe the shape of the measured spectrum indicated by the bump at approximately $3\,\mathrm{GeV}/c$. In the case of the η meson, both tunes reproduce the measured spectrum for $p_{\mathrm{T}} > 1.5\,\mathrm{GeV}/c$ within experimental uncertainties. For lower momenta below $p_{\mathrm{T}} < 1.5\,\mathrm{GeV}/c$, both tunes deviate significantly in magnitude and shape from data. Apparently, the tuning parameters of the soft QCD part of PYTHIA fail to describe the measured η meson spectrum for this p_{T} region while both tunes are consistent within uncertainties with the π^0 measurement for $0.3 < p_{\mathrm{T}} < 1.5\,\mathrm{GeV}/c$.

The π^0 and η meson spectra shown in Fig. 6.2.25 exhibit a similar power law behavior, see Eq. 2.3.15 for its definition. For high momenta of $p_{\mathrm{T}} > 3.5\,\mathrm{GeV}/c$, the respective values of the power n are found to be rather similar: $n_{\pi^0} = 5.936 \pm 0.012(\mathrm{stat}) \pm 0.023(\mathrm{sys})$ and $n_\eta = 5.930 \pm 0.029(\mathrm{stat}) \pm 0.044(\mathrm{sys})$, which is also reflected in the flatness of the η/π^0 ratio in this p_{T} region as shown in Fig. 6.2.28. In this p_{T} region, the ratio is found to obey a constant of

$C^{\eta/\pi^0} = 0.455 \pm 0.006(\text{stat}) \pm 0.014(\text{sys})$. The quoted uncertainties are obtained by fitting the ratio with a constant, once using only statistical and again by attaching the total uncertainties to the data point in each p_{T} bin. The systematic uncertainties are then computed by quadratically subtracting the statistical from the total uncertainties and extracting the root.

The η/π^0 ratio is reproduced fairly well by the NLO pQCD calculations although they fail to describe the individual neutral meson spectra. It has to be noted that a different FF for the π^0 is used to compile the theory curve, namely DSS07 [75], since there is no recent calculation for the η available which could be compared to the recent DSS14 prediction for the π^0. The two PYTHIA tunes are at tension with the measurement. However, they are still in agreement down to $p_{\mathrm{T}} \approx 1.5\,\text{GeV}/c$ within the experimental uncertainties although it seems that the shape cannot be fully reproduced. Below $p_{\mathrm{T}} < 1.5\,\text{GeV}/c$, the clear deviations of the PYTHIA tunes from data can also be seen in the η/π^0 ratio.

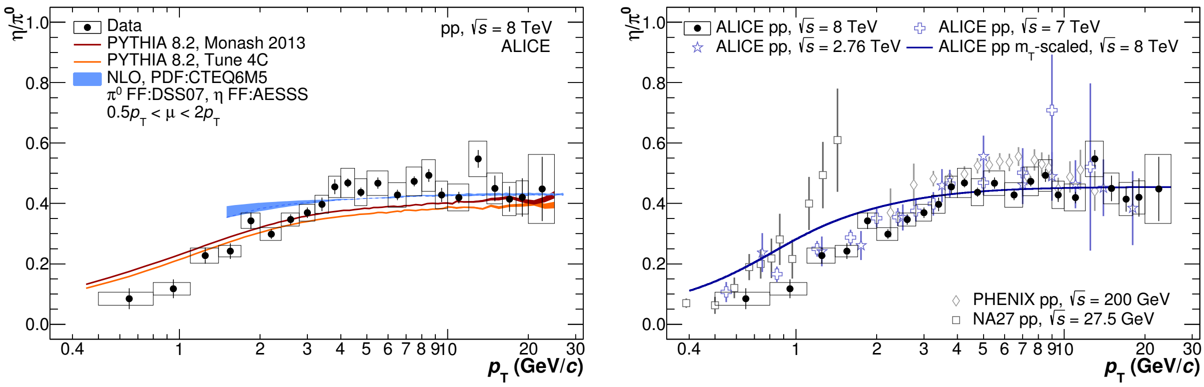

a) b)

Figure 6.2.28: a) The measured η/π^0 ratio is compared to NLO pQCD predictions using PDF CTEQ6M5 and FFs DSS07 for the π^0 and AESSS for the η as well as PYTHIA 8.210 calculations using the tunes 4C and Monash 2013. The total uncertainties of the measured η/π^0 ratio are of the order of 10 % for most of the p_{T} bins covered, increasing for lower and higher momenta due to limited statistics as well as systematic effects. b) Comparison of the η/π^0 ratio to previous ALICE measurements [8, 10] as well as other experiments at lower collision energies for which total uncertainties are drawn. Furthermore, a comparison to the η/π^0 ratio obtained with m_{T} scaling is added, which will be discussed later in Sec. 6.3.

In Fig. 6.2.28b, the η/π^0 measurement is compared to results from experiments before the LHC era. In this context, PHENIX and NA27 provide the η/π^0 ratio with highest accuracy at high and low p_{T} and, hence, are compared to the η/π^0 measurement in pp collisions at $\sqrt{s} = 8\,\text{TeV}$. The PHENIX measurement at $\sqrt{s} = 200$ GeV is only available for $p_{\mathrm{T}} > 2.25\,\text{GeV}/c$ [258] for which it has to be noted that no secondary π^0 correction concerning weak decays is applied in contrast to ALICE. Measurements of π^0 and η production cross sections in pp collisions at $\sqrt{s} = 27.5$ GeV from NA27 [259] are used to obtain the η/π^0 ratio in the p_{T} range of $0.4 < p_{\mathrm{T}} < 1.6\,\text{GeV}/c$, for which the paper does not mention any secondary correction of the π^0 measurement. The first NA27 points at $p_{\mathrm{T}} < 1\,\text{GeV}/c$ are consistent with data from pp collisions at $\sqrt{s} = 2.76$ [8], 7 [10] and 8 TeV [4] within uncertainties. For $p_{\mathrm{T}} > 1\,\text{GeV}/c$, uncertainties become significant and no conclusion can be drawn.

6.3 Measurement of Neutral Mesons in pp Collisions at $\sqrt{s} = 0.9$ & 7 TeV

ALICE did already publish a paper on neutral meson production at $\sqrt{s} = 0.9$ and 7 TeV [10] for which only measurements of PCM and PHOS were available though. In this thesis, the EMCal-related measurements are performed for these datasets for the first time. Additionally, the latest reconstruction pass is used in this context, doubling the available statistics due to issues fixed which occurred during data reconstruction. An overview of the different meson reconstruction methods used in this thesis is given in Tab. 6.3.12 for pp collisions at $\sqrt{s} = 0.9$ and 7 TeV. The respective references are also given and the covered p_{T} intervals of the full combination of all individual methods are listed in addition.

reconstruction method	available p_{T} reach (GeV/c) π^0	η	η/π^0	reference
		pp, $\sqrt{s} = 0.9$ TeV		
PCM	0.4 – 3.5	0.9 – 3.0	0.9 – 3.0	MSc thesis by N. Schmidt [244]
EMCal	1.2 – 10.0	N/A	N/A	this thesis
PCM-EMCal	0.8 – 4.0	N/A	N/A	this thesis
PHOS	0.6 – 7.0	N/A	N/A	published by ALICE [10]
combination	0.3 – 10.0	0.9 – 3.0	0.9 – 3.0	this thesis
		pp, $\sqrt{s} = 7$ TeV		
PCM	0.3 – 16.0	0.4 – 10.0	0.4 – 10.0	MSc thesis by N. Schmidt [244]
EMCal	1.2 – 16.0	2.2 – 14.0	2.2 – 14.0	this thesis
PCM-EMCal	0.8 – 16.0	1.0 – 12.0	1.0 – 12.0	this thesis
PHOS	0.8 – 25.0	1.0 – 15.0	1.0 – 15.0	PhD thesis by P. Parek [260]
combination	0.3 – 25.0	0.4 – 15.0	0.4 – 15.0	this thesis

Table 6.3.12: A summary of the different reconstruction methods available for neutral meson measurements at $\sqrt{s} = 0.9$ and 7 TeV with the corresponding p_{T} reach. All measurements are purely based on MB triggers since no calorimeter triggers were recorded for these datasets. The PCM measurement is performed by Nicolas Schmidt, documented in Ref. [244]. The PHOS measurement at $\sqrt{s} = 0.9$ TeV is taken from the previous ALICE publication [10], whereas the PHOS measurements of both π^0 and η mesons at $\sqrt{s} = 7$ TeV are provided by Pooja Parek [260].

The p_{T} ranges as introduced in Tab. 6.3.12 are split into bins which can be deduced from the figures shown in the remaining part of this chapter or Sec. B.2.2. All analysis are performed independently from each other so that the results obtained with the different reconstruction methods are combined as described in Sec. 6.3.2. The measurements described in this section closely follow the analysis at 8 TeV, introduced and elaborated in the previous Sec. 6.2. All definitions, procedures and corrections also apply here if not explicitly defined differently.

6.3.1 Signal Extraction & MC Corrections of Raw Spectra

The measurement of neutral mesons in pp collisions at $\sqrt{s} = 0.9$ and 7 TeV for both EMCal and PCM-EMCal reconstruction methods involves the analysis of MB triggered events only, see Sec. 4.1, from which the invariant cross sections are determined according to Eq. 6.1.4. Example bins are shown in Fig. 6.3.29 for both reconstruction methods for which clear π^0 and η meson peaks are visible on top of combinatorial background. The respective definitions and explanations given in Sec. 6.1 concerning Fig. 6.1.1 and the previous Sec. 6.2.1 also apply here.

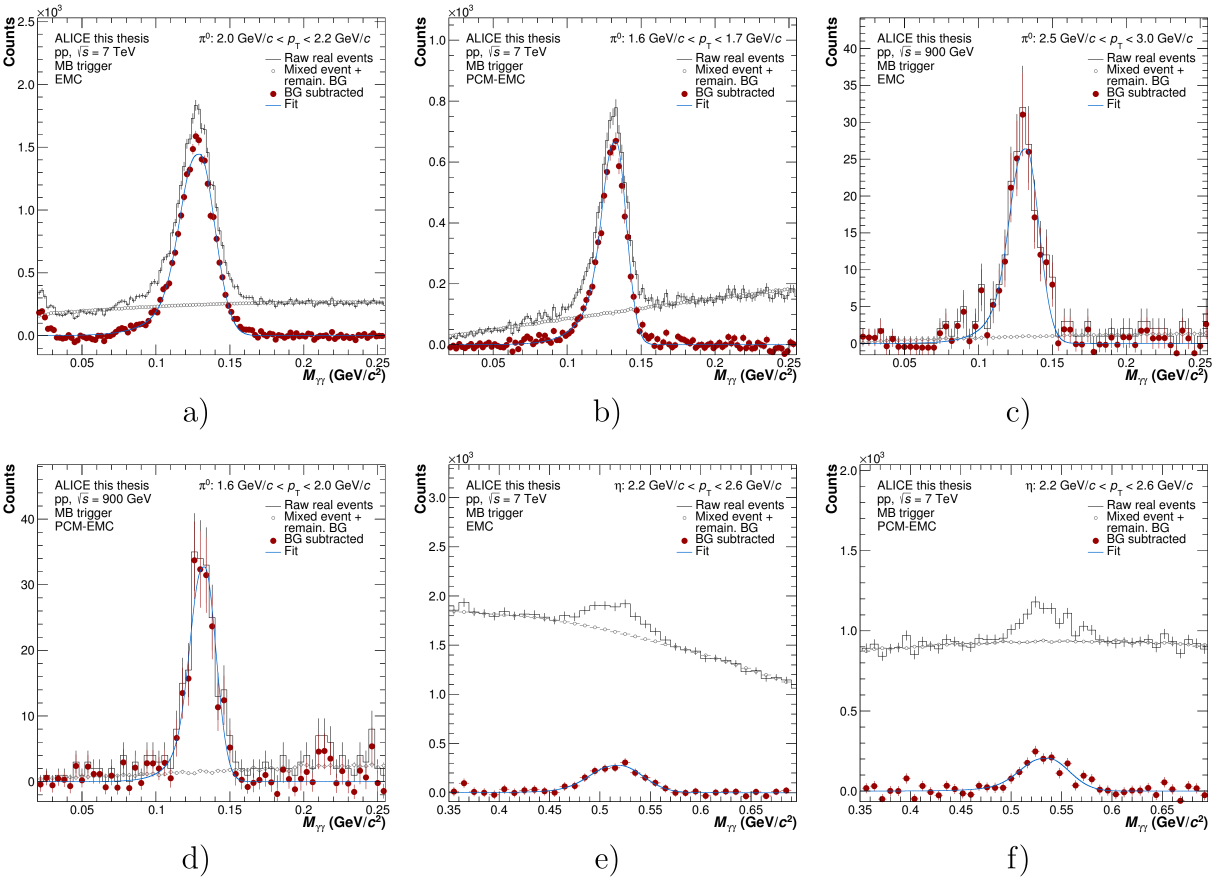

Figure 6.3.29: Example invariant mass distributions for the reconstruction methods EMCal and PCM-EMCal obtained for V0OR (INT1) MB triggered events in pp collisions at $\sqrt{s} = 0.9$ and 7 TeV showing π^0, a) − d), and η meson candidates, e) and f).

An overview of the complete signal extraction for all p_{T} bins used for the analysis is given in Sec. B.2.2 for both EMCal and PCM-EMCal methods for $\sqrt{s} = 0.9$ and 7 TeV. The respective normalization ranges employed to scale the mixed-event background are summarized in Tab. 6.3.13.

		pp, $\sqrt{s} = 0.9$ and 7 TeV	
reconstruction method	trigger	normalization range $[M_{\gamma\gamma}^{\mathrm{low}}, M_{\gamma\gamma}^{\mathrm{high}}]$ (GeV/c^2)	
		π^0	η
EMCal	INT1	[0.19, 0.30]	[0.67, 0.80]
PCM-EMCal		[0.19, 0.30]	[0.65, 0.75]

Table 6.3.13: The normalization ranges for the reconstruction methods PCM-EMCal and EMCal for the π^0 and η meson analysis at $\sqrt{s} = 0.9$ and 7 TeV.

The following Fig. 6.3.30 shows the reconstructed mass peak positions and extracted peak widths of π^0 and η mesons for the EMCal and PCM-EMCal methods and, in addition, for the remaining input measurements from the PCM and the PHOS as introduced in Tab. 6.3.12. A comparison of these quantities between data and MC simulations, visualized by full and open markers respectively, confirms a proper detector response in the simulation for all reconstruction methods. The peak width ordering, $\sigma_{\text{PCM}} < \sigma_{\text{PHOS}} < \sigma_{\text{PCM-EMCal}} < \sigma_{\text{EMCal}}$, is also observed like in Fig. 6.2.13 which is a direct consequence of the respective energy and momentum resolutions of the different photon reconstruction techniques. Moreover, the mass positions using PCM and PHOS are found to be close to the PDG masses which are indicated by the horizontal gray lines. The mass position for the EMCal method varies as a function of p_{T} since the MC cluster energies are calibrated to data as introduced in Sec. 5.2.1.

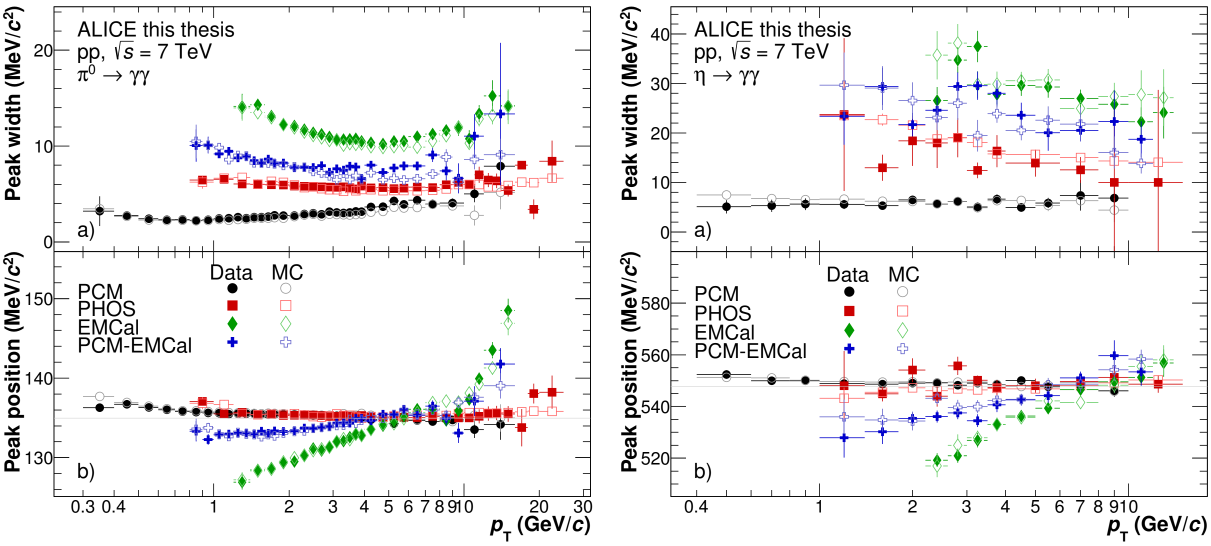

a) b)

Figure 6.3.30: The reconstructed peak widths and peak positions for π^0, a), and η, b), mesons for all methods used in the 7 TeV analysis. Full markers show results from data, whereas open markers represent the obtained values from MC simulations. The corresponding plots for $\sqrt{s} = 0.9$ TeV can be found in Fig. B.2.17.

The integration ranges used to determine the mesons' raw yields are listed in Tab. 6.3.14 for the different reconstruction methods. They are chosen to cover at least $[-3\,\sigma, +3\,\sigma]$ around the reconstructed mass positions for both mesons, M_{π^0} and M_η, where σ is the standard deviation of the Gaussian part of the fit function.

		pp, $\sqrt{s} = 0.9$ and 7 TeV	
reconstruction method	trigger	integration range $[M_{\gamma\gamma}^{\text{low}}, M_{\gamma\gamma}^{\text{high}}]$ (GeV/c^2)	
		π^0	η
EMCal	INT1	$[M_{\pi^0}$ - 0.050, M_{π^0} + 0.040$]$	$[M_\eta$ - 0.080, M_η + 0.080$]$
PCM-EMCal		$[M_{\pi^0}$ - 0.032, M_{π^0} + 0.022$]$	$[M_\eta$ - 0.060, M_η + 0.055$]$

Table 6.3.14: The integration ranges used to obtain the raw yields of π^0 and η mesons in pp collisions at $\sqrt{s} = 0.9$ and 7 TeV, applied to all p_{T} bins used in the analysis.

The determination of the raw yields $N^{\pi^0(\eta)}$ for each p_T bin is performed by bin counting the background-subtracted signal, shown in red color in Fig. 6.3.29, in the given integration ranges summarized in Tab. 6.3.14.

According to Eq. 6.1.4 in Sec. 6.1, the obtained π^0 raw spectra are corrected for secondary π^0 mesons from weak decays and material interactions which is further elaborated in Sec. 6.2.3. The production cross sections of the three main particles relevant for the secondary correction due to weak decays, K^0_S, K^0_L and Λ, are not well enough described by MC event generators for this analysis. However, the relevant particle spectra are already published by ALICE for pp collisions at $\sqrt{s}$ = 0.9 [251, 261] and 7 TeV [253, 262, 263]. These spectra are parameterized and used as weights in a PYTHIA 6.4 generator level simulation for which the subsequent steps to estimate the secondary π^0 contributions are analog to Sec. 6.2.3. The effective secondary π^0 corrections of the leading contribution from K^0_S decays are summarized in Fig. 6.3.31 for the reconstruction methods PCM, EMCal and PCM-EMCal, while the remaining cases can be found in Fig. B.2.18. The corrections are of the order of $1-3\,\%$ for K^0_S, $<0.5\,\%$ for K^0_L, $\lesssim 0.02\,\%$ for Λ and $0.1-2\,\%$ for π^0 mesons from material interactions, varying within the given values for the different reconstruction methods.

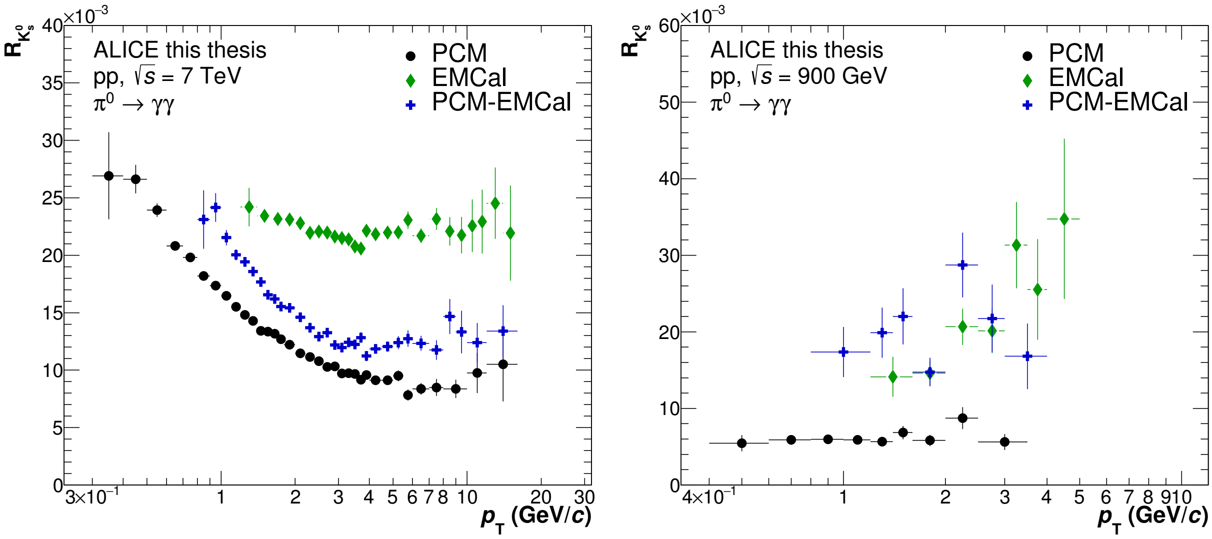

a) b)

Figure 6.3.31: Effective corrections for secondary π^0 mesons originating from K^0_S, summarized for the methods PCM, PCM-EMCal and EMCal for pp collisions at $\sqrt{s} = 0.9$ and 7 TeV. The fractions of secondary π^0 mesons $R_{K^0_S}$ are plotted as a function of p_T. The remaining plots for K^0_L and Λ decays as well as for hadronic interactions are shown in Fig. B.2.18.

The normalized correction factors ε are shown in Fig. 6.3.32 for the different reconstruction methods used for the π^0 analysis in pp collisions at $\sqrt{s}$ = 0.9 and 7 TeV. The factors contain the detector acceptances and the respective reconstruction efficiencies, which are determined according to Eq. 6.2.12 and Eq. 6.2.13 using PYTHIA 6 MC simulations, see Tab. 4.1.1. Compared to Fig. 6.2.17, the correction factors for the EMCal and PCM-EMCal are found to be smaller since only four EMCal supermodules were installed during data taking of pp collisions at $\sqrt{s} = 0.9$ and 7 TeV compared to ten active modules for $\sqrt{s} = 8$ TeV, see Tab. 3.2.4.

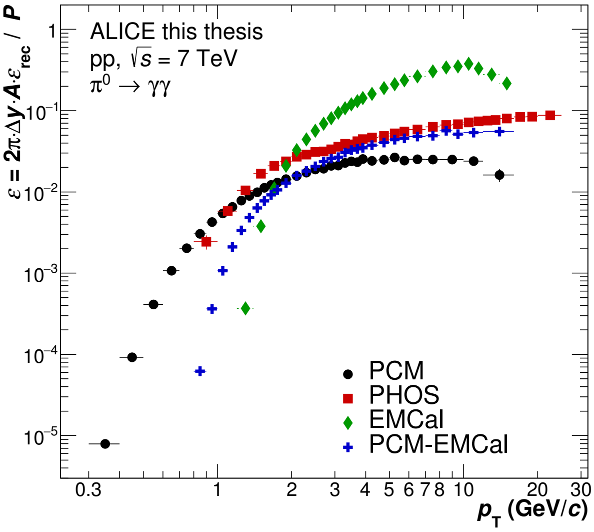

a)

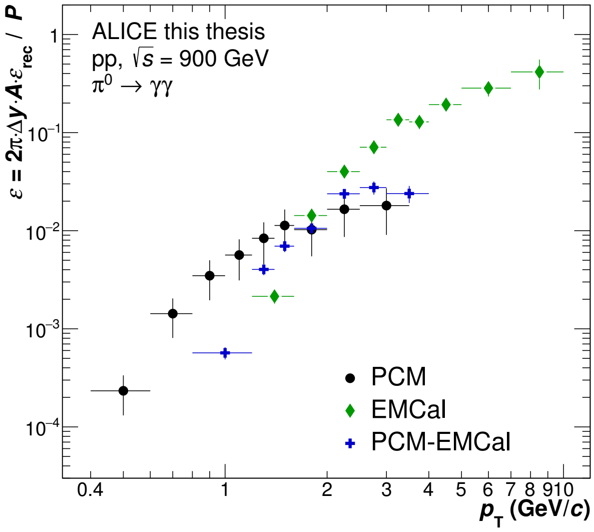

b)

Figure 6.3.32: The normalized correction factors ε are plotted as a function of p_{T} for each reconstruction method used for π^0 mesons for pp collisions at $\sqrt{s} = 7$, a), and 0.9 TeV, b). The corresponding plot for the η meson at 7 TeV can be found in Fig. B.2.27.

6.3.2 Systematic Uncertainties & Combination of Individual Measurements

The determination of systematic uncertainties of the neutral meson measurements provided by EMCal and PCM-EMCal in pp collisions at $\sqrt{s} = 0.9$ and 7 TeV is analog to the previous Sec. 6.2.4 which concerns pp collisions at $\sqrt{s} = 8$ TeV. All definitions and explanations given in Sec. 6.2.4 also apply here. The systematic uncertainties are estimated by varying the applied cuts used in the analysis, which are introduced in Chap. 4, Chap. 5 and Chap. 6. In this context, each source of systematic uncertainty is considered in the global picture by incorporating all available information, including the knowledge about systematic effects obtained from $\sqrt{s} = 8$ TeV which particularly relates to the p_{T} region beyond a couple of GeV/c.

For the measurements carried out at $\sqrt{s} = 0.9$ and 7 TeV, the same sources of systematic uncertainties are identified as for $\sqrt{s} = 8$ TeV, see Sec. 6.2.4, where the different systematic uncertainty sources are summarized into eleven categories. Since no EMCal triggers were recorded for $\sqrt{s} = 0.9$ and 7 TeV, the systematic uncertainty related to the trigger normalization does not apply and the category is therefore reduced to relate to pileup only. The respective systematic sources are categorized and the according systematic uncertainties are summarized for the reconstruction methods EMCal and PCM-EMCal in Tab. 6.3.15, Tab. 6.3.16 and Tab. 6.3.17 for the neutral mesons π^0 and η as well as their ratio η/π^0. In these tables, the uncertainties are given in percent and refer to relative systematic uncertainties of the measured values for three different p_{T} bins respectively, illustrating the relative strengths of the reconstruction methods. In Tab. 6.3.15, one example bin is devoted to the measurement at $\sqrt{s} = 0.9$ TeV for which, because of the limited statistics available, the same systematic uncertainties are assigned as for the corresponding 7 TeV measurements despite the signal extraction. This approach is chosen since the data taking at $\sqrt{s} = 0.9$ TeV took place in between the data taking periods at 7 TeV, see Tab. 3.2.3, so that the same detector configuration and experimental conditions were present.

A detailed overview of the p_T-dependent systematic uncertainties decomposed into the different sources can be found in Fig. B.2.20 for $\sqrt{s} = 0.9$ and Fig. B.2.21 for 7 TeV. All these individual uncertainties from the different sources are summed quadratically for each p_T bin. The systematic uncertainty of the η/π^0 ratio is independently determined in addition to the respective mesons π^0 and η. For this purpose, the π^0 signal is extracted using the same bin widths as defined for the η meson. As indicated in Tab. 6.3.17, many uncertainties cancel in this case such as the material-related systematics. Furthermore, all uncertainties given in the following represent a $1\,\sigma$ level of deviation. They are visualized in Fig. B.2.23 for $\sqrt{s} = 0.9$ and in Fig. B.2.22 for 7 TeV as a function of p_T for the different reconstruction methods used for the respective π^0, η and η/π^0 measurements, for which example bins are also quoted in Tab. 6.3.15, Tab. 6.3.16 and Tab. 6.3.17 as already introduced.

	pp, $\sqrt{s} = 7$ TeV						pp, $\sqrt{s} = 0.9$ TeV	
π^0 measurement	$1.8 - 2.0$ GeV/c		$5.0 - 5.5$ GeV/c		$9.0 - 10.0$ GeV/c		$2.5 - 3.0$ GeV/c	
category	PCM-EMCal	EMCal	PCM-EMCal	EMCal	PCM-EMCal	EMCal	PCM-EMCal	EMCal
signal extraction	1.9	2.0	2.0	1.3	3.2	1.9	3.6	2.3
inner material	4.5	–	4.5	–	4.5	–	4.5	–
outer material	2.1	4.2	2.1	4.2	2.1	4.2	2.1	4.2
PCM track rec.	0.4	–	0.4	–	0.4	–	0.4	–
PCM electron PID	0.3	–	0.5	–	0.8	–	0.3	–
PCM photon PID	0.5	–	0.8	–	1.6	–	1.2	–
clus. description	2.4	3.6	2.3	3.3	2.5	3.4	2.3	3.3
clus. energy calib.	2.2	2.3	2.1	2.2	2.1	2.2	2.1	2.2
track-to-clus. mat.	0.2	2.1	0.5	1.5	1.4	1.8	1.0	1.7
efficiency	2.0	2.5	2.0	2.5	2.0	2.5	2.0	2.5
pileup	0.2	0.2	0.2	0.2	0.2	0.2	0.2	0.2
total sys. unc.	6.6	7.1	6.6	6.6	7.4	6.9	7.4	6.9
statistical unc.	1.5	1.7	4.4	2.2	13.0	4.9	20.1	13.2

Table 6.3.15: Summary of relative systematic uncertainties of the measurement of π^0 mesons for selected p_T bins in percent. The statistical uncertainties are given in addition to the total systematic uncertainties for each bin. The uncertainties from the cross section determination of the MB triggers, see Tab. 4.2.4, is independent from the reported measurements and is separately indicated in the following plots in Sec. 6.3.3.

In analogy to Sec. 6.2.2, the final results for the different meson measurements are obtained by combining the individual results provided by the different reconstruction methods by exploiting the BLUE method [246–250]. The determined systematic correlation factors for $\sqrt{s} = 0.9$ and 7 TeV can be found in Fig. B.2.24 which are used to determine the respective weights for the different reconstruction methods as shown in Fig. 6.3.33. The relative total, statistical and systematic uncertainties obtained after performing the combination of all individual measurements are shown in Fig. 6.3.34.

	pp, $\sqrt{s} = 7\,\mathrm{TeV}$					
η measurement	$2.2 - 2.6\,\mathrm{GeV}/c$		$5.0 - 6.0\,\mathrm{GeV}/c$		$8.0 - 10.0\,\mathrm{GeV}/c$	
category	PCM-EMCal	EMCal	PCM-EMCal	EMCal	PCM-EMCal	EMCal
signal extraction	9.9	9.3	5.9	5.1	6.8	5.2
inner material	4.5	–	4.5	–	4.5	–
outer material	2.1	4.2	2.1	4.2	2.1	4.2
PCM track reconstruction	1.8	–	1.8	–	1.8	–
PCM electron PID	1.0	–	1.0	–	1.0	–
PCM photon PID	2.9	–	2.9	–	2.9	–
cluster description	3.0	4.0	3.0	3.7	3.1	4.0
cluster energy calibration	3.8	4.0	3.8	4.0	3.8	4.0
track-to-cluster matching	1.5	2.5	1.5	2.5	1.5	2.9
efficiency	5.0	4.3	5.0	4.3	5.0	4.3
pileup	0.2	0.2	0.2	0.2	0.2	0.2
total systematic uncertainty	13.6	12.7	11.1	9.9	11.6	10.2
statistical uncertainty	9.9	19.0	13.5	10.5	30.7	18.5

Table 6.3.16: Summary of relative systematic uncertainties of the measurement of η mesons for selected p_{T} bins in percent. The statistical uncertainties are given in addition to the total systematic uncertainties for each bin, see also explanations in caption of Tab. 6.3.15.

	pp, $\sqrt{s} = 7\,\mathrm{TeV}$					
η/π^0 measurement	$2.2 - 2.6\,\mathrm{GeV}/c$		$5.0 - 6.0\,\mathrm{GeV}/c$		$8.0 - 10.0\,\mathrm{GeV}/c$	
category	PCM-EMCal	EMCal	PCM-EMCal	EMCal	PCM-EMCal	EMCal
signal extraction	10.0	9.4	6.2	5.2	7.4	5.5
PCM track reconstruction	1.8	–	1.8	–	1.8	–
PCM electron PID	1.1	–	1.2	–	1.3	–
PCM photon PID	3.0	–	3.3	–	3.9	–
cluster description	3.7	5.0	3.6	4.8	4.1	5.0
cluster energy calibration	4.2	4.6	4.2	4.6	4.2	4.6
track-to-cluster matching	1.5	2.5	1.6	2.5	2.0	2.9
efficiency	5.4	4.5	5.4	4.5	5.4	4.5
total systematic uncertainty	13.3	12.7	10.8	9.9	11.9	10.3
statistical uncertainty	10.0	19.1	13.9	10.6	31.7	18.8

Table 6.3.17: Summary of relative systematic uncertainties of the measurement of the η/π^0 ratio for selected p_{T} bins in percent. The statistical uncertainties are given in addition to the total systematic uncertainties for each bin, see also the explanations given in the caption of Tab. 6.3.15.

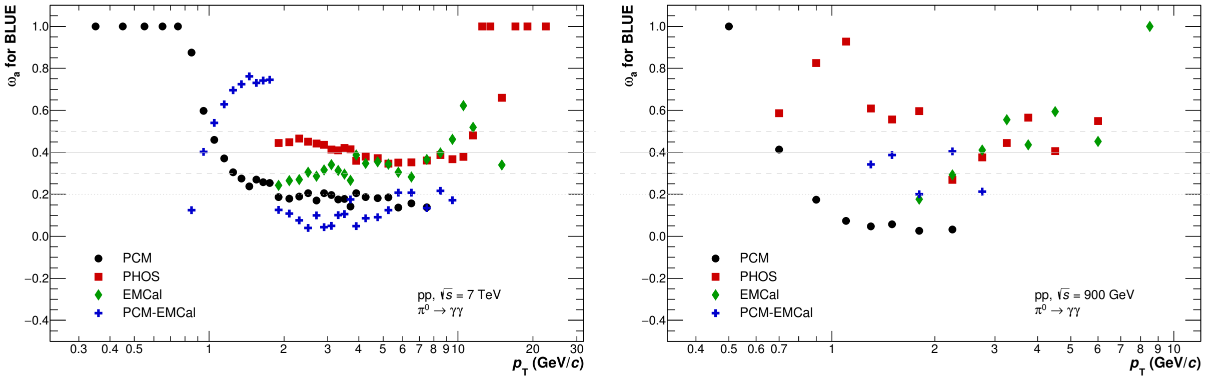

a) b)

Figure 6.3.33: The obtained weights $\omega_a(p_T)$ using the BLUE method for the combination of π^0 measurements for $\sqrt{s} = 7$ TeV, a), which are shown using all inputs summarized in Tab. 6.3.12 and for the π^0 measurement at $\sqrt{s} = 0.9$ TeV, b). The weights for the corresponding η and η/π^0 measurements can be found in Fig. B.2.19.

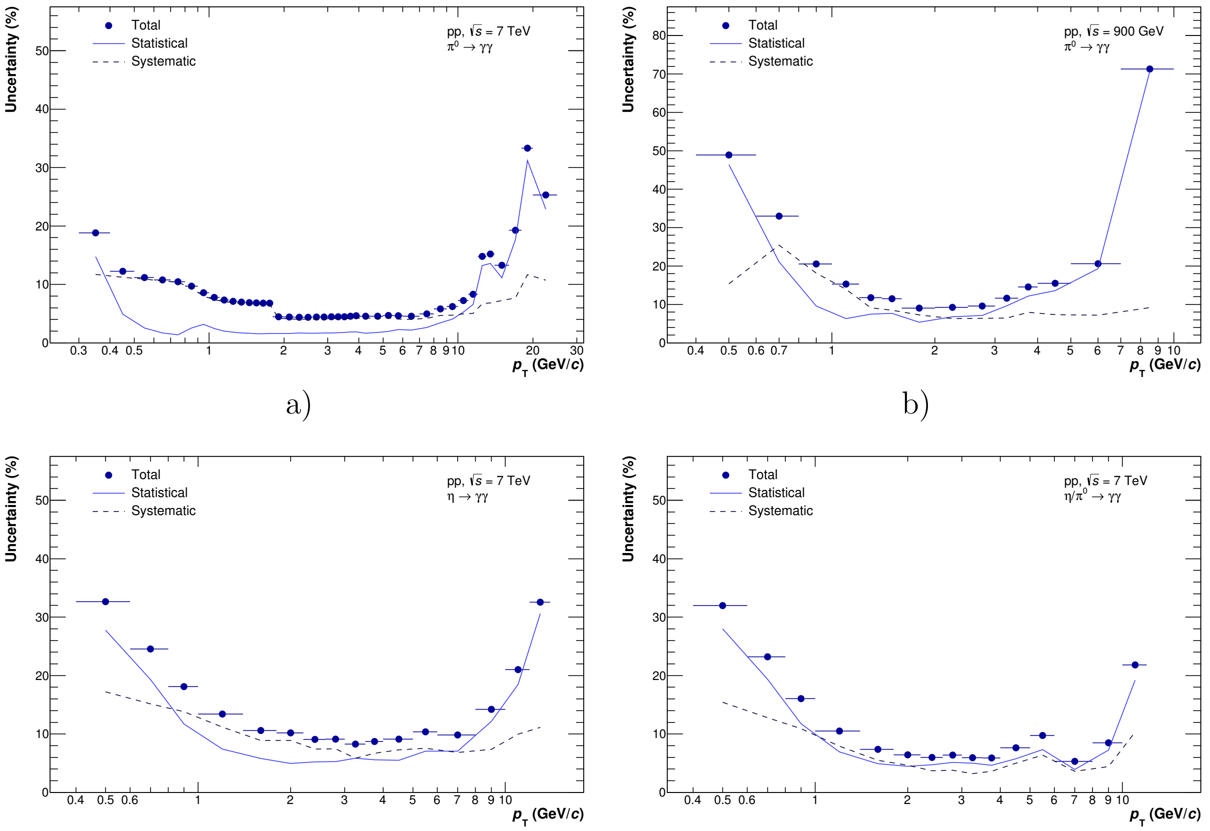

a) b)

c) d)

Figure 6.3.34: The relative total, statistical and systematic uncertainties as a function of p_T for the combination of π^0, η and η/π^0 measurements are shown in a), c) and d) for $\sqrt{s} = 7$ TeV and for the π^0 at $\sqrt{s} = 0.9$ TeV, b).

6.3.3 Results

The measurements of the invariant differential cross sections of inclusive π^0 and η meson production at mid-rapidity in pp collisions at $\sqrt{s} = 7\,\text{TeV}$ cover p_T ranges of $0.3 < p_\text{T} < 25.0\,\text{GeV}/c$ and $0.4 < p_\text{T} < 16.0\,\text{GeV}/c$ respectively, which are shown in Fig. 6.3.35 together with various theory predictions. Moreover, the π^0 and η meson cross sections measured at mid-rapidity in pp collisions at $\sqrt{s} = 0.9\,\text{TeV}$ are also shown, covering $0.3 < p_\text{T} < 10.0\,\text{GeV}/c$ and $0.9 < p_\text{T} < 3.0\,\text{GeV}/c$ respectively. All combined results are obtained according to the combination procedure described in Sec. 6.3.2 using the weights shown in Fig. 6.3.33.

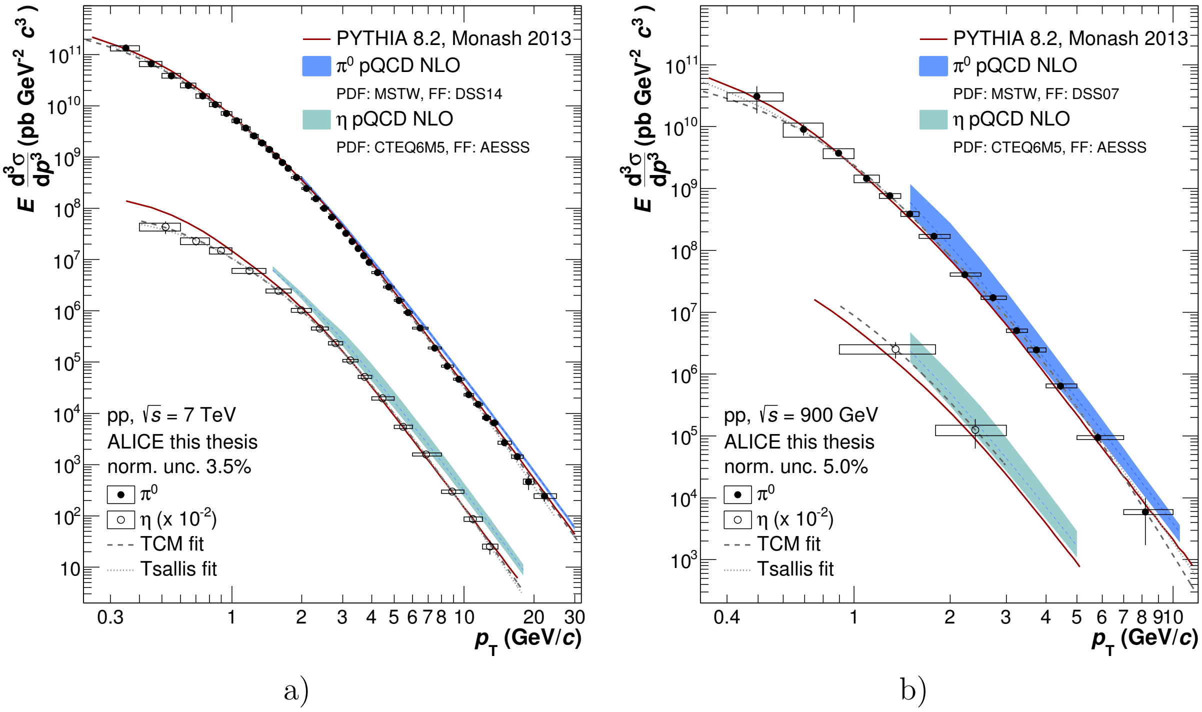

Figure 6.3.35: Combined invariant cross sections for neutral meson production in pp collisions at $\sqrt{s} = 0.9$ and $7\,\text{TeV}$ compared to PYTHIA 8.210 Monash 2013 tune as well as NLO pQCD predictions using PDFs MSTW08 with FFs DSS14 (DSS07) for the π^0 and CTEQ6M5 and AESSS for the η meson, see Sec. 6.4 for further details.

The vertical error bars represent the statistical uncertainties, whereas the boxes quantify the bin widths in horizontal direction and the systematic uncertainties in vertical direction. The total uncertainties of the measurements, calculated by quadratically adding the combined statistical and systematic uncertainties, are shown in Fig. 6.3.34 as a function of p_T. They increase for low and high momenta mainly due to statistical limitations.

The combined neutral meson spectra are fitted by default using a TCM [69] fit function, see Eq. 2.3.12 in Sec. 2.3, using the total uncertainties for each p_T bin. The results of the different reconstruction methods entering the combination procedure are compared by calculating the ratios of the spectra measured by each reconstruction method to the TCM fit of the combined spectrum which is shown in Fig. 6.3.36. All respective measurements agree within uncertainties over the full p_T range.

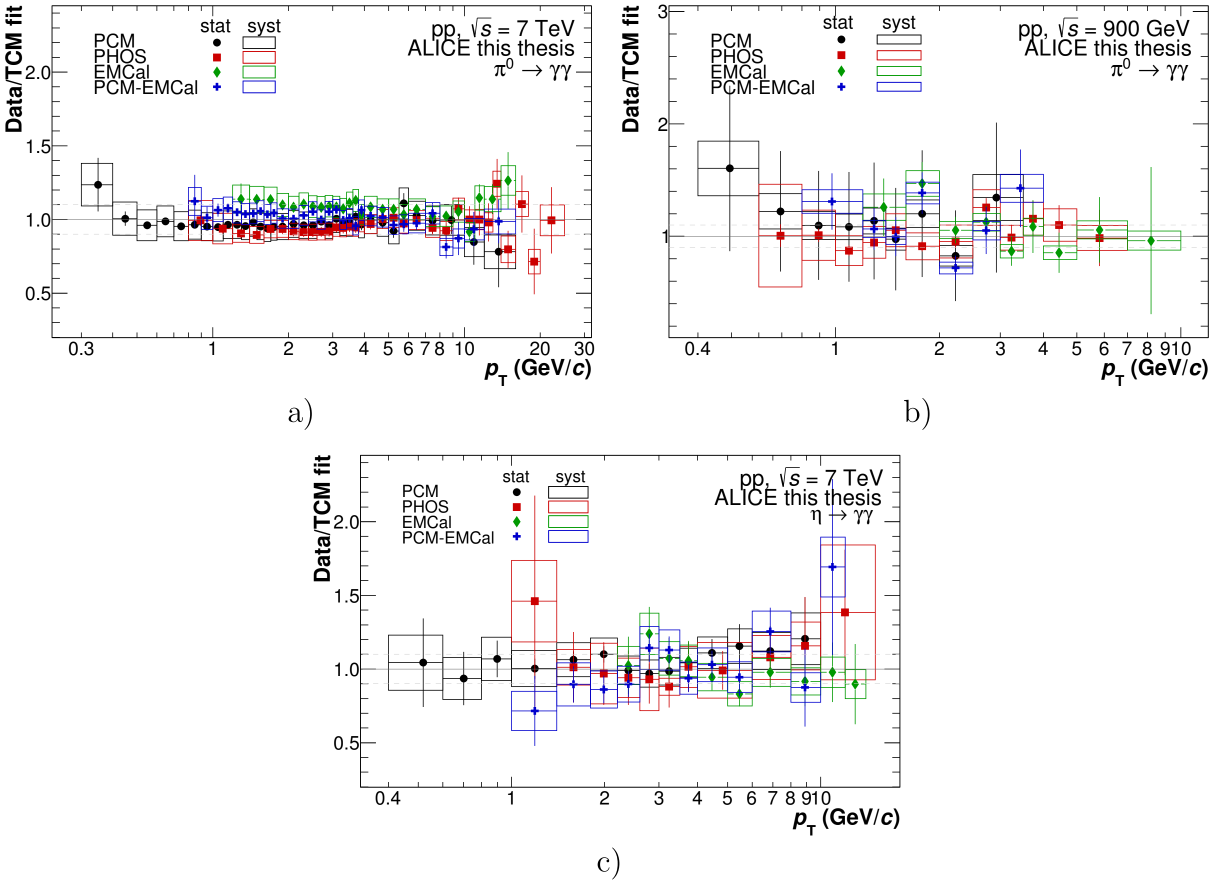

Figure 6.3.36: Ratios of the measured π^0, a), and η, c), spectra by each reconstruction method to the TCM fit of the respective combined spectrum for pp collisions at $\sqrt{s} = 7$ TeV. In b), the analog plot is shown for the π^0 at $\sqrt{s} = 0.9$ TeV.

Moreover, the combined spectra are fitted with a Tsallis function, see Eq. 2.3.13, and the corresponding ratios of the spectra to the fit result are computed which is demonstrated in Fig. B.2.26 for the π^0 and η respectively. This figure also includes a comparison with a modified Hagedorn fit, see Eq. 2.3.14, and a pure power law, see Eq. 2.3.15. All fit functions perform a reasonable job in describing the spectra which is a valid statement in case of the power law only beyond 4 GeV/c as expected.

For momenta above $p_{\mathrm{T}} > 3.5$ GeV/c, power laws are fitted to the measured spectra and similar powers of $n_{\pi^0} = 5.993 \pm 0.021(\mathrm{stat}) \pm 0.030(\mathrm{sys})$ and $n_{\eta} = 5.990 \pm 0.092(\mathrm{stat}) \pm 0.080(\mathrm{sys})$ are obtained for $\sqrt{s} = 7$ TeV, which is also reflected by the flatness of the η/π^0 ratio in this p_{T} region as shown in Fig. 6.3.37. For 0.9 TeV, a power of $n_{\pi^0} = 7.463 \pm 0.461(\mathrm{stat}) \pm 0.201(\mathrm{sys})$ is found. In Fig. 6.3.37, the η/π^0 ratios for both pp collisions at $\sqrt{s} = 0.9$ and 7 TeV are shown. For the latter center of mass energy, the ratio is found to obey a constant of $C^{\eta/\pi^0} = 0.468 \pm 0.011(\mathrm{stat}) \pm 0.009(\mathrm{sys})$ for $p_{\mathrm{T}} > 3.5$ GeV/c. It is reproduced reasonably well by the superimposed NLO pQCD calculations although no reliable conclusions can be drawn for $\sqrt{s} = 0.9$ TeV because of the limited data points and statistics, from which large uncertainties arise. Further comparisons and discussions of the measurements carried out in pp collisions at $\sqrt{s} = 0.9$ and 7 TeV are provided in the following Sec. 6.4.

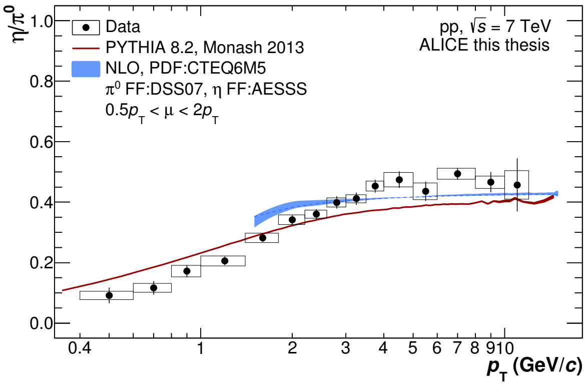

a)

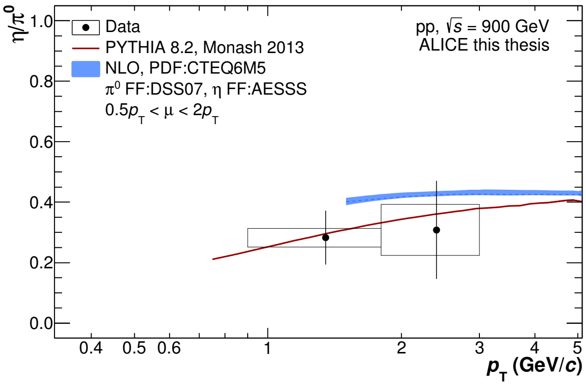

b)

Figure 6.3.37: The measured η/π^0 ratios are compared to NLO pQCD predictions using the PDF CTEQ6M5 and FFs DSS07 for the π^0 and AESSS for the η. Furthermore, the ratios are compared to PYTHIA 8.210 calculations using the Monash 2013 tune. The η/π^0 ratio is shown in a) for pp collisions at $\sqrt{s} = 7$ while the analog plot is shown in b) for 0.9 TeV. The total uncertainties of the measured η/π^0 ratio at $\sqrt{s} = 7$ TeV are shown in Fig. 6.3.34, d).

6.4 Neutral Meson Measurements in pp Collisions at $\sqrt{s}$ = 0.9, 2.76, 7 & 8 TeV

The invariant differential cross sections of inclusive π^0 and η meson production at mid-rapidity in pp collisions at $\sqrt{s}$ = 0.9, 2.76 [8], 7 and 8 TeV [4] are shown in Fig. 6.4.38. The measurements enable a study of the dependency of particle spectra on $\sqrt{s}$. Independently, additional normalization uncertainties from the cross section determination, see Tab. 4.2.4 and Ref. [8], enter at a level of 5.0 %, 2.5 %, 3.5 % and 2.6 % respectively. Note that the measured spectra and the according theory predictions are multiplied with different powers of ten in order to clearly separate and visualize the respective spectra. Different theory predictions are superimposed and compared to the measurements, involving comparisons with PYTHIA 8.2 predictions using the Monash 2013 tune [81, 117]. Furthermore, NLO pQCD calculations [76, 77] using the PDF MSTW [114] and the FF DSS14 [77] are superimposed for the π^0, for which the uncertainty bands reflect the choice of the factorization scale μ with $0.5p_T < \mu < 2p_T$. The η meson spectra are compared to analog calculations using the PDF CTEQ6M5 [256] and the FF AESSS [76], for which the different choices of μ are represented by the differently dotted blue curves as defined in the legends. The vertical error bars represent the statistical uncertainties, whereas the boxes quantify the bin widths in horizontal direction and the systematic uncertainties in vertical direction which also applies to all upcoming plots shown in this section.

All spectra are fitted with TCM and Tsallis functions, see Eq. 2.3.12 and Eq. 2.3.13 respectively, for which the obtained fit parameters are summarized in Tab. 6.4.18 and Tab. 6.4.19 for all collision energies. The latter table also contains the results of pure power law fits, summarizing the power n of spectra for the different $\sqrt{s}$. The quoted uncertainties of the parameters represent the fit uncertainties. A direct comparison of the TCM and Tsallis fits can be found in Fig. 6.4.38, where both fits are plotted in addition to the measured spectra and theory calculations.

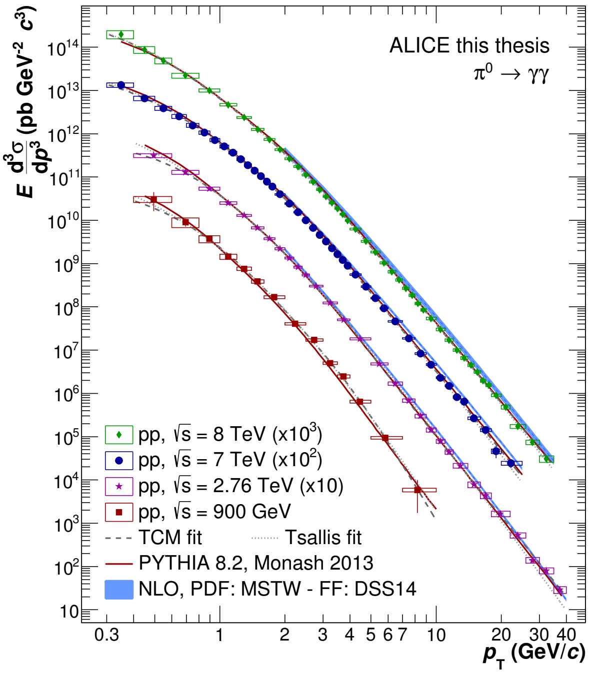

a)

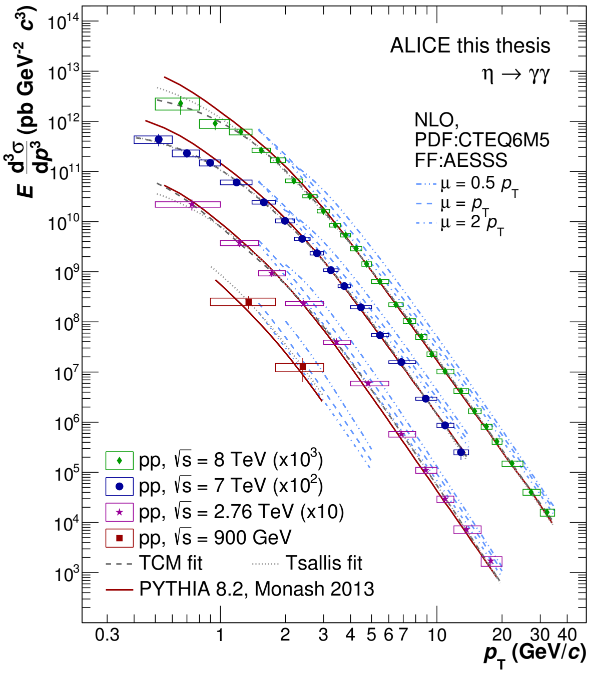

b)

Figure 6.4.38: The invariant differential cross sections of π^0, a), and η, b), production measured in pp collisions at $\sqrt{s} = 0.9$, 2.76 [8], 7 and 8 TeV [4]. Independently, additional normalization uncertainties from the cross section determination, see Tab. 4.2.4 and Ref. [8], enter at a level of 5.0 %, 2.5 %, 3.5 % and 2.6 % respectively. The measurements are fitted with TCM as well as Tsallis functions which are plotted in addition. The PYTHIA 8.2 prediction using the Monash 2013 tune is also shown together with pQCD NLO calculations using the PDF MSTW and FF DSS14 for the π^0 as well as CTEQ6M5 and AESSS for the η.

As previously introduced in Sec. 6.2.6 for the measurements at $\sqrt{s} = 8$ TeV, the TCM is chosen as the standard fit function since it better describes the spectra at low and high p_T than the Tsallis counterpart, see Fig. 6.2.27. This fact is also observed for the other center of mass energies, see Fig. B.2.26 for 7 TeV and Ref. [8] for 2.76 TeV. The improved description of the TCM compared to the Tsallis is also reflected in the smaller values obtained for the reduced χ^2_{red} of the respective fits which are recorded in Tab. 6.4.18 and Tab. 6.4.19. The only exception is the case of the π^0 measurement at $\sqrt{s} = 0.9$ TeV. However, both χ^2_{red} values are very close which could be caused due to the limited amount of data points and the large uncertainties leading to the situation that the Tsallis fit is favored. For the η at same energy, no χ^2_{red} values could be extracted for the TCM and the power law. This is due to the fact that the spectrum only includes two measured data points below 3 GeV/c which prevents any of both fits to be performed. For the Tsallis fit, the parameter n is fixed in order to be able to approximate the only two data points with the remaining two free parameters. The value is chosen to be $n = 8$ according to the obtained power n of the π^0 spectrum which itself shows large uncertainties though. The χ^2_{red} values are calculated without assuming any correlation of systematic uncertainties and, hence, are found to be rather small for both fits as the total uncertainties of meson spectra are used for their calculation.

pp, $\sqrt{s}$ (TeV)	TCM fit parameters A_e (pb GeV$^{-2}c^3$)	T_e (GeV)	A (pb GeV$^{-2}c^3$)	T (GeV)	n	χ^2_{red}
			π^0 meson			
0.9	(1.00±0.71)·10^{11}	0.224±0.051	(0.79±1.59)·10^{9}	1.060±0.442	4.384±1.076	0.88
2.76	(7.87±3.50)·10^{8}	0.566±0.035	(7.43±1.30)·10^{10}	0.441±0.021	3.083±0.027	0.45
7	(3.97±1.33)·10^{11}	0.155±0.024	(3.22±1.09)·10^{10}	0.608±0.042	3.077±0.029	0.27
8	(6.84±2.79)·10^{11}	0.142±0.020	(3.68±0.89)·10^{10}	0.597±0.030	3.028±0.018	0.28
			η meson			
0.9	–	–	–	–	–	–
2.76	(1.85±2.21)·10^{10}	0.149±0.071	(1.39±1.05)·10^{9}	0.852±0.136	3.319±0.123	0.32
7	(8.30±4.62)·10^{9}	0.195±0.075	(1.80±1.16)·10^{9}	0.917±0.133	3.233±0.132	0.16
8	(1.62±4.35)·10^{9}	0.229±0.203	(2.89±1.81)·10^{9}	0.810±0.103	3.043±0.045	0.33

Table 6.4.18: Obtained TCM fit parameters for the π^0 and η invariant differential cross sections in pp collisions at $\sqrt{s} = 0.9$, 2.76 [8], 7 and 8 TeV [4].

Besides the obtained parameters for the Tsallis fits of spectra, Tab. 6.4.19 also lists the obtained powers n from pure power law fits to the spectra according to Eq. 2.3.15. No power law fit is possible for the η at $\sqrt{s} = 0.9$ TeV since both data points are below the fitting region of the power law of $p_{\mathrm{T}} > 3.5$ GeV/c.

pp, $\sqrt{s}$ (TeV)	Tsallis fit parameters C (pb)	T (GeV)	n	χ^2_{red}	power law fit n
		π^0 meson			
0.9	(0.73±0.20)·10^{11}	0.143±0.019	8.346±0.583	0.82	7.463 ± 0.503
2.76	(1.29±0.10)·10^{11}	0.128±0.004	7.046±0.068	1.52	6.290 ± 0.045
7	(1.87±0.10)·10^{11}	0.135±0.003	6.770±0.055	0.41	5.993 ± 0.037
8	(2.46±0.18)·10^{11}	0.121±0.004	6.465±0.042	0.57	5.936 ± 0.026
		η meson			
0.9	(1.59±3.74)·10^{10}	0.162±0.279	8.000 (fixed)	–	–
2.76	(1.12±0.26)·10^{10}	0.207±0.024	7.133±0.335	0.52	6.380 ± 0.175
7	(1.34±0.13)·10^{10}	0.254±0.016	7.360±0.299	0.18	5.990 ± 0.122
8	(1.56±0.19)·10^{10}	0.221±0.012	6.560±0.113	0.59	5.930 ± 0.052

Table 6.4.19: Obtained Tsallis as well as power law (for $p_{\mathrm{T}} > 3.5$ GeV/c) fit parameters for the π^0 and η invariant differential cross sections in pp collisions at $\sqrt{s} = 0.9$, 2.76 [8], 7 and 8 TeV [4].

Taken together all obtained fit results, the TCM does a much better job in describing the spectra at low and high p_{T} in comparison to the Tsallis, especially when the measurements reach up to very high p_{T} involving many data points. With increasing $\sqrt{s}$, the particle spectra become harder so that the power n of the power law fits are expected to decrease. This is in fact observed since the different powers n line up reasonably. The measurements at $\sqrt{s} = 0.9$ TeV show the highest value of about $n \approx 7.5$ which decreases to about $n \approx 6.3$ for 2.76 TeV. Furthermore, values of about $n \approx 6.0$ and $n \approx 5.9$ are obtained for 7 TeV and 8 TeV. The latter two values are found to be are rather close, matching the expectation due to the small relative difference in $\sqrt{s}$. Hence, the spacing of the determined values n reflects the change of the center of mass energy $\sqrt{s}$ and consequently the hardening of spectra.

The determined TCM fit parameters follow the expected $\sqrt{s}$ behavior as well, indicated by the increasing normalization parameters A and decreasing powers n within the quoted uncertainties. The measurements at $\sqrt{s} = 2.76$ TeV seem to be off, though, and do not follow the global trends. Its obtained parameter A_e does not fit the global trend seen in Tab. 6.4.18 and also T_e is much larger at about 0.566 GeV. Compared to the other values, both parameters would naively be expected to lie in between the $\sqrt{s} = 0.9$ and 7 TeV. The same can be stated for the parameters A and T, whereas n at least fits the global decreasing trend. This could be partially caused by a potential bias still present at high p_{T} as the π^0 measurement at $\sqrt{s} = 2.76$ TeV is the only one involving the merged EMCal analysis [8] which dominantly enters the measurement in the highest p_{T} bins. Note that due to a different definition of the power n in the case of the TCM which reflects the hardness of the spectra, the corresponding values are found to be lower than for the classical simple power law fit. For the η meson, the experimental uncertainties of the measurements, especially at low p_{T}, are higher compared to the π^0. Additionally, a limited amount of data points is available to constrain the parameters of the fit at low and high p_{T}. Therefore, substantial uncertainties are found for most of the TCM fit parameters in these cases. Despite the uncertainties, however, the provided description of spectra is found to be much better than using the Tsallis counterpart, indicated by the obtained χ^2_{red} values. For the Tsallis fits the conclusion can be drawn that in general the obtained values follow the expected $\sqrt{s}$ ordering. The fits of the spectra measured at $\sqrt{s} = 2.76$ TeV show by far the largest χ^2_{red} among all Tsallis fits while the η meson at $\sqrt{s} = 0.9$ TeV can only be rudimentary approximated by fixing the power n in that case.

The measurements of neutral meson cross sections at the different $\sqrt{s}$ energies, which are shown in Fig. 6.4.38, are compared with the corresponding theory predictions in the following Fig. 6.4.39. The ratios of the measured data points as well as theory predictions are computed with respect to the TCM fits of the spectra. In case of the η at $\sqrt{s} = 0.9$ TeV, the Tsallis fit can only be used. A comparison of the data with PYTHIA calculations using the Monash 2013 tune [81, 117] indicates a good agreement in general, considering the given experimental uncertainties. The statistical uncertainties of the PYTHIA calculations are visualized by the respective line thickness which becomes broader the larger the corresponding uncertainties are. The measurement of the π^0 at $\sqrt{s} = 0.9$ TeV exhibits substantial uncertainties for which the shape of the TCM fit and the PYTHIA predictions seem to grow some tension beyond $p_{\mathrm{T}} > 2\,\mathrm{GeV}/c$ although PYTHIA is within 20 % throughout the p_{T} region covered by the measurement. For the π^0 at $\sqrt{s} = 2.76$ TeV, a good agreement can be stated while for $\sqrt{s} = 7$ and 8 TeV the PYTHIA predictions overshoot the measurements by approximately 10 % to 20 %. The shape of the measured spectra can be reasonably described although the presence of a bump in the ratio is indicated at around 3 GeV/c. For the η, the PYTHIA description is within ≈ 20 % for all $\sqrt{s}$ energies. At low p_{T}, however, PYTHIA is not able to describe the spectra at $\sqrt{s} = 7$ and 8 TeV and deviates significantly.

Furthermore, Fig. 6.4.39 shows comparisons with NLO pQCD calculations using the PDF MSTW [114] and the FF DSS14 [77] for the π^0. The uncertainty bands reflect the choice of the factorization scale μ with $0.5p_{\mathrm{T}} < \mu < 2p_{\mathrm{T}}$, whereas the case $\mu = p_{\mathrm{T}}$ is visualized by

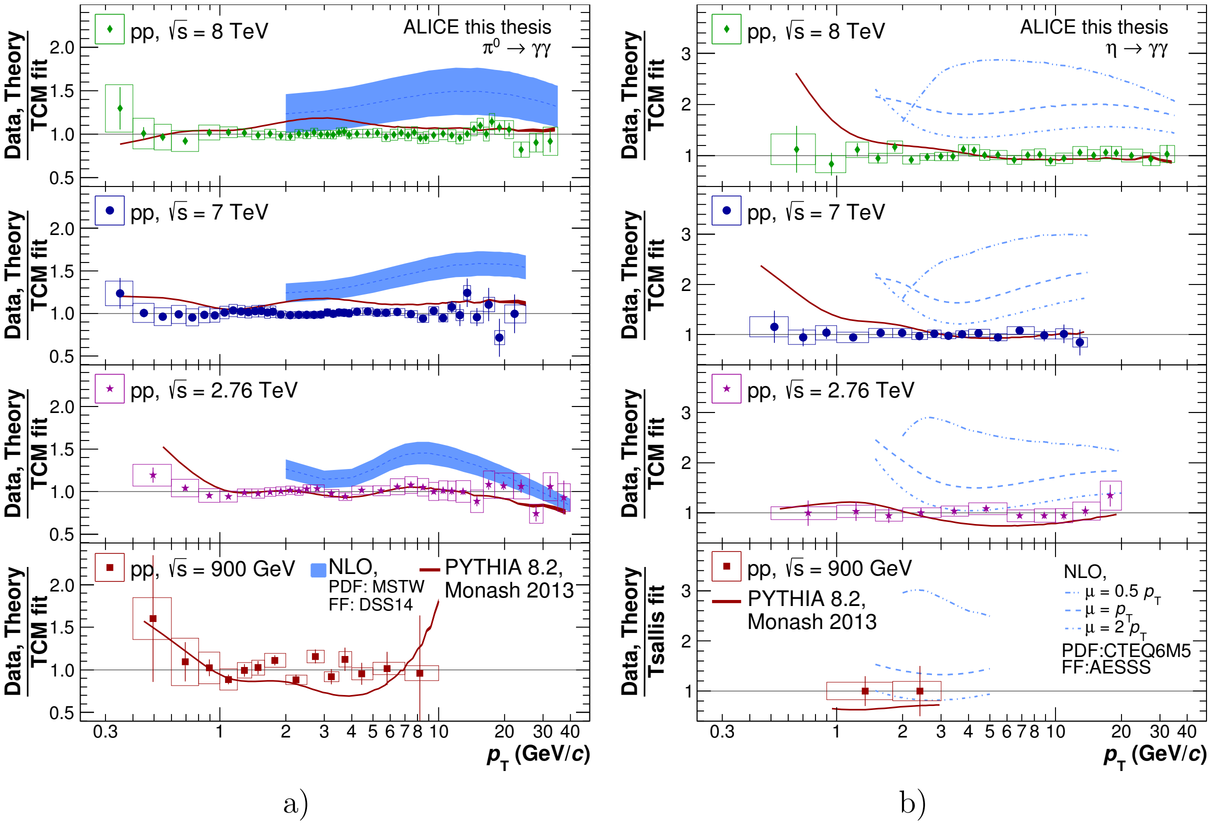

Figure 6.4.39: Ratios of data, PYTHIA and pQCD predictions to TCM fits of the measured π^0, a), and η, b), meson spectra for $\sqrt{s} = 0.9$, 2.76 [8], 7 and 8 TeV [4].

dotted lines. For $\sqrt{s} = 0.9$ TeV, no DSS14 calculation was made available for comparisons. All pQCD calculations overestimate the measured cross sections for which the respective magnitude is strongly p_T-dependent as well as $\sqrt{s}$-dependent. The highest deviation of up to approximately 60 % for $\mu = p_T$ is seen for $\sqrt{s} = 7$ TeV. However, these predictions do a much better job compared to the analog calculations for the η meson spectra using the PDF CTEQ6M5 [256] and the FF AESSS [76] which are also shown in Fig. 6.4.39. In this case, the different choices of μ are represented by the differently dotted blue curves as defined in the legend. For the η, the deviations are partially of the order of 100% and even beyond. Additionally, the scale uncertainties are observed to be much larger in comparison. In contrast to the π^0, however, the FFs of the η meson have not been updated for quite a while and hence do not include LHC data at all in the global fits. The availability of η measurements covering wide p_T intervals would help to further constrain the FFs in this case and, thus, help to reduce the uncertainties and significantly reduce the observed deviations. This could already be achieved for the π^0 for which the update from DSS07 [75], which had comparable discrepancies than AESSS for the η, to its successor DSS14 lead to a major improvement in the description of measurements.

The evolution the π^0 spectra as a function of $\sqrt{s}$ is studied using the following Fig. 6.4.40. In this context, rather different p_T bin widths and total number of bins are present for the various measurements available for the different $\sqrt{s}$ energies. Hence, bin-by-bin comparisons are shown in Fig. 6.4.40 which are computed by exploiting an algorithm that merges the available p_T bins of two measurements in as little steps as possible until a common p_{T} binning is obtained, for which the ratios are calculated. The comparisons involve the π^0 and $\pi^\pm$ spectra measured in pp collisions at $\sqrt{s} = 2.76$, 7 and 8 TeV. However, no measurement of $\pi^\pm$ is available for $\sqrt{s} = 8$ TeV at the time this thesis is compiled.

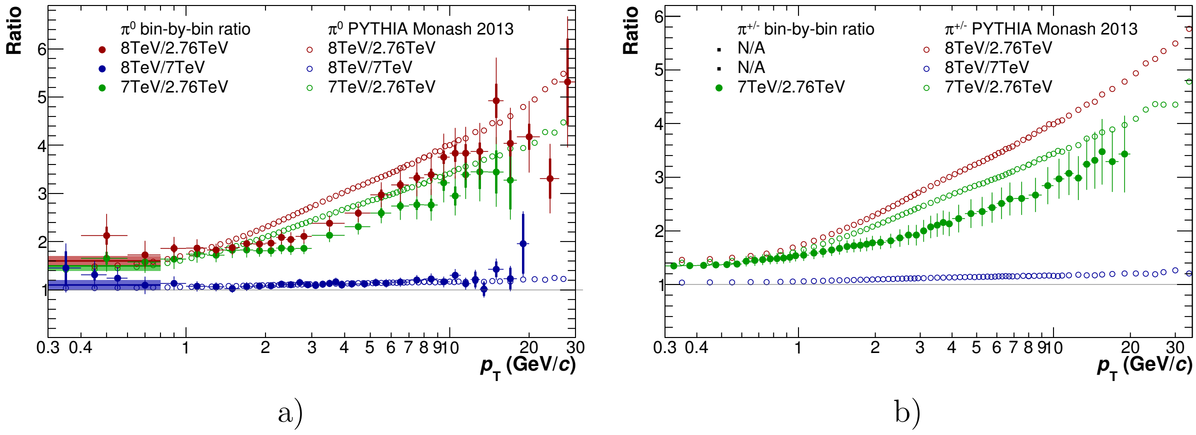

Figure 6.4.40: Bin-by-bin ratios of the measured π^0 cross sections in pp collisions at $\sqrt{s}$ = 2.76 [8], 7 and 8 TeV [4]. The corresponding ratios are also calculated using the PYTHIA, Monash 2013 tune. They are shown for the π^0, a), and its charged equivalents $\pi^\pm$, b), for which no measurement at $\sqrt{s} = 8$ TeV is available though.

The bin-by-bin ratios shown in Fig. 6.4.40 are computed not only for the available π^0 and $\pi^\pm$ measurements but also for the corresponding PYTHIA predictions. A similar plot is shown in Ref. [264] for the evolution of charged particle spectra. In Fig. 6.4.40, thick vertical error bars represent statistical uncertainties, whereas thin error bars stand for the total uncertainties. The PYTHIA predictions do not show a considerable difference between π^0 and $\pi^\pm$ due to isospin symmetry. For the π^0, these comparisons are an extremely important tool to confirm a working pileup removal procedure [244] which is of crucial importance for the PCM measurements that dominate the combined spectra below 0.8 GeV/c. Because of different running conditions, less pileup, and partially even almost no pileup, was present at $\sqrt{s}$ = 2.76 and 7 TeV, whereas difficult running conditions were faced throughout the data taking at 8 TeV, see Chap. 4. The colored horizontal lines represent the expected evolution of spectra at low p_{T}, estimated based on Fig. 2.3.5a for which systematic uncertainties of about 10 % are assumed. All ratios shown in Fig. 6.4.40 agree with these expectations within one sigma for all p_{T} bins which demonstrates that the evolution of spectra follows the expectations. For higher p_{T}, the measurement do show a different shape than the PYTHIA predictions which is also observed for the $\pi^\pm$ ratio between $\sqrt{s} = 7$ and 2.76 TeV. Other than that, the PYTHIA prediction of the ratio of yields at $\sqrt{s} = 7$ and 8 TeV suggests a small enhancement of a couple of percent, little varying as a function of p_{T}. In fact, this behavior is well confirmed by measurements over the full reported p_{T} range.

The η/π^0 ratios measured in pp collisions at $\sqrt{s}$ = 0.9, 2.76, 7 and 8 TeV are summarized in Fig. 6.4.41a. The respective ratios are fitted with a constant for $p_{\mathrm{T}} > 3.5$ GeV/c yielding:

- $C^{\eta/\pi^0} = 0.474 \pm 0.015(\mathrm{stat}) \pm 0.024(\mathrm{sys})$ for 2.76 TeV;
- $C^{\eta/\pi^0} = 0.468 \pm 0.011(\mathrm{stat}) \pm 0.009(\mathrm{sys})$ for 7 TeV;
- $C^{\eta/\pi^0} = 0.455 \pm 0.006(\mathrm{stat}) \pm 0.014(\mathrm{sys})$ for 8 TeV.

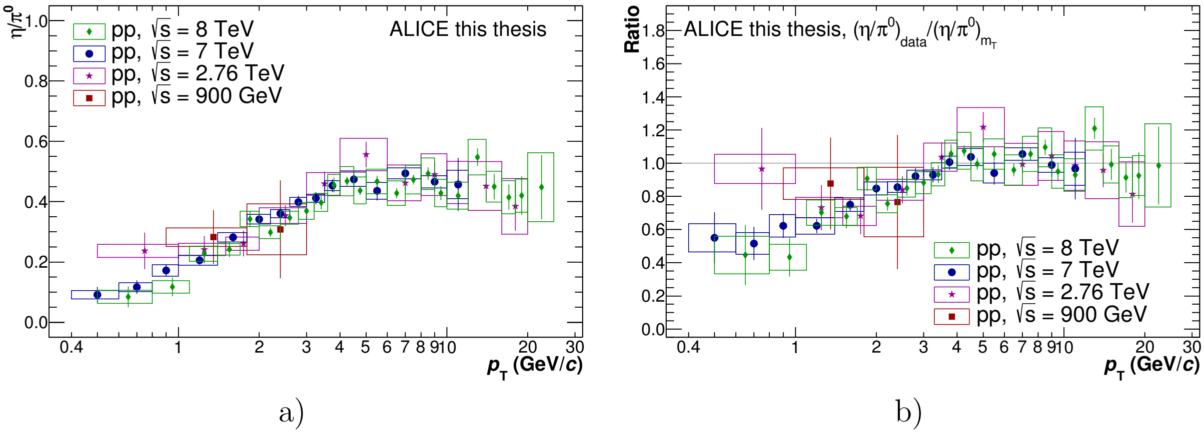

Figure 6.4.41: a) η/π^0 ratios measured in pp collision at $\sqrt{s} = 0.9$, 2.76 [8], 7 and 8 TeV [4]. b) Ratios of the measured η/π^0 ratios over the η/π^0 ratios obtained with m_{T} scaling for the different pp energies.

The obtained values C^{η/π^0} for the different center of mass energies are consistent with each other within uncertainties for the given p_{T} range. For the region $p_{\mathrm{T}} < 3.5\,\mathrm{GeV}/c$, all collision energies covered by ALICE also agree within experimental uncertainties so that η/π^0 ratios may be claimed to be consistent within accuracy for all ALICE measurements in pp collisions at $\sqrt{s} = 0.9$, 2.76, 7 and 8 TeV. The measurements compiled in Fig. 6.4.41 and the comparisons shown in Fig. 6.2.28 thus confirm a universal behavior of the η/π^0 ratio seen for NA27, PHENIX and ALICE data for pp collisions from $\sqrt{s} = 27.5$ GeV up to $\sqrt{s} = 8$ TeV within experimental uncertainties.

In Fig. 6.4.41b, the validity of m_{T} scaling is tested by means of the η/π^0 ratio. Such a m_{T} scaling prediction for the η/π^0 ratio is already illustrated in Fig. 6.2.28. The term m_{T} scaling denotes an empirical rule observed in relative particle yields. It allows estimates of the hadronic background of rare probes such as direct photons, dileptons and heavy-quark production. Using m_{T} scaling, the p_{T}-dependent differential cross sections of most of particles can be derived from the well measured light-flavor mesons, like pions and kaons, by assuming that the meson spectra can be described as a function of transverse mass m_{T}:

$$E\frac{\mathrm{d}^3\sigma}{\mathrm{d}p^3} = C^h f(m_{\mathrm{T}}), \tag{6.4.14}$$

where the function $f(m_{\mathrm{T}})$ is universal for all hadron species so that their spectra share the same shape up to a normalization factor C^h [265]. Hence, this empirical scaling rule is widely used in the context of rare probes to estimate the various background sources, for which no measurements are available.

Before the LHC era, the precision of η/π^0 measurements was not sufficient to probe m_{T} scaling over broad ranges of p_{T} with high statistics. Almost all lower-energy experiments from ISR to RHIC confirm the validity of this empirical rule in particle production within experimental uncertainties over the complete p_{T} regions covered by the measurements, i.a. for kaons, ϕ and J/ψ in pp collisions at $\sqrt{s} = 0.2$ TeV [266, 267]. However, recent phenomenological analysis of LHC data indicates that m_{T} scaling only holds at higher p_{T} compared to lower collision energies, for which, down to lower p_{T} than at the LHC, the empirical law is still followed [265, 268].

In order to study the validity of the m_{T} scaling rule for the precise measurements of the η/π^0 ratio shown in Fig. 6.4.41a, the TCM parameterizations of the measured π^0 spectrum are used which are given in Tab. 6.4.18. The corresponding η spectrum is obtained via the application of m_{T} scaling by replacing the π^0 mass with the η mass and using the respective normalization ratio C^{η/π^0} as quoted earlier. From these two spectra, the η/π^0 ratio is constructed which is, for example, represented by the blue curve in Fig. 6.2.28b. The ratio of the measured η/π^0 ratio over the η/π^0 ratio obtained with m_{T} scaling is computed and plotted in Fig. 6.4.41b for the different center of mass energies. It can be deduced from the plot that the ratio is consistent with unity above $p_{\mathrm{T}} > 3.5\,\mathrm{GeV}/c$. For $p_{\mathrm{T}} < 3.5\,\mathrm{GeV}/c$, however, the computed ratio constantly decreases and reaches values of about 0.4 at around $1\,\mathrm{GeV}/c$ as shown in Fig. 6.4.41b. For the example of 8 TeV [4], the m_{T} scaling prediction is estimated to be broken with a significance of $6.2\,\sigma$ below $3.5\,\mathrm{GeV}/c$. The significance is calculated by reflecting the statistical and systematic uncertainties of each p_{T} bin, from which the corresponding deviations from unity are expressed in $n\,\sigma$ leading to the total observed significance. No statement can obviously be made for $\sqrt{s} = 0.9\,\mathrm{TeV}$, whereas there is indication for a m_{T} scaling violation with $2.1\,\sigma$ for 2.76 TeV [8]. A significant disagreement well beyond $5\,\sigma$ from the m_{T} scaling hypothesis is observed for $\sqrt{s} = 7\,\mathrm{TeV}$ as well. Hence, all η/π^0 ratios are found to be consistently violating m_{T} scaling for $p_{\mathrm{T}} < 3.5\,\mathrm{GeV}/c$. Whether the magnitude of m_{T} scaling violation depends on the collision energy could be clarified in future by the ongoing measurements of hadron spectra in pp collisions at $\sqrt{s} = 13\,\mathrm{TeV}$ by ALICE.

The integrated yields $\mathrm{d}N/\mathrm{d}y|_{y\,\approx\,0}$ and the mean transverse momenta $\langle p_{\mathrm{T}}\rangle$ are determined for the neutral meson measurements at mid-rapidity as shown in Fig. 6.4.38. For this purpose, the reported spectra are transformed into differential yields by dividing with the respective inelastic cross section, see Tab. 4.2.4, and multiplying with p_{T}. The resulting spectra are shown in Fig. 6.4.42 and Fig. B.2.29, illustrating the differential yield per inelastic collision. Furthermore, fits to the spectra using the modified Hagedorn, TCM and Tsallis parameterizations are shown in Fig. 6.4.42. The default fit function used to obtain $\mathrm{d}N/\mathrm{d}y|_{y\,\approx\,0}$ and $\langle p_{\mathrm{T}}\rangle$ is the modified Hagedorn, defined in Eq. 2.3.14. It provides the best description of the neutral meson spectra at lowest p_{T} measured which is the crucial part of the spectra with regard to $\mathrm{d}N/\mathrm{d}y|_{y\,\approx\,0}$ and $\langle p_{\mathrm{T}}\rangle$, see Fig. 6.2.27 and Fig. B.2.26. Moreover, the TCM and Tsallis fit functions are used in this context to estimate systematic uncertainties, see Eq. 2.3.12 and Eq. 2.3.13 for their definitions.

In order to determine $\mathrm{d}N/\mathrm{d}y|_{y\,\approx\,0}$, the neutral meson spectra are integrated in the measured p_{T} region using the available data points, whereas the fit function is used to estimate the yield in the unmeasured p_{T} regions. The systematic uncertainty of the determined integrated yield is obtained by moving the data points to the maximum and minimum $1\,\sigma$ variations according to the corresponding systematic uncertainties. After the data points are moved in each direction, the fit procedure is repeated using the same functional form. Doing so, one can obtain the maximum and minimum yield which is still in accordance with the systematic uncertainties given for each p_{T} bin. Another systematic uncertainty arises from the necessary extrapolation of spectra to determine $\mathrm{d}N/\mathrm{d}y|_{y\,\approx\,0}$ for which the dominant contribution is found to be at low p_{T}. In this region, the estimated yield is primarily obtained by means of the extrapolation function. To estimate the systematic uncertainty due to this necessary extrapolation step, two other fit functions, the TCM and Tsallis, are taken into account and the corresponding results for $\mathrm{d}N/\mathrm{d}y|_{y\,\approx\,0}$ are compared to each other. The variation of the fit function is kept separate from the other sources of systematic uncertainties as it heavily depends on the choice of fit functions to extrapolate the spectra and might improve in the future.

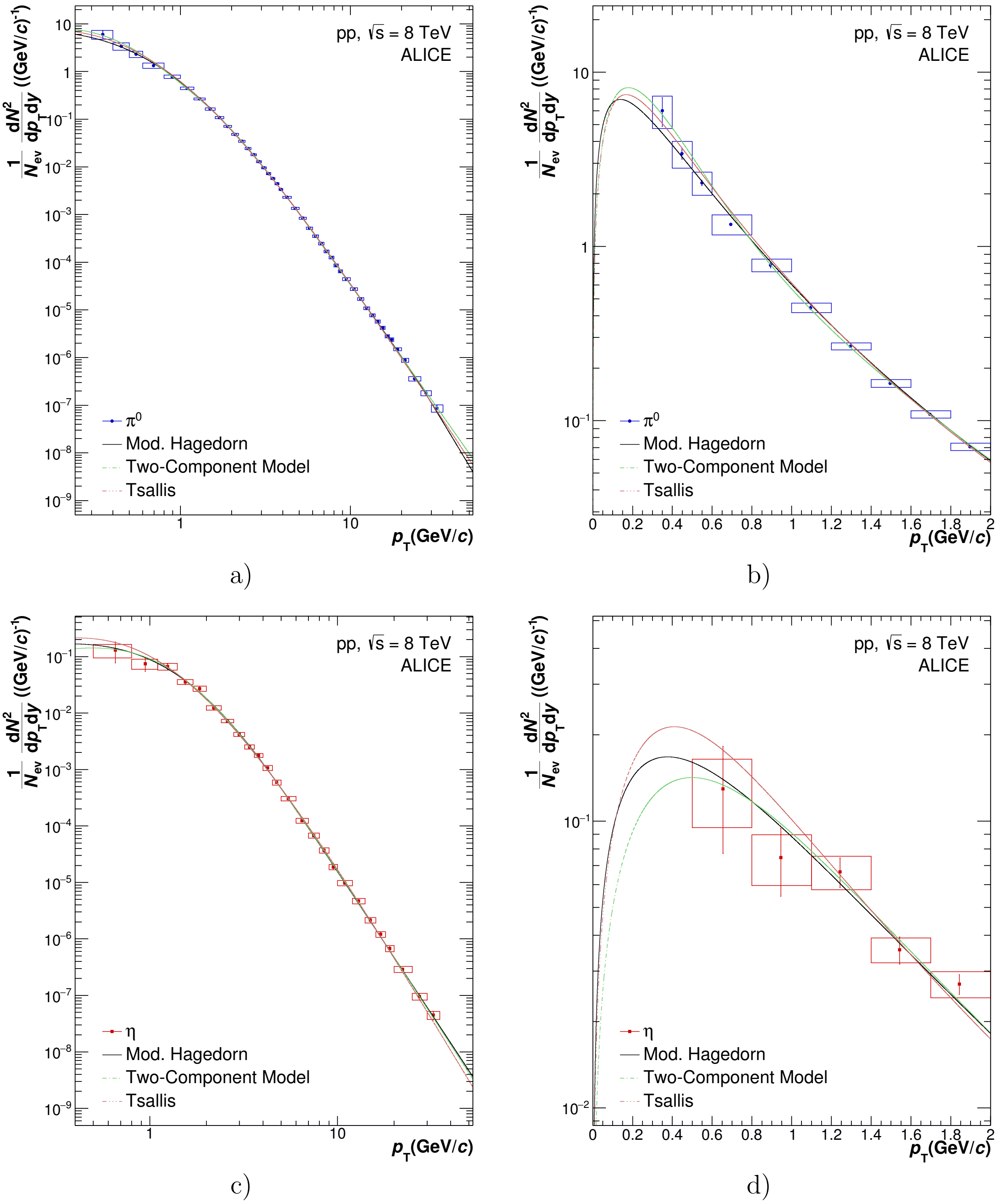

Figure 6.4.42: The neutral meson spectra measured in pp collisions at $\sqrt{s} = 8\,\text{TeV}$ [4] are shown with logarithmic abscissa (left) and for the low momentum region $p_T < 2\,\text{GeV}/c$ with a linear scale on the abscissa (right). The different fits are shown which are used to determine the integrated yields and mean p_T values. The corresponding spectra and fits for 0.9 and 7 TeV can be found in Fig. B.2.28 and Fig. B.2.29.

A similar procedure is followed to obtain the $\langle p_{\mathrm{T}} \rangle$ of the respective particle species. In contrast to the previous case, the data points are shifted such that they represent the hardest and softest possible spectrum in order to obtain the corresponding systematic uncertainties. Analog to the previous paragraph, an additional uncertainty from the choice of the functional from is taken into account as an independent contribution to the systematics.

The obtained values for $\mathrm{d}N/\mathrm{d}y|_{y\approx 0}$ and $\langle p_{\mathrm{T}} \rangle$ for π^0 and η mesons are listed in Tab. 6.4.20 for the different $\sqrt{s}$ energies, where the corresponding statistical and systematic uncertainties are quoted in addition. The additional uncertainty term denoted with "fit sys" reflects the differences of the results due to choice of the fitting function. The extrapolation fractions F_{ext} are also given which are significant throughout. This is also reflected by the estimated uncertainties of the different values. Additionally, the integrated η/π^0 ratio is estimated and can be found in Tab. 6.4.20 as well. Within their substantial uncertainties, the η/π^0 ratios determined for all $\sqrt{s}$ energies are found to be consistent.

pp, $\sqrt{s}$ (TeV)		$\langle p_{\mathrm{T}} \rangle$ (GeV/c)	$\mathrm{d}N/\mathrm{d}y\|_{y\approx 0}$	F_{ext}
0.9	π^0	$0.369 \pm 0.023_{(\mathrm{stat})} \pm 0.047_{(\mathrm{sys})} \pm 0.227_{(\mathrm{fit})}$	$2.122 \pm 0.271_{(\mathrm{stat})} \pm 0.959_{(\mathrm{sys})} \pm 1.157_{(\mathrm{fit})}$	67%
	η	–	–	–
	η/π^0	–		
2.76	π^0	$0.451 \pm 0.008_{(\mathrm{stat})} \pm 0.014_{(\mathrm{sys})} \pm 0.152_{(\mathrm{fit})}$	$1.803 \pm 0.058_{(\mathrm{stat})} \pm 0.352_{(\mathrm{sys})} \pm 0.646_{(\mathrm{fit})}$	59%
	η	$0.647 \pm 0.068_{(\mathrm{stat})} \pm 0.040_{(\mathrm{sys})} \pm 0.140_{(\mathrm{fit})}$	$0.250 \pm 0.050_{(\mathrm{stat})} \pm 0.052_{(\mathrm{sys})} \pm 0.063_{(\mathrm{fit})}$	52%
	η/π^0	$0.139 \pm 0.028_{(\mathrm{stat})} \pm 0.040_{(\mathrm{sys})} \pm 0.061_{(\mathrm{fit})}$		
7	π^0	$0.451 \pm 0.005_{(\mathrm{stat})} \pm 0.022_{(\mathrm{sys})} \pm 0.035_{(\mathrm{fit})}$	$2.632 \pm 0.072_{(\mathrm{stat})} \pm 0.507_{(\mathrm{sys})} \pm 0.250_{(\mathrm{fit})}$	45%
	η	$0.815 \pm 0.047_{(\mathrm{stat})} \pm 0.051_{(\mathrm{sys})} \pm 0.067_{(\mathrm{fit})}$	$0.209 \pm 0.021_{(\mathrm{stat})} \pm 0.047_{(\mathrm{sys})} \pm 0.021_{(\mathrm{fit})}$	31%
	η/π^0	$0.079 \pm 0.008_{(\mathrm{stat})} \pm 0.024_{(\mathrm{sys})} \pm 0.011_{(\mathrm{fit})}$		
8	π^0	$0.431 \pm 0.006_{(\mathrm{stat})} \pm 0.020_{(\mathrm{sys})} \pm 0.012_{(\mathrm{fit})}$	$3.252 \pm 0.128_{(\mathrm{stat})} \pm 0.918_{(\mathrm{sys})} \pm 0.146_{(\mathrm{fit})}$	45%
	η	$0.929 \pm 0.110_{(\mathrm{stat})} \pm 0.126_{(\mathrm{sys})} \pm 0.085_{(\mathrm{fit})}$	$0.164 \pm 0.033_{(\mathrm{stat})} \pm 0.052_{(\mathrm{sys})} \pm 0.023_{(\mathrm{fit})}$	34%
	η/π^0	$0.050 \pm 0.010_{(\mathrm{stat})} \pm 0.022_{(\mathrm{sys})} \pm 0.008_{(\mathrm{fit})}$		

Table 6.4.20: The mean transverse momenta $\langle p_{\mathrm{T}} \rangle$ and integrated yields $\mathrm{d}N/\mathrm{d}y|_{y\approx 0}$ for π^0 and η mesons in pp collisions at $\sqrt{s}$ = 0.9, 2.76 [8], 7 and 8 TeV [4] are summarized. It has to be noted that the uncertainties from the measurements of the inelastic cross sections are not included for the given numbers which can be found in Tab. 4.2.4. Moreover, the integrated η/π^0 ratios are quoted for the different systems.

Within the substantial uncertainties, the expected natural ordering of increasing $\mathrm{d}N/\mathrm{d}y|_{y\approx 0}$ and $\langle p_{\mathrm{T}} \rangle$ for increasing $\sqrt{s}$ is observed since more particles are produced and spectra get harder. Only the determined yields for η meson seem to be in contradiction. However, the uncertainties are significant and according to the global trends that are observed in upcoming Fig. 6.4.43, the measurement at $\sqrt{s}$ = 2.76 TeV tends to give a central value for the yield which seems to be too high while for 8 TeV a too low central value for the yield seems to be obtained.

The following Fig. 6.4.43 summarizes the obtained results for the π^0 and η mesons concerning $\langle p_{\mathrm{T}} \rangle$ and $\mathrm{d}N/\mathrm{d}y|_{y\approx 0}$ for all available $\sqrt{s}$ energies. Furthermore, the results from charged pions $\pi^{\pm}$ and charged kaons $K^{\pm}$ are also superimposed using open markers [252, 262, 269, 270]. To ensure consistency, all integrated yields and $\langle p_{\mathrm{T}} \rangle$ values are obtained using the same method. Due to the current systematic uncertainties especially at low p_{T} and the large extrapolation fractions of the π^0 and η meson spectra with respect to the charged particles, the uncertainties of $\langle p_\mathrm{T}\rangle$ and $\mathrm{d}N/\mathrm{d}y|_{y\,\approx\,0}$ are found to be considerably larger for the neutral mesons. These points also affect the uncertainties of the integrated η/π^0 ratios.

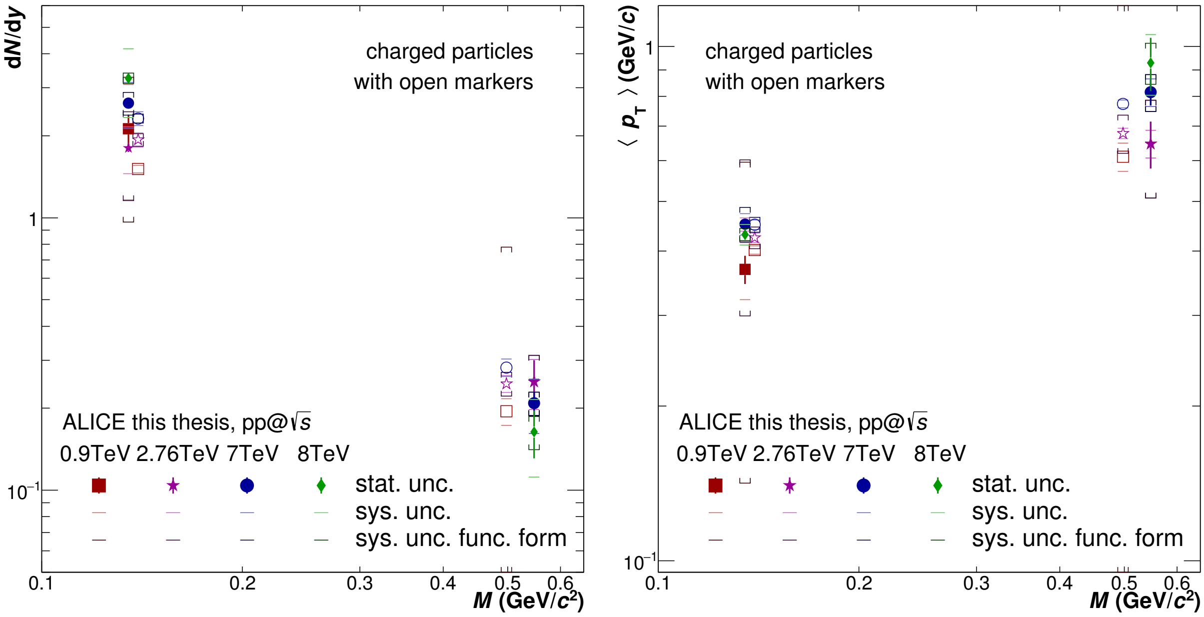

a) b)

Figure 6.4.43: The integrated yields $\mathrm{d}N/\mathrm{d}y|_{y\,\approx\,0}$, a), and the mean transverse momenta $\langle p_\mathrm{T}\rangle$, b), are plotted as a function of particle mass for pp collisions at $\sqrt{s} = 0.9$, 2.76, 7 and 8 TeV. Open markers represent charged particles, whereas full markers stand for neutral particles. Statistical and systematic uncertainties are given in both plots, represented by vertical error bars and colored lines, as well as the systematic uncertainty due to the choice of the fitting function shown in colored brackets.

Some general trends can be clearly deduced from Fig. 6.4.43. The higher the particle mass the more $\mathrm{d}N/\mathrm{d}y|_{y\,\approx\,0}$ decreases. In contrast, $\langle p_\mathrm{T}\rangle$ increases with rising particle mass. Moreover, for increasing $\sqrt{s}$ energy, both $\mathrm{d}N/\mathrm{d}y|_{y\,\approx\,0}$ and $\langle p_\mathrm{T}\rangle$ are found to become larger as well. Hence, it can be stated that the determined $\langle p_\mathrm{T}\rangle$ and $\mathrm{d}N/\mathrm{d}y|_{y\,\approx\,0}$ values for neutral mesons fit the general picture. The comparisons with measurements of $\langle p_\mathrm{T}\rangle$ of charged particles [269] and with results concerning charged-particle multiplicity [270] suggest this statement. Furthermore, all integrated yields quoted in Tab. 6.4.20 are consistent within experimental uncertainties with the results from charged particle measurements [252, 262]. The obtained yields for neutral mesons can be used to further constrain theoretical models describing global properties like the thermal model of particle production [271].

Chapter 7

Direct Photon Measurements

This chapter presents measurements of inclusive and direct photon production in pp collisions at $\sqrt{s} = 8\,\mathrm{TeV}$. The p_{T}-differential inclusive photon spectrum is measured by exploiting the PCM and the EMCal methods, see Sec. 5.1 and Sec. 5.2 for the respective reconstruction principles of photon candidates. From this measurement, the direct photon spectra are obtained according to the subtraction method introduced in Eq. 2.3.17, for which a precise knowledge of R_γ, see Eq. 2.3.18, is needed. In this context, a detailed knowledge about the decay photon contamination is required which, in fact, dominate the inclusive photon spectrum. Therefore, Sec. 7.1 introduces the decay photon simulation which is necessary to estimate the amount of decay photons as a function of p_{T} and to perform secondary photon corrections for photons originating from weak decays and material interactions. Such MC based corrections to the photon sample but also the estimation of detector acceptances and reconstruction efficiencies are summarized and elaborated in Sec. 7.2. The systematic uncertainties of the measurements are described in Sec. 7.2.2. Finally, the obtained results are summarized in Sec. 7.2.4. The presented photon measurements are published by ALICE [6, 7] which further includes the results in pp collisions at $\sqrt{s} = 2.76\,\mathrm{TeV}$ [219]. The chapter concludes with a short outlook on the π^0-tagging technique, see Sec. 7.3, which is a promising method to further reduce the experimental uncertainties in the future.

7.1 Decay Photon Simulation for pp Collisions at $\sqrt{s} = 8\,\mathrm{TeV}$

The main experimental challenge is to distinguish direct photons from the large background of decay photons which originate from particle decays and, in fact, represent the dominant contribution to the total amount of inclusive photons. For this purpose, the decay photon spectrum needs to be well known to the best possible precision since it is a key ingredient for the measurement of R_γ, defined in Eq. 2.3.18. Because MC event generators do not match the required precision in this context, the decay photon spectra are estimated using a particle decay simulation. This simulation is anchored to measured particle spectra and is commonly also known as “cocktail simulation”. The full decay chain is simulated for all input particles which are unstable. Hence, the simulation is also used to estimate the secondary π^0 spectra from weakly decaying particles, see Sec. 6.2.3 and Sec. 6.3.1 for the relevant information in this context. For the photon measurements, on the other hand, the simulation is used to estimate the amount of secondary photons from weak decays and to correct for them analog to the corresponding meson measurements. Most importantly, it is of main relevance for the extraction of the direct photon spectrum due to its connection via R_γ as already implied.

particle	mass (MeV/c^2)	decay channels	branching ratio	C_{m_T}	references
π^0	134.98	$\gamma\gamma$	9.882 E-01	–	this thesis [4]
		$e^+e^-\gamma$	1.174 E-02		
K^0_S	497.61	$\pi^0\pi^0$	3.065 E-01	–	interpolation [252, 253, 262, 272] $K^\pm$ proxy
		$\pi^+\pi^-\gamma$	1.787 E-03		
K^0_L	497.61	$\pi^0\pi^0\pi^0$	1.946 E-01	–	interpolation [252, 253, 262, 272] $K^\pm$ proxy
		$\pi^+\pi^-\pi^0$	1.250 E-01		
		$\pi^\pm e^\mp\nu\gamma$	3.988 E-03		
		$\pi^0\pi^0$	8.630 E-04		
		$\gamma\gamma$	5.500 E-04		
		$\pi^\pm\mu^\mp\nu\gamma$	4.920 E-04		
		$\pi^+\pi^-\gamma$	4.200 E-05		
η	547.85	$\gamma\gamma$	3.941 E-01	–	this thesis [4]
		$\pi^+\pi^-\gamma$	4.220 E-02		
		$e^+e^-\gamma$	6.899 E-03		
		$\mu^+\mu^-\gamma$	3.090 E-04		
		$\pi^0\gamma\gamma$	2.560 E-04		
ρ^0	775.49	$\pi^+\pi^-\gamma$	9.900 E-03	1.0±0.2	m_T scaling from π^0
		$\pi^0\gamma$	6.000 E-04		
		$\eta\gamma$	4.000 E-04		
		$\pi^0\pi^0\gamma$	4.500 E-05		
ρ^+	775.49	$\pi^+\gamma$	4.500 E-04	1.0±0.2	same as for ρ^0
ρ^-	775.49	$\pi^-\gamma$	4.500 E-04		
ω	782.65	$\pi^0\gamma$	8.350 E-02	0.85±0.10	m_T scaling from π^0
		$\eta\gamma$	4.600 E-04		
		$\pi^0\pi^0\gamma$	7.000 E-05		
p	938.27	–	–	–	interpolation [252, 262, 272]
η'	957.66	$\rho^0\gamma$	2.908 E-01	0.4±0.2	m_T scaling from π^0
		$\omega\gamma$	2.746 E-02		
		$\gamma\gamma$	2.198 E-02		
		$\mu^+\mu^-\gamma$	1.080 E-04		
ϕ	1019.46	$\eta\gamma$	1.310 E-02	–	interpolation [272–274]
		$\pi^0\gamma$	1.273 E-03		
		$\pi^0\pi^0\gamma$	1.130 E-04		
		$\pi^0\eta\gamma$	7.300 E-05		
		$\eta'\gamma$	6.300 E-05		
		$\pi^+\pi^-\gamma$	4.100 E-05		
		$\mu^+\mu^-\gamma$	1.400 E-05		
Λ	1115.68	nπ^0	3.580 E-01	–	interpolation [252, 253, 272]
		nγ	8.400 E-04		
Σ^0	1192.64	$\Lambda\gamma$	1.000 E+00	0.49±0.0245	m_T scaling from p
Δ^0	1232.00	nγ	6.000 E-03	1.0±0.5	m_T scaling from p
Δ^+	1232.00	pγ	6.000 E-03		

Table 7.1.1: List of input particles for the decay photon simulation including references.

The particle decay simulation is based on the PYTHIA 6.4 particle decayer [79] which performs a random generation of mother particles uniformly distributed in the rapidity range $|y| < 1.0$, in full azimuth $0 \leq \varphi < 2\pi$ and in the transverse momentum range $0 \leq p_{\mathrm{T}} \leq 50\,\mathrm{GeV}/c$. Subsequently, the respective particle decays are simulated taking into account their full decay kinematics. The parameterizations of the invariant yields of the respective mother particles as a function of p_{T} are utilized to apply proper weights in order to obtain the correct particle abundances in the generator level simulation. An overview of all input particles used for the decay photon simulation is given in Tab. 7.1.1 which lists the relevant mesons and baryons according to their rest masses. For each particle, the relevant decay channels are given with the corresponding branching ratios. Furthermore, references are given for each case indicating if the respective particle spectrum is measured by ALICE, interpolated from available measurements at different $\sqrt{s}$ energies or obtained via m_{T} scaling.

The dominant contributions to the total amount of decay photons are given by decays of π^0 and η mesons. Therefore, it is crucial to have as precise measurements as possible available for both meson production cross sections. For the particle decay simulation performed for pp collisions at $\sqrt{s} = 8$ TeV, the π^0 and η measurements reported in this thesis are used as input, see Chap. 6 or Refs. [4, 5], providing a combination of up to four different reconstruction methods measuring the production cross section of each meson. However, besides the π^0 and η meson spectra reported in this thesis, no further ALICE measurement of a relevant particle spectrum in pp collisions at $\sqrt{s} = 8$ TeV was available in coincidence with this analysis. Hence, the p_{T}-differential cross sections of $K^{\pm}$, ϕ, Λ and p production in pp collisions at $\sqrt{s} = 8$ TeV are obtained by an interpolation procedure as indicated in Tab. 7.1.1 which uses the respective measured spectra at $\sqrt{s} = 2.76$, 7 and 13 TeV [252, 253, 262, 272–274] as input. In this context, the neutral kaons K^0_S and K^0_L, representing relevant sources of secondary photons, are approximated by the average of the charged kaon $K^{\pm}$ measurements for which a better precision and p_{T} coverage is available in comparison. The interpolation is performed on a bin-by-bin basis in p_{T} assuming a power law evolution of the respective particle cross sections with increasing center of mass energies. For the remaining particles listed in Tab. 7.1.1 for which no measurements are available, the spectra are obtained via m_{T} scaling. For that purpose, the π^0 parameterization is used as a basis B to estimate the meson spectra, whereas the p parameterization is used for the baryons. Therefore, the proton is listed in Tab. 7.1.1 as well although it is evidentially a stable particle. The m_{T} scaling factors, $C^X_{m_{\mathrm{T}}} = (\mathrm{d}N_X/\mathrm{d}m_{\mathrm{T}})/(\mathrm{d}N_B/\mathrm{d}m_{\mathrm{T}})$, for each particle X at high p_{T} are derived from the respective spectra in PYTHIA which are also given in Tab. 7.1.1. The known incapability of m_{T} scaling regarding the description of spectra at low p_{T}, see Sec. 6.4 or Refs. [4, 265], can be neglected because the m_{T} scaled particles only contribute with a tiny fraction to the total yield of decay photons as it can be deduced from the upcoming Fig. 7.1.3. This m_{T} scaling limitation is nevertheless considered in the determination of systematic uncertainties, see Sec. 7.2.2, for which the respective factors $C_{m_{\mathrm{T}}}$ are varied within the given intervals.

The measured and interpolated p_{T}-differential particle spectra are parametrized using their statistical uncertainties by fitting a modified Hagedorn function, see Eq. 2.3.14, multiplied by p_{T}. These parameterizations are then used as an input for the generation of the decay photon simulation. In this context, a dedicated decay photon simulation is performed for each π^0 reconstruction method; PCM, EMC and PCM-EMCal, for which the individual π^0 spectra enter that are exclusively measured with the corresponding reconstruction method instead of using the combined π^0 spectrum. This approach is needed to allow a cancellation of systematic uncertainties for the R_{γ} which is defined in Eq. 2.3.18. The following Fig. 7.1.1a shows an example of a modified Hagedorn fit to the measured π^0 spectrum using PCM-EMCal in MB triggered events. Furthermore, ratios of data and the fit result are computed and visualized in the bottom part of the figure.

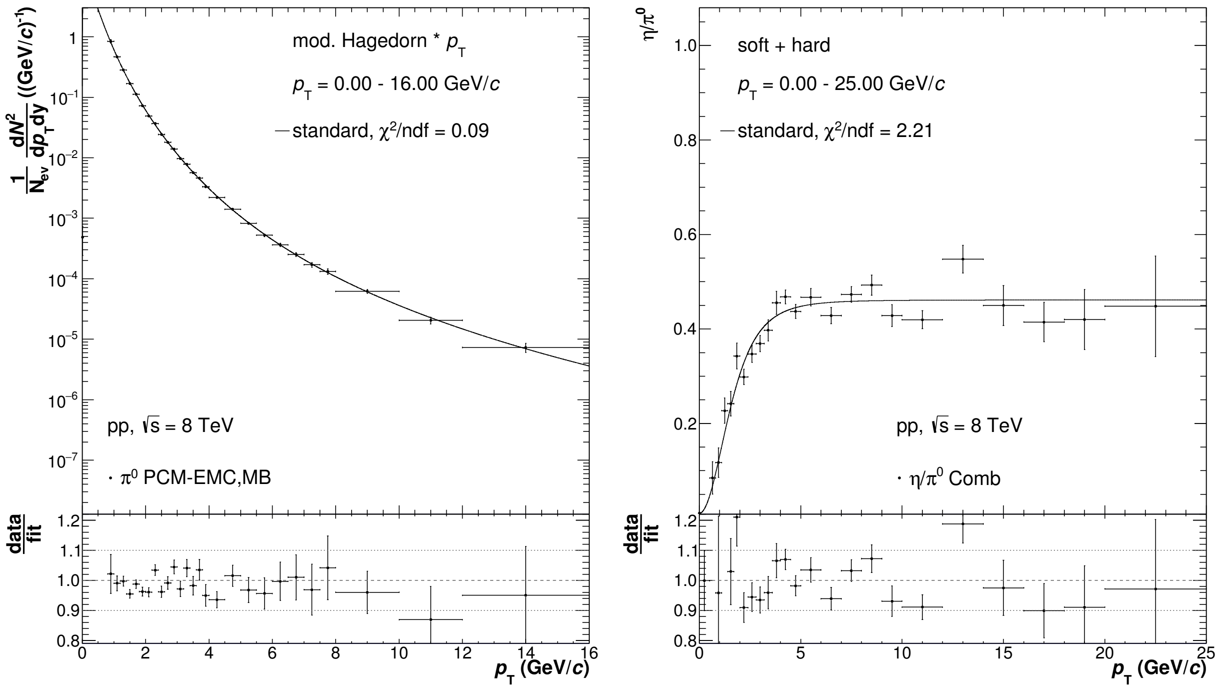

a) b)

Figure 7.1.1: Parameterizations of the invariant π^0 yield measured with PCM-EMCal in MB triggered events and the combined η/π^0 ratio for which statistical uncertainties are used. Further example parameterizations are given in Fig. B.3.30.

The parameterization of the combined η/π^0 ratio for pp at $\sqrt{s} = 8\,\text{TeV}$ is shown in Fig. 7.1.1b, from which a more reliable parameterization for the η meson yield up to highest p_T is proven to be found. The η/π^0 ratio is fitted with an empirical function that contains two separate contributions from soft and hard processes [265]. It is approximated by the following formula:

$$\frac{\eta}{\pi^0}(p_\mathrm{T}) = \frac{A \cdot \exp\left(\frac{\beta p_\mathrm{T} - m_\mathrm{T}^{\eta}}{T\sqrt{1-\beta^2}}\right) + C \cdot B \cdot \left(1 + \left(\frac{p_\mathrm{T}}{p_0}\right)^2\right)^{-n}}{\exp\left(\frac{\beta p_\mathrm{T} - m_\mathrm{T}^{\pi^0}}{T\sqrt{1-\beta^2}}\right) + B \cdot \left(1 + \left(\frac{p_\mathrm{T}}{p_0}\right)^2\right)^{-n}}, \tag{7.1.1}$$

where B is the relative normalization between the soft and hard part of the parameterization. The soft part is based on a blast wave inspired function [275] with radial flow velocity β and kinetic freeze-out temperature T. On the other hand, the hard part is described by the two power law like terms entering in numerator and denominator. The variable C is the constant ratio between the two particle species which is approached at high p_T and A, p_0 as well as n are additional free parameters. The parametrization of the η spectrum is then obtained by multiplying the parametriations of the η/π^0 ratio and the π^0. Taken together, all input parametrizations are found to describe the measurements within a maximum of $\approx 10\,\%$ deviation over the full p_T range.

The spectra of all mesons and baryons entering the particle decay simulation are summarized in Fig. 7.1.2a which are either measured, interpolated or m_{T} scaled. The ratios of the respective spectra to the π^0 reference are compiled in Fig. 7.1.2b. Both figures exemplify the usage of the π^0 spectrum provided by the PCM-EMCal reconstruction method. Using the EMCal method, the corresponding plots are found to be very similar, basically indistinguishable. By construction, the particle ratios of mesons to the π^0 generally tend to be flat for high p_{T}. A significant drop of the ratio is observed for the baryon to π^0 ratios since the scaling is performed based on the p spectra.

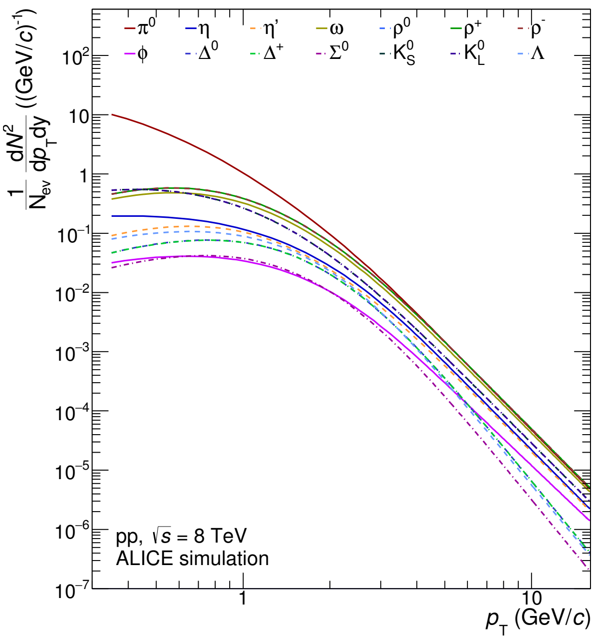

a)

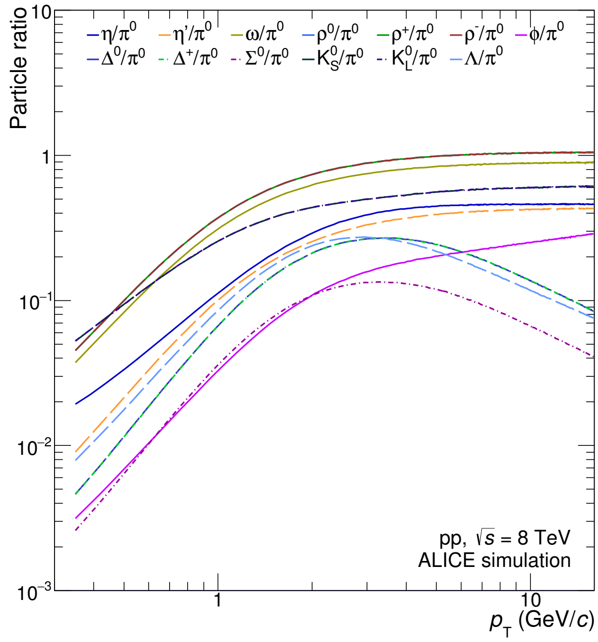

b)

Figure 7.1.2: a) The input spectra of all relevant mesons and baryons, denoted mother particles in this context, for the decay photon simulation using the π^0 parameterization provided by the PCM-EMCal method for pp collisions at $\sqrt{s}$ = 8 TeV. b) The ratios of the respective mother particle spectra to the π^0 reference spectrum.

After generating the decay photon cocktail, only such decay photons are kept that fulfill the condition $|y| < 0.9$ in order to match the hadron rapidity range used for the corresponding analysis. The decay photon spectra, which are obtained for the different mother particles, are shown in Fig. 7.1.3a. The contributions of each individual decay photon source to the total amount of decay photons from the simulation are shown in Fig. 7.1.3b.

The dominant contribution of decay photons originates from π^0 decays with about $\sim 85\,\%$ of the total amount of such photons at high p_{T}. The second highest contribution stems from η meson decays which account for a fraction of approximately $\sim 10\,\%$ at high p_{T}. Moreover, the fraction of decay photons from ω and η' mesons are below $\sim 3\,\%$ and $\sim 1.5\,\%$ respectively. All remaining sources of decay photons are actually negligible as shown in Fig. 7.1.3b. This holds in very good approximation as the sensitivity limit of the π^0 input measurements is reached, regarding their total uncertainties in comparison with the expected photon signals stemming from all these remaining mother particles.

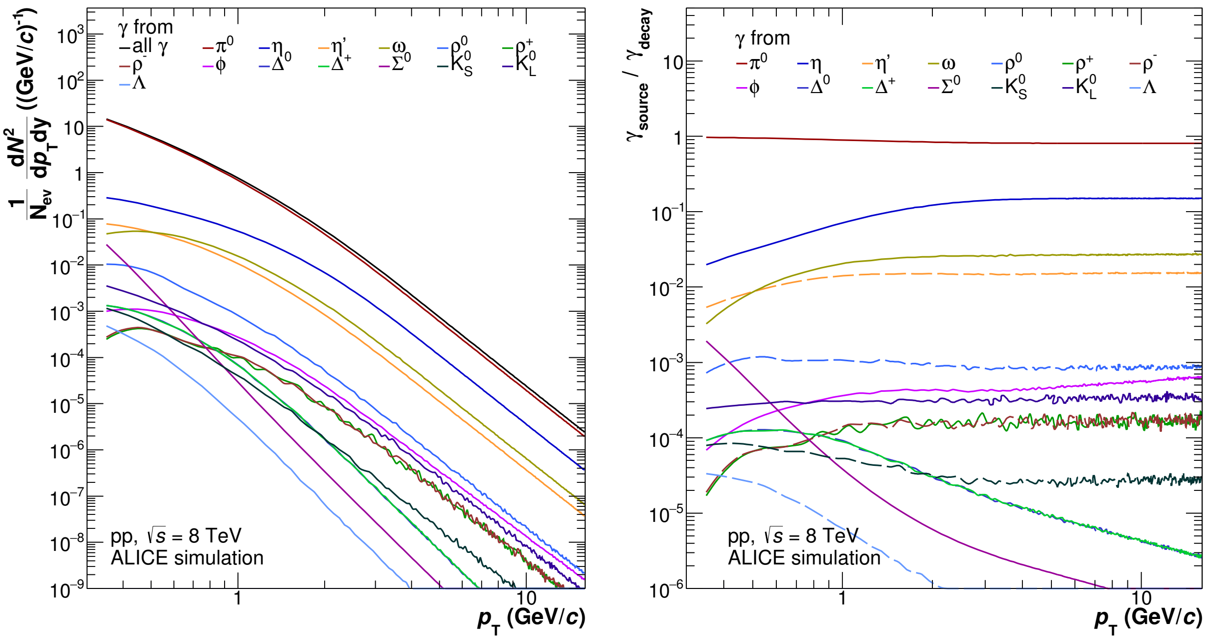

a) b)

Figure 7.1.3: a) The decay photon spectra, subdivided into the different sources, which are obtained from the decay photon simulation using the mother particle spectra shown in Fig. 7.1.2 as input. b) The contributions of the decay photons from the different mother particles, as indicated in the legend, with respect to the total amount of decay photons as a function of photon p_{T}.

7.2 Inclusive & Direct Photon Measurements in pp Collisions at $\sqrt{s}$ = 8 TeV

The results concerning inclusive and direct production in pp collisions at $\sqrt{s} = 8\,\mathrm{TeV}$ presented in this thesis are published by ALICE [6, 7]. An overview of the different photon reconstruction methods used in that publication is given in Tab. 7.2.2 which also lists the covered p_{T} intervals for each method and the subsequent combination of all measurements.

reconstruction method	available p_{T} reach (GeV/c) $Y_{\gamma_{\mathrm{incl}}}$	R_γ	reference
PCM	0.3 – 12.0	0.3 – 12.0	MSc thesis by N. Schmidt [244]
EMCal	1.2 – 16.0	1.2 – 16.0	this thesis
PCM-EMCal	0.8 – 16.0	0.8 – 16.0	this thesis
combination	0.3 – 16.0	0.3 – 16.0	published by ALICE [6]

Table 7.2.2: A summary of the available measurements of the invariant cross sections of inclusive $Y_{\gamma_{\mathrm{incl}}}$ and direct photon $Y_{\gamma_{\mathrm{dir}}}$ production in pp collisions at $\sqrt{s} = 8\,\mathrm{TeV}$. To determine $Y_{\gamma_{\mathrm{dir}}}$, the measurement of R_γ is also carried out. Only MB event triggers are consulted for the reported measurements since the low p_{T} region is of interest for $Y_{\gamma_{\mathrm{dir}}}$ production. The PCM measurement is provided by Nicolas Schmidt [244].

The PCM-EMCal method uses PCM photons as input for $Y_{\gamma_{\text{incl}}}$ and $Y_{\gamma_{\text{dir}}}$, also denoted as PCM* in the following, for which the applied selection criteria can be found in Tab. 5.1.1. Compared to the PCM method, slightly different photon selection criteria are utilized in this case. The hybrid method uses a wider cut on the electron/positron energy loss hypothesis of $-4 < n\sigma_e < 5$ compared to $-3 < n\sigma_e < 5$ for the PCM. Moreover, the p_{T} restriction of the charged pion $\mathrm{d}E/\mathrm{d}x$ cut is loosened, $n\sigma_\pi > 1$ for $p > 0.4$ GeV/c, which is only performed up to $p < 3.5\,\text{GeV}/c$ for the PCM. Furthermore, the respective lists of good runs do not coincide entirely. Hence, statistical and systematic uncertainties are largely correlated between the PCM and PCM* measurements. Although the combination of the PCM and PCM* measurements does not improve the uncertainties a lot for $Y_{\gamma_{\text{incl}}}$, the hybrid method, which is using the PCM* sample, provides a significant improvement with regard to the R_γ measurement because of the additional independent measurement of the π^0 contributing significantly to the corresponding uncertainties of R_γ.

The invariant differential cross section $Y_{\gamma_{\text{incl}}}$ of inclusive photon production, $pp \rightarrow \gamma + X$, at mid-rapidity is obtained via:

$$E\frac{\mathrm{d}^3\sigma^{pp\rightarrow\gamma+X}}{\mathrm{d}p^3} = \frac{1}{2\pi p_{\text{T}}}\frac{1}{\mathscr{L}_{\text{int}}}\frac{1}{\varepsilon_{\text{rec}}}\frac{\varepsilon_{\text{pur}}}{P_{\text{conv}}}\frac{C_{\text{pileup}}\cdot N^\gamma - N^\gamma_{\text{sec}}}{\Delta y \Delta p_{\text{T}}}, \tag{7.2.2}$$

where, besides the factor $(2\pi p_{\text{T}})^{-1}$, the respective experimental quantities to be determined are the following:

- $\mathscr{L}_{\text{int}}$ stands for the integrated luminosity, see Tab. 4.2.5;
- ε_{rec} is the photon reconstruction efficiency;
- ε_{pur} represents the photon purity;
- P_{conv} is the photon conversion probability in case of the PCM method, otherwise it is set to $P_{\text{conv}} = 1$ for the inclusive photon measurement using EMCal;
- C_{pileup} represents the fraction of out-of-bunch pileup which is estimated for the PCM case, otherwise it is set to $F_{\text{pileup}} = 1$ for the measurement using EMCal;
- N^γ is the raw photon yield for a given bin width in rapidity and transverse momentum, $\Delta y \Delta p_{\text{T}}$;
- N^γ_{sec} stands for the estimated amount of secondary photons from weak decays of K^0_S, K^0_L, Λ and material interactions.

Once the inclusive photon spectrum is determined, the direct photon spectrum $Y_{\gamma_{\text{dir}}}$ is obtained via the subtraction method introduced in Eq. 2.3.17: $\gamma_{\text{dir}} = \left(1 - R_\gamma^{-1}\right)\cdot\gamma_{\text{inc}}$. For this purpose, a precise knowledge of R_γ is needed which is the ratio of the inclusive and decay photon yields and, according to Eq. 2.3.18, it can be written as: $R_\gamma = \left(\gamma_{\text{inc}}/\pi^0\right)_{\text{meas}} / \left(\gamma_{\text{dec}}/\pi^0_{\text{param}}\right)_{\text{sim}}$. It is also referred to as double ratio in common speech. As input, the measured inclusive photon spectrum and the according π^0 measurement are needed. Furthermore, the photon decay spectrum and the parameterized π^0 spectrum have to be provided exploiting the decay photon simulation, see Sec. 7.1 for details. In this context, the double ratio is computed using the individual inclusive photon and π^0 spectra provided by the same reconstruction methods and the decay photon simulation based on parameterizations of the same π^0 spectrum. Like this, the cancellation of systematic uncertainties is maximized and, moreover, possible biases affecting both photon and meson measurements can be avoided.

7.2.1 Signal Extraction & MC Corrections of Raw Spectra

The raw photon yield N^{γ} is extracted for each p_{T} bin defined in the analysis by applying the respective photon selection criteria, summarized in Tab. 5.1.1 for the PCM* and Tab. 5.2.2 for the EMCal, on the inclusive set of reconstructed photon candidates for each method. The invariant cross section of inclusive photon production is then obtained by applying the MC based corrections to those extracted raw yields, involving the respective terms introduced in the previous Sec. 7.2, which will be elaborated in detail in the following. The MC based corrections are evaluated using the same MC simulations as for the neutral meson measurements, see Chap. 4 and Chap. 6. For pp collisions at $\sqrt{s} = 8\,\mathrm{TeV}$, MC simulations using the PYTHIA 8 and PHOJET event generators are available. The subsequent step of propagating the particles through the ALICE detector is taken over by GEANT3. The same reconstruction algorithms and photon selection criteria are applied for data and MC simulations. Both PYTHIA and PHOJET MC productions are found to be consistent for the correction step and, hence, are combined to reduce statistical uncertainties.

Whereas events showing in-bunch pileup can be reliably removed using the SPD pileup detection algorithms, see Sec. 4.2, out-of-bunch pileup is caused by multiple primary interactions occurring closely in time. Due to the high ion drift times within the TPC gas volume, see Sec. 3.2.1, the outgoing particles produced in the different interactions overlap within the detector's drift volume. Hence, the occurrence of out-of-bunch pileup is linked with the delivered luminosity during data taking as well as the actual filling scheme and present bunch spacing in the LHC. Therefore, the presence of a high luminosity environment requires an out-of-bunch pileup correction if solely TPC information is used which applies to reconstructing photon candidates using PCM. In contrast, once a detector with a short readout time is involved which is quick enough to resolve the respective bunch crossings, the ITS or the EMCal for example, there is no need for such a correction. The out-of-bunch pileup correction for the PCM method is based on the $\mathrm{DCA_z}$ information of photon candidates which are extracted for each p_{T} bin used in the analysis. In this context, PCM photons are separated into three categories depending on the readout time of the different detectors involved during the reconstruction of its both daughter particles:

1) both conversion daughters are reconstructed solely using TPC information which is valid for all photon candidates beyond $R_{\mathrm{conv}} \geq 50\,\mathrm{cm}$;

2) one of the conversion daughters is associated with at least two recorded hits in the different ITS layers;

3) both daughters produced at least two hits in the ITS layers.

The largest amount of photon candidates belongs to category 1), whereas category 2) shows the least amount of candidates. This observation is expected as it is very unlikely for one daughter track to generate multiple ITS hits while the other one is completely missed by the ITS coverage. In fact, such a case may occur from time to time due to dead areas or shared ITS clusters between both daughters. Therefore, the $\mathrm{DCA_z}$ distributions are plotted for category 1) and 3) in Fig. 7.2.4 which shows example $\mathrm{DCA_z}$ distributions for three different p_{T} bins.

In Fig. 7.2.4, much broader $\mathrm{DCA_z}$ distributions, exhibiting additional underlying contributions, can be observed for category 1) compared to 3). The underlying distribution is produced if reconstructed photon candidates are associated to the wrong primary vertex which is being displaced with respect to the true primary vertex, from which the photon actually originated. Due

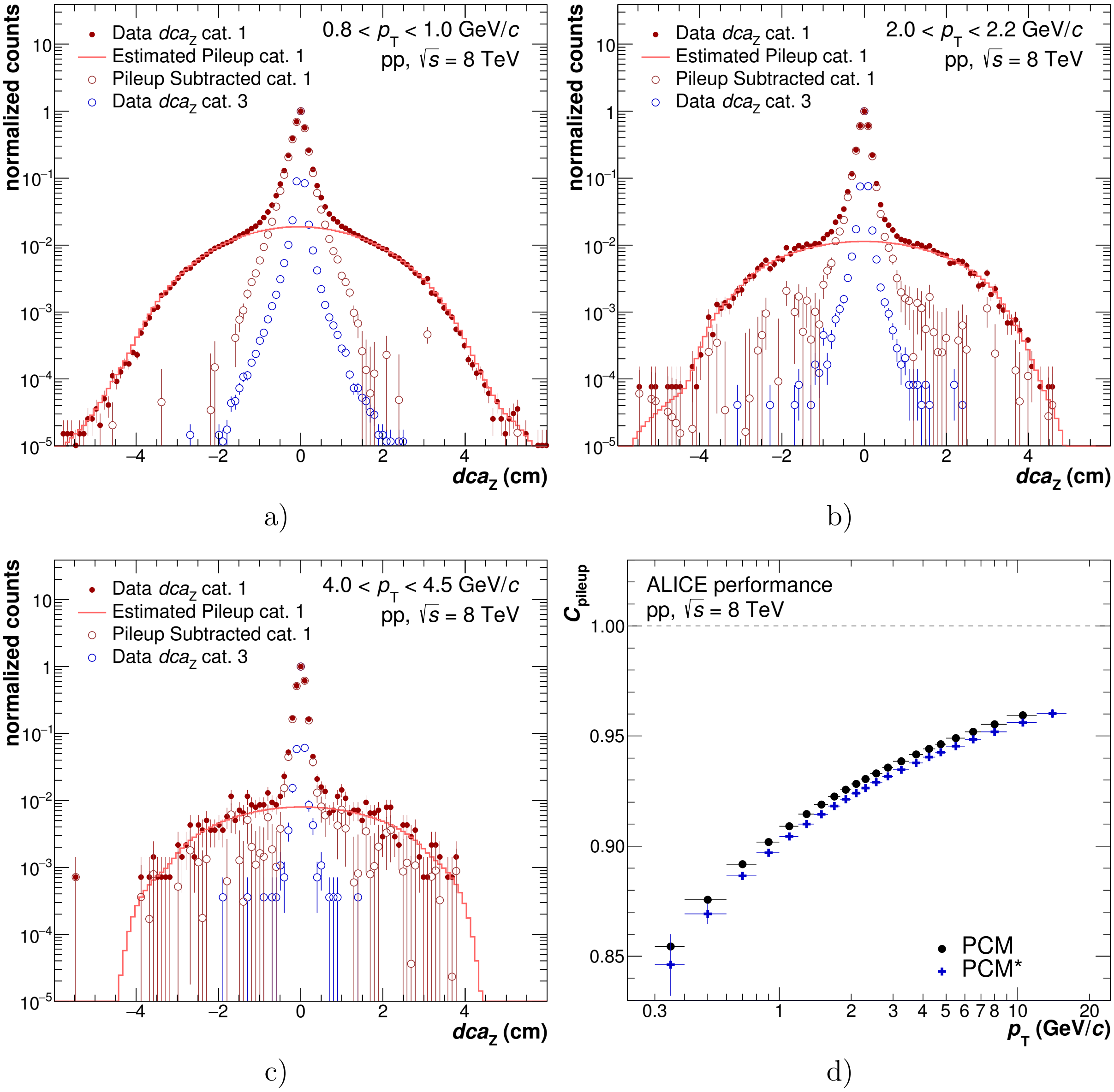

Figure 7.2.4: Selected $\mathrm{DCA_z}$ distributions for photon candidates with respect to the reconstructed primary vertex are shown in a), b) and c) for different p_{T} intervals for pp, $\sqrt{s} = 8\,\mathrm{TeV}$. The underlying distributions, estimated by the red curves, are caused by photons originating from out-of-bunch pileup. b) The obtained pileup correction factors C_{pileup} for both PCM and PCM* methods as a function of p_{T}.

to the fast readout of the ITS, category 3) is not expected to include out-of-bunch pileup which is reasonably demonstrated by the narrow $\mathrm{DCA_z}$ distributions in this case. Hence, the additional contribution in category 1) caused by out-of-bunch pileup is estimated using a background estimator implemented in the ROOT framework named "TH1::ShowBackground". This estimator uses an iterative procedure to subsequently exclude the actual peak region and estimate the remaining background. A total of seven iterations are used in this analysis, a number that is varied for systematic studies, see Sec. 7.2.2. This method is proven to give a better estimate of the background than a Gaussian fit or any other related functional terms. As shown in Fig. 7.2.4, the estimator is capable of describing the background for which remaining differences can be associated by the reduced tracking performance for the case of solely using TPC information. The pileup correction factor C_{pileup} is calculated by the following formula:

$$C_{\mathrm{pileup}}(p_{\mathrm{T}}) = \frac{\gamma^{\mathrm{cat\ 1}}_{\mathrm{subtracted}}(p_{\mathrm{T}}) + \gamma^{\mathrm{cat\ 2}}_{\mathrm{subtracted}}(p_{\mathrm{T}}) + \gamma^{\mathrm{cat\ 3}}_{\mathrm{all}}(p_{\mathrm{T}})}{\gamma^{\mathrm{cat\ 1}}_{\mathrm{all}}(p_{\mathrm{T}}) + \gamma^{\mathrm{cat\ 2}}_{\mathrm{all}}(p_{\mathrm{T}}) + \gamma^{\mathrm{cat\ 3}}_{\mathrm{all}}(p_{\mathrm{T}})}, \tag{7.2.3}$$

where $\gamma^{\mathrm{cat\ X}}_{\mathrm{all}}$ represents all photons associated to the respective category X, represented by full red markers in Fig. 7.2.4 a) to c), as a function of reconstructed photon p_{T}. The integrated number of photons surviving the out-of-bunch correction is described by $\gamma^{\mathrm{cat\ X}}_{\mathrm{subtracted}}$ for each category X, visualized by open red markers in Fig. 7.2.4. The obtained out-of-bunch pileup correction factors for the two PCM-based measurements are shown in Fig. 7.2.4d, emphasizing the importance of this correction especially at low p_{T} where it reaches up to $\sim 15\,\%$. The offset between both methods is due to the slightly different photon selection criteria applied.

For the inclusive photon measurements, contributions of secondary photons from weak decays and hadronic interactions are estimated and removed analog to Sec. 6.2.3 for the measurement of π^0 mesons. The majority of photons from weak decays originate from K^0_S but also contributions from K^0_L and Λ are considered. The decay photon simulation described in Sec. 7.1 is used to estimate the invariant secondary photon yields which originate from the weakly decaying mother particles. The respective reconstruction efficiencies for the secondary photons from the different sources are determined using the full ALICE GEANT3 MC simulations. Combining the invariant yields and the determined reconstruction efficiencies, the estimated raw yields of secondary photons are then subtracted from the inclusive photon raw yields for each p_{T} bin. The correction for secondary photons, which are produced in hadronic interactions with the detector material, are purely obtained from true MC information. All effective corrections for the different sources of secondary photons are summarized in Fig. 7.2.5. The term 'Rest' denotes the totality of photons produced from material interactions as well as from all other particles classified as secondary interactions. However, the material interactions represent far more than 99 % in this category. The effective corrections for secondary photons are of the order of $1.0-4.0\,\%$ for K^0_S, $\lesssim 0.4\,\%$ for K^0_L, $\lesssim 0.08\,\%$ for Λ and $0.1-4.0\,\%$ for material interactions depending on p_{T} and the respective method used to reconstruct photons. The different magnitude of the corrections for the EMCal can be attributed to the larger amount of material in front of the calorimeter and the worse momentum resolution for these photons.

The photon purity is defined as the fraction of true photons contained in the photon sample which passed all selection criteria. In other words, it is a measure of the remaining contamination, also denoted background, of the photon sample. The determination of the purity $\varepsilon_{\mathrm{pur}}$ of the photon sample is fully based on MC simulations using validated true MC information. It is computed after the estimated number of validated true secondaries $\gamma^{\mathrm{true}}_{\mathrm{secondary}}$ are removed from the reconstructed photon sample γ^{all}. The definition of $\varepsilon_{\mathrm{pur}}$ is as follows:

$$\varepsilon_{\mathrm{pur}}(p_{\mathrm{T}}) = \frac{\gamma^{\mathrm{true}}_{\mathrm{primary}}(p_{\mathrm{T}})}{\gamma^{\mathrm{all}}(p_{\mathrm{T}}) - \gamma^{\mathrm{true}}_{\mathrm{secondary}}(p_{\mathrm{T}})}, \tag{7.2.4}$$

where $\gamma^{\mathrm{true}}_{\mathrm{primary}}$ stands for the number of validated true primary photons reconstructed in the photon sample. The applied photon selection criteria are chosen to remove as much contamination as feasible, still maintaining an efficiency as large as possible for the reconstruction of

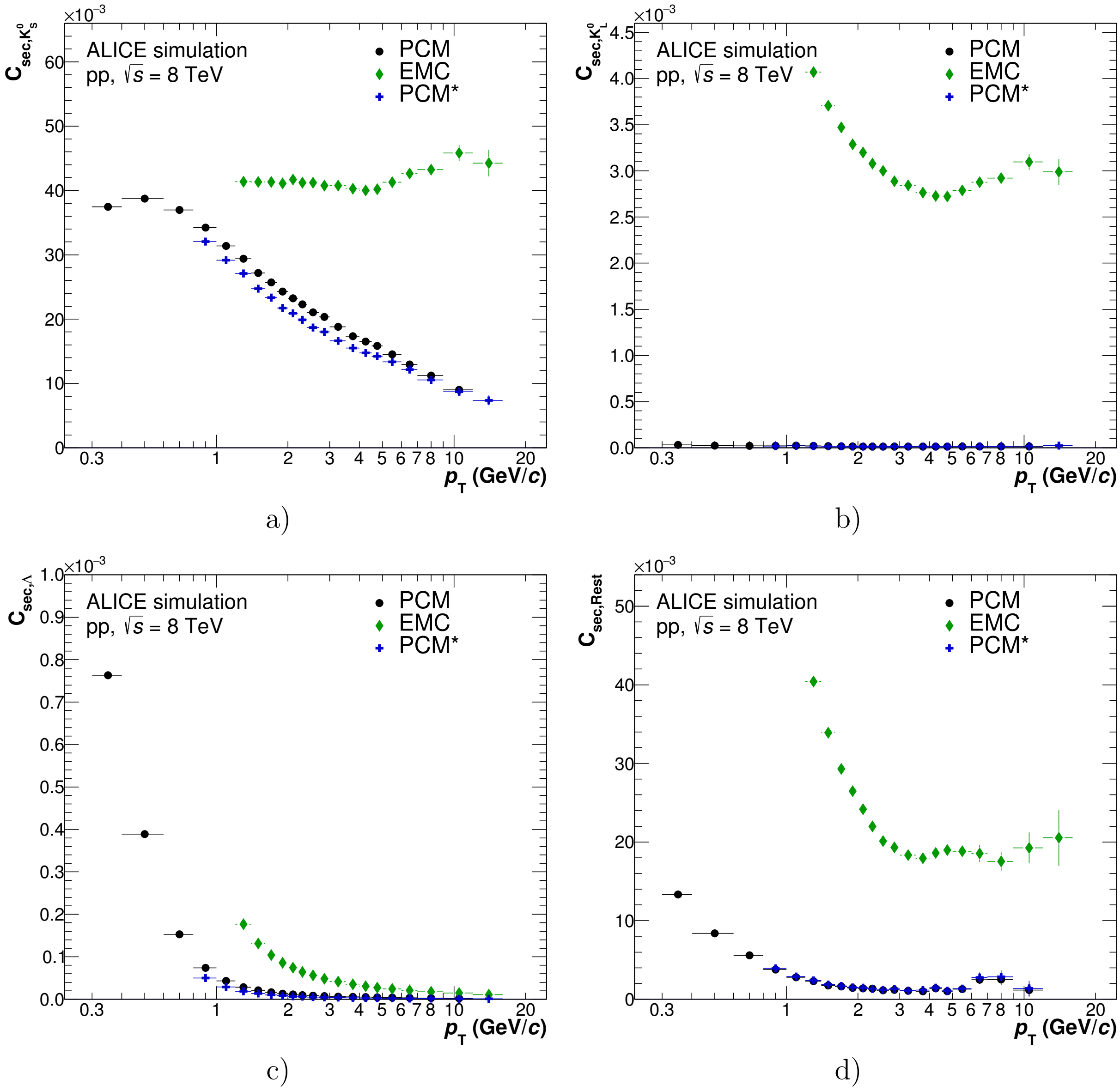

Figure 7.2.5: Effective corrections concerning secondary photons originating from K^0_S, K^0_L and Λ decays as well as from the 'Rest', which mainly includes secondaries from hadronic interactions with the detector material of ALICE, are summarized for the methods PCM, PCM* and EMCal from a) to d). The fractions of secondary photons from the different sources are plotted as a function of photon p_{T}.

true primary photons. The more strict cuts are applied, the higher purities can be achieved in general. Hence, the interplay of these effects disfavors too loose selection criteria as well as too strict selections, because in either way too much reliance would be imposed on the MC simulations which would need to describe the data almost perfectly in these cases.

Using the true MC information, the contamination of the reconstructed photon samples is separated into the different contributions which is shown in Fig. 7.2.6a for the PCM* and in Fig. 7.2.6b for the EMCal method. According to the figure labels, the fractions C_{i} of true identified background components with respect to the total number of true primary photons are plotted as a function of photon p_{T}. Like this, the purity can be estimated and the different sources of the background photons can be identified using true MC information. The purities $\varepsilon_{\mathrm{pur}}$, which visualize the sum of the respective background components subtracted from unity, are shown in Fig. 7.2.6c for the three methods PCM, PCM* and EMCal.

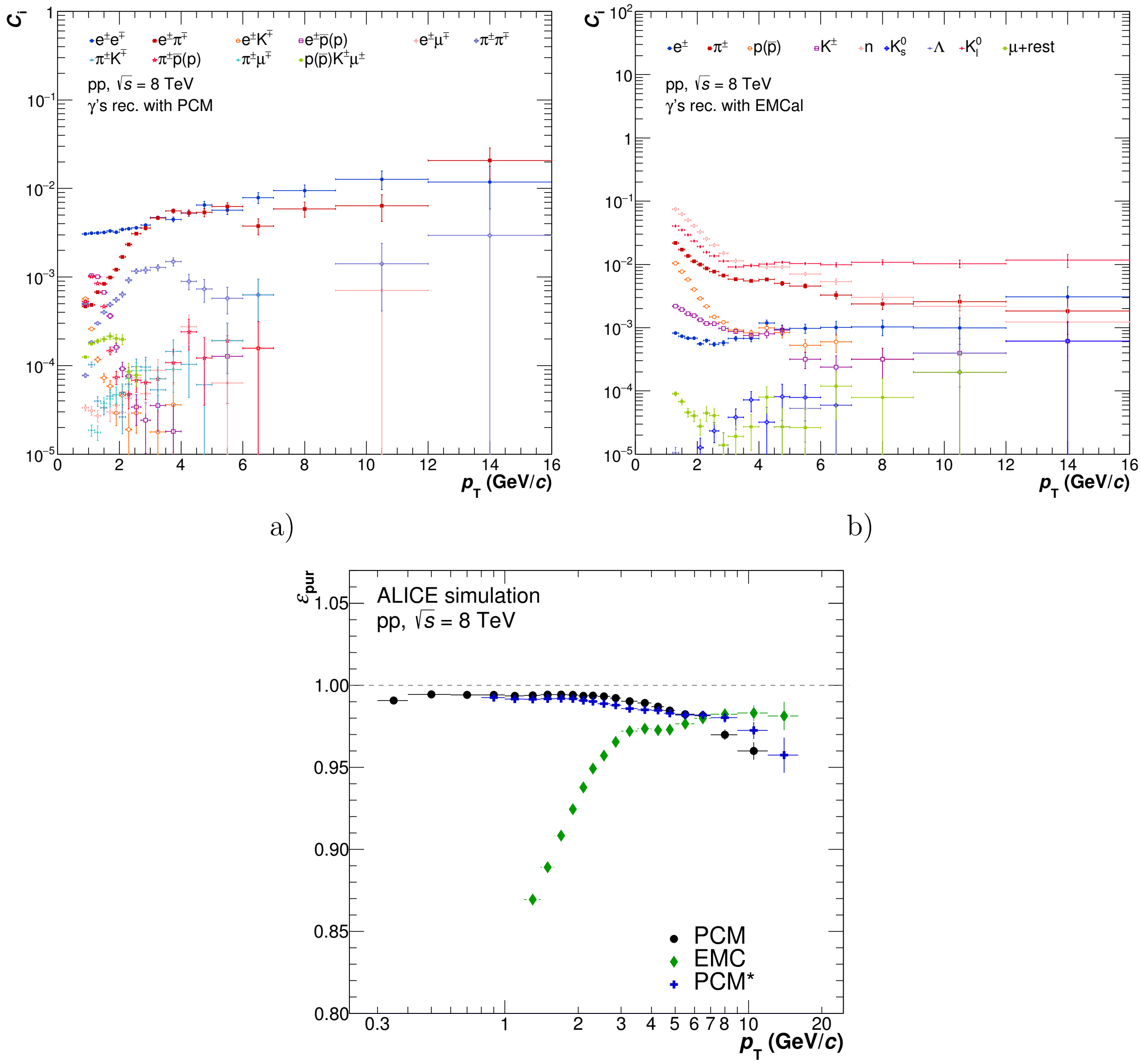

c)

Figure 7.2.6: The ratios C_{i} of identified background contributions to the total amount of true primary photons as a function of photon p_{T} for the PCM* and EMCal methods in a) and b). The purity $\varepsilon_{\mathrm{pur}}$ of the reconstructed photon sample for the methods PCM, PCM* and EMCal is shown in c) as a function of photon p_{T}.

The ratios C_{i} of the respective identified background sources to the true primary photons is shown in Fig. 7.2.6a for the PCM* measurement. The dominant contribution at low p_{T} is due to wrong combinations of $e^{\mp}$-$e^{\pm}$ pairs, including like-sign combinations as well, whereas the $e^{\pm}$-$\pi^{\mp}$

contamination takes over at higher p_{T}. Such track pairs show a similar topology as real photon conversions and, hence, survive all photon selection criteria. The purity of the photon sample reconstructed with PCM* is found to be approximately 99 % up to 3 GeV/c, decreasing towards 96 % for highest p_{T} of about 10 GeV/c mainly due to an increasing contamination from $e^{\pm}$-$\pi^{\mp}$ pairs as well as wrong combinations of $e^{\mp}$-$e^{\pm}$. Due to the looser electron PID cuts, the PCM* measurements shows a slightly lower purity compared to PCM.

For the photon reconstruction using EMCal, a significantly worse purity at low p_{T} is observed compared to PCM* although for higher momenta $\varepsilon_{\mathrm{pur}}$ becomes comparable or even better in comparison. The purity correction is the largest for $p_{\mathrm{T}} < 3$ GeV/c, where purities rise from 87 % up to 97 % as a function of p_{T}. On the other hand, reasonable purities of about 97 % are reached for high p_{T}. In Fig. 7.2.6b, the identified background contributions with respect to the true photon candidates are broken down for the EMCal. The main contributions stem from falsely identified photon candidates created by neutrons and antineutrons at low p_{T} and by neutral kaons at high p_{T}, where in particular the K^0_L contributes. In addition, the EMCal photon sample is corrected for impurities from direct $e^{\pm}$, $\pi^{\pm}$, $\mu^{\pm}$, $K^{\pm}$, K^0_S, $p\bar{p}$, Λ and heavier particles. The contamination from charged particles reflects the track finding as well as track matching inefficiencies which are demonstrated to be below the percent level except for $\pi^{\pm}$ at a level of 1 − 2 % below 2 GeV/c.

To correct for the finite momentum resolution of the photon detection methods, Bayesian unfolding [276, 277] is employed to convert from the reconstructed to the true p_{T} of the photons. For this purpose, the respective detector response is used by the unfolding procedure which is supplied by the RooUnfold package [278]. The unfolding algorithm has to find a solution for the following equation:

$$p_{\mathrm{T}}^{\mathrm{rec}} = \mathcal{A} \cdot p_{\mathrm{T}}^{\mathrm{true}}, \tag{7.2.5}$$

where $\mathcal{A}$ is the detector response matrix, $p_{\mathrm{T}}^{\mathrm{rec}}$ the reconstructed transverse momentum and $p_{\mathrm{T}}^{\mathrm{true}}$ the true p_{T} of the photon. The detector response matrices $\mathcal{A}$ are shown in Fig. 7.2.7 for PCM* and EMCal. For PCM*, the matrix shows the effect of bremsstrahlung with the shift of points towards $p_{\mathrm{T}}^{\mathrm{true}}$ ($p_{\mathrm{T}}^{\mathrm{MC}}$). For EMCal, the reconstructed p_{T} is often higher than the true p_{T} since two EMCal clusters closely located on the detector's surface can merge into single clusters. Exploiting RooUnfold package, the response matrix $\mathcal{A}$ can be inverted to calculate $p_{\mathrm{T}}^{\mathrm{true}}$. However, there could be large biases present or it could be even impossible to perform this step in the presence of statistical fluctuations. Such limitations can be avoided by following the Bayesian theorem [276, 277] using an iterative unfolding approach. The first prior used in this context is the MC photon momentum distribution. Consecutive iterations use the unfolded result of the previous iteration as updated prior. A total of four iterations is used. The results are cross-checked with the Singular Value Decomposition (SVD) unfolding method [279] which is also implemented in the RooUnfold package. The differences are below the level of a percent, hence the unfolding procedure is found to be stable.

The photon measurement using PCM is based on the conversion of the photons into e^-e^+ pairs. The probability for such a conversion to occur depends on the amount of detector material being traversed by the photons. It is not considered by the reconstruction efficiency $\varepsilon_{\mathrm{rec}}$ but it is reflected using a separate term denoted for the PCM measurement. This additional correction is based on the true MC information and is applied to account for the conversion probability of the PCM photons in the detector material. It depends on how well the present amount of detector

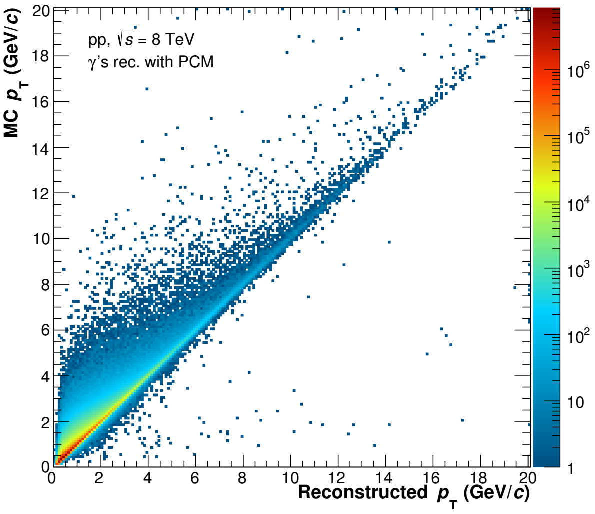

a)

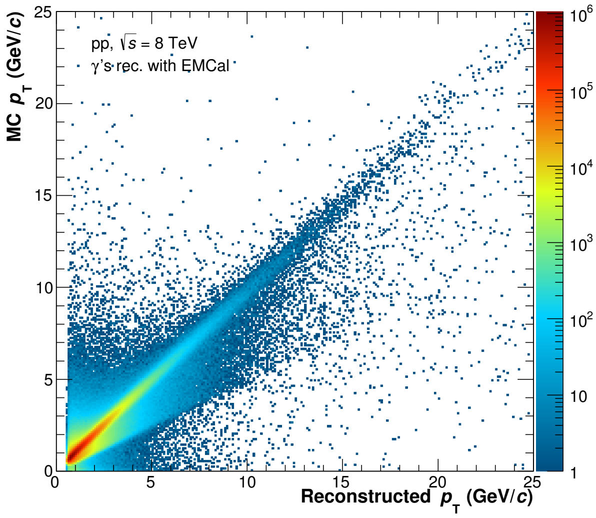

b)

Figure 7.2.7: The detector response matrices $\mathcal{A}$ for photons reconstructed with the PCM*, a), and the EMCal, b), in pp collisions at $\sqrt{s} = 8\,\text{TeV}$.

material is reproduced in the simulation and is calculated using the following formula:

$$P_{\text{conv}}(p_{\text{T}}) = \frac{\gamma^{\text{true converted}}_{\text{primary}}(p_{\text{T}})}{\gamma^{\text{true}}_{\text{primary}}(p_{\text{T}})}, \tag{7.2.6}$$

where $\gamma^{\text{true}}_{\text{primary}}$ represents all validated true primary photons and $\gamma^{\text{true converted}}_{\text{primary}}$ the subset of the first category which converted into a lepton pair. The obtained conversion probability P_{conv} is shown in Fig. 7.2.8a for the two PCM-based measurements. It can be deduced that P_{conv} levels out at about $\sim 8.9\,\%$ for large p_{T}, whereas towards low p_{T} a decrease of the probability is visible. This behavior is due to the electron low momentum cut-off as the electron acceptance is folded into the P_{conv} distribution, leading to an increase from $\sim 5.6\,\%$ at lowest p_{T} up to $\sim 8.9\,\%$ for the highest measured p_{T}.

The photon reconstruction efficiency ε_{rec} is calculated by dividing the true validated MC photon spectrum by all photons from the simulation:

$$\varepsilon_{\text{rec}}(p_{\text{T}}) = \frac{\gamma^{\text{true rec}}_{\text{primary}}(p_{\text{T}})}{\gamma^{\text{all}}_{\text{primary}}(p_{\text{T}})}, \tag{7.2.7}$$

where $\gamma^{\text{all}}_{\text{primary}}$ represents all photons for EMCal and all converted photons for the PCM*. The numerator $\gamma^{\text{true rec}}_{\text{primary}}$ includes all validated true primary photons which are reconstructed. The efficiency inherently corrects for differences in the particle p_{T} resolution in data and MC simulations. The following Fig. 7.2.8b shows the reconstruction efficiencies for the three measurements obtained from the unfolding method, $\varepsilon_{\text{rec}}(p_{\text{T}}^{\text{true}})$, as well as before unfolding, $\varepsilon_{\text{rec}}(p_{\text{T}}^{\text{rec}})$. The difference between these two efficiencies is caused by energy loss due to radiative processes for the PCM methods. Below $2\,\text{GeV}/c$, the effective correction from the momentum resolution becomes smaller and both efficiencies are getting closer. The maximum value for $\varepsilon_{\text{true}}$ is found at approximately $2.5\,\text{GeV}/c$ with about $72\,\%$ for the PCM methods. The efficiencies decrease towards low

p_T due to the minimum p_T cut-off for the conversion daughters. Moreover, the respective conversion daughters may be stopped prior to reaching the required track length within the TPC drift volume and also the applied photon selection criteria have some influence. For high p_T, the strict rejection cuts for charged pions as well as strict photon quality cuts reduce the efficiencies. For the EMCal photon reconstruction efficiencies, the effect of the momentum resolution correction is found to be smaller. The unfolding yields an approximately 10% higher correction at low p_T. With increasing p_T, the correction decreases until at around 4 GeV/c EMCal clusters start to merge. In such a case, too much energy is contained in a cluster so that the resolution correction causes a lower reconstruction correction beyond this momentum. The maximum value for $\varepsilon_\mathrm{true}$ is found at approximately 5.0 GeV/c with about 52 %.

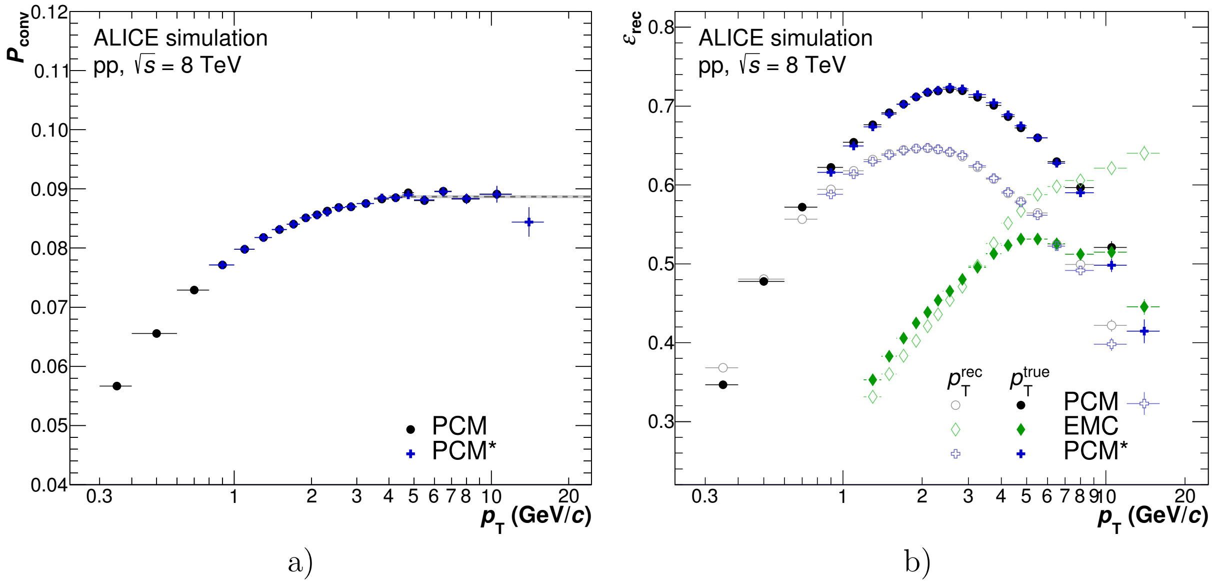

Figure 7.2.8: The photon conversion probability, a), for the PCM and PCM* methods as well as the photon reconstruction efficiency, b), for which the EMCal method is shown in addition.

The total correction factors $\varepsilon = \varepsilon_\mathrm{rec} \cdot P_\mathrm{conv}/\varepsilon_\mathrm{pur}$ are shown in Fig. B.3.31 in the appendix, which are computed for PCM, PCM* and EMCal respectively. The major difference between the factors ε obtained for the EMCal and the PCM-related measurements is the photon conversion probability, leading to a difference of about an order of magnitude.

Besides the inclusive photon cross sections, the corresponding π^0 and η meson measurements in the same collision system are needed to extract R_γ from Eq. 2.3.18, which are described in detail in Chap. 6 but also in Ref. [4]. The results of the decay photon simulation are also needed in this context which is described in Sec. 7.1. The direct photon spectra are then obtained via the subtraction method, see Eq. 2.3.17.

7.2.2 Systematic Uncertainties

Different sources of systematic uncertainties are identified for the described measurements using the reconstruction methods PCM-EMCal and EMCal, closely related to the determination and estimation of systematic effects described in Sec. 6.2.4 and Sec. 6.3.2. Compared to the reported neutral meson measurements, an additional category related to the decay photon simulation enters. Hence, the total of twelve categories of systematic uncertainties are summarized in Tab. 7.2.3 for the measurements of $Y_{\gamma_{\mathrm{incl}}}$ and R_γ. For three different p_{T} bins respectively, the uncertainties are given in percent and refer to relative systematic uncertainties of the measured values, illustrating the relative strengths of each reconstruction method. The systematic effects are estimated by varying different aspects of the analysis, for example by processing the analysis with modified event and photon selection criteria as introduced in Chap. 4 and Chap. 5. All uncertainties are evaluated on the level of the obtained invariant cross sections for $Y_{\gamma_{\mathrm{incl}}}$ and directly on R_γ. For these measurements, a detailed overview of the p_{T}-dependent systematic uncertainties decomposed into the different sources can be found in Fig. B.3.32 for PCM-EMCal and EMCal.

The determination of the systematic uncertainties of R_γ involve the contributions from the $Y_{\gamma_{\mathrm{incl}}}$ and the π^0 measurements as well as the decay photon simulation. The systematics related to the π^0 measurement, which enters for the direct photon excess ratio R_γ, is discussed in Sec. 6.2.4 in detail. Partially, common systematic uncertainties from $Y_{\gamma_{\mathrm{incl}}}$ and π^0 measurements are found to cancel for the case of R_γ. Hence, the magnitude of most systematic effects is found to be different but also the p_{T}-behavior may be altered as for both $Y_{\gamma_{\mathrm{incl}}}$ measurements one photon candidate from the same reconstruction method enters in the numerator as well as the denominator. For the PCM-EMCal measurement, PCM photons are used for $Y_{\gamma_{\mathrm{incl}}}$ and also one PCM photon enters the hybrid method exploited for π^0 reconstruction, leading to a partial cancellation of uncertainties. The analog is found for EMCal which involves two EMCal photons for the π^0 measurement compared to the single contribution of one photon for $Y_{\gamma_{\mathrm{incl}}}$. The estimated systematic uncertainties for the different categories are introduced in the following. They are further elaborated with respect to the $Y_{\gamma_{\mathrm{incl}}}$ and R_γ measurements carried out and the respective cancellations which are found.

π^0 Signal Extraction

This systematic uncertainty applies only for R_γ as it relates to the signal extraction uncertainty in the context of the π^0 meson reconstruction. The same variations are used as introduced in Sec. 6.2.4, where the systematic uncertainties of the π^0 measurements are discussed in detail which enter the calculation of R_γ. The uncertainty ranges between $\sim 2-3\,\mathrm{GeV}/c$ depending on p_{T} and the considered reconstruction method.

Inner Material

The systematic uncertainty is estimated to be 4.5 % per PCM photon for which further details can be found in Refs. [10, 232]. It is the main contributor to the systematic uncertainties of the PCM photon reconstruction and is of same size as determined for the neutral meson measurements, see Sec. 6.2.4. For the PCM-EMCal method, it contributes once to the uncertainty of the inclusive photon $Y_{\gamma_{\mathrm{incl}}}$ measurement. On the other hand, it cancels out completely for the R_γ as it enters once the $Y_{\gamma_{\mathrm{incl}}}$ and once the π^0 uncertainties. This fact represents the main advantage of the PCM-EMCal measurement of R_γ for which only the outer material uncertainty enters.

$Y_{\gamma_{\mathrm{incl}}}$ and R_γ meas.	$1.6-1.8\,\mathrm{GeV}/c$				$4.0-4.5\,\mathrm{GeV}/c$				$9.0-12.0\,\mathrm{GeV}/c$			
category	PCM-EMCal		EMCal		PCM-EMCal		EMCal		PCM-EMCal		EMCal	
	$Y_{\gamma_{\mathrm{incl}}}$	R_γ	$Y_{\gamma_{\mathrm{incl}}}$	R_γ	$Y_{\gamma_{\mathrm{incl}}}$	R_γ	$Y_{\gamma_{\mathrm{incl}}}$	R_γ	$Y_{\gamma_{\mathrm{incl}}}$	R_γ	$Y_{\gamma_{\mathrm{incl}}}$	R_γ
π^0 signal extraction	–	1.8	–	2.7	–	2.2	–	2.4	–	3.1	–	2.8
inner material	4.5	–	–	–	4.5	–	–	–	4.5	–	–	–
outer material	–	2.1	2.1	3.0	–	2.1	2.1	3.0	–	2.1	2.1	3.0
PCM track rec.	0.1	0.2	–	–	0.1	0.2	–	–	0.1	0.2	–	–
PCM electron PID	0.3	0.3	–	–	0.6	0.8	–	–	0.6	0.8	–	–
PCM photon PID	1.3	1.0	–	–	1.3	1.0	–	–	2.2	1.7	–	–
cluster description	–	2.5	2.6	3.0	–	2.4	2.6	2.7	–	3.0	2.6	4.0
cluster energy calib.	–	2.3	1.4	2.3	–	1.8	0.9	1.8	–	1.8	0.9	1.8
track-to-clus. mat.	–	0.2	1.8	1.5	–	0.3	1.5	1.0	–	1.9	1.9	1.5
efficiency	0.5	2.1	1.8	2.7	0.5	2.1	1.8	2.7	0.5	2.1	1.8	2.7
cocktail	0.1	1.0	0.3	0.8	0.1	1.7	0.3	0.9	0.1	2.0	0.3	1.4
pileup	2.7	2.7	0.1	–	2.4	2.4	0.1	–	3.0	3.0	0.1	–
total sys. unc.	5.4	5.7	4.4	6.4	5.3	5.7	4.2	5.8	5.9	7.1	4.3	6.9
statistical unc.	0.3	2.1	0.2	2.7	1.4	3.4	0.6	2.2	4.1	9.9	2.1	4.7

Table 7.2.3: Summary of relative systematic uncertainties in percent for selected p_{T} bins for the $Y_{\gamma_{\mathrm{incl}}}$ and R_γ measurements in pp collisions at $\sqrt{s} = 8\,\mathrm{TeV}$. The statistical uncertainties are given in addition to the total systematic uncertainty. The visible cross section uncertainty of 2.6 % is independent from reported uncertainties and is separately indicated in the upcoming figures shown in Sec. 7.2.4.

Outer Material

This category summarizes the systematic effect of the description of the outer detector material of ALICE beyond the radial center of the TPC. It is estimated analog to Sec. 6.2.4 for $Y_{\gamma_{\mathrm{incl}}}$ and R_γ. If one EMCal photon is involved, which is true for the R_γ measurement using PCM-EMCal and the reconstruction of $Y_{\gamma_{\mathrm{incl}}}$ using EMCal, it is found to be 2.1 % in accordance with the neutral meson measurements. Otherwise, for the R_γ measurement using EMCal a partial cancellation of the outer material uncertainty is observed which is found to be 3.0 % in this case.

PCM Track Reconstruction

This category summarizes the systematic uncertainties related to the secondary track finding used for the PCM method, see also Sec. 6.2.4. It is found to be one of the insignificant uncertainties at around 0.1 % for $Y_{\gamma_{\mathrm{incl}}}$ and approximately 0.2 % for R_γ by varying the selection criteria applied with regard to the number of TPC clusters and the minimum track p_{T}.

PCM Electron PID

The systematic uncertainties related to the electron PID used to reconstruct and select PCM photons are summarized in this category. In detail, the TPC $\mathrm{d}E/\mathrm{d}x$ cuts on $n\sigma_e$ used for electron PID and $n\sigma_\pi$ used for charged pion suppression are varied to study the systematics. The uncertainty ranges from 0.1 % at lowest p_T up to 0.6 % at highest p_T available for the Y_{γ_incl} measurement. For the R_γ, it increases from 0.1 % up to approximately 0.8 % with increasing p_T. The p_T dependence for both Y_{γ_incl} and R_γ is caused by the fact that the $\pi^\pm$ $\mathrm{d}E/\mathrm{d}x$ band approaches the $e^\pm$ $\mathrm{d}E/\mathrm{d}x$ band for higher p_T so that $\pi^\pm$ cannot be rejected as efficient as at lower p_T any longer.

PCM Photon PID

This category includes all systematic uncertainties related to the selection of PCM photon candidates. It is estimated by varying the selection criteria applied to χ^2_red, ψ_pair and to the 2D Armenteros-Podolanski plot. For the Y_{γ_incl} measurement, the uncertainty ranges from about 1.3 % at low p_T up to 3.5 % for the highest p_T used in analysis. The same p_T dependence is observed for the R_γ measurement which is explained in both cases by the increasing charged pion contamination. Part of the uncertainty cancels for R_γ, for which it is found to be approximately 0.8 % at low p_T with increasing magnitude up to 2.4 % as a function of p_T.

Cluster Description

The cluster description uncertainty quantifies the mismatch in the description of the clusterization process between data and MC simulations for the EMCal, leading to possible influences on the reconstruction efficiencies. The relevant selection criteria are the minimum energy cut on EMCal cluster level, the cluster shape cut σ^2_long, the minimum number of cells contained in the reconstructed cluster and the cut on the cluster time. Furthermore, variations on the energy thresholds of E_seed and E_min in the context of the clusterization are included as well at timing cuts on the cell level. For the R_γ measurement using PCM-EMCal, it ranges from 2.3 % at intermediate p_T up to approximately 4.0 % (3.3 %) for lowest (highest) p_T used in the analysis. For the EMCal, the uncertainty is found to be $\sim$ 2.6 % for the Y_{γ_incl} measurement, whereas for R_γ it is minimal at intermediate p_T with about 2.6 % with increasing behavior for lower and higher momenta. At lowest (highest) p_T, it reaches values of 3.7 % (5.1 %).

Cluster Energy Calibration

The uncertainty due to the finite accuracy of the EMCal cluster energy calibration is represented by this category. It incorporates the difference between the available energy calibration schemes as well as the remaining difference of the reconstructed mass positions of neutral mesons between data and MC simulations after the calibration procedure is performed, from which an uncertainty of the energy scale is deduced. For the Y_{γ_incl} measurement using EMCal, it is found to be 0.9 % at high p_T rising up to 2.2 % for the lowest p_T bin available. There is a partial cancellation of the uncertainty for the corresponding R_γ measurement present so that the magnitude is comparable to the R_γ measurement using PCM-EMCal. It is about 1.8 % at highest p_T and increases up to 3.1 % for the p_T bin $1.2-1.4\,\mathrm{GeV}/c$.

Track-to-Cluster Matching

The uncertainty caused by imperfections of the track-to-cluster matching procedure when comparing data and MC simulations is reflected in this category. As for the neutral meson measurements, see Sec. 6.2.4, it is assessed by varying the matching residuals. For the measurement of R_γ using PCM-EMCal, it is estimated to about 0.2 % at low p_T, increasing up to approximately 2.9 % for the highest p_T bin reported. For the EMCal in comparison, the effect of the variations is observed to be higher. For the Y_{γ_incl}, it is estimated to be $\sim 1.5\,\%$ at intermediate p_T of about $4\,\mathrm{GeV}/c$, rising towards lower and higher p_T up to 2 % approximately. A partial cancellation for the R_γ is deduced for which values of around 1 % at intermediate p_T are found that increase to the order of 2 % at lowest and highest p_T.

Efficiency

The systematic uncertainty denoted efficiency is estimated using different MC generators to vary the input spectra used for the determination of reconstruction efficiencies which are compared to the obtained validated efficiencies using true MC information in addition. The choice of the generator has an influence on the purity of the EMCal photons and the π^0 reconstruction efficiency as these depend partially on the underlying event description so that the influence is found to be bigger for the EMCal than for the PCM. Concerning the Y_{γ_incl} measurement, the uncertainty is estimated to be 0.5 % and 1.8 % for PCM-EMCal and EMCal respectively, showing no dependence on p_T. For R_γ, values of 2.1 % and 2.7 % for PCM-EMCal and EMCal are found without a dependence on p_T.

Cocktail

As already elaborated, a dedicated decay photon simulation is produced for each π^0 reconstruction method. Hence, separate decay simulations for EMCal and PCM-EMCal are available. Each reconstruction method features its own systematic uncertainties which are not reflected for the default parameterizations entering the standard decay photon simulation. In fact, this is of particular importance since the measured particle spectra need to be extrapolated to cover the full p_T region of $0 \leq p_\mathrm{T} \leq 50\,\mathrm{GeV}/c$ for which the fits need to be well constrained. Including the systematic uncertainties would leave too much freedom for the fits and the choice of the functional forms to obtain reliable parameterizations for each case. Therefore, the input spectra are modified within their systematic uncertainties, for which different decay photon simulations are performed, in order to obtain the impact of these uncertainties on the decay photon simulation. The largest contribution to the systematics in this context is caused by modifications of the input π^0 and η meson spectra as they dominate the sample of inclusive decay photons. For these meson spectra, however, large parts of the determined systematic uncertainties are p_T independent, for example those related to the description of the inner and outer material. Such shifts would cancel for R_γ since photons and mesons would be shifted by the same amount. Therefore, such uncertainties are not taken into account for the determination of systematic uncertainties due to the decay photon simulation. Hence, only the remaining uncertainties are used to shift the measured data points of the input spectra within their given systematic uncertainties as it is shown in Fig. 7.2.9 for the π^0 input spectrum measured with EMCal and the combined η/π^0 ratio. For this purpose, the factors $C(p_\mathrm{T})$, shown in Fig. 7.2.9 a) and b), visualize

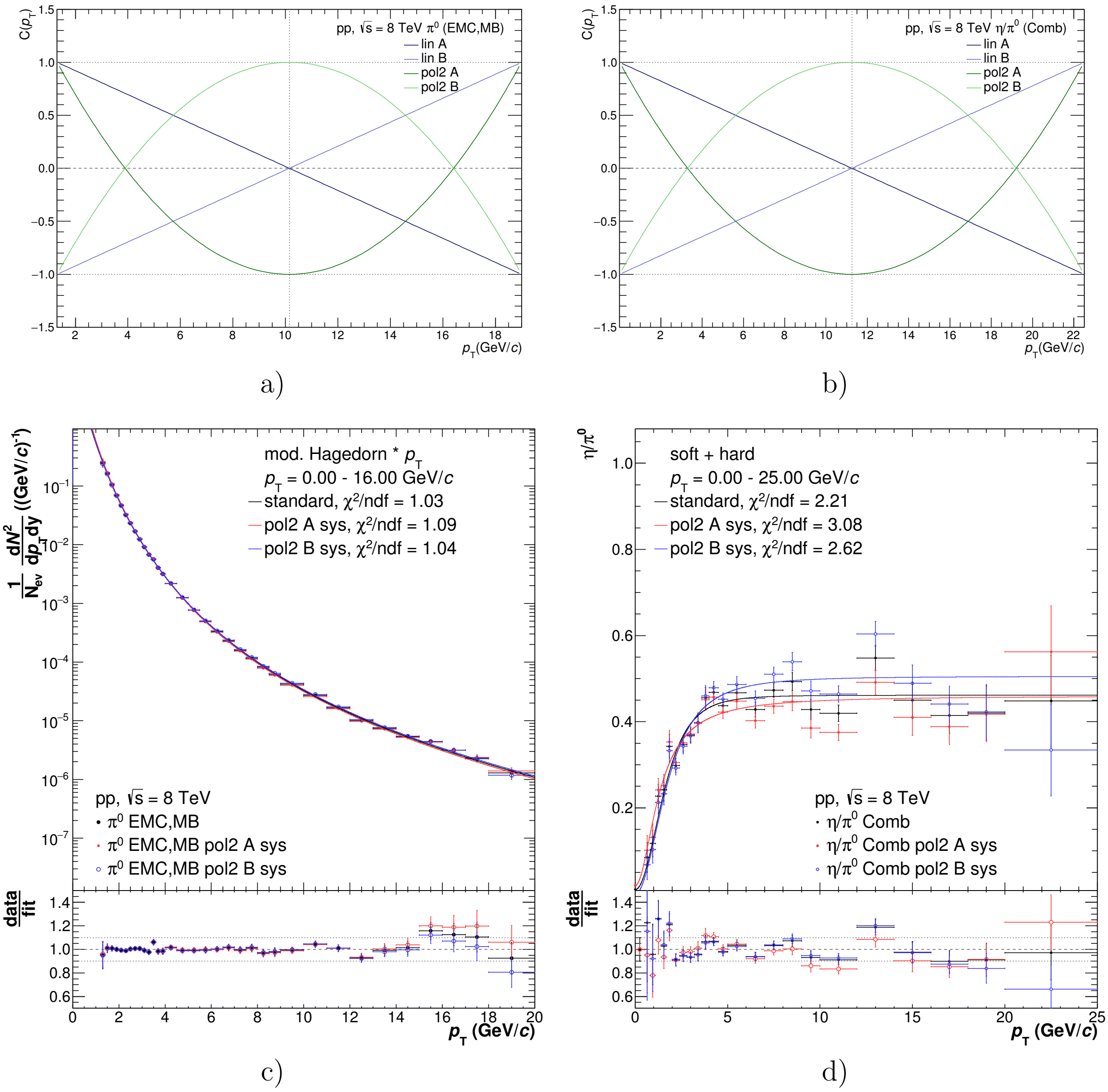

Figure 7.2.9: The fraction $C(pT)$ of the respective systematic uncertainties used to shift the central values are shown in a) and b) for the EMCal π^0 spectrum and the combined η/π^0 ratio which enter the decay photon simulation. The actual spectra and ratios are shown in c) and d), where the effects of the shifts are visualized. The black points denote the actual inputs, whereas the red and blue markers show the shifted inputs according to a) and b). In Fig. B.3.33, the corresponding plots are shown for the π^0 input spectrum reconstructed with PCM-EMCal.

the extent of the respective shifts for each measured data point. The value for $C(p_{\mathrm{T}})$, which can be read off from the y-axis as a function of p_{T}, represents the shift of the respective data point quantified in $C \cdot \sigma_{\mathrm{sys}}$. In total, four different scenarios are realized which are subdivided into two linear functions as well as two polynomials of second order. They are facilitated to vary the input spectra within their systematics to generate different slopes of these spectra since constant offsets do not matter for R_γ as already explained. In this context, the linear functions shift the input spectra by $\pm1 \cdot \sigma_{\mathrm{sys}}$ for the lowest p_{T} bin and by $\mp1 \cdot \sigma_{\mathrm{sys}}$ for the highest p_{T} bin respectively. In between these p_{T} bins, shifts of $C \cdot \sigma_{\mathrm{sys}}$ are applied where C changes linearly from ±1 to ∓1 within the covered p_{T} interval of the respective measurement. On the other hand, the polynomial scenarios perform shifts of $\pm1 \cdot \sigma_{\mathrm{sys}}$ for the lowest and highest p_{T} bin while shifting the median p_{T} bin by $\mp1 \cdot \sigma_{\mathrm{sys}}$. The outcomes of these operations are shown in Fig. 7.2.9 c) and d) for the example of polynomial shifts of the π^0 input spectrum measured with EMCal and the combined η/π^0 ratio. The standard data points are drawn in black, whereas the two systematic variations of the input spectra are drawn in red and blue as denoted in the respective legends. The fits are repeated for the shifted data points and the results are superimposed.

The elaborated shifting procedure is carried out for each shifting scenario for all input spectra of the decay photon simulation at the same time. For each of these scenarios, a full decay photon simulation is performed and the differences on the extracted $Y_{\gamma_{\mathrm{incl}}}$ spectra and on R_γ regarding the different scenarios are determined in order to obtain the associated systematic uncertainties. As already introduced in Tab. 7.1.1, the m_{T} scaling constants $C_{m_{\mathrm{T}}}$ used to estimate the spectra of the unmeasured particles are also varied within the associated uncertainties listed in this table, for which two additional decay photon simulations are carried out for the variation upwards and downwards of the constants $C_{m_{\mathrm{T}}}$. Taken together, the estimated uncertainty of R_γ, which is related the decay photon simulations, is found to be 0.8 % at low p_{T} for the EMCal measurement, rising up to about 1.6 % for the highest p_{T} bin reported. For PCM-EMCal, the uncertainty is estimated to be 1.0 % at low p_{T} with a similar dependence on p_{T}, so that about 2 % is reached for the highest p_{T} bin used in the analysis. Furthermore, the same procedure is used to estimate the uncertainty related to the secondary photon correction of the $Y_{\gamma_{\mathrm{incl}}}$ measurement which is found to be approximately 0.25 % for EMCal and which is estimated to be of the order of 0.1 % for PCM-EMCal. The same approach is followed to determine the uncertainties related to the secondary π^0 correction for the π^0 measurements described in Sec. 6.2.4 and Sec. 6.3.2.

Pileup

The uncertainty on the out-of-bunch pileup correction for PCM is estimated by running the background estimator repeatedly using different sets of iterations. The variations are chosen such that the smallest and highest background fractions are found for which the estimations still provide a reasonable description of the $\mathrm{DCA_z}$ distributions. Furthermore, the pileup systematic uncertainty reflects the finite efficiency of the SPD concerning the rejection of in-bunch pileup, which applies for the both PCM-EMCal and EMCal. For the $Y_{\gamma_{\mathrm{incl}}}$ measurement using EMCal, the uncertainty due to the SPD inefficiency is found to be approximately 0.1 % while it cancels for R_γ. For PCM-EMCal, the pileup uncertainty involves both contributions from in-bunch and out-of-bunch corrections. It is estimated to be $\sim 2.3\,\%$ for $Y_{\gamma_{\mathrm{incl}}}$ at intermediate p_{T}, rising for both directions towards lowest and highest p_{T} bins up to 3.4 %. The same uncertainty as found for $Y_{\gamma_{\mathrm{incl}}}$ is denoted for the related R_γ measurement.

The following Fig. 7.2.10 summarizes the relative statistical and systematic uncertainties for the $Y_{\gamma_{\mathrm{incl}}}$ and R_γ measurements using the different reconstruction methods PCM, PCM-EMCal and EMCal for pp collisions at $\sqrt{s} = 8\,\mathrm{TeV}$. The estimated systematic uncertainties on $Y_{\gamma_{\mathrm{incl}}}$ amount to approximately 5.5 – 6.0 % for the PCM measurements and to about 4.0 % for the EMCal. The corresponding statistical uncertainties are well below 1 % for $p_{\mathrm{T}} < 3\,\mathrm{GeV}/c$ so that the $Y_{\gamma_{\mathrm{incl}}}$ measurement is limited in its precision due to its systematics. The systematic uncertainties estimated for the direct photon excess ratio R_γ are larger than for the $Y_{\gamma_{\mathrm{incl}}}$ counterparts due to the addition of the uncertainties related to the respective π^0 measurements. They range around 5 − 7 %, depending on p_{T} and the respective method, and rise to about 12 % for the lowest p_{T} bin covered by the PCM method. The corresponding statistical uncertainties are at the level of a couple of percent and rise significantly for all methods towards higher p_{T}.

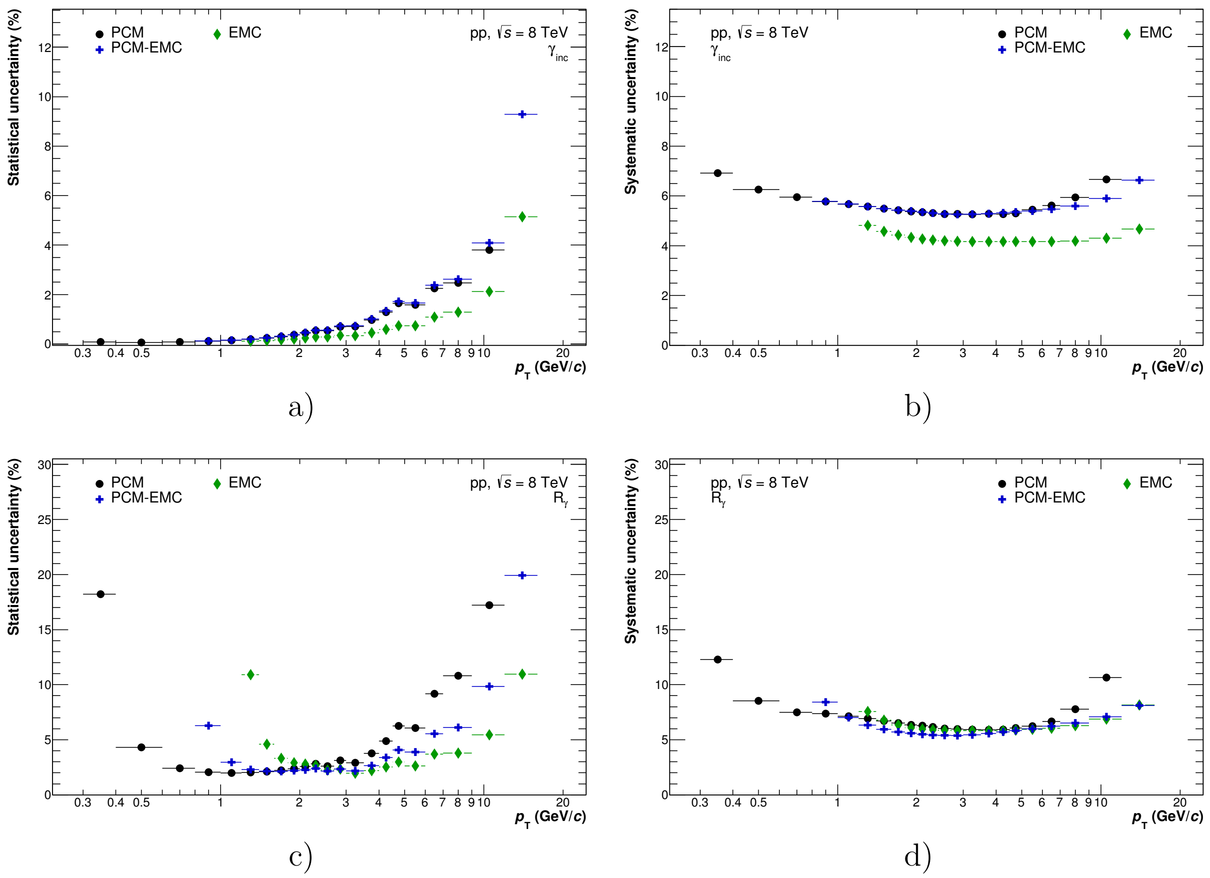

Figure 7.2.10: Relative statistical, a), and systematic, b), uncertainties in percent for all available reconstruction methods for $Y_{\gamma_{\mathrm{incl}}}$ and R_γ measurements in pp, $\sqrt{s} = 8$ TeV.

7.2.3 Combination of Individual Measurements

The individual measurements, introduced in Tab. 7.2.2, of the p_{T}-differential invariant yields of inclusive photon production $Y_{\gamma_{\mathrm{incl}}}$ and the direct photon excess ratio R_γ at mid-rapidity in pp collisions at $\sqrt{s} = 8$ TeV are shown in Fig. 7.2.11. The plots indicate a good agreement of all available measurements within their associated statistical and systematic uncertainties. Moreover, Fig. 7.2.11 also visualizes the p_{T} ranges for which the respective measurements are available, representing the input for the combination procedure described in this section.

In analogy to the combination of the neutral meson spectra, introduced in detail in Sec. 6.2.2 and Sec. 6.2.5, the final results on $Y_{\gamma_{\mathrm{incl}}}$ and R_γ are obtained by combining the individual results provided by the three reconstruction methods exploiting the BLUE method [246–250]. For this

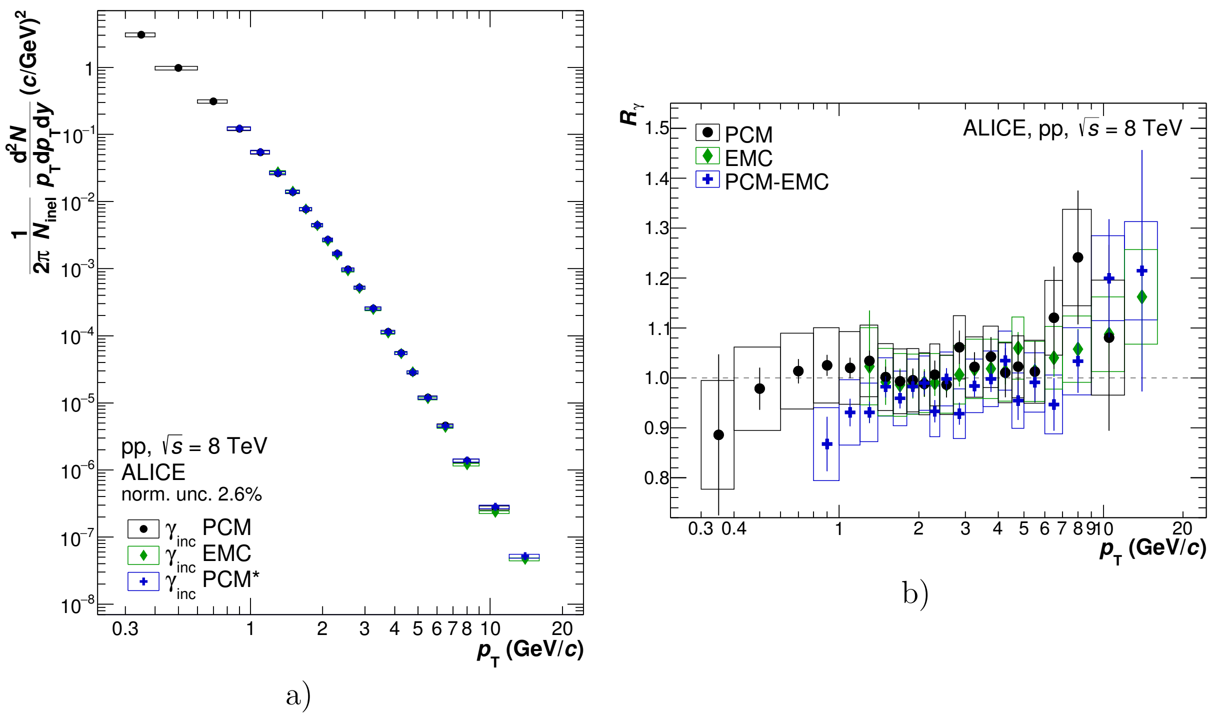

Figure 7.2.11: The different measurements of $Y_{\gamma_{\text{incl}}}$ provided by PCM, PCM* and EMCal are shown in a), while the inputs for R_γ are shown in b). The vertical error bars represent statistical uncertainties, whereas the boxes quantify the p_{T} bin widths in horizontal direction as well as the systematic uncertainties in vertical direction.

purpose, the correlations of statistical and systematic uncertainties among the different measurements are estimated. In contrast to the combination of meson measurements, there are also correlations of statistical uncertainties present for $Y_{\gamma_{\text{incl}}}$ and R_γ for which the corresponding factors $\rho_{ij}(p_{\text{T}})$ are shown in Fig. 7.2.12. As already indicated, the measurements of $Y_{\gamma_{\text{incl}}}$ provided by PCM and PCM* are strongly correlated as it can be deduced from Fig. 7.2.12a so that correlation factors well beyond 0.9 are found independent of p_{T}. This is an expected consequence as the two methods differ only by the selection of good run lists and some photon selection criteria. On the other hand, both PCM-related measurements of $Y_{\gamma_{\text{incl}}}$ are assumed to be statistically independent with respect to the EMCal equivalent, see also Sec. 6.2.5 for further explanations which also apply here. This statement also holds with regard to the statistical correlations of R_γ for which the π^0 measurements enter. For R_γ, however, all three π^0 measurements are found to be statistically independent, see Sec. 6.2.5. This fact leads to a significant decrease of the statistical correlation between PCM and PCM-EMCal for the R_γ which can be seen in Fig. 7.2.12b. In this case, they range between 0.2 and 0.5 depending on p_{T}.

The correlations of the systematic uncertainties of $Y_{\gamma_{\text{incl}}}$ and R_γ are shown in Fig. 7.2.13. For PCM and PCM*, the correlation factors are found to be well beyond 0.9 for $Y_{\gamma_{\text{incl}}}$, since only parts of the systematic effects related to the photon reconstruction cancel. The same statement concerning the cancellation is also valid for R_γ, however, in this case the systematic uncertainties from the independent π^0 measurements enter. For example, the material budget, pileup and signal extraction uncertainties of the PCM π^0 measurement are assumed to be independent with

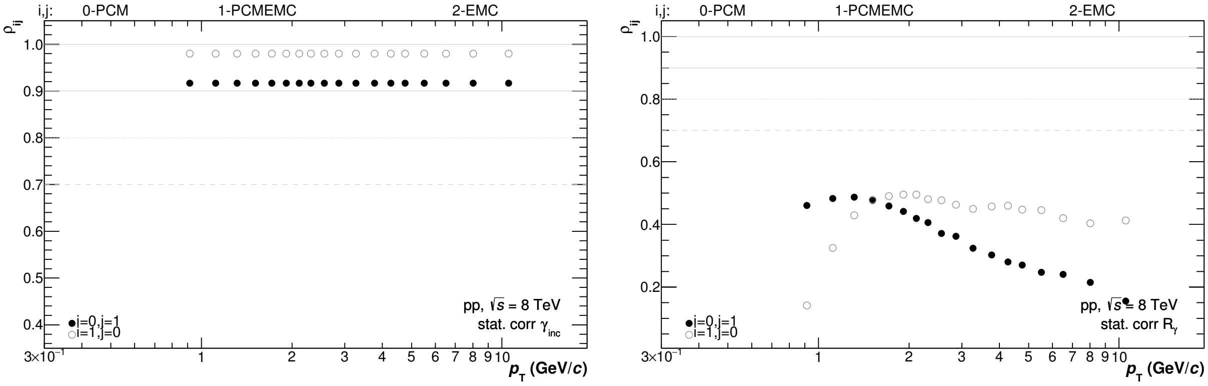

a) b)

Figure 7.2.12: The p_{T}-dependent correlation factors $\rho_{ij}(p_{\mathrm{T}})$ visualizing the fraction of correlated statistical uncertainties between the methods PCM and PCM* for the $Y_{\gamma_{\mathrm{incl}}}$ and R_γ measurements in a) and b).

respect to the corresponding measurement using PCM-EMCal. On the contrary, the EMCal related systematics as well as the signal extraction are the most important categories which are independent with respect to PCM. Hence, the correlation factors for R_γ range approximately between 0.4 and 0.6 for PCM and PCM-EMCal so that the addition of the R_γ measurement using the hybrid method does improve the precision of the final result significantly. The only correlated systematic uncertainty between both PCM-related measurements of $Y_{\gamma_{\mathrm{incl}}}$ and the equivalent using the EMCal is the uncertainty related to the removal of in-bunch pileup. Hence, the factors are found to be tiny in this case of the order of 0.02 to 0.03. For R_γ, the only correlated uncertainty between PCM and EMCal is found to be the one related to the cocktail uncertainty which cancels partially, leading to the estimated values at around 0.02. Between PCM-EMCal and EMCal, the PCM-related uncertainties are found to be independent as well as part of the uncertainties from both π^0 measurements so that the measurement are found to be highly correlated at around 0.8 to 0.9 with respect to their systematics.

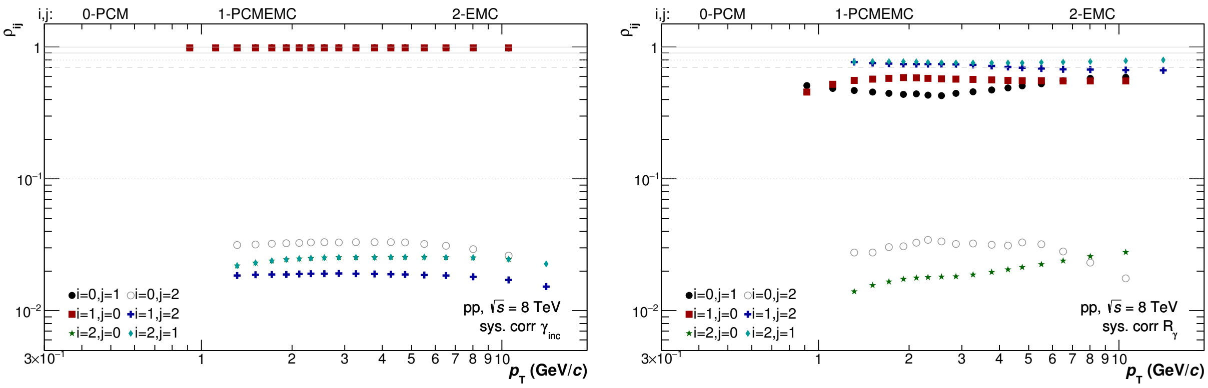

a) b)

Figure 7.2.13: The p_{T}-dependent correlation factors $\rho_{ij}(p_{\mathrm{T}})$ visualizing the fraction of correlated systematic uncertainties for the $Y_{\gamma_{\mathrm{incl}}}$ and the R_γ measurements, in a) and b), for all combinations of the methods PCM, PCM-EMCal and EMCal.

Using the determined correlation factors for the statistical and systematic uncertainties, the combination of the individual measurements is performed following the BLUE method. The obtained weights ω_a for the individual measurements provided by the different reconstruction methods are shown in the left part of Fig. 7.2.14. In most p_{T} bins, the EMCal dominates the combinations of both $Y_{\gamma_{\mathrm{incl}}}$ and R_γ measurements because it provides high statistics as well as the best precision with respect to the associated systematics uncertainties. For $Y_{\gamma_{\mathrm{incl}}}$, the PCM and PCM* measurements are highly correlated while for R_γ the degree of correlation decreases because of the different π^0 measurements entering, so that the weights of the PCM-related measurements are higher compared to the EMCal weights.

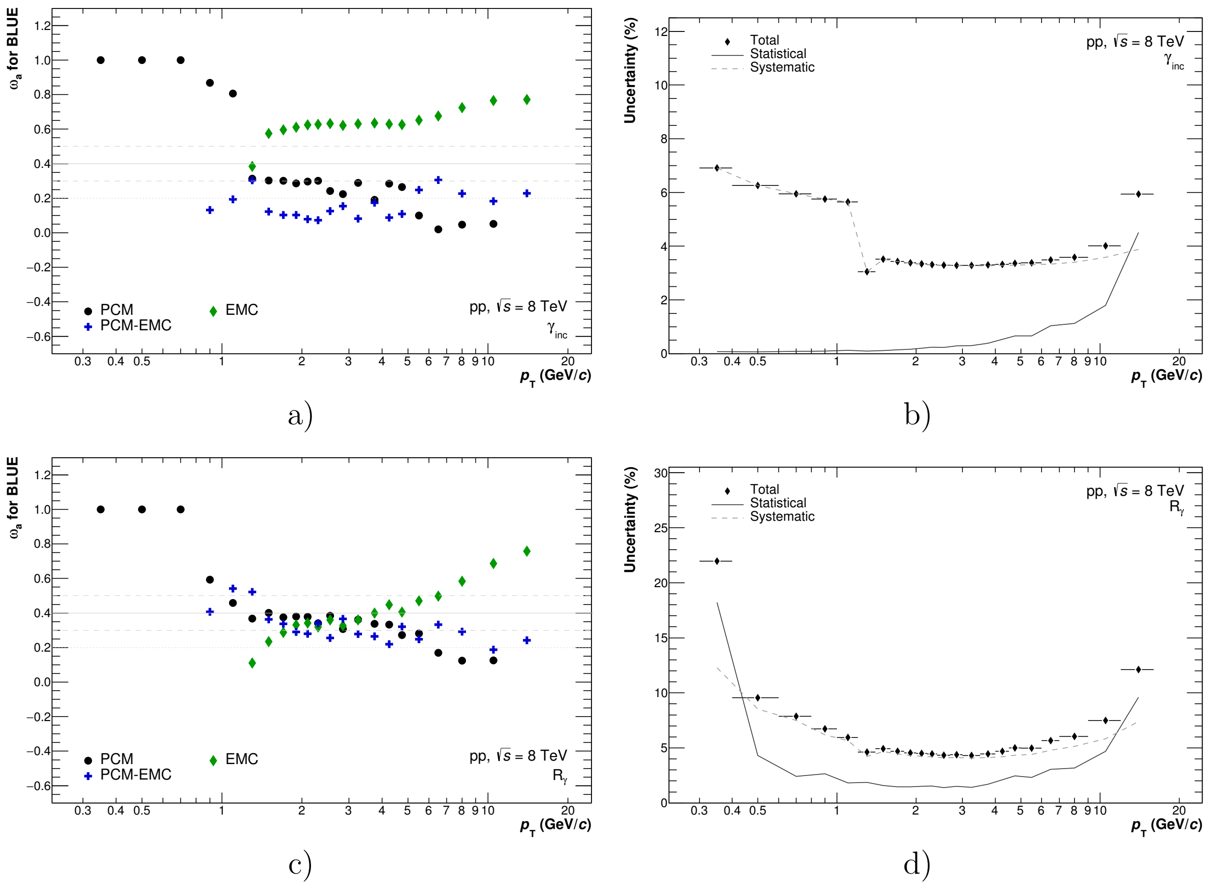

Figure 7.2.14: The obtained weights $\omega_a(p_{\mathrm{T}})$ using the BLUE method for the combination of $Y_{\gamma_{\mathrm{incl}}}$, a), and R_γ, c), measurements using all inputs summarized in Tab. 7.2.2 for pp collisions at $\sqrt{s} = 8\,\mathrm{TeV}$. The corresponding total, statistical and systematic uncertainties for the combined results are shown in b) and d).

Furthermore, the total, statistical and systematic uncertainties of the combined results for $Y_{\gamma_{\mathrm{incl}}}$ and R_γ are shown in the right parts of Fig. 7.2.14 as well. For $Y_{\gamma_{\mathrm{incl}}}$, total uncertainties of about $3\,\%$ are achieved if all three measurements enter the combination, observing a modest rise for higher p_{T} due to a lack of statistics. Otherwise, the total uncertainties are dominated by the systematics and values of approximately $6\,\%$ are accomplished below $1\,\mathrm{GeV}/c$. The R_γ is measured with a precision of about $5\,\%$ in most of the p_{T} bins, limited by statistical effects both at low and high p_{T}.

Correction for Finite Bin Width

Analog to the correction for the finite bin width for the meson measurements, which is described in Sec. 6.2.5, a similar correction is applied for $Y_{\gamma_{\mathrm{incl}}}$ and R_γ. The shifts are performed along the vertical axis for the $Y_{\gamma_{\mathrm{incl}}}$ and the corresponding π^0 measurements so that the respective results on R_γ can be combined. The bin shift corrections for $Y_{\gamma_{\mathrm{incl}}}$ are shown in Fig. 7.2.15 for PCM-EMCal and EMCal which are applied in order to shift the data points along the vertical axis.

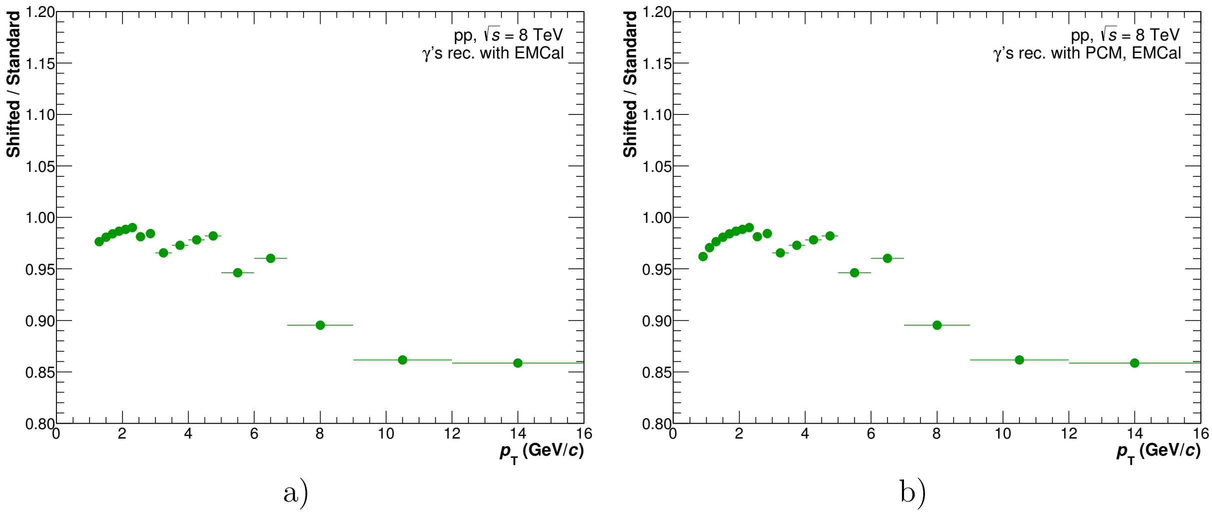

Figure 7.2.15: The size of the bin width corrections for the combined $Y_{\gamma_{\mathrm{incl}}}$ measurements are shown for EMCal, a), and PCM-EMCal, b), shifting the spectra along the vertical direction.

The corresponding input π^0 spectra are also shifted along the vertical axis so that the resulting shifts on the R_γ are determined which are visualized in Fig. B.3.34. The corrections are nearly equal on the $Y_{\gamma_{\mathrm{incl}}}$ and π^0 spectra so that they are found to be at the sub-percent level. Only for the PCM, the correction is of the order of 2 % for the lowest p_{T} bins used in the analysis.

7.2.4 Results

The measurement of the invariant differential cross section of inclusive photon production $Y_{\gamma_{\mathrm{incl}}}$ in pp collisions at $\sqrt{s} = 8\,\mathrm{TeV}$ covers a transverse momentum range of $0.3 < p_{\mathrm{T}} < 16\,\mathrm{GeV}/c$. It is shown in the Fig. 7.2.16a. This presented result on $Y_{\gamma_{\mathrm{incl}}}$ is accomplished by combining the individual measurements provided by the PCM, PCM* and EMCal methods, which is described in Sec. 7.2.3. As usual, the vertical error bars represent the statistical uncertainties, whereas the boxes quantify the bin widths in horizontal direction and the systematic uncertainties in vertical direction. For the combined $Y_{\gamma_{\mathrm{incl}}}$ result, the statistical uncertainties are predominantly below 1 % while the systematic uncertainties are found to be in the region of 3 − 3.5 % for the p_{T} interval of $1.4 < p_{\mathrm{T}} < 8\,\mathrm{GeV}/c$. The exact magnitudes of both uncertainties for each p_{T} bin can also be deduced from the previously shown Fig. 7.2.14. Independently, an additional normalization uncertainty from the cross section determination, see Tab. 4.2.4 in Sec. 4.2, enters at a level

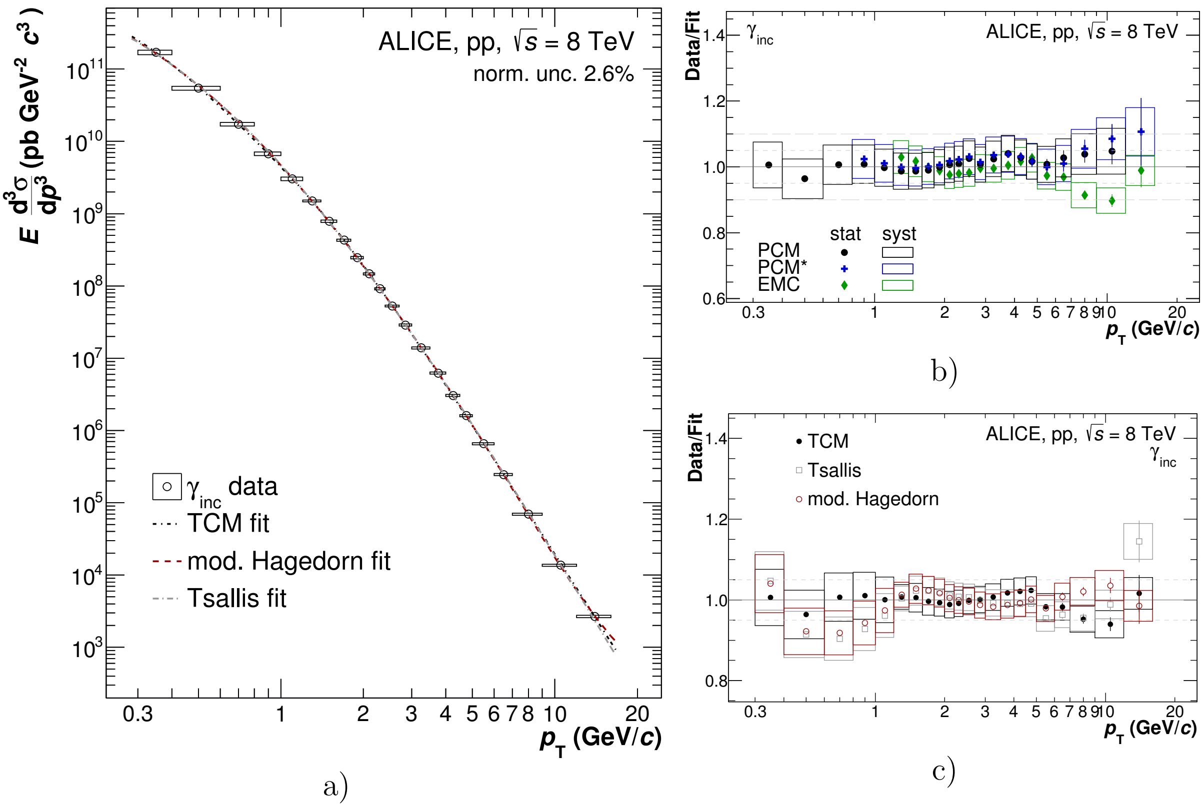

Figure 7.2.16: a) The invariant cross section $Y_{\gamma_{\mathrm{incl}}}$ at mid-rapidity obtained from the combination of all input measurements for pp collisions at $\sqrt{s} = 8$ TeV which is plotted together with different fits of the spectrum. b) The ratios of the individual measurements to the TCM fit of the combined $Y_{\gamma_{\mathrm{incl}}}$ spectrum are shown in a). c) The ratios of the $Y_{\gamma_{\mathrm{incl}}}$ data to the fits using three different functional forms: a TCM, a Tsallis as well as a modified Hagedorn.

of 2.6 %. By default, the $Y_{\gamma_{\mathrm{incl}}}$ spectrum is fitted using a TCM function which is defined in Eq. 2.3.12. The obtained TCM fit, using the total uncertainties of the respective data points computed by the quadratic combination of statistical and systematic uncertainties, is also plotted in Fig. 7.2.16a. Beyond that, the extracted TCM fit parameters are summarized in Tab. 7.2.4, where the fit uncertainties on the different parameters are also given. The TCM fit is used to parameterize the $Y_{\gamma_{\mathrm{incl}}}$ spectrum which also allows a comparison of the individual results provided by the different reconstruction methods. This comparison is shown in Fig. 7.2.16b, where the ratios of the respective data points and the TCM fit of the combined $Y_{\gamma_{\mathrm{incl}}}$ spectrum are presented. This figure demonstrates that the $Y_{\gamma_{\mathrm{incl}}}$ cross sections measured with the PCM, PCM* and EMCal methods agree to each other within the given uncertainties. Some tension between the methods could be indicated at around 10 GeV/c, which is not significant though.

Furthermore, the $Y_{\gamma_{\mathrm{incl}}}$ spectrum is fitted using two additional functions: a Tsallis and a modified Hagedorn, which are defined in Eq. 2.3.13 as well as Eq. 2.3.14 and which are being used in the context of neutral meson measurements, too. The respective fit results using these two functional forms are also superimposed in Fig. 7.2.16a, where the result of the default TCM fit is visualized as well. The ratios of the $Y_{\gamma_{\mathrm{incl}}}$ data points and the respective parameterizations of the spectra

$Y_{\gamma_{\mathrm{incl}}}$ in pp, $\sqrt{s} = 8\,\mathrm{TeV}$					
TCM fit parameters					χ^2_{red}
A_e (pb GeV$^{-2}c^3$)	T_e (GeV)	A (pb GeV$^{-2}c^3$)	T (GeV)	n	
$(3.54\pm8.77)\cdot10^{12}$	0.106 ± 0.083	$(0.64\pm1.09)\cdot10^{10}$	0.472 ± 0.176	2.993 ± 0.206	$1.9\cdot10^{-3}$

Tsallis fit parameters			χ^2_{red}
C (pb)	T (GeV)	n	
$(3.08\pm1.20)\cdot10^{11}$	0.084 ± 0.017	6.476 ± 0.393	$9.0\cdot10^{-3}$

Table 7.2.4: The TCM and Tsallis fit parameters which are found to approximate the $Y_{\gamma_{\mathrm{incl}}}$ spectrum shown in Fig. 7.2.16 for pp, $\sqrt{s} = 8\,\mathrm{TeV}$.

using the different fit functions are shown in Fig. 7.2.16c. The ratios indicate that in principle all three functions may describe the $Y_{\gamma_{\mathrm{incl}}}$ spectrum over the complete p_{T} interval covered by the measurement. However, the TCM fit does show the best agreement for the complete range which is found to be within 10 % regarding each p_{T} bin. Furthermore, the smallest χ^2_{red} value of all fit functions is obtained for this case which is quoted in Tab. 7.2.4 as well. The magnitude of χ^2_{red} is found to be small since the fitting is performed using the total uncertainties of $Y_{\gamma_{\mathrm{incl}}}$ without assuming any correlations of the respective contributions of systematic uncertainties. The corresponding value as well as the obtained fit parameters for the Tsallis function are quoted in Tab. 7.2.4 in addition. The Tsallis struggles to provide a reasonable description at low p_{T} but delivers a decent description of the spectrum beyond that. Finally, Fig. 7.2.16 also includes comparisons with the modified Hagedorn function, which provides a fairly good description for higher p_{T} comparable to the TCM but also fails to describe the spectrum at low p_{T}.

Based on the measurement of $Y_{\gamma_{\mathrm{incl}}}$, the direct photon excess ratio R_γ is determined. It is defined as the ratio of the inclusive and decay photon yields which can be rewritten according to Eq. 2.3.18 as follows: $R_\gamma = \left(\gamma_{\mathrm{inc}}/\pi^0\right)_{\mathrm{meas}} / \left(\gamma_{\mathrm{dec}}/\pi^0_{\mathrm{param}}\right)_{\mathrm{sim}}$. The input π^0 measurement is described in Sec. 6.2, see also Ref. [4], while the extraction of the decay photon yield $Y_{\gamma_{\mathrm{decay}}}$ as well as the parameterization of the π^0 spectrum is described in Sec. 7.1. Using these input measurements, the direct photon excess ratio R_γ is computed for pp collisions at $\sqrt{s} = 8\,\mathrm{TeV}$ and shown in Fig. 7.2.17a, covering a p_{T} range of $0.3 < p_{\mathrm{T}} < 16\,\mathrm{GeV}/c$. The presented R_γ is the result of the combination of the three individual measurements displayed in Fig. 7.2.11. Over the complete p_{T} range, they are found to be in agreement with each other within uncertainties. The combined R_γ features systematic uncertainties of about 4.5 – 5.5 % between $1 < p_{\mathrm{T}} < 7\,\mathrm{GeV}/c$. Furthermore, the combined statistical uncertainties range in the order of 2 – 3 % in the same p_{T} interval. More details concerning both uncertainties can also be deduced from the previously shown Fig. 7.2.14 from which they can be read off as a function of p_{T}.

If a value of R_γ is measured that is greater than unity for a certain p_{T} bin, $R_\gamma > 1$, an indication for a direct photon signal is found. However, it is also experimentally possible to obtain values smaller than unity due to experimental uncertainties. With the present accuracy of the R_γ measurement shown in Fig. 7.2.17a, no significant direct photon excess is observed for $p_{\mathrm{T}} < 7\,\mathrm{GeV}/c$. Furthermore, the onset of prompt photon production above $p_{\mathrm{T}} > 7\,\mathrm{GeV}/c$, which is predicted by various NLO pQCD calculations, is consistently observed in data although the experimental accuracy is not good enough to state a significant effect. However, this finding

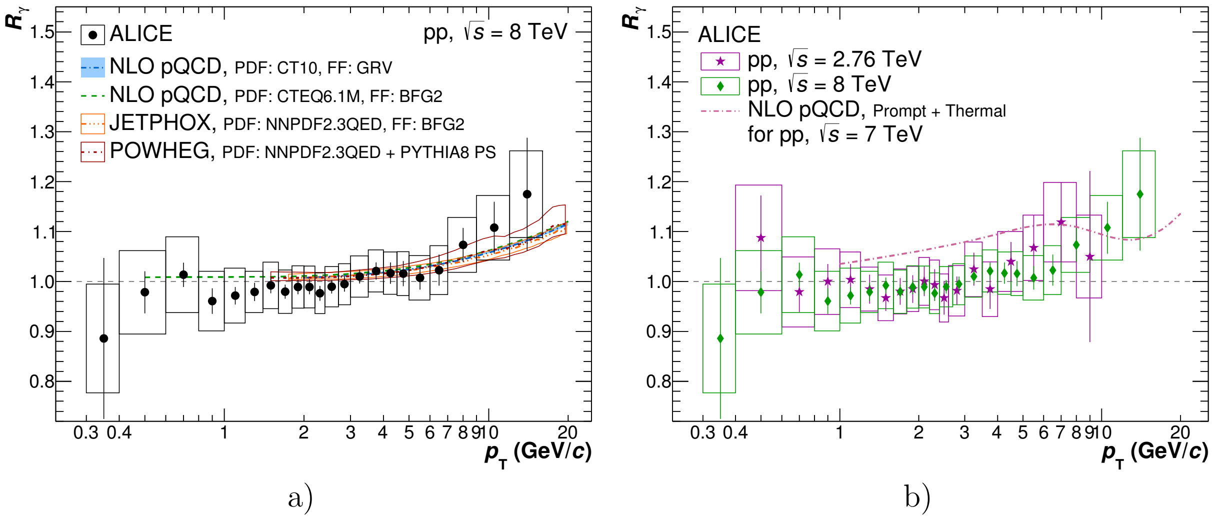

Figure 7.2.17: a) The direct photon excess ratio R_γ measured in pp, $\sqrt{s} = 8$ TeV. Different theory predictions are superimposed as summarized in the legend. b) A comparison of the measured R_γ for pp, $\sqrt{s} = 2.76$ and 8 TeV. Furthermore, a NLO pQCD calculation is included which predicts an additional thermal component of direct photons already in pp collisions at $\sqrt{s} = 7$ TeV [3].

provides indeed evidence for the rise of R_γ being consistent with theory calculations at high p_T. These prompt photon expectations from theory, which are shown in Fig. 7.2.17a, are calculated via the following formula:

$$R_\gamma^{\rm NLO} = 1 + \frac{Y_{\gamma_{\rm dir}}^{\rm NLO}}{Y_{\gamma_{\rm decay}}}, \tag{7.2.8}$$

using $Y_{\gamma_{\rm decay}}$ extracted from the particle decay simulation, see Sec. 7.1, to enable a comparison of the respective $Y_{\gamma_{\rm dir}}^{\rm NLO}$ calculations on the level of R_γ as shown in Fig. 7.2.17a. These pQCD predictions for $Y_{\gamma_{\rm dir}}^{\rm NLO}$ are based on different PDFs and FFs. The calculations labeled as NLO pQCD [96, 280] are using CT10 [281–283] and CTEQ6.1M [284] proton PDFs together with GRV [285] and BFG2 [286] FFs. Furthermore, a JETPHOX [287] calculation based on the proton PDF NNPDF2.3QED [288] and the FF BFG2 is provided as well as a POWHEG [287] prediction based on the same PDF but exploiting the PYTHIA 8 parton shower algorithm instead of a fragmentation function. The uncertainty bands of the respective theory calculations, which are shown in Fig. 7.2.17a, are estimated by variations of the factorization scale value μ within $0.5p_T < \mu < 2p_T$ regarding the factorization, renormalization and fragmentation scales at the same time. Given the present experimental uncertainties of R_γ, all pQCD calculations are in agreement with data over the complete p_T interval covered by the measurement. Moreover, all theory calculations are found to be consistent with each other within their associated uncertainties. In this context, it is not possible to discriminate between different PDFs or FFs which are used as input for the different predictions.

In Fig. 7.2.17b, a comparison of the R_γ measurements in pp collisions at $\sqrt{s} = 2.76$ and 8 TeV is shown. Both measurements are in fact part of the ALICE publication on the direct photon production at low p_T [6, 7] for which the R_γ measurement at $\sqrt{s} = 2.76$ TeV is mainly contributed by Friederike Bock [219]. The two R_γ results are found to be consistent with each other and show no indication of a direct photon signal in pp collisions below 7 GeV/c. Mainly due to statistical limitations, the measurement at $\sqrt{s} = 2.76$ TeV provides less accuracy for higher p_{T} beyond 4 GeV/c. Furthermore, a thermal prediction [3] is also shown in Fig. 7.2.17b which is exemplary mentioned in Chap. 1 as one of the references predicting a direct photon excess at low p_{T} due to an additional thermal component already being present in pp collisions. However, the measurements evidently disfavor such an assumption. No hint for such a signal at the predicted magnitude can be observed below 7 GeV/c.

By exploiting the subtraction method, which is introduced in Eq. 2.3.17, the direct photon spectra $Y_{\gamma_{\mathrm{dir}}}$ are determined using R_γ and $Y_{\gamma_{\mathrm{incl}}}$ as follows: $\gamma_{\mathrm{dir}} = \left(1 - R_\gamma^{-1}\right) \cdot \gamma_{\mathrm{inc}}$. The obtained $Y_{\gamma_{\mathrm{dir}}}$ result is presented in Fig. 7.2.18 together with theory predictions and the $Y_{\gamma_{\mathrm{incl}}}$ spectrum.

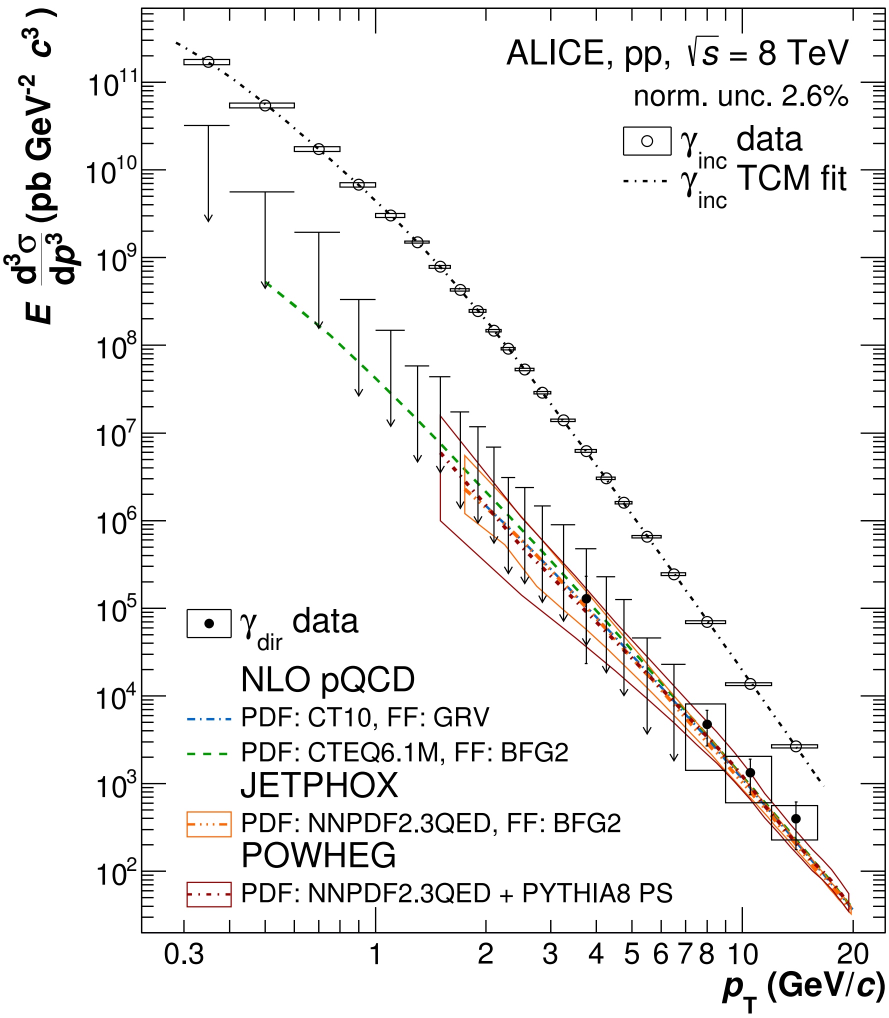

a)

Figure 7.2.18: The invariant cross sections, and upper limits respectively, of $Y_{\gamma_{\mathrm{incl}}}$ and $Y_{\gamma_{\mathrm{dir}}}$ production at mid-rapidity in pp collisions at $\sqrt{s} = 8$ TeV. Different theory predictions for $Y_{\gamma_{\mathrm{dir}}}$ are superimposed. The normalization uncertainty of 2.6 % is quoted independently and needs to be taken into account, see Tab. 4.2.4. If no data points could be extracted for $Y_{\gamma_{\mathrm{dir}}}$, upper limits at 90 % C.L. are shown.

In Fig. 7.2.18, the $Y_{\gamma_{\rm incl}}$ spectrum is plotted together with its parameterization provided by the TCM function. The additional normalization uncertainty, independently entering from the cross section determination, enters at a level of 2.6 % in addition, see Tab. 4.2.4 in Sec. 4.2. For $Y_{\gamma_{\rm dir}}$, three data points can be extracted between $7 < p_{\rm T} < 16\,{\rm GeV}/c$ for which the R_γ, considering its total uncertainties, is found to be above unity. For the other data points, upper limits at 90 % C.L. are calculated which are represented by the horizontal bars at the end of the arrows. They are determined for each $p_{\rm T}$ bin for which the central value of the R_γ measurement does not exceed unity respecting its total uncertainty at a level of $1\,\sigma$. This is the case for all $p_{\rm T}$ bins below 7 GeV/c. If the central value of R_γ, considering either $1\,\sigma$ of statistical or systematic uncertainty, is found to be above unity, the direct photon cross section $Y_{\gamma_{\rm dir}}$ is determined and only a marker or a box is drawn in addition to the upper limit, which in fact only applies to the $p_{\rm T}$ bin at 4 GeV/c. The calculated upper limits of direct photon production $Y_{\gamma_{\rm dir}}$ are obtained at 90 % C.L. which is equivalent to $1.28\,\sigma$ of the total uncertainty. The same NLO pQCD predictions are plotted in Fig. 7.2.18 as previously shown for the R_γ in Fig. 7.2.17a. All theory calculations agree with the extracted data points on $Y_{\gamma_{\rm dir}}$ well within the given statistical uncertainties. Their predicted cross section is also well compatible with the upper limits which can be quoted for $p_{\rm T} < 7\,{\rm GeVc}$ at 90 % C.L.

The ALICE publication [6] reporting the measurement of direct photon production at low $p_{\rm T}$ involves not only the result just presented for pp collisions at $\sqrt{s} = 8\,{\rm TeV}$ but also the corresponding measurement at $\sqrt{s} = 2.76\,{\rm TeV}$ which is mainly provided by Friederike Bock [219]. The measurements of both $Y_{\gamma_{\rm incl}}$ and $Y_{\gamma_{\rm dir}}$ spectra are more accurate at $\sqrt{s} = 8\,{\rm TeV}$ though, for which the onset of R_γ beyond 7 GeV/c due to contributions of prompt pQCD photons is seen. Although this is not a significant observation, it provides evidence and motivates further measurements involving EMCal triggers in order to improve the accuracy in this $p_{\rm T}$ region, see also the upcoming Sec. 7.3. On the other side, the measurement of R_γ and the determination of upper limits regarding $Y_{\gamma_{\rm dir}}$ in pp collisions at $\sqrt{s} = 2.76\,{\rm TeV}$ is of importance in the context of Pb-Pb measurements [105] which are shown in Fig. 2.3.11 in Sec. 2.3.3. The same plots are presented in the following Fig. 7.2.19 but the pp reference measured at the same center of mass energy is superimposed this time. In Fig. 7.2.19a, the corresponding upper limits for the pp reference are plotted, scaled by the average number of binary collisions $\langle N_{\rm coll}\rangle$. However, the precision of the pp measurement is not sufficient to confirm the expected $N_{\rm coll}$ scaling behavior at high $p_{\rm T}$. The corresponding R_γ measurement is shown in Fig. 7.2.19b. While there is no excess of direct photons seen for pp collisions, R_γ is found to be larger than unity for the Pb-Pb case in contrast. This comparison further strengthens the interpretation of the heavy-ion results for which the QGP is considered to be a source of thermal photons additionally contributing to the inclusive sample of direct photons at low $p_{\rm T}$.

7.3 Outlook: Improving the Precision of Direct Photon Measurements

In order to improve the precision of direct photon measurements and to possibly add more data points to the $Y_{\gamma_{\rm dir}}$ spectrum shown in Fig. 7.2.18 as well as Fig. 7.2.19a, the experimental accuracy on $Y_{\gamma_{\rm incl}}$ and R_γ needs to be increased.

The precision of the $Y_{\gamma_{\rm incl}}$ result may further be improved by conducting the measurement using the PHOS and adding it to the combination, which would yield another independent

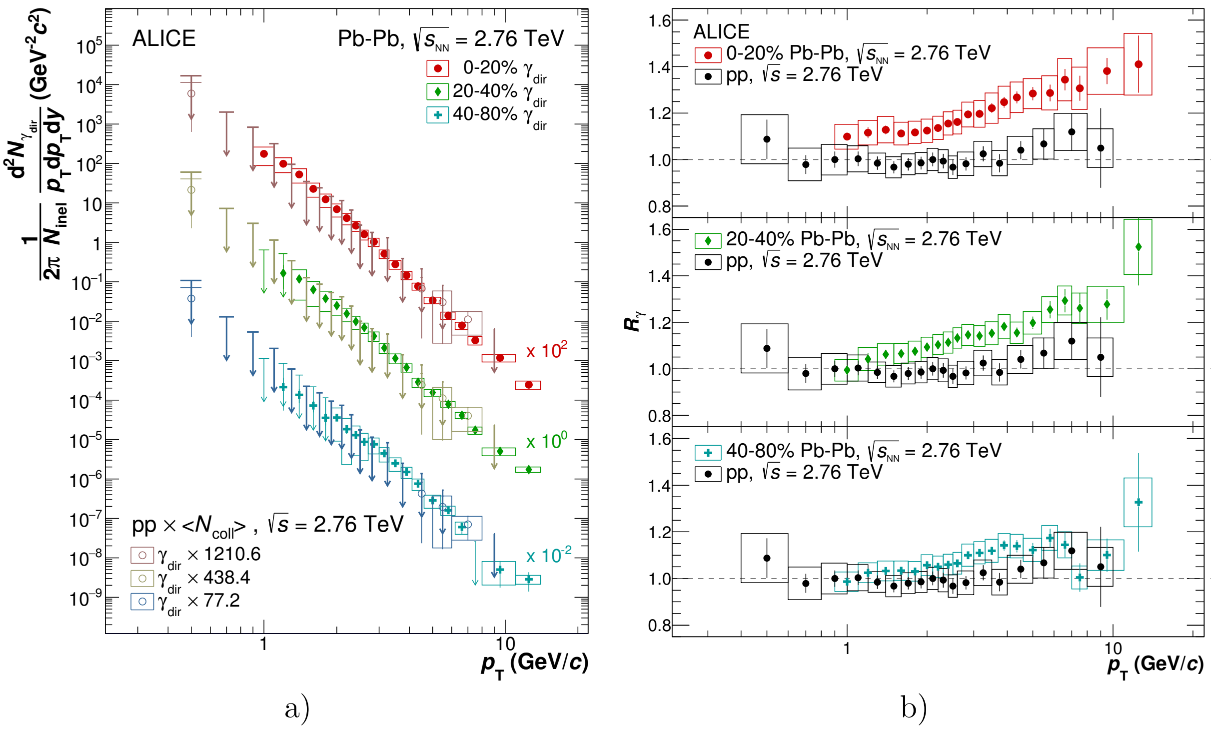

Figure 7.2.19: The invariant yields of direct photon production $Y_{\gamma_{\rm dir}}$, a), and the corresponding values of R_γ, b), measured for three different centrality classes of Pb-Pb collisions at $\sqrt{s_{\rm NN}} = 2.76\,\rm TeV$ which are compared to various theory predictions [105]. In addition, the corresponding measurements for pp collisions at $\sqrt{s} = 2.76\,\rm TeV$ are shown. The pp reference on concerning $Y_{\gamma_{\rm dir}}$ is scaled by the average number of binary collisions $\langle N_{\rm coll}\rangle$ for each centrality class. Since no data points could be extracted for $Y_{\gamma_{\rm dir}}$ in this case, upper limits at 90 % C.L. are shown for comparison.

measurement of $Y_{\gamma_{\rm incl}}$ regarding both statistical and systematic uncertainties. The precision of the existing EMCal-related measurements beyond $p_{\rm T} > 5\,{\rm GeV}/c$ can be increased by performing the $Y_{\gamma_{\rm incl}}$ analysis using EMCal triggered data. This also applies for the PHOS measurement to be carried out for which related triggers were also recorded. Furthermore, another possible way is to attempt to reduce the systematic uncertainties of the existing EMCal and PCM measurements even further. Concerning the EMCal, some focus could be set on the thorough understanding of the cluster shape $\sigma^2_{\rm long}$ in data and MC simulations and the related cluster merging effects. Moreover, the contributions related to the knowledge of the outer material budget as well as the cluster energy calibration could be focused in this context. For the PCM, the material budget uncertainty is the biggest contributor to the systematics which can be improved by resolving the difference of the material description between data and MC. Such an approach is followed by applying a weighting procedure as a function of the photon conversion radius which is still being developed and studied in detail. For LHC Run 3, a dedicated photon converter of well-known material thickness will be available to be used as a reference in this context. Additionally, the understanding of the different pileup contributions may possibly be enhanced by further studies so that the precision of the related correction procedure may be improved in order to reduce the associated systematic uncertainties.

As it is the case for Y_{γ_incl}, the R_γ measurement is also dominated by the EMCal results at high p_T and the PCM at low p_T. The increase of R_γ beyond $p_\mathrm{T} > 7\,\mathrm{GeV}/c$ may be studied by conducting the respective EMCal-related analysis on EMCal triggered data, which would allow to further test the theory predictions concerning this contribution from pQCD photons. Such measurements based on triggered data will be followed subsequent to this thesis since the first focus for publication was set on direct photon at low p_T. The related PHOS measurement of R_γ could also be carried out and combined with the existing results. Moreover, a better understanding of the systematic effects and their related systematic uncertainties can be followed as described for the Y_{γ_incl} measurement. Some improvement can still be achieved for the input π^0 measurements used to construct the R_γ for which more reconstruction methods like PCM-PHOS and PCM-Dalitz can be added to the combination. For LHC Run 2, the DCal and PCM-DCal methods are also available in principle. Such progress would also lead to improving the precision of $Y_{\gamma_\mathrm{decay}}$ extracted from the decay photon simulation, for which additional measurements of input particles which soon become available could lead to a reduction of the associated systematic uncertainty. Another method to measure R_γ at lowest p_T is also foreseen to be pursued, the so-called π^0-tagging. It represents a different way to compute the double ratio for which the PCM material budget uncertainty cancels out completely. On the other hand, however, EMCal-related uncertainties enter in this case that are expected to dominate the remaining systematic uncertainties, i.a. the energy scale uncertainty at low p_T. This method would also strongly profit from incorporating EMCal triggers into the measurements to extend the measurement to higher p_T.

Trivially, recording simply more statistics in upcoming LHC runs will also help to improve the measurements of Y_{γ_incl} and R_γ. However, the effect would be limited for the Y_{γ_incl}, only leading to an enhancement of the p_T reach covered by the experiments. This is due to the fact that only the systematic uncertainties basically limit the precision at low p_T. Hence, substantial efforts to further reduce the systematic uncertainties are still required for this low p_T region. Furthermore, the reported meson measurements using the different reconstruction methods awaits its application to Pb-Pb data, for which commonly only PCM and PHOS entered in recent publications. The new LHC Run 2 data may also provide many new insights for which pp and p-Pb data of highest statistics including large amounts of calorimeter triggers are available. These triggers are also of relevance for the neutral meson measurements to improve their precision as well as to further provide accurate measurements of the R_{pA} and R_{AA} in the high p_T region.

Summary

This thesis reports on measurements of neutral meson, namely π^0 and η, production in pp collisions at $\sqrt{s} = 0.9$, 2.76, 7 and 8 TeV. Furthermore, measurements of the inclusive and direct photon production are presented for pp collisions at $\sqrt{s} = 2.76$ and 8 TeV. The different collision systems were provided by the LHC and the data was recorded using the ALICE experiment. The neutral mesons π^0 and η are reconstructed via their two-gamma decay channels, $\pi^0(\eta) \rightarrow \gamma\gamma$, by means of invariant mass analysis. Photons are reconstructed using two fundamentally different detection methods exploiting the ALICE detector. The first method utilizes the fact that photons may convert into e^-e^+ pairs within the inner detector material of ALICE, located between the interaction point and the radial midpoint of the TPC. These e^-e^+ pairs, originating from secondary vertices, can be reconstructed using the main tracking system of ALICE centered at mid-rapidity which consists of the ITS and the TPC. The second method of photon reconstruction employs the measurement of photons using electromagnetic calorimeters, in particular the EMCal. If a photon enters such a calorimeter, it generates an electromagnetic shower spreading over multiple adjacent cells. These cells can be grouped into so-called clusters so that the full energy of impinging photons can be reconstructed.

The reported neutral meson measurements involve the results for the invariant differential cross sections of inclusive π^0 and η meson production at mid-rapidity in pp collisions at $\sqrt{s} = 8$ TeV which cover transverse momentum ranges of $0.3 < p_{\mathrm{T}} < 35.0\,\mathrm{GeV}/c$ and $0.5 < p_{\mathrm{T}} < 35.0\,\mathrm{GeV}/c$ respectively. These results are subject of a recent ALICE publication [4, 5] which was written and published in the context of this thesis. The analog measurements at $\sqrt{s} = 7$ TeV span p_{T} ranges of $0.3 < p_{\mathrm{T}} < 25.0\,\mathrm{GeV}/c$ for the π^0 and $0.4 < p_{\mathrm{T}} < 16.0\,\mathrm{GeV}/c$ for the η, whereas for $\sqrt{s} = 0.9$ TeV intervals of $0.3 < p_{\mathrm{T}} < 10.0\,\mathrm{GeV}/c$ and $0.9 < p_{\mathrm{T}} < 3.0\,\mathrm{GeV}/c$ are covered respectively. They are foreseen to enter an upcoming ALICE publication planned to update the current Ref. [10] which exhibits some limitations on the sampled statistics and the available input measurements. Moreover, the corresponding meson measurements were carried out for pp collisions at $\sqrt{s} = 2.76$ TeV as well, see Ref. [8], for which analysis contributions were provided. The production cross sections are measured for the p_{T} intervals $0.3 < p_{\mathrm{T}} < 25.0\,\mathrm{GeV}/c$ for the π^0 and $0.4 < p_{\mathrm{T}} < 16.0\,\mathrm{GeV}/c$ for the η meson. Beyond that, analysis contributions were also provided for the recently published ALICE paper [9] on neutral meson production in p-Pb collisions with respect to the EMCal-related analysis and the basic quality assurance of the datasets.

The measured meson spectra are parameterized by default using a TCM fit function since it provides the best description in comparison to a Tsallis, a modified Hagedorn and a pure power law function, which are all employed as well to describe the measured spectra. With increasing center of mass energy, the particle spectra become harder so that the powers n of the power law fits are observed to decrease, lining up reasonably. The measurements at $\sqrt{s} = 0.9$ TeV show the highest value of about $n \approx 7.5$, decreasing to about $n \approx 6.3$ for $\sqrt{s} = 2.76$ TeV. Furthermore, values of approximately $n \approx 6.0$ and $n \approx 5.9$ are obtained for $\sqrt{s} = 7$ and 8 TeV. The determined TCM and Tsallis fit parameters are also observed to follow the expected $\sqrt{s}$ behavior.

Different theory calculations are compared to the measurements involving comparisons with PYTHIA 8.2 predictions using the Monash 2013 tune [81, 117]. In general, good agreement is found between data and the Monash 2013 tune within the given experimental uncertainties. The measurement of the π^0 at $\sqrt{s} = 0.9$ TeV exhibits substantial uncertainties, for which the

PYTHIA prediction is nevertheless within 20 % throughout the p_{T} region covered. For the π^0 at $\sqrt{s} = 2.76$ TeV, a good agreement can be stated while the PYTHIA predictions overshoot the measurements for $\sqrt{s} = 7$ and 8 TeV by approximately 10 % to 20 %. The shape of the measured spectra can be reasonably described besides the presence of a bump in the ratio which is indicated at around 3 GeV/c. For the η, the PYTHIA description is within $\sim$20 % for all center of mass energies. At low p_{T}, however, PYTHIA is not able to describe the η spectra at $\sqrt{s} = 7$ and 8 TeV and deviates significantly.

Furthermore, the π^0 measurements are compared to NLO pQCD calculations [76, 77] using the PDF MSTW [114] and the FF DSS14 [77]. All pQCD calculations overestimate the measured cross sections for which the respective magnitude is found to be strongly p_{T}-dependent as well as $\sqrt{s}$-dependent. The highest deviation of up to approximately 60 % for $\mu = p_{\mathrm{T}}$ is seen for $\sqrt{s} =$ 7 TeV. However, these predictions do a much better job compared to the analog calculations for the η meson spectra using the PDF CTEQ6M5 [256] and the FF AESSS [76]. In this case, the deviations are partially of the order of 100 % and even beyond compared to the η measurement. In contrast to the π^0, however, the FFs of the η meson have not been updated for quite a while and hence do not include LHC data in the global fits at all. In the meantime, high precision η measurements covering wide p_{T} intervals became available, as reported in this thesis, which would help to further constrain the FFs in this case and consequently help to significantly decrease the uncertainties in order to reduce the observed deviations. This could already be achieved for the π^0 for which the update from DSS07 [75], which had comparable discrepancies like the AESSS for the η, to its successor DSS14 significantly improved the description of measurements.

The η/π^0 ratios measured in pp collisions at $\sqrt{s} = 0.9$, 2.76, 7 and 8 TeV using the ALICE detector are consistent with each other within uncertainties. Moreover, a universal behavior of the η/π^0 ratio is confirmed for NA27, PHENIX and ALICE data for pp collisions starting from $\sqrt{s} = 27.5$ GeV up to 8 TeV within experimental uncertainties. In addition, the validity of m_{T} scaling, which is widely used to estimate the hadronic background of rare probes such as direct photons, dileptons and heavy-quark production, is tested by means of the η/π^0 ratio. Using m_{T} scaling, the p_{T}-dependent differential cross sections of most particles can be derived from the well measured light-flavor mesons, from pions or kaons for example, by assuming that the meson spectra can be described as a function of transverse mass m_{T}. Hence, this empirical scaling rule is widely used in the context of rare probes to estimate the various background sources for which no measurements are available. However, it is found that for $\sqrt{s} = 8$ TeV the m_{T} scaling prediction is estimated to be broken with a significance of $6.2\,\sigma$ for $p_{\mathrm{T}} < 3.5$ GeV/c [4]. No statement can be made for $\sqrt{s} = 0.9$ TeV, whereas there is indication for a m_{T} scaling violation with $2.1\,\sigma$ for 2.76 TeV [8]. A significant disagreement well beyond $5\,\sigma$ from the m_{T} scaling hypothesis is observed for $\sqrt{s} = 7$ TeV as well. Hence, all η/π^0 ratios are found to be consistently violating m_{T} scaling for $p_{\mathrm{T}} < 3.5$ GeV/c if the η reference is calculated using this scaling law. Whether the magnitude of m_{T} scaling violation depends on the collision energy could be clarified in future by the ongoing measurements of hadron spectra in pp collisions at $\sqrt{s} = 13$ TeV by ALICE.

The integrated yields $\mathrm{d}N/\mathrm{d}y|_{y\,\approx\,0}$ and the mean transverse momenta $\langle p_{\mathrm{T}}\rangle$ are also determined for the neutral meson measurements carried out at mid-rapidity for pp collisions at $\sqrt{s} =$ 0.9, 2.76, 7 and 8 TeV. Due to the considerable systematic uncertainties obtained for the π^0 and η meson measurements and the high extrapolation fractions down to zero p_{T}, substantial uncertainties are found for the yields and mean momenta. Nevertheless, the expected natural ordering of increasing $\mathrm{d}N/\mathrm{d}y$ and $\langle p_{\mathrm{T}}\rangle$ for increasing center of mass energy is observed since more particles are produced and spectra become harder. For the η meson, the measurement at $\sqrt{s} = 2.76\,\mathrm{TeV}$ tends to give a central value for the $\mathrm{d}N/\mathrm{d}y|_{y\,\approx\,0}$ which seems to be too high, whereas for $8\,\mathrm{TeV}$ a too low central value seems to be obtained when comparing to the global trends. However, no real conclusion can be drawn as the uncertainties are found to be significant concerning $\mathrm{d}N/\mathrm{d}y$ and $\langle p_{\mathrm{T}} \rangle$. The results are compared to measurements of the $\langle p_{\mathrm{T}} \rangle$ of charged particles [269] and to results concerning charged-particle multiplicity [270], for which an increase of $\langle p_{\mathrm{T}} \rangle$ is observed for increasing particle mass. Furthermore, all integrated yields are consistent within experimental uncertainties with the results from charged particle measurements [252, 262]. Another observation is made for the $\mathrm{d}N/\mathrm{d}y$ which is found to decrease if the mass of a particle increases. Hence, it can be stated that the determined $\langle p_{\mathrm{T}} \rangle$ and $\mathrm{d}N/\mathrm{d}y|_{y\,\approx\,0}$ values for neutral mesons fit the general picture. These values can be used to further constrain theoretical models describing global properties like the thermal model of particle production [271].

The measurement of light neutral mesons is of relevance and special interest since no other ALICE measurement of identified particle spectra is available for such wide p_{T} ranges from the order of a hundred MeV/c up to way more than $100\,\mathrm{GeV}/c$. This range is expected to be reached for pp collisions at $\sqrt{s} = 8\,\mathrm{TeV}$ using the merged EMCal single cluster analysis described in Ref. [8]. Moreover, not only a reliable reference for heavy-ion collisions is provided but the neutral meson spectra are also a relevant input and provide important constraints for PDFs and FFs in the context of pQCD calculations. Here, the LHC energies enable to probe rather low values of $x \sim 0.001$ and $z \sim 0.1$. In this context, the π^0 is of interest because it is the lightest hadron being produced most abundantly, originating dominantly from gluon fragmentation. Only above $20\,\mathrm{GeV}/c$, quark fragmentation also starts to play a role. On the other hand, the η is relevant because of its hidden strangeness component. Furthermore, high precision measurements of neutral meson cross sections are also needed to obtain essential knowledge about decay photons which are a dominant background source for many measurements related to direct photons, dileptons and heavy-quark production, for example.

In addition, the measurement of the invariant differential cross section of inclusive photon production $Y_{\gamma_{\mathrm{incl}}}$ in pp collisions at $\sqrt{s} = 8\,\mathrm{TeV}$, which covers a transverse momentum range of $0.3 < p_{\mathrm{T}} < 16\,\mathrm{GeV}/c$, is presented in this thesis. Based on the measurement of $Y_{\gamma_{\mathrm{incl}}}$, the direct photon excess ratio R_γ is determined which is defined as the ratio of the inclusive and decay photon yields for a given p_{T} bin. For this purpose, the π^0 and η meson production cross sections at $\sqrt{s} = 8\,\mathrm{TeV}$, which are determined in the context of thesis, are a crucial input for the decay photon simulation used to estimate the decay photon spectrum. The dominant contribution is found to be due to π^0 decays with about $\sim 85\,\%$ of the total amount of such photons at high p_{T}. The second highest contribution stems from η meson decays which account for a fraction of approximately $\sim 10\,\%$ at high p_{T}.

With the present accuracy of the R_γ measurement, no significant direct photon excess is observed for $p_{\mathrm{T}} < 7\,\mathrm{GeV}/c$ in pp collisions at $\sqrt{s} = 8\,\mathrm{TeV}$. Furthermore, the onset of prompt photon production above $p_{\mathrm{T}} > 7\,\mathrm{GeV}/c$, which is predicted by various NLO pQCD calculations, is consistently observed in data although the experimental accuracy is not good enough to state a significant effect. However, this finding provides indeed evidence for the rise of R_γ being consistent with theory calculations at high p_{T}. The NLO pQCD [96, 280] predictions of the direct photon yield are based on different PDFs and FFs involving CT10 [281–283] and CTEQ6.1M [284] proton PDFs together with GRV [285] and BFG2 [286] FFs. Furthermore, a JETPHOX [287] calculation based on the proton PDF NNPDF2.3QED [288] and the FF BFG2 is compared as well as a POWHEG [287] prediction based on the same PDF but exploiting the PYTHIA8 parton shower algorithm instead of a fragmentation function. Given the present experimental uncertainties of R_γ, all pQCD calculations are in agreement with data over the complete p_T interval covered by the measurement. Moreover, all theory calculations are found to be consistent with each other within their associated uncertainties. In this context, it is not possible to discriminate between different PDFs or FFs which are used as input for the respective predictions.

Furthermore, a thermal prediction [3] is also compared to data which is one of the references predicting a direct photon excess at low p_T due to an additional thermal component already being present in pp collisions. However, the measurements evidently disfavor such an assumption. No hint for such a signal at the predicted magnitude can be observed below $7\,\mathrm{GeV}/c$. By exploiting the subtraction method, the direct photon spectra Y_{γ_dir} are determined using R_γ and Y_{γ_incl}. For Y_{γ_dir}, three data points can be extracted between $7 < p_\mathrm{T} < 16\,\mathrm{GeV}/c$ for which the R_γ, considering its total uncertainties, is found to be above unity. For the other data points, upper limits at $90\,\%$ C.L. are calculated and presented. All theory calculations agree with the extracted data points on Y_{γ_dir} well within the given statistical uncertainties. Their predicted cross section is also well compatible with the upper limits which can be quoted for $p_\mathrm{T} < 7\,\mathrm{GeV}/c$ at $90\,\%$ C.L. Taken together, these results on inclusive and direct photon are published by ALICE, see Refs. [6, 7], which also contains the corresponding measurements performed for pp collisions at $\sqrt{s} = 2.76\,\mathrm{TeV}$. While there is no excess of direct photons seen for pp collisions at $\sqrt{s} = 2.76\,\mathrm{TeV}$, R_γ is found to be larger than unity for the Pb-Pb case at the equivalent center of mass energy in contrast. This comparison further strengthens the interpretation of the heavy-ion results for which the QGP is considered to be a source of thermal photons additionally contributing to the inclusive sample of direct photons at low p_T.

Finally, this thesis concludes with a discussion on how to further improve the precision of direct photon measurements in order to possibly add more data points to the Y_{γ_dir} spectrum for which the experimental accuracy on Y_{γ_incl} and R_γ needs to be increased.

Zusammenfassung

Diese Arbeit berichtet über Messungen der Produktion neutraler π^0- und η-Mesonen in pp Kollisionen bei $\sqrt{s} = 0.9$, 2.76, 7 und 8 TeV. Weiterhin werden Messungen der gesamten und direkten Photonenproduktion in pp Kollisionen bei $\sqrt{s} = 2.76$ und 8 TeV präsentiert. Für die verschiedenen Kollisionssysteme, bereitgestellt vom LHC, wurden Daten vom ALICE Experiment aufgenommen. Die neutralen π^0- und η-Mesonen werden mittels der invarianten Masse über ihre Zerfallskanäle in zwei Photonen rekonstruiert, $\pi^0(\eta) \rightarrow \gamma\gamma$. Die Photonen werden dabei über zwei fundamental verschiedene Methoden mit Hilfe des ALICE Detektors rekonstruiert. Die erste Methode nutzt die Tatsache, dass Photonen innerhalb des inneren Detektormaterials von ALICE zwischen dem Interaktionspunkt sowie dem Mittelpunkt der TPC in radialer Richtung in e^-e^+ Paare konvertieren können. Solche e^-e^+ Paare, die von sekundären Vertices stammen, können mit Hilfe des zentralen Spurrekonstruktionssystems von ALICE rekonstruiert werden, welches bei mittlerer Rapidität zentriert ist und sich aus dem ITS und der TPC zusammensetzt. Die zweite Messmethode nutzt elektromagnetische Kalorimeter, wobei im Speziellen das EMCal zur Verfügung steht. Wenn ein Photon auf ein solches Kalorimeter trifft, generiert es einen elektromagnetischen Schauer, der sich über mehrere angrenzende Zellen ausbreitet. Diese Zellen können zu sogenannten Clustern zusammengefasst werden, sodass die komplette Energie des einfallenden Photons rekonstruiert werden kann.

Die Messungen neutraler Mesonen beinhalten die Ergebnisse bezüglich der invarianten differenziellen Wirkungsquerschnitte für die gesamte π^0- und η-Mesonen Produktion bei mittlerer Rapidität in pp Kollisionen bei $\sqrt{s} = 8$ TeV, welche Transversalimpulsintervalle von jeweils $0.3 < p_{\mathrm{T}} < 35.0$ GeV/c und $0.5 < p_{\mathrm{T}} < 35.0$ GeV/c abdecken. Diese Resultate sind Bestandteil einer neueren ALICE-Publikation [4, 5], welche im Rahmen dieser Arbeit geschrieben und veröffentlicht worden ist. Die äquivalenten Messungen bei $\sqrt{s} = 7$ TeV umfassen Transversalimpulsintervalle von $0.3 < p_{\mathrm{T}} < 25.0$ GeV/c für π^0- und $0.4 < p_{\mathrm{T}} < 16.0$ GeV/c für η-Mesonen, während für $\sqrt{s} = 0.9$ TeV die jeweiligen Intervalle von $0.3 < p_{\mathrm{T}} < 10.0$ GeV/c sowie $0.9 < p_{\mathrm{T}} < 3.0$ GeV/c abgedeckt werden. Es ist vorgesehen, mit diesen Messungen die derzeitige ALICE-Publikation aus Ref. [10] zu aktualisieren, die einige Limitationen bezüglich der Statistik sowie den verfügbaren Messmethoden aufweist. Außerdem wurden die entsprechenden Messungen ebenfalls für pp Kollisionen bei $\sqrt{s} = 2.76$ TeV durchgeführt, siehe Ref. [8], wofür Beiträge zur Analyse geleistet worden sind. Die Produktionswirkungsquerschnitte sind in diesem Falle in den Intervallen $0.3 < p_{\mathrm{T}} < 25.0$ GeV/c für π^0- und $0.4 < p_{\mathrm{T}} < 16.0$ GeV/c für η-Mesonen gemessen. Darüber hinaus wurden Beiträge zur Analyse auch für die zuletzt veröffentlichte ALICE-Publikation [9] bezüglich der Produktion neutraler Mesonen in p-Pb Kollisionen hinsichtlich der EMCal Analyse sowie der grundlegenden Qualitätssicherung der Daten geleistet.

Die gemessenen Mesonenspektren werden standardmäßig mit einer TCM Fitfunktion parametrisiert, welche die beste Beschreibung der Spektren liefert im Vergleich zu einer Tsallis- und modifizierter Hagedorn-Funktion sowie einem einfachen Potenzgesetz, welche alle genutzt werden, um die gemessenen Spektren zu beschreiben. Mit ansteigender Schwerpunktenergie werden die Teilchenspektren härter, sodass entsprechend kleiner werdende Potenzen n der jeweiligen Fits mit einem Potenzgesetz beobachtet werden können. Die Messungen bei $\sqrt{s} = 0.9$ TeV zeigen den höchsten Wert von ungefähr $n \approx 7.5$, welcher sich verkleinert zu $n \approx 6.3$ für $\sqrt{s} = 2.76$ TeV Weiterhin werden Werte von ungefähr $n \approx 6.0$ und $n \approx 5.9$ für $\sqrt{s} = 7$ und 8 TeV extrahiert. Die erhaltenen TCM und Tsallis Fitparameter folgen ebenfalls dieser erwarteten $\sqrt{s}$-Abhängigkeit.

Verschiedene Theorieberechnungen, unter anderem Vorhersagen des PYTHIA 8.2 Monash 2013 Tunes [81, 117], sind mit den Messungen verglichen. Im Allgemeinen wird eine gute Übereinstimmung zwischen den Daten und den Vorhersagen dieses Tunes innerhalb der experimentellen Unsicherheiten festgestellt. Die Messung des π^0 bei $\sqrt{s} = 0.9$ TeV weist substanzielle Unsicherheiten auf, die jedoch mit der PYTHIA Vorhersage innerhalb von 20 % über den gesamten abgedeckten p_{T}-Bereich übereinstimmt. Für das π^0 bei $\sqrt{s} = 2.76$ TeV kann eine gute Übereinstimmung festgestellt werden, wobei die PYTHIA Vorhersagen die Messungen bei $\sqrt{s} = 7$ und 8 TeV um zirka 10 % bis 20 % überschätzen. Die Form der gemessenen Spektren kann angemessen beschrieben werden mit Ausnahme einer Abweichung bei ungefähr 3 GeV/c, welche im Verhältnis deutlich präsent ist. Für das η stimmt die PYTHIA Vorhersage innerhalb von ~ 20 % für alle Schwerpunktenergien überein. Bei kleinen p_{T} ist PYTHIA jedoch nicht in der Lage, die η Spektren bei $\sqrt{s} = 7$ und 8 TeV zu beschreiben, wobei eine signifikante Abweichung festgestellt wird.

Weiterhin sind die π^0 Messungen mit NLO pQCD Berechnungen [76, 77] unter der Nutzung der Partonenverteilungsfunktion (PDF) MSTW [114] mit der Fragmentationsfunktion (FF) DSS14 [77] verglichen. Alle pQCD Berechnungen überschätzen die gemessenen Wirkungsquerschnitte, wobei die genaue Abweichung sowohl von p_{T} als auch $\sqrt{s}$ abhängt. Die größte Abweichung von bis zu 60 % für $\mu = p_{\mathrm{T}}$ wird für $\sqrt{s} = 7$ TeV festgestellt. Diese Vorhersagen liefern jedoch eine viel bessere Beschreibung im Vergleich mit analogen Rechnungen für die η-Mesonenspektren unter Nutzung der PDF CTEQ6M5 [256] mit der FF AESSS [76]. In diesem Falle sind die Abweichungen im Hinblick auf die η Messung teilweise von bis zu 100 % und sogar höher. Im Gegensatz zum π^0 jedoch wurden die FFs der η-Mesonen für eine längere Zeit nicht aktualisiert, sodass überhaupt keine LHC Daten in den globalen Fits berücksichtigt sind. In der Zwischenzeit sind präzise Messungen des η-Mesons für breite Transversalimpulsintervalle verfügbar geworden, wie sie auch in dieser Arbeit vorgestellt werden, die einen wichtigen Beitrag zur weiteren Einschränkung der FFs liefern und somit zur Verkleinerung der Unsicherheiten beitragen können, um damit die beobachteten Abweichungen zu reduzieren. Dies konnte bereits für das π^0 erreicht werden, für welches eine Update von DSS07 [75], das vergleichbare Diskrepanzen wie AESSS für das η aufwies, zu dem Nachfolger DSS14 erfolgte, sodass eine bedeutende Verbesserung der Beschreibung der Messungen erreicht werden konnte.

Die von ALICE gemessenen η/π^0 Verhältnisse in pp Kollisionen bei $\sqrt{s} = 0.9$, 2.76, 7 und 8 TeV sind innerhalb der Unsicherheiten konsistent. Außerdem kann ein allgemeingültiges Verhalten des η/π^0 Verhältnisses für die NA27, PHENIX und ALICE Messungen in pp Kollisionen von $\sqrt{s} = 27.5$ GeV bis zu 8 TeV innerhalb der experimentellen Unsicherheiten bestätigt werden. Zusätzlich wird die Gültigkeit des m_{T}-Skalierungsverhaltens mit Hilfe des η/π^0 Verhältnisses getestet, welches weit verbreitet genutzt wird, um den hadronischen Hintergrund für rare Sonden wie direkte Photonen, Dileptonen oder der Produktion von schweren Quarks zu beschreiben. Mit Hilfe des m_{T}-Skalierungsverhaltens können die p_{T}-abhängigen differenziellen Wirkungsquerschnitte für die meisten Teilchen von den präzise gemessenen leichten Mesonen wie Pionen oder Kaonen hergeleitet werden, indem angenommen wird, dass die Mesonenspektren in Abhängigkeit der transversalen Masse m_{T} beschrieben werden können. Daher ist die Nutzung dieses empirischen Skalierungsverhaltens weit verbreitet im Zusammenhang mit raren Sonden, um jene Hintergrundquellen abzuschätzen für die keine Messungen verfügbar sind. Für $\sqrt{s} = 8$ TeV wird jedoch festgestellt, dass die m_{T}-Hypothese mit einer Signifikanz von $6.2\,\sigma$ für $p_{\mathrm{T}} < 3.5$ GeV/c widerlegt wird [4]. Keine Aussage kann für $\sqrt{s} = 0.9$ TeV getroffen werden, wohingegen ein Hinweis für die Verletzung dieses Skalierungsverhaltens mit $2.1\,\sigma$ für 2.76 TeV [8] existiert. Eine signifikante Abweichung über $5\,\sigma$ wird für $\sqrt{s} = 7$ TeV ebenfalls beobachtet. Somit verletzen die

η/π^0 Verhältnisse konsistent die m_T-Hypothesen für $p_\mathrm{T} < 3.5\,\mathrm{GeV}/c$. Ob das Ausmaß dieser Verletzung von der Schwerpunktenergie abhängt kann in der Zukunft beantwortet werden mit Hilfe der ALICE-Ergebnisse hinsichtlich der Hadronenspektren in pp Kollisionen bei $\sqrt{s} = 13\,\mathrm{TeV}$.

Die integrierten Ausbeuten $\mathrm{d}N/\mathrm{d}y|_{y\,\approx\,0}$ und mittleren Transversalimpulse $\langle p_\mathrm{T}\rangle$ sind ebenfalls ermittelt für die neutralen Mesonen bei mittlerer Rapidität in pp Kollisionen bei $\sqrt{s} = 0.9$, 2.76, 7 und 8 TeV. Aufgrund der erheblichen systematischen Unsicherheiten der π^0- und η-Meson Messungen und der großen Extrapolationsanteile bis hin zu verschwindenden Transversalimpulsen werden wesentliche Unsicherheiten für die integrierte Ausbeute und die mittleren Transversalimpulse gefunden. Nichtsdestotrotz kann das erwartete Verhalten von ansteigenden $\mathrm{d}N/\mathrm{d}y$ und $\langle p_\mathrm{T}\rangle$ für steigende Schwerpunktenergien beobachtet werden, da mehr und mehr Teilchen produziert sowie die Spektren immer härter werden. Für das η-Meson scheint die Messung bei $\sqrt{s} = 2.76\,\mathrm{TeV}$ einen tendenziell zu hohen zentralen Wert für $\mathrm{d}N/\mathrm{d}y$ zu liefern, wohingegen für 8 TeV ein zu kleiner zentraler Wert bestimmt wird im Vergleich zu den globalen Trends. Es kann jedoch keine wirkliche Schlussfolgerung getroffen werden, da signifikante Unsicherheiten hinsichtlich $\mathrm{d}N/\mathrm{d}y$ und $\langle p_\mathrm{T}\rangle$ bestehen. Die Resultate sind mit Messungen des $\langle p_\mathrm{T}\rangle$ von geladenen Teilchen [269] verglichen und mit Resultaten in Bezug auf der Multiplizität geladener Teilchen [270], für welche ein Anstieg von $\langle p_\mathrm{T}\rangle$ für zunehmende Teilchenmassen beobachtet wird. Darüber hinaus sind die integrierten Ausbeuten konsistent innerhalb der experimentellen Unsicherheiten mit den Ergebnissen der Messungen geladener Teilchen [252, 262]. Eine weitere Beobachtung bezüglich $\mathrm{d}N/\mathrm{d}y$ ist dessen Abnahme im Hinblick auf zunehmende Teilchenmassen. Daher kann die Aussage getroffen werden, dass die für die neutralen Mesonen ermittelten Werte $\langle p_\mathrm{T}\rangle$ und $\mathrm{d}N/\mathrm{d}y|_{y\,\approx\,0}$ in das globale Bild passen. Diese Messungen stehen nun zur Verfügung, um theoretische Modelle wie zum Beispiel das thermische Modell [271] weiter einzuschränken.

Die Messung leichter, neutraler Mesonen ist relevant und von besonderer Bedeutung, da keine andere ALICE Messung identifizierter Teilchenspektren für derartig weite p_T Intervalle von der Größenordnung einiger hundert MeV/c bis hin zu weit mehr als $100\,\mathrm{GeV}/c$ verfügbar ist. Es ist zu erwarten, dass dieses Intervall für pp Kollisionen bei $\sqrt{s} = 8\,\mathrm{TeV}$ mit Hilfe derjenigen EMCal Analyse erreicht werden kann, die einzelne fusionierte Cluster verwendet und in Ref. [8] beschrieben ist. Außerdem wird nicht nur eine verlässliche Referenz für Schwerionenkollisionen bereitgestellt, sondern mittels der neutralen Mesonenspektren auch ein relevanter Beitrag sowie wichtige Beschränkungen für die PDFs und FFs im Zusammenhang mit pQCD Berechnungen zur Verfügung gestellt. Hierbei ermöglichen die LHC Energien eher kleine Werte von $x \sim 0.001$ und $z \sim 0.1$ zu untersuchen. In diesem Zusammenhang ist das π^0 von Interesse, da es das leichteste Hadron ist, welches am häufigsten produziert wird und hauptsächlich von Gluonfragmentation stammt. Erst über $20\,\mathrm{GeV}/c$ beginnt die Quarkfragmentation eine größere Rolle zu spielen. Auf der anderen Seite ist das η relevant, da es eine versteckte Strangeness Komponente beinhaltet. Weiterhin werden hoch präzise Messungen der Produktionswirkungsquerschnitte neutraler Mesonen benötigt, um grundlegendes Wissen über die Zerfallsphotonen zu erlangen, welche eine dominante Hintergrundkomponente für viele Messungen wie beispielsweise für direkte Photonen, Dileptonen oder auch der Produktion schwerer Quarks sind.

Zusätzlich präsentiert diese Arbeit die Messung des invarianten differentiellen Wirkungsquerschnittes für die gesamte Photonenproduktion Y_{γ_incl} in pp Kollisionen bei $\sqrt{s} = 8\,\mathrm{TeV}$, die ein Transversalimpulsintervall von $0.3 < p_\mathrm{T} < 16\,\mathrm{GeV}/c$ abdeckt. Neben der Messung von Y_{γ_incl} ist ebenfalls das Überschussverhältnis direkter Photonen bestimmt, R_γ, welches definiert ist als das Verhältnis der gesamten sowie der Zerfallsphotonenausbeute für ein gegebenes p_T-Intervall. Zu diesem Zweck liefern die π^0- und η-Mesonenproduktionswirkungsquerschnitte bei $\sqrt{s} = 8\,\mathrm{TeV}$, die in dieser Arbeit ebenfalls präsentiert sind, einen wesentlichen Beitrag für die Zerfallsphotonensimulation, welche genutzt wird, um das Zerfallsphotonenspektrum zu beschreiben. Der dominante Beitrag wird bei hohen p_{T} mit ungefähr $\sim 85\,\%$ der Gesamtheit aller derartiger Photonen durch π^0-Zerfälle verursacht. Der zweithöchste Beitrag stammt von η-Mesonenzerfällen, welche für einen Anteil von ungefähr $\sim 10\,\%$ bei hohen p_{T} verantwortlich sind.

Mit der gegebenen Genauigkeit der R_γ-Messung kann kein Überschuss direkter Photonen für $p_{\mathrm{T}} < 7\,\mathrm{GeV}/c$ in pp Kollisionen bei $\sqrt{s} = 8\,\mathrm{TeV}$ beobachtet werden. Darüber hinaus kann der Beginn der Produktion prompter Photonen über $p_{\mathrm{T}} > 7\,\mathrm{GeV}/c$, der von vielen NLO pQCD Berechnungen vorhergesagt wird, konsistent in den Daten beobachtet werden, obwohl die experimentelle Genauigkeit nicht ausreicht um einen signifikanten Effekt festzustellen. Trotzdem liefert diese Erkenntnis gewiss Anzeichen, dass der Anstieg von R_γ konsistent mit den Theorieberechnungen bei hohen p_{T} ist. Die NLO pQCD [96, 280] Vorhersagen für die Produktion direkter Photonen basieren auf verschiedenen PDFs und FFs wie den Proton PDFs CT10 [281–283] und CTEQ6.1M [284] zusammen mit den FFs GRV [285] und BFG2 [286]. Ferner sind eine JETPHOX [287] Berechnung basierend auf der Proton PDF NNPDF2.3QED [288] und der FF BFG2 verglichen wie auch eine POWHEG [287] Vorhersage basierend auf der gleichen PDF und dem PYTHIA8 Parton-Shower Algorithmus, der an Stelle einer Fragmentationsfunktion genutzt wurde. Innerhalb der gegebenen experimentellen Unsicherheiten von R_γ sind alle pQCD Berechnungen in Übereinstimmung mit den Daten über das komplette p_{T} Intervall, welches durch die Messung erschlossen wird. Zudem sind alle Theorieberechnungen konsistent untereinander innerhalb der assoziierten Unsicherheiten. In diesem Zusammenhang ist es nicht möglich, zwischen den verschiedenen PDFs oder FFs zu unterscheiden, die für die verschiedenen Vorhersagen genutzt worden sind.

Außerdem wird eine thermische Vorhersage [3] auch mit den Daten verglichen, die eine derjenigen Referenzen ist, die einen Überschuss direkter Photonen bei kleinen p_{T} aufgrund einer zusätzlichen thermischen Komponente bereits in pp Kollisionen vorhersagt. Die Messungen weisen eine solche Annahme jedoch augenscheinlich zurück. Kein Hinweis für ein derartiges Signal in der vorhergesagten Größenordnung kann unter $7\,\mathrm{GeV}/c$ beobachtet werden. Die direkten Photonenspektren $Y_{\gamma_{\mathrm{dir}}}$ sind mit Hilfe der Subtraktionsmethode sowie R_γ und $Y_{\gamma_{\mathrm{incl}}}$ bestimmt. Für $Y_{\gamma_{\mathrm{dir}}}$ können drei Datenpunkte zwischen $7 < p_{\mathrm{T}} < 16\,\mathrm{GeV}/c$ extrahiert werden, für welche R_γ-Werte über Eins innerhalb der gesamten Unsicherheiten gefunden werden. Für die anderen Datenpunkte sind obere Limits mit $90\,\%$ C.L. präsentiert. Alle Theorieberechnungen stimmen gut mit den extrahierten $Y_{\gamma_{\mathrm{dir}}}$-Datenpunkten bereits innerhalb der statistischen Unsicherheiten überein. Die vorhergesagten Wirkungsquerschnitte sind weiterhin gut vereinbar mit den oberen Limits, die für $p_{\mathrm{T}} < 7\,\mathrm{GeV}/c$ mit $90\,\%$ C.L. angegeben werden. Zusammenfassend sind alle Resultate bezüglich der gesamten und direkten Photonenproduktion für $\sqrt{s} = 8\,\mathrm{TeV}$ publiziert, siehe ALICE-Ref. [6], die ebenfalls die entsprechende Messung für pp Kollisionen bei $\sqrt{s} = 2.76\,\mathrm{TeV}$ beinhaltet. Während kein Überschuss direkter Photonen in pp Kollisionen bei $\sqrt{s} = 2.76\,\mathrm{TeV}$ festgestellt werden kann, ist R_γ im Gegensatz durchweg über Eins für Pb-Pb Kollisionen bei der äquivalenten Schwerpunktenergie. Dieser Vergleich bestärkt die Interpretation der Schwerionenresultate, für welche das QGP als zusätzliche Quelle thermischer Photonen berücksichtigt wird, die zur gesamten Ausbeute direkten Photonen bei kleinen p_{T} beiträgt.

Letztendlich schließt diese Arbeit mit einer Diskussion ab, wie die Präzision der direkten Photonenmessungen weiter verbessert werden kann, um möglicherweise mehr $Y_{\gamma_{\mathrm{dir}}}$-Datenpunkte zu erhalten, wofür die experimentelle Genauigkeit hinsichtlich $Y_{\gamma_{\mathrm{incl}}}$ und R_γ weiter gesteigert werden muss.

Appendix A

Acronyms & Technical Terms

2D	Two-Dimensional
3D	Three-Dimensional
ACORDE	ALICE Cosmic Ray Detector
ADC	Analog-to-Digital Converter
AGK	Abramowski-Gribov-Kancheli
AGS	Alternating Gradient Synchrotron
ALEPH	A Detector for Electron-Positron Annihilations at LEP
ALICE	A Large Ion Collider Experiment
AliEn	ALICE Environment
AOD	Analysis Object Data
ATLAS	A Toroidal LHC Apparatus
APD	Avalanche Photodiode
BG	Background
BLUE	Best Linear Unbiased Estimate
BNL	Brookhaven National Laboratory
BOOSTER	Proton Synchrotron Booster
BR	Branching Ratio
CASTOR	CERN Advanced Storage Manager
CERN	European Organization for Nuclear Research
CMS	Compact Muon Solenoid
CCMF	Conv-Calo Mass Fit
CMF	Calo Mass Fit
CCRF	Conv-Calo Ratio Fit
CRF	Calo Ratio Fit

CPV	Charged Particle Veto
CTEQ	Coordinated Theoretical-Experimental Project
CTP	Central Trigger Processor
DAQ	Data Acquisition
DCA	Distance of Closest Approach
DCal	Di-jet Calorimeter
DCS	Detector Control System
DDL	Detector Data Link
DGLAP	Dokshitzer-Gribov-Lipatov-Altarelli-Parisi
DPM	Dual Parton Model
EBDS	Event Building and Distribution System
ECRIS	Electron Cylcotron Resonance Ion Source
ECS	Experiment Control System
EMC	Electromagnetic Calorimeter
EMCal	Electromagnetic Calorimeter
ESD	Event Summary Data
FEE	Front End Electronics
FF	Fragmentation Function
FIFO	First In, First Out
FLUKA	Fluktuierende Kaskade
FMD	Forward Multiplicity Detector
FPGA	Field Programmable Gate Array
FSR	Final State Radiation
GA	Gammas and Neutral Mesons
GDC	Global Data Collector
GEANT	Geometry and Tracking Software
GEM	Gas Electron Multiplier
GUT	Grand Unified Theory
HEP	High Energy Physics
HL	High Luminosity
HLT	High-Level Trigger
HMPID	High Momentum Particle Identification Detector

HV	High Voltage
IP	Interaction Point
ISR	Initial State Radiation
ITS	Inner Tracking System
I/O	Input/Output
L0	Level-0
L1	Level-1
L2	Level-2
LCG	LHC Computing Grid
LEGO	Lightweight Environment for Grid Operations
LEP	Large Electron Positron Collider
LEIR	Low Energy Ion Ring
LHC	Large Hadron Collider
LHCb	LHC beauty Experiment
LHCf	LHC forward
L3	L3 Experiment
LDC	Local Data Concentrator
LHA	Les Houches Accord
LHEF	Les Houches Event Files
LINAC	Linear Accelerator
LO	Leading Order
LS	Long Shutdown
LTU	Local Trigger Unit
LQCD	Lattice QCD
MB	Minimum Bias
MC	Monte Carlo
MCH	Muon Chambers
MIB	Machine-Induced Background
MIP	Minimum Ionizing Particle
MoEDAL	Monopole and Exotics Detector at the LHC
MPI	Multiparton Interaction
MRPC	Multigap Resistive Plate Chamber

MSTW	Martin-Stirling-Thorne-Watt
MTR	Muon Trigger
MUON	Muon Spectrometer
MWPC	Multi-Wire Proportional Chamber
NLO	Next-to-Leading Order
O^2	Online and Offline Computing System
PCG	Photon Conversion Group
PDF	Parton Distribution Function
PHOS	Photon Spectrometer
RICH	Ring Imaging Cherenkov
PCA	Point of Closest Approach
PCM	Photon Conversion Method
PDG	Particle Data Group
PDF	Parton Distribution Function
PDS	Permanent Data Storage
PHENIX	Pioneering High Energy Nuclear Interactions Experiment
PID	Particle Identification
PMD	Photon Multiplicity Detector
PMT	Photomultiplier Tube
pQCD	perturbative QCD
PS	Proton Synchrotron
PSEL	Physics Selection
PWG	Physics Working Group
QA	Quality Assurance
QCD	Quantum Chromodynamics
QED	Quantum Electrodynamics
QFT	Quantum Field Theory
QGP	Quark-Gluon Plasma
RCT	Run Condition Table
RF	Trigger Rejection Factor
RHIC	Relativistic Heavy Ion Collider
RPC	Resistive Plate Chamber

SC	Synchrocyclotron
SDD	Silicon Drift Detector
SM	Standard Model
SPD	Silicon Pixel Detector
SPS	Super Proton Synchrotron
SSD	Silicon Strip Detector
SVD	Singular Value Decomposition
T0	Timing and Trigger Detector
T0A	T0 sub-detector on A-side
T0C	T0 sub-detector on C-side
TCM	Two-Component Model
TCP/IP	Transmission Control Protocol/Internet Protocol
TDC	Time-to-Digital Converter
TDR	Technical Design Report
TDS	Transient Data Storage
Tl	Transfer line
TOF	Time-Of-Flight Detector
TOTEM	Total Elastic and Diffractive Cross Section Measurement
TPC	Time Projection Chamber
TR	Transition Radiation
TRD	Transition Radiation Detector
TRG	Trigger System
TRU	Trigger Region Unit
V^0	Secondary Vertex
V0	Triggering and Centrality Detector
V0A	V0 sub-detector on A-side
V0C	V0 sub-detector on C-side
vdM	van der Meer
ZDC	Zero Degree Calorimeter
ZEM	Zero Degree Electromagnetic Calorimeter
ZN	Zero Degree Neutron Calorimeter
ZP	Zero Degree Proton Calorimeter

Appendix B

Additional Figures

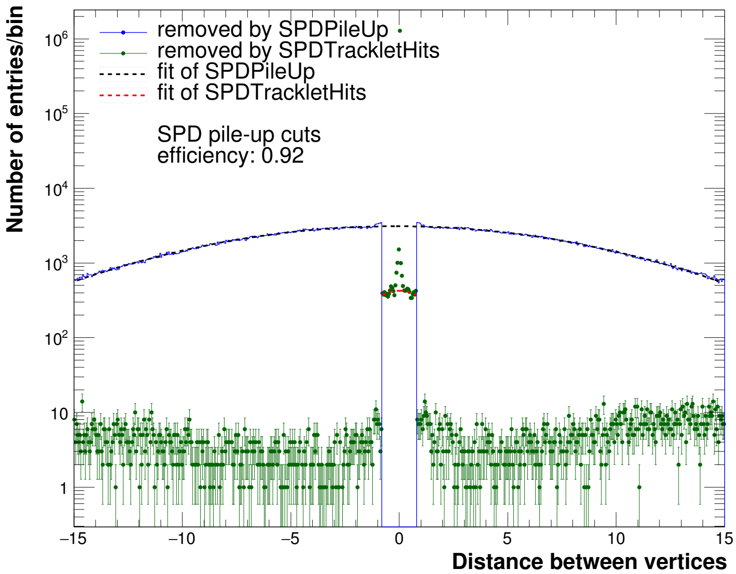

a)

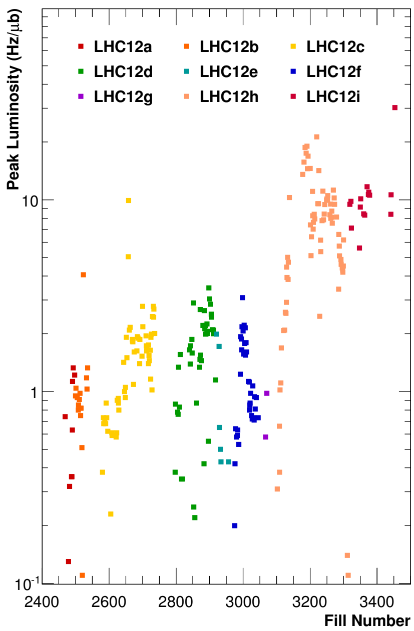

b)

Figure B.0.1: a) The largest distance between two reconstructed primary vertices in a V0AND-triggered pp collisions at $\sqrt{s} = 8\,\text{TeV}$ given in units of cm, if more than one vertex could be reconstructed. The blue line represents the rejection by the SPD pileup cut, which is only effective for distances greater than 0.9 cm, whereas in green color the rejection by the SPD background cut is shown which rejects some part of pileup below 0.9 cm. Assuming a Gaussian shape of the underlying distribution, the blue curve is fitted in the whole range visualized by the dotted black line, from which the pileup removal efficiency of 92 % can be estimated. b) The peak luminosity for each fill of the LHC used for data taking for pp, $\sqrt{s} = 8\,\text{TeV}$.

B.1 Additional Tables

pp, $\sqrt{s} = 0.9\,\text{TeV}$ - MB trigger V0OR (INT1)
LHC10c
118506, 118507, 118512, 118518, 118556, 118558, 118560, 118561, 121039, 121040

Table B.1.1: List of good runs used for analysis for the MB trigger V0OR in pp, $\sqrt{s} = 0.9\,\text{TeV}$, separated by the respective data taking periods.

pp, $\sqrt{s} = 7\,\text{TeV}$ - MB trigger V0OR (INT1)
LHC10b
115393, 115399, 115401, 116102, 116288, 116402, 116403, 116643, 116645, 117050, 117052, 117053, 117059, 117060, 117063, 117099, 117109, 117112, 117116, 117220, 117222
LHC10c
119159, 119161, 119163, 119841, 119842, 119844, 119845, 119846, 119853, 119856, 119859, 119862, 120067, 120069, 120072, 120076, 120079, 120244, 120503, 120504, 120505, 120616, 120617, 120671, 120741, 120820, 120821, 120822, 120823, 120824, 120825, 120829
LHC10d
122374, 122375, 125630, 125632, 125633, 125842, 125843, 125844, 125847, 125848, 125849, 125850, 125851, 125855, 126004, 126007, 126008, 126073, 126078, 126081, 126082, 126088, 126090, 126097, 126158, 126160, 126167, 126168, 126284, 126285, 126351, 126352, 126359, 126403, 126404, 126405, 126406, 126407, 126408, 126409, 126422, 126424, 126425, 126432
LHC10e
128486, 128494, 128495, 128498, 128503, 128504, 128505, 128506, 128582, 128590, 128592, 128594, 128596, 128605, 128609, 128611, 128615, 128621, 128677, 128678, 128777, 128778, 128819, 128820, 128823, 128824, 128833, 128834, 128835, 128836, 128843, 128850, 128853, 128855, 128913, 129042, 129512, 129513, 129514, 129515, 129516, 129519, 129520, 129521, 129523, 129524, 129525, 129527, 129528, 129536, 129540, 129586, 129587, 129599, 129639, 129641, 129647, 129650, 129651, 129652, 129653, 129659, 129666, 129723, 129726, 129729, 129734, 129735, 129736, 129738, 129742, 129744, 129959, 129960, 129961, 129962, 129966, 129983, 130149, 130151, 130157, 130158, 130168, 130172, 130178, 130343, 130354, 130356, 130358, 130360, 130375, 130480, 130481, 130517, 130519, 130696, 130704, 130793, 130795, 130798, 130799, 130834, 130840, 130842, 130844, 130847, 130848
LHC10f
133006, 133007, 133010, 133327, 133329, 133330, 133414, 133670, 133762, 133800, 133920, 133969, 133982

Table B.1.2: List of good runs used for analysis for the MB trigger V0OR in pp, $\sqrt{s} = 7\,\text{TeV}$, separated by the respective data taking periods.

pp, $\sqrt{s} = 8\,\mathrm{TeV}$ - MB trigger V0AND (INT7)
LHC12a
176715, 176730, 176749, 176752, 176753, 176849, 176854, 176859, 176924, 176926, 176927, 176929, 177011
LHC12b
177580, 177592, 177597, 177612, 177620, 177624, 177671, 177679, 177680, 177681, 177682, 177798, 177799, 177802, 177804, 177805, 177942
LHC12c
179569, 179571, 179584, 179585, 179591, 179618, 179621, 179639, 179796, 179803, 179806, 179858, 179859, 179916, 179917, 179918, 179919, 179920, 180000, 180042, 180044, 180129, 180130, 180131, 180132, 180133, 180199, 180200, 180500, 180501, 180515, 180517, 180561, 180564, 180567, 180569, 180716, 180717, 180719, 180720, 182017, 182018, 182022, 182023, 182106, 182110, 182111, 182207, 182289, 182295, 182297, 182299, 182300, 182302, 182322, 182323, 182324, 182325, 182624, 182635, 182684, 182686, 182687, 182691, 182692, 182724, 182725, 182728, 182729, 182730, 182741, 182744
LHC12d
183913, 183916, 183932, 183933, 183934, 183935, 183936, 183937, 183938, 183942, 183946, 184126, 184127, 184131, 184132, 184134, 184135, 184137, 184138, 184140, 184144, 184145, 184147, 184183, 184188, 184208, 184209, 184210, 184215, 184216, 184371, 184383, 184389, 184673, 184678, 184682, 184687, 184784, 184786, 185029, 185031, 185116, 185126, 185127, 185132, 185133, 185134, 185157, 185160, 185164, 185189, 185196, 185198, 185203, 185206, 185208, 185217, 185221, 185282, 185284, 185289, 185291, 185292, 185293, 185296, 185299, 185300, 185302, 185303, 185349, 185350, 185351, 185356, 185359, 185360, 185361, 185362, 185363, 185368, 185371, 185375, 185378, 185461, 185465, 185474, 185574, 185578, 185580, 185581, 185582, 185583, 185588, 185589, 185659, 185687, 185738, 185764, 185765, 185768, 185775, 185776, 185778, 185784, 186007, 186009, 186011, 186163, 186164, 186165, 186167, 186205, 186208, 186319, 186320
LHC12f
186668, 186688, 186689, 186690, 186692, 186694, 186811, 186814, 186937, 186938, 186939, 186966, 186969, 186990, 186992, 186994, 187143, 187145, 187146, 187147, 187148, 187149, 187150, 187151, 187152, 187202, 187203, 187339, 187340, 187341, 187487, 187488, 187489, 187510, 187623, 187624, 187627, 187656, 187698, 187739, 187749, 187783, 187785, 187791, 187796, 188093, 188101
LHC12h
189306, 189310, 189315, 189316, 189350, 189351, 189352, 189353, 189400, 189407, 189409, 189410, 189411, 189577, 189578, 189602, 189603, 189605, 189610, 189611, 189612, 189616, 189621, 189623, 189647, 189648, 189650, 189654, 189656, 189658, 189659, 189696, 189697, 189698, 190150, 190209, 190210, 190212, 190213, 190214, 190215, 190216, 190240, 190303, 190305, 190307, 190335, 190337, 190338, 190340, 190341, 190342, 190344, 190386, 190388, 190389, 190390, 190392, 190393, 190416, 190417, 190418, 190419, 190421, 190422, 190424, 190425, 190895, 190898, 190903, 190904, 190968, 190970, 190974, 190975, 190979, 190981, 190983, 190984, 191129, 191227, 191229, 191230, 191231, 191245, 191247, 191248, 191450, 191451, 192072, 192073, 192075, 192128, 192136, 192140, 192141, 192172, 192174, 192177, 192194, 192197, 192199, 192200, 192201, 192202, 192205, 192246, 192344, 192347, 192348, 192349, 192415, 192417, 192453, 192461, 192468, 192471, 192492, 192499, 192505, 192510, 192535, 192542, 192548, 192551, 192729, 192731, 192732
LHC12i
192772, 192775, 192778, 192779, 192820, 192822, 192824, 193004, 193005, 193007, 193008, 193010, 193011, 193014, 193047, 193049, 193051, 193092, 193093, 193094, 193097, 193148, 193155, 193156, 193187, 193188, 193189, 193194

Table B.1.3: List of good runs used for analysis for the MB trigger V0AND in pp, $\sqrt{s} = 8\,\mathrm{TeV}$, separated by the respective data taking periods.

pp, $\sqrt{s} = 8\,\mathrm{TeV}$ - rare trigger EMCal-L0 (EMC7)
LHC12b
177798, 177799
LHC12c
179796, 179803, 179806, 179858, 179859, 179916, 179917, 179918, 179919, 179920, 180000, 180042, 180044, 180129, 180130, 180131, 180132, 180133, 180199, 180200, 180500, 180501, 180515, 180517, 180561, 180564, 180567, 180569, 180716, 180717, 180719, 180720, 182017, 182018, 182022, 182023, 182106, 182110, 182111, 182207, 182289, 182295, 182297, 182299, 182300, 182302, 182322, 182323, 182324, 182325, 182624, 182635, 182684, 182686, 182687, 182691, 182692, 182724, 182725, 182728, 182729, 182730, 182741, 182744
LHC12d
183913, 183916, 183932, 183933, 183934, 183935, 183936, 183937, 183938, 183942, 183946, 184126, 184127, 184131, 184132, 184134, 184135, 184137, 184138, 184140, 184144, 184145, 184147, 184183, 184188, 184208, 184209, 184210, 184215, 184216, 184371, 184383, 184389, 184673, 184678, 184682, 184687, 184784, 184786, 185029, 185031, 185116, 185126, 185127, 185132, 185133, 185134, 185157, 185160, 185164, 185189, 185196, 185198, 185203, 185206, 185208, 185217, 185221, 185282, 185284, 185289, 185292, 185293, 185296, 185299, 185300, 185302, 185303, 185349, 185350, 185351, 185356, 185359, 185360, 185361, 185362, 185363, 185368, 185371, 185375, 185378, 185461, 185465, 185474, 185574, 185578, 185580, 185581, 185582, 185583, 185588, 185589, 185659, 185687, 185738, 185764, 185765, 185768, 185775, 185776, 185778, 185784, 186003, 186006, 186007, 186009, 186011, 186163, 186164, 186165, 186167, 186205, 186208, 186319, 186320
LHC12f
186668, 186688, 186689, 186690, 186692, 186694, 186811, 186814, 186937, 186938, 186939, 186966, 186969, 186990, 186992, 186994, 187143, 187145, 187146, 187147, 187148, 187149, 187150, 187151, 187152, 187202, 187203, 187339, 187340, 187341, 187487, 187488, 187489, 187510, 187623, 187624, 187627, 187656, 187698, 187739, 187749, 187783, 187785, 187791, 187796, 188093, 188101
LHC12h
190209, 190210, 190212, 190213, 190214, 190215, 190216, 190240, 190303, 190305, 190307, 190335, 190337, 190338, 190340, 190341, 190342, 190344, 190386, 190388, 190389, 190390, 190392, 190393, 190416, 190417, 190418, 190419, 190421, 190422, 190424, 190425, 191129, 191227, 191229, 191230, 191231, 191245, 191247, 191248, 191450, 191451, 192072, 192073, 192075, 192128, 192136, 192140, 192141, 192172, 192174, 192177, 192194, 192197, 192199, 192200, 192201, 192202, 192205, 192246, 192344, 192347, 192348, 192349, 192415, 192417, 192453, 192461, 192468, 192471, 192492, 192499, 192535, 192542, 192548, 192551, 192729, 192731, 192732
LHC12i
192772, 192775, 192778, 192779, 192820, 192822, 192824, 193004, 193005, 193007, 193008, 193010, 193011, 193014, 193047, 193049, 193051, 193092, 193093, 193094, 193097, 193148, 193155, 193156, 193187, 193188, 193189, 193194

Table B.1.4: List of good runs used for analysis for the EMCal-L0 trigger EMC7 in pp, $\sqrt{s} = 8\,\mathrm{TeV}$, separated by the respective data taking periods.

pp, $\sqrt{s} = 8\,\text{TeV}$ - rare trigger EMCal-L1 (EGA)
LHC12c
179796, 179803, 179806, 179858, 179859, 179916, 179917, 179918, 179919, 179920, 180000, 180042, 180044, 180129, 180130, 180131, 180132, 180133, 180199, 180200, 180500, 180501, 180515, 180517, 180561, 180564, 180567, 180569, 180716, 180717, 180719, 180720, 182017, 182018, 182022, 182023, 182106, 182110, 182111, 182207, 182289, 182295, 182297, 182299, 182300, 182302, 182322, 182323, 182324, 182325, 182624, 182635, 182684, 182686, 182687, 182691, 182692, 182724, 182725, 182728, 182729, 182730, 182741, 182744
LHC12d
183913, 183916, 183932, 183933, 183934, 183935, 183936, 183937, 183938, 183942, 183946, 184126, 184127, 184131, 184132, 184134, 184135, 184137, 184138, 184140, 184144, 184145, 184147, 184183, 184188, 184208, 184209, 184210, 184215, 184216, 184371, 184383, 184389, 184673, 184678, 184682, 184687, 184784, 184786, 185029, 185031, 185116, 185126, 185127, 185132, 185133, 185134, 185157, 185160, 185164, 185189, 185196, 185198, 185203, 185206, 185208, 185217, 185221, 185282, 185284, 185289, 185292, 185293, 185296, 185299, 185300, 185302, 185303, 185349, 185350, 185351, 185356, 185359, 185360, 185361, 185362, 185363, 185368, 185371, 185375, 185378, 185461, 185465,(185474),185574, 185578, 185580, 185581, 185582, 185583, 185588, 185589, 185659, 185687, 185738, 185764, 185765, 185768, 185775, 185776, 185778, 185784, 186003, 186006, 186007, 186009, 186011, 186163, 186164, 186165, 186167, 186205, 186208, 186319, 186320
LHC12f
186668, 186688, 186689, 186690, 186692, 186694, 186811, 186814, 186937, 186938, 186939, 186966, 186969, 186990, 186992, 186994, 187143, 187145, 187146, 187147, 187148, 187149, 187150, 187151, 187152, 187202, 187203, 187339, 187340, 187341, 187487, 187488, 187489, 187510, 187623, 187624, 187627, 187656, 187698, 187739, 187749, 187783, 187785, 187791, 187796, 188093, 188101
LHC12h
189400, 189407, 189409, 189410, 189411, 189602, 189603, 189605, 189610, 189611, 189612, 189616, 189621, 189623, 189647, 189648, 189650, 189654, 189656, 189658, 189659, 189696, 189697, 189698, 190209, 190210, 190212, 190213, 190214, 190215, 190216, 190240, 190303, 190305, 190307, 190335, 190337, 190338, 190340, 190341, 190342, 190344, 190386, 190388, 190389, 190390, 190392, 190393, 190416, 190417, 190418, 190419, 190421, 190422, 190424, 190425, 191129, 191227, 191229, 191230, 191231, 191245, 191247, 191248, 191450, 191451, 192072, 192073, 192075, 192128, 192136, 192140, 192141, 192172, 192174, 192177, 192194, 192197, 192199, 192200, 192201, 192202, 192205, 192246, 192344, 192347, 192348, 192349, 192415, 192417, 192453, 192461, 192468, 192471, 192492, 192499, 192535, 192542, 192548, 192551, 192729, 192731, 192732
LHC12i
192772, 192775, 192778, 192779, 192820, 192822, 192824, 193004, 193005, 193007, 193008, 193010, 193011, 193014, 193047, 193049, 193051, 193092, 193093, 193094, 193097, 193148, 193155, 193156, 193187, 193188, 193189, 193194

Table B.1.5: List of good runs used for analysis for the EMCal-L1 trigger EGA in pp, $\sqrt{s} = 8\,\text{TeV}$, separated by the respective data taking periods.

	list of anchor runs for LHC16c2				
period	LHC12c	LHC12d	LHC12f	LHC12h	LHC12i
$N^{\text{EGA}}_{\text{collected}}$	$3.8 \cdot 10^5$	$4.9 \cdot 10^5$	$2.5 \cdot 10^5$	$9.8 \cdot 10^5$	$2.4 \cdot 10^5$
runs with fraction of generated statistics	180720 (8.13 %) 182692 (8.13 %)	184215 (16.75 %) 185687 (4.19 %)	187488 (10.78 %)	189616 (6.66 %) 190393 (5.90 %) 192073 (14.58 %) 192349 (14.58 %)	193051 (10.32 %)

Table B.1.6: List of anchor runs for the PYTHIA 8 Jet-Jet production 'LHC16c2'. The selection of runs is based on the list which is shown in Tab. B.1.5, requiring approximately $2.5 \cdot 10^6$ recorded events per anchor run. Additionally, the varying acceptance of the EMCal for the different runs was properly considered.

min $p_{\mathrm{T,hard}}$ (GeV/c)	max $p_{\mathrm{T,hard}}$ (GeV/c)	N_{trials}	σ_{event}	$N_{\mathrm{generated\ events}}$	ω_{JJ}
5	7	$1.54392 \cdot 10^{7}$	26.5537	$1.64488 \cdot 10^{7}$	28.3084
7	9	$1.59332 \cdot 10^{7}$	7.92493	$1.69479 \cdot 10^{7}$	8.43277
9	12	$1.55818 \cdot 10^{7}$	3.83319	$1.65593 \cdot 10^{7}$	4.07753
12	16	$1.55815 \cdot 10^{7}$	1.4517	$1.65612 \cdot 10^{7}$	1.54812
16	21	$1.54717 \cdot 10^{7}$	0.511408	$1.64587 \cdot 10^{7}$	0.543997
21	28	$1.54482 \cdot 10^{7}$	0.196645	$1.64526 \cdot 10^{7}$	0.208601
28	36	$1.53611 \cdot 10^{7}$	0.0616515	$1.63700 \cdot 10^{7}$	0.0652923
36	45	$1.75912 \cdot 10^{7}$	0.0217118	$1.68646 \cdot 10^{7}$	0.0187104
45	57	$1.69320 \cdot 10^{7}$	0.00926498	$1.66335 \cdot 10^{7}$	0.00834861
57	70	$1.69476 \cdot 10^{7}$	0.00324228	$1.69524 \cdot 10^{7}$	0.00301551
70	85	$1.65147 \cdot 10^{7}$	0.0013259	$1.66884 \cdot 10^{7}$	0.00125972
85	99	$1.65432 \cdot 10^{7}$	0.000491328	$1.68616 \cdot 10^{7}$	0.000474541
99	115	$1.61887 \cdot 10^{7}$	0.000249832	$1.65804 \cdot 10^{7}$	0.000244081
115	132	$1.60438 \cdot 10^{7}$	0.00012086	$1.65079 \cdot 10^{7}$	0.000119259
132	150	$1.63231 \cdot 10^{7}$	$6.12943 \cdot 10^{-5}$	$1.68666 \cdot 10^{7}$	$6.09870 \cdot 10^{-5}$
150	169	$1.60302 \cdot 10^{7}$	$3.23291 \cdot 10^{-5}$	$1.66121 \cdot 10^{7}$	$3.24178 \cdot 10^{-5}$
169	190	$1.58894 \cdot 10^{7}$	$1.82594 \cdot 10^{-5}$	$1.65020 \cdot 10^{7}$	$1.84328 \cdot 10^{-5}$
190	212	$1.57749 \cdot 10^{7}$	$9.95101 \cdot 10^{-6}$	$1.64190 \cdot 10^{7}$	$1.00931 \cdot 10^{-5}$
212	235	$1.58268 \cdot 10^{7}$	$5.58825 \cdot 10^{-6}$	$1.64917 \cdot 10^{7}$	$5.68605 \cdot 10^{-6}$
235	∞	$1.58591 \cdot 10^{7}$	$8.17691 \cdot 10^{-6}$	$1.65580 \cdot 10^{7}$	$8.38078 \cdot 10^{-6}$

Table B.1.7: Information about the PYTHIA 8 Jet-Jet MC production 'LHC16c2' which is anchored to the periods 'LHC12c-i'. The anchor run list can be found in Tab. B.1.6. The respective $p_{\mathrm{T,hard}}$ bin intervals can be extracted from this table as well as the number of trials, N_{trials}, and the corresponding cross sections, σ_{event}. The number of generated events for each $p_{\mathrm{T,hard}}$ bin are given, $N_{\mathrm{generated\ events}}$, and finally the calculated weights for each bin, ω_{JJ}.

dataset	scheme	MC generator	p_0	p_1	p_2
LHC10b-f	CCRF	PYTHIA 6	0.95503	-3.76064	-0.19318
	CRF		0.96116	-3.61217	-0.61404
LHC12a-i	CCRF	PYTHIA 8	0.95503	-3.76064	-0.19318
		Phojet	0.95520	-3.80387	-0.20055
	CRF	PYTHIA 8	0.96116	-3.61217	-0.61404
		Phojet	0.95970	-3.62239	-0.55626
LHC12c-i	CCRF	Jet-Jet PYTHIA 8	0.95834	-3.85842	-0.40528
	CRF		0.95868	-3.48444	-0.76686

Table B.1.8: A summary of the obtained parameters for the energy calibration schemes CCRF and CRF for the different datasets analyzed.

B.2 Additional Neutral Meson Plots

B.2.1 π^0 & η Mesons in pp, $\sqrt{s} = 8$ TeV

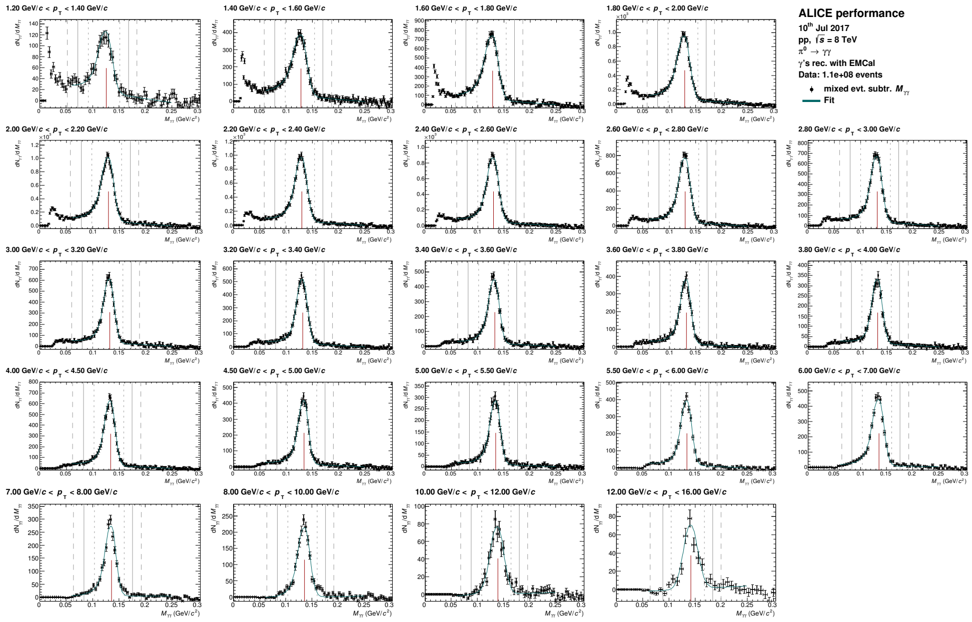

a)

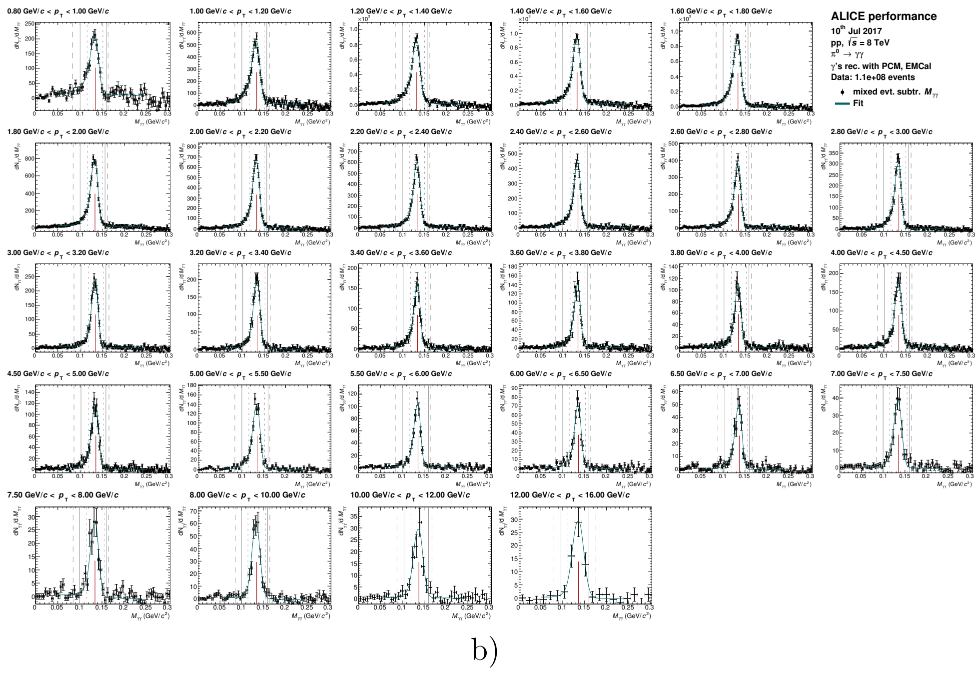

b)

Figure B.2.2: The invariant mass distributions of π^0 candidates are shown for MB triggers using the EMCal, a), and PCM-EMCal, b), method. The reconstructed mass position obtained from the fit of Eq. 6.1.3 (light blue) is visualized by the red lines. Moreover, the integration ranges are visualized used to extract the signal.

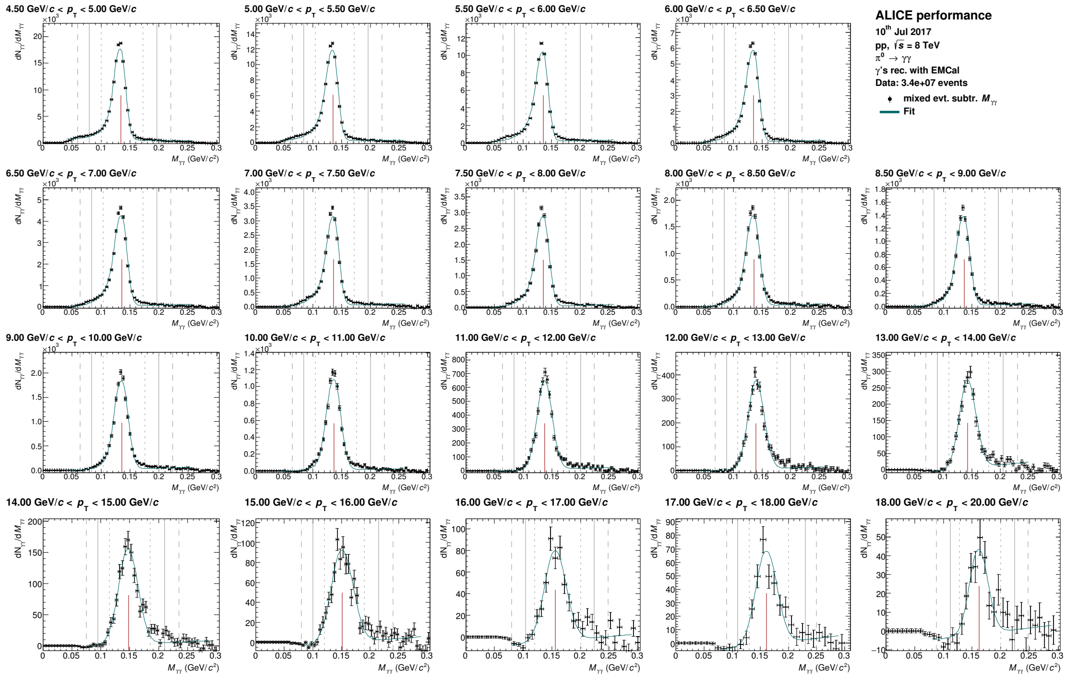

a)

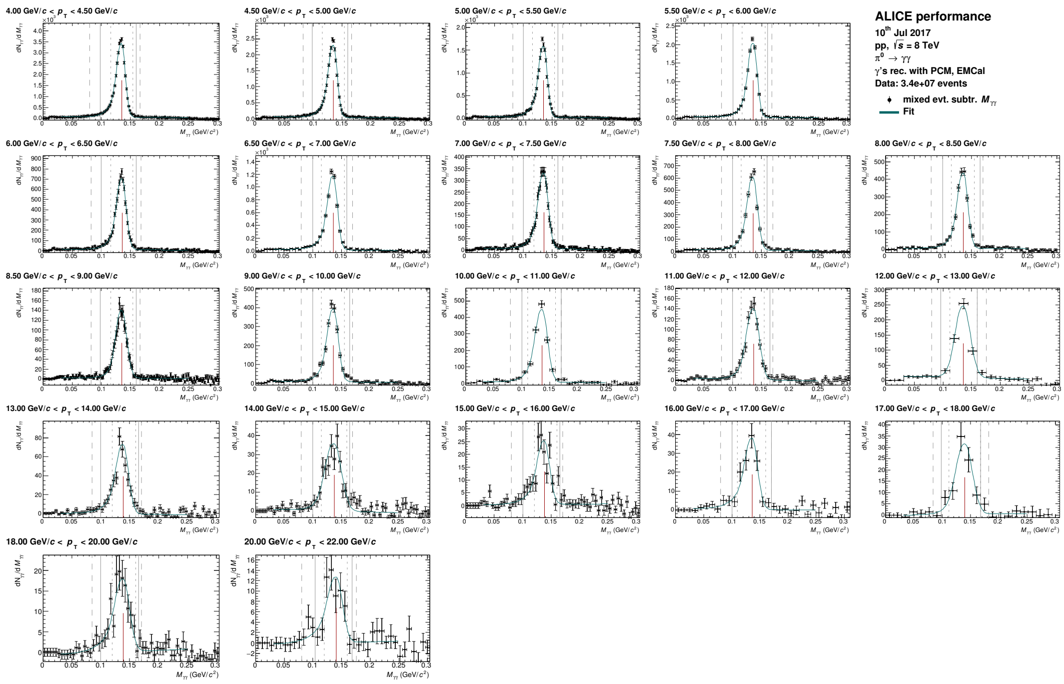

b)

Figure B.2.3: The invariant mass distributions of π^0 candidates are shown for EMC7 triggers using the EMCal, a), and PCM-EMCal, b), method. The reconstructed mass position obtained from the fit of Eq. 6.1.3 (light blue) is visualized by the red lines. Moreover, the integration ranges are visualized used to extract the signal.

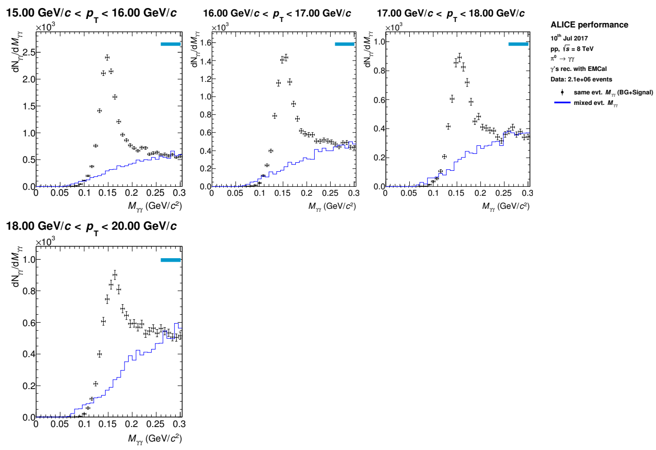

a)

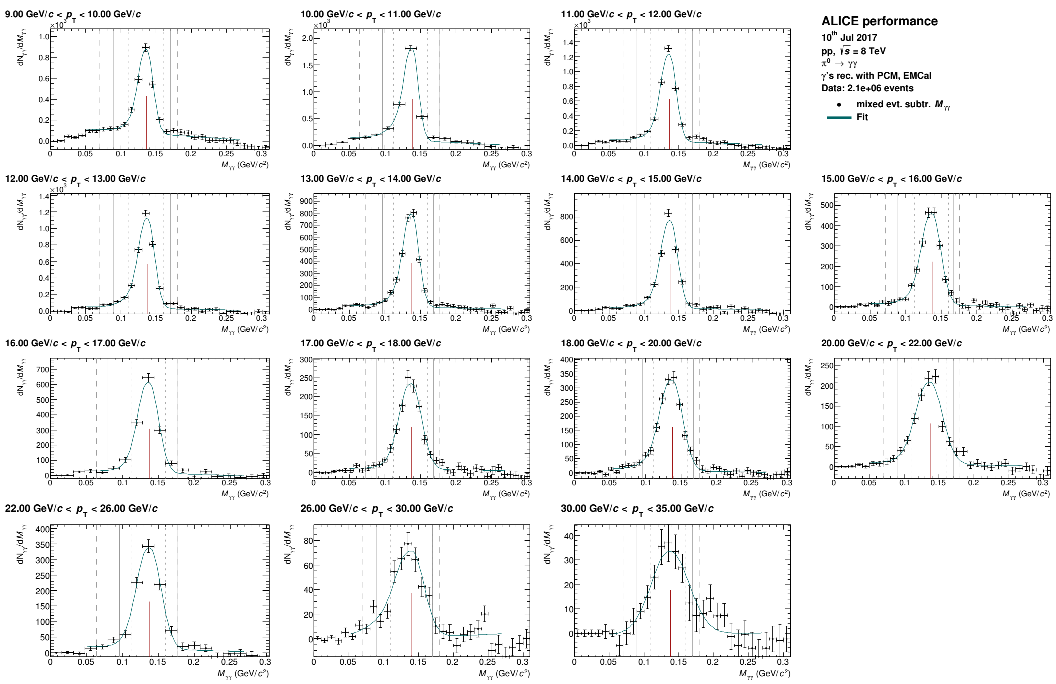

b)

Figure B.2.4: The invariant mass distributions of π^0 candidates are shown for EGA triggers using the EMCal, a) (in this example before the subtraction of the mixed-event background), and PCM-EMCal, b), method. The reconstructed mass position obtained from the fit of Eq. 6.1.3 (light blue) is visualized by the red lines. Moreover, the integration ranges are visualized used to extract the signal.

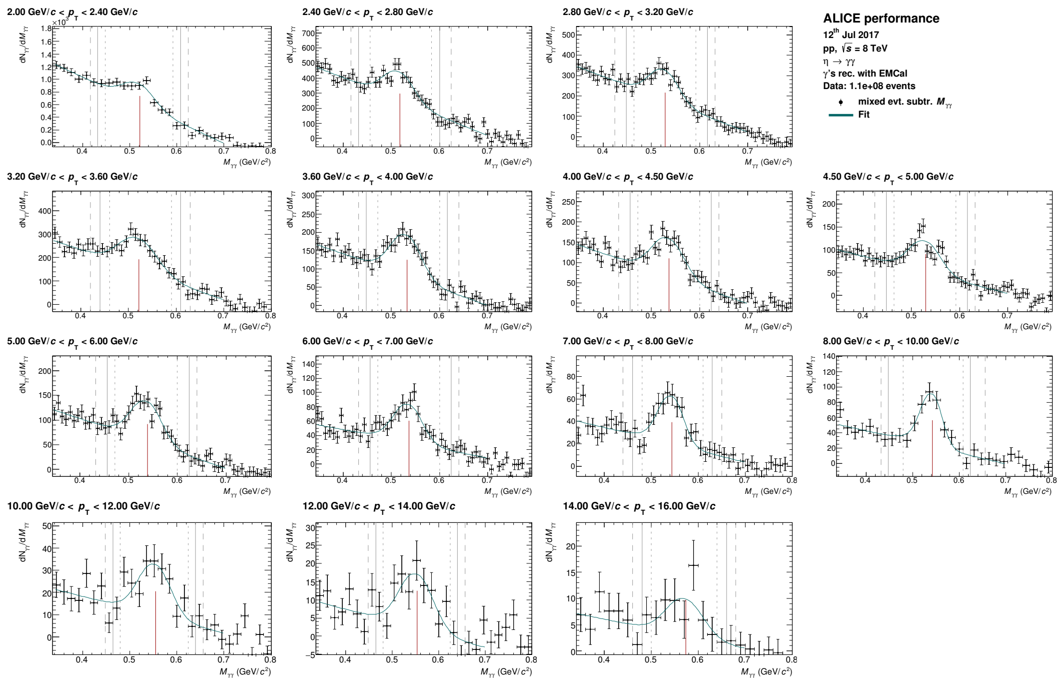

a)

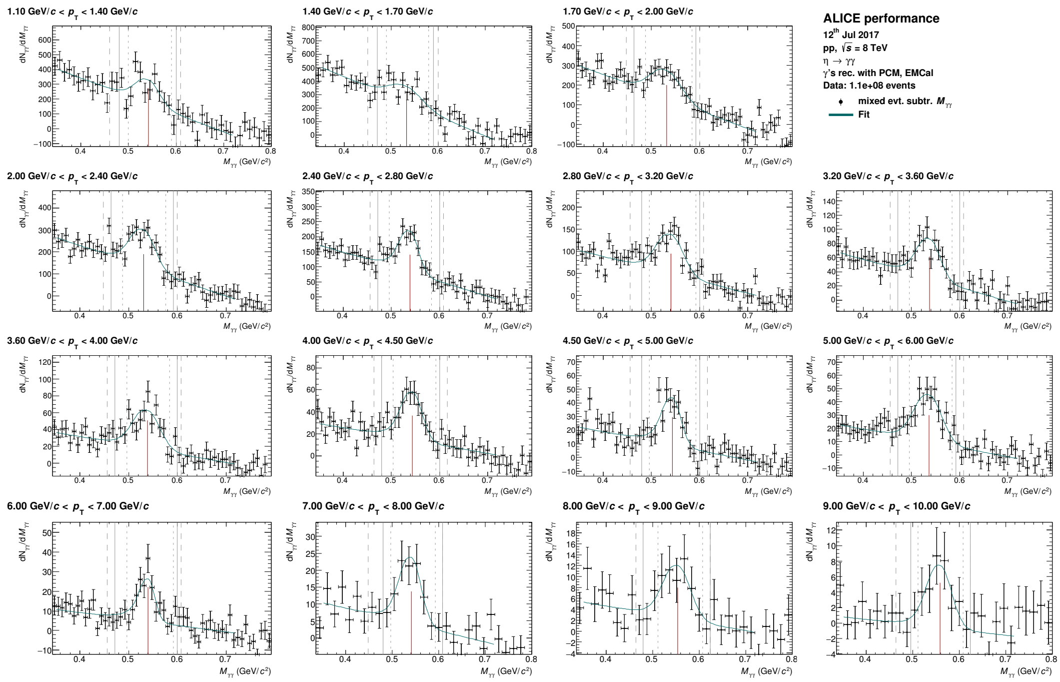

b)

Figure B.2.5: The invariant mass distributions of η candidates are shown for MB triggers using the EMCal, a), and PCM-EMCal, b), method. The reconstructed mass position obtained from the fit of Eq. 6.1.3 (light blue) is visualized by the red lines. Moreover, the integration ranges are visualized used to extract the signal.

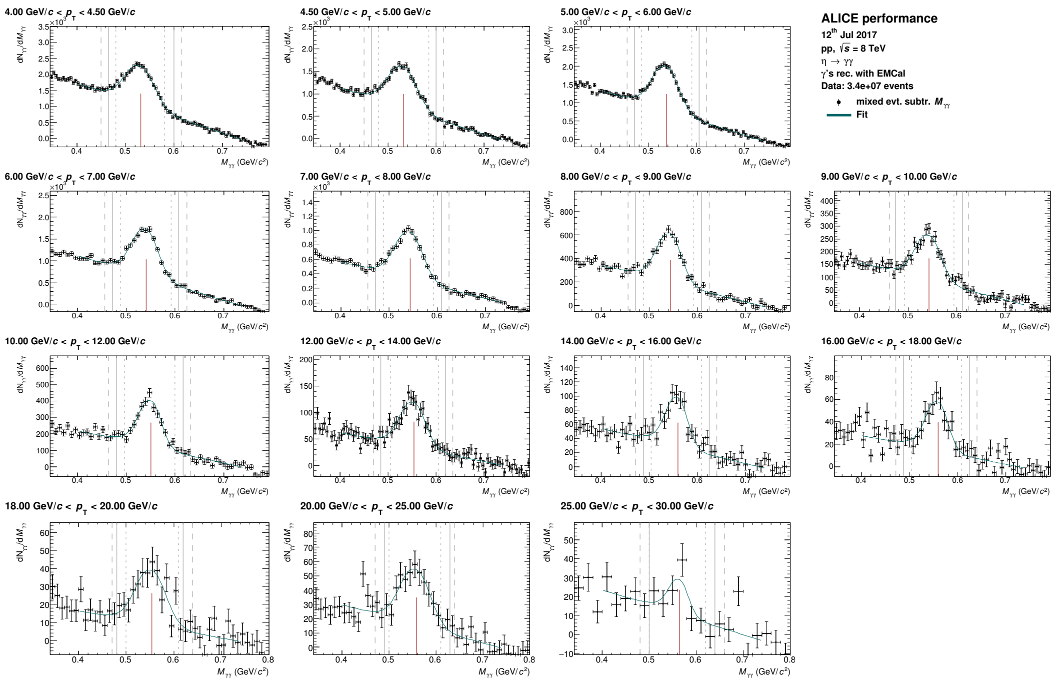

a)

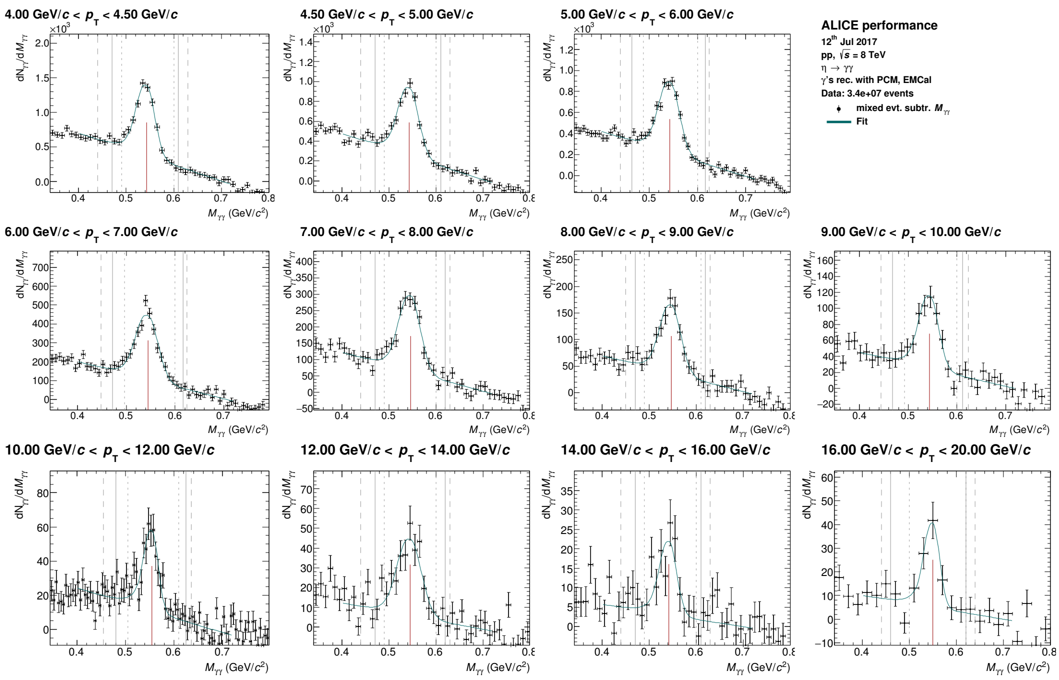

b)

Figure B.2.6: The invariant mass distributions of η candidates are shown for EMC7 triggers using the EMCal, a), and PCM-EMCal, b), method. The reconstructed mass position obtained from the fit of Eq. 6.1.3 (light blue) is visualized by the red lines. Moreover, the integration ranges are visualized used to extract the signal.

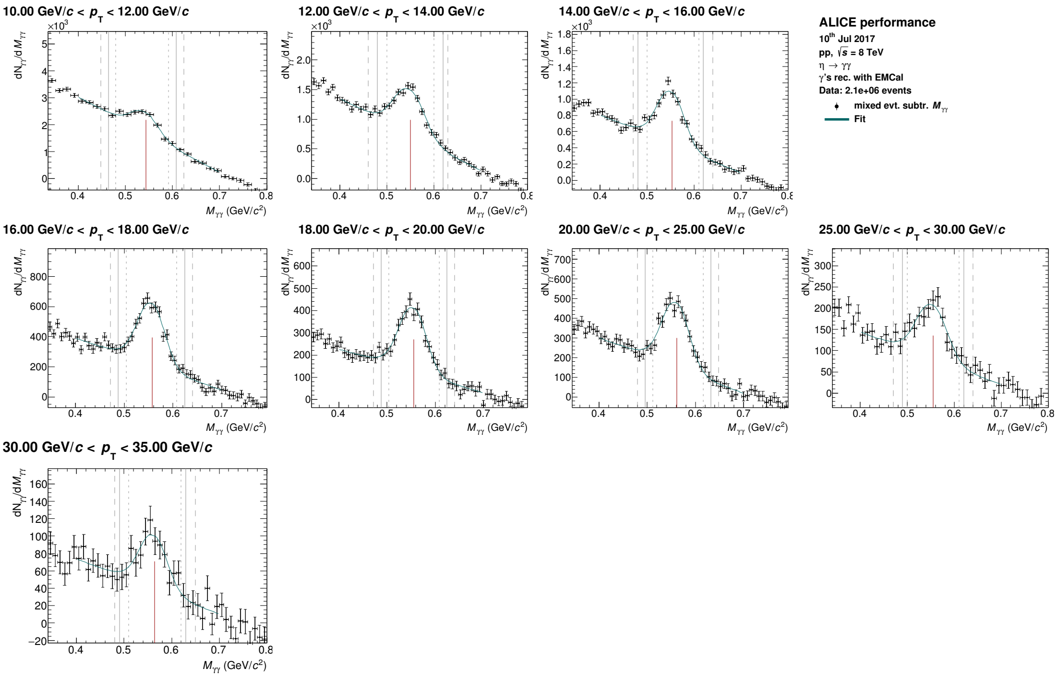

a)

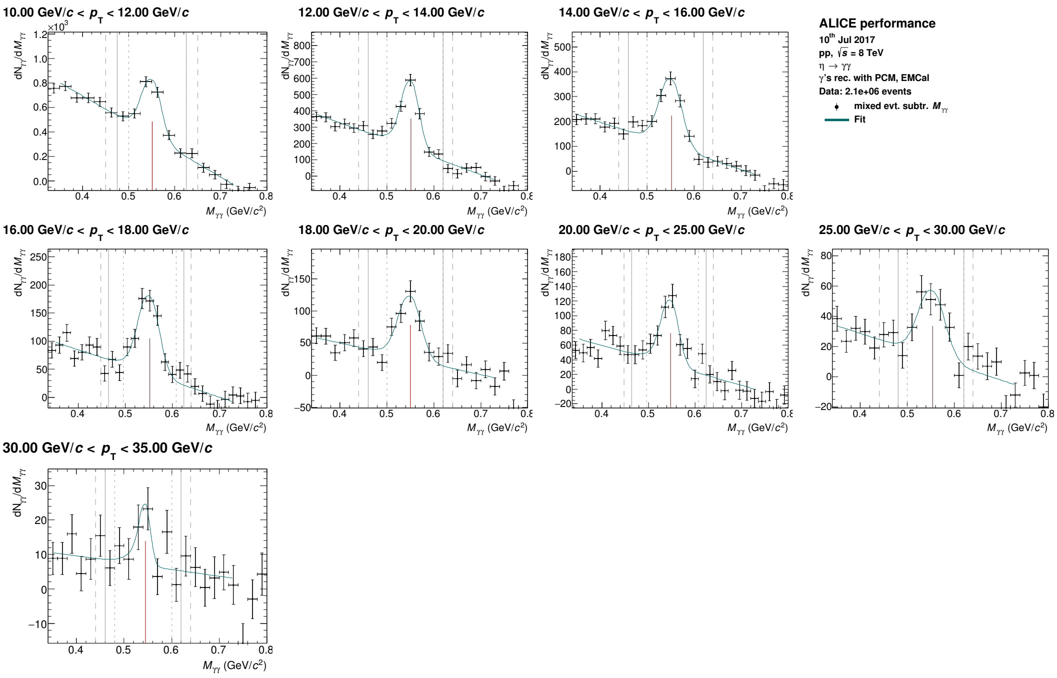

b)

Figure B.2.7: The invariant mass distributions of η candidates are shown for EGA triggers using the EMCal, a), and PCM-EMCal, b), method. The reconstructed mass position obtained from the fit of Eq. 6.1.3 (light blue) is visualized by the red lines. Moreover, the integration ranges are visualized used to extract the signal.

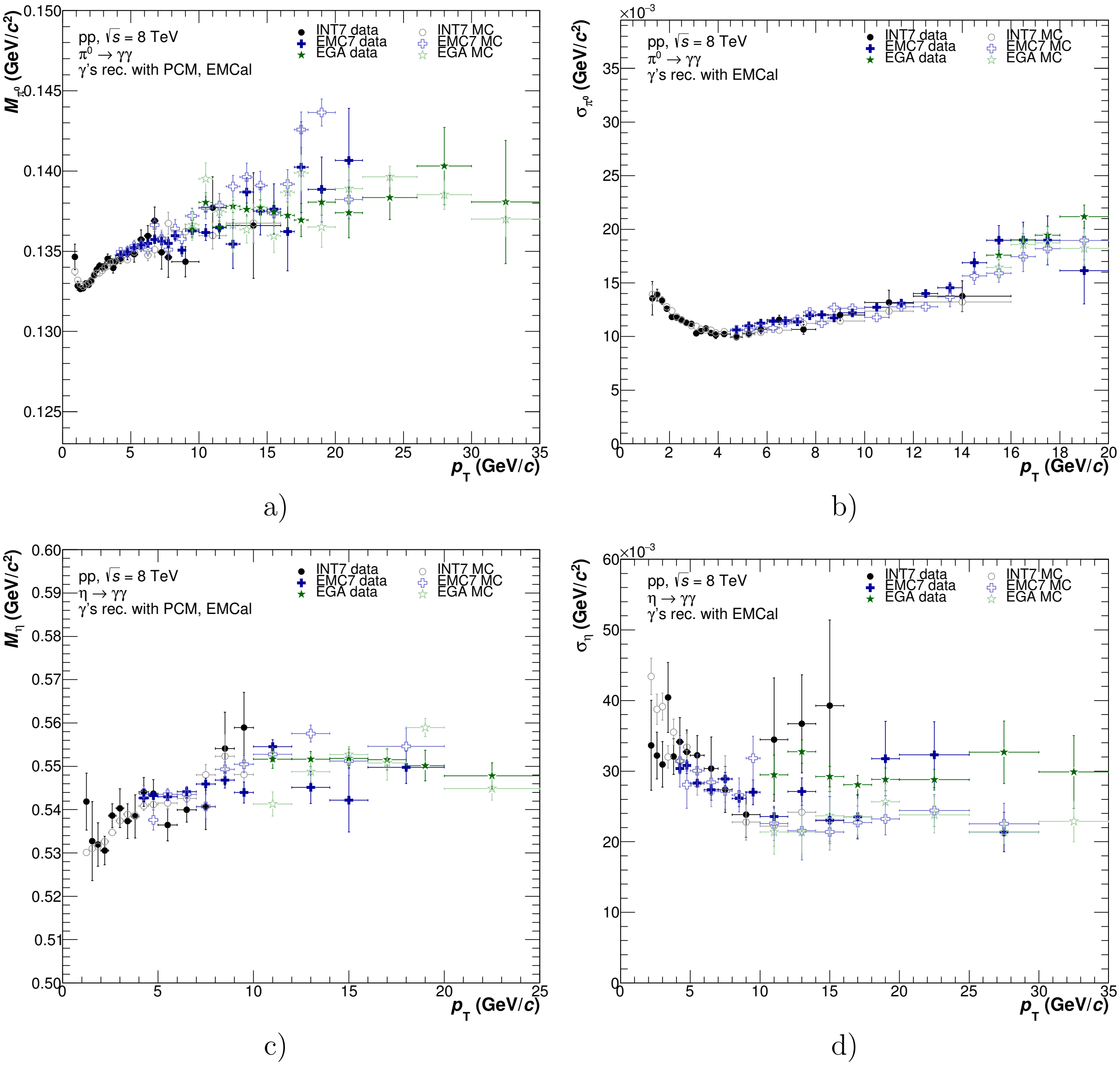

Figure B.2.8: The extracted mass positions, M_{π^0} and M_η, and extracted peak widths, $\sigma_{M_{\pi^0}}$ and σ_{M_η}, by fitting Eq. 6.1.3 to the background-subtracted signal, drawn as a function of p_{T} for real data and MC simulations for the three available triggers. The other distributions can be found in Fig. 6.2.7 and Fig. 6.2.8.

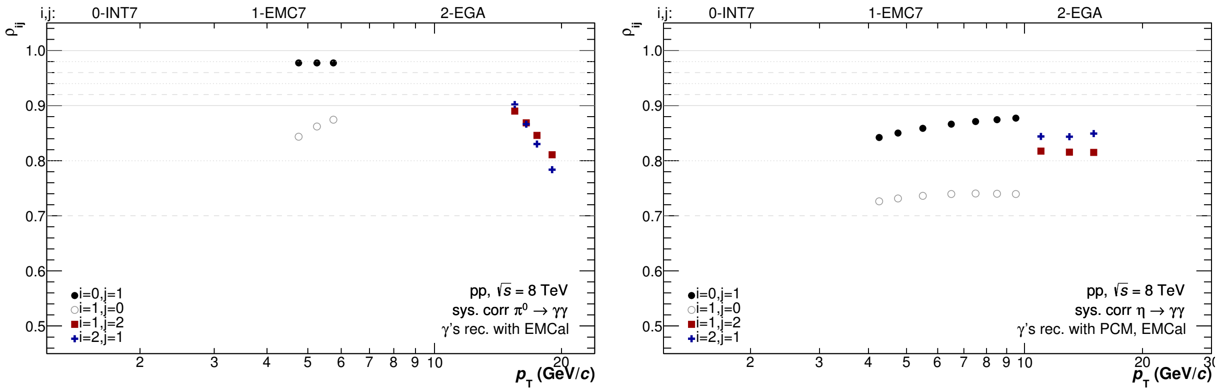

a) b)

Figure B.2.9: The p_{T}-dependent correlation factors $\rho_{ij}(p_{\mathrm{T}})$ visualizing the fraction of correlated systematic uncertainty of trigger i with respect to trigger j. The factors are shown for the example of the π^0 for EMCal, a), and the η for PCM-EMCal, b). The remaining plots showing the other cases can be found in Fig. 6.2.11 and Fig. B.2.10.

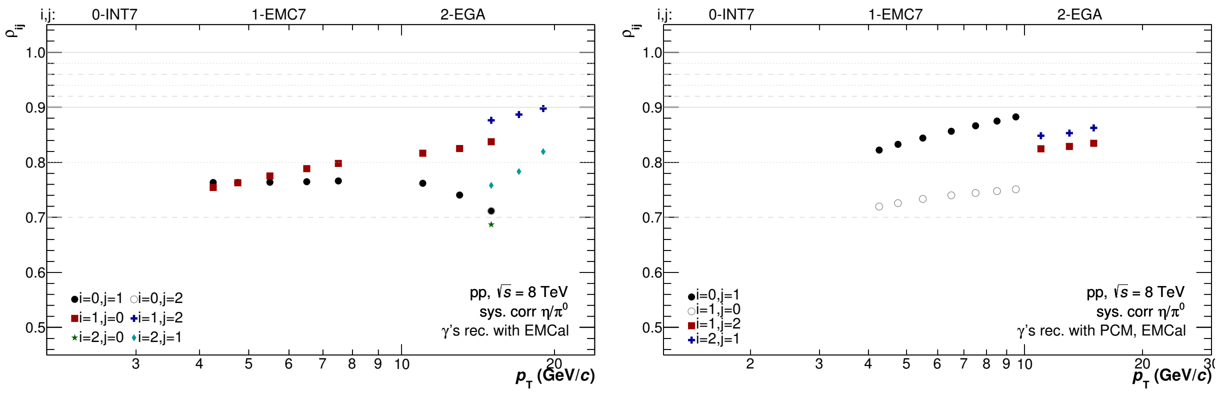

a) b)

Figure B.2.10: The p_{T}-dependent correlation factors $\rho_{ij}(p_{\mathrm{T}})$ visualizing the fraction of correlated systematic uncertainty of trigger i with respect to trigger j. The factors are shown for the example of the η/π^0 for EMCal, a), and PCM-EMCal, b). The remaining plots for the π^0 and η can be found in Fig. 6.2.11 and Fig. B.2.9.

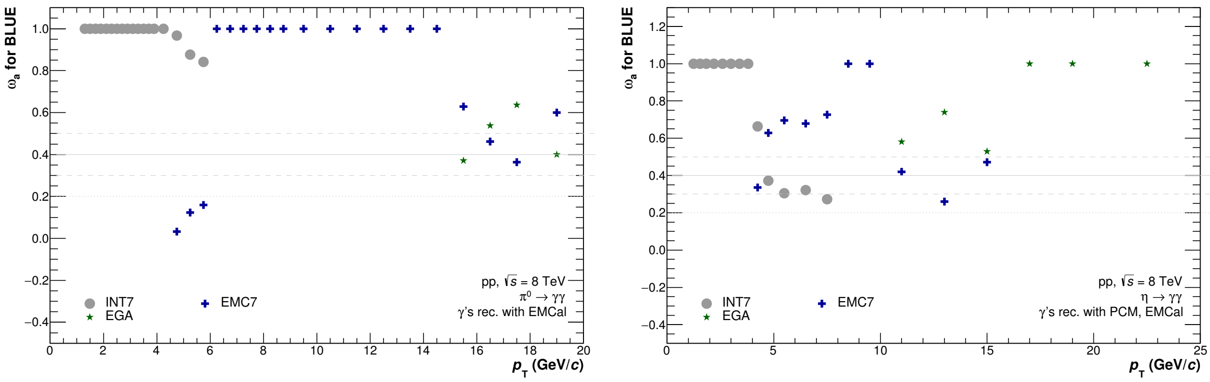

a) b)

Figure B.2.11: The obtained weights $\omega_a(p_\mathrm{T})$ using the BLUE method for the combination of π^0 measurements using EMCal, a), and for the η using PCM-EMCal, b). The remaining plots showing the weights for all other cases can be found in Fig. 6.2.12 and Fig. B.2.12.

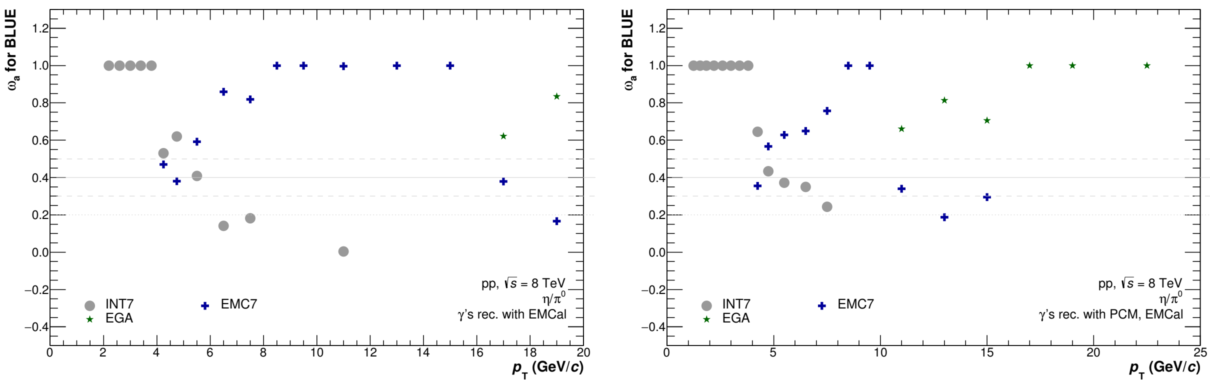

a) b)

Figure B.2.12: The obtained weights $\omega_a(p_\mathrm{T})$ using the BLUE method for the combination of η/π^0 measurements using EMCal, a), and using PCM-EMCal, b). The remaining plots showing the weights for all other cases can be found in Fig. 6.2.12 and Fig. B.2.11.

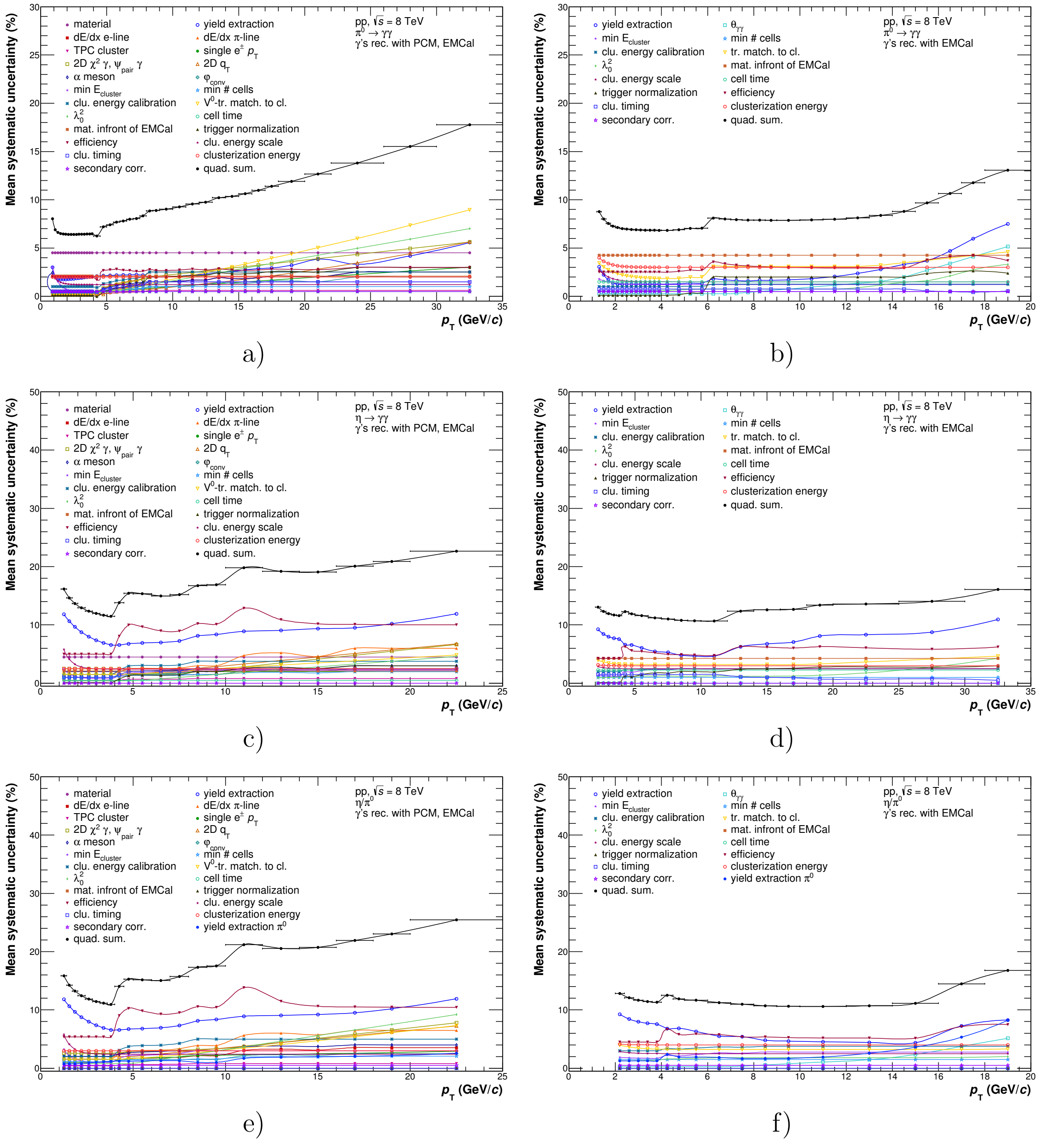

Figure B.2.13: Detailed overviews of the p_{T}-dependent systematic uncertainties decomposed into the different sources as indicated in the legends for π^0, η and η/π^0 measurements using PCM-EMCal (left) and EMCal (right) for pp, $\sqrt{s} = 8\,\mathrm{TeV}$. In black, the quadratic sum of all respective sources is given. The respective plots show the combined uncertainties for all three triggers used for analysis which explains the different shapes of the uncertainty sources as a function of p_{T}.

B.2.2 π^0 & η Mesons in pp, $\sqrt{s} = 0.9$ & 7 TeV

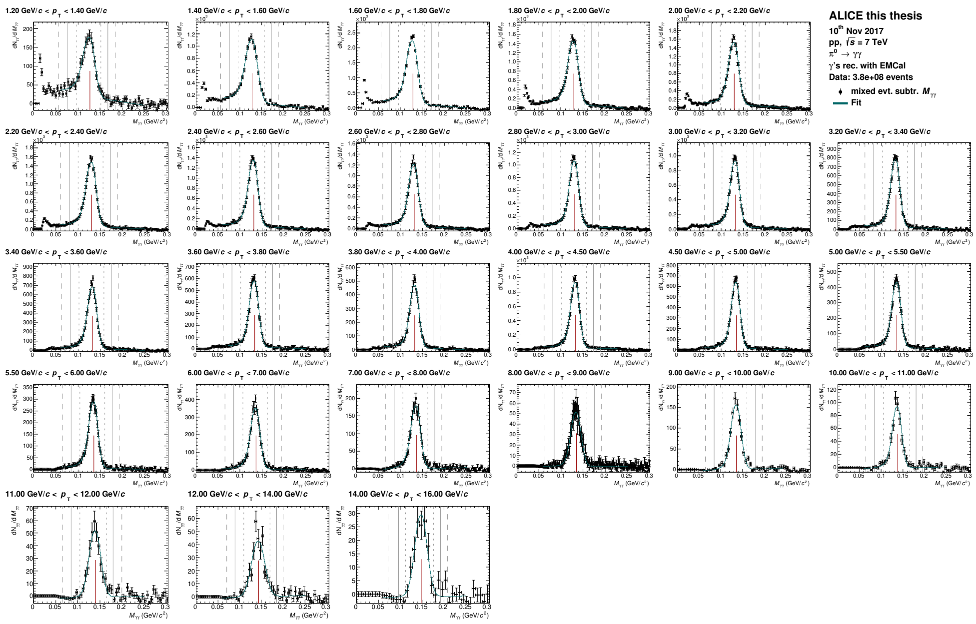

a)

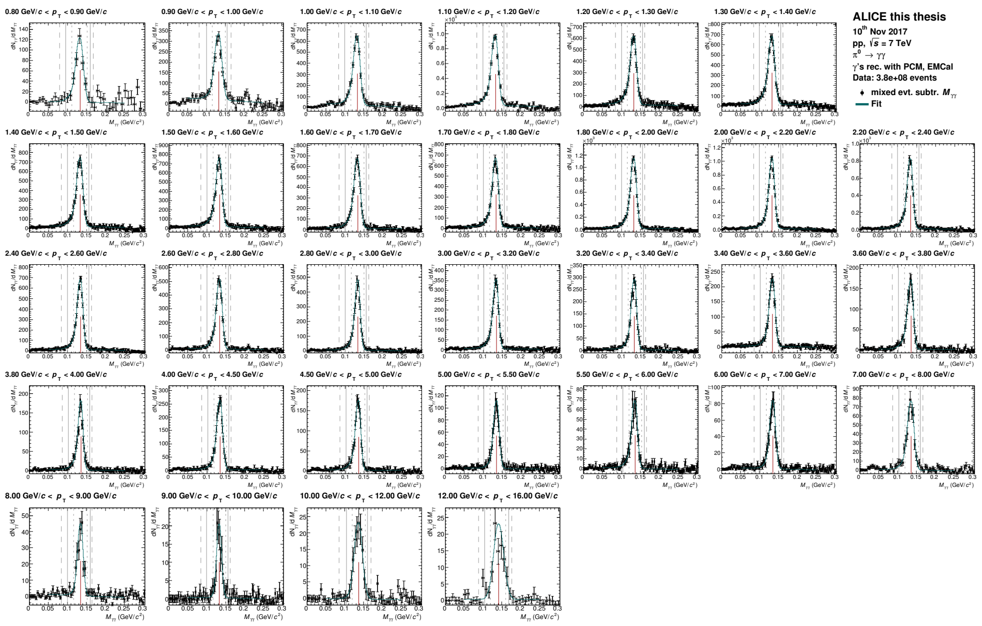

b)

Figure B.2.14: The invariant mass distributions of π^0 candidates are shown for MB triggers using the EMCal, a), and PCM-EMCal, b), method. The reconstructed mass position obtained from the fit of Eq. 6.1.3 (light blue) is visualized by the red lines. Moreover, the integration ranges are visualized used to extract the signal.

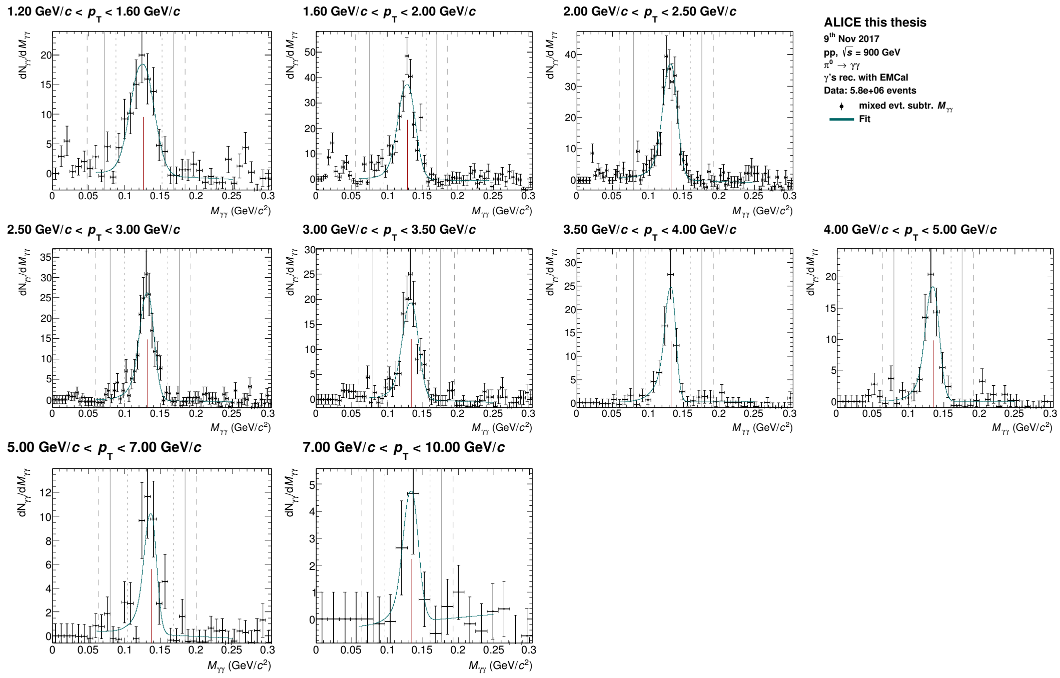

a)

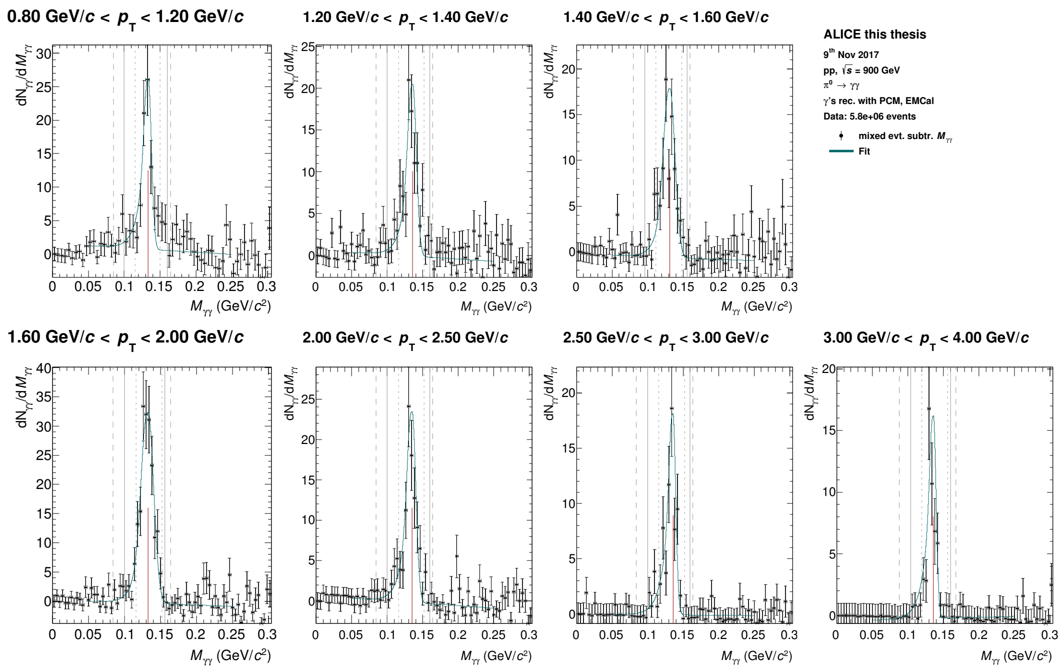

b)

Figure B.2.15: The invariant mass distributions of π^0 candidates are shown for MB triggers using the EMCal, a), and PCM-EMCal, b), method. The reconstructed mass position obtained from the fit of Eq. 6.1.3 (light blue) is visualized by the red lines. Moreover, the integration ranges are visualized used to extract the signal.

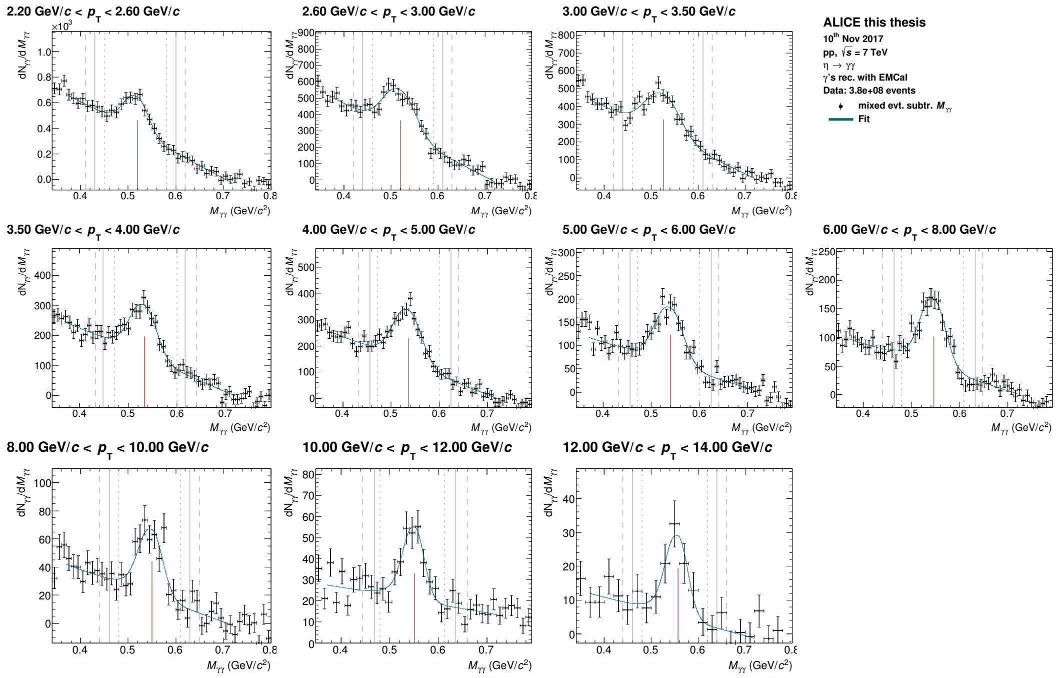

a)

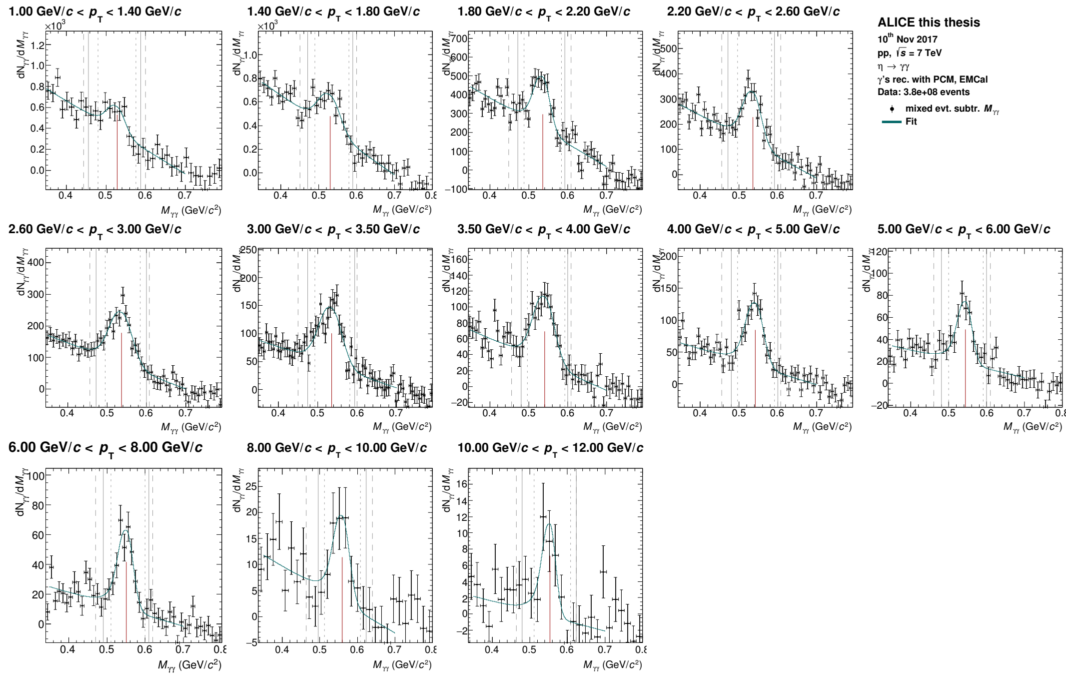

b)

Figure B.2.16: The invariant mass distributions of η candidates are shown for MB triggers using the EMCal, a), and PCM-EMCal, b), method. The reconstructed mass position obtained from the fit of Eq. 6.1.3 (light blue) is visualized by the red lines. Moreover, the integration ranges are visualized used to extract the signal.

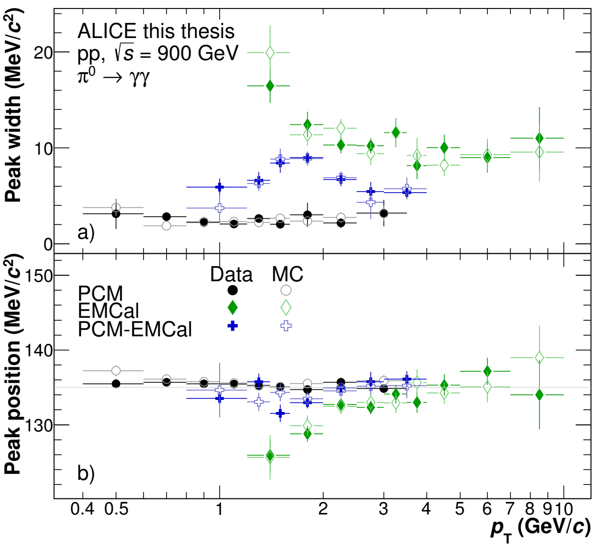

a)

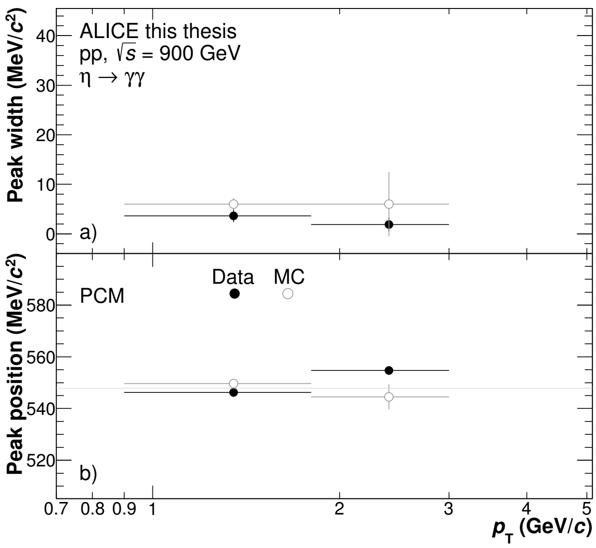

b)

Figure B.2.17: The reconstructed peak widths and peak positions for the π^0 (left) and η (right) mesons for all reconstruction methods used in the analysis of pp, $\sqrt{s} = 0.9\,\mathrm{TeV}$. Full markers show results from data, whereas open markers represent the obtained values from MC simulations.

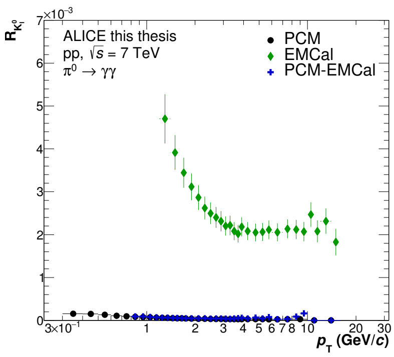

a)

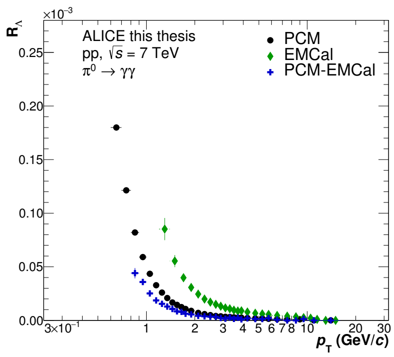

b)

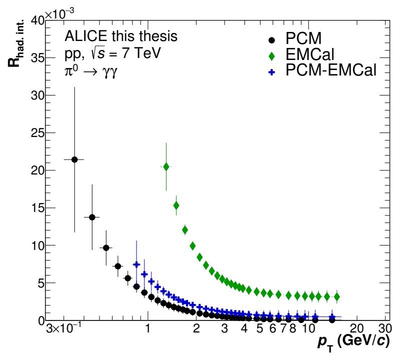

c)

Figure B.2.18: Effective corrections concerning secondary π^0 mesons originating from K^0_L and Λ decays as well as hadronic interactions with the detector material of ALICE, from a) to c), summarized for the methods PCM, PCM-EMCal and EMCal for pp collisions at $\sqrt{s} = 7\,\mathrm{TeV}$. The respective fractions of secondary π^0 mesons are plotted as a function of p_{T}.

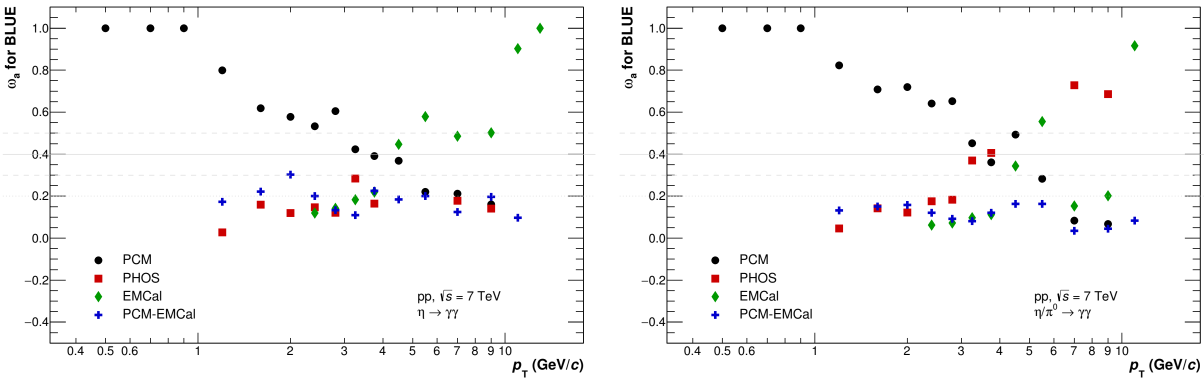

a) b)

Figure B.2.19: The obtained weights $\omega_a(p_\mathrm{T})$ using the BLUE method for the combination of η and η/π^0 measurements are shown in a) and b) using all inputs summarized in Tab. 6.3.12 for pp collisions at $\sqrt{s} = 7\,\mathrm{TeV}$.

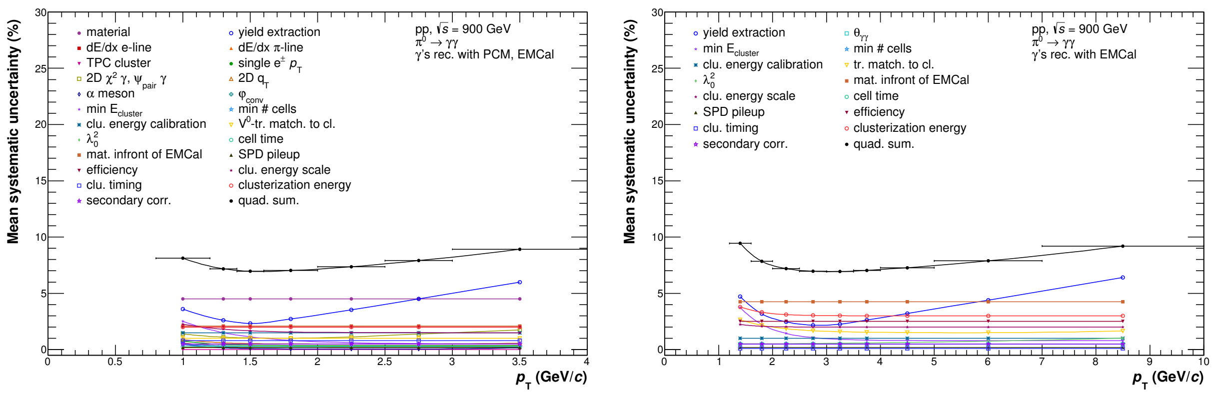

a) b)

Figure B.2.20: Detailed overviews of the p_T-dependent systematic uncertainties decomposed into the different sources as indicated in the legends for π^0 measurements using PCM-EMCal, a), and EMCal, b) for pp, $\sqrt{s} = 0.9\,\mathrm{TeV}$. In black, the quadratic sum of all respective sources is given. The respective plots show the combined uncertainties for all three triggers used for analysis which explains the different shapes of the uncertainty sources as a function of p_T.

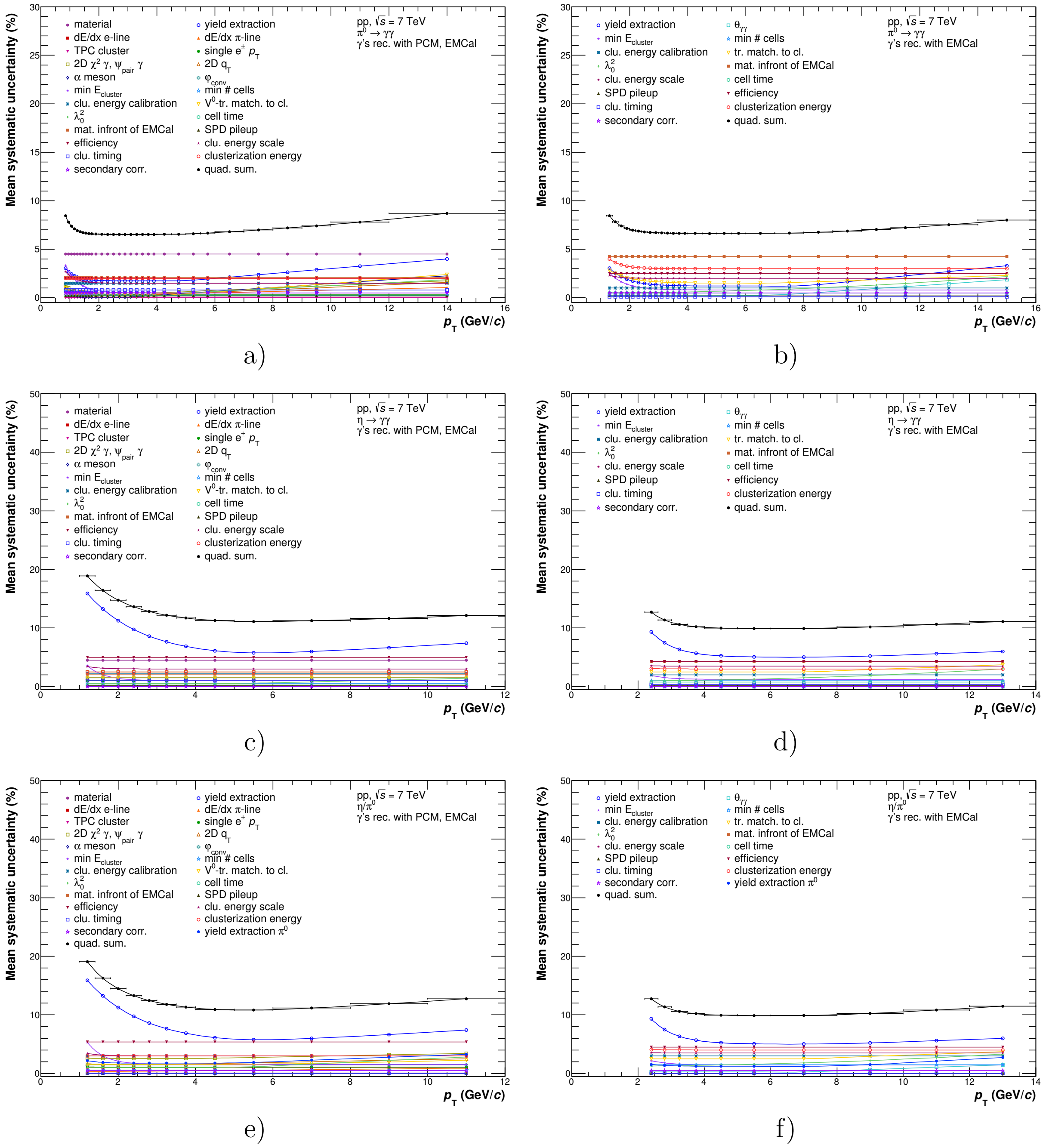

Figure B.2.21: Detailed overviews of the p_{T}-dependent systematic uncertainties decomposed into the different sources as indicated in the legends for π^0, η and η/π^0 measurements using PCM-EMCal (left) and EMCal (right) for pp, $\sqrt{s}$ = 7 TeV. In black, the quadratic sum of all respective sources is given. The respective plots show the combined uncertainties for all three triggers used for analysis which explains the different shapes of the uncertainty sources as a function of p_{T}.

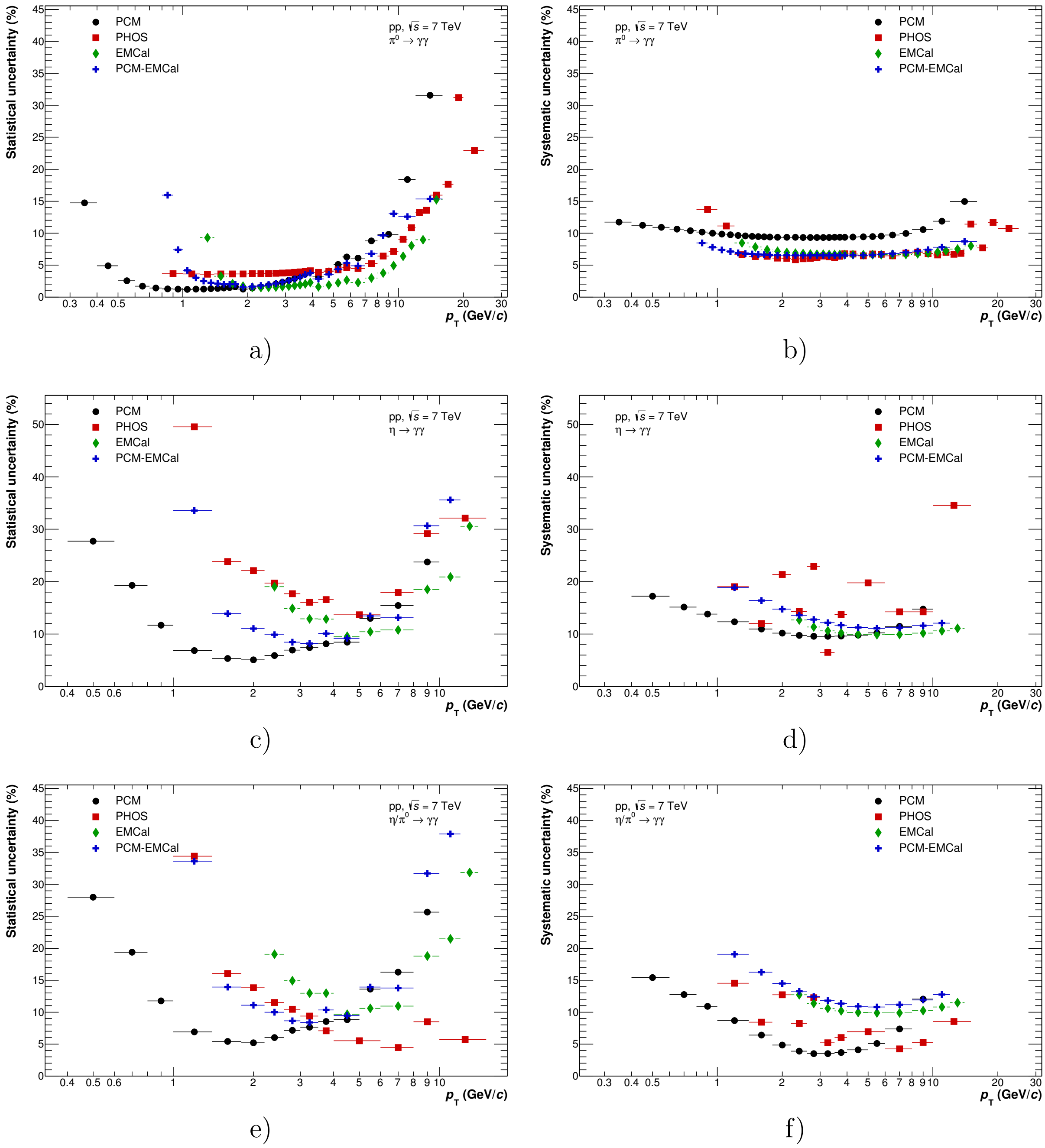

Figure B.2.22: Relative statistical (left) and systematic (right) uncertainties, given in percent, for all available reconstruction methods for π^0, η and η/π^0 measurements in pp collisions at $\sqrt{s} = 7\,\text{TeV}$.

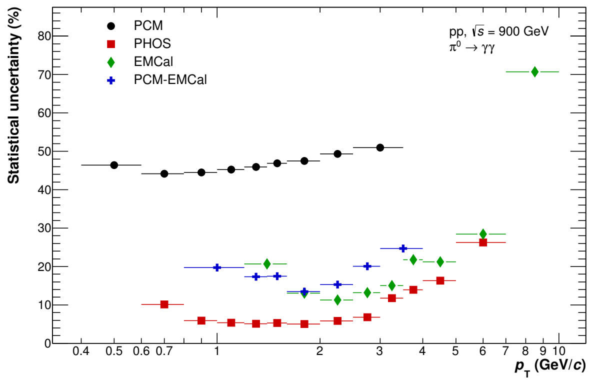

a)

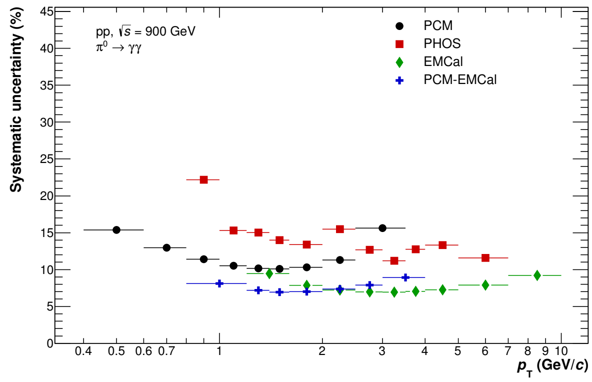

b)

Figure B.2.23: Relative statistical (left) and systematic (right) uncertainties in percent for all available reconstruction methods measuring π^0 mesons in pp, $\sqrt{s} = 0.9\,\text{TeV}$.

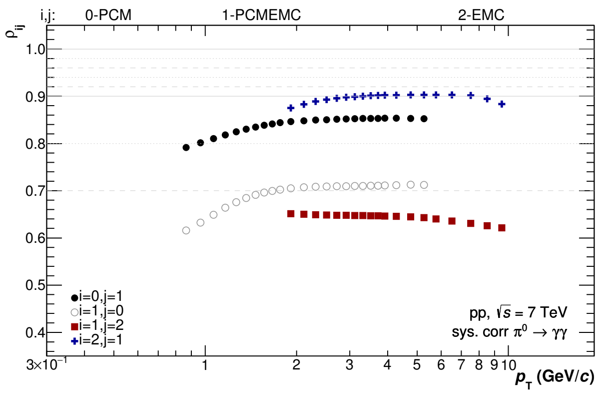

a)

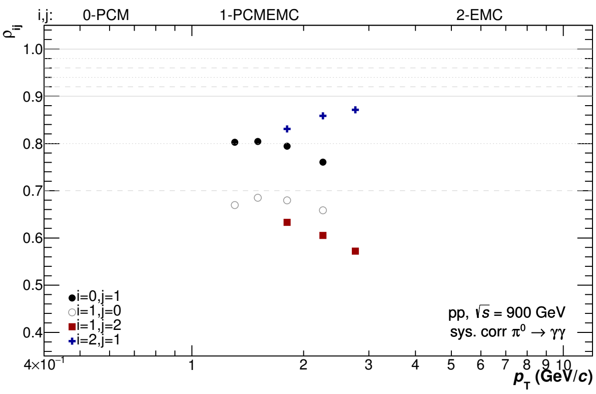

b)

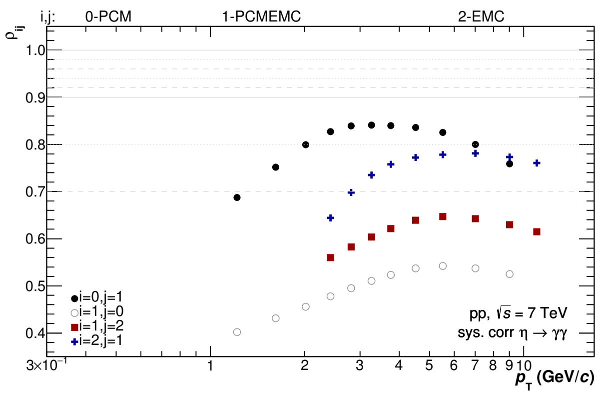

c)

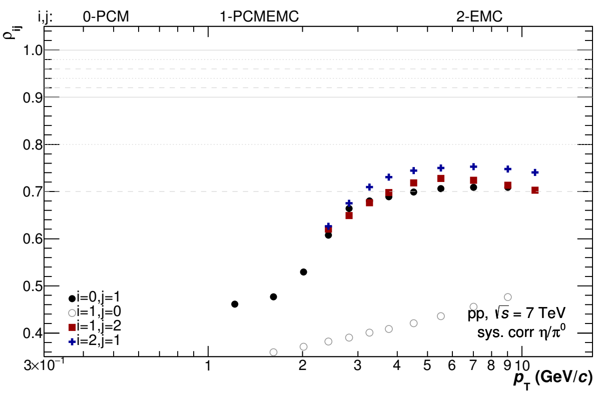

d)

Figure B.2.24: The p_T-dependent correlation factors $\rho_{ij}(p_T)$ visualizing the fraction of correlated systematic uncertainty of reconstruction method i with respect to method j. The factors are shown for all available measurements of π^0 and η meson production, a) and c), and the η/π^0 ratio, d), in pp collisions at $\sqrt{s} = 7\,\text{TeV}$. Furthermore, the analog plot is shown in b) for the π^0 at $\sqrt{s} = 0.9\,\text{TeV}$.

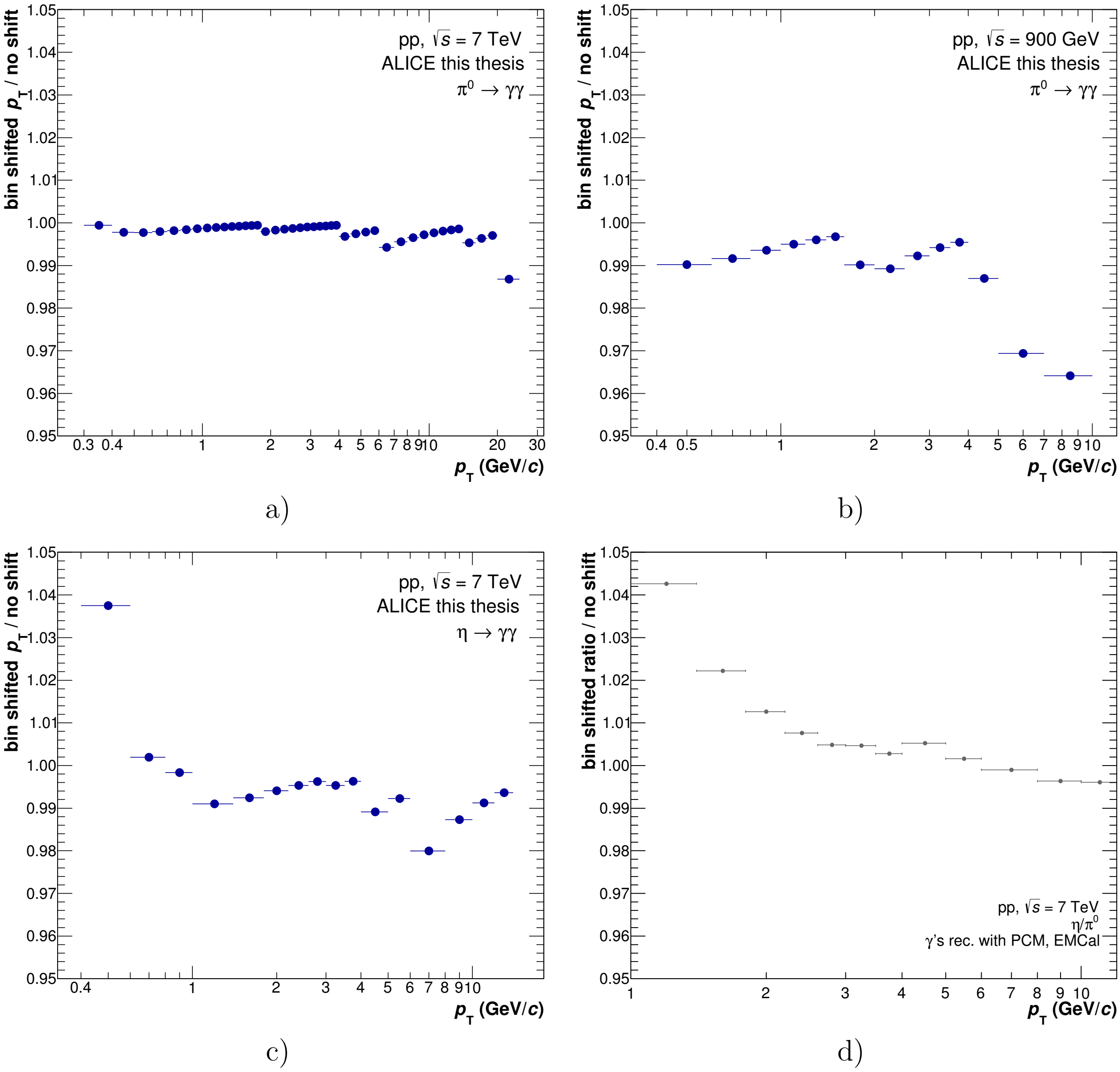

Figure B.2.25: The size of the bin width corrections for the combined π^0 and η meson spectra are shown for pp, $\sqrt{s}$ = 7 TeV in a) and c). Furthermore, the obtained bin width correction for the corresponding η/π^0 ratio is shown for the PCM-EMCal method in d). Moreover, the bin width correction for the π^0 measured in pp, $\sqrt{s}$ = 0.9 TeV is shown in b).

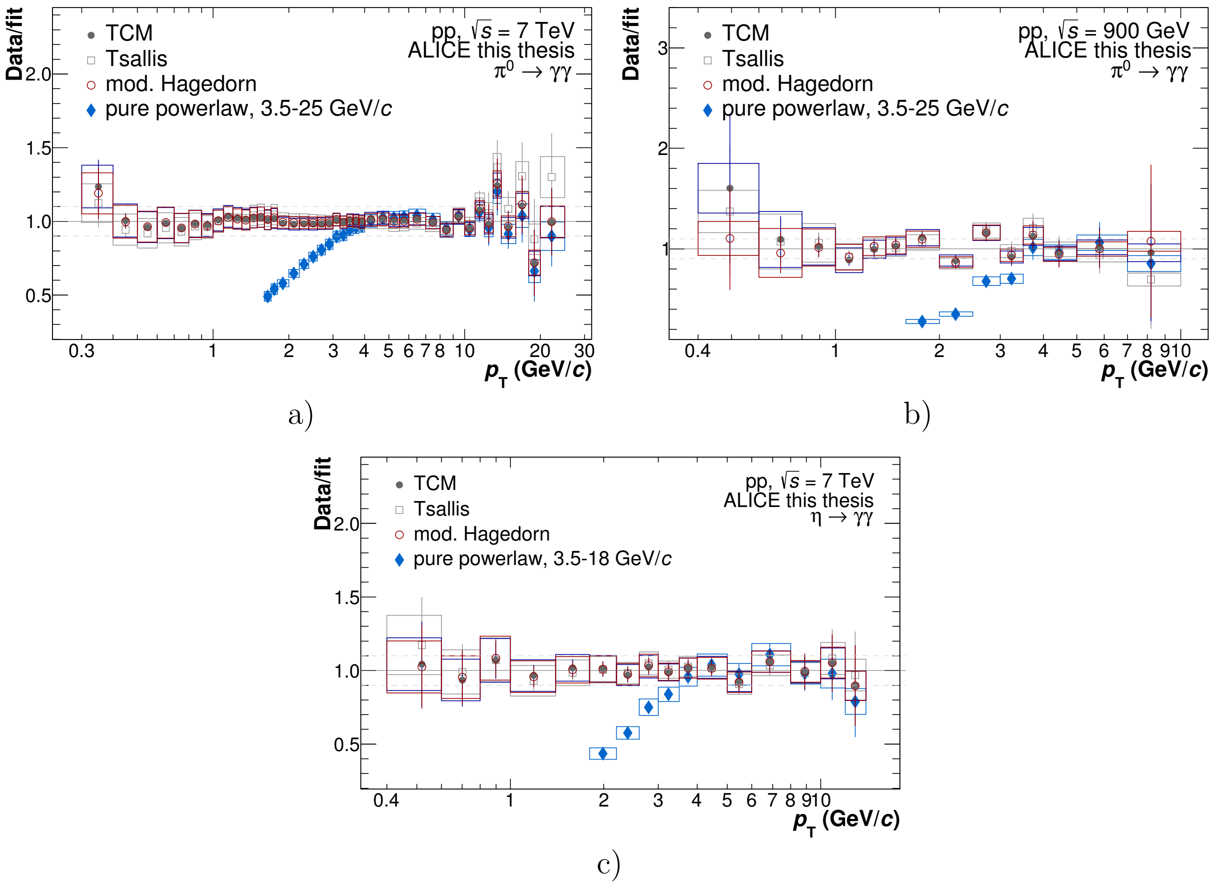

Figure B.2.26: Ratios of the measured π^0 and η spectra from each reconstruction method to the TCM fit of the combined spectrum are shown in a) and c) for pp, $\sqrt{s} = 7\,\text{TeV}$. Furthermore, the analog plot is shown in b) for the π^0 at $\sqrt{s} = 0.9\,\text{TeV}$.

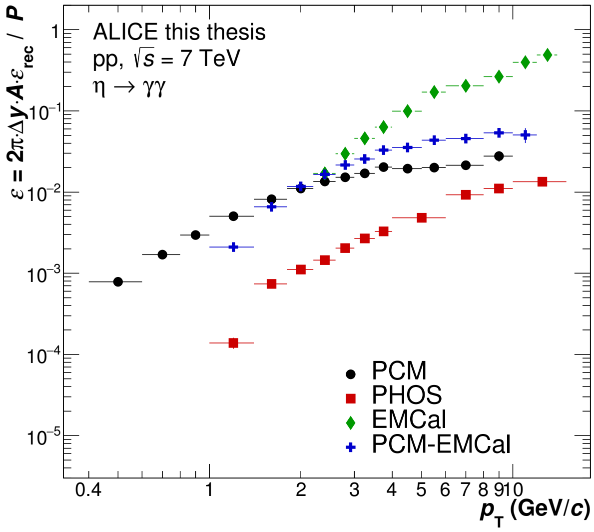

a)

Figure B.2.27: The normalized correction factors ε are plotted as a function of p_{T} for each reconstruction method used for η mesons for pp collisions at $\sqrt{s} = 7$.

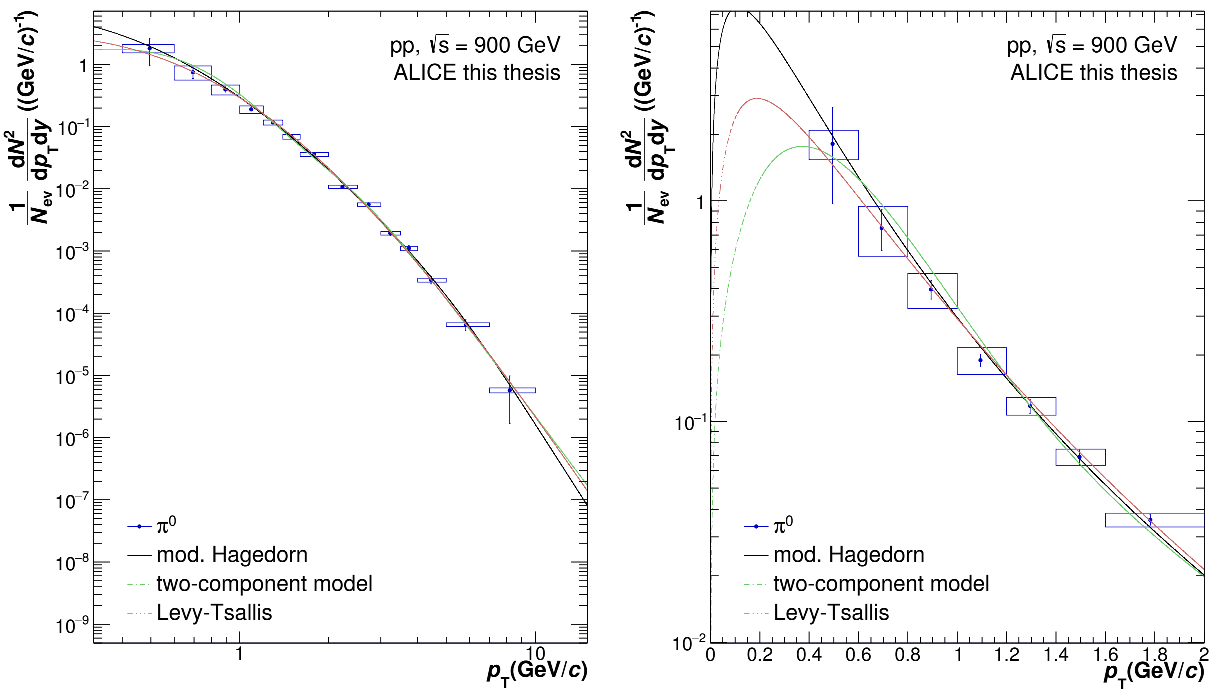

a) b)

Figure B.2.28: The neutral pion spectrum measured in pp collisions at $\sqrt{s} = 0.9\,\mathrm{TeV}$ is shown with logarithmic abscissa (left) and for the low momentum region $p_{\mathrm{T}} < 2\,\mathrm{GeV}/c$ with a linear scale on the abscissa (right). Furthermore, the different fits are shown which are used to determine the integrated yields and mean p_{T} values.

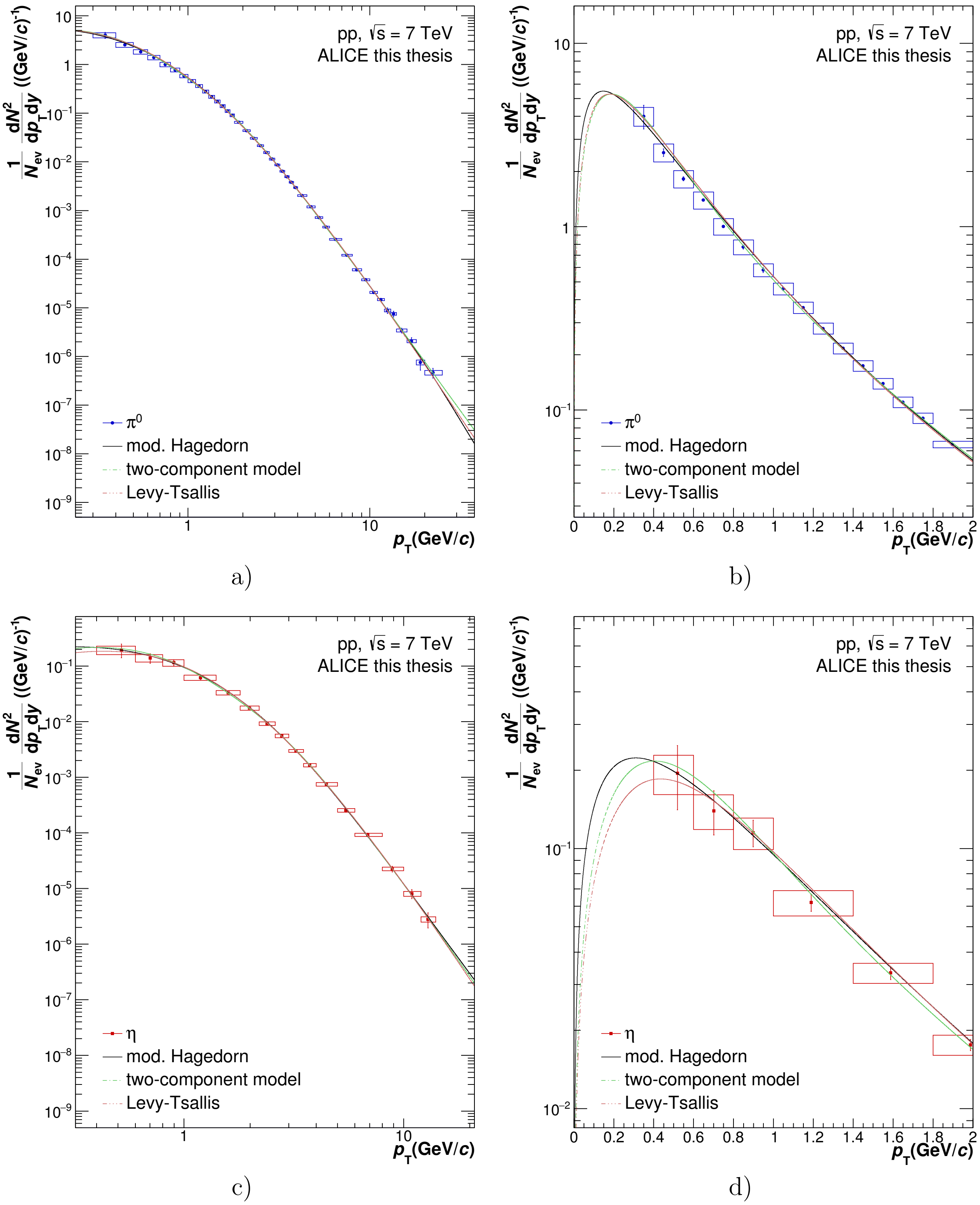

Figure B.2.29: The neutral meson spectra measured in pp collisions at $\sqrt{s} = 7\,\mathrm{TeV}$ are shown with logarithmic abscissa (left) and for the low momentum region $p_\mathrm{T} < 2\,\mathrm{GeV}/c$ with a linear scale on the abscissa (right). Furthermore, the different fits are shown which are used to determine the integrated yields and mean p_T values.

B.3 Additional Direct Photon Plots

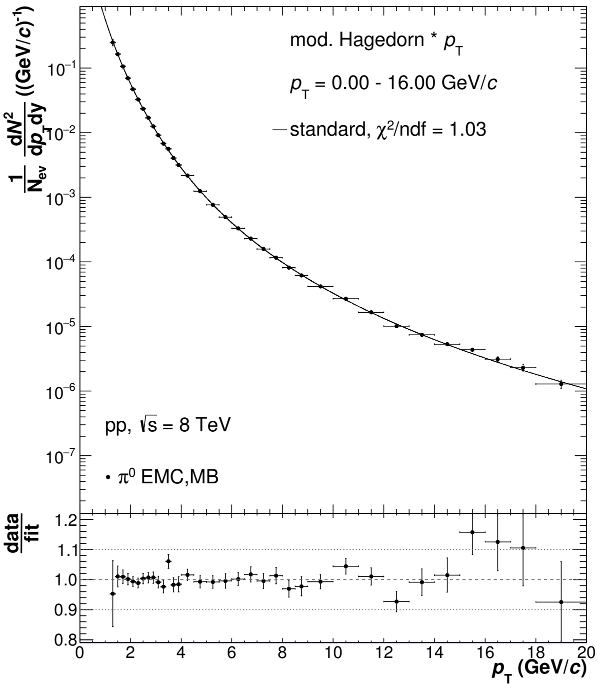

a)

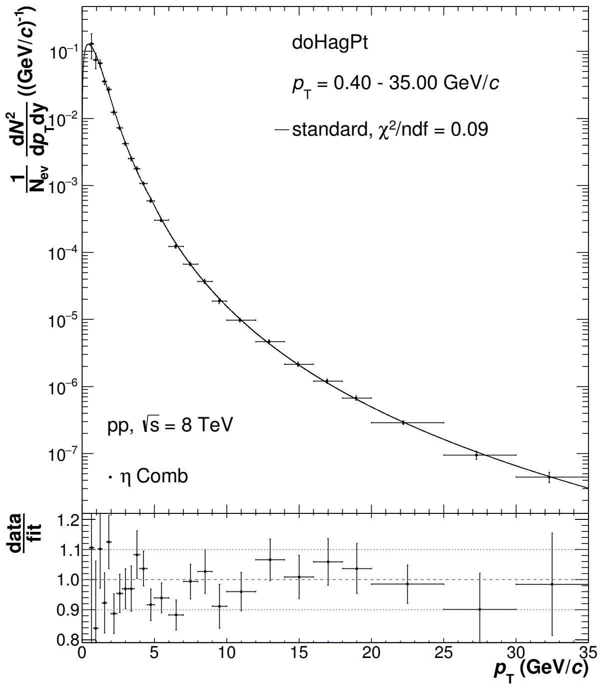

b)

Figure B.3.30: Parameterizations of the invariant π^0 yield measured with EMCal in MB triggered events and the combined η measurement, for which only statistical uncertainties are used that are drawn in the plots.

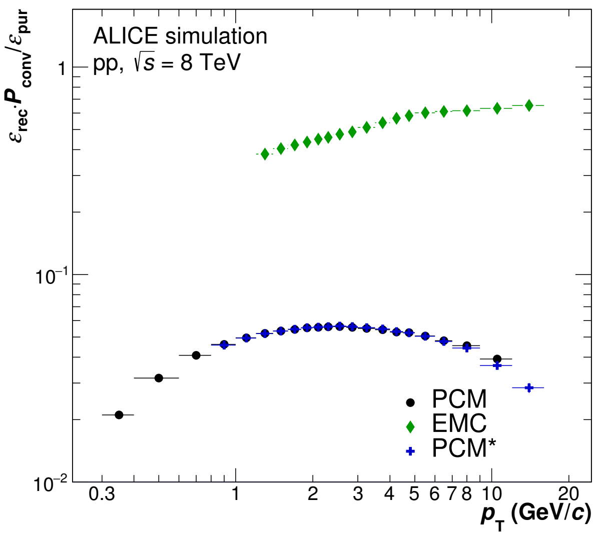

a)

Figure B.3.31: The total correction factors ε for the $Y_{\gamma_{\mathrm{incl}}}$ measurements. The major difference between the EMCal and the PCM is due to the photon conversion probability.

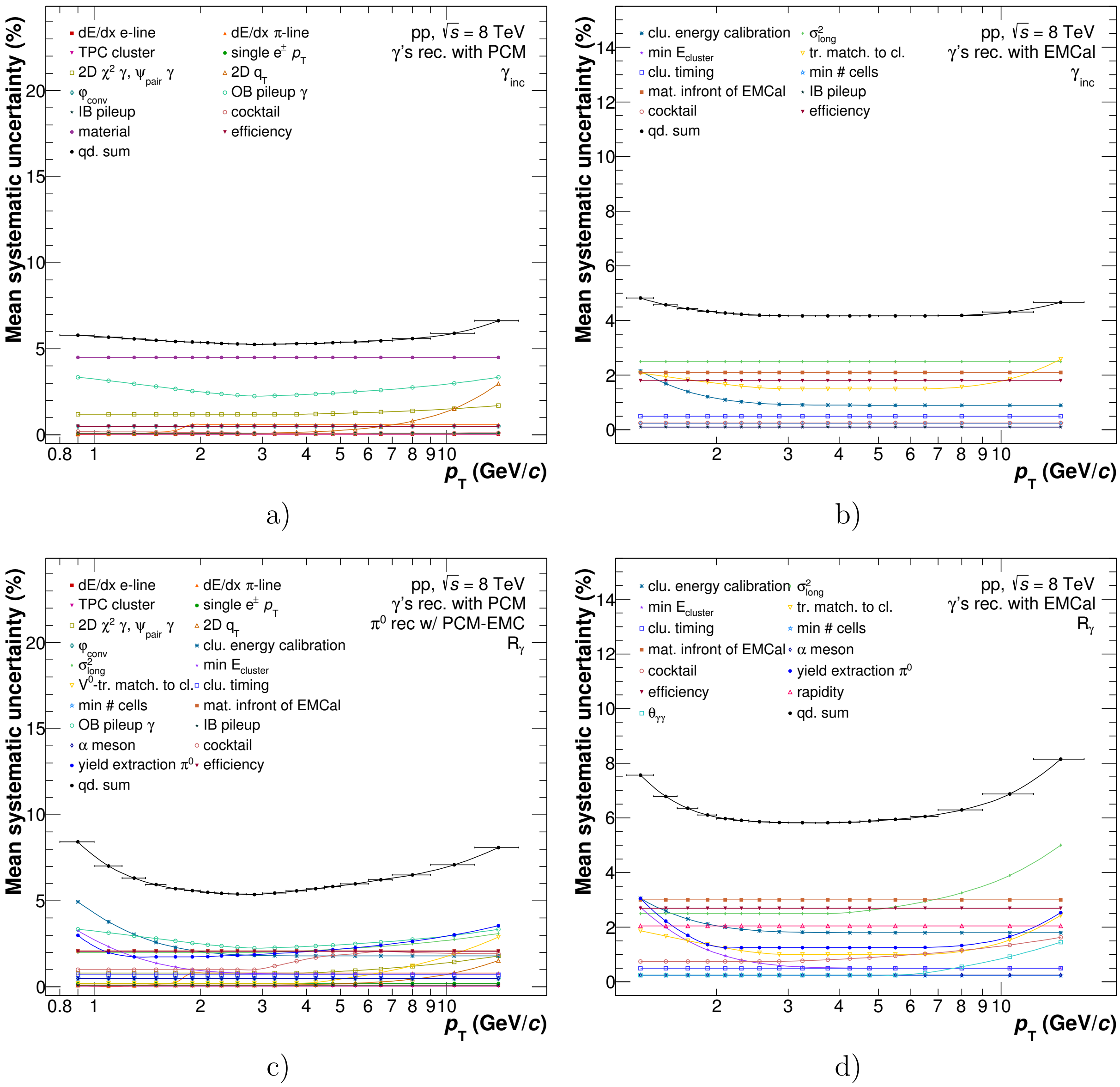

Figure B.3.32: Detailed overviews of the p_{T}-dependent systematic uncertainties decomposed into the different sources as indicated in the legends for the $Y_{\gamma_{\mathrm{incl}}}$ and R_γ measurements using PCM-EMCal (left) and EMCal (right) for pp, $\sqrt{s} = 8\,\mathrm{TeV}$. In black, the quadratic sum of all respective sources is given.

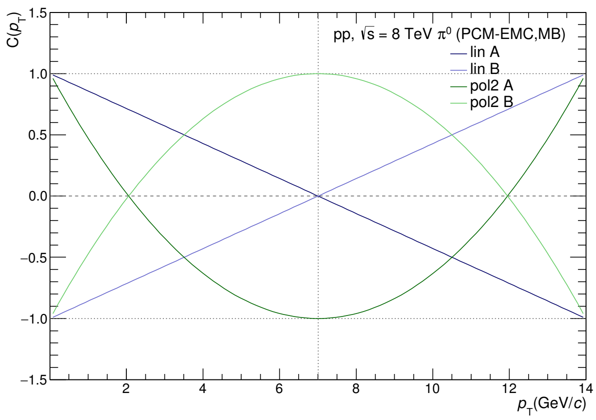

a)

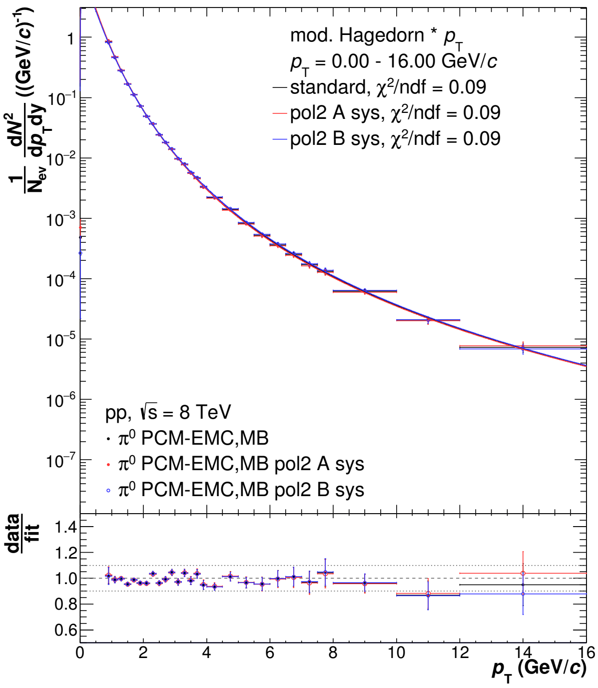

b)

Figure B.3.33: The fraction $C(pT)$ of the systematic uncertainties used to shift the central values is shown in a) for the PCM-EMCal π^0 input spectrum entering the decay photon simulation. The actual spectrum is shown in b), where the effects of the shifts are visualized. The black points denote the actual input spectrum, whereas the red and blue markers show the shifted inputs according to a), which are separately fitted using the same functional forms as for the standard case.

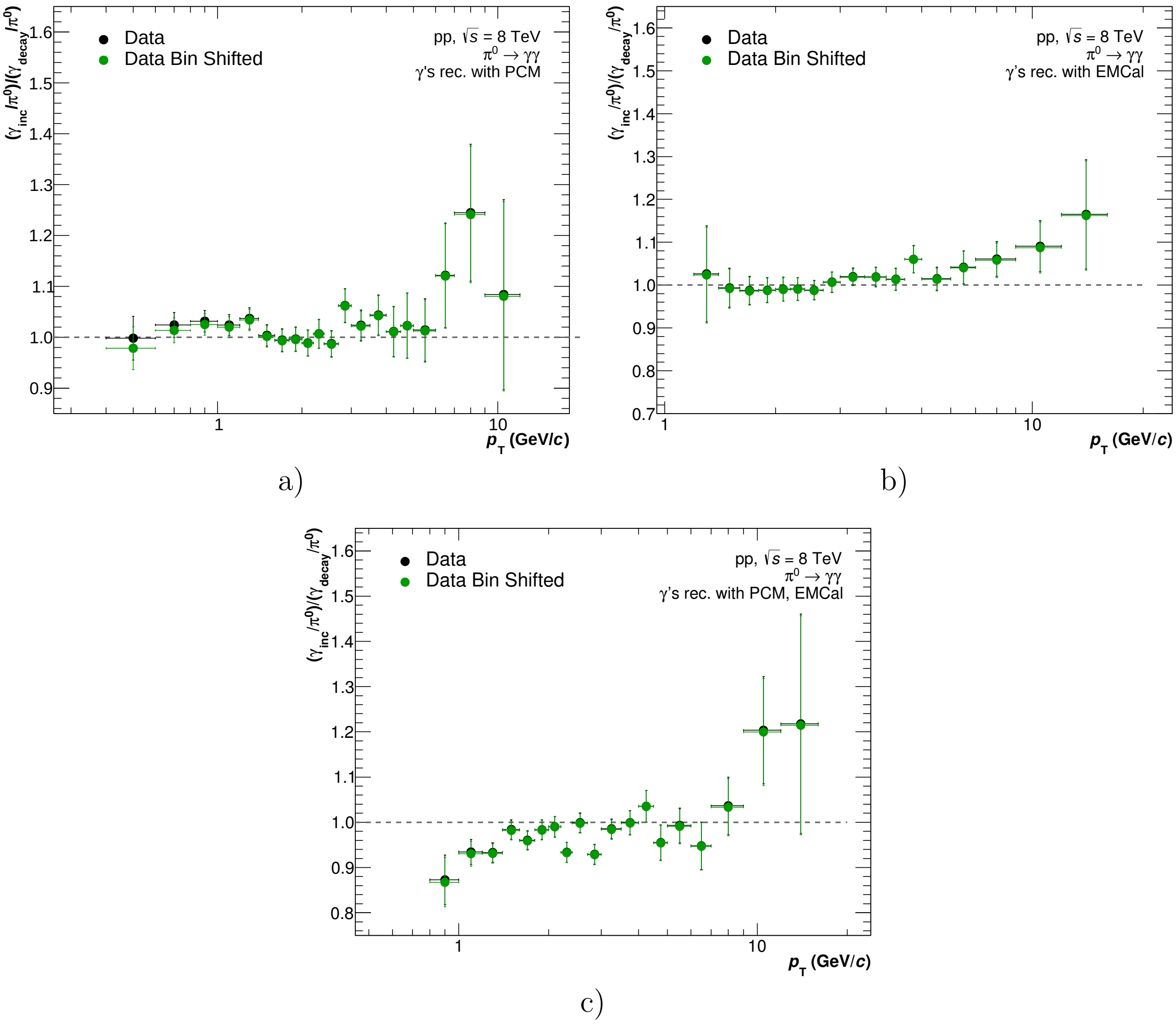

Figure B.3.34: The size of the resulting bin width corrections for the combined R_γ measurements are shown for PCM, EMCal and PCM-EMCal, shifting both input $Y_{\gamma_{\mathrm{incl}}}$ and π^0 spectra along the vertical direction.

List of Tables

List of Figures

Bibliography

[1] S. F. Novaes, "Standard model: An Introduction," in *Proceedings, 10th Jorge Andre Swieca Summer School*, pp. 5–102. 1999. arXiv:hep-ph/0001283 [hep-ph].

[2] C. Loizides, "Experimental overview on small collision systems at the LHC," *Nucl. Phys.* **A956** (2016) 200–207, arXiv:1602.09138 [nucl-ex].

[3] F.-M. Liu and K. Werner, "Direct photons at low transverse momentum: A QGP signal in pp collisions at LHC," *Phys. Rev. Lett.* **106** (2011) 242301, arXiv:1102.1052 [hep-ph].

[4] **ALICE** Collaboration, S. Acharya *et al.*, "π^0 and η meson production in proton-proton collisions at $\sqrt{s} = 8$ TeV," *Eur. Phys. J.* **C78** (2018) 263, arXiv:1708.08745 [hep-ex].

[5] **ALICE** Collaboration, S. Acharya *et al.*, "Supplemental figures: π^0 and η meson production in proton-proton collisions at $\sqrt{s} = 8$ TeV," ALICE-PUBLIC-2017-009. http://cds.cern.ch/record/2282851.

[6] **ALICE** Collaboration, S. Acharya *et al.*, "Direct photon production at low transverse momentum in proton-proton collisions at $\sqrt{s} = 2.76$ and 8 TeV," arXiv:1803.09857 [nucl-ex].

[7] **ALICE** Collaboration, S. Acharya *et al.*, "Supplemental figures: Direct photon production at low transverse momentum in proton-proton collisions at $\sqrt{s} = 2.76$ and 8 TeV,". http://cds.cern.ch/record/2310535.

[8] **ALICE** Collaboration, S. Acharya *et al.*, "Production of π^0 and η mesons up to high transverse momentum in pp collisions at 2.76 TeV," *Eur. Phys. J.* **C77** (2017) 339, arXiv:1702.00917 [hep-ex].

[9] **ALICE** Collaboration, S. Acharya *et al.*, "Neutral pion and η meson production in p-Pb collisions at $\sqrt{s_{NN}} = 5.02$ TeV," arXiv:1801.07051 [nucl-ex].

[10] **ALICE** Collaboration, B. Abelev *et al.*, "Neutral pion and η meson production in proton-proton collisions at $\sqrt{s} = 0.9$ TeV and $\sqrt{s} = 7$ TeV," *Phys. Lett.* **B717** (2012) 162–172, arXiv:1205.5724 [hep-ex].

[11] D. Kazakov, "The Higgs Boson is found: what is next?," *Phys. Usp.* **57** no. 9, (2014) 930–942, arXiv:1405.5495 [hep-ph]. [Usp. Fiz. Nauk184,no.9,1004(2014)].

[12] S. L. Glashow, "Partial Symmetries of Weak Interactions," *Nucl. Phys.* **22** (1961) 579–588.

[13] A. Salam, "Weak and Electromagnetic Interactions," *Conf. Proc.* **C680519** (1968) 367–377.

[14] S. Weinberg, "A Model of Leptons," *Phys. Rev. Lett.* **19** (1967) 1264–1266.

[15] Nobel Media AB, "The Nobel Prize in Physics 1979." `http://www.nobelprize.org/nobel_prizes/physics/laureates/1979/`. [accessed August 07, 2018].

[16] G. Altarelli, "Collider Physics within the Standard Model: a Primer," `arXiv:1303.2842 [hep-ph]`.

[17] **SLD Electroweak Group, DELPHI, ALEPH, SLD, SLD Heavy Flavour Group, OPAL, LEP Electroweak Working Group, L3** Collaboration, S. Schael *et al.*, "Precision electroweak measurements on the Z resonance," *Phys. Rept.* **427** (2006) 257–454, `arXiv:hep-ex/0509008 [hep-ex]`.

[18] G. Aad *et al.*, "Observation of a new particle in the search for the Standard Model Higgs boson with the ATLAS detector at the LHC," *Phys. Lett.* **B716** (2012) 1 – 29.

[19] S. Chatrchyan *et al.*, "Observation of a new boson at a mass of 125 GeV with the CMS experiment at the LHC," *Phys. Lett.* **B716** (2012) 30 – 61.

[20] M. Baak, M. Goebel, J. Haller, A. Hoecker, D. Kennedy, R. Kogler, K. Moenig, M. Schott, and J. Stelzer, "The Electroweak Fit of the Standard Model after the Discovery of a New Boson at the LHC," *Eur. Phys. J.* **C72** (2012) 2205, `arXiv:1209.2716 [hep-ph]`.

[21] Y. Choquet-Bruhat, *Introduction to General Relativity, Black Holes, and Cosmology.* Oxford University Press, New York, 2015.

[22] **Virgo, LIGO Scientific** Collaboration, B. P. Abbott *et al.*, "Observation of Gravitational Waves from a Binary Black Hole Merger," *Phys. Rev. Lett.* **116** no. 6, (2016) 061102, `arXiv:1602.03837 [gr-qc]`.

[23] H. Georgi and S. L. Glashow, "Unity of All Elementary Particle Forces," *Phys. Rev. Lett.* **32** (1974) 438–441.

[24] S. Hawking, *The Theory Of Everything.* Jaico Publishing House, 2006.

[25] C. Rovelli, "Notes for a brief history of quantum gravity," in *Proceedings, MG'9*, pp. 742–768. 2000. `arXiv:gr-qc/0006061 [gr-qc]`.

[26] K. Freese, "Review of Observational Evidence for Dark Matter in the Universe and in upcoming searches for Dark Stars," *EAS Publ. Ser.* **36** (2009) 113–126, `arXiv:0812.4005 [astro-ph]`.

[27] B. Penning, "The pursuit of dark matter at colliders—an overview," *J. Phys.* **G45** no. 6, (2018) 063001, `arXiv:1712.01391 [hep-ex]`.

[28] J. Liu, X. Chen, and X. Ji, "Current status of direct dark matter detection experiments," *Nature Phys.* **13** no. 3, (2017) 212–216, `arXiv:1709.00688 [astro-ph.CO]`.

[29] J. M. Gaskins, "A review of indirect searches for particle dark matter," *Contemp. Phys.* **57** no. 4, (2016) 496–525, `arXiv:1604.00014 [astro-ph.HE]`.

[30] M. Thomson, *Modern Particle Physics*. Cambridge University Press, Cambridge, 2013.

[31] P. Skands, "Introduction to QCD," in *Proceedings, TASI 2012*, pp. 341–420. 2013. arXiv:1207.2389 [hep-ph]. [,63(2107)].

[32] **Particle Data Group** Collaboration, C. Patrignani *et al.*, "Review of Particle Physics," *Chin. Phys.* **C40** no. 10, (2016) 100001.

[33] Prof. Xiangdong Ji, University of Maryland, "Lecture Notes on Phys 741." https://www.physics.umd.edu/courses/Phys741/xji/chapter5.pdf. [accessed August 07, 2018].

[34] C. Klein-Bösing, *Study of the Quark-Gluon Plasma with Hard and Electromagnetic Probes*. Habilitation, Westfälische-Wilhelms Universität Münster, 2013. https://www.uni-muenster.de/imperia/md/content/physik_kp/agwessels/thesis_db/ag_wessels/klein-boesing_c_2013_habilitation.pdf.

[35] **CMS** Collaboration, V. Khachatryan *et al.*, "Constraints on parton distribution functions and extraction of the strong coupling constant from the inclusive jet cross section in pp collisions at $\sqrt{s} = 7$ TeV," *Eur. Phys. J.* **C75** no. 6, (2015) 288, arXiv:1410.6765 [hep-ex].

[36] **CMS** Collaboration, V. Khachatryan *et al.*, "Measurement of the inclusive 3-jet production differential cross section in proton–proton collisions at 7 TeV and determination of the strong coupling constant in the TeV range," *Eur. Phys. J.* **C75** no. 5, (2015) 186, arXiv:1412.1633 [hep-ex].

[37] A. Deur, S. J. Brodsky, and G. F. de Teramond, "The QCD Running Coupling," *Prog. Part. Nucl. Phys.* **90** (2016) 1–74, arXiv:1604.08082 [hep-ph].

[38] D. H. Perkins, *Introduction to High Energy Physics*. Cambridge University Press, Cambridge, 2000.

[39] D. J. Gross and F. Wilczek, "Asymptotically Free Gauge Theories. 1," *Phys. Rev.* **D8** (1973) 3633–3652.

[40] M. Creutz, *Quarks, Gluons and Lattices*. Cambridge University Press, Cambridge, 1983.

[41] J. B. Kogut, "A Review of the Lattice Gauge Theory Approach to Quantum Chromodynamics," *Rev. Mod. Phys.* **55** (1983) 775.

[42] K. G. Wilson, "Confinement of Quarks," *Phys. Rev.* **D10** (1974) 2445–2459. [,319(1974)].

[43] A. S. Kronfeld, "Twenty-first Century Lattice Gauge Theory: Results from the QCD Lagrangian," *Ann. Rev. Nucl. Part. Sci.* **62** (2012) 265–284, arXiv:1203.1204 [hep-lat].

[44] **CTEQ** Collaboration, R. Brock *et al.*, "Handbook of perturbative QCD: Version 1.0," *Rev. Mod. Phys.* **67** (1995) 157–248.

[45] J. C. Collins and D. E. Soper, "Parton Distribution and Decay Functions," *Nucl. Phys.* **B194** (1982) 445–492.

[46] R. Placakyte, "Parton Distribution Functions," in *Proceedings, PIC 2011*. 2011. arXiv:1111.5452 [hep-ph].

[47] A. Metz and A. Vossen, "Parton Fragmentation Functions," *Prog. Part. Nucl. Phys.* **91** (2016) 136–202, arXiv:1607.02521 [hep-ex].

[48] N. Cabibbo and G. Parisi, "Exponential Hadronic Spectrum and Quark Liberation," *Phys. Lett.* **59B** (1975) 67–69.

[49] J. C. Collins and M. J. Perry, "Superdense Matter: Neutrons Or Asymptotically Free Quarks?," *Phys. Rev. Lett.* **34** (1975) 1353.

[50] P. Braun-Munzinger and J. Stachel, "The quest for the quark-gluon plasma," *Nature* **448** (2007) 302–309.

[51] R. Hagedorn, "Statistical thermodynamics of strong interactions at high-energies," *Nuovo Cim. Suppl.* **3** (1965) 147–186.

[52] Y. Aoki, S. Borsanyi, S. Durr, Z. Fodor, S. D. Katz, S. Krieg, and K. K. Szabo, "The QCD transition temperature: results with physical masses in the continuum limit II.," *JHEP* **06** (2009) 088, arXiv:0903.4155 [hep-lat].

[53] **HotQCD** Collaboration, A. Bazavov *et al.*, "Equation of state in (2+1)-flavor QCD," *Phys. Rev.* **D90** (2014) 094503, arXiv:1407.6387 [hep-lat].

[54] M. Cheng *et al.*, "The Transition temperature in QCD," *Phys. Rev.* **D74** (2006) 054507, arXiv:hep-lat/0608013 [hep-lat].

[55] P. Braun-Munzinger and J. Wambach, "The Phase Diagram of Strongly-Interacting Matter," *Rev. Mod. Phys.* **81** (2009) 1031–1050, arXiv:0801.4256 [hep-ph].

[56] F. Karsch and E. Laermann, "Thermodynamics and in medium hadron properties from lattice QCD," arXiv:hep-lat/0305025 [hep-lat].

[57] R. J. Fries and B. Muller, "Heavy ions at LHC: Theoretical issues," *Eur. Phys. J.* **C34** (2004) S279–S285, arXiv:nucl-th/0307043 [nucl-th].

[58] U. W. Heinz, "The Little bang: Searching for quark gluon matter in relativistic heavy ion collisions," *Nucl. Phys.* **A685** (2001) 414–431, arXiv:hep-ph/0009170 [hep-ph].

[59] A. M. Cooper-Sarkar, R. C. E. Devenish, and A. De Roeck, "Structure functions of the nucleon and their interpretation," *Int. J. Mod. Phys.* **A13** (1998) 3385–3586, arXiv:hep-ph/9712301 [hep-ph].

[60] **LHCb** Collaboration, R. Aaij *et al.*, "Observation of $J/\psi\phi$ structures consistent with exotic states from amplitude analysis of $B^+ \to J/\psi\phi K^+$ decays," *Phys. Rev. Lett.* **118** no. 2, (2017) 022003, arXiv:1606.07895 [hep-ex].

[61] **LHCb** Collaboration, R. Aaij *et al.*, "Observation of $J/\psi p$ Resonances Consistent with Pentaquark States in $\Lambda_b^0 \to J/\psi K^- p$ Decays," *Phys. Rev. Lett.* **115** (2015) 072001, arXiv:1507.03414 [hep-ex].

[62] R. F. Lebed, R. E. Mitchell, and E. S. Swanson, "Heavy-Quark QCD Exotica," *Prog. Part. Nucl. Phys.* **93** (2017) 143–194, arXiv:1610.04528 [hep-ph].

[63] S. L. Olsen, "Multiquark Hadrons," *JPS Conf. Proc.* **17** (2017) 111001, arXiv:1611.01277 [hep-ex].

[64] V. Crede and W. Roberts, "Progress towards understanding baryon resonances," *Rept. Prog. Phys.* **76** (2013) 076301, arXiv:1302.7299 [nucl-ex].

[65] S. L. Adler, "Axial vector vertex in spinor electrodynamics," *Phys. Rev.* **177** (1969) 2426–2438. [,241(1969)].

[66] B. M. K. Nefkens and J. W. Price, "The Neutral decay modes of the eta meson," *Phys. Scripta* **T99** (2002) 114–122, arXiv:nucl-ex/0202008 [nucl-ex].

[67] **TOTEM** Collaboration, G. Antchev *et al.*, "Luminosity-independent measurements of total, elastic and inelastic cross-sections at $\sqrt{s} = 7$ TeV," *EPL* **101** no. 2, (2013) 21004.

[68] **ALICE** Collaboration, K. Aamodt *et al.*, "Charged-particle multiplicity density at mid-rapidity in central Pb-Pb collisions at $\sqrt{s_{NN}} = 2.76$ TeV," *Phys. Rev. Lett.* **105** (2010) 252301, arXiv:1011.3916 [nucl-ex].

[69] A. Bylinkin, N. S. Chernyavskaya, and A. A. Rostovtsev, "Predictions on the transverse momentum spectra for charged particle production at LHC-energies from a two component model," *Eur. Phys. J.* **C75** (2015) 166, arXiv:1501.05235 [hep-ph].

[70] C. Tsallis, "Possible Generalization of Boltzmann-Gibbs Statistics," *J. Stat. Phys.* **52** (1988) 479–487.

[71] **ALICE** Collaboration, B. B. Abelev *et al.*, "Neutral pion production at midrapidity in pp and Pb-Pb collisions at $\sqrt{s}$= 2.76 TeV," *Eur. Phys. J.* **C74** (2014) 3108, arXiv:1405.3794 [nucl-ex].

[72] **PHENIX** Collaboration, A. Adare *et al.*, "Detailed measurement of the e^+e^- pair continuum in $p + p$ and Au + Au collisions at $\sqrt{s_{NN}} = 200$ GeV and implications for direct photon production," *Phys. Rev. C* **81** (2010) 034911, arXiv:0912.0244 [nucl-ex].

[73] M. Connors, C. Nattrass, R. Reed, and S. Salur, "Review of Jet Measurements in Heavy Ion Collisions," arXiv:1705.01974 [nucl-ex].

[74] A. Majumder and M. Van Leeuwen, "The Theory and Phenomenology of Perturbative QCD Based Jet Quenching," *Prog. Part. Nucl. Phys.* **66** (2011) 41–92, arXiv:1002.2206 [hep-ph].

[75] D. de Florian, R. Sassot, and M. Stratmann, "Global analysis of fragmentation functions for pions and kaons and their uncertainties," *Phys. Rev.* **D75** (2007) 114010, arXiv:hep-ph/0703242 [hep-ph].

[76] C. A. Aidala, F. Ellinghaus, R. Sassot, J. P. Seele, and M. Stratmann, "Global Analysis of Fragmentation Functions for Eta Mesons," *Phys. Rev.* **D83** (2011) 034002, arXiv:1009.6145 [hep-ph].

[77] D. de Florian, R. Sassot, M. Epele, R. J. Hernández-Pinto, and M. Stratmann, "Parton-to-Pion Fragmentation Reloaded," *Phys. Rev.* **D91** (2015) 014035, arXiv:1410.6027 [hep-ph].

[78] A. Buckley *et al.*, "General-purpose event generators for LHC physics," *Phys. Rept.* **504** (2011) 145–233, arXiv:1101.2599 [hep-ph].

[79] T. Sjostrand, S. Mrenna, and P. Z. Skands, "PYTHIA 6.4 Physics and Manual," *JHEP* **05** (2006) 026, arXiv:hep-ph/0603175 [hep-ph].

[80] T. Sjostrand, S. Mrenna, and P. Z. Skands, "A Brief Introduction to PYTHIA 8.1," *Comput. Phys. Commun.* **178** (2008) 852–867, arXiv:0710.3820 [hep-ph].

[81] T. Sjöstrand, S. Ask, J. R. Christiansen, R. Corke, N. Desai, P. Ilten, S. Mrenna, S. Prestel, C. O. Rasmussen, and P. Z. Skands, "An Introduction to PYTHIA 8.2," *Comput. Phys. Commun.* **191** (2015) 159–177, arXiv:1410.3012 [hep-ph].

[82] R. Engel, "PHOJET manual," *University of Siegen - preprint* (1995) 95–05.

[83] R. Engel, J. Ranft, and S. Roesler, "Hard diffraction in hadron hadron interactions and in photoproduction," *Phys. Rev.* **D52** (1995) 1459–1468, arXiv:hep-ph/9502319 [hep-ph].

[84] X. Artru and G. Mennessier, "String model and multiproduction," *Nucl. Phys.* **B70** (1974) 93–115.

[85] J. Bellm *et al.*, "Herwig 7.0/Herwig++ 3.0 release note," *Eur. Phys. J.* **C76** no. 4, (2016) 196, arXiv:1512.01178 [hep-ph].

[86] D. Amati and G. Veneziano, "Preconfinement as a Property of Perturbative QCD," *Phys. Lett.* **83B** (1979) 87–92.

[87] B. Andersson and P. A. Henning, "On the dynamics of a color rope: The Fragmentation of interacting strings and the longitudinal distributions," *Nucl. Phys.* **B355** (1991) 82–105.

[88] C. Bierlich, G. Gustafson, L. Lönnblad, and A. Tarasov, "Effects of Overlapping Strings in pp Collisions," *JHEP* **03** (2015) 148, arXiv:1412.6259 [hep-ph].

[89] B. Andersson, G. Gustafson, G. Ingelman, and T. Sjostrand, "Parton Fragmentation and String Dynamics," *Phys. Rept.* **97** (1983) 31–145.

[90] B. Andersson, *The Lund Model*. Cambridge University Press, Cambridge, 2005.

[91] **JADE** Collaboration, W. Bartel *et al.*, "Particle Distribution in Three Jet Events Produced by e+ e- Annihilation," *Z. Phys.* **C21** (1983) 37.

[92] C. Bierlich, "Rope Hadronization and Strange Particle Production," *EPJ Web Conf.* **171** (2018) 14003, arXiv:1710.04464 [nucl-th].

[93] W. Chen, S. Cao, T. Luo, L. Pang, and X.-N. Wang, "Jet-induced medium excitation in γ-hadron correlation at RHIC," *Nucl. Phys.* **A967** (2017) 488–491.

[94] R. Chatterjee, H. Holopainen, I. Helenius, T. Renk, and K. J. Eskola, "Elliptic flow of thermal photons from event-by-event hydrodynamic model," *Phys. Rev.* **C88** (2013) 034901, arXiv:1305.6443 [hep-ph].

[95] C. Shen, U. W. Heinz, J.-F. Paquet, and C. Gale, "Thermal photons as a quark-gluon plasma thermometer reexamined," *Phys. Rev.* **C89** no. 4, (2014) 044910, `arXiv:1308.2440 [nucl-th]`.

[96] J.-F. Paquet, C. Shen, G. S. Denicol, M. Luzum, B. Schenke, S. Jeon, and C. Gale, "Production of photons in relativistic heavy-ion collisions," *Phys. Rev.* **C93** no. 4, (2016) 044906, `arXiv:1509.06738 [hep-ph]`.

[97] O. Linnyk, V. Konchakovski, T. Steinert, W. Cassing, and E. L. Bratkovskaya, "Hadronic and partonic sources of direct photons in relativistic heavy-ion collisions," *Phys. Rev.* **C92** no. 5, (2015) 054914, `arXiv:1504.05699 [nucl-th]`.

[98] P. Marmier, *Kernphysik, 1. Vorlesungen von P. Marmier.* Zürich, 1960.

[99] C. Grupen, *Teilchendetektoren.* BI-Wiss.-Verlag, Mannheim, 1993.

[100] C. Grupen and I. Buvat, *Handbook of Particle Detection and Imaging.* Springer Science & Business Media, Berlin Heidelberg, 2012.

[101] S. W. Li and J. F. Beacom, "Spallation Backgrounds in Super-Kamiokande Are Made in Muon-Induced Showers," *Phys. Rev.* **D91** no. 10, (2015) 105005, `arXiv:1503.04823 [hep-ph]`.

[102] S. Sarkar, H. Satz, and B. Sinha, "The physics of the quark-gluon plasma," *Lect. Notes Phys.* **785** (2010) pp.1–369.

[103] **ALICE** Collaboration, B. Abelev *et al.*, "Centrality determination of Pb-Pb collisions at $\sqrt{s_{NN}}$ = 2.76 TeV with ALICE," *Phys. Rev.* **C88** no. 4, (2013) 044909, `arXiv:1301.4361 [nucl-ex]`.

[104] L. Leardini, "Direct photon R_{AA} in 0-20% Pb-Pb collisions compared to the neutral mesons R_{AA} in 0-10% Pb-Pb collisions and in 0-100% NSD p-Pb collisions." ALICE Internal Figure Repository. `https://aliceinfo.cern.ch/Figure/node/12577`. [accessed August 07, 2018].

[105] **ALICE** Collaboration, J. Adam *et al.*, "Direct photon production in Pb-Pb collisions at $\sqrt{s_{\mathrm{NN}}}$ = 2.76 TeV," *Phys. Lett.* **B754** (2016) 235–248, `arXiv:1509.07324 [nucl-ex]`.

[106] **ALICE** Collaboration, S. Acharya *et al.*, "Neutral pion and η meson production at mid-rapidity in Pb-Pb collisions at $\sqrt{s_{NN}}$ = 2.76 TeV," `arXiv:1803.05490 [nucl-ex]`.

[107] **ALICE** Collaboration, S. Acharya *et al.*, "Direct photon elliptic flow in Pb-Pb collisions at $\sqrt{s_{NN}}$ = 2.76 TeV," `arXiv:1805.04403 [nucl-ex]`.

[108] **ALICE** Collaboration, K. Aamodt *et al.*, "Elliptic flow of charged particles in Pb-Pb collisions at 2.76 TeV," *Phys. Rev. Lett.* **105** (2010) 252302, `arXiv:1011.3914 [nucl-ex]`.

[109] R. Snellings, "Elliptic Flow: A Brief Review," *New J. Phys.* **13** (2011) 055008, `arXiv:1102.3010 [nucl-ex]`.

[110] **PHENIX** Collaboration, A. Adare *et al.*, "Observation of direct-photon collective flow in $\sqrt{s_{NN}}$ = 200 GeV Au+Au collisions," *Phys. Rev. Lett.* **109** (2012) 122302, `arXiv:1105.4126 [nucl-ex]`.

[111] P. D. B. Collins, *An Introduction to Regge Theory and High-Energy Physics*. Cambridge Monographs on Mathematical Physics. Cambridge Univ. Press, Cambridge, UK, 2009. `http://www-spires.fnal.gov/spires/find/books/www?cl=QC793.3.R4C695`.

[112] A. Donnachie and P. V. Landshoff, "Total cross-sections," *Phys. Lett.* **B296** (1992) 227–232, `arXiv:hep-ph/9209205 [hep-ph]`.

[113] **CTEQ** Collaboration, H. L. Lai, J. Huston, S. Kuhlmann, J. Morfin, F. I. Olness, J. F. Owens, J. Pumplin, and W. K. Tung, "Global QCD analysis of parton structure of the nucleon: CTEQ5 parton distributions," *Eur. Phys. J.* **C12** (2000) 375–392, `arXiv:hep-ph/9903282 [hep-ph]`.

[114] A. D. Martin, W. J. Stirling, R. S. Thorne, and G. Watt, "Parton distributions for the LHC," *Eur. Phys. J.* **C63** (2009) 189–285, `arXiv:0901.0002 [hep-ph]`.

[115] B. Andersson, S. Mohanty, and F. Soderberg, "Recent developments in the Lund model," in *Proceedings, PINP 2002*. 2002. `arXiv:hep-ph/0212122 [hep-ph]`.

[116] R. Corke and T. Sjöstrand, "Interleaved Parton Showers and Tuning Prospects," *JHEP* **03** (2011) 032, `arXiv:1011.1759 [hep-ph]`.

[117] P. Skands, S. Carrazza, and J. Rojo, "Tuning PYTHIA 8.1: the Monash 2013 Tune," *Eur. Phys. J.* **C74** (2014) 3024, `arXiv:1404.5630 [hep-ph]`.

[118] F. W. Bopp, R. Engel, and J. Ranft, "Rapidity gaps and the PHOJET Monte Carlo," in *Proceedings, LISHEP'98*, pp. 729–741. 1998. `arXiv:hep-ph/9803437 [hep-ph]`.

[119] A. Capella, U. Sukhatme, C.-I. Tan, and J. Tran Thanh Van, "Dual parton model," *Phys. Rept.* **236** (1994) 225–329.

[120] V. N. Gribov, "A REGGEON DIAGRAM TECHNIQUE," *Sov. Phys. JETP* **26** (1968) 414–422. [Zh. Eksp. Teor. Fiz.53,654(1967)].

[121] V. A. Abramovsky, V. N. Gribov, and O. V. Kancheli, "Character of Inclusive Spectra and Fluctuations Produced in Inelastic Processes by Multi - Pomeron Exchange," *Yad. Fiz.* **18** (1973) 595–616. [Sov. J. Nucl. Phys.18,308(1974)].

[122] R. Engel and J. Ranft, "Hadronic photon-photon interactions at high-energies," *Phys. Rev.* **D54** (1996) 4244–4262, `arXiv:hep-ph/9509373 [hep-ph]`.

[123] R. K. Ellis, W. J. Stirling, and B. R. Webber, "QCD and collider physics," *Camb. Monogr. Part. Phys. Nucl. Phys. Cosmol.* **8** (1996) 1–435.

[124] T. G. Pickavance, "Synchrocyclotrons, and the CERN 600 MeV machine," *Nuovo Cim.* **2** no. 1suppl, (1955) 403–412.

[125] E. Regenstreif, "The CERN proton synchrotron. 1.," CERN-59-29.

[126] J. Redfearn, "SPS: CERN's New Super Proton Synchrotron," *Phys. Bull.* **27** (1976) 499.

[127] **LEP** Collaboration, "LEP Design Report: Vol.2. The LEP Main Ring," CERN-LEP-84-01.

[128] L. Evans and P. Bryant, "LHC Machine," *JINST* **3** (2008) S08001.

[129] **ALICE** Collaboration, K. Aamodt *et al.*, "The ALICE experiment at the CERN LHC," *JINST* **3** (2008) S08002.

[130] **ATLAS** Collaboration, G. Aad *et al.*, "The ATLAS Experiment at the CERN Large Hadron Collider," *JINST* **3** (2008) S08003.

[131] **CMS** Collaboration, S. Chatrchyan *et al.*, "The CMS Experiment at the CERN LHC," *JINST* **3** (2008) S08004.

[132] **LHCb** Collaboration, A. A. Alves, Jr. *et al.*, "The LHCb Detector at the LHC," *JINST* **3** (2008) S08005.

[133] **LHCf** Collaboration, O. Adriani *et al.*, "The LHCf detector at the CERN Large Hadron Collider," *JINST* **3** (2008) S08006.

[134] **MoEDAL** Collaboration, J. Pinfold *et al.*, "Technical Design Report of the MoEDAL Experiment,".

[135] **TOTEM** Collaboration, G. Antchev *et al.*, "Performance of the TOTEM Detectors at the LHC," *Int. J. Mod. Phys.* **A28** (2013) 1330046, `arXiv:1310.2908 [physics.ins-det]`.

[136] O. S. Bruning, P. Collier, P. Lebrun, S. Myers, R. Ostojic, J. Poole, and P. Proudlock, "LHC Design Report Vol.1: The LHC Main Ring," CERN-2004-003-V1, CERN-2004-003.

[137] J.-L. Caron, "LHC Layout." CERN document server, 1997. `http://cds.cern.ch/record/841573`. [accessed August 07, 2018].

[138] B. Todd, *A beam interlock system for CERN high energy accelerators*. PhD thesis, Brunel U., 2006. `http://weblib.cern.ch/abstract?CERN-THESIS-2007-019`.

[139] J. Jowett *et al.*, "The 2015 Heavy-Ion Run of the LHC," in *Proceedings, IPAC*, p. TUPMW027. 2016. `http://inspirehep.net/record/1469938/files/tupmw027.pdf`.

[140] C. De Melis, "The CERN accelerator complex." CERN document server, 2016. `https://cds.cern.ch/record/2119882`. [accessed August 07, 2018].

[141] J. Lettry, R. Scrivens, M. Kronberger, D. Kuchler, O. Midttun, M. M. Paoluzzi, H. Pereira, and C. Schmitzer, "Overview of the Status and Developments on Primary Ion Sources at CERN," *Conf. Proc.* **C110904** (2011) 3474–3476.

[142] C. Fabjan and J. Schukraft, "The Story of ALICE: Building the dedicated heavy ion detector at LHC," in *The Large Hadron Collider: A marvel technology*. 2011. `arXiv:1101.1257 [physics.ins-det]`. `http://inspirehep.net/record/883486/files/arXiv:1101.1257.pdf`.

[143] **ALICE** Collaboration, P. Cortese *et al.*, "ALICE: Physics performance report, volume I," *J. Phys.* **G30** (2004) 1517–1763.

[144] **ALICE** Collaboration, P. Cortese *et al.*, "ALICE: Physics performance report, volume II," *J. Phys.* **G32** (2006) 1295–2040.

[145] **ALICE** Collaboration, B. B. Abelev *et al.*, "Performance of the ALICE Experiment at the CERN LHC," *Int. J. Mod. Phys.* **A29** (2014) 1430044, arXiv:1402.4476 [nucl-ex].

[146] J. Thaeder, "3D ALICE Schematic - with Description." ALICE Internal Figure Repository. https://aliceinfo.cern.ch/Figure/node/3400. [accessed August 07, 2018].

[147] **ALICE** Collaboration, L. Betev *et al.*, "Definition of the ALICE Coordinate System and Basic Rules for Sub-detector Components Numbering." ALICE-INT-2003-038. http://edms.cern.ch/document/406391.

[148] **ALICE** Collaboration, "The Mechanical Properties of the Space Frame Supporting Detectors," ALICE-INT-1997-32, CERN-ALICE-INT-1997-32.

[149] **ALICE** Collaboration, I. A. Shelaev, Y. A. Shishov, A. S. Vodopyanov, and W. Flegel, "The (large) ALICE Magnet System," ALICE-INT-1993-23, CERN-ALICE-INT-1993-23.

[150] **L3** Collaboration, B. Adeva *et al.*, "The construction of the L3 experiment," *Nucl. Instrum. Meth.* **A289** (1990) 35 – 102.

[151] **ALICE** Collaboration, G. Dellacasa *et al.*, "ALICE technical design report of the inner tracking system (ITS)," CERN-LHCC-99-12.

[152] **ALICE** Collaboration, G. Dellacasa *et al.*, "ALICE: Technical design report of the time projection chamber," CERN-OPEN-2000-183, CERN-LHCC-2000-001.

[153] **ALICE** Collaboration, P. Cortese, "ALICE transition-radiation detector," ALICE-TDR-9, CERN-LHCC-2001-021, LYCEN-2001-97.

[154] **ALICE** Collaboration, G. Dellacasa *et al.*, "ALICE technical design report of the time-of-flight system (TOF)," CERN-LHCC-2000-012.

[155] **ALICE** Collaboration, P. Cortese *et al.*, "ALICE: Addendum to the technical design report of the time of flight system (TOF)," CERN-LHCC-2002-016.

[156] **ALICE** Collaboration, P. Cortese *et al.*, "ALICE electromagnetic calorimeter technical design report," CERN-LHCC-2008-014, CERN-ALICE-TDR-014.

[157] **ALICE** Collaboration, J. Allen *et al.*, "ALICE DCal: An Addendum to the EMCal Technical Design Report Di-Jet and Hadron-Jet correlation measurements in ALICE," CERN-LHCC-2010-011, ALICE-TDR-14-add-1.

[158] **ALICE** Collaboration, G. Dellacasa *et al.*, "ALICE technical design report of the photon spectrometer (PHOS)," CERN-LHCC-99-04.

[159] **ALICE** Collaboration, S. Beole *et al.*, "ALICE technical design report: Detector for high momentum PID," CERN-LHCC-98-19.

[160] **ALICE** Collaboration, K. Aamodt *et al.*, "Alignment of the ALICE Inner Tracking System with cosmic-ray tracks," *JINST* **5** (2010) P03003, arXiv:1001.0502 [physics.ins-det].

[161] **ALICE** Collaboration, P. Kuijer, "The inner tracking system of the Alice experiment," *Nucl. Instrum. Meth.* **A530** (2004) 28–32.

[162] Y. C. Morales, "ITS performance." ALICE Internal Figure Repository. `https://aliceinfo.cern.ch/Figure/node/9865`. [accessed August 07, 2018].

[163] J. Alme *et al.*, "The ALICE TPC, a large 3-dimensional tracking device with fast readout for ultra-high multiplicity events," *Nucl. Instrum. Meth.* **A622** (2010) 316–367, `arXiv:1001.1950 [physics.ins-det]`.

[164] **ALICE** Collaboration, D. Rohr, "Tracking performance in high multiplicities environment at ALICE," in *Proceedings, LHCP 2017*. 2017. `arXiv:1709.00618 [physics.ins-det]`. `http://inspirehep.net/record/1621494/files/arXiv:1709.00618.pdf`.

[165] W. Blum, W. Riegler, and L. Rolandi, *Particle Detection with Drift Chambers*. Springer Science & and Business Media, Berlin Heidelberg, 2008.

[166] **ALICE** Collaboration, S. Acharya *et al.*, "The ALICE Transition Radiation Detector: construction, operation, and performance," *Nucl. Instrum. Meth.* **A881** (2018) 88–127, `arXiv:1709.02743 [physics.ins-det]`.

[167] **ALICE EMCal** Collaboration, U. Abeysekara *et al.*, "ALICE EMCal Physics Performance Report," `arXiv:1008.0413 [physics.ins-det]`.

[168] **PANDA** Collaboration, R. W. Novotny, "The electromagnetic calorimetry of the PANDA Detector at FAIR," *J. Phys. Conf. Ser.* **404** (2012) 012063.

[169] S. Moser, W. Harder, C. Hurlbut, and M. Kusner, "Principles and practice of plastic scintillator design," *Radiation Physics and Chemistry* **41** no. 1, (1993) 31 – 36. `http://www.sciencedirect.com/science/article/pii/0969806X9390039W`.

[170] H. Kolanoski and N. Wermes, *Teilchendetektoren - Grundlagen und Anwendungen*. Springer-Verlag, Berlin Heidelberg New York, 2016.

[171] M. Dialinas, "Overview of DCal and PHOS." Indico - DCal design review. `https://indico.cern.ch/event/194127/contributions/358613/attachments/280846/392718/DR_DCAL_Insertion_Tooling_130612.pdf`. [accessed August 07, 2018].

[172] M. Brice, "One module of the ALICE photon spectrometer.." CERN-EX-0603026, 2006. `http://cds.cern.ch/record/946050`. [accessed August 07, 2018].

[173] **ALICE** Collaboration, M. Yu. Bogolyubsky *et al.*, "Charged Particle Veto Detector for the PHOS Spectrometer," ALICE-INT-1999-08, CERN-ALICE-INT-1999-08.

[174] D. Swoboda, L. Leistam, L. Pigni, D. Cacaut, E. Kochournikov, and A. Vodopianov, "Status of the ALICE magnet system," *IEEE Transactions on Applied Superconductivity* **12** (2002) 432 – 437.

[175] **ALICE** Collaboration, P. Cortese *et al.*, "ALICE technical design report on forward detectors: FMD, T0 and V0," CERN-LHCC-2004-025.

[176] **ALICE** Collaboration, G. Dellacasa *et al.*, "ALICE technical design report: Photon multiplicity detector (PMD)," CERN-LHCC-99-32, CERN-OPEN-2000-184.

[177] **ALICE** Collaboration, P. Cortese *et al.*, "ALICE: Addendum to the technical design report of the Photon Multiplicity Detector (PMD)," CERN-LHCC-2003-038.

[178] **ALICE** Collaboration, G. Dellacasa *et al.*, "ALICE technical design report of the zero degree calorimeter (ZDC)," CERN-LHCC-99-05.

[179] **ALICE** Collaboration, G. Dellacasa *et al.*, "ALICE technical design report of the dimuon forward spectrometer," CERN-LHCC-99-22.

[180] **ALICE** Collaboration, G. Dellacasa *et al.*, "ALICE dimuon forward spectrometer," ALICE-TDR-5-add-1, CERN-LHCC-2000-046.

[181] **ACORDE** Collaboration, A. Fernández *et al.*, "ACORDE a Cosmic Ray Detector for ALICE," *Nucl. Instrum. Meth.* **A572** (2007) 102–103, arXiv:physics/0606051 [physics.ins-det].

[182] **ALICE Muon Spectrometer** Collaboration, C. Finck, "The muon spectrometer of the ALICE," *J. Phys. Conf. Ser.* **50** (2006) 397–401.

[183] A. Fernandez Tellez, "ACORDE, The ALICE Cosmic Ray Detector," in *Proceedings, ICRC 2007*, pp. 1201–1204. 2007. http://indico.nucleares.unam.mx/contributionDisplay.py?contribId=35&confId=4.

[184] G. Apollinari, O. Brüning, T. Nakamoto, and L. Rossi, "High Luminosity Large Hadron Collider HL-LHC," *CERN Yellow Report* no. 5, (2015) 1–19, arXiv:1705.08830 [physics.acc-ph].

[185] **ALICE** Collaboration, P. Antonioli, A. Kluge, and W. Riegler, "Upgrade of the ALICE Readout & Trigger System," CERN-LHCC-2013-019, ALICE-TDR-015. https://cds.cern.ch/record/1603472.

[186] **ALICE** Collaboration, P. Buncic, M. Krzewicki, and P. Vande Vyvre, "Technical Design Report for the Upgrade of the Online-Offline Computing System," CERN-LHCC-2015-006, ALICE-TDR-019.

[187] **ALICE** Collaboration, C. Lippmann, "Upgrade of the ALICE Time Projection Chamber," CERN-LHCC-2013-020, ALICE-TDR-016.

[188] **ALICE** Collaboration, B. Abelev *et al.*, "Technical Design Report for the Upgrade of the ALICE Inner Tracking System," *J. Phys.* **G41** (2014) 087002.

[189] **ALICE** Collaboration, G. Martinez-Garcia and W. Riegler, "Technical Design Report for the Muon Forward Tracker," CERN-LHCC-2015-001, ALICE-TDR-018. https://cds.cern.ch/record/1981898.

[190] **ALICE** Collaboration, D. Swoboda, P. Van de Vyvre, and O. Villalobos Baillie, "Data Acquisition, Control and Trigger : common Report for the preparation of the ALICE Technical Design Reports.," ALICE-INT-1998-23, CERN-ALICE-INT-1998-23.

[191] **ALICE** Collaboration, C. W. Fabjan, L. Jirdén, V. Lindestruth, L. Riccati, D. Rorich, P. Van de Vyvre, O. Villalobos Baillie, and H. de Groot, "ALICE trigger data-acquisition high-level trigger and control system: Technical Design Report," CERN-LHCC-2003-062, ALICE-TDR-10. `http://cds.cern.ch/record/684651`.

[192] F. Follin and D. Jacquet, "Implementation and experience with luminosity levelling with offset beam," in *Proceedings, BB2013*, pp. 183–187. 2014. `arXiv:1410.3667 [physics.acc-ph]`.

[193] **ALICE** Collaboration, P. Cortese, F. Carminati, C. W. Fabjan, L. Riccati, and H. de Groot, "ALICE computing: Technical Design Report," CERN-LHCC-2005-018, ALICE-TDR-12. `http://cds.cern.ch/record/832753`.

[194] B. Stroustrup, "The C++ Programming Language." `http://www.stroustrup.com/index.html`. [accessed August 07, 2018].

[195] B. Stroustrup, *The C++ Programming Language*. Addison-Wesley Publishing Company, Inc., 1986. ISBN-020112078X.

[196] Git project, "Git - a distributed version control system." `https://git-scm.com/`. [accessed August 07, 2018].

[197] R. Brun and F. Rademakers, "ROOT: An object oriented data analysis framework," *Nucl. Instrum. Meth.* **A389** (1997) 81–86.

[198] R. Brun and F. Rademakers, "ROOT - a Data Analysis Framework." `https://root.cern.ch/`. [accessed August 07, 2018].

[199] **ALICE** Collaboration, "ALICE Software Framework." `https://github.com/alisw/AliRoot`. [accessed August 07, 2018].

[200] S. Roesler, R. Engel, and J. Ranft, "The Monte Carlo event generator DPMJET-III," in *Proceedings, MC2000*, pp. 1033–1038. 2000. `arXiv:hep-ph/0012252 [hep-ph]`.

[201] X.-N. Wang and M. Gyulassy, "HIJING: A Monte Carlo model for multiple jet production in p p, p A and A A collisions," *Phys. Rev.* **D44** (1991) 3501–3516.

[202] Z.-W. Lin, C. M. Ko, B.-A. Li, B. Zhang, and S. Pal, "A Multi-phase transport model for relativistic heavy ion collisions," *Phys. Rev.* **C72** (2005) 064901, `arXiv:nucl-th/0411110 [nucl-th]`.

[203] R. Brun, F. Bruyant, M. Maire, A. McPherson, and P. Zanarini, "GEANT3," *CERN-DD-EE-84-1* (1987) BASE001 1–3.

[204] **GEANT4** Collaboration, S. Agostinelli *et al.*, "GEANT4: A Simulation toolkit," *Nucl. Instrum. Meth.* **A506** (2003) 250–303.

[205] A. Ferrari, P. R. Sala, A. Fasso, and J. Ranft, "FLUKA: A multi-particle transport code (Program version 2005)," CERN-2005-010, SLAC-R-773, INFN-TC-05-11.

[206] S. Gorbunov and I. Kisel, "Reconstruction of decayed particles based on the Kalman filter," *CBM-SOFT-note* **003** (2007) 1–16. `http://web-docs.gsi.de/~ikisel/reco/CBM/DOC-2007-May-14-1.pdf`.

[207] R. Fruhwirth, "Application of Kalman filtering to track and vertex fitting," *Nucl. Instrum. Meth.* **A262** (1987) 444–450.

[208] P. Billoir, "Track Fitting With Multiple Scattering: A New Method," *Nucl. Instrum. Meth.* **A225** (1984) 352–366.

[209] **ALICE** Collaboration, "ALICE Analysis Repository." `https://github.com/alisw/AliPhysics`. [accessed August 07, 2018].

[210] **ALICE** Collaboration, P. Cerello, "Grid computing: Concepts and applications," CERN-ALI-2001-048, CERN-ALICE-PUB-2001-48. `http://cds.cern.ch/record/523297`.

[211] I. Bird, K. Bos, N. Brook, D. Duellmann, C. Eck, I. Fisk, D. Foster, B. Gibbard, C. Grandi, F. Grey, *et al.*, "LHC computing Grid. Technical design report," CERN-LHCC-2005-024.

[212] S. Bagnasco, L. Betev, P. Buncic, F. Carminati, C. Cirstoiu, C. Grigoras, A. Hayrapetyan, A. Harutyunyan, A. J. Peters, and P. Saiz, "AliEn: ALICE Environment on the GRID," *J. Phys. Conf. Ser.* **119** (2008) 062012.

[213] **ALICE** Photon Conversion Group, "Indico - Weekly Meetings." `https://indico.cern.ch/category/4027/`. [accessed August 07, 2018].

[214] **ALICE** Collaboration, M. Zimmermann, "The ALICE analysis train system," *J. Phys. Conf. Ser.* **608** no. 1, (2015) 012019, `arXiv:1502.06381 [hep-ex]`.

[215] **ALICE** Photon Conversion Group, "Afterburner Framework - AnalysisSoftware." `https://gitlab.cern.ch/alice-pcg/AnalysisSoftware`. [accessed August 07, 2018].

[216] **ALICE** Photon Conversion Group, "Photon Conversion Group Tutorial." `https://friederikebock.gitbooks.io/pcgtutorial/content/`. [accessed August 07, 2018].

[217] **ALICE** Photon Conversion Group, "Tutorial for the Software Framework." `https://github.com/FriederikeBock/ALICEPCGtutorial`. [accessed August 07, 2018].

[218] Courtesy of F. Bock, "ALICE Event Displays.". friederike.bock@cern.ch, private communication.

[219] F. Bock, *Measurement of Direct Photons and Neutral Mesons in Small Collisions Systems with the ALICE Experiment at the LHC*. PhD thesis, University of Heidelberg, 2017. `http://www.ub.uni-heidelberg.de/archiv/23888`.

[220] **ALICE** Collaboration, B. Abelev *et al.*, "Measurement of inelastic, single- and double-diffraction cross sections in proton–proton collisions at the LHC with ALICE," *Eur. Phys. J.* **C73** (2013) 2456, `arXiv:1208.4968 [hep-ex]`.

[221] J. Kral, T. Awes, H. Muller, J. Rak, and J. Schambach, "L0 trigger for the EMCal detector of the ALICE experiment," *Nucl. Instrum. Meth.* **A693** (2012) 261–267.

[222] D. Wang *et al.*, "Level-0 trigger algorithms for the ALICE PHOS detector," *Nucl. Instrum. Meth.* **A629** (2011) 80–86.

[223] **ALICE EMCal** Collaboration, O. Bourrion, N. Arbor, G. Conesa-Balbastre, C. Furget, R. Guernane, and G. Marcotte, "The ALICE EMCal L1 trigger first year of operation experience," *JINST* **8** (2013) C01013, arXiv:1210.8078 [physics.ins-det].

[224] O. Bourrion, R. Guernane, B. Boyer, J. L. Bouly, and G. Marcotte, "Level-1 jet trigger hardware for the ALICE electromagnetic calorimeter at LHC," *JINST* **5** (2010) C12048, arXiv:1010.2670 [physics.ins-det].

[225] L. Lijiao, *L0/L1 trigger generation by the ALICE PHOS detector*. PhD thesis, Bergen U., 2011. http://inspirehep.net/record/1382032/files/liu_materie.pdf.

[226] S. van der Meer, "Calibration of the Effective Beam Height in the ISR." CERN-ISR-PO-68-31, 1968.

[227] V. Balagura, "Notes on van der Meer Scan for Absolute Luminosity Measurement," *Nucl. Instrum. Meth.* **A654** (2011) 634–638, arXiv:1103.1129 [physics.ins-det].

[228] **ALICE** Collaboration, S. Acharya *et al.*, "ALICE luminosity determination for pp collisions at $\sqrt{s} = 8$ TeV," ALICE-PUBLIC-2017-002. https://cds.cern.ch/record/2255216.

[229] **UA5** Collaboration, G. J. Alner *et al.*, "Antiproton-proton cross sections at 200 and 900 GeV c.m. energy," *Z. Phys.* **C32** (1986) 153–161.

[230] **TOTEM** Collaboration, G. Antchev *et al.*, "Luminosity-Independent Measurement of the Proton-Proton Total Cross Section at $\sqrt{s} = 8$ TeV," *Phys. Rev. Lett.* **111** (2013) 012001.

[231] K. Koch, *Measurement of π^0 and η mesons with photon conversions in ALICE in proton-proton collisions at $\sqrt{s} = 0.9$, 2.76 and 7 TeV*. PhD thesis, University of Heidelberg, 2012. http://www.ub.uni-heidelberg.de/archiv/13113.

[232] F. Bock, "ALICE Capabilities for Studying Photon Physics with the Conversion Method at LHC Energies," Bachelor thesis, University of Heidelberg, 2010. http://www.physi.uni-heidelberg.de//Publications/Bock-Bachelorthesis.pdf.

[233] F. Bock, "Neutral Pion and Eta Meson Production in pp and Pb-Pb Collisions at the LHC with the ALICE Detector," Master's thesis, University of Heidelberg, 2012. http://www.physi.uni-heidelberg.de//Publications/Bock-Masterthesis.pdf.

[234] T. Dahms, "Measurement of photons via conversion pairs with the PHENIX experiment at RHIC," Master's thesis, Stony Brook University, 2005. https://www.phenix.bnl.gov/WWW/publish/tdahms/master-thesis/tdahms_thesis.pdf.

[235] J. Podolanski and R. Armenteros, "III. Analysis of V-events," *Phil. Mag.* **45** (1954) 13–30.

[236] **ALICE** Collaboration, H. Muller, R. Pimenta, Z.-B. Yin, D.-C. Zhou, X. Cao, Q.-X. Li, Y.-Z. Liu, F.-F. Zou, B. Skaali, and T. C. Awes, "Configurable electronics with low noise and 14-bit dynamic range for photodiode-based photon detectors," *Nucl. Instrum. Meth.* **A565** (2006) 768–783.

[237] Courtesy of N. Schmidt, "Schematic of the Working Principle of the V2 Clusterizer.". nicolas.schmidt@cern.ch, private communication.

[238] M. G. Bekishev and V. N. Ivanchenko, "A Method of electromagnetic shower identification and measuring of its position in segmented calorimeters," *Nucl. Instrum. Meth.* **A361** (1995) 138–148.

[239] T. Awes, F. Obenshain, F. Plasil, S. Saini, S. Sorensen, and G. Young, "A simple method of shower localization and identification in laterally segmented calorimeters," *Nucl. Instrum. Meth.* **A311** (1992) 130 – 138.

[240] **ALICE** Collaboration, "Energy resolution and linearity of the ALICE-EMCal calorimeter." Internal document - to be published. https://aliceinfo.cern.ch/Notes/node/480. [accessed August 07, 2018].

[241] T. Matulewicz *et al.*, "Response of BaF2 detectors to photons of 3-50 MeV energy," *Nucl. Instrum. Meth.* **A289** (1990) 194–204.

[242] **ALICE** Collaboration, K. Koch, "π^0 and η measurement with photon conversions in ALICE in proton-proton collisions at sqrt(s) = 7 TeV," *Nucl. Phys.* **A855** (2011) 281–284, arXiv:1103.2217 [hep-ex].

[243] J. Thaeder, "General ALICE Cross-Section without L3 Magnet." ALICE Internal Figure Repository. https://aliceinfo.cern.ch/Figure/node/3395. [accessed August 07, 2018].

[244] N. Schmidt, "Neutral meson and direct photon measurements with conversions in ALICE in proton-proton collisions at $\sqrt{s} = 0.9$, 7 and 8 TeV," Master's thesis, University of Heidelberg, 2017. http://www.physi.uni-heidelberg.de//Publications/masterthesis_nschmidt.pdf.

[245] S. Yano, *Neutral Pion Production in Proton+Proton Collisions at $\sqrt{s} = 8$ TeV and Insight into Hadron Production Mechanism.* PhD thesis, Hiroshima University, Mar, 2018. https://cds.cern.ch/record/2310803. CERN-THESIS-2018-023.

[246] L. Lyons, D. Gibaut, and P. Clifford, "How to Combine Correlated Estimates of a Single Physical Quantity," *Nucl. Instrum. Meth.* **A270** (1988) 110.

[247] A. Valassi, "Combining correlated measurements of several different physical quantities," *Nucl. Instrum. Meth.* **A500** (2003) 391–405.

[248] L. Lyons, *Statistics For Nuclear And Particle Physicists.* Cambridge, UK: Univ. Pr., 1986.

[249] R. J. Barlow, *Statistics: a guide to the use of statistical methods in the physical sciences*, vol. 29. John Wiley & Sons, 1989.

[250] A. Valassi and R. Chierici, "Information and treatment of unknown correlations in the combination of measurements using the BLUE method," *Eur. Phys. J.* **C74** (2014) 2717, arXiv:1307.4003 [physics.data-an].

[251] **ALICE** Collaboration, K. Aamodt *et al.*, "Strange particle production in proton-proton collisions at $\sqrt{s} = 0.9$ TeV with ALICE at the LHC," *Eur. Phys. J.* **C71** (2011) 1594, arXiv:1012.3257 [hep-ex].

[252] **ALICE** Collaboration, B. B. Abelev *et al.*, "Production of charged pions, kaons and protons at large transverse momenta in pp and Pb–Pb collisions at $\sqrt{s_{\rm NN}}$ =2.76 TeV," *Phys. Lett.* **B736** (2014) 196–207, arXiv:1401.1250 [nucl-ex].

[253] **ALICE** Collaboration, J. Adam *et al.*, "Enhanced production of multi-strange hadrons in high-multiplicity proton-proton collisions," *Nature Phys.* **13** (2017) 535–539, arXiv:1606.07424 [nucl-ex].

[254] R. Barlow, "Systematic errors: Facts and fictions," in *Proceedings, Advanced Statistical Techniques in Particle Physics 2002*, pp. 134–144. 2002. arXiv:hep-ex/0207026 [hep-ex].
http://www.ippp.dur.ac.uk/Workshops/02/statistics/proceedings//barlow.pdf.

[255] G. Lafferty and T. Wyatt, "Where to stick your data points: The treatment of measurements within wide bins," *Nucl. Instrum. Meth.* **A355** (1995) 541–547.

[256] W. Tung, H. Lai, A. Belyaev, J. Pumplin, D. Stump, and C.-P. Yuan, "Heavy quark mass effects in deep inelastic scattering and global QCD analysis," *JHEP* **02** (2007) 053, arXiv:hep-ph/0611254 [hep-ph].

[257] **PHENIX** Collaboration, A. Adare *et al.*, "Inclusive cross section and double-helicity asymmetry for π^0 production at midrapidity in p+p collisions at $\sqrt{s} = 510$ GeV," *Phys. Rev.* **D93** (2016) 011501, arXiv:1510.02317 [hep-ex].

[258] **PHENIX** Collaboration, A. Adare *et al.*, "Cross section and double helicity asymmetry for eta mesons and their comparison to neutral pion production in p+p collisions at $\sqrt{s} = 200$ GeV," *Phys. Rev.* **D83** (2011) 032001, arXiv:1009.6224 [hep-ex].

[259] **LEBC-EHS** Collaboration, M. Aguilar-Benitez *et al.*, "Inclusive particle production in 400 GeV/c pp-interactions," *Z. Phys.* **C50** (1991) 405–426.

[260] P. Parek, *Neutral pion and Direct Photon Measurement in p+p in ALICE Experiment at LHC*. PhD thesis, Indian Institute of Technology Indore, 2018. [in preparation].

[261] **ALICE** Collaboration, K. Aamodt *et al.*, "Production of pions, kaons and protons in *pp* collisions at $\sqrt{s} = 900$ GeV with ALICE at the LHC," *Eur. Phys. J.* **C71** (2011) 1655, arXiv:1101.4110 [hep-ex].

[262] **ALICE** Collaboration, J. Adam *et al.*, "Measurement of pion, kaon and proton production in proton–proton collisions at $\sqrt{s} = 7$ TeV," *Eur. Phys. J.* **C75** (2015) 226, arXiv:1504.00024 [nucl-ex].

[263] **ALICE** Collaboration, J. Adam *et al.*, "Multiplicity dependence of charged pion, kaon, and (anti)proton production at large transverse momentum in p-Pb collisions at $\sqrt{s_{NN}}$ = 5.02 TeV," *Phys. Lett.* **B760** (2016) 720–735, arXiv:1601.03658 [nucl-ex].

[264] **ALICE** Collaboration, J. Adam *et al.*, "Pseudorapidity and transverse-momentum distributions of charged particles in proton–proton collisions at $\sqrt{s} = 13$ TeV," *Phys. Lett.* **B753** (2016) 319–329, arXiv:1509.08734 [nucl-ex].

[265] L. Altenkämper, F. Bock, C. Loizides, and N. Schmidt, "Applicability of transverse mass scaling in hadronic collisions at energies available at the CERN Large Hadron Collider," *Phys. Rev.* **C96** (2017) 064907, arXiv:1710.01933 [hep-ph].

[266] M. Bourquin and J.-M. Gaillard, "A simple phenomenological description of hadron production," *Nucl. Phys.* **B114** (1976) 334 – 364.

[267] P. K. Khandai, P. Shukla, and V. Singh, "Meson spectra and m_T scaling in $p+p$, d+Au, and Au + Au collisions at $\sqrt{s_{NN}} = 200$ GeV," *Phys. Rev.* **C84** (2011) 054904, arXiv:1110.3929 [hep-ph].

[268] K. Jiang, Y. Zhu, W. Liu, H. Chen, C. Li, L. Ruan, Z. Tang, Z. Xu, and Z. Xu, "Onset of radial flow in p+p collisions," *Phys. Rev.* **C91** (2015) 024910, arXiv:1312.4230 [nucl-ex].

[269] **ALICE** Collaboration, B. B. Abelev *et al.*, "Multiplicity dependence of the average transverse momentum in pp, p-Pb, and Pb-Pb collisions at the LHC," *Phys. Lett.* **B727** (2013) 371–380, arXiv:1307.1094 [nucl-ex].

[270] **ALICE** Collaboration, J. Adam *et al.*, "Charged-particle multiplicities in proton–proton collisions at $\sqrt{s} = 0.9$ to 8 TeV," *Eur. Phys. J.* **C77** (2017) 33, arXiv:1509.07541 [nucl-ex].

[271] A. Andronic, P. Braun-Munzinger, K. Redlich, and J. Stachel, "The statistical model in Pb-Pb collisions at the LHC," *Nucl. Phys.* **A904-905** (2013) 535c–538c, arXiv:1210.7724 [nucl-th].

[272] **ALICE** Collaboration, S. Acharya *et al.*, "INTERNAL PAPER DRAFT: Production of light flavor hadrons in pp collisions at $\sqrt{s} = 7$ and 13 TeV." https://alice-publications.web.cern.ch/node/3429. [internal communication].

[273] **ALICE** Collaboration, J. Adam *et al.*, "K*(892)^0 and $\phi(1020)$ meson production at high transverse momentum in pp and Pb-Pb collisions at $\sqrt{s_{\mathrm{NN}}} = 2.76$ TeV," *Phys. Rev.* **C95** (2017) 064606, arXiv:1702.00555 [nucl-ex].

[274] **ALICE** Collaboration, B. Abelev *et al.*, "Production of $K^*(892)^0$ and $\phi(1020)$ in pp collisions at $\sqrt{s} = 7$ TeV," *Eur. Phys. J.* **C72** (2012) 2183, arXiv:1208.5717 [hep-ex].

[275] E. Schnedermann, J. Sollfrank, and U. W. Heinz, "Thermal phenomenology of hadrons from 200-A/GeV S+S collisions," *Phys. Rev.* **C48** (1993) 2462–2475, arXiv:nucl-th/9307020 [nucl-th].

[276] R. Bayes, "An essay toward solving a problem in the doctrine of chances," *Phil. Trans. Roy. Soc. Lond.* **53** (1764) 370–418.

[277] G. D'Agostini, "A Multidimensional unfolding method based on Bayes' theorem," *Nucl. Instrum. Meth.* **A362** (1995) 487–498.

[278] T. Adye, "Unfolding algorithms and tests using RooUnfold," in *Proceedings, PHYSTAT 2011*, pp. 313–318, CERN. CERN, Geneva, 2011. arXiv:1105.1160 [physics.data-an]. https://inspirehep.net/record/898599/files/arXiv:1105.1160.pdf.

[279] A. Hocker and V. Kartvelishvili, "SVD approach to data unfolding," *Nucl. Instrum. Meth.* **A372** (1996) 469–481, arXiv:hep-ph/9509307 [hep-ph].

[280] B. Jager, A. Schafer, M. Stratmann, and W. Vogelsang, "Next-to-leading order QCD corrections to high p(T) pion production in longitudinally polarized pp collisions," *Phys. Rev.* **D67** (2003) 054005, arXiv:hep-ph/0211007 [hep-ph].

[281] H.-L. Lai, M. Guzzi, J. Huston, Z. Li, P. M. Nadolsky, J. Pumplin, and C. P. Yuan, "New parton distributions for collider physics," *Phys. Rev.* **D82** (2010) 074024, arXiv:1007.2241 [hep-ph].

[282] J. Gao, M. Guzzi, J. Huston, H.-L. Lai, Z. Li, P. Nadolsky, J. Pumplin, D. Stump, and C. P. Yuan, "CT10 next-to-next-to-leading order global analysis of QCD," *Phys. Rev.* **D89** no. 3, (2014) 033009, arXiv:1302.6246 [hep-ph].

[283] M. Guzzi, P. Nadolsky, E. Berger, H.-L. Lai, F. Olness, and C. P. Yuan, "CT10 parton distributions and other developments in the global QCD analysis," arXiv:1101.0561 [hep-ph].

[284] D. Stump, J. Huston, J. Pumplin, W.-K. Tung, H. L. Lai, S. Kuhlmann, and J. F. Owens, "Inclusive jet production, parton distributions, and the search for new physics," *JHEP* **10** (2003) 046, arXiv:hep-ph/0303013 [hep-ph].

[285] M. Gluck, E. Reya, and A. Vogt, "Parton fragmentation into photons beyond the leading order," *Phys. Rev.* **D48** (1993) 116. [Erratum: Phys. Rev.D51,1427(1995)].

[286] L. Bourhis, M. Fontannaz, and J. P. Guillet, "Quarks and gluon fragmentation functions into photons," *Eur. Phys. J.* **C2** (1998) 529–537, arXiv:hep-ph/9704447 [hep-ph].

[287] M. Klasen, C. Klein-Bösing, and H. Poppenborg, "Prompt photon production and photon-jet correlations at the LHC," *JHEP* **03** (2018) 081, arXiv:1709.04154 [hep-ph].

[288] **NNPDF** Collaboration, R. D. Ball, V. Bertone, S. Carrazza, L. Del Debbio, S. Forte, A. Guffanti, N. P. Hartland, and J. Rojo, "Parton distributions with QED corrections," *Nucl. Phys.* **B877** (2013) 290–320, arXiv:1308.0598 [hep-ph].

List of Scientific Contributions

- Currently (8.8.2018) 147 publications as a member of the ALICE Collaboration, see https://inspirehep.net/search?ln=en&p=Daniel+Mühlheim for the full list of publications
- List of publications subject of this thesis (or closely related)
  - ▷ with major contributions to data analysis/paper writing:
    1) *"π^0 and η meson production in proton-proton collisions at $\sqrt{s} = 8$ TeV"*[4, 5]
    2) *"Direct photon production at low transverse momentum in proton-proton collisions at $\sqrt{s} = 2.76$ and 8 TeV"*[6, 7]
  - ▷ with analysis contributions to the related EMCal and PCM-EMCal measurements:
    3) *"Production of π^0 and η mesons up to high transverse momentum in pp collisions at 2.76 TeV"*[8]
    4) *"Neutral pion and η meson production in p-Pb collisions at $\sqrt{s_{NN}} = 5.02$ TeV"*[9]
- Contributions to conferences and seminars: talks & posters
  - ▷ 09/2014, ALICE Week (Primošten, Croatia): *"TRD - Supermodule Assembly and Schedule Towards Run2"*
  - ▷ 03/2015, DPG-Frühjahrstagung (Heidelberg): *"Tagging Neutral Mesons using Photons from Conversions and Calorimeters in ALICE"*
  - ▷ 03/2016, DPG-Frühjahrstagung (Darmstadt): *"Measurement of neutral mesons via combination of calorimeter and conversion photons in pp collisions with ALICE at the LHC"*
  - ▷ 09/2016, ALICE Germany Meeting (Altensteig-Warte): *"Neutral Meson Measurements in pp Collisions at 8 TeV with ALICE"*
  - ▷ 02/2017, Quark Matter 2017 (Chicago, USA): *"Poster: Neutral meson measurements in proton-proton collisions at 8 TeV with ALICE"*
  - ▷ 07/2017, Hausseminar (Münster): *"Measurement of neutral mesons and direct photons in pp collisions with ALICE"*
  - ▷ 09/2017, PANIC (Peking, China): *"Neutral Mesons and Direct Photons in ALICE"*
  - ▷ 09/2017, ALICE Germany Meeting (Buchenau): *"Neutral Mesons and Direct Photons in ALICE"*
  - ▷ 02/2018, DPG-Frühjahrstagung (Bochum): *"Measurements of Neutral Mesons and Direct Photons in pp collisions with ALICE"*
  - ▷ 05/2018, Quark Matter (Venice, Italy): *"Poster: Measurement of Neutral Mesons and Direct Photons in pp collisions with the ALICE EMCal detector at the LHC"*
  - ▷ 06/2018, GRK Student Seminar (Münster): *"Hadronization"*
- Since 03/2017: coordinator of the Photon Conversion Group (PCG), a subgroup within the physics working group related to photons and neutral mesons, PWG-GA, in ALICE
- Since 04/2014: mediator of educational particle physics masterclasses offered for school classes within the Netzwerk Teilchenwelt: http://www.teilchenwelt.de/

Lebenslauf

Name:	Daniel Mühlheim
Geburtsdatum:	27.04.1988
Geburtsort:	Gießen
Staatsangehörigkeit:	deutsch
Eltern:	Arnold Mühlheim Gabriele Mühlheim, geb. Juretzka
Schulausbildung	
08/1994 - 07/1998	Grundschule Krofdorf-Gleiberg
08/1998 - 07/2004	Wettenbergschule
08/2004 - 06/2007	Herdergymnasium
06/2007	Allgemeine Hochschulreife
Wehr- oder Zivildienst	
01/2007 - 01/2012	Freigestellter Helfer im Katastrophenschutz bei der Feuerwehr Wettenberg
Studium	
09/2007 - 08/2010	Studium der Physik an der Justus-Liebig-Universität in Gießen
08/2010	Bachelor of Science
09/2010 - 07/2011	Auslandsjahr an der University of Washington in Seattle, USA (DAAD Austauschprogramm)
08/2011 - 08/2013	Studium der Physik an der Justus-Liebig-Universität in Gießen
08/2013	Master of Science
Seit 09/2013	Promotionsstudium an der Westfälischen Wilhelms-Universität Münster

Münster, den 8.8.2018

Danksagung

Zu guter Letzt möchte ich mich gerne bei allen bedanken, die zum Gelingen dieser Arbeit beigetragen haben.

Besonders danke ich in diesem Zusammenhang zunächst Prof. Dr. Johannes Wessels für die Möglichkeit diese Arbeit anfertigen zu können und damit ein für mich völlig neues Experiment samt Arbeitsgruppe kennenzulernen. Weiterhin gilt besonderer Dank an PD Dr. Christian Klein-Bösing für die hervorragende Betreuung und die immerzu hilfreichen Ratschläge. Darüber hinaus bedanke ich mich für die vielfältigen Möglichkeiten und Gelegenheiten, meine Forschungsinteressen in Münster wie auch am CERN sowie auf diversen Konferenzen zu verfolgen und dabei vieles Neues kennenzulernen.

Ein großes Dankeschön gilt Friederike Bock für die geduldige Hilfe zum Einstieg sowie die effektive und produktive Zusammenarbeit über die ganzen Jahre, die mir immer viel Freude bereitet hat und bei der ich immer viel über die technischen Seiten als auch über die Physik gelernt habe. In dem Zusammenhang danke ich auch Nicolas Schmidt für die gute Zusammenarbeit, auch besonders im Hinblick auf die beiden Publikationen und den damit verbundenen Analysen.

Zudem bedanke ich mich bei der gesamten Photon Conversion Group wie auch der PWG-GA für die kritischen Fragen, konstruktiven Diskussionen und hilfreichen Anmerkungen. Ebenso möchte ich allen danken, die an den Publikationen mitgewirkt haben - sei es beim Verfassen, Korrektur lesen oder kritischem Hinterfragen der Methoden. Dafür gilt auch ein Dank den jeweiligen Paper Committees.

Einen besonderen Dank möchte ich der gesamten Arbeitsgruppe für das gute Arbeitsklima aussprechen sowie der Mittags- und Kaffeerunde für die unterhaltsamen Pausen, um auch mal auf andere Gedanken zu kommen. Des Weiteren bedanke ich mich bei all meinen Bürokollegen, die sich bei Problemen oder Fragen immer als erste Ansprechpartner erwiesen haben und dafür auch jederzeit ein offenes Ohr hatten. Vielen Dank auch an alle, die diese Arbeit - oder Teile davon - Korrektur gelesen haben und mir viele hilfreiche Hinweise gegeben haben.

Schließlich gilt ein großes Dankeschön an meine Familie, insbesondere meinen Eltern sowie meiner Frau für die stetige Unterstützung sowie der schier unerschöpflichen Verständnis für meine Interessen.